EXPERIMENTAL REFERENCE STRESS TECHNIQUES FOR THE PREDICTION OF CREEP DEFORMATIONS USING LEAD ALLOY MODELS

by

T. H. Hyde

Thesis submitted to the University of Nottingham for the degree of Doctor of Philosophy, February 1976

SUMMARY

It is necessary at the design stage to predict the creep behaviour of components and structures operating at high temperature. The direct calculation of the creep behaviour requires extensive material data for the long service lives of the components and engineering methods are needed to minimise the amount of data needed. This can be achieved in some cases by use of the so called Reference stress method and the objective of this work was the experimental prediction of the creep deformation of some components using developments of this idea. It has been achieved by the determination of Reference stresses from accelerated room temperature creep tests of lead alloy models.

Reference stresses, which characterise the creep response of components in relation to uniaxial tests, have previously been determined by calculation. Reference stresses determined by the new experimental methods have been compared with analytical predictions for beams in pure bending, cantilevers, thin cylinders and thin spheres under internal pressure. Acceptable agreement was found for the Reference stresses and consequent predictions of creep deformations. The method has also been used successfully to predict creep strains in a cylindrical pressure vessel with a hemispherical end.

The methods of chill-casting models from a lead-antimony-arsenic alloy have been improved and the material has been calibrated by constant and stepped load, uniaxial and biaxial (combined pressure and torsion of thin cylinders) tests. The creep strains cannot be characterised by separate stress and time functions; a strain hardening law best describes its stepped load response; the von-Mises criterion gives accurate predictions of creep strains in the tension-compression quadrant but underestimates the creep strains in the tension-tension quadrant.

CONTENTS

10. Summary of conclusions

Acknowledgements

References

Appendix 1 Beams in Pure Bending

Appendix 2 2-Bar structure

Appendix 3 Cantilevers With Transverse End Loads

Appendix 4 Internal pressurisation of long closed end cylinders

Appendix 5 Torsion of Cylinders

Appendix 6 Internal pressurisation of spheres

Notation

A, B, C	constants
B(n)	a function of n
E	Youngs Modulus
F( ), L( )	functions
J_1, J_2'	first stress invariant and second deviatoric stress invariant respectively
K	a constant
P	load
Q	activation energy
R	Boltzmanns constant
T	temperature
X	a constant
b	a constant
f( ), g( )	functions
k	a constant
m	time index
n	creep stress index
p	pressure
q	initial stress index
t	time
$\Gamma(t)$, $\Gamma(\sigma,t)$	functions of time, and stress and time respectively
$\alpha, \beta, \gamma, \xi, \chi$	constants
δ_{ij}	Kronecker delta
ε	strain
ν	Poissons ratio
σ	stress
τ	shear stress
ϕ	component deformation
ω	Kachanovs damage parameter

other symbols are described where used

Subscripts

A	Araldite
a	axial
c	creep
i	initial
L	lead
m	melting point
mod	model
nom	nominal
O	normalised
prot	prototype
R	rupture
r	radial
red	redistribution
sc	stationary creep
ss	stationary state
TR	tresca
ult	ultimate
VM	von Mises
Y	yield
θ	hoop

Superscripts

*	effective
-	reference
'	particular value

CHAPTER 1

1. INTRODUCTION

Failure of engineering components may be due to either excessive deformations or rupture. Therefore, design codes are usually based upon a combination of both these criteria. When a component is operating at an elevated temperature, creep deformations may become significant and a knowledge of the magnitude of these will be necessary.

Creep deformations can be obtained from measurements of a prototype under the operating conditions. However, components such as those used in generating plants are very expensive and are expected to last for 20 years or more, which makes this type of test unacceptable. Usually, some uniaxial creep data is available for the component material from which a constituitive equation may be obtained. This constituitive equation, together with some assumptions about the multiaxial behaviour of the material may be used to obtain either analytical or numerical solutions to the creep problem.

An alternative approach to the solution of creep problems is the Reference Stress method. Ideally a Reference Stress, which is associated with the deformation (strain or displacement) at a point in a component*, is a quantity which characterises the dependence of the deformation at the point on the material properties. Although the Reference Stress itself should be independent of the component material behaviour, the deformation at the point in the component can be predicted from the data of a single uniaxial test of the component material in its working environment. A single solution for the deformation of the point in the component when subjected to loads proportional to the working loads and the uniaxial data at the Reference Stress in the environment appropriate to the test are also required. The method is powerful

---

* It is important to state that, in general, the Reference Stresses differ for different points in the component and for different modes of deformation at each point. This is proved in Appendix 3 for a cantilever.

because this single solution for the component deformation may be for a relatively simple case such as the initial elastic deformation. This solution can then be used to predict the deformation of the component when subjected to a load history involving plasticity and creep. Direct solutions for such load histories may be difficult to obtain and would require an extensive knowledge of the component material behaviour in the operating environment.

It is doubtful if ideal Reference Stresses, as described above, exist for real components and materials subject to linear and non-linear elasticity, plasticity, creep, stress redistribution and all forms of load variation. However, for many real situations, approximate Reference Stresses, which are insensitive to material behaviour laws rather than independent of them, can be determined. These approximate Reference Stresses allow the prediction of deformations to an acceptable degree of accuracy.

As Reference Stresses are insensitive to the material behaviour laws, they can be determined analytically or numerically by using constituitive equations which are analytically convenient but do not necessarily describe the material behaviour accurately. Analytical solutions have been published for a few simple components such as beams, plates and tubes. Reference Stresses may be determined numerically for any component, but for many engineering components the calculation is a formidable task due to their complex shapes.

The concepts and application of experimental methods for the determination of Reference Stresses are described. The methods require the measurement of the deformations of models of the component and the experimental determination of the uniaxial properties of the model material. Again because of the insensitivity of Reference Stresses to material behaviour laws, it is possible to use model materials which do not necessarily behave in the same way as the actual component

material. Model materials which are experimentally convenient because they creep at room temperature have been used. The accuracy of this experimental method is assessed by comparing values of Reference Stress determined experimentally from some lead alloy models of some simple components with values obtained analytically. An Sb-As- lead alloy was chosen as the model material because reasonable creep strains may be obtained under small loads at room temperature.

The simple components for which experimental Reference Stresses were obtained were beams, cantilevers and pressure vessels. These components were made from castings produced in the laboratory.

Chapters 2 and 3 give the general theoretical background and the theory on which the experimental Reference Stress method is based. In Chapter 4, the development and results of the production of the lead alloy castings is described. Chapters 5 and 7 describe the uniaxial and biaxial calibration of the lead alloy. Tests on simple components (beams and cantilevers) are described in Chapter 6 and tests on more complex components (pressure vessels) are described in Chapter 8. These two chapters also show the method of obtaining experimental Reference Stresses.

CHAPTER 2

2. GENERAL THEORETICAL BACKGROUND AND LITERATURE SURVEY

2.1 Introduction

Creep data is usually obtained by measuring the principal strains in statically determinate structures with uniform stress fields (e.g. tensile loading of bars or torsion, internal pressure and axial loading of thin cylinders).

When subjected to a uniform stress field, most metals at temperatures above about 0.5 T_m (the melting temperature) will deform in a manner similar to that shown in Fig. 2.1.0A is the initial strain obtained upon loading and may include both elastic and plastic components, AB is the primary region of creep during which the creep strain rate is reducing, BC is the secondary region of creep during which the creep strain rate is constant and CD is the tertiary region of creep in which the creep strain rate is increasing until rupture at D.

The shape of the basic creep curve (Fig.2.1) and any variations in the shape of this creep curve for a particular material depends on the creep mechanisms which are operating. Rotherham (1), Hoffmann (2) and Finnie and Heller (3) give accounts of the creep mechanisms associated with creep of various metals. Creep depends upon the movement of atoms within grains and grain boundaries. The extent to which either the grains or the grain boundaries contribute to the creep strains depends upon the material under consideration and its operating temperature. Since contributions to creep are due to movement of atoms within grains and grain boundaries, creep deformations may be greatly dependent upon grain size.

The mechanisms involved in creep deformation and eventual rupture include glide of close-packed planes in the close-packed direction, movement of dislocations and sliding of grain boundaries. Under the

influence of stress and high temperature, the grain size and grain structure of some alloys may change (e.g. precipitation, recrystallisation or fragmentation may occur) which may cause the creep resistance of a material to change.

Attempts have been made to relate creep deformations and creep rupture to the micro structural properties of materials, but even in the primary creep range where the creep mechanisms are usually considered to be similar to those occurring during plastic deformation, the problems are enormous. It is for this reason that engineers prefer to use macroscopic creep data obtained by measurements of the gross deformations of specimens subjected to uniform stress fields.

2.2 Constant load uniaxial creep and creep rupture

The most commonly used tests for obtaining material data are the constant load, constant temperature, uniaxial tensile, creep and creep rupture tests. For small deformation, these tests may be regarded as constant stress tests. The data from the constant load creep tests is most conveniently presented as initial strain (ε_i) against stress (σ) and creep strain (ε_c) against time (t) with stress and temperatures as parameters.

Eventually, the specimen may rupture and the rupture data is conveniently presented as stress against time (or log(time)) to rupture (t_R) and ductility (% elongation and % reduction in area) against time (or log(time)) to rupture. Typical examples of these types of plots of tensile and creep data are given in Chapter 5 (Figs.5.4, 5.7 and 5.23(a)). In these raw data plots, all of the basic information is presented, from which any particular representation (such as isochronous stress-strain curves) may be easily produced.

However, most of the material data for steels is obtained from

interrupted creep tests and therefore, the initial and creep strains cannot be separated. With the use of uniaxial tensile data, an estimate of the initial strains can be made but when the initial plastic strains are large, this method must be regarded as being very approximate.

For the purpose of obtaining analytical solutions for stresses and deformations within a structure undergoing creep and to estimate rupture times, it is necessary to represent the constant load uniaxial data by creep and creep rupture laws.

2.2.1 Primary and secondary creep laws

For creep in the primary and secondary regions, the most general form of creep law is

$$\varepsilon_c = f(\sigma, T, t) \qquad (2.1)$$

which is usually approximated (for analytical convenience) to a commutative law, i.e.

$$\varepsilon_c = f_1(\sigma)\, f_2(T)\, f_3(t) \qquad (2.2)$$

Many forms have been suggested for these functions and Finnie and Heller (3), Hult (4) and Penny and Marriott (5) have all reviewed the most commonly used functions. It must be noted that a law of this form cannot generally be used for the tertiary regions of creep.

The simplest and therefore the most widely used form for the stress function is that due to Norton (see ref. 5), i.e.

$$f_1(\sigma) \alpha \sigma^n \qquad (2.3a)$$

which is a good approximation over small stress ranges and for some materials over wide stress ranges. However, n is usually found to increase with stress. For this reason and because creep may be considered as a solid state rate process, a more acceptable form for

the stress function is

$$f_1(\sigma)\alpha \sinh\left[\frac{\sigma}{C}\right] \tag{2.3b}$$

The time function is usually taken to be

$$f_3(t)\alpha t^m + bt \tag{2.4}$$

for the primary and secondary regions of creep and when b = 0, the time function suggested by Bailey (see ref. 5) is obtained. It will be shown later that for stationary creep analysis, the time function does not need to be defined explicitly and a simple creep law of the form

$$\varepsilon_c = f_1(\sigma)\,\Gamma(t) \tag{2.5}$$

is assumed.

Therefore, at constant temperature, the most widely used creep law is the Norton-Bailey law

$$\varepsilon_c = A\sigma^n t^m \tag{2.6}$$

but as has already been stated, this type of law is of most value over limited ranges of stress and time. The constants A, n and m in equation 2.6 are temperature dependent. However, over small temperature ranges n and m are practically constant.

The temperature dependence of creep has been investigated by Dorn (6) who suggests that the temperature function should be of the form

$$f_2(T) = \exp(-Q/RT) \tag{2.7}$$

where Q is the activation energy and R is Boltzmann's constant. Dorn also suggests that the time and temperature functions are not separable and that the creep strain should be represented by

$$\varepsilon_c = f_1(\sigma)\, f_4(t \exp(-Q/RT)) \tag{2.8}$$

If simple power functions are considered, this again falls into line with the Norton-Bailey creep equation, i.e.

$$\varepsilon_c = B(\exp(-Q/RT))^m \sigma^n t^m \qquad (2.9)$$

Other temperature-time parameters such as the Larson-Miller parameter $T(C + \log t_R)$, ref. 7, have been suggested but none of the parameters is consistently good over large temperature ranges.

2.2.2 Creep laws which include tertiary creep

Graham and Walles (8), Johnson, Henderson and Khan (9) and Kachanov (10) have investigated the possibility of representing creep data into the tertiary range by a single expression. Graham and Walles suggest that an expression of the form

$$\varepsilon_c = c_1\sigma^{n_1} t^{1/3} + c_2\sigma^{n_2} t + (c_3\sigma^{n_3} + c_4\sigma^{n_4})t^3 \qquad (2.10)$$

may be used to accurately describe creep data up to and including tertiary creep. This is hardly surprising when it is considered that there are eight material constants incorporated. However, although equations of this type may accurately represent the material data it is practically impossible to use them to obtain analytical solutions to structural problems. Similarly, the expressions suggested by Johnson et al (9)

$$\varepsilon_c = At + Bt^m + Ce^{Kt} \qquad (2.11)$$

(where A, B, C and K are dependent on σ and m is a constant) are difficult to use analytically.

Kachanov (10) introduced a damage parameter (ω) into the creep equation, where ω may be interpreted as the fraction of the cross-sectional area which is currently occupied by cracks. Therefore, this method is particularly applicable to brittle materials. Kachanov proposed that

$$\frac{d\varepsilon_c}{dt} = f(\sigma, \omega) \qquad (2.12a)$$

and $\frac{d\omega}{dt} = g(\sigma, \omega)$ (2.12b)

where f and g are usually taken to be simple power functions

i.e. $\frac{d\varepsilon_c}{dt} = A \left[\frac{\sigma}{1-\omega}\right]^n$ (2.13a)

$\frac{d\omega}{dt} = B \left[\frac{\sigma}{1-\omega}\right]^\nu$ (2.13b)

Using this formulation, Hayhurst et al (11) have obtained accurate predictions of the rupture life for some simple components.

2.2.3 Creep rupture

Similar types of temperature-time parameters to those suggested by Dorn (Equation 2.8) have been fitted to creep rupture data, but these have been more for the purpose of extrapolation than for use in structural analysis. Rather than use analytical methods for obtaining rupture times, it is usual to obtain a design stress for a given structure under its operating conditions and to compare this with the raw data (e.g. Fig. 5.23(a)). From this data and the design stress, the rupture time and ductility may be obtained. If the time is greater than the required life of the component and if the ductility is high enough at the time of rupture to ensure that the component will not rupture in areas with high initial stress concentrations, then the design should be safe. Because of the inevitable degree of approximation in a method of this sort, the design stress must include a high safety factor.

2.2.4 Correlation between creep and creep rupture

Murphy (12) has shown that there is a correlation between creep deformation and creep rupture which is valid over a range of values of times and temperatures and for different materials. Murphy has shown

that if the stress to cause rupture in a given time is plotted against the stress to reach a given percentage strain in the same time a linear relationship is obtained which incorporates different times, temperatures and materials, e.g. Murphy has shown that $\frac{1}{2}$Cr Mo V and $2\frac{1}{4}$Cr Mo steels fall on the same straight line for a number of different heat treatments, temperatures and times. From this simple relationship it is possible to estimate creep data for materials for which only creep rupture data is known.

2.3 Variable load uniaxial creep and creep rupture

Most engineering structures are statically indeterminate, therefore stress redistribution will occur during creep and, since structures seldom have constant loads applied to them, it is therefore necessary to have a knowledge of the effect of variable loading on creep and creep rupture. This behaviour of materials is most conveniently obtained from uniaxial stepped load tests, i.e. tests in which the load is changed after a certain amount of creep has occurred at a different load.

2.3.1 Effect of variable loading on creep

Many theories have been proposed for creep under variable load conditions, the simplest of which is the "total strain theory" in which the creep strain is assumed to be dependent upon the current stress and time as shown in Figs. 2.2(a) and 2.2(b). It can be seen that the variations in creep stain are very sensitive to changes in stress. On the other hand, the "time hardening theory" in which the creep strain rate is assumed to be dependent upon the current stress and time, the variations in creep strain are relatively insensitive to changes in stress as shown in Figs. 2.2(a) and 2.2(b). The sensitivity of changes in creep strain with stress predicted by the "strain hardening", "work hardening" and "hereditary" theories falls between that of the "total strain" and "time hardening" theories.

The "strain hardening theory" predicts that the creep strain rate is dependent upon the current stress and plastic strain (figs. 2.2(a) and 2.2(b)). Although this theory is usually nearer to actual material behaviour than the "time hardening theory", it is more difficult to use and is therefore not used as often as the time hardening theory.

The "work hardening theory" which has been discussed by Rabotnov (13) assumes that the creep strain rate depends upon the current stress and plastic work. The creep strains predicted by the "work hardening theory" are more sensitive to changes in stress than those predicted by the "strain hardening theory" (Figs. 2.2(a) and 2.2(b)) which was found to be the case for some of the lead alloy specimens tested (Chapter 5). However, the predictions based upon these two theories are so similar that the simpler one (strain hardening) is adequate, particularly when it is considered that creep has a lot of scatter associated with it.

Graham and Walles (8) and Rabotnov (14) have suggested hereditary theories which are qualitatively capable of predicting reverse creep but are quantitatively inaccurate and are therefore not used for structural analysis.

2.3.2 Effect of variable loading on creep rupture

The most generally accepted variable load rupture criterion is the life fraction rule which assumes that at rupture

$$\sum_i \frac{t_i}{t_{R_i}} = 1 \qquad (2.14)$$

where t_i is the time for which a specimen is subjected to a stress which would cause rupture in time t_{R_i}. Experimental work by Johnson et al (9) confirms this.

Using Kachanov's formulations (i.e. equations 2.13(a) and 2.13(b)), together with the assumption that $\omega = 0$ at $t = 0$ and $\omega = 1$ at $t = t_R$, the rupture time of a uniaxial specimen is given by

$$1 = \int_0^{t_R} B(1+V)(\sigma(t))^V \, dt \qquad (2.15)$$

For the case of constant loading equation 2.15 reduces to

$$t_R = \frac{1}{B(1+V)\sigma^V} \qquad (2.16)$$

2.4 Multiaxial creep and creep rupture

2.4.1 Multiaxial creep laws

When formulating multiaxial creep laws it is usually assumed that

a) creep is an isotropic process,

b) creep is a constant volume process (i.e. $(\varepsilon_{ii})_c = 0$),

c) the principal axes of current stresses and strain increments are coincident,

d) hydrostatic stress has no effect on creep,

e) effective stress and strain are related in the same way as uniaxial stress and strain (i.e. $\varepsilon_c^* = f_1(\sigma^*) f_2(T) f_3(t)$), where the effective stresses and strains are usually taken to be the same as those used in plasticity analysis,

f) the components of strain are dependent upon the deviatoric stresses.

Johnson et al (9) have shown that at low and moderate stresses, initial isotropy is preserved. However, at high stresses, pronounced anisotropy may be obtained which is associated with high initial plastic or creep strains. Johnson et al also state that their experimental work on thin cylinder biaxial specimens verifies the

assumptions of constant volume, coincidence of principal axes of stress and strain and that hydrostatic stress has no effect on creep. These results may not be directly applicable to structural analysis because only tensile-compressive combinations of stress are considered, whereas tensile-tensile stresses are more commonly found in engineering structures.

Following the methods developed for the predictions of plastic deformations the von Mises and Tresca yield criteria have been used in creep analysis and it is generally accepted that the von Mises yield criterion fits observations better than the Tresca yield criterion.

Using the von Mises yield criterion, the multiaxial constituitive equations corresponding to the uniaxial equation (2.5) are

$$\varepsilon_c^* = f_1(\sigma^*)\Gamma(t) \tag{2.17a}$$

$$(\varepsilon_{ij})_c = \frac{3}{2}\,\frac{f_1(\sigma^*)}{\sigma^*}\,S_{ij}\,\Gamma(t) \tag{2.17b}$$

where $S_{ij} = \sigma_{ij} - \frac{1}{3}\,\delta_{ij}\,\sigma_{kk}$ are the deviatoric stresses,

$\sigma^* = \sqrt{3\,S_{ij}\,S_{ij}/2}$ is the effective stress

and $\varepsilon^*_c = \sqrt{2(\varepsilon_{ij})_c\,(\varepsilon_{ij})_c/3}$

Similarly, using the Tresca yield criterion, the constituitive equations are

$$\varepsilon_c^* = \frac{3}{2}\,f_1(\sigma^*)\Gamma(t) \tag{2.18a}$$

$$(\varepsilon_{ij})_c = \frac{3}{2}\,\frac{f_1(\sigma^*)}{\sigma^*}\,S_{ij}\,\Gamma(t) \tag{2.18b}$$

where $\sigma^* = \sigma_1 - \sigma_3$ is the effective stress ($\sigma_1 > \sigma_2 > \sigma_3$),

and $\varepsilon_c^* = \varepsilon_{c_1} - \varepsilon_{c_2}$ is the effective creep strain.

Although it is usually assumed that the von Mises formulation (Equations 2.17(a) and 2.17(b)) is the most acceptable form for the constituitive equations, Greenwood (15) and Dyson (16) have suggested that the hydrostatic component of stress and the maximum tensile stress also have an effect. Finnie (17) has shown this to be the case for aluminium and lead containing 6% Sb. The author's present work also shows this to be the case for lead containing 1.6% Sb and 0.16% As. This is contrary to the results of Johnson et al but as has already been stated, the results of Johnson et al only cover the combined tension-compression regions of creep.

2.4.2 Multiaxial creep rupture laws

Johnson et al (9) have investigated the biaxial creep rupture behaviour in the tension-compression quadrant for six materials. For materials which exhibit general and progressive crack propagation in the tertiary creep range, the criterion of fracture was found to be the maximum principal stress. Materials which fall into this category are copper at 250°C, Nimonic 75 at 650°C and 0.5% Mo steel at 550°C for which a creep rupture law may be written in the form

$$\log(t_R) = L(\sigma_1) \qquad (2.19)$$

where L was found to be a linear function of maximum tensile stress, σ_1.

For 0.2% C steel at 450°C, an aluminium alloy (RR59) at 150 and 200°C and a 2% Al magnesium alloy at 20°C, Johnson et al found that no cracking was microscopically visible until fracture occured and the criterion for fracture was found to be the von Mises effective stress.

Hayhurst (18) has shown that, although the rupture criteria presented by Johnson et al are accurate in the tension-compression quadrant, the same criteria may overestimate the rupture times in the tension-tension quadrant, particularly for the materials for which the maximum principal stress criterion is applicable. Hayhurst suggestsa creep rupture law of the form

$$t_R = A(\alpha\sigma_1 + \beta J_1 + \gamma J_2'^{\frac{1}{2}})^{-\chi} \qquad (2.20)$$

where σ_1 is the maximum tensile stress,

$$J_1 = \sigma_1 + \sigma_2 + \sigma_3$$

and $J_2' = \frac{1}{6}((\sigma_1 - \sigma_2)^2 + (\sigma_2 - \sigma_3)^2 + (\sigma_3 - \sigma_1)^2)$.

The maximum principal stress criterion is obtained when $\alpha = 1$ and $\beta = \gamma = 0$, the maximum octahedral shear stress criterion is obtained when $\gamma = 1$ and $\alpha = \beta = 0$ and a maximum hydrostatic stress criterion is obtained when $\beta = 1$ and $\alpha = \gamma = 0$.

By putting $\Sigma_i = \sigma_i/\sigma_o$ and $T' = t/t_{o_R}$, where t_{o_R} is the time to rupture in a uniaxial specimen at stress σ_o, Hayhurst normalises equation (2.20) and for biaxial stress systems with $\Sigma_2/\Sigma_1 = \xi$ and $\Sigma_3 = 0$, the normalised equation is

$$T' = (\alpha + \beta(\xi^2 + 2\xi + 1)^{\frac{1}{2}} + \gamma(\xi^2 - \xi + 1)^{\frac{1}{2}})^{-\chi}\Sigma_1^{-\chi} \qquad (2.21)$$

where $\alpha + \beta + \gamma = 1$.

With equation 2.21, which contains only four material constants, Hayhurst has obtained good correlation with experimental results.

2.5 Component Behaviour

When a component which is operating in the creep range is loaded, initial stresses and deformation will occur which may be elastic or elastic-plastic, depending upon the magnitude of the loading and the yield stress of the material. After the initial deformation, creep will begin and the stresses will redistribute. If the material creep behaviour is governed by a law with separable stress and time functions, which implies that the creep curves are the same shape for all stresses and that the transitions from primary to secondary creep and from secondary to tertiary creep depend only upon time and not upon stress, then a stationary state will eventually be reached. In the stationary state, creep will occur without any change in the stress distribution. However, the transition from primary to secondary creep and from secondary to tertiary creep is not independent of stress, therefore a true stationary state will not exist. In the primary and secondary regions of creep, the fact that the transition is stress dependent is unlikely to greatly effect the stress distribution and an approximately stationary state stress distribution will develop.

Eventually, some part of the component will enter the tertiary range of creep and the strain in this part will be restrained by other parts of the component causing further stress redistribution. As more and more parts of the structure enter the tertiary creep range, some part will become so weakened that rupture will occur. For a brittle material, the tertiary region of creep may be very small or may not exist at all, in which case, cracks will develop with subsequent stress redistribution, particularly in the region of the cracks where stress concentrations will occur. These cracks will propagate and cause eventual failure.

2.5.1 'Exact' theoretical creep solutions

It is possible to use "raw" uniaxial data (or at least interpolated "raw" data) in conjunction with some assumptions about the multi-axial behaviour of a material to obtain solutions to creep problems with initial elastic and plastic deformations. However, most 'exact' solutions have been obtained for structures with initial elastic stresses and strains using either "time hardening" or "strain hardening" uniaxial creep laws. The creep laws are assumed to have simple separable power functions of stress and time and the von Mises yield criterion and the Prandtl-Reuss relations usually assumed, i.e. the constituitive equations, are usually assumed to be

$$\varepsilon_{ij} = c_{ij\,kl}\sigma_{kl} + \frac{3}{2} A \sigma^{*n-1} s_{ij}\, t^{m} \qquad (2.22)$$

Using this constituitive equation in conjunction with both "time hardening" and "strain hardening" laws, Marriott and Leckie (19) have computed the variations of stress and strain with time for a rectangular beam in pure bending, a thick cylinder under internal pressure, a rotating disc and an encastré beam with a uniformly distributed load. These results show that, for steadily loaded structures, the "time hardening" and "strain hardening" predictions are very similar and the stationary state stress distributions and deformation rates are identical. A similar method has been used by Frederick and Lewis (20) to compute the primary deformations and variations of stresses in beams of complicated and tapered cross-sections for time hardening materials. Penny and Marriott (5) and Sim (21),(22) present similar results obtained by this method.

For the relatively simple components discussed so far, a method based upon the simple "strength of materials" approach has been used. However, for more complicated structures, it is not possible to use

this method. Parkes and Webster (23) have computed the stress and strain variations during creep in a thin shell axisymmetric pressure vessel and a split turbine casing by the finite element method. Their results which are based upon a "strain hardening" law show that, although the highest effective stresses reduce during redistribution, the hoop stresses at these positions increase during redistribution.

The 'exact' method requires the development of complicated computer programmes and expensive computing time for all but the simplest of problems. In the early stages of design, such expense may not be justified and simpler 'approximate' methods of analysis have advantages.

2.5.2 "Approximate" theoretical creep solutions for steadily loaded components

For materials which have separable stress and time functions, the deformation at a point in a component under steady load may be exactly represented by

$$\phi = \phi_i + \phi_c = \phi_i + (\phi_{sc} + \delta\phi) \qquad (2.23)$$

where ϕ is a general deformation parameter (i.e. ϕ may be a component of displacement, rotation, curvature or strain). ϕ_i is the initial deformation upon loading and ϕ_c is the subsequent time dependent deformation which may be conveniently split up into a stationary creep component ϕ_{sc} and a component $\delta\phi$ which is a consequence of the redistribution of stress within the component. The components of total deformation are illustrated in the plot of deformation against the time function, $\Gamma(t)$, in Fig. 2.3. The total deformation is asymptotic to a line which has the same gradient as the stationary creep deformation ϕ_{sc}. $\Delta\phi$ is the magnitude of $\delta\phi$ when the stationary state has been reached. The stationary state deformation is usually obtained from

either closed form analytical solutions or from the stationary state solution obtained from an 'exact' analysis. This stationary state deformation is added to the initial deformation to give an approximate solution to the creep problem, the degree of approximation being governed by the magnitude of $\Delta\phi$ and the service life of the component.

These solutions show that the stationary state creep deformation at a particular point may be expressed in the form

$$\dot{\phi}_{sc} \doteq (\sigma_{nom})^n \, F_1(n) \, F_2(\text{dimensions}) \, \dot{\Gamma}(t) \qquad (2.24)$$

where F_1 and F_2 are functions of stress index n and dimensions respectively and σ_{nom} is a nominal stress which is proportional to the magnitude of the loading.

To illustrate the form of the stationary state solutions, the stationary state creep curvature K_{sc} of a beam of depth d and breadth b in pure bending (see Appendix 1), is given by

$$K_{sc} = \left[\frac{M}{bd^2}\right]^n \left[\frac{2n+1}{n}\right]^n \frac{2^{n+1}}{d} \, \dot{\Gamma}(t) \qquad (2.25)$$

i.e. $F_1(n) = 2^{n+1} \left[\frac{2n+1}{n}\right]^n$

$F_2(\text{dimensions}) = 1/d$

and $\sigma_{nom} = \frac{M}{bd^2}$

In many applications the deformation due to stress redistribution $\Delta\phi$, may be neglected. At "long time" $\Delta\phi$ is negligible compared with the total deformation and Penny and Marriott (5) and Marriott (24), (25) have shown that $\Delta\phi$ is also negligible for "short times" for n values less than 9, which includes most practical materials. Marriott (24), (25) and Leckie and Martin (26) have shown how bounds on $\Delta\phi$ may be obtained. These bounds on $\Delta\phi$ have been shown to be proportional

to the difference between the strain energy at the stationary state and at the initial elastic state. The constant of proportionality is dependent upon the stress index and the type of hardening law assumed. Ponter and Leckie (27), (28) have extended these ideas to include bodies which creep in the plastic range.

As already stated, Marriott (24), (25) and Leckie and Martin (26) have shown that at "long times" the effect of redistribution may be ignored. Therefore, if stationary creep analysis is to be used an estimate of the redistribution time t_{red} (which may be regarded as a "long time" for the structure) must be made. Calladine (29) has shown how the redistribution time may be estimated from a knowledge of the maximum stress in the structure, the initial strains and the creep properties of the material. Calladine shows that

$$t_{red} \doteq \frac{2.3}{n} t^* \qquad (2.26)$$

where t_{red} is the time taken for $(\hat{\sigma} - \hat{\sigma}_{SS})$ to reach 10% of its initial value, n is the stress index in the creep law and t* is the time taken for the creep strain to become equal to the initial elastic strain in a uniaxial specimen subjected to a stress of $\hat{\sigma}_{SS}$ (the maximum stationary state stress in the structure).

For some creeping structures for which it is not possible to obtain closed form analytical solutions, Hoff (30) has pointed out that a creeping structure may be considered as an analogous non-linear elastic structure by replacing strain rates and displacement rates by strains and displacement. This analogy allows the elastic energy theorems to be used to solve creep problems. Calladine and Drucker (31), (32) have shown how the stationary creep deformation of a structure may be bounded by using the elastic and plastic solutions to the problem and Calladine (33) has also shown how a close approximation

to stationary state stress distributions may be obtained by interpolating the elastic and plastic solutions. Martin (34) and Palmer (35) show how upper and lower bounds on stationary creep deformation may be obtained. Both of these methods, which are based upon energy dissipation rates, have the advantage of being able to optimise the bounds.

All of the methods described so far require the creep law to be of the form $\varepsilon_c = \sigma^n \Gamma(t)$ which in turn requires an extensive program of creep testing and curve fitting to creep data. Since these creep tests last for several years at elevated temperature, the cost of such a test program is very great. A method has been developed which reduces to an absolute minimum the amount of creep testing required and therefore reduces the cost of testing to a minimum. This method is called the "Reference Stress" method.

2.5.3 The theoretical Reference Stress method

In order to pursue the Reference Stress concept, it is convenient to normalise the nominal stress, σ_{nom}, in the general stationary creep solution (equaltion 2.24) by introducing an arbitrary stress, σ_o. From equation 2.5,

$$\Gamma(t) = \frac{\varepsilon_{co}}{\sigma_o^n} \qquad (2.27)$$

where ε_{co} is the creep strain obtained from a uniaxial specimen subjected to stress σ_o.

By substitution of equation (2.27) into equation (2.24), the normalised stationary creep solution is obtained, i.e.

$$\phi_{sc} = \left[\frac{\sigma_{nom}}{\sigma_o}\right]^n F_1(n)\, F_2(\text{dimensions})\, \varepsilon_{co} \qquad (2.28a)$$

$$= B(n)\, F_2\,(\text{dimensions})\, \varepsilon_{co} \qquad (2.28b)$$

Anderson et al (36) investigated the stationary creep behaviour of uniformly loaded beams and found that by a suitable choice of σ_o, the function $B(n) = ((\sigma_{nom})/\sigma_o)^n F_1(n))$ is made weakly dependent upon n; this value of σ_o is called the Reference Stress $\bar{\sigma}_o$; i.e. when $\sigma_o = \bar{\sigma}_o$, $B(n) = \bar{B}$ which is approximately constant over a range of values of n. Anderson et al chose the value of $\bar{\sigma}_o$ by inspection.

Mackenzie (37) obtained Reference Stresses for beams, circular plates, thin cylinders and thick cylinders by formalising the approach used by Anderson et al. The formalisation was based on the fact that if B(n) is independent of n, then the Reference Stress can be obtained by substituting any two values of n into B(n) and equating them. One of the values chosen by Mackenzie was n = 1, the other value, n', was chosen to suit the particular application. Equating the expressions for $\bar{B}$ obtained for n = 1 and n = n' gives

$$\bar{B} = \left[\frac{\sigma_{nom}}{\bar{\sigma}_o}\right] F_1(1) = \left[\frac{\sigma_{nom}}{\bar{\sigma}_o}\right]^{n'} F_1(n') \qquad (2.29)$$

from which

$$\bar{\sigma}_o = \sigma_{nom} \left[\frac{F_1(n')}{F_1(1)}\right]^{\frac{1}{n'-1}} \qquad (2.30)$$

Substituting $\bar{\sigma}_o$ into equation (2.28) gives

$$\phi_{sc} = \bar{B} \; F_2(\text{dimensions}) \; \bar{\varepsilon}_{co} \qquad (2.31)$$

where $\bar{\varepsilon}_{co}$ is the uniaxial creep strain of the material at the Reference Stress $\bar{\sigma}_o$, which is obtained from equation (2.30). The function $\bar{B}$ given by equation (2.29), is weakly dependent on the stress index of the constituitive equation (2.5) and is thus insensitive, to some extent, to the material behaviour laws. F_1 in equations (2.29) and(2.30)

and F_2 in equation (2.31) are determined from the expressions for the stationary creep deformation.

To illustrate the method, the beam in pure bending will again be considered. Normalising equation (2.25) gives

$$K_{sc} = \left[\frac{M}{\sigma_o bd^2}\right]^n \left[\frac{2n+1}{n}\right]^n \frac{2^{n+1}}{d} \varepsilon_{co} \qquad (2.32)$$

Using equations (2.29) and (2.30), $\bar{B}$ and $\bar{\sigma}_o$ are obtained, i.e.

$$\bar{\sigma}_o = \left[\left[\frac{2n'+1}{n'}\right] \frac{2^{n'+1}}{12}\right]^{\frac{1}{n'-1}} \frac{M}{bd^2} = \frac{1}{\alpha} \frac{M}{bd^2} \qquad (2.33a)$$

$$\text{and } \bar{B} = 12 \left[\left[\frac{n'}{2n'+1}\right] \frac{12}{2^{n'+1}}\right]^{\frac{1}{n'-1}} = 12\alpha \qquad (2.33b)$$

Therefore,

$$K_{sc} = 12\alpha \frac{\varepsilon_{co}}{d} \qquad (2.34)$$

and for n = 1.1 to 7, α = 0.233 to 0.247.

Equation 2.34 illustrates the power of the Reference Stress approach in so far as it expresses the stationary creep deformation in terms of the uniaxial data for a single value of stress.

Johnsson (38) shows how the Reference Stress may be obtained more accurately for materials whose approximate stress index is known. He defines the Reference Stress as the value of σ_o which renders the rate of change of B(n), in the closed form creep solution, equation 2.28, stationary with respect to n for the appropriate value of n.

Sim (21), (22), (39), (40) has shown how Reference Stresses may be obtained for components for which closed form solutions cannot be found. Sim solves the creep problem with the aid of a digital computer

for small increments of time until the stationary state is reached. From the creep deformation rates, $d\phi_{sc}/d\sigma(t)$ is obtained at the stationary state for two values of n and a similar method to that applied by Mackenzie may be used to obtain the Reference Stress. He also obtains numerical solutions in the form of equation (2.31) which expresses the stationary creep deformation in terms of the uniaxial creep strain of the component material at the Reference Stress.

Marriott and Leckie (19) have shown that in certain cases the Reference Stress can be identified with the stress at a point in a structure. This point, known as the "skeletal point" is that point in a structure where the stress at the beginning and end of redistribution is the same. For the beam in pure bending previously considered (Appendix 1), the stress at the skeletal point is $4.06 \frac{M}{bd^2}$ (for a material with n = 5) which is the bending stress 0.338d from the neutral axis. This is an example where the Reference Stress may be associated with a point in the structure. However, the analysis of a simple two bar structure outlined in Appendix 2 is an example of a structure for which a Reference Stress exists but not a "skeletal point". Marriott and Leckie also show that the position of the "skeletal point" is the same whether the material is assumed to be time or strain hardening. This suggests that the Reference Stress obtained by Mackenzie's method may be applicable for the component whether the material is regarded as time or strain hardening. Fairbairn (41) has examined a number of stress functions and concluded that the skeletal point concept is applicable to some stress functions other than simple power relationships and hence is applicable to a wide range of engineering materials.

Penny and Marriott (5) report that Sim obtained an approximate value of the Reference Stress by using the similarity of the creep

solution for $n = \infty$ to the rigid-perfectly plastic solution. He states that

$$\bar{\sigma}_o \doteq \frac{P}{P_{ult}} \sigma_y \qquad (2.35)$$

where σ_y is the yield stress of the material, P the load and P_{ult} the collapse load of the component. This gives an easily obtainable value of the Reference Stress but it is not stated which position and to which deformation it refers to. Appendix 3 which outlines the analysis of a cantilever beam shows that for complex structures, each mode of deformation at each point in a structure has a different Reference Stress. The simple examples of the beam in pure bending and the two bar structure did not bring out this point because a single deformation totally characterises all other deformation of the structures, namely the curvature and the nett downward displacement respectively.

Intuitively, it is believed that the Reference Stress given by equation (2.35) may be an upper bound for the Reference Stresses for any deformation but it is particularly appropriate to those deformations which become infinite at the collapse load.

Penny and Marriott (5) show that the stationary state deformation may be related to the initial deformation through the relationship

$$\frac{\phi_{sc}}{\phi_i} = \frac{\bar{\varepsilon}_{co}}{\bar{\varepsilon}_{io}} \qquad (2.36)$$

where $\bar{\varepsilon}_{co}$, $\bar{\varepsilon}_{io}$ are the creep and initial strains respectively, obtained from a uniaxial test carried out at $\bar{\sigma}_o$. This equation may be used to predict stationary creep deformations from initial deformations and the uniaxial material data at the Reference Stress, but it will be shown (Chapter 3) that great care must be taken in the application of this equation.

Penny and Marriott (42) have used equation (2.36) in conjunction with (2.35) to predict the creep deformation of a pressure vessel.

2.5.4 Creep of components subjected to variable loading

As in the case of the creep analysis of steadily loaded structures, it is also possible to obtain 'exact' solutions to variable loading problems by solving the problem for small increments of time by means of a digital computer. Chubb (43) has used this type of method to compute the deformations and stresses in a tube operating in the plastic range to which both variable loads and temperatures are applied. However, in the early stages of design, this method may be unjustifiably expensive.

Frederick and Armstrong (44) have shown that the amount of computation required for structures undergoing cyclic loading may be greatly reduced because a cyclic state of stress develops after a small number of load cycles. Therefore, the computation need only be continued until the cyclic state is reached.

An alternative approach for components subjected to proportional load changes is to use the Reference Stress method which has been suggested by Penny and Marriott (5). Since the Reference Stress for a component is linearly dependent on the loading, then if the Reference Stress is taken through the same load history as the component, an approximate solution to the variable load problem may be obtained. In this way, the amount of creep testing is reduced to a minimum and the hardening law is automatically incorporated. Using the Reference Stress method in this manner also allows variable temperatures and environments to be included by merely taking the uniaxial specimen through the same history of temperature and environment. Sim (22) has shown the method to be valid by using it to predict the deformation of aluminium beams subjected to cyclic pure bending.

moments. Using Sim's approximate Reference Stress, Penny and Marriott (42) have obtained predictions for the deflection and strains of a pressure vessel under variable loading. The deflection and strains were predicted fairly accurately, but the value chosen for the yield stress of the material (σ_y) was somewhat arbitrary.

Sim (45) has shown that it is also possible to obtain Reference Stresses for structures subjected to thermal gradients. His analysis of spheres and cylinders under internal pressure and having radial temperature gradients show that a Reference Temperature may be obtained at which a uniaxial specimen must be tested at the Reference Stress. The results he obtained show that the Reference Temperature is equal to or slightly less than the average of the inside and outside wall temperatures.

2.5.5 Creep rupture of structures

As already mentioned, the normal method of obtaining the rupture time for a structure is to obtain a design stress based upon the stress distribution in the structure. A large safety factor is incorporated and Carlton et al (46) have discussed the need to estimate the amount of redistribution of stress which occurs and the time taken for redistribution to take place.

Martin and Leckie (47) have obtained lower bounds on creep rupture times for components made of a material which obeys equations 2.13(a) and 2.13(b) and for which damage is associated with only the maximum tensile stress. Their results for a thick cylinder under internal pressure show that a point exists at which the hoop stress remains constant even when a great deal of damage has occurred.

The rupture time for a uniaxial specimen at this value of hoop stress, is very close to the theoretically predicted rupture time which implies that the Reference Stress concepts may also be applicable for rupture properties.

Hayhurst et al (11) have obtained Reference Stresses to predict creep rupture for materials which rupture according to an effective shear stress criterion and for materials which rupture according to a maximum principal stress criterion. The Reference Stress for the effective shear stress criterion is the same as that obtained for the approximate Reference Stress to predict creep deformations, namely $\bar{\sigma}_{oR} = (P/P_{ult})\sigma_y$. Reference Stresses were obtained for the creep rupture of circular torsion bars and circular notched tension bars. The prediction of rupture times based upon these Reference Stresses compare favourably with experimental evidence. Penny and Marriott (42) have also used the approximate Reference Stress $((P/P_{ult})\sigma_y)$ to predict the rupture time of an aluminium pressure vessel and obtained accurate predictions.

Goodall and Cockroft (48) have also obtained bounds on the life of structures. The lower bound is taken as the time for the first point in the structure to enter the tertiary creep range. This is likely to be very inaccurate except for brittle materials. The upper bound on the rupture time is obtained when the average stress over a certain period of time (t) lies on the failure surface appertaining to that time (t). Although the physical basis of this upper bound is not fully understood, the application of the bounds by Goodall (49) show that the method gives close bounds which are similar to those used by Hayhurst et al (11) and Penny and Marriott (42). Goodall (49) states that the load on a structure which causes rupture in time $\bar{t}$

is bounded as follows

$$\frac{P_{ult}\ \sigma_R(\bar{t})}{\sigma_y(1 + (\chi - 1)/n)} \leqslant P(\bar{t}) \leqslant \frac{P_{ult}}{\sigma_y}\ \sigma_R(\bar{t}) \qquad (2.37)$$

where $\sigma_R(\bar{t})$ is the uniaxial stress which causes rupture in a time $\bar{t}$ and χ is the ratio of the maximum effective stress in the elastic state to the maximum effective stress for a perfectly plastic material.

2.6 Model techniques

For components with complicated shapes and loading conditions it may not be possible to obtain accurate predictions of creep deformations and rupture times. Since it may not be feasible to test full size components under actual working conditions because of the time and cost involved it may be necessary to carry out model tests. Model tests are not only useful for prototype predictions, but are also invaluable in the testing of the methods upon which analytical solutions are based, such as the finite element solutions obtained by Parkes and Webster (23).

Frederick (50) has derived model correlations for investigating creep and relaxation in structures. In his investigation, Frederick found that the correlation between model and prototype depends upon the form of the prototype creep law and the hardening law. For prototype materials obeying equation 2.5, it is necessary for the model material to have the same stress index and also necessary for both model and prototype to be in an initially elastic state. For both time hardening and strain hardening materials, correlation is obtained at equivalent times given by

$$\left[E\sigma^{n-1}\,\Gamma(t)\right]_{prot} = \left[E\sigma^{n-1}\,\Gamma(t)\right]_{model} \qquad (2.38)$$

and equivalent strains are given by

$$\left[\frac{E\varepsilon_c}{\sigma}\right]_{prot} = \left[\frac{E\varepsilon_c}{\sigma}\right]_{model} \qquad (2.39)$$

Similar correlations exist for materials obeying more complex creep laws. In theory it should be possible to extend these correlations to include the tertiary region of creep and creep rupture. However, it would be practically impossible to obtain a model material to fit all of the requirements. Fessler, Gill and Stanley (51) and Fessler and Bellamy (52) have developed lead alloys (0.2% Sb, 0.02% As-Pb and 1.2% Sb, 0.12% As-Pb) which may be used for predicting creep deformations in the primary and secondary regions. However, the loads required to ensure that the models are in the elastic range are so small that creep deformations are difficult to measure. Apart from the difficulty of obtaining a model material, the major drawback with the above modelling method is that the prototype creep properties must be well defined, i.e. a large amount of expensive prototype material testing is required.

An alternative approach may be adopted if the effect of redistribution may be neglected. Sim's approximate Reference Stress may be obtained by obtaining the collapse load of a model structure, $(P_{ult})_{model}$, which may be scaled up to give the collapse load of the prototype structure, $(P_{ult})_{prot}$. The collapse load of the prototype structure may be used in conjunction with equations 2.35 and 2.36 to predict prototype deformations. However, the Reference Stress obtained from equation 2.35 may be very inaccurate as the example of the cantilever beam (Appendix 3) shows. Also, equation 2.36 is strictly only applicable to problems with one dimensional stress systems. However, in Chapter 3 it will be shown that an equation similar to equation 2.36 exists which may be used in conjunction with more thorough model tests to give accurate predictions

of Reference Stresses. It will also be shown in Chapter 3 that, since the Reference Stress is independent of the material creep law, no correlations between model and prototype material are required, which makes the selection of a model material much easier. Therefore, a model material may be chosen which has creep rupture properties which correlate with the prototype creep rupture properties, the only restriction being that small grained, homogeneous and isotropic castings can be produced with the model material from which reasonable creep strains can be obtained for small loads at moderate temperatures (eg. 1% creep strain in 200 h at 20°C).

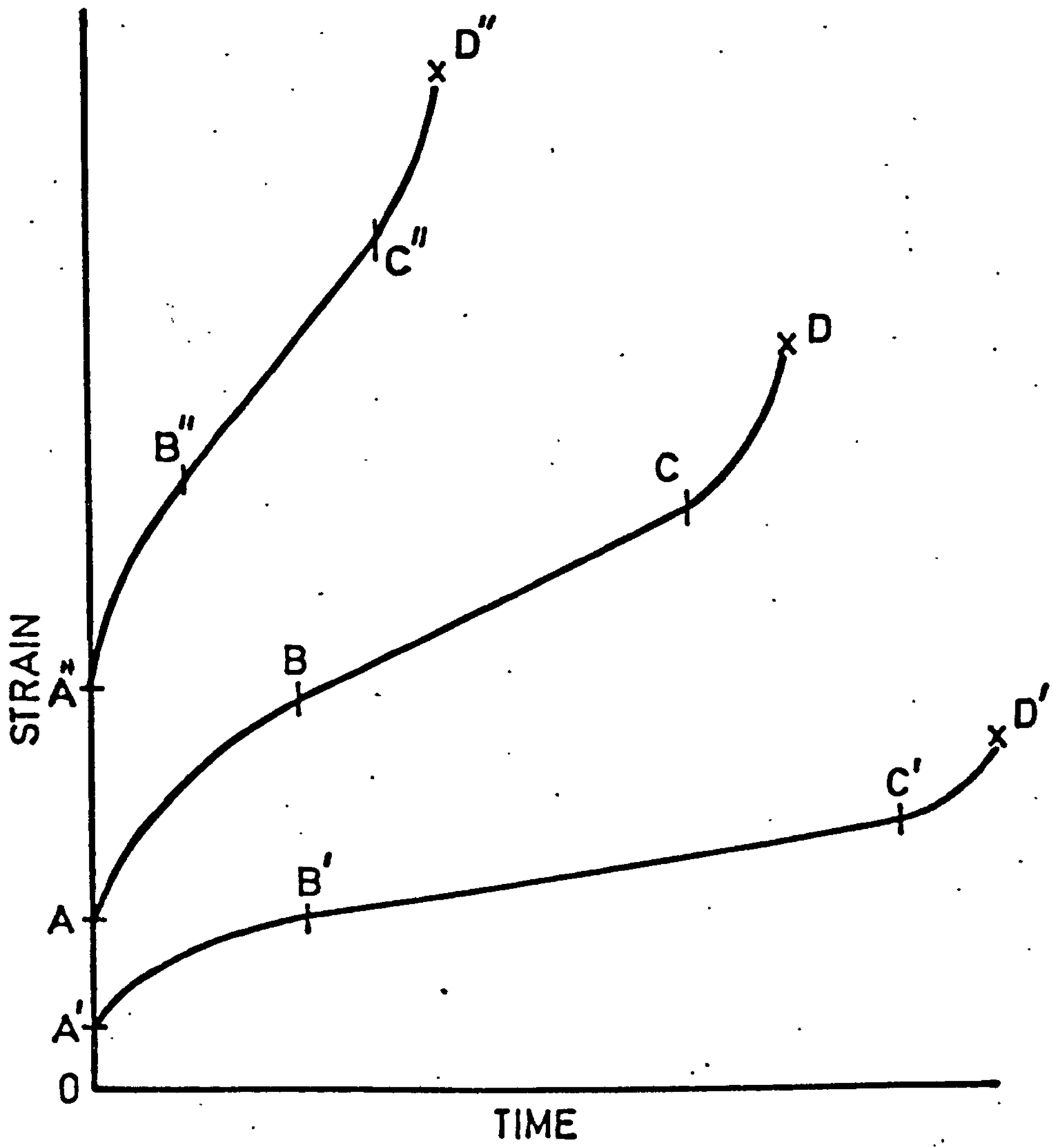

FIG.2.1 TYPICAL CREEP CURVES.

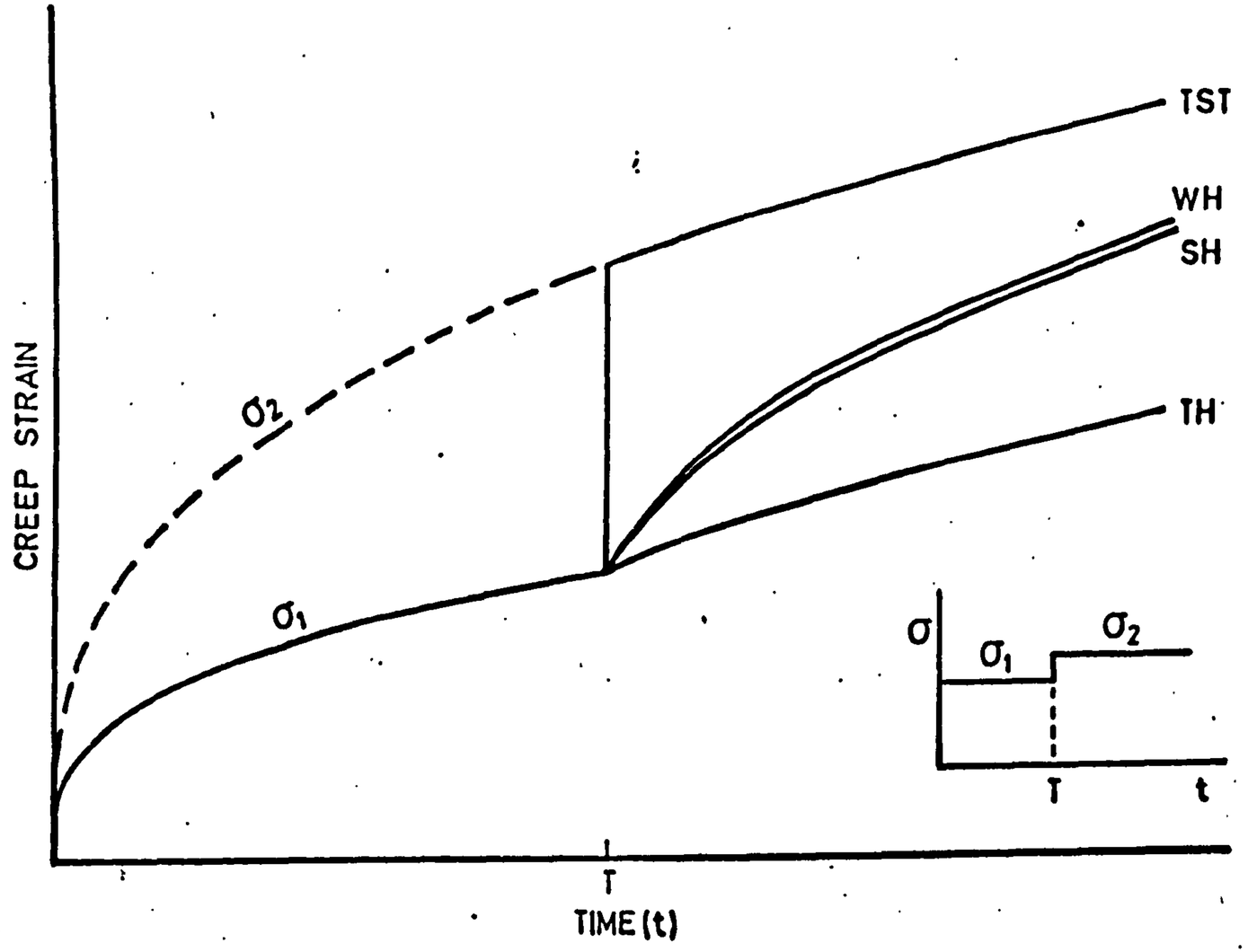

FIG. 2.2(a) STEPPED UP LOADING.

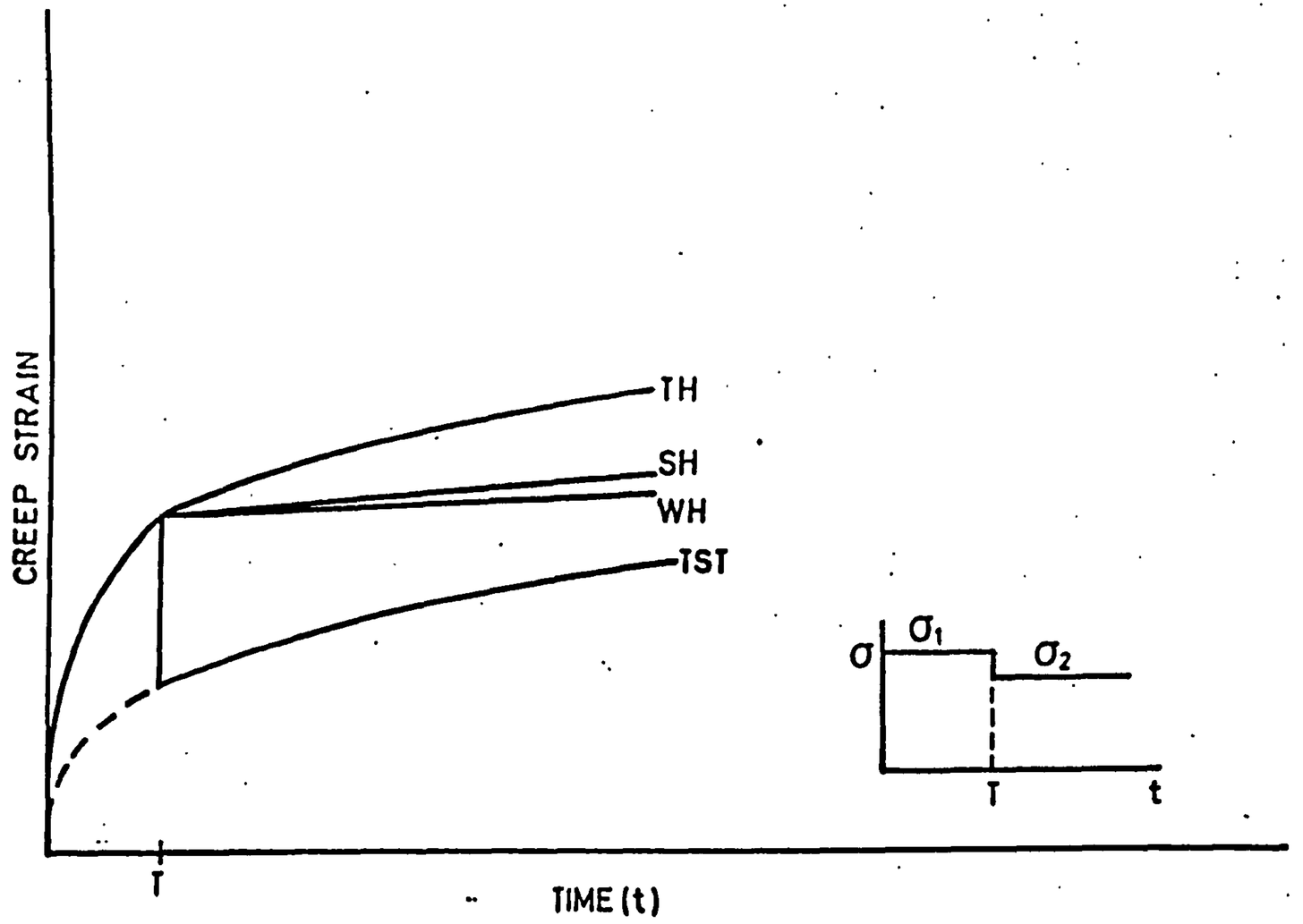

FIG.2.2(b) STEPPED DOWN LOADING.

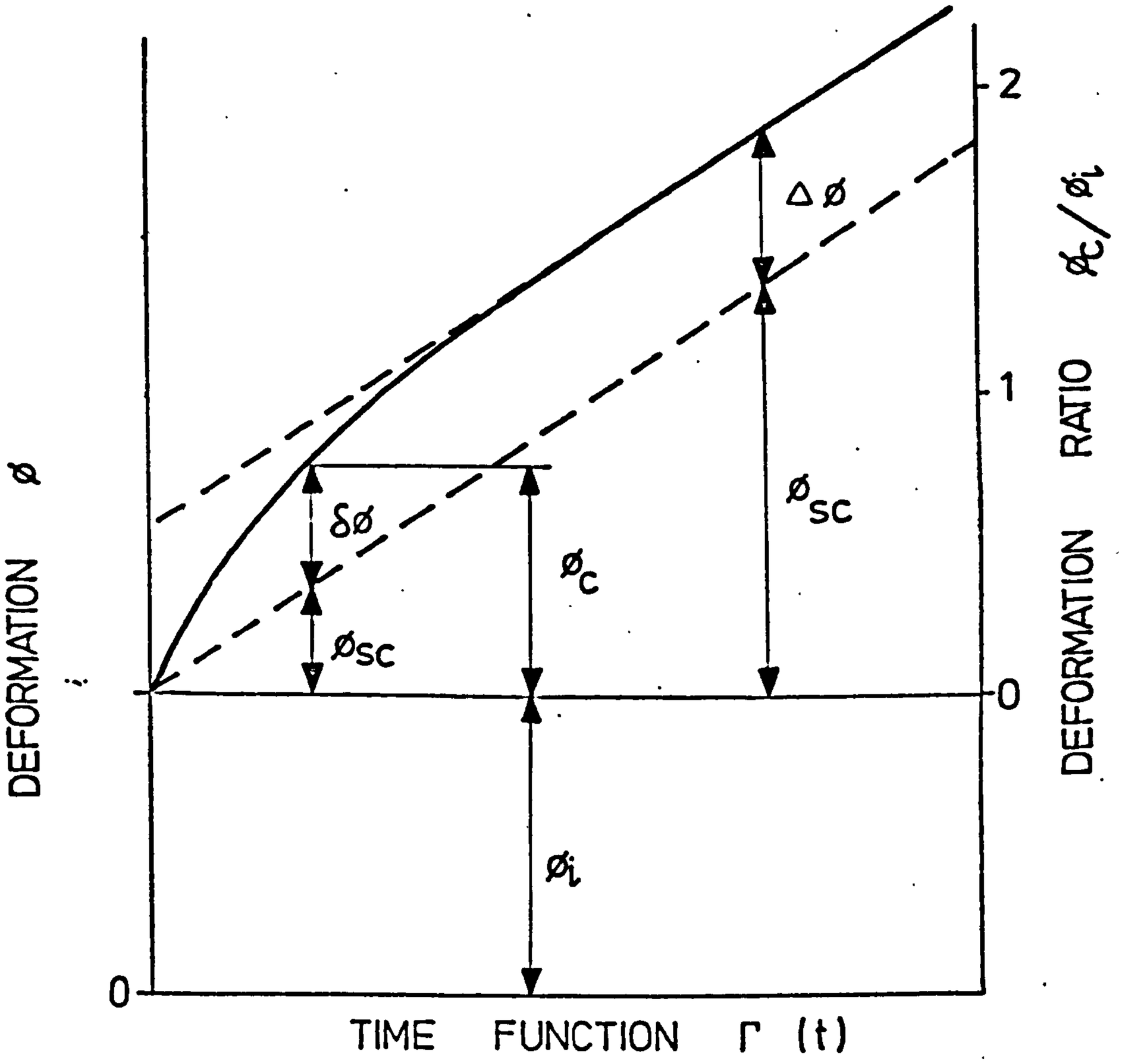

FIG. 2.3 COMPONENT DEFORMATION

CHAPTER 3

3. THE EXPERIMENTAL REFERENCE STRESS METHOD

3.1 Introduction

Ideally, a Reference Stress is a quantity which characterises the dependence of the deformation at a point in a component on the material properties. This ideal Reference Stress would be capable of predicting the total deformation at the point of interest in the component (i.e. elastic, plastic, creep and redistribution deformation), under any load history. It is doubtful if ideal Reference Stresses, as described above, exist for real components and materials. However, for many real situations, approximate Reference Stresses, which are insensitive to material behaviour laws rather than independent of them, can be determined. These approximate Reference Stresses allow the prediction of deformations to an acceptable degree of accuracy.

As Reference Stresses are insensitive to material behaviour laws, they can be determined analytically or numerically by using constituitive equations which are analytically convenient but do not necessarily describe the material behaviour accurately. Therefore, the basis of the experimental Reference Stress method will be developed for a simple separable stress and time 'n-power' creep law (which conveniently allows the variation in material properties by varying the value of n) and this will be extended to show how the experimental Reference Stress may be obtained from models made of materials which obey more complex creep laws.

3.2 Reference Stresses from model tests

3.2.1 Theoretical basis for one-dimensional stress systems

These include straight and curved beams and plane frames.

It is assumed that the initial stress-strain relationship of the material may be approximated by

$$\varepsilon_i = k\sigma^q \qquad (3.1)$$

This may include the effect of initial plasticity and/or non-linear elasticity; for the linear elastic case, k = 1/E and q = 1.

Fig 2.1 shows, for a typical material, uniaxial creep data which are assumed to be represented in the primary and secondary region by

$$\varepsilon_c = \sigma^n \Gamma(t) \qquad (3.2)$$

For the purpose of obtaining the stationary creep deformation (ϕ_{sc}) of a component, it is convenient to linearise and normalise the primary and secondary creep strains with respect to the initial strains by plotting $\varepsilon_c/\varepsilon_i$ against the time function $\Gamma(t)$. This is illustrated in Fig.3.1 for a material characterised by equation 3.2. If a component made of such a material has a one-dimensional stress system applied to it, the initial deformation will be governed by the initial constituitive equation and the equations of equilibrium and compatability. The "stationary state" creep deformations will be governed by the same equations of equilibrium and compatability (for small deformation) together with the creep constituitive equations of the material, which leads to the "initial" and "stationary creep" relationships for the component having similar forms, i.e.

$$\phi_i = k(\sigma_{nom})^q F_1(q) F_2(\text{dimensions}) \qquad (3.3a)$$

and $$\phi_{sc} = \Gamma(t)(\sigma_{nom})^n F_1(n) F_2(\text{dimensions}) \qquad (3.3b)$$

(Hoff (30) has used this "initial deformation analogue" to obtain "steady state" creep solutions to some simple problems for which non-linear elastic solutions are possible.)

From equations 3.1 and 3.2, $k = \varepsilon_{io}/\sigma_o^q$ and $\Gamma(t) = \varepsilon_{co}/\sigma_o^n$ where σ_o is an arbitrary stress and ε_{io}, ε_{co} are the initial and creep strains respectively, obtained from a uniaxial specimen subjected to this stress. Substitution of the above relations into equations

3.3 gives

$$\phi_i = \left[\frac{\sigma_{nom}}{\sigma_o}\right]^q F_1(q)\, F_2(\text{dimensions})\,\varepsilon_{io} \qquad (3.4a)$$

and $$\phi_{sc} = \left[\frac{\sigma_{nom}}{\sigma_o}\right]^n F_1(n)\, F_2(\text{dimensions})\,\varepsilon_{co} \qquad (3.4b)$$

$(\sigma_{nom}/\sigma_o)^q F_1(q)$ and $(\sigma_{nom}/\sigma_o)^n F_1(n)$ can be made weakly dependent on q and n respectively by a suitable choice of σ_o, namely $\bar{\sigma}_o$, the Reference Stress. Equations 3.4 then become

$$\phi_i = \bar{B}\, F_2(\text{dimensions})\,\bar{\varepsilon}_{io} \qquad (3.5a)$$

and $$\phi_{sc} = \bar{B}\ F_2(\text{dimensions})\,\bar{\varepsilon}_{co} \qquad (3.5b)$$

where $\bar{B}$ is a constant (or, more accurately, a weakly dependent function of n or q) and $\bar{\varepsilon}_{io}$, $\bar{\varepsilon}_{co}$ are the initial and creep strains respectively obtained from a uniaxial specimen subjected to the Reference Stress $\bar{\sigma}_o$. Dividing (3.5b) by (3.5a) gives

$$\frac{\phi_{sc}}{\phi_i} = \frac{\bar{\varepsilon}_{co}}{\bar{\varepsilon}_{io}} \qquad (3.6)$$

3.2.2 Experimental evaluation

Relationship 3.6 is used in conjunction with model tests to determine Reference Stresses. It is called the 'single model' equation because it can be used to determine the Reference Stresses from the initial and creep deformation of a single model of the component and its uniaxial material data.

The value of stress for which the material uniaxial data satisfy the relationship (equation 3.6) throughout the creep process is the Reference Stress. A difficulty arises in determining the Reference Stress because a creep test on a model yields the total creep deformation, $\phi_c = \phi_{sc} + \Delta\phi$, rather than the stationary creep ϕ_{sc}. The stationary creep deformation

is most readily obtained from a plot of the total creep deformation ϕ_c against the time function $\Gamma(t)$ as shown in Fig. 2.3. A time function which is independent of stress only exists for materials whose uniaxial creep data can be represented by the product of separable stress and time functions,

$$\text{i.e. } \varepsilon_c = f_1(\sigma)\,\Gamma(t)$$

For such materials the time function can be evaluated from the uniaxial creep data. The stationary creep deformation is then determined from a plot of the total creep deformation against this time function $\Gamma(t)$ and the Reference Stress is determined by using Equation 3.6. Some of the techniques which may be used are not described here because the method is only applicable to materials with separable stress-time creep laws.

3.2.3 The use of a generalised time function

Many materials, (53), (54), (55) and the material used for the experimental work described later, do not have separable stress-time creep laws. However, a plot, similar in form to the ϕ - $\Gamma(t)$ curve in Fig. 2.3, should be obtained for materials with a completely general uniaxial creep law by plotting $\phi_c(t)$ against $\bar{\varepsilon}_{co}(\bar{\sigma}_o, t)$, i.e. the creep deformation at time t is plotted against the uniaxial creep strain at the Reference Stress at the same time t for a range of values of t. It may be seen from equation 3.6 that the gradient of the ϕ_{sc} line on the plot, $(\phi_{sc}/\bar{\varepsilon}_{co})$, should be equal to $(\phi_i/\bar{\varepsilon}_{io})$. This procedure can be used to determine the Reference Stress by taking successive trial values σ_o for the Reference Stress. Graphs of $\phi_c(t)$ against $\varepsilon_{co}(\sigma_o, t)$ for each trial value are plotted and the curve corresponding to the Reference Stress should have the characteristic shape of the creep deformation curve illustrated in Fig. 2.3 and the gradient of its ϕ_{sc} line should be equal to $\phi_{io}/\varepsilon_{io}$. The uniaxial creep data for each trial value is required and it is improbable that this data will be available

for the Reference Stress. However, the Reference Stress may be interpolated from the gradients of the ϕ_{sc} lines and values of $\phi_{io}/\varepsilon_{io}$ for the trial values. This procedure would be tedious and time consuming if Reference Stresses for deformations at many points in a component are required and a more efficient graphical procedure has been developed.

Considering a more general uniaxial creep law of the form:

$$\varepsilon_c = f_1(\sigma)\,\Gamma(\sigma,t) \qquad (3.7)$$

where the time function $\Gamma(\sigma, t)$ is now a function of both stress and time and is defined as

$$\Gamma(\sigma, t) = \frac{\varepsilon_c(\sigma,t)}{\varepsilon_c(\sigma,t_o)} \qquad (3.8)$$

This time function for a stress σ is the ratio of the uniaxial creep strain at time t to the creep strain at some conveniently chosen time t_o, i.e. $f_1(\sigma) = \varepsilon_c(\sigma, t_o)$. The normalised creep strain $\varepsilon_c/\varepsilon_i$, for each constant stress uniaxial creep test, is plotted against its appropriate time function $\Gamma(\sigma,t)$ to give a series of straight lines passing through the origin. The gradients of these lines are $\varepsilon_c(\sigma, t_o)/\varepsilon_i(\sigma)$. Fig. 3.2 shows such a plot for the uniaxial data of the material used for the model creep tests described later. Superimposed on this graph are constant time curves. The constant time curve for the time t_o is a line parallel to the $\varepsilon_c/\varepsilon_i$ axis.

The following procedure enables a graph of (ϕ_c/ϕ_i) against the time function $\Gamma(\bar{\sigma}_o, t)$, corresponding to the Reference Stress, to be constructed on a piece of tracing paper, Fig. 3.3. Lines of constant (ϕ_c/ϕ_i), to the same scale as $(\varepsilon_c/\varepsilon_i)$ in Fig. 3.2 are drawn on the tracing paper, Fig. 3.3, for the same times as the isochronous curves in Fig. 3.2. The tracing paper, Fig. 3.3, is overlaid on the creep data plot, Fig. 3.2, and moved vertically until the intersections of the (ϕ_c/ϕ_i) lines

and their corresponding isochronous curves form a curve which has the characteristics of a ϕ_c against $\Gamma(\bar{\sigma}, t)$ curve as shown in Fig. 2.3. The stationary creep line associated with this total creep deformation curve will be parallel to the uniaxial creep data line for the Reference Stress. The value of Reference Stress is obtained from the gradients of the (ϕ_{sc}/ϕ_i) line and the uniaxial creep data lines by interpolation. Estimates for the redistribution deformation $\Delta\phi$ and the redistribution time ($t_{red}^{\cdot}$) are readily obtained from the total creep deformation curve.

3.2.4 Theoretical basis for complex stress systems

Equation 3.6 which forms the basis of the determination of Reference Stresses for one dimensional stress systems is based on the assumption that the material behaviour laws, equations 3.1 and 3.2, governing the initial and creep deformations respectively are of similar form. The creep law for complex stress systems corresponding to equation 3.2 for uniaxial stress is

$$(\varepsilon_{ij})_c = \frac{3}{2}(\sigma^*)^{n-1} s_{ij} \Gamma(t) \qquad (3.9)$$

Therefore, if equation 3.6 is to be applicable for components subjected to complex stress systems, the initial deformation law for the material must be of a similar form to equation 3.9. An initial deformation law which satisfies this similarity condition is

$$(\varepsilon_{ij})_i = \frac{3}{2} k(\sigma^*)^{q-1} s_{ij} \qquad (3.10)$$

(N.B. the suffix i outside the brackets on the L.H.S. of equation 3.10 is not part of the tensorial notation but indicates "initial").

Equation 3.10 is a behaviour law for an incompressible material (i.e. for $V = \frac{1}{2}$). Thus equation 3.6 is only strictly applicable to multi-dimensional stress systems if the initial deformation of the model material is incompressible. This is not usually so for the materials which are suitable for creep models. However, this difficulty

may be overcome by determining the initial deformation and material data for a second model made from an incompressible material. Araldite, which is a widely used model material for experimental stress and deformation analysis, is compressible in its 'rubber' state (at temperatures above its 'stress freezing' temperature).

The initial deformation of a model made from an incompressible material and the creep deformation of a geometrically similar model with similar loading, whose material behaviour laws are defined by equations 3.10 and 3.9 respectively, are derived like equations 3.4 as

$$(\phi_i)_A = \left[\frac{(\sigma_{nom})_A}{(\sigma_o)_A}\right]^q F_1(q) \; (F_2(\text{dimensions}))_A \; (\varepsilon_{io})_A \qquad (3.11a)$$

$$(\phi_{sc})_L = \left[\frac{(\sigma_{nom})_L}{(\sigma_o)_L}\right]^n F_1(n) \; (F_2(\text{dimensions}))_L \; (\varepsilon_{co})_L \qquad (3.11b)$$

where suffix A refers to the initially incompressible model material (Araldite) and L refers to the creep model material (Lead). $(\varepsilon_{io})_A$ is the initial uniaxial strain of material A at a stress of $(\sigma_o)_A$ and $(\varepsilon_{co})_L$ is the uniaxial creep strain of the material L at a stress of $(\sigma_o)_L$. The functions F_1 and F_2 in equations 3.11 a and 3.11b are identical because the models and their loads are geometrically similar and the material behaviour laws are of the same form.

The functions $((\sigma_{nom})_A/(\sigma_o)_A)^q F_1(q)$ and $((\sigma_{nom})_L/(\sigma_o)_L)^n F_1(n)$ are made weakly dependent on q and n respectively by choosing $(\sigma_o)_A$ and $(\sigma_o)_L$ to be equal to the (two, different) Reference Stresses $(\bar{\sigma}_o)_A$ and $(\bar{\sigma}_o)_L$ respectively. Equations 3.11 can then be written in the form:

$$(\phi_i)_A = \bar{B} \; (F_2(\text{dimensions}))_A \; (\bar{\varepsilon}_{io})_A \qquad (3.12a)$$

$$(\phi_{sc})_L = \bar{B} \; (F_2(\text{dimensions}))_L \; (\bar{\varepsilon}_{co})_L \qquad (3.12b)$$

where

$$\bar{B} = \left[\frac{(\sigma_{nom})_A}{(\bar{\sigma}_o)_A}\right]^q F_1(q) = \left[\frac{(\sigma_{nom})_L}{(\bar{\sigma}_o)_L}\right]^n F_1(n) \qquad (3.13)$$

and $(\bar{\varepsilon}_{io})_A$ and $(\bar{\varepsilon}_{co})_L$ are the initial and creep uniaxial strains in the materials A and L at the (two, different) Reference Stresses $(\bar{\sigma}_o)_A$ and $(\bar{\sigma}_o)_L$ respectively. Both Reference Stresses are proportional to the two nominal stresses and are related by:

$$\frac{(\sigma_{nom})_A}{(\bar{\sigma}_o)_A} = \frac{(\sigma_{nom})_L}{(\bar{\sigma}_o)_L} \qquad (3.14)$$

Eliminating $\bar{B}$ from equations 3.12 gives

$$\beta_{AL} \cdot \frac{(\phi_{sc})_L}{(\phi_i)_A} = \frac{(\bar{\varepsilon}_{co})_L}{(\bar{\varepsilon}_{io})_A} \qquad (3.15)$$

where $\beta_{AL} = (F_2(\text{dimensions}))_A/(F_2(\text{dimensions}))_L$ is unity if the deformations are strains or is the scale ratio of the two models if the deformations are displacements or the reciprocal of the scale ratio if the deformations are curvatures.

Equation 3.15 is applicable to complex stress systems if the initial deformation of material A is incompressible. However, it is also applicable to one dimensional stress systems. It may be used to determine the Reference Stress from the initial deformation of a material A model, the creep deformation of a material L model and the uniaxial data for both materials. It is referred to as the 'two model' equation.

The techniques used to determine Reference Stresses for one dimensional stress systems from equation 3.6 can be used to determine Reference Stresses for complex stress systems from equation 3.15. For example in the graphical method the time function is

$$\Gamma(\sigma,t) = \frac{(\varepsilon_c(\sigma,t))_L}{(\varepsilon_c(\sigma,t_o))_L} \qquad (3.16)$$

The uniaxial creep strains in material L are normalised with respect to the initial strains in material A at the appropriate stresses (as shown in Fig. 3.4 for the material used for the model creep tests described later). The appropriate stresses are such that the ratios of the stresses applied to the A and L material specimens are equal to the ratio of the nominal stresses in the A and L material models respectively. The creep deformation curve is a plot of $\beta_{AL}(\phi_{sc})^{\cdot}_{L}/(\phi_i)_A$ against the time function $\Gamma(\bar{\sigma}_o, t)$ for the Reference Stress. If material A is linear elastic $(\varepsilon_i)_A = E_A(\sigma)_A$ and does not have to be obtained experimentally.

3.3 Prediction of prototype stationary creep deformation

Previous studies (50) and (52) of the prediction of prototype creep deformations from model test results, based on satisfying precisely the necessary similarity conditions between model and prototype, show that such predictions are only possible if a number of conditions relating to the model and prototype materials are satisfied. A typical requirement is that the uniaxial creep data for both materials shall be expressable as products of independent functions of stress and time and that the stress functions for both materials are identical. The resulting predictions are for the total creep deformation, including the deformation due to stress redistribution. Generally it would be difficult to find model materials which satisfy the necessary similarity conditions.

The Reference Stress approach provides a means for the prediction of prototype creep behaviour from model tests. These predictions are not as complete as thosebased on satisfying the similarity conditions because they allow the prediction of the initial deformation and stationary creep deformation, but not the deformation due to stress redistribution. It is difficult to define precisely the necessary requirements of a material for it to be applicable to the Reference

Stress approach. However theoretical and experimental studies indicate that many analytical material models and most real materials satisfy the requirements, at least approximately.

A Reference Stress characterises the dependence of a deformation of a component on its material behaviour in so far as the deformation can be expressed in terms of the uniaxial strain of the material at the Reference Stress. This property enables prototype deformations to be predicted from model test results, the uniaxial data for the model material and uniaxial data for the prototype material at the Reference Stress appropriate to the deformations of interest. The prediction of stationary creep deformations for the more general case of multi-dimensional stress systems only is considered here.

Equation 3.15 is a relationship between the stationary creep deformation of a creep model, the initial deformation of a model made from an initially incompressible material and the uniaxial data for the two materials L and A. Following the derivation of equation 3.15, the following relationship between the stationary creep deformation of a prototype and the initial deformation of the initially incompressible model is obtained.

$$\beta_{AP} \frac{(\phi_{sc})_P}{(\phi_i)_A} = \frac{(\bar{\varepsilon}_{co})_P}{(\bar{\varepsilon}_{io})_A} \qquad (3.17)$$

Equation 3.17 may be expressed in the form

$$\beta_{AP} \frac{(\phi_{sc})_P}{(\bar{\varepsilon}_{co})_p} = \frac{(\phi_i)_A}{(\bar{\varepsilon}_{io})_A} \qquad (3.18)$$

Having followed the experimental method described above for determining the Reference Stress, the quantities on the right hand side of Equation 3.18 will be known, and the value of the right hand side will be some known quantity X.

Equation 3.18 may be expressed as:

$$(\phi_{sc})_P = \frac{1}{\beta_{AP}} \cdot X \cdot (\bar{\varepsilon}_{co})_P \qquad (3.19)$$

where $X = \dfrac{(\phi_i)_A}{(\bar{\varepsilon}_{io})_A}$

Equation 3.19 may be used to predict the stationary creep of a prototype component from the quantity X, determined from the model test results, and the uniaxial creep data of the prototype material without further reference to the model results.

3.4 Reference Stresses from non-creep models

The main application of the Reference Stress method is in the prediction of stationary creep deformations, it was therefore considered advisable to obtain Reference Stresses from creep model tests. However, it is possible to obtain Reference Stresses capable of predicting prototype creep deformations from tests carried out on two non-creeping models. It is necessary for the two non-creeping model materials to have different q values and if Reference Stresses are required for complex stress systems, the materials must be incompressible.

To illustrate the method, a one-dimensional stress system will be considered and for simplicity the two models will be assumed to be the same size and have the same loads applied to them.

Consider two models made of materials having uniaxial laws of the form

$$(\varepsilon_i)_1 = k_1 \sigma^{q_1} \qquad (3.20a)$$

$$(\varepsilon_i)_2 = k_2 \sigma^{q_2} \qquad (3.20b)$$

where $q_1 \neq q_2$ and there is no restriction on the values of k_1 and k_2

(i.e. k_1 may be the same as k_2).

The expressions for the deformations of the two models will be similar to equation 3.3a, i.e.

$$(\phi_i)_1 = k_1(\sigma_{nom})^{q_1} F_1(q_1) F_2(\text{dimensions}) \qquad (3.21a)$$

$$(\phi_i)_2 = k_2(\sigma_{nom})^{q_2} F_1(q_2) F_2(\text{dimensions}) \qquad (3.21b)$$

By a similar method to that already described, equations 3.21a and 3.21b may be expressed in the form

$$(\phi_i)_1 = \bar{B} F_2(\text{dimensions}) \ (\bar{\varepsilon}_{io})_1 \qquad (3.22a)$$

$$(\phi_i)_2 = \bar{B} F_2(\text{dimensions}) \ (\bar{\varepsilon}_{io})_2 \qquad (3.22b)$$

where $(\bar{\varepsilon}_{io})_1$ and $(\bar{\varepsilon}_{io})_2$ are the strains obtained from uniaxial specimens, made of materials 1 and 2 respectively, when subjected to a stress of $\bar{\sigma}_o$, the Reference Stress.

Dividing equation 3.22a by equation 3.22b gives

$$\frac{(\phi_i)_1}{(\phi_i)_2} = \frac{(\bar{\varepsilon}_{io})_1}{(\bar{\varepsilon}_{io})_2} \qquad (3.23)$$

From uniaxial tests, a plot of $(\varepsilon_i(\sigma))_1/(\varepsilon_i(\sigma))_2$ against stress (σ) may be obtained (illustrated in Fig. 3.5 for the model tests described later). The deformation ratio $(\phi_i)_1/(\phi_i)_2$, obtained from model tests, may then be used to identify the Reference Stress (as shown in Fig. 3.5).

A similar equation to equation 3.19 may then be used to predict stationary creep prototype deformations, i.e.

$$(\phi_{sc})_P = \frac{1}{\beta_{1P}} \cdot X \cdot (\bar{\varepsilon}_{co})_P \qquad (3.24a)$$

$$\text{or} \quad (\phi_{sc})_P = \frac{1}{\beta_{2P}} \cdot X \cdot (\bar{\varepsilon}_{co})_P \qquad (3.24b)$$

where $X = \dfrac{(\phi_i)_1}{(\bar{\varepsilon}_{io})_1} = \dfrac{(\phi_i)_2}{(\bar{\varepsilon}_{io})_2}$ (3.25)

and β_{1P}, β_{2P} are the model to prototype scale ratios.

Following the previous analysis, a similar method may be used to obtain Reference Stresses and prototype predictions for components with complex stress systems.

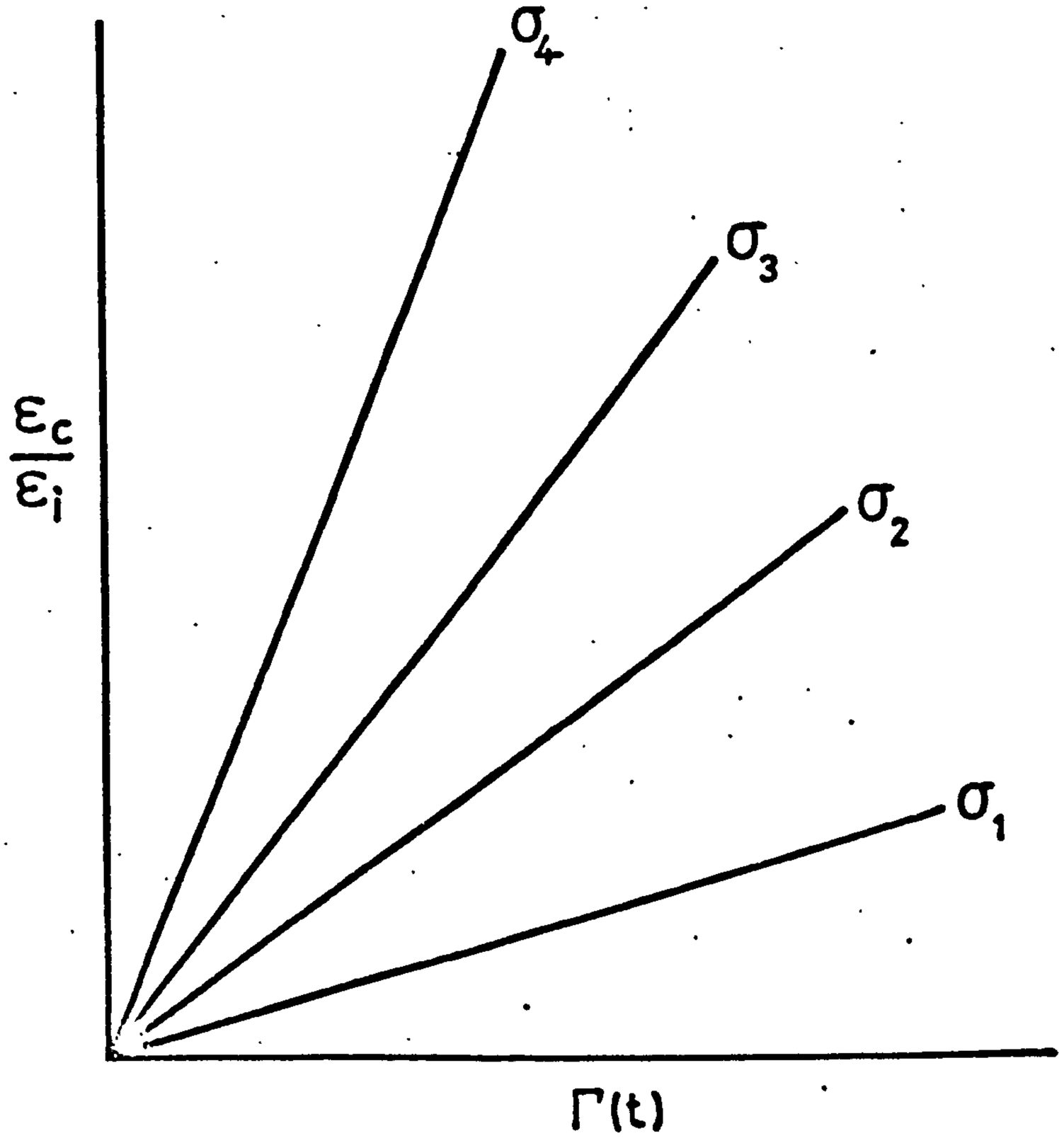

FIG. 3.1 NORMALISED CREEP DATA
(FOR A MATERIAL OBEYING $\varepsilon_c = f_1(\sigma)\Gamma(t)$)

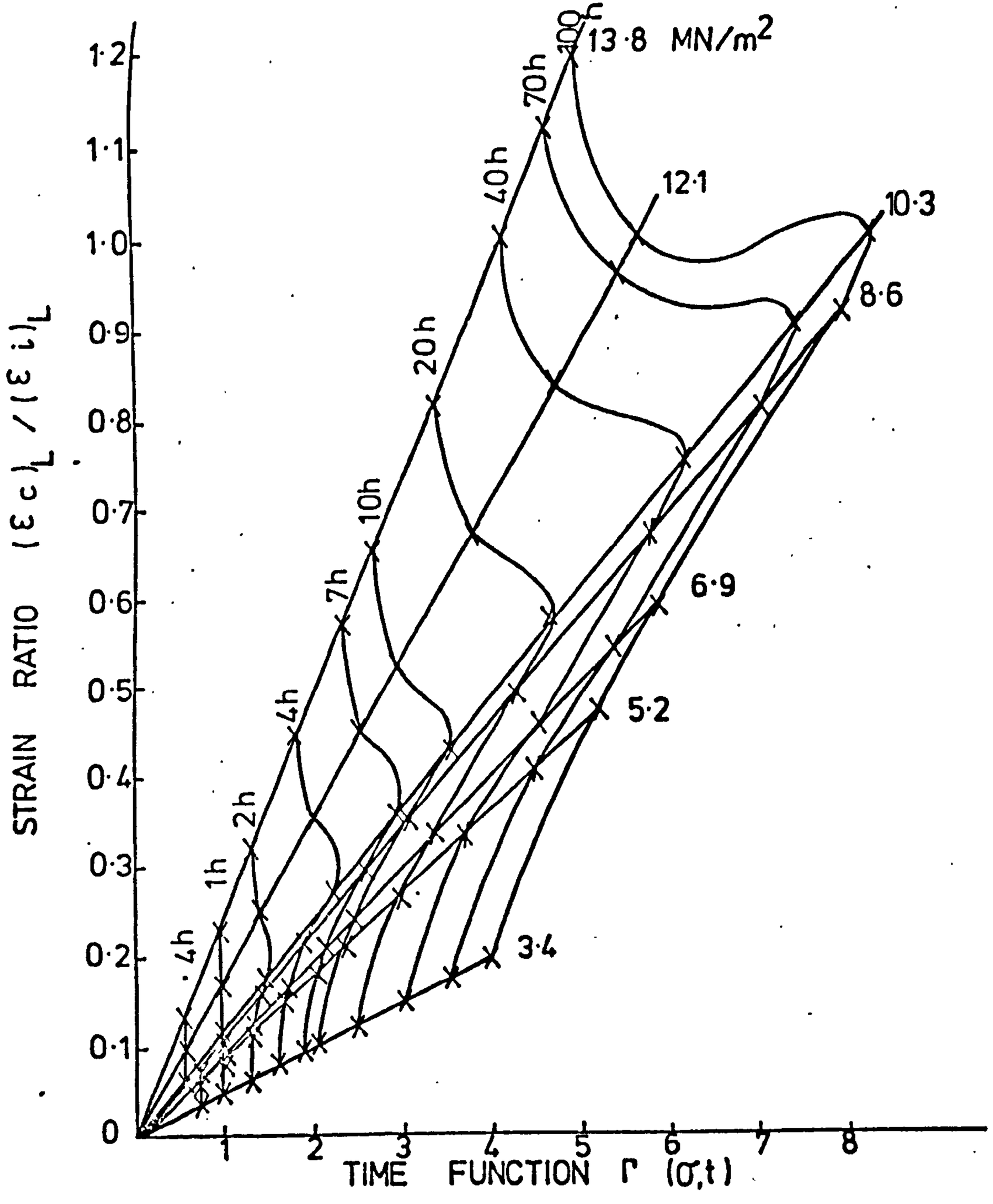

FIG.3.2 SINGLE MODEL CREEP DATA FOR CASTING P9

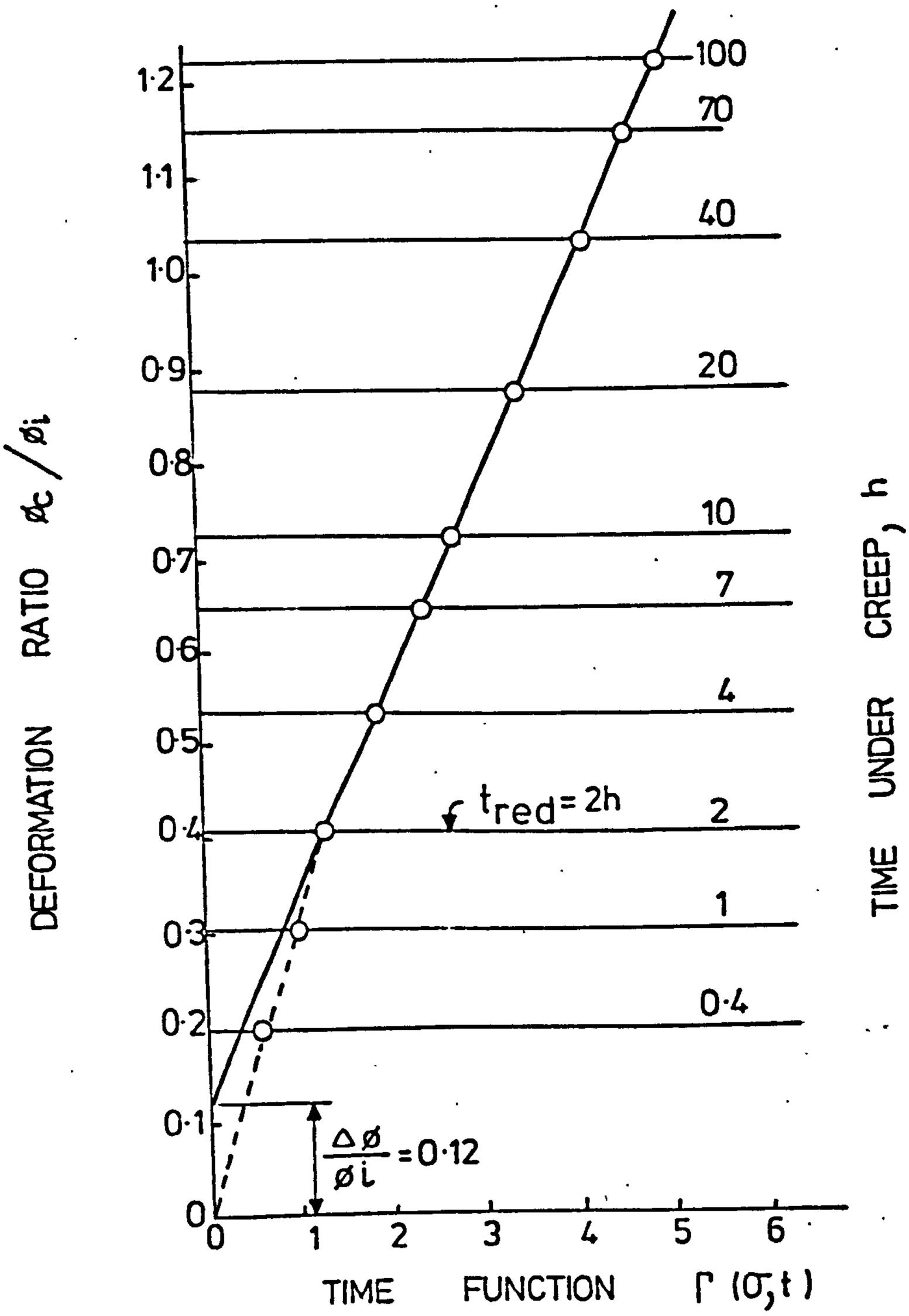

FIG.3.3 DEFORMATION RATIO FOR A BEAM IN PURE BENDING MADE FROM CASTING P9

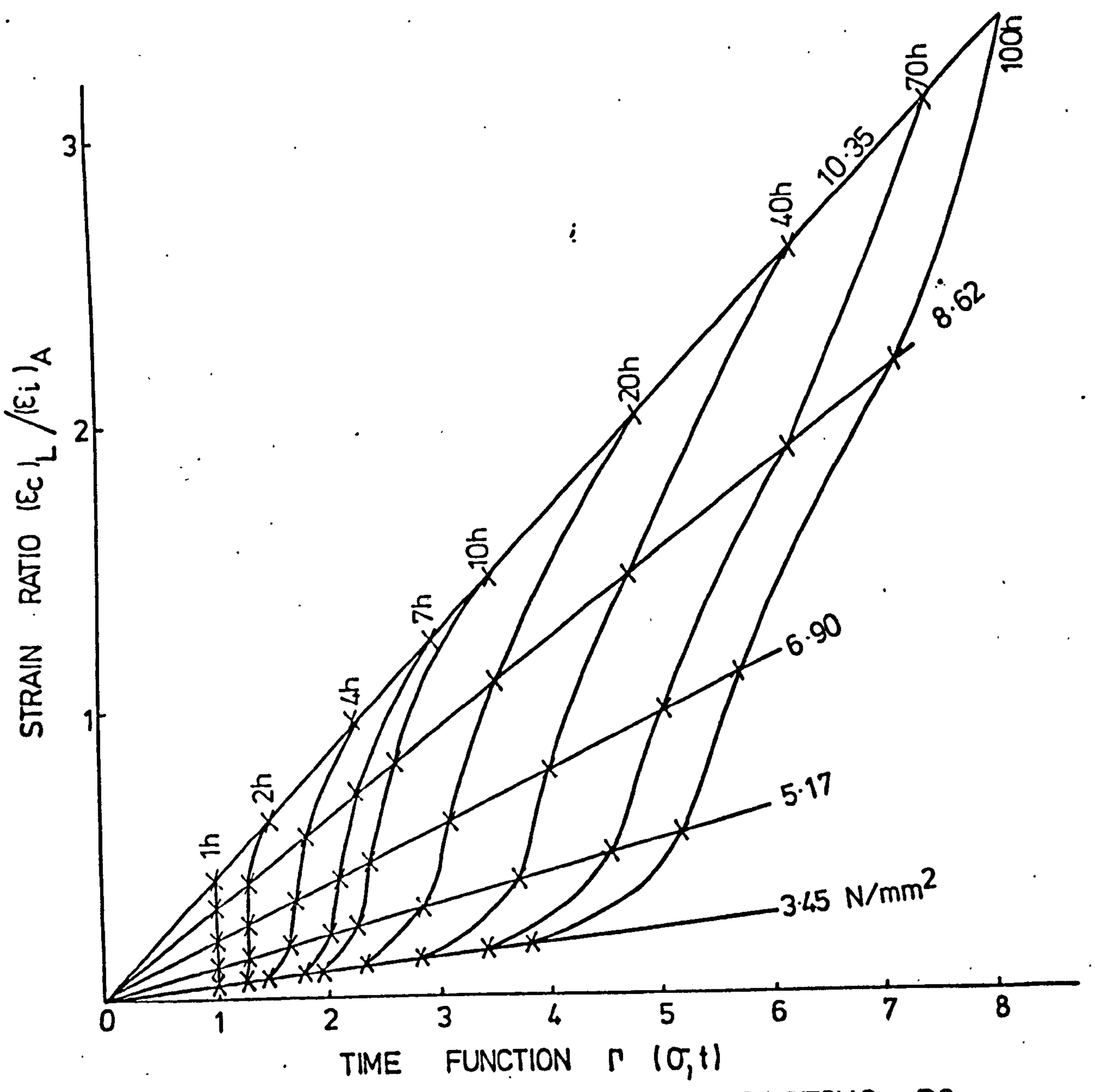

FIG.3.4 TWO MODEL CREEP DATA FOR CASTING P9

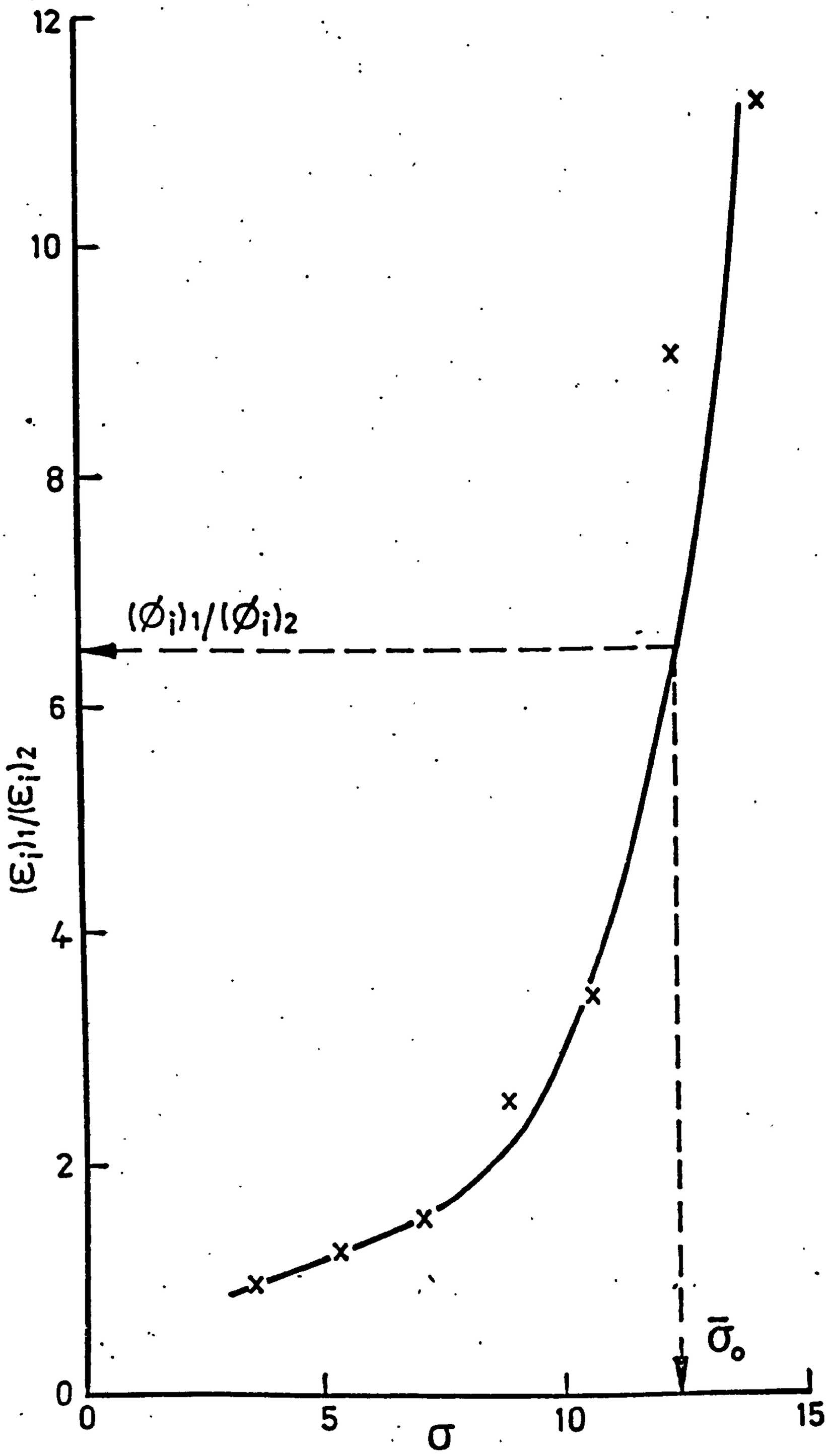

FIG.3.5 NON-CREEP MODEL DATA (P9 CASTING)

CHAPTER 4

4. THE PRODUCTION OF LEAD ALLOY CASTINGS

4.1 Introduction

In order to obtain an isotropic and homogeneous casting, it is necessary to ensure that the casting has small grains. Unfortunately, the grain structure of the lead alloy cannot be refined by subsequent heat treatment. The grain structure may be refined by cold working but this process is very difficult to carry out repeatably and is likely to give the lead alloy directional properties. Therefore, the only practical methods of producing fine grained lead alloy castings is to either use a chill casting technique or use an alloying material which will act as a nucleating agent.

Antimony is one of the materials alloyed with the lead and this material acts as a nucleating agent. However, when sufficient antimony is alloyed with the lead to make the grain structure fine and virtually independent of the casting temperatures (i.e. mould and melt temperatures), the material is too brittle and therefore not useful as a creep model material.

With low percentages of antimony in the lead alloy, nucleation is still caused by the antimony but not to a sufficient extent to make the casting temperatures unimportant. Therefore, the molten lead alloy (the melt) must be introduced into the casting cavity as quickly as possible and the mould and melt temperatures must be adjusted so as to produce the finest possible grain structure. There is however, a limit to how low the temperatures of the mould and melt can be allowed to drop, this is because the lead must not be allowed to freeze before the mould has filled or "cold runs" will result.

Because the lead alloy must be introduced into the mould at a fixed position, it is inevitable that this region of the mould becomes hotter than the rest. Therefore, solidification of the casting at the pouring position will be slower than anywhere else and larger grains will be produced at this "hot spot". The extent of a "hot spot" may be reduced by increasing the thermal capacity of the mould in the vicinity of the "hot spot". This may be done by increasing the specific heat and thermal conductivity of the mould material at the "hot spot" or more simply (if possible) by introducing an extra mass of metal to the mould at the position of the "hot spot".

The relative coefficients of expansion of the mould material and the lead alloy are of importance, particularly if a solid core is incorporated in the mould. If the relative coefficients of expansion are such that the casting shrinks tightly onto a part of the mould, it may be difficult to extract the casting and the casting may, in an extreme case, be cracked within the mould. Even if the above difficulties are not encountered, the possibility of work hardening certain parts of the casting may exist and this must be eliminated in order to ensure that the casting has homogeneous mechanical properties.

Porosity is probably the most undesirable feature of castings. This is because the material properties may be affected quite drastically by its presence. The presence of porosity can usually be associated with:

(i) the expansion of air which has been trapped in some part of the mould;

(ii) turbulence due to either excessive flow velocities or flow around tight corners and over sharp edges, causing cavitation.

(iii) a "hot spot" which has no means of being fed with molten lead

Because the lead, antimony and arsenic all have different densities, there will be a tendency for gravity segregation to take place within the melt. However, since pouring and solidification are fast compared with the process of gravity segregation, stirring the melt just prior to pouring will eliminate this.

Casting properties depend upon the following independent variables,

a) the melt composition and purity,

b) the velocity of pouring, which is controlled by the "head" of lead in the crucible and the size of pouring nozzle,

c) the melt temperature,

d) the latent heat of the melt and the specific heats of the molten lead and the solid lead,

e) the time for which the heating elements are left on and the time for whichthe mould is left to cool after the heating elements are switched off,

f) the thermal capacity and thermal conductivity of the mould and core (if one is used), and the positioning of the various masses of the mould, i.e. greater mass concentrations near "hot spots", etc. and

g) the coefficients of expansion of the lead alloy and mould material.

Casting properties depend upon the following dependent variables,

a) the mould temperature distribution before and after casting,

b) the mould filling time and

c) the solidification rate at various parts of the mould.

4.2 Mould design and development

4.2.1 The multi-cylinder mould (KK mould)

The KK mould was designed so that five biaxial test specimens could be produced from a single casting, five in line cylinders being the maximum number possible with the available heating box. Making as many cylinders as possible from a single casting eliminates possible scatter in the experimental results due to cast to cast variations in composition.

It was decided that where possible, the biaxial specimens should be cast to size (the biaxial specimen is shown in Fig. 7.2), which eliminates the risk of work hardening the material during the machining process. Because cores would have been too long to cast the inside diameter of the biaxial specimen to size, the cylinders were cast without cores but the outside diameters were cast to size.

Another advantage of casting the outside diameter to size is that the smallest grains in the casting are found close to the mould walls. Therefore, casting the outside diameter to size ensures that the smallest grains possible will exist in the biaxial specimens.

Fig. 4.1 shows the basic mould design, the central cylinder being used for pouring into. The other four cylinders are filled from the bottom by means of the channel connecting the bottoms of the cylinders. Because the 'bottom pouring' method is used, the mould must be split to allow extraction. The two halves of the mould are located by means of two dowels and clamped together by eight bolts.

A typical casting from the mould is shown in Fig. 4.2.

Problems were encountered with the flow, clamping and cooling.

4.2.1.1 The flow conditions

The inside of one half of the KK mould is shown in Fig. 4.3. All the edges of the mould which are exposed to the flow have been rounded to reduce the turbulence caused by flow separation and hence the risk of producing porous castings. The guide at the bottom of the central cylinder smoothes the flow at the bottom of this cylinder to eliminate splash and reduce the risk of seperation.

Turbulence and therefore porosity may be caused by having excessive flow velocities. For this reason, the flow channels connecting the bottoms of the cylinders were made as large as possible.

Table 4.1 (KK1 to KK5) shows what effect rounding the corners, reducing flow velocities and guiding the flow had on the castings produced. It can be seen that these methods reduced the porosity considerably but did not completely eliminate it. It was also found (Table 4.1, KK6) that the clamping conditions (i.e. the method by which the two halves of the mould were held together) also had a considerable effect on the porosity of the castings.

4.2.1.2 The clamping conditions

After the first heating up run was carried out on the mould, it was found that the two halves of the mould had warped, causing a flash to be present between all the cylinders. This warping may have been due to stress relieving of the steel from which the mould was made or it may have been due to the fact that the eight bolts used to clamp the mould together were tightened through lugs on the side of the mould. Tightening the bolts by means of lugs, causes the edges of the mould to be forced together, but causes the centre of the mould to bow outwards. This warping, caused a gap of about 0.5 mm at some parts of the mould which produced a flash of the same thickness.

At first, it was thought that these gaps would not cause any trouble, apart from the inconvenience of having to remove the flash from the castings. However, after work had been done to improve the flow conditions of the mould, it became apparent that there was another factor which was also responsible for causing porosity. This was found to be that air trapped in the gaps between the cylinders was expanding during casting. This expanded air caused minute bubbles to be present in the casting (i.e. porosity). To eliminate this, clamps were designed which applied a force into each of the V-grooves of the mould, thus getting rid of the gaps between the cylinders.

It was found that the work carried out on the flow conditions and on the clamping conditions completely removed the causes of porosity. Table 4.1 shows that after casting KK5 no porosity was observed.

4.2.1.3 The cooling conditions

It was found that with the basic mould design, it was not possible to produce small grains in cylinders 2 and 4 (cylinder numbers are defined in Fig. 4.1), particularly on those parts of these cylinders which were nearest cylinder number 3 (see Table 1, KK1 to KK7). Even when the mould and melt temperatures were reduced enough to cause flow lines (i.e. positions where solidification is so rapid that the mould does not fill) in cylinders 1 and 5 the grain size in cylinders 2 and 4 was unacceptable (see Table 4.1, KK4).

In order to try and eliminate these large grains, extra masses of steel were introduced into the V-grooves connecting cylinders 2, 3 and 4, and the sides of the mould on cylinders 2 and 4.

Since any reduction in the temperature of the lead entering cylinders 1 and 5 would mean that trouble would be caused by flow

lines, it was decided that the extra masses of steel in the V-grooves connecting cylinders 2, 3 and 4 should be insulated from cylinder number 3, (i.e. the pouring cylinder). This was done by introducing pieces of Syndanyo strip into the V-grooves as shown in Fig. 4.1 Therefore, the added pieces of steel extract heat from the lead entering cylinders 2 and 4 but have very little effect on the heat extracted from cylinders 1 and 5.

The final mould design is shown in Fig. 4.4 on which the thermocouple positions are also shown.

4.2.2 The pressure vessel mould (P mould)

The P mould is used for making the pots shown in Fig. 4.5. The mould and core are shown in Figs. 4.6(a) - (e). To allow for various shapes of flange and end closure, the steel mould was made in three parts. Since the core can only lose its heat either through the lead or through the top, the hemispherical end of the core tends to retain its heat for quite a long time. In order to increase the rate at which the heat is extracted from the core (through the lead alloy casting) at the hemispherical end, the thermal capacity of the mould was made much larger in this region by having a large mass of steel there.

Consideration of a greatly simplified idealisation of the cooling process involved will show why aluminium was chosen as the core material. Referring to Fig. 4.7, after pouring, the melt will cool to the liquidus point (L) and it will take a short time to reach the solidus point (S) at which point the casting will be completely solid. At this point, the temperature difference between the casting and the mould (the core is assumed to be at the same temperature as the mould at this particular time) will be ΔT. The value of ΔT must be large enough to cause the solidification process to occur quickly (in order to produce small grains) but at the same time, not large enough to cause the casting to

contract too much while the core is still expanding. Since it is arranged for ΔT to be fairly small, this does not present a great problem. A greater problem arises when T_{EXT} (the core extraction temperature) is reached. If the core extraction is left too long, the casting may suffer a permanent strain which will work harden the lead alloy and may also give it directional properties. The shrinking of the lead alloy onto the core may be so severe that it may be impossible to extract the core without damaging the casting. In order to eliminate this effect, the mould should have a coefficient of expansion less than that of the lead alloy and the core should have a coefficient of expansion greater than that of the lead alloy. Since few metals have a coefficient of expansion greater than lead and since none of these are of practical use as a core material, a practical core material with the highest possible coefficient of expansion must be chosen. Thus, it was decided that aluminium should be used as the core material and steel should be used as the mould material.

Collapsible sand cores were also considered but were discarded because of the risk of contaminating the lead alloy with sand particles. Instead of a solid aluminium core, a thin collapsible aluminium core with a tin filling was considered. The tin which has a melt temperature lower than that of the melt temperature of the lead alloy was to have been used to give the core a large heat capacity, this large heat capacity being obtained by allowing the tin to melt (i.e. the heat capacity would include the latent heat of solidification of the tin). This was also discarded because of the development time that would have been required to produce a usable core of this type.

Even with a solid aluminium core, it can be seen that the lead alloy will shrink onto the core because the lead alloy has got a greater coefficient of expansion than that of the aluminium. Apart from the friction force which must be overcome before the core may be extracted,

a vacuum force of about 2 KN must also be overcome. Since the temperature of the casting, at the time of extraction is fairly close to the melt temperature, the forces required to remove the core would be capable of tearing the casting apart. In order to overcome these difficulties, it was decided that a split core arrangement should be used (shown in Figs. 4.6.) With this arrangement, the core may be left for 20 minutes without any great difficulty being encountered in extracting it. However, it is advisable to extract the core as quickly as possible to avoid the possibility of strain hardening the lead alloy.

With the split core arrangement, it has been found that although the full diameter is still present, the force normal to the sides of the core (due to shrinkage of the lead alloy) is reduced greatly. It has been found that if the core should still not release, due to a flash being caused between the two halves of the core, a slight rotation of the core by means of tapping the cross-bar lightly soon breaks down the resistance and the core can be extracted without any difficulty.

The two parts of the core are located in the cross-bar and held in position by five bolts, the centre bolt also being used to aid in the extraction of the lower part of the core.

The core is located with respect to the mould be means of 4 dowels which are located in the arms of the cross-bar and in the mould, as shown in Figs. 4.6. When the core is located, it is clamped in position by means of the "quick release clamps" and the dowels are then removed. The removal of the dowels is to prevent damage (and/or seizure) due to the differential expansions of the mould and cross-bar, this being due to their difference in temperatures and due to the fact that the cross-bar is clamped to the aluminium core.

Because the best temperatures of the mould and melt can only be obtained by experiment, the length of the core was originally set to its nominal value (i.e. allowance was not made for expansion). When the best casting and mould temperatures were found, the thickness of the hemispherical part of the casting was then matched to the cylindrical part of the casting by "shimming up" the four arms of the cross-bar.

Because the coefficients of expansion of the steel "centre-bolt" and the aluminium core are different, it is necessary to leave the bolt loose before the mould is heated. The correct amount of "slack" is set by means of a feeler gauge.

The mould is fixed to the base of the heating box by means of four bolts to avoid lifting the mould when the core is being extracted.

The vacuum force created between the mould and casting tends to pull the casting flanges down onto the mould, this prevents the casting from being extracted immediately after casting. However, if the casting is left to cool for about 12 hours, the slow seepage of air past the flange allows it to be removed without any difficulty. The casting is extracted by means of "lifting dogs" which are cast into the flange.

Three thermocouples were placed on the outside of the mould and one thermocouple was placed on the inside of the core, their positions are shown in Fig. 4.6(a).

In the P mould there are no narrow cavities for the molten lead alloy to flow through and there are no sharp corners or edges for the lead to flow round, therefore, porosity was not such a problem as it was with the KK mould.

4.3 The casting equipment

A schematic diagram of the casting set-up is shown in Fig. 4.8. From this diagram, it can be seen that there are four main features, which are:

a) the mould,

b) the heating box,

c) the crucible and

e) the control of the level of cast in the mould.

4.3.1 The heating box

If cooling of the lead alloy is too rapid, "flow lines" and contraction cracks will result. Therefore, the mould must be preheated, this is done by means of a heating box (shown in Fig. 4.9).

The same heating box was used for both the KK mould and the P mould. The heating box is made of 13 mm. thick Syndanyo board with a reflective aluminium lining. A 1 mm. aluminium lining was chosen to reduce warping of the aluminium thus reducing the possibility of electrical shorting. The Syndanyo box is placed inside a hardboard box and fibre glass insulation is placed between these two boxes. This system provides very good insulation.

This arrangement, which constitutes the heating box, is situated on a tray which is in turn mounted on a trolley. The tray is necessary in order to contain the molten lead if there should be a catastrophic overflow. The trolley makes it easy to manoeuvre the heating box and mould in and out of the casting area beneath the crucible.

Originally, 4 x 1 KW pencil-type heating elements were clamped vertically to provide the maximum direct heat to the mould. The wiring to these heating elements was kept to the outside of the Syndanyo box except for very short lengths near to the terminals of the heating

elements. This was done to prevent the wires from being "fouled up" and destroyed by the spillage of molten lead alloy. Aluminium splash guards were made to go above the heating elements to stop lead from splashing on them; this was done to avoid heating elements burning out during the heating up process. However, it was found that these pencil-type heating elements would only last for three or four castings. Therefore, electrical heating elements of the type used for the heating rings of electrical cookers were substituted. With these heating elements, twenty castings have been made without the need for replacement.

To make it easy to dismantle the heating box to either work on the mould, change the mould or clean out any lead which may have spilled in the bottom of the heating box, the tray, which formed the base of the heating box was made to slip inside the sides of the box and no screws, nuts or such-like protrusions were in the bottom 50 mm. of the box. Therefore spillage of lead cannot cause the base and sides of the heating box to seize together. Thus, dismantling the heating box merely entails lifting the sides of the box from the base.

4.3.2 The melt heating equipment

The crucible is described in detail by Bellamy (56), therefore, only the main features will be outlined here.

The crucible is made of steel and contains about 200 kg of lead when full. Hot gas flows through spiral passages around the side of the crucible and the whole assembly is insulated by surrounding it with a hollow cylinder. In between the crucible (and spiral passages) and the hollow cylinder, vermiculate insulation is placed. The crucible is mounted in a fume cupboard to extract lead vapour, gas exhaust and lead oxide dust. The crucible is bottom pouring to prevent scum from entering the mould. A solenoid actuates the valve in the bottom of the crucible. When the lead reaches a predetermined level in the mould,

a level switch cuts out the solenoid and the valve closes.

With the crucible initially full, the KK mould fills in about 4 seconds and the P mould fills in about 1.5 seconds.

4.3.3 The level control

The valve is automatically closed by means of a "hold on" relay in the solenoid circuit. The circuit is broken when the lead in the mould reaches a predetermined contact position.

In order to avoid the possibility of the valve being caused to close prematurely by lead splashing onto the contact, a level switch of the type shown in Fig. 4.10 was used. Because the flow must enter a small hole and the contact is withdrawn up the tube, away from the hole, it is very unlikely that contact would be made even if a splash of lead did enter this hole. With the contact arranged in this manner, 49 castings were made with only one failure occurring due to splash.

4.3.4 The thermocouples

The positions of the thermocouples on the KK mould and P mould are shown in Figs. 4.4 and 4.6 respectively.

In order to ensure that a uniform grain structure is produced on the surface of a casting, it is necessary to ensure that the surface temperature of the mould is uniform before casting takes place. Due to the positioning of the heating elements, localised hot spots will be produced during the heating up process. Therefore, in order to obtain a uniform temperature distribution, the mould must be overheated and then allowed to cool. This is particularly important for the P mould, because the core temperature lags behind the mould temperature

due to the fact that the core has to be heated across a 10 mm. air gap. Tables 4.1, 4.2 and 4.3 show the temperature distributions before and after casting for both the KK mould and the P mould.

The melt temperature is also measured by means of a thermocouple which is situated at about half the depth of the lead alloy in the crucible.

The thermocouples are calibrated by introducing a known voltage into the circuit. This known voltage artificially simulates the voltage produced by the thermocouple. The reading produced on the automatic cold junction compensated temperature gauges should then be that which is equivalent to the input voltage. If it is not, the resistance of the circuit must be increased or decreased to bring the input voltage and the temperature output reading into line with one another.

4.4 Casting procedure

The casting procedure described will be that developed for the 1.6% Sb, 0.16% As lead alloy. The various stages of the development are summarised in Tables 4.1 and 4.2 Table 4.3 gives a summary of the casting conditions used for other compositions of antimony and arsenic. Because so few castings were made of each composition of antimony and arsenic (apart from 1.6% sb), the conditions given in Table 4.3 are not necessarily the optimum conditions.

4.4.1 The KK mould casting procedure

(i) The two halves of the mould are cleaned to remove all traces of dirt and lead alloy using a clean dry cloth, then the surfaces of the mould are painted with a thin layer of anti-seize when necessary.

(ii) The two halves of the mould are located by means of the two dowels and they are held together by means of six of the eight "lug" bolts. The two "lug" bolts at the top of the mould are not used at this stage.

(iii) The Syndanyo stripsand cooling masses are placed in the V-grooves (as shown in Fig. 4.1) and then clamped in position by means of the two clamping straps.

(iv) By shining a light into the cylinders of the KK mould, it is possible to see whether the mould is completely closed (i.e. whether a flash will be formed during casting). The clamps are tightened, forcing the Syndanyo strip and cooling masses into the V-grooves, until the centre cylinder is completely closed. The other cylinders are closed by tightening bolts into the other V-grooves (also shown in Fig. 4.1).

(v) The additional cooling masses (for cylinders 2 and 4) are then placed in position and another clamp used to hold them in position.

(vi) The level switch is then assembled, checked and placed in position. The other two "lug" bolts are then put into the top two lugs of the mould. These two bolts serve the dual purpose of clamping the top of the mould together and of holding the splash plate in position.

(vii) Lead splashes are then removed from the heating elements, particularly in the vicinity of the terminals and the heating elements are switched on to make sure that they are working.

(ix) With the heating box splash guards removed, the KK mould is then lowered into the heating box, making sure that it is reasonably central and that it is not touching the heating elements, then the splash guards are fastened in position above the heating elements.

(x) The lid is placed in position and the pouring funnel placed in position to make sure that it fits correctly, then the funnel is removed and the fibre glass lagging is placed on top of the lid.

(xi) The initial mould temperatures are recorded and then the heating elements are switched on.

(xii) The heating elements are switched off after 50 minutes at which time, the approximate temperatures will be $T_1 = 280^{\circ}C$, $T_2 = 270^{\circ}C$ and $T_3 = 250^{\circ}C$.

(xiii) 40 minutes before casting, the crucible burner is ignited to melt the lead and the extractor fan in the fume cupboard is switched on.

(xiv) When the melt reaches a temperature of $445^{\circ}C$ the crucible burners are turned down in order to maintain the melt at this temperature. If necessary, the melt is topped up to a level about 50 mm. below the top of the crucible, the temperature being maintained at $445^{\circ}C$.

(xv) Between 50 and 55 minutes after switching the heating elements off, the mould temperatures will be approximately $T_1 = 210^{\circ}C$, $T_2 = 210^{\circ}C$ and $T_3 = 195^{\circ}C$. At this stage, the fibre glass is removed from the heating box, the funnel is placed in position, the heating box is pushed under the fume cupboard and the "pour extractor fan" is switched on.

(xvi) The molten lead is then stirred and all temperatures are recorded.

(xvii) The solenoid circuit is then activated. When the mould has filled, the solenoid should automatically switch off; if it does not, this must be done manually.

(xviii) Immediately after pouring, all temperatures are recorded and the mould is pulled out from under the fume cupboard.

(xix) The "pour extractor fan" is then switched off.

(xx) When the melt temperature has fallen below the solidus temperature, the fume cupboard extractor fan is switched off.

(xxi) When the casting has reached room temperature, usually after about 12 h, the heating box lid and splash guards are removed and the mould is lifted out of the heating box (using block and tackle).

(xxii) The casting is removed from the mould be reversing the procedure (ii) to (vi). If the two halves of the mould should not come apart easily, they may be separated by lightly tapping the "lugs" around the sides of the mould.

(xxiii) Care must be taken at this stage to prevent any damage to the casting (i.e. work hardening of the surface must be avoided.)

4.4.2 The P mould casting procedure

(i) The mould and core are wiped with a clean dry cloth to remove all dirt and lead particles.

(ii) The core is then assembled taking particular care to exclude any dirt form the mating faces of the split core.

(iii) Lead splashes are then removed from the heating elements, particularly near the terminals.

(iv) The heating elements are switched on to make sure that they are working and then they are switched off (this should only take a matter of seconds).

(v) The thermocouple circuits are checked by placing a known voltage across their terminals and noting the implied temperature reading.

(vi) If necessary, the mould and core are coated with an anti-seize solution.

(vii) The level switch is then assembled, checked and placed in position, putting the "lifting lugs" in position at the same time.

(viii) The core is lowered into position and it is shimmed up to the correct height (relative to the mould).

(ix) The core is then located relative to the mould by means of the four locating dowels (the core will only fit in one of the four possible positions, this is clearly marked).

(x) The core is locked in position by means of the "quick release" clamps.

(xi) The splash plate is locked in position by tightening the bolts provided on two of the cross-bar arms.

(xii) The core centre-bolt is set with a feeler gauge.

(xiii) The four locating dowels are removed.

(xiv) The lid is placed in position and the pouring funnel placed in position to make sure that it fits correctly, then the funnel is removed and the fibre-glass lagging is placed on top of the lid.

(xv) The initial mould and core temperatures are recorded and the heating elements are switched on.

(xvi) After 95 minutes, the heating elements are switched off, at this time the approximate mould and core temperatures will be $T_1 = 380^{\circ}C$, $T_2 = 430^{\circ}C$, $T_3 = 220^{\circ}C$ and $T_4 = 260^{\circ}C$.

(xvii) About 40 minutes before casting, the crucible burner is ignited to melt the lead and the extractor fan in the fume cupboard is switched on.

(xviii) When the melt reaches a temperature of $440^{\circ}C$, the crucible burners are turned down in order to maintain the melt at this temperature. If necessary the melt is topped up to a level about 50 mm. below the top of the crucible, the temperature being maintained at $440^{\circ}C$.

(xix) Between 95 and 100 minutes after switching the heating elements off, the approximate mould and melt temperatures will be $T_1 = 220^{\circ}C$, $T_2 = 180^{\circ}C$, $T_3 = 240^{\circ}C$ and $T_4 = 180^{\circ}C$. At this stage, the fibre-glass is removed from the heating box, the funnel is placed in position, the heating box is pushed under the fume cupboard and the "pour extractor fan" is switched on.

(xx) The molten lead is stirred and all temperatures are recorded.

(xxi) The solenoid circuit is activated. When the mould has filled, the solenoid should automatically switch off; if it does not, this must be done manually.

(xxii) Immediately after pouring, all temperatures are recorded and the mould is pulled out from under the fume cupboard.

(xxiii) The "pour extractor fan" is then switched off.

(xxiv) The heating box lid is removed and the casting is allowed to cool.

(xxv) Between 15 and 20 minutes after casting, the temperature of the casting will be low enough to allow the core to be extracted (N.B. the casting will have solidified almost immediately after casting, but at high temperatures near the melt point the cohesive forces are so small that the casting may easily be torn apart, it must therefore, be allowed to cool further). At this time, the core temperature will be about $240^{\circ}C$. The lower core bolts are removed and the centre bolt is undone by 2 or 3 threads.

(xxvi) The "quick release" bolts are then undone and the core is lifted with the use of the lifting tackle which is attached to two of the four cross-bar arms. The core should split into two which allows it to be lifted without any difficulty.

(xxvii) When the core is completely removed, the casting is filled with fibre glass and the heating box lid is replaced. This prevents contraction cracking caused by too rapid cooling of the surface of the casting.

(xxviii) When the melt temperature has fallen below the solidus temperature, the fume cupboard extractor fan is switched off.

(xxiv) When the casting has reached room temperature, after about 12 h, the heating box lid is removed and the lifting tackle is attached to the lifting lugs cast into the casting.

(xxx) The casting is then lifted out of the mould. This should be done very slowly by two people, one person raising the casting and the other person guiding the casting out of the mould to prevent the casting from jamming. Jamming of the casting must be avoided because the areas where jamming occurs will be work hardened.

(xxxi) The lifting lugs are removed from the casting (using a hammer and chisel) with as little force as possible.

4.5 Casting results and observations

4.5.1 Castability

Pot castings have been produced with various compositions of antimony and arsenic. The nominal range of antimony composition was varied between 1.2% and 6% by weight.

It was found that for high percentages of antimony, the castings were very easy to produce. The grain size being very small (too small to see with the naked eye) over a large range of mould and melt temperatures. From Table 3 (castings 1 to 7), it can be seen that for 6% antimony composition, (i) variations in mould temperature between 200 and 240°C, (ii) variations in core temperature between 190 and 220°C, and (iii) variations in melt temperature between 420 and 440°C had no

visible effect on grain size.

Also, with 6% antimony there was no trouble with cold runs, porosity and blow holes. Some difficulty was observed because of a "hot spot" at the hemispherical end of the casting. However, it was found that by raising the mould off the base of the heating box, thus allowing the hemispherical end to lose its heat more quickly, this "hot spot" was eliminated.

Similar results to those obtained for the 6% (nominal) antimony were also obtained for 3.6% (nominal) and a 1.8% (nominal) antimony. It was however observed that as the antimony content was reduced the grain size and blow holes were becoming more pronounced; they were still good enough to be of acceptable quality but the casting temperatures were much more critical.

Castings produced with a 1.6% antimony, 0.16% arsenic lead alloy gave more trouble as Table 4.1shows. It was found that the grain size, cold runs, hot spots and blow holes were very dependent upon the casting temperatures. However, it was found that by systematically varying the mould, core and melt temperatures, a casting was produced with small grains and no visible porosity or blow holes. Very slight "hot spots" and "cold runs" are present over very small regions of the castings at these optimum temperatures but these regions were considered to be small enough to have no effect.

Because of the very complex flow and cooling conditions of the KK mould, a large number of test conditions needed to be tried in order to obtain the optimum temperatures. However, it can be seen from Table 4.1 that by a systematic variation in mould and melt temperatures, castings were produced for which the grain size was very similar to that of the pots (i.e. KK 16 to KK 20).

Although the castability of the lead alloy becomes better as the antimony content is increased, the material properties make it unfavourable as a room temperature model material. Therefore, although the castability of the 1.6% antimony, 0.16% arsenic lead alloy is not as good as the higher percentage alloys the more promising possibilities of using this material as a room temperature (20°C) model material made it the obvious choice.

4.5.2 Dimensional accuracy

Measurements were taken of wall thickness and inner and outer radii for pot numbers 2, 4, 5, 7, 10, 12 and P7 (see Tables 4.2 and 4.3). These measurements showed that the wall thickness in all seven castings fell within the range 9.246 ± 0.28 mm. The clearance between the mould and core was checked at room temperature and was found to be 9.525 ± 0.025 mm. Therefore, it was concluded that the variations in wall thickness and radii were due to temperature differences at various parts of the mould, these occurring at the instant of pouring. Also, the cooling rate could possibly affect the wall thickness since the maximum wall thickness was at the hottest place and the minimum wall thickness was at the coolest place.

From dimension measurements made on two KK castings (KK1 and KK2), it was found that the diameter of all 10 cylinders fell in the range 57.075 ± 0.25 mm. The differences between the dimensions of the two castings were small. Typically, the "out of round" of a cylinder is 0.305 mm. and the axial variations in diameter are 0.152 mm.

4.5.3 Grain structure

Specimens were etched from a pressure vessel (P5) casting and a cylinder casting (KK20). The etching was carried out in order to find out whether there was any directional grain growth within the casting

and to see whether the small grain structure present on the surface of the castings was also present inside the castings.

The grain structure of the P5 pressure vessel casting was found to have no preferred direction of growth but slightly larger grain were found within the casting than on the casting surface. The number of grains through the wall thickness (nominally 10 mm) varies between 20 and 60, which was considered to be large enough to ensure homogeneous material properties.

Similar grain structures were found in the KK20 casting. The number of grains in the thin cylinders of the biaxial specimens was found to be between 5 and 20 (in a nominal wall thickness of 3 mm).

4.5.4 Antimony and Arsenic composition

The composition of the castings was obtained by means of an X-ray flourescence method and the percentage compositions by weight are given in Table 4.4. The samples upon which the analysis was based were taken from the melt just before casting. The antimony content was found to be 1.49% ± 0.17% and the arsenic content was found to be 0.15% ± 0.01%, the exception being casting 13 which had an arsenic composition of 0.21%. However, casting 13 was not made from the same batch of material.

TABLE 4.1 CASTING CONDITIONS FOR THE CYLINDERS

Casting No.	Mould Temps. (°C)						Melt Temp. (°C)	Comments					
	Before casting			After casting				Grain Size	Cold Spots	Hot Spots	Porosity	Blow Holes	Action
	T1	T2	T3	T1	T2	T3							
KK1 4.10.74	208	211	213	319	308	310	440	Large	None	Centre cylinder & insides of other cylinders	A lot, particularly in cyl's 2 and 4	None visible	
KK2 7.10.74	216	221	222			295	440	"	"	"	"	"	Round off corner to reduce turbulence
KK3 8.10.74			182			289	420	Small in cyl's 1 & 5 larger grains at bottom & inside of cyl's 2 & 4	"	"	Slightly reduced	Slight	Increase channel area ∴ reduce velocity ∴ reduce turbulence
KK4 10.10.74			174			285	400	Small, except cyl. No. 3 & bottoms of cyl's 2 & 4	Flow lines at bottom of cyl's 1 & 5	Centre cyl. and inside of cyl's 2 & 4	"	None visible	Introduce guide at bottom of cyl. 3 to eliminate some of turbulence
KK5 16.10.74			185			288	400	"	"	"	Reduced further except near the flash	Slight	Clamp the mould to avoid flash, Introduce extra metal to cyl's 2 & 4 to reduce grain size
KK6 17.10.74			246			269	400	As above + smaller grains near centre tube of cyl's 2 & 4	"	"	None visible	"	Introduce more metal to sides of cyl's 2 & 4
KK7 21.10.74			248			270	400	Very small grains everywhere except a small band on cyl's 2 & 4	"	"	"	"	Do not put Anti-seize on mould
KK8 23.10.74			258			278	400	"	"	"	"	Blow holes reduced	
KK9 25.10.74		200			299		400	"	Very slight on cyl's 1 & 5	"	"	None on cyl's 3, 4 & 5	Specimens to be made from cyl's 3, 4, 5.
KK10 26.10.74		200			294		402	"	Flow lines at bottom of cyl's 1 & 5	"	"	Quite a large number KK9 may be a fluke	
KK11 29.10.74		198			295		420	"	"	"	"	As above + impurities present in casting	Raise melt temp. to eliminate blow holes & flow lines. Clean melt thoroughly
KK12 30.10.74	200			278			420	"	Slightly reduced	"	"	Slightly reduced	
KK13 31.10.74	201			270			440	Small but slightly larger	Flow lines almost gone	"	"	Impurities almost gone blow holes gone	Take more care when cleaning melt
KK14 1.11.74	208	201	189	268	290	284	439	"	"	"	"	Very slight impurities	"
KK15 4.11.74	198	185	182	256	248	280	440	"	"	"	"	"	Increase melt temp. to eliminate slight flow lines
KK16 7.11.74	189	189	188	260	269	284	445	Majority less than $\frac{1}{16}$ mm everywhere, some larger ie 1mm	None	"	"	None on gauge lengths needed	
KK17 8.11.74	212	215	199	280	248	299	445	"	"	"	"	"	
KK18 11.11.74	215	220	201	280	320	286	445	"	"	"	"	"	
KK19 13.11.74	212	214	198	276	322	289	445	"	"	"	"	"	
KK20 14.11.74	201	203	196	270	322	284	445						

Positions at which temperatures were recorded are shown in Fig. 4.1

Sb, As compositions given in Table 4.4

TABLE 4.2 CASTING CONDITIONS FOR THE POTS (1.0% Sb, 0.16% As-Pb)

T_1, T_4 = Temps. before casting; T_2, T_5 = Temps. after casting; T_3, T_6 = Temps. on extraction

Casting No.	Mould Temp. (°C)			Core Temp. (°C)			Melt Temp. (°C)	Time from Pour to Ext. (min)	Comments					
	T_1	T_2*	T_3	T_4	T_5*	T_6			Extraction	Grain Size	Cold Runs	Hot Spots	Porosity	Blow Holes
P1 9.9.74	197	255	204	214	250	213	420	22	Core Stuck, slight force required	Very small	50% of the cylinder opposite the pour position	Near pour position, about 20% of cylinder	None visible	Slight, mainly on hemi-spherical end
P2 10.9.74	205	280	206	222	256	215	426	25	"	"	As P1 but less pronounced	"	"	Slight
P3 11.9.74	203	278	207	227	259	216	425	28	"	"	Internal runs are very slight	"	"	"
P4 12.9.74	222	248	209	224	260	219	430	31	Core stuck, great force, casting destroyed	"	Slight runs over ≏ 40% of the cylinder	"	"	"
P5 16.9.74	209	253	219	228	265	231	430	17	O.K.	Largest less than ½ mm, most too small to see	"	"	"	"
P6 17.9.74	214	262	220	230	269	229	436	25	Core stuck, slight force required	"	Very slight worst on the inside	"	"	"
P7 18.9.74	220	272	229	234	268	228	440	19	O.K.	"	No runs	"	"	"
P8 19.9.74	220	272	222	241	272	238	440	18	O.K.	"	"	"	"	"
P9 20.9.74	218	273	219	243	274	236	440	14	O.K.	"	"	Very slight near the pour posⁿ.	Very slight near specⁿ. Posⁿ. 14	Almost non-existent
P10 23.9.74	217	272	223	244	272	238	440	17	O.K.	"	"	"	None visible	Very slight near specⁿ posⁿ. 14
P11 24.9.74	223	269	227	237	270	239	440	18	O.K.	Small	Slight	Slight	None visible	Slight
P12 25.9.74	220	280	222	240	270	239	440	18	O.K.	"	"	"	"	"
P13 26.9.74	220	275	236	238	266	235	440	17	"	"	"	"	"	"
P14 27.9.74	216	279	221	241	272	238	440	18	"	About ½ mm at pour position	"	Approx. 20% of cylinder near pour posⁿ.	"	"
P15 30.9.74	220	262	232	238	262	249	440	7	Tight, mould did not fill	Small	Many	None	None visible	None visible
P16 1.10.74	218	279	225	241	272	240	440	16	O.K.	"	Slight	Slight	"	"

TABLE 4.3 CASTING CONDITIONS FOR THE POTS OF VARIOUS ALLOYING COMPOSITION

Casting No. and nominal Sb Composition	Mould Temp. (°C)			Core Temp. (°C)			Melt Temp. (°C)	Time from Pour to Ext. (min)	Comments					
	T_1	T_2*	T_3	T_4	T_5*	T_6			Extraction	Grain Size	Cold Runs	Hot Spots	Porosity	Blow Holes
1 19.12.73 6%	198	210		194	235		440	7	O.K.	Very small	None	Was not solid	None visible	None visible
2 20.10.73 6%	215	242	220	223	243	229	425	20	"	"	"	Slight around pour position	"	"
3 2.1.74 6%	238	259	230	211	242	236	420	20	"	"	"	Was not solid	"	"
4 8.1.74 6%	222	232	151	221	232	208	425	35	"	"	"	Slight	"	"
5 9.1.74 6%	220	240	151	218	252	201	430	57	Core stuck, force required	"	"	"	"	"
6 11.4.74 6%	209	236	189				425	34	O.K.	"	"	"	"	"
7 17.4.74 6%	211	239	193				420	35	O.K.	Very small	None	Slight	None visible	None visible
8 15.5.74 3.6%				213	239	200	428	36	"	"	"	"	"	"
9 16.5.74 3.6%				211	242	198	422	39	"	"	"	"	"	"
10 12.6.74 1.8%	212	237	188	208	233	198	425	29	"	"	"	"	"	"
11 26.6.74 1.6%	209	238	191	229	250	210	420	43	"	Large	"	"	"	"
12 27.6.74 1.6%	200	264	182	209	238	210	420	57	"	Very small	"	"	"	"
13 28.6.74 1.6%	206	235	195	209	235	201	420	30	"	"	"	"	"	"

TABLE 4.4 LEAD ANALYSIS

Specimen Number	% Composition (by weight)	
	Arsenic (As)	Antimony (Sb)
P1	0.15	1.53
P3	0.15	1.38
P4	0.14	1.33
P5	0.14	1.43
P6	0.14	1.28
P7	0.15	1.56
P9	0.15	1.66
P10	0.15	1.54
P11	0.16	1.75
P12	0.14	1.53
P13	0.15	1.42
P14	0.16	1.67
P15	0.16	1.48
P16	0.15	1.49
13	0.21	1.43
KK9	0.14	1.34
KK16	0.14	1.37
KK17	0.15	1.38
KK18	0.14	1.31
KK19	0.15	1.45
KK20	0.15	1.48

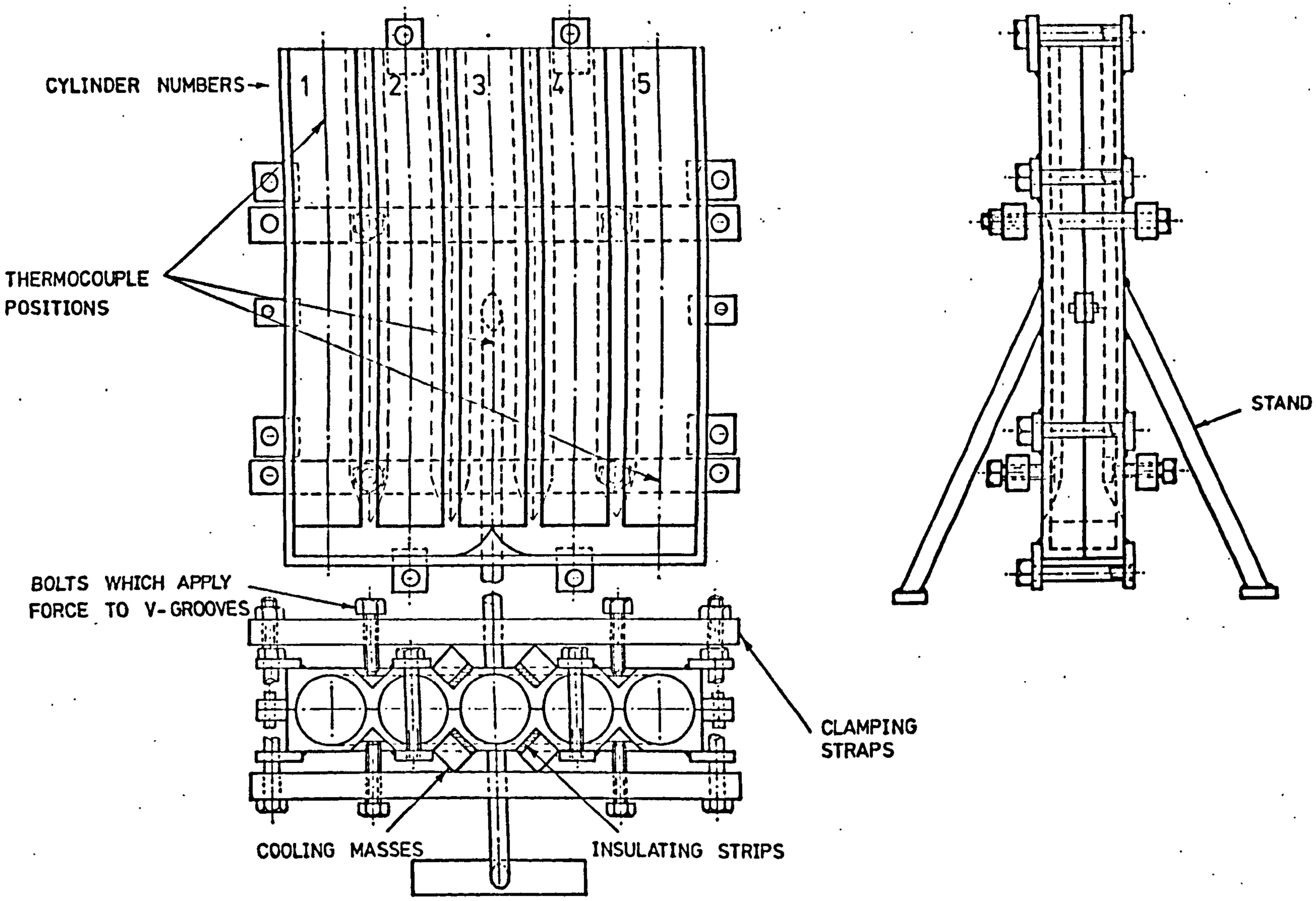

FIG. 4.1 THE MULTI-CYLINDERS MOULD

FIG. 4.2 A MULTI-CYLINDERS CASTING

FIG. 4.3 INSIDE OF THE MULTI-CYLINDERS MOULD

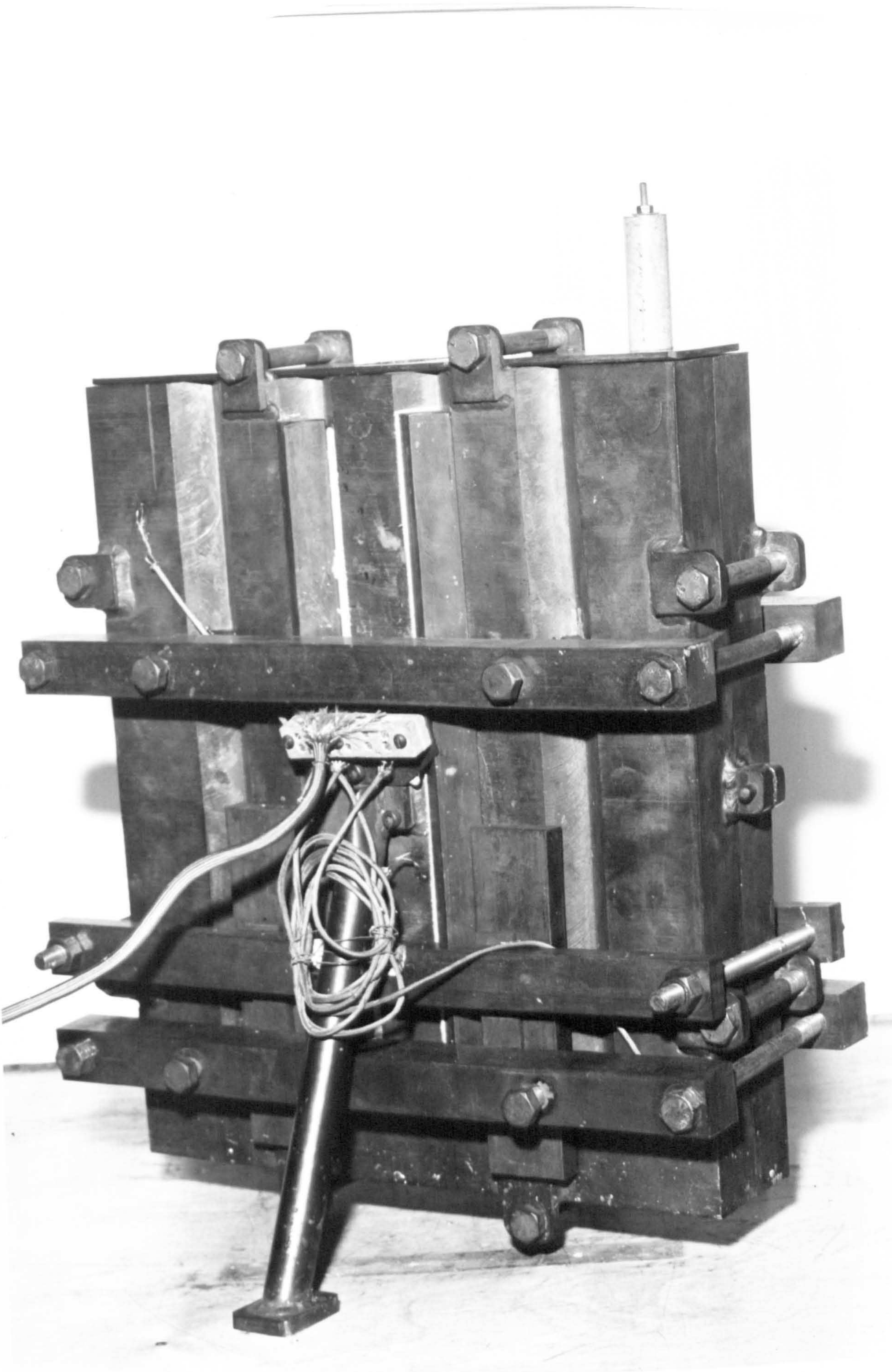

FIG. 4.4 THE MULTI-CYLINDER MOULD

FIG. 4.5 PRESSURE VESSEL CASTINGS

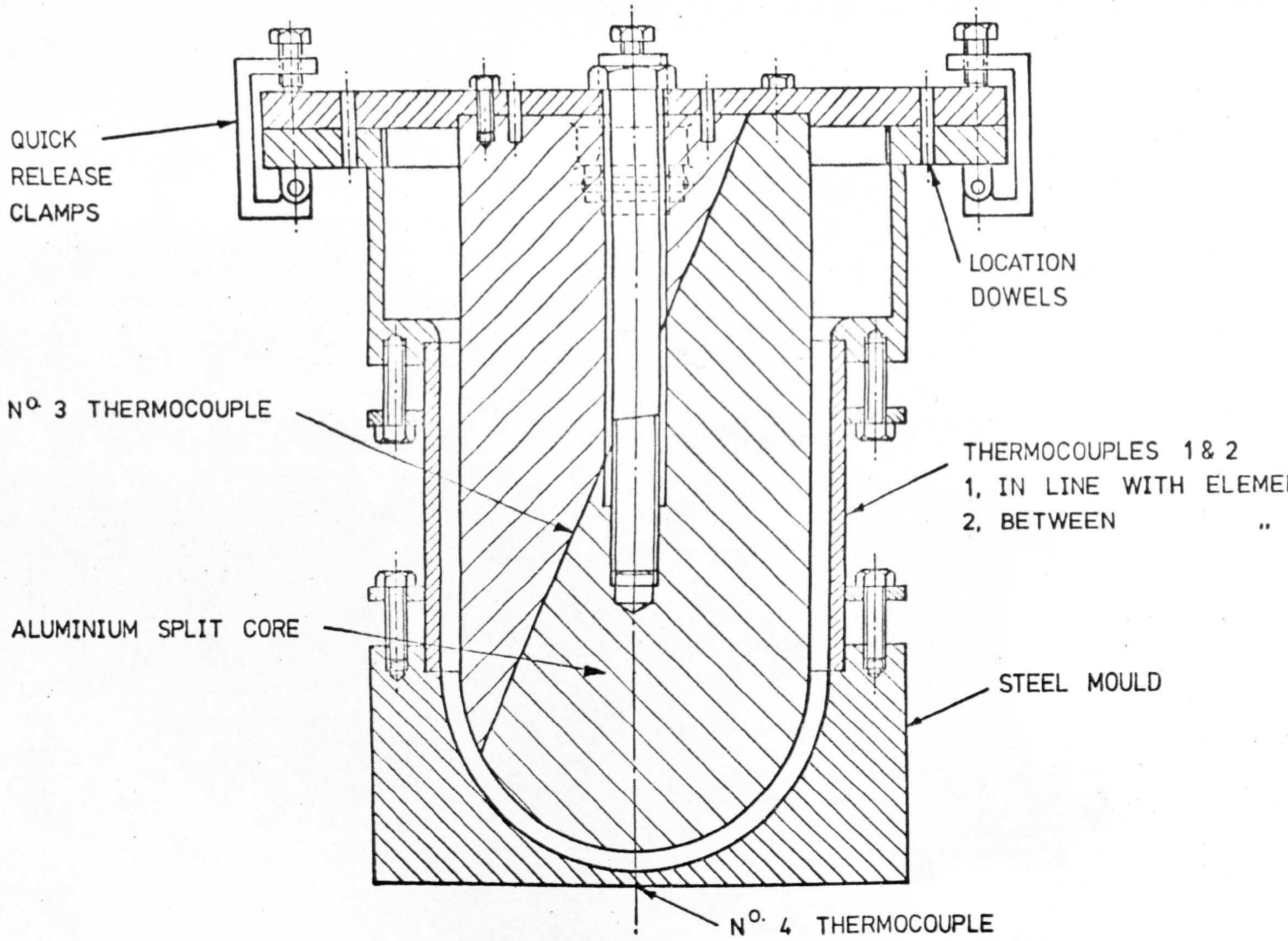

FIG. 4.6(a) THE PRESSURE VESSELS MOULD

FIG. 4.6(b) THE PRESSURE VESSEL MOULD

FIG. 4.6(c)

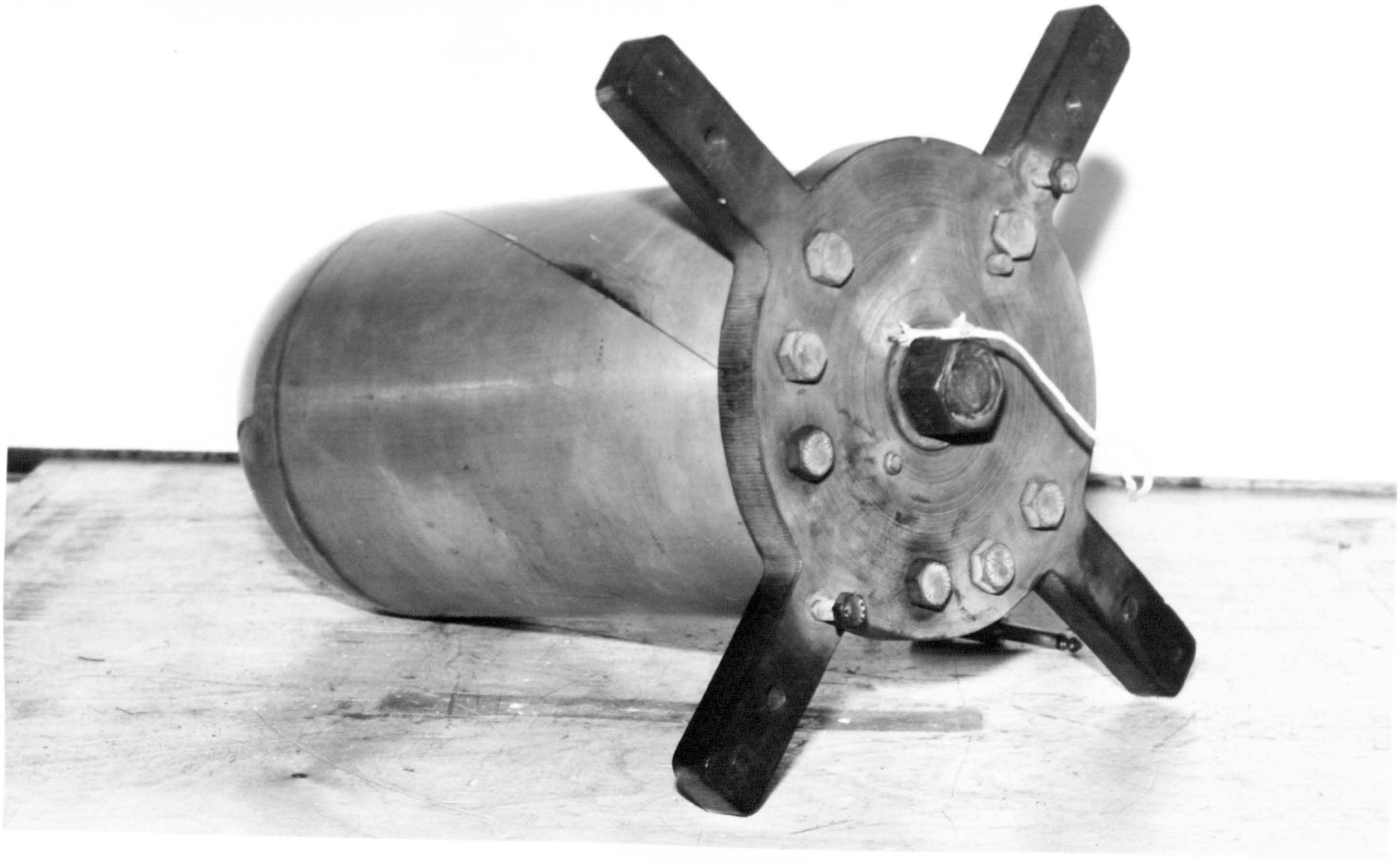

FIG. 4.6(d)

FIG. 4.6(e)

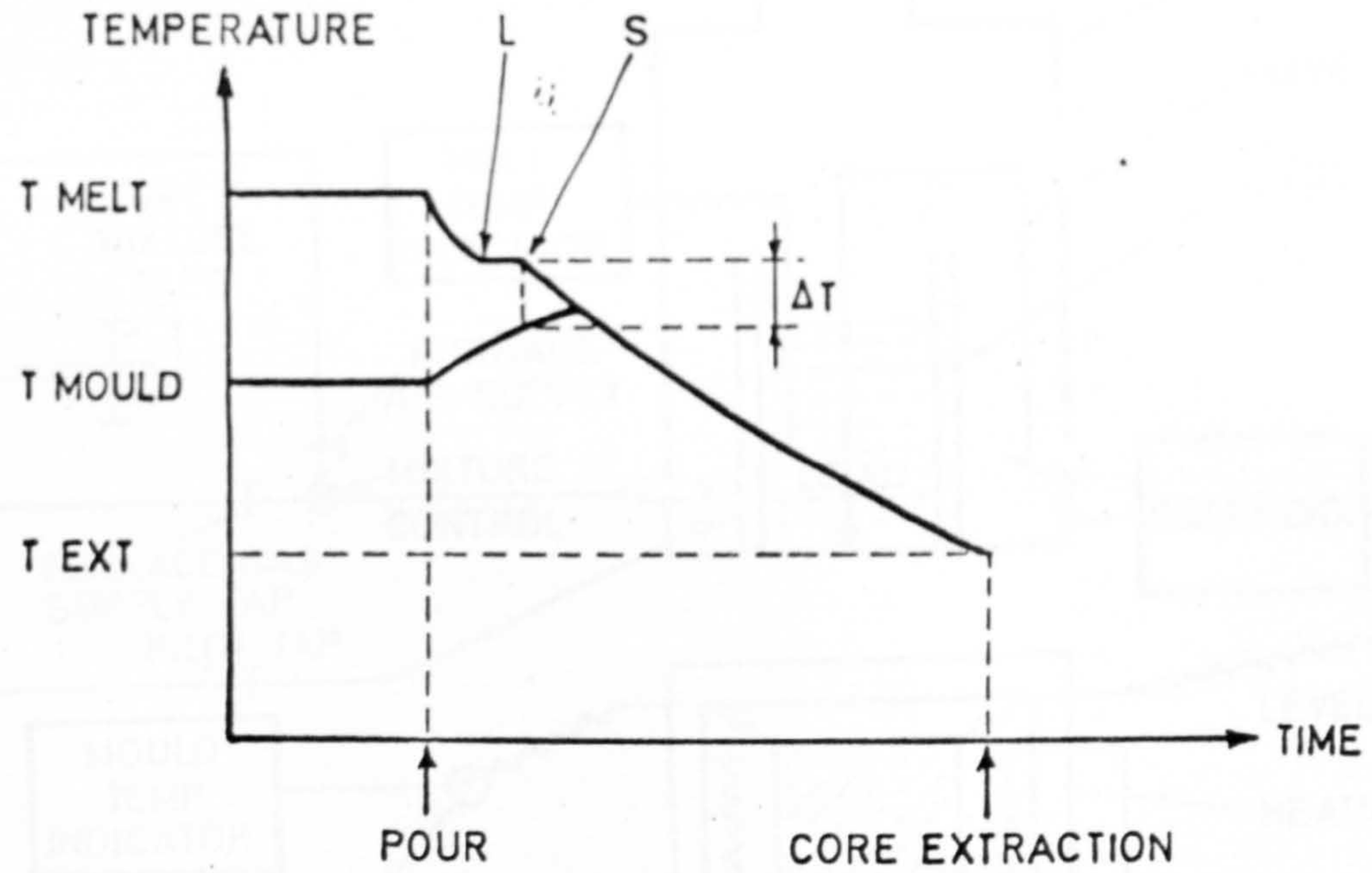

FIG. 4.7 THE COOLING PROCESS (IDEALISED)

FIG. 4.9 THE HEATING BOX

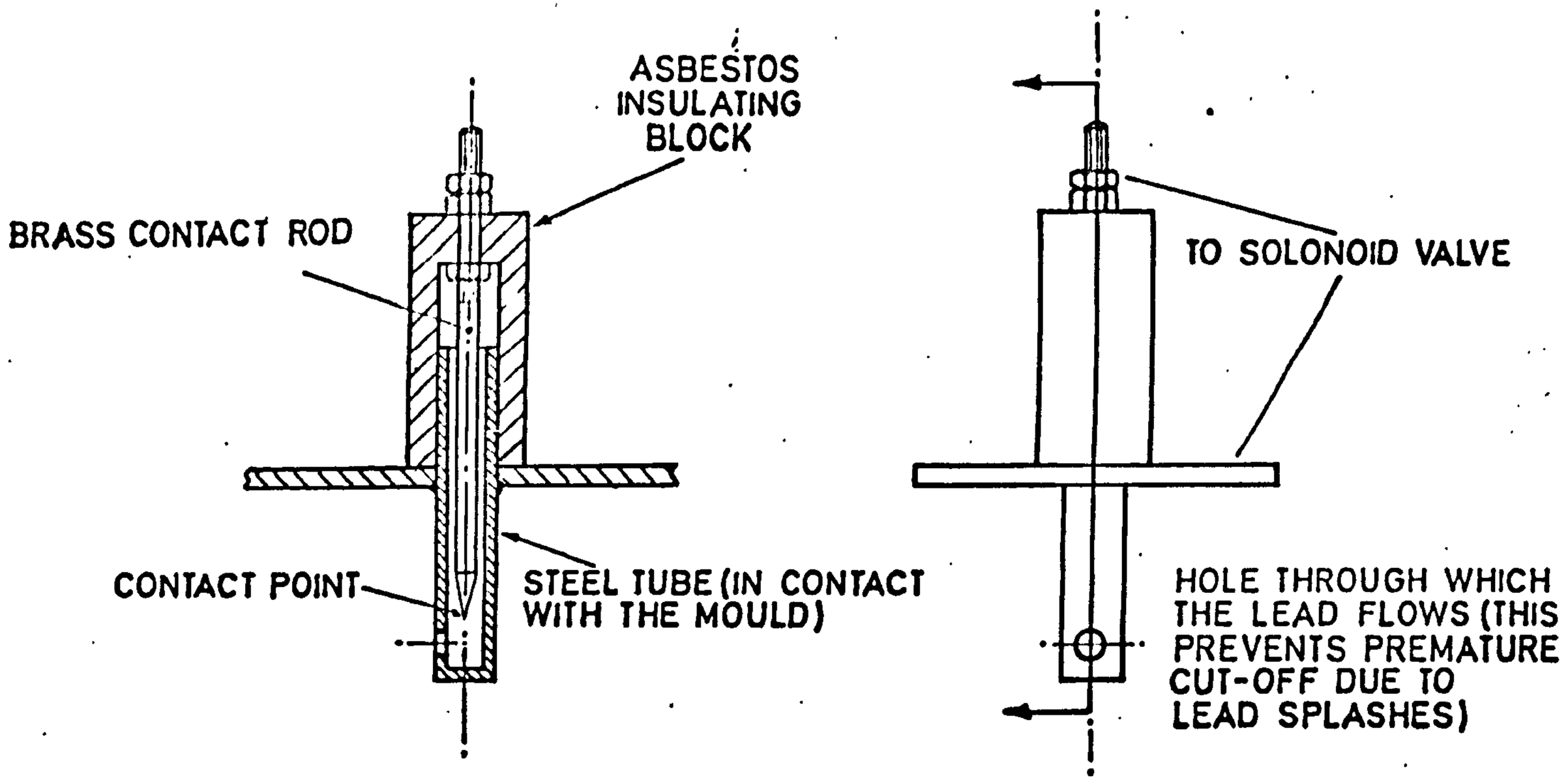

FIG. 4.10 THE LEVEL SWITCH

CHAPTER 5

5. UNIAXIAL CALIBRATION OF CHILL CAST Sb-As ALLOYS OF LEAD

5.1 Objectives

a) To obtain an alloy suitable for

(i) deformation model testing,

(ii) rupture model testing

b) To represent the uniaxial creep data of this alloy by a single creep law.

5.2 Experimental requirements

In order to achieve the objectives, five types of tests were carried out:

(i) tensile tests,

(ii) constant load creep tests (in which both initial and creep deformationswere measured),

(iii) stepped load creep tests (to obtain the variable load characteristics of the material, i.e. "time" or "strain" hardening, etc.),

(iv) constant load creep rupture tests, and

(v) stepped load creep rupture tests.

5.3 Calibration of 1.2% Sb, 0.12% As lead alloy

The material for the specimens made of this composition was obtained from a chill cast model of the thick flanged turbine casing T14 (Ref. 57). The uniaxial data from this casting was used to assess various creep laws and to obtain a single creep law to represent the data over wide ranges of stress.

5.3.1 Experimental conditions

The uniaxial clamps and loading rigs are shown in Figs. 5.1(a)-(c) and the uniaxial specimen is shown in Figs. 5.2 and 6.1.

Previous experience by Bellamy (56) on the application of a uniaxial load through sharply pointed cones showed that the points soon become rounded and cause a non-axial load to be applied. To overcome the problem of wear, a system which incorporates circular knife edges (Fig. 5.1(b)) was devised. The circular knife edges were machined so that they could be accurately positioned between the two clamping plates when the two concentric dowels on the circular knife edges pass through the dowel holes in the clamping plates. Fig.5.1(c) shows one of a pair of 'leaf spring' alignment jigs. With the uniaxial specimen (Fig. 5.2) lightly clamped in position by means of the two clamping studs, the four feet of each of the alignment jigs are made to touch the concentric dowels of the circular knife edges and a load of about 20 kgf is applied to the centre of the leaf springs so that the uniaxial specimen is lightly clamped between the "specimen clamping points". At this stage, the specimen is clamped in position by means of the clamping studs and a line joining the centres of the circular knife edges should pass along the axis of the uniaxial specimen. With the sides of the load hangers parallel to the sides of the clamping plates and the G-shaped knife edges placed in the centre of the load hangers, the system should pull axially. The loading is applied to the uniaxial specimen through an 8:1 lever arrangement. The three knife edges on the lever arm are in line and the lever arm is stiff enough to ensure that the three knife edges stay in line when the load is applied, which ensures that the lever ratio remains constant while the lever rotates. With this loading arrangement, which incorporates six

knife edges, tests carried out on an aluminium uniaxial specimen show that the load is applied axially to within 0.03 mm. TML strain gauges (type PL20) were used in conjunction with Tecquipment strain bridges in order to measure the strains. The temperature was maintained at $20^{o}C$ $\pm \frac{1}{2}^{o}C$. The positions from which the specimens were taken are shown in Fig. 5.3.

5.3.2 "Zero Time" data

The instantaneous strains upon loading are shown in Fig. 5.4 together with an unloading line obtained from a specimen with small plastic strain shown in Fig. 5.5.

From Figs. 5.4 and 5.5 it can be seen that the Young's modulus is 2.15×10^{4} N/mm^2 and the yield stress is about 6 N/mm^2. Poisson's ratio is 0.44; this was obtained from an unloading test carried out on a biaxial specimen (see chapter 7). Hoffmann (2) confirms these values for the elastic constants.

5.3.3 Creep data

Uniaxial tests were carried out at seven stress levels ranging from 2.76 N/mm^2 to 11.06 N/mm^2. In an eighth test, a stress of 15.21 N/mm^2 caused immediate rupture. The "raw" data from the creep tests is shown in Figs. 5.6, 5.7 and 5.8.

Straight lines were drawn through the log (ε_c) v log (t) plots. However, due to the scatter at 2.76 N/mm^2 it was decided to obtain a relationship between the gradient of these straight lines (the time index "m") and the stress and to extrapolate to 2.76 N/mm^2 by using this function. A quadratic was fitted to the data by a "least squares" method and the result is shown in Fig. 5.9.

It was found that

$$m = 0.1265 + 0.02375\,\sigma + 0.001143\,\sigma^{2} \qquad 5.1$$

with a standard derivation of 0.0224. This gave a value of m = 0.206 at $\sigma = 2.76$ N/mm^2. A straight line with this gradient was then drawn

through the points corresponding to $\sigma = 2.76\ N/mm^2$ on Fig. 5.8.

N.B. This gives the best value for m at $\sigma = 2.76\ N/mm^2$ taking all six other stress levels into account. However, from Fig. 5.9, it can be seen that a discontinuity exists at a stress value in the region of the yield stress. If two different curves had been fitted (on either side of the discontinuity) a higher value of m at $\sigma = 2.76\ N/mm^2$ would have been obtained.

Fig. 5.10 shows isochronous strain v stress plots at 0.1, 1,10 and 100 h. It was initially assumed that an "n power" law could be fitted to the creep data.

$$\text{i.e. } \varepsilon_c = \sigma^n \Gamma(t) \qquad 5.2$$

where n is a constant and $\Gamma(t)$ is a function of time only. However, when the "n power" law was fitted to the data of Fig. 5.10 at times 0.1, 1, 10 and 100 h (the results displayed in Table 5.1) it was found that n was not a constant. The "n power" laws were fitted to the actual data (not the log (data)) so as not to give undue weighting to the lower strain values. Using these n power laws, the prediction of creep strains at low stresses is very inaccurate, (e.g. the "n power" law at 100 h predicts a creep strain of $1\mu\varepsilon$ at a stress of $2.76\ N/mm^2$ whereas the actual strain reading was $35\mu\varepsilon$). It was therefore decided that the "n power" law could not be used for stresses below $7\ N/mm^2$.

In order to obtain a better fit to the low stress data, it was decided to fit a "sinh" law to the creep data

$$\text{i.e. } \varepsilon_c = \sinh\left[\frac{\sigma}{C}\right] \Gamma(t) \qquad 5.3$$

The standard deviations in Table 5.2 show that the fit is much better. However, it can be seen from Table 5.2 that C is not a constant but is time dependent whereas $\Gamma(t)$ is approximately independent of time and C. This implies that equation 5.3 should be changed to the form

$$\varepsilon_c = B \sinh \left[\frac{\sigma}{C(t)}\right] \qquad 5.4$$

where B is a constant

and C(t) is a function of time.

Because of the uncertainty of extrapolating C(t) to small times it was decided to fit a law of the form

$$\varepsilon_c = A t^{(a + b\sigma + c\sigma^2)} \sinh\left[\frac{\sigma}{C}\right] \qquad 5.5$$

where a, b and c are obtained from equation 5.1 and A and C are the best fit constants over a range of time. From Fig. 5.10 and Table 5.3 it can be seen that fitting this law at times 0.1, 1, 10 and 100 h gives good results without great loss of accuracy at low stress values.

Table 5.3 also shows the same law fitted at times 25, 50, 75 and 100 h and there is practically no difference between the results.

The law

$$\varepsilon_c = c\, t^{0.333} \sinh\left[\frac{\sigma}{c}\right] \qquad 5.6$$

was also fitted to the data at times 0.1, 1, 10 and 100h but a very poor fit was obtained (particularly at high stress levels). However, if this law were only applied to the data for which little initial plasticity was obtained (i.e. 7 N/mm^2 and below) it is expected that a reasonable fit would be obtained. The results of this law are given in Table 5.3.

5.3.4 Conclusion

The best creep law to fit the data was found to be

$$\varepsilon_c = 11.977 \sinh\left[\frac{\sigma}{3.262}\right] t^{(0.1265 + 0.02375\sigma + 0.001143\sigma^2)} \qquad 5.7$$

t in h, σ in N/mm^2, ε_c in $\mu\varepsilon$

which is shown (by a dotted line) on Figs. 5.6, 5.7, 5.8 and 5.10.

5.4 Selection of model material

5.4.1 Basis of material selection

The modelling method used by R.A. Bellamy (56) requires various correlation between the model and prototype material properties. However, it has been shown (Chapter 3) that the stationary creep solution can be obtained from tests on model components, without the rigorous correlations previously required. Therefore, in order to predict creep strains, the model material need only be chosen such that

(a) small grained, homogeneous and isotropic castings can be produced in a laboratory,

(b) reasonable creep strains can be obtained for small loads at moderate temperatures (i.e. 1% creep strain in 200 h at 20°C).

In order to predict prototype rupture, the model material must be chosen such that its ductility is similar to that of the prototype material. The reasons for this are,

(a) the model and prototype must be dimensionally similar at the time of rupture,

(b) the place at which the model and prototype rupture must be the same (i.e. the modes of failure must be the same, brittle or ductile).

Although it is realised that the tensile and creep rupture properties may not be closely related, it was decided (because of the time required for creep rupture testing), that the selection of the model material should be based upon the tensile rupture properties of the model and prototype materials.

5.4.2 Tensile data

One prototype material, $2\frac{1}{4}$ Cr Mo steel in the normalised and tempered state, is fully described in Section 5.6. Only the tensile properties (ref.(58)) are required for the present application. The tensile ductility properties of $2\frac{1}{4}$ Cr Mo steel (in the normalised and tempered

state) are shown in Fig. 5.11. It should be noted that the ductility of $2\frac{1}{4}$ Cr Mo steel is similar to that of many other steels, which means that if the model material is suitable for modelling $2\frac{1}{4}$ Cr Mo steel, it may also be applied to other steels.

In order to obtain a suitable model material, tensile tests were carried out on uniaxial specimens made from chill cast Sb - As alloys of lead with various antimony and arsenic compositions (the As composition was fixed at 10% of the Sb composition for all castings). The tensile tests were carried out on a Hounsfield Tensometer (Type W) motor driven to give a straining rate of 0.16%/sec using number 12 test pieces. Table 5.4 summarises the data obtained from the tensile tests (for nominal alloying compositions) and Table 5.5 gives the average data (excluding faulty specimens). The results of Table 5.5 are shown plotted in Figs. 5.12 and 5.13.

On the basis of these tests, and tests carried out by Bellamy (56) on a 1.2% Sb, 0.12% As - lead alloy, it was decided that the composition of the lead alloy should be 1.6% Sb, 0.16% As and castings were produced with this nominal material composition, the exact composition being obtained by an X-ray fluorescence method. The exact compositions of these castings are given in Table 4.4.

The results of tensile tests carried out on specimens taken from two of the castings (P7 and P9) are shown in Tables 5.6 and 5.7 (the points are also shown in Figs. 5.12 and 5.13).

From Tables 5.6 and 5.7 it can be seen that the tensile properties of the "exact" material are very consistent.

The UTS obtained for the 1.6% Sb - 0.16% As - Pb was found to be 25.8 N/mm^2, which compares favourably with published work carried out on a similar material (ref. 2) from which the UTS for a 1.5% Sb - Pb alloy is quoted as 23.4 N/mm^2.

5.5 Calibration of 1.6% Sb, 0.16% As lead alloy

5.5.1 Experimental conditions

Creep tests were carried out on 58 test specimens obtained from 4 castings (of two different types). The casting numbers are P7, P9, KK19 and KK20 and the compositions are given in Table 4.4. The positions from which the specimens were taken are shown in Figs. 5.14 and 5.15. The test specimens and loading rigs were the same as those used to test the 1.2% Sb, 0.12% As lead alloy. The method of obtaining the strains was improved by incorporating a 100 channel "data logging" system capable of taking readings at time intervals of about 0.3 sec.

5.5.2 "Initial" data

The instantaneous strains upon loading and unloading for all tests performed at stresses of 14.10 N/mm^2 and below for which strain gauges were used are shown in Figs. 5.16(a) and 5.16(b) respectively.

From the unloading strains, the Young's modulus of the material of each casting and the overall Young's modulus were found and are shown in Table 5.8. The yield stress for all of the castings was found to be about 7 N/mm^2, this was not very well defined, but the 0.1% proof stress was found to be between 12 N/mm^2 and 14 N/mm^2 for all of the castings (as shown by Fig. 5.16(a)).

5.5.3 Constant load creep data

For the P7, P9, KK19 and KK20 castings, 40 uniaxial creep tests were carried out on strain gauged specimens, at stress levels between 3.5 N/mm^2 and 14.1 N/mm^2, 18 additional high stress tests with stresses up to 26.4 N/mm^2 were carried out on specimens for which dial gauges were used to obtain the strains (most of these being on the specimens from the P7 casting). Table 5.9 shows the initial stress at which each of the specimens was tested. The symbols relating to each test which were used for producing the material data plots are also shown in Table 5.9.

The "raw" data from these creep tests are shown in Fig. 5.17(a) for casting P7, 5.17(b) for casting P9 and Fig. 5.17(c) for castings KK19 and KK20. This data is also shown plotted for each individual stress level in Figs. 5.18(a)-(n).

From the experience obtained in analysing the 1.2% Sb, 0.12% As lead alloy, it was decided that the best representation of creep data is obtained by fitting a law of the form of equation 5.5. Since the majority of the creep tests were carried out for stresses up to 14.1 N/mm^2 it was decided to fit creep laws (equation 5.5) up to 14.1 N/mm^2 only. Following the procedure of section 5.3.3, quadratics were fitted to the time indices for each of the sets of data and for the overall data. The results of this curve fitting are given in Table 5.10 and Figs. 5.19(a)-(d). It was found that the average of the constants obtained for the individual castings were practically the same as the constants obtained for the overall data, but no good reason for this could be found to justify using this to predict creep laws for other compositions.

Using these quadratic forms for the m values, the constants A and C in equation 5.5 were obtained by a least squares curve fitting method, using the appropriate values of a, b and c for each set of data. The results of this curve fitting are given in Table 5.11. The accuracy of the individually "fitted" creep laws may be seen from Figs. 5.17(a)-(c) to be very good (as the standard deviations of Table 5.11 imply), particularly at low stress levels (Figs. 5.20(a)-(c)). The accuracy of the overall law was not so good, which may be seen from Figs. 5.18(a)-(g), and as indicated by the standard deviation of Table 5.11. However, Figs. 5.18(a)-(g) show that the overall creep law falls within the scatter band at each of the stress levels at which tests were performed and again the results were particularly good at low stress levels (Figs 5.21(a)-(d)), which is where the "n power" law is not suitable.

5.5.4 Stepped load creep tests

In the previous section, only constant loads were considered. However, some of the uniaxialtests were stepped load tests. Stepped up loading was usually performed after 100 h (in which case the first 100 h of the test could be used in the uniaxial calibration) and stepped down loading was usually performed between 5 and 20 h after initial loading.

The stepped loadings were chosen so that the effect on creep behaviour could be studied when stepping from

(i) an initial elastic to an initial elastic stress (up and down)

(ii) an initial elastic to an initial plastic stress (up)

(iii) an initial plastic to an initial elastic stress (down)

and (iv) an initial plastic to an initial plastic stress (up and down)

Table 5.12 shows the stepped load tests which were performed and Figs. 5.22(a)-(h) show these tests plotted to natural scales. Superimposed on these curves are the strain hardening predictions obtained from the individual creep laws for each of the castings (Tables 5.10 and 5.11) and also the strain hardening and time hardening predictions obtained from the raw creep data. From these figures, it can be seen that the strain hardening law fits the data very well for all stress ranges, both stepped up and stepped down loading. However, although the strain hardening law gives a better fit, the fit obtained by using the time hardening law at the lower stresses, is not greatly in error, particularly for the case of stepped down loading, when the time hardening prediction is a "safe" prediction. Cyclic loading tests were carried out on two additional specimens from the P9 casting, the results of which are plotted in Figs. 5.22(i) and 5.22(j). These results also confirm that the strain hardening law gives accurate predictions of strains.

The "total strain" and "hereditary" laws were also considered but they were found to greatly overestimate the amount of creep recovery and, therefore, they were not as good as the "strain hardening" law.

5.5.5 Rupture tests

Rupture tests have been performed on 18 uniaxial specimens having nominal stresses between 19.32 N/mm^2 and 26.35 N/mm^2. Details of the tests are given in Table 5.13. One of the tests (specimen P7/ 6) was a stepped load test for which the life fraction rule (i.e. $1 = \sum t(\sigma)/t_R(\sigma)$) gave a value of 0.76 as opposed to unity.

The percentage elongation and reduction in area at rupture were measured as well as the time to rupture, the results are shown in Fig. 5.23(a) and Table 5.13. From Fig. 5.23(a), it can be seen that with the exception of specimen P7/17, which broke at the clamps, there is very little scatter. Two of the specimens (P7/8 and P9/21) were found to have blow holes which caused the nominal stress to increase. An estimate of the nominal stress was made by taking the size of the blow hole into account. By taking the blow hole into account, the results of these tests fell into line with the other results. The implication of this is that the ductility of the material was such that the effect of the stress concentrations around the blow holes was negligible.

Fig. 5.23(b) shows the creep rupture data in relation to the creep strain data. This plot of stress against time shows the raw data, together with the predictions based upon the overall creep law. Since the overall creep law was only fitted to the data with stresses of 14.10 N/mm^2 and below, the other data points in Fig. 5.23(b) (above 14.10 N/mm^2) have had curves sketched through them to show the general trend.

Using the creep law curves and the sketched curves of Fig. 5.23(b) the plots of stress to cause rupture agains stress to cause a particular

creep strain in the same time (suggested by Murphy (12)) were produced, Fig. 5.23(c). The plots produced by Murphy for a number of steels with different heat treatments were approximated by straight lines. However, as can be seen from Fig. 5.23(c) this is not the case for the lead alloy. Because of the shortage of creep rupture data, it was not possible to produce Fig. 5.23(c) using raw data, therefore it is possible that the curved appearance of Fig. 5.23(c) would not be present if the raw data were used rather than the smoothed data.

5.6 Prototype material

5.6.1 Prototype data requirements

Because of its widespread use in high temperature engineering and because it is currently being considered as a likely candidate for use in nuclear engineering, it was decided that the prototype material should be $2\frac{1}{4}$ Cr Mo steel in the normalised and tempered state (N & T).

Because the creep data which was supplied (ref. 59) was interrupted creep data, the initial plastic strain was not measured. Therefore, it was necessary to obtain tensile data for this material. As already explained in Section 5.4.1, this tensile data (ref. 58) was also used to select a model material suitable for creep rupture testing.

5.6.2 Data sources for $2\frac{1}{4}$ Cr Mo Steel (N & T)

There are no known conventional publications which give the creep properties but the following were made available.

a) BSCC book (ref. 60). Both the tensile and creep data were found to be sparse, e.g. only 0.2% and 1% proof stresses were quoted for the tensile properties.

b) NEL report Z3/17/71 gives some complete creep curves but insufficient data at any one temperature for a reliable creep law to be obtained (ref. 61).

c) Creep data from BSCC (T1 STDDED) (ref. 59) this provided information obtained from interrupted creep tests.

d) Babcock and Wilcox Report No. 1/72/550 provided data from which the initial strains could be estimated for the data obtained from interrupted creep tests (ref. 58).

5.6.3 Analysis of data for $2\frac{1}{4}$% Cr 1% Mo steel (N & T)

To determine creep laws (of the form of "n power" laws or "sinh" laws), it is necessary to have creep data at several stress levels at each temperature of interest. The number of stress levels available are shown in Table 5.14. The most comprehensive data were found in ref. 59, all of these data available are given in Table 5.15 for completeness. The 575°C values used are all plotted in Fig. 5.24.

The data come from several sources and, as large differences between corresponding strains from different sources were found, it was not considered to be worth analysing data with less than three stress levels. Therefore, only two temperatures could be considered as shown in Table 5.16.

To determine the instantaneous plastic strain component of the total plastic strains presented, the average values of four sets of stress-strain data were used to obtain stress (to produce a given plastic strain) v temperature curves, as shown in Fig. 5.25. From these curves, stress v initial plastic strain curves were obtained at 575°C and 600°C, as shown in Figs. 5.26 and 5.27. The latter two curves show that at a stress of 11 tonf/in^2, which is the highest stress used in the creep data, the initial plastic strain is negligible and that at all other stresses, the initial plastic strain is zero. Therefore, the total plastic strain obtained from the interrupted creep tests could be used in the analysis as creep strain.

Although all of the data used was for $2\frac{1}{4}$ Cr Mo steel (nominally) in the normalised and tempered state, the results obtained from each individual source differed quite considerably, as shown in Table 5.16. The stress index (n) used in the creep law

$$\varepsilon_c = A\sigma^n t^m$$

was obtained by a "least squares" method of curve fitting to

(a) the log ε_c v log σ data (Method 1)

and (b) the actual data (Method 2)

The differences in n value for the same temperature and times were attributed to unknown differences in chemical composition, heat treatment, method of production, shape and size of the forgings. To obtain some general impression, these differences were subsequently ignored and combining all the data from Table 5.16 for any one time and temperature, the results shown in Table 5.17 were obtained.

Method 1 fitted straight lines to log strain-log stress data and therefore gave undue weight to the small (less accurate) values. These results are shown in Figs. 5.28 to 5.30 together with the best sinh curves obtained by fitting to the actual data (shown as Method 3 in Table 5.17).

Comparing the "n-values" obtained for the lead alloy (Table 5.1) and for the $2\frac{1}{4}$ Cr Mo steel (Table 5.17), it can be seen that the lead alloy has possibilities for use as a model material for the method used by Bellamy (56) as well as for the proposed experimental Reference Stress model method.

5.7 Discussion

A theoretical analysis of the effects of bending on the creep strain in a tensile specimen has been carried out by Penny and Leckie (62). They show that for n values between 3 and 7 (which is within the range of most engineering materials), the bending can have a significant effect and they suggest that the eccentricity of loading of a uniaxial

specimen should be less than 1% of the radius of the test specimen. The uniaxial testing rig used was such that the eccentricity was within $\frac{1}{2}$% and this was therefore considered to have a small effect on the scatter.

Creep tests carried out by G. Brearley (63) on a lead alloy similar to the lead alloy under present consideration showed that for a 50°C increase in temperature (20°C to 70°C), the creep strains obtained from uniaxial specimens subjected to the same stress were approximately doubled. The temperature variations of 20°C $\pm$ $\frac{1}{2}$°C were therefore considered to have very little effect on the creep strains obtained. The effect of this variation in temperature based upon a linear interpolation, which would overestimate the errors, is less than $\frac{1}{2}$%. Since the weights which were used were accurate to within $\frac{1}{4}$%, it was found that possible errors in the measured strains due to the test equipment are about 2 or 3%.

Since the scatter of creep data within a casting is more than the predicted 2 or 3% (i.e. about 10%) and from casting to casting it is a great deal more (i.e. about 200%), it must be concluded that the scatter is genuine material scatter.

From Table 4.2 it can be seen that the core temperature for casting P9 was slightly greater than that for casting P7 and the creep strains obtained from specimens made from casting P9 were greater than those for casting P7. However, a similar difference in mould temperature for castings KK19 and KK20 caused no significant difference in creep strains obtained from uniaxial specimens cut from the two casting. It was therefore concluded that the casting temperatures were not a critical factor in causing scatter of creep strains.

All of the specimens were tested within a period of 2 to 9 months after casting and no ageing effect was noticed within this time.

A large grained specimen (KK20/3/10) having grains of about 2 mm diameter which was taken from the centre cylinder of casting KK20 was tested at a stress of 7.03 N/mm^2. Three other small grained specimens taken from the same casting were also tested at 7.03 N/mm^2 but although the large grained specimen was slightly more creep resistant, the difference in creep strain were small compared to the cast to cast variations (see Fig. 5.18(c)). However some of the specimens cut from castings P7 and P9 at positions at about 90^o to the pour position were found to be slightly more creep resistant than specimens taken from other parts of the castings (i.e. see specimens P7/3, P7/5, P7/20 in Fig. 5.17(a)). This contradicts the previous findings and therefore it must be concluded that the experimental evidence on the effect of grain size is inconclusive. However, it is obvious that any effect due to grain size is small. It is possible that the creep properties may depend upon the direction in which the stress is applied relative to the direction of flow of the lead alloy during casting. This would account for the slightly different creep properties at 90^o to the pour position in the P7 and P9 castings.

Castings KK19 and KK20 have almost identical antimony compositions (1.45% and 1.48% respectively) and as Fig. 5.17(c) shows, the creep strains obtained from uniaxial specimens taken from these two casting are almost identical with no definite trend towards one or the other being the most creep resistant. However, castings P7 and P9 have antimony compositions which are different to that of castings KK19 and KK20 (1.56% and 1.66% respectively). From these various antimony compositions, it can be seen (Figs. 5.18(a)-(n)) that within the range 1.45 to 1.66% Sb,

the creep strains increase with increasing antimony composition. Hoffman (2) has presented results for different ranges of antimony composition and has shown that the opposite is true, it therefore appears that a plot of creep resistance against antimony composition is of a form similar to that shown in Fig. 5.31. However, the results presented by Hoffmann are sparse and from a number of different sources, which makes it difficult to quantify the relationship illustrated in Fig. 5.31. As well as the creep strains increasing with antimony composition, there is a tendency for the time index "m" to increase with antimony composition and since the "C" value in the "sinh" law decreases with increasing antimony composition, the stress index "n" in the simple "n-power" law also increases with antimony composition. However, there does not appear to be a simple relationship between the constants in the creep laws and the antimony composition. Many tests were carried out at stresses of 7.03 and 8.78 N/mm^2 from which the ratio of the maximum creep strains (in casting P9) to the minimum creep strains (in castings KK19 and KK20) is about 4 to 1. Although it does not seem possible to relate the creep law to the antimony composition, by plotting the creep data as creep strain obtained at a particular stress and time against antimony composition (as shown in Fig. 4.32), the creep strain at the same stress and time may be obtained for any antimony composition from a curve drawn through the data points. By this method, a set of creep data may be generated for any antimony composition and a law may be fitted to this generated creep data.

From Fig. 5.32 it can be seen that a linear relationship between creep strain (at a particular stress and time) and antimony composition will give a reasonable fit to the data and a better fit may be obtained if two straight lines are drawn (shown dotted in Fig. 5.32). Using this fact, the creep law for a particular antimony composition may be obtained without the need for further curve fitting to generated creep data.

For two alloys with different antimony compositions (X_1% and X_2%) the creep laws are

$$(\varepsilon_c)_{X_1} = A_1 \sinh \left[\frac{\sigma}{c_1}\right] t^{m_1(\sigma)}$$

and $$(\varepsilon_c)_{X_2} = A_2 \sinh \left[\frac{\sigma}{c_1}\right] t^{m_2(\sigma)}$$

On the assumption that a linear relatinshop exists between creep strain and antimony composition, the creep strains in an alloy with an antimony composition of X_3% will be given by $(X_1 < X_3 < X_2)$

$$(\varepsilon_c)_{X_3} = \frac{(X_2 - X_3)}{(X_2 - X_1)} (\varepsilon_c)_{X_1} + \frac{(X_3 - X_1)}{(X_2 - X_1)} (\varepsilon_c)_{X_2}$$

i.e.

$$(\varepsilon_c)_{X_3} = \frac{(X_2 - X_3)}{(X_2 - X_1)} A_1 \sinh \left[\frac{\sigma}{c_1}\right] t^{m_1(\sigma)} + \frac{(X_3 - X_1)}{(X_2 - X_1)} A_2 \sinh \left[\frac{\sigma}{c_2}\right] t^{m_2(\sigma)}$$

From Figs. 5.18(f)-(l) it can be seen that at stresses greater than about 12 N/mm^2, there is a tendency for the material to become significantly more creep resistant after a time of between 10 and 20 h. In order to gain some insight into this effect, a specimen (P7/22) was loaded with a stress of 14.05 N/mm^2 and was then immediately unloaded and left unloaded for 10 h. Upon reloading after 10h, it was found that the specimen was more creep resistant than the virgin material. The result of this test confirmed the suspicion that the effect of increased creep resistance was time dependent rather than strain dependent. Although there is no metallurgical evidence, this increase in creep resistance may be due to recrystallisation, fragmentation or precipitation

hardening. Finnie and Heller (3) show that a similar effect is obtained from 18% Cr, 8% Ni steel with small amounts of titanium and columbium. Their precipitation as carbide takes place in part within the grains and enhances creep resistance.

On the basis of a limited number of tests shown in Fig. 5.23 the rupture time and rupture ductility do not appear to be strongly dependent upon the antimony composition.

TABLE 5.1

Individual "n Power" laws

TIME	$\Gamma(t)$	n	$\sum(\text{error})^2$	St. Dev.
0.1	0.835	1.654	44.43	2.519
1	0.143	2.968	404.03	7.597
10	0.0235	4.293	2631.40	19.389
100	0.00679	5.372	20127.59	53.622

TABLE 5.2

Individual "Sinh" laws

TIME(h)	$\Gamma(t)$	C	$\sum(\text{error})^2$	St. Dev.
0.1	10.6863	5.092	17.397	1.576
1	8.7824	2.962	53.999	2.777
10	8.9700	2.179	418.95	7.736
100	10.5715	1.766	7530.28	32.799

TABLE 5.3

Overall Laws

LAW (ε_c =)	TIMES FITTED	A	C	$\sum error^2$	St. Dev.
$At^{a+b\sigma+c\sigma^2} \sinh\left[\frac{\sigma}{C}\right]$	0.1, 1, 10 and 100 h	11.877	3.262	9353.34	18.28
"	25, 50, 75 and 100 h	11.933	3.268	19234.99	26.21
$At^{0.333} \sinh\left[\frac{\sigma}{C}\right]$	0.1, 1, 10 and 100 h	2.4726	1.823	511236.98	135.12

Table 5.4 Tensile Properties for Nominal Material

Strain Rate = 0.16%/sec *Faulty Specimen

Material and Source	UTS (N/mm^2)	Elong. %	R.A. %
(A)			
6% Sb, 0.6% As-Pb (NOM)	42.2	16	13
CASTING 2	38.8	16	14
CAST DATE 20.12.73	38.8	17.5	15
TEST DATE 8.1.74	39.4	16	14
(B)			
3.6% Sb, 0.36% As-Pb (NOM)	37.2	14	16
CASTING 9	35.7	13	19
CAST DATE 16.5.74	*32.9	5	5
TEST DATE 9.6.74	36.3	14	12
	36.3	15	21
(C)			
1.8% Sb, 0.18% As-Pb (NOM)	*28.4	4	5
CASTING 10	36.3	16	25
CAST DATE 12.6.74	*32.0	11	12
TEST DATE 19.6.74	*31.8	9	11
(D)			
1.6% Sb, 0.16% As-Pb (NOM)	31.2	25	35
CASTING 12	32.6	24	35
CAST DATE 27.6.74	31.8	21	32
TEST DATE 10.7.74	29.0	23	36
	30.6	28	38
	*25.3	12	19
(E)			
1.6% Sb, 0.16% As-Pb (NOM)	32.3	20	29
CASTING 13	31.8	15	22
CAST DATE 28.6.74	32.9	18	35
TEST DATE 12.8.74	31.5	26	36
	30.9	20	37
	30.6	24	38

Table 5.5 Average Tensile Properties For Nominal Material

Material *	UTS (N/mm^2)	Elong. %	R.A. %
A	39.8	16.4	14.0
B	36.4	14.0	17.0
C	36.3	16.0	25.0
D	31.0	24.2	35.2
E	31.7	20.5	32.8

* referenced in Table 5.4

Table 5.6 Tensile Properties

Material and Source	UTS (N/mm^2)	Elong. %	R.A. %
(A)			
1.56% Sb, 0.15% As-Pb	25.0	27	35
CASTING P7	24.7	26	36
CAST DATE 18.9.74	27.3	28	39
TEST DATE 27.9.74	26.1	34	41
	25.9	32	38
(B)			
1.66% Sb, 0.15% As-Pb	25.9	35	42
CASTING P9	26.0	30	40
CAST DATE 20.9.74	27.3	34	44
TEST DATE 9.1.75	25.4	23	28
	25.5	29	39
	25.3	28	37

Table 5.7 Average Tensile Properties

Material Reference in Table 5.6	UTS (N/mm^2)	Elong %	R.A. %
A	25.8	29.4	37.8
B	25.9	29.8	38.3

Table 5.8 Young's moduli

Casting No.	E(N/mm^2)
P7	2.28×10^4
P9	2.34×10^4
*KK19 & 20	2.34×10^4
OVERALL	2.32×10^4
T14	2.15×10^4

* KK19 and 20 are included together because so few tests were done on each and because the compositions are almost identical (Table 4.4)

Table 5.9 Uniaxial Creep Tests

STRESS LEVEL (N/mm^2)	P7			P9			KK19			KK20			T14		
	SPEC.	SYM-BOL	TEST TIME (h)	SPEC.	SYM-BOL	TEST TIME (h)	SPEC.	SYM-BOL	TEST TIME (h)	SPEC.	SYM-BOL	TEST TIME (h)	SPEC.	SYM-BOL	TEST TIME (h)
2.81													9		990
3.51	31	+	70	7	◐	100				5/2	◒	100			
4.50													8		1020
5.27	12 20	× ○	210	20	◭	263	1/12	▬	239						
5.62													2		190
7.03	3 15 21 30	△ ◁ ▽ △	645 210 100 5	4 13 28	▽ ▷ ◁	214 100 5				5/1 4/8 4/9 3/10	◭ ◁ ▽ ◁	239 100 5 239	11		315
8.43													5		188
8.78	7 11 29	□ ◇ ⊕	645 210 10	6 12 22	◖ ◧ ◭	214 10 100	1/13	◆	100	5/3	▬	10			
9.84													6		340
10.54	2 9 28	⊗ ◐ △	114 210 20	5 29	◭ ◓	214 20	1/14	◀	20	5/4	◆	239			
11.24													1		320
12.30	4	▽	549	11	△	214									
14.05	1 5 22	▷ ▣ ◁	120 203°	27	▽	214				4/7	⊞	239			
15.46													10		0
15.81	26D	◇	100												
17.57	18D	⊥	100	15D	▷										
19.32	17D	⊼	503(R)												
21.08	24D	◑	935(R)												
22.84	6D 10D 16D 32D	◭ ▽ ▷ ◁	46.2 73.1(R) 0(R) 162.7(R)	23D	◁		1/11D	◀	209.9R	5/5D	⊠				
24.59	8D 27D	▯ ◊	0.583(R) 30.85(R)	21D	◊	1.15R				5/6D	⊕	0(R)			
26.35	23D 25D	⊽ ◔	0.425(R) 0.56												

• Immediately unloaded and then reloaded after 10h.

Symbols are used in Figs. 5.17(a)-(c), 5.18(a)-(n), 5.22(a)-(h).

Table 5.10 Constants of the time index quadratic

Casting	a	b	c	St. Dev.
P7	.17221	.032093	-0.0006886	.0190
P9	.07004	.068899	-0.0031190	.0271
KK19 & 20	.17476	.027408	-0.0006512	.0109
OVERALL	.13877	.042849	-0.0014744	.0230
AVE. OF P7, P9 & KK's	.13900	.042800	-0.0014845	
T14	.12650	.023752	0.0016263	.0224

Table 5.11 Sinh Laws:- $\varepsilon_c = B \sinh\left[\frac{\sigma}{C}\right] t^{m(\sigma)}$

Casting Number	B	C (N/mm^2)	St. Dev. $\mu\varepsilon$	Stress Range (N/mm^2)
P7	3.9023	2.443	312.2	3.51 to 14.05
P9	5.5638	2.273	366.6	" "
KK19 & 20	3.750	2.733	52.871	" "
OVERALL (1.6 nom)	5.5178	2.503	826.2	" "
AVE. OF P7, P9 & KK's	5.8603	2.763		
T14	11.877	3.316	26.21	2.81 to 11.24

Table 5.12 Stepped Load Tests

Casting	Spec.	Initial Stress (N/mm^2)	Stepped Stress (N/mm^2)	Time before step (h)	Total time of test (h)	Symbol
P7	26D	15.81	17.55	100	Still on	
	18D	17.57	19.32	100	Still on	
	20	5.27	7.03	100	213	
	21	7.03	8.78	100	213	
	6D	22.84	24.59	46.2	50.5R	
	28	10.54	8.78	20	213	
	29	8.78	7.03	10	213	
	30	7.03	5.27	5	213	
	31	3.51	5.27	70	213	
P9	28	7.03	5.27	5	213	
	29	10.54	8.78	20	213	
	7	3.51	5.27	100	263	
	12	8.78	7.03	10	263	
	13	7.03	8.78	100	263	
	22	8.78	10.54	100	263	
KK19	1/14	10.54	8.78	20	213	
	1/13	8.78	10.54	100	214	
KK20	5/2	3.51	5.27	100	214	
	4/8	7.03	8.78	100	214	
	5/3	8.78	7.03	10	214	
	4/9	7.03	5.27	5	214	

D indicates that the creep strains were obtained by use of dial gauges rather than ERS gauges.

Table 5.13 Rupture Data

Casting	Spec.	Stress (N/mm^2)	Life (h)	% Elong.	% R.A.	Symbol
P7	25	26.35	0.558	29.43	37.55	
	27	24.59	30.85	22.93	17.77	
	32	22.84	162.7	18.87	22.53	
	10	22.84	73.1	14.57	22.50	
	23	26.35	0.425	28.97	42.97	
	8	24.59 (26.14*)	0.583	15.27	28.57 (32.60)	
	6	22.84 to 24.59 @ 46.2 h	50.5	22.53	17.62	
	16	22.84	0	7.0 +	6.57	
	17	19.32	503	9.90 x	4.14	
	24	21.00	935	22.7	14.82	
P9	23	22.84	2624	17.1	23.4	
	21	24.59 (26.14*)	1.15	26.5	28.88 (33.08)	
KK19	1/11	22.84	209.9	30.4	24.5	
KK20	5/5	22.84	5184	still on		
	5/6	24.59	0	7.90 +	5.36	
T14	10	15.46	0	30.77 +	35.23	
KK16	5/1	23.93	75.9	17.44	15.44	
KK16	4/4	24.82	47.3	23.67	17.29	
KK16	4/5	22.5	2688.5	15.03	17.70	

x Broke at clamp

\+ Broke immediately

* Nominal stress when blow hole is taken into account (at t = 0)

Table 5.14 Summary of available data

Temperature °C	Number of stress levels after					
	100h	300h	1000h	3000h	10 000h	30 000h
550	1	2	2	2	2	0
565 & 566	4	4	3	2	1	1
575	1	6	7	6	4*	1
580	2	2	1	0	0	0
593	0	0	1	1	0	0
600	4	4	2	1	1	0
621	4	3	2	0	0	0
625	0	2	2	1	0	0
640	2	1	0	0	0	0

* very small range 56 to 70 N/mm^2

Table 5.15 Total Plastic Strain Data for 2¼ Cr Mo Steel (Normalised and Tempered)

Temperature °C	Stress N/mm²	Cast No. or Identity	Total Plastic Strain at 100h	300h	1000h	3000h	10 000h	30 000h	Final Duration h	Final Strain %
550	93	61987	-	0.5	0.58	0.78	1.6	-	17000	3.2
	93	62526	-	0.11	0.21	0.42	1.2	-	17000	2.2
	93	H7484	-	0.18	0.24	-	-	-	2100	0.31
	85	MCRR1C2	0.045	0.095	0.27	0.78	3.3	-	24000	20
565	154	H7484	0.32	0.64	-	-	-	-	550	1.0
	154	H7484	0.53	0.82	-	-	-	-	460	1.0
	124	H7484	0.31	0.72	-	-	-	-	360	0.95
	124	H7484	0.19	0.36	0.80	-	-	-	1400	1.0
	93	H7484	0.16	0.23	0.33	0.63	-	-	5000	1.0
	62	H7484	0.95	0.13	0.19	-	-	-	2000	0.24
566	70	DS	-	-	-	0.41	0.72	1.6	70000	25
	70	DQ	-	-	-	-	0.56	2.1	54000	39
	70	DR	-	-	-	0.35	0.68	3.4	46000	34
575	170	61987	-	2.2	-	-	-	-	660	15
	170	61802	-	5.2	-	-	-	-	440	27
	139	61987	-	0.66	1.8	-	-	-	1900	10.5
	139	62526	-	2.1	29	-	-	-	1000	29
	139	61802	-	1.8	6.0	-	-	-	1170	21
	124	61987	-	0.6	1.4	-	-	-	2900	26
	124	62526	-	1.7	3.4	10.0	-	-	5400	50
	124	61802	-	0.8	1.6	10.0	-	-	3200	31
	116	PR	-	-	1.8	-	-	-	2200	22
	116	PM	-	-	2.7	-	-	-	2150	29
	100	PR	-	-	-	6.5	-	-	3300	23
	100	PP	-	-	-	-	-	-	2700	23
	93	61987	-	0.3	0.59	0.4	-	-	7200	30
	93	62526	-	0.45	0.86	2.4	-	-	6400	28
	93	61802	-	0.23	0.47	1.06	-	-	6400	2.2
	70	PR	-	-	-	-	3.2	-	12000	7.2
	70	PP	-	-	0.32	0.74	5.5	-	12000	16
	70	PM	-	-	-	-	2.0	-	16000	24
	62	62526	-	0.16	0.35	0.66	1.05	-	17500	1.25
	62	61987	-	0.14	0.4	0.7	1.8	-	19500	22
	59	MCRR/CR	0.073	0.155	0.36	0.72	2.1	13.5	35000	20
	56	PP	-	-	-	-	1.4	-	22500	24
580	124	H7484	0.36	0.60	-	-	-	-	780	1.03
	93	H7484	0.21	0.30	0.55	-	-	-	2000	1.05
593	85	DR	-	-	0,62	2.1	-	-	5600	54
	85	DQ	-	-	0.65	1.9	-	-	6000	46
	85	DS	-	-	1.2	3.2	-	-	7000	43
600	139	H7484	3.7	15	-	-	-	-	310	15.5
	139	61987	-	-	-	-	-	-	410	300
	139	61802	-	-	-	-	-	-	380	29
	124	H7484	0.59	1.0	-	-	-	-	300	1.0
	124	61987	-	1.2	-	-	-	-	810	15
	124	61802	-	2.4	-	-	-	-	740	28
	124	62526	-	-	-	-	-	-	460	30
	93	H7484	0.3	0.51	-	-	-	-	700	1.0
	93	61987	-	0.56	1.8	-	-	-	1900	24
	93	61802	-	0.66	1.4	-	-	-	2900	29
	93	62526	-	0.64	1.05	-	-	-	2500	46
	62	H7484	0.12	0.25	0.72	-	-	-	1400	1.0
	62	61987	-	0.28	0.58	1.6	-	-	8400	34
	62	61802	-	0.24	0.44	1.0	8.5	-	11200	29
	62	62526	-	0.22	0.42	1.06	-	-	9560	34
	62	1/4786T	-	-	-	1.1	-	-	3900	2.1
	62	1/4786L	-	-	-	1.3	-	-	3900	1.9
	62	1/4786	-	-	-	-	-	-	9500	54
621	124	H7484	-	-	-	-	-	-	33	1.0
	93	H7484	0.55	-	-	-	-	-	200	1.0
	62	H7484	0.11	0.38	-	-	-	-	590	1.0
	48	H7434	0.16	0.29	1.1	-	-	-	1000	1.1
	39	H7484	0.088	0.17	0.54	-	-	-	1500	1.0
625	93	61987	-	1.75	-	-	-	-	540	22
	93	61802	-	1.2	-	-	-	-	850	25
	93	62526	-	1.7	-	-	-	-	660	28
	62	61987	-	0.66	2.2	-	-	-	2000	30
	62	61802	-	0.72	1.85	-	-	-	2500	31
	62	62526	-	0.74	2.1	-	-	-	2200	34
	46	61987	-	-	1.03	2.4	-	-	5700	37
	46	61802	-	-	1.00	4.1	-	-	4200	30
	46	62526	-	-	0.76	1.9	-	-	6000	28
640	108	H7484	-	-	-	-	-	-	24	1.0
	93	H7848	-	-	-	-	-	-	45	1.0
	62	H7484	0.94	-	-	-	-	-	105	1.0
	46	H7484	0.26	0.7	-	-	-	-	410	1.0

Table 5.16 Useful data and stress indices for each set

Material Reference	Temperature °C	Time h	Stress Index n	No. of stress levels
61802	575	300	5.20	4
61987	575	300	2.52	4
62526	575	300	3.31	4
61802	575	1000	5.94	3
61987	575	1000	1.90	4
62526	575	1000	4.88	4
62526	575	3000	3.86	3
H7484	600	100	3.63	4
61802	600	300	3.27	3
61987	600	300	2.07	3
H7484	600	300	4.11	4

Table 5.17 Results for combined data

Temp.	Time	Method 1			Method 2			Method 3		
°C	h	$\log_{10}A$	n	ST. DEV	$A(x10^9)$	n	ST. DEV	B	C	ST. DEV
575	300	-6.746	3.24	0.108	1.63	4.37	0.670	0.0821	37.61	0.648
575	1000	-5.288	2.67	0.194	14.5	3.77	1.134	0.0389	26.26	1.125
600	300	-5.002	2.45	0.107	554	3.07	0.364	0.0730	33.19	0.359

A is in N, mm, h units

σ_0 is in N/mm^2

ε_c is in % strain.

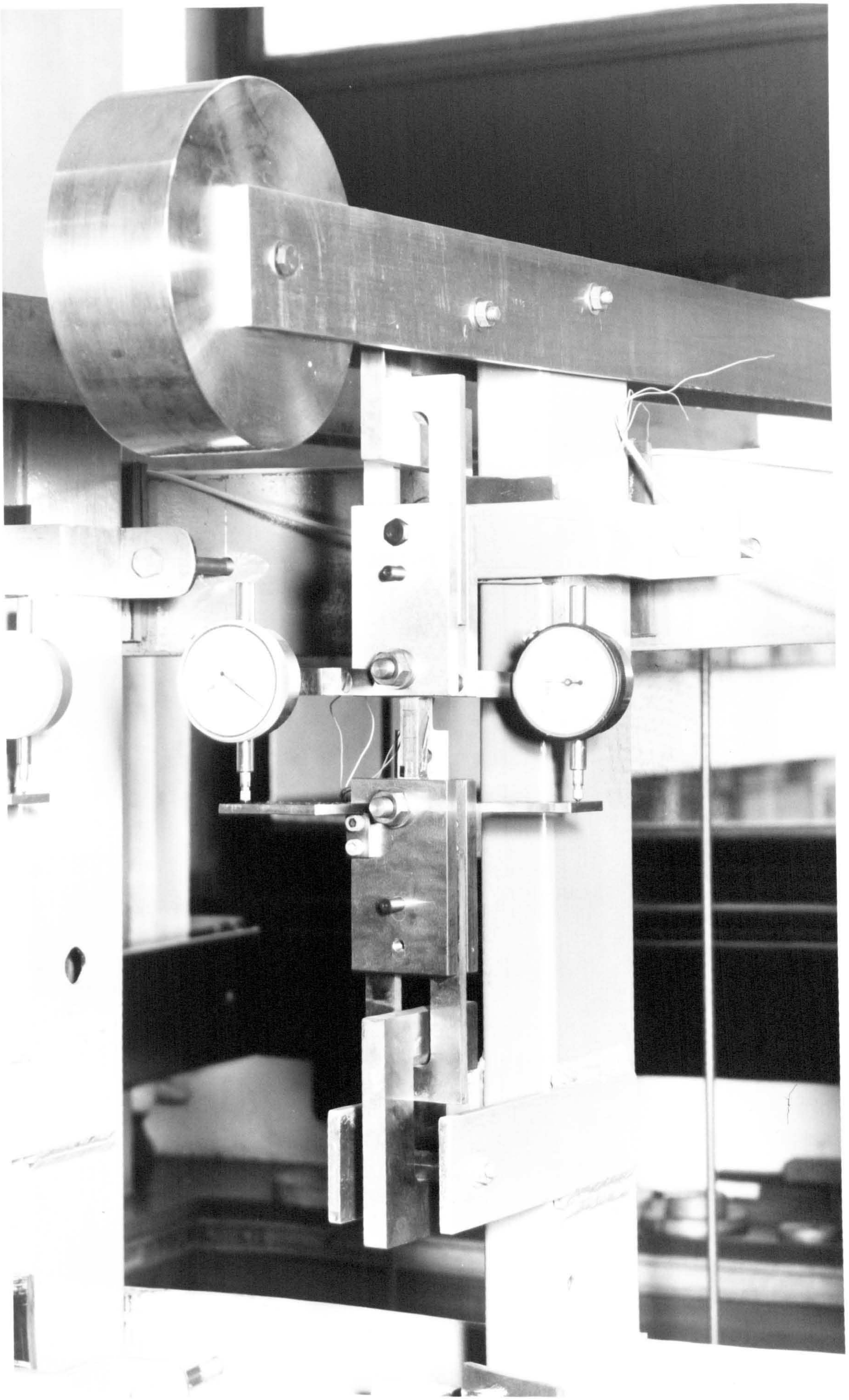

FIG. 5.1(a) UNIAXIAL LOADING RIG

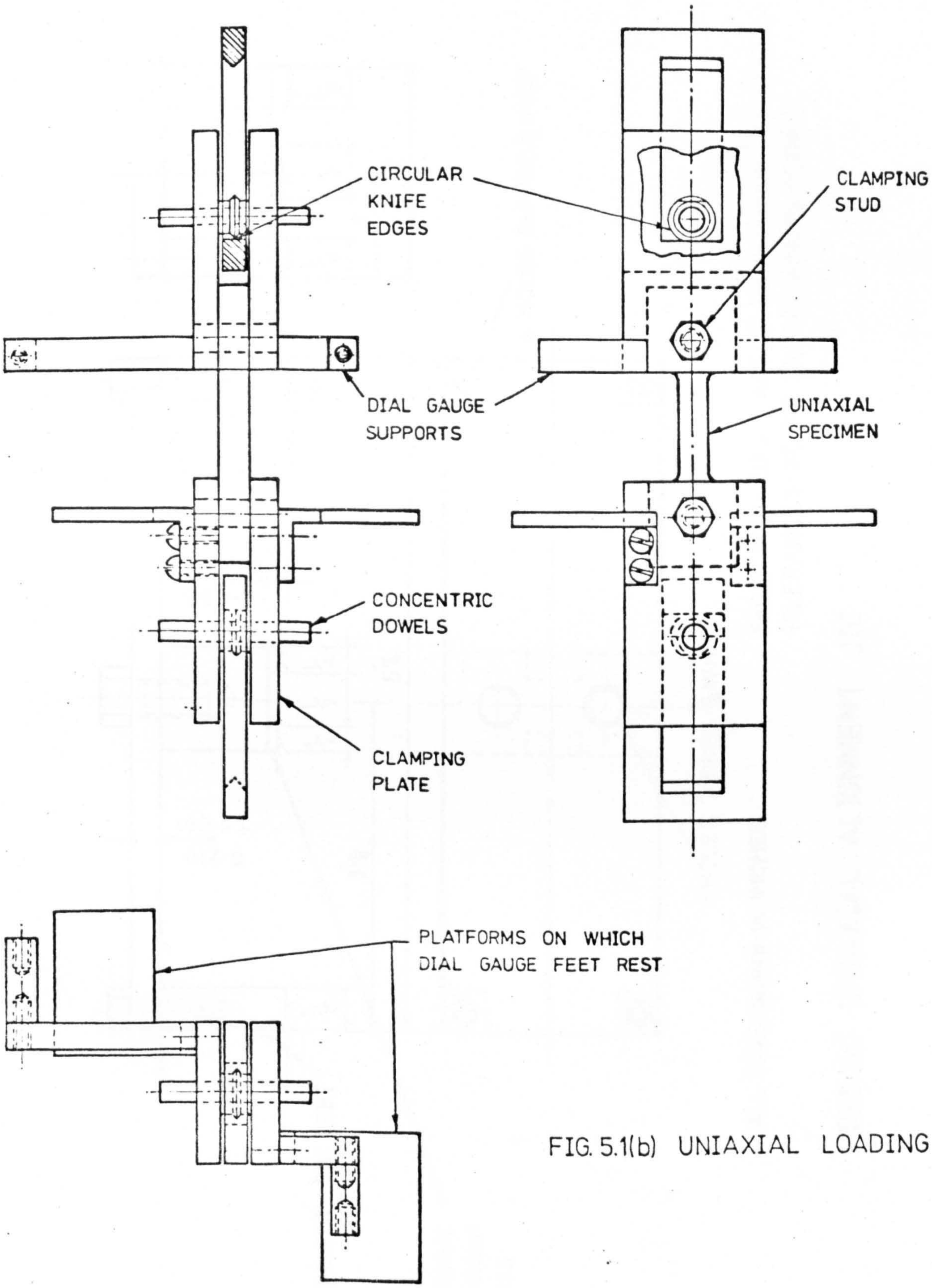

FIG. 5.1(b) UNIAXIAL LOADING RIG

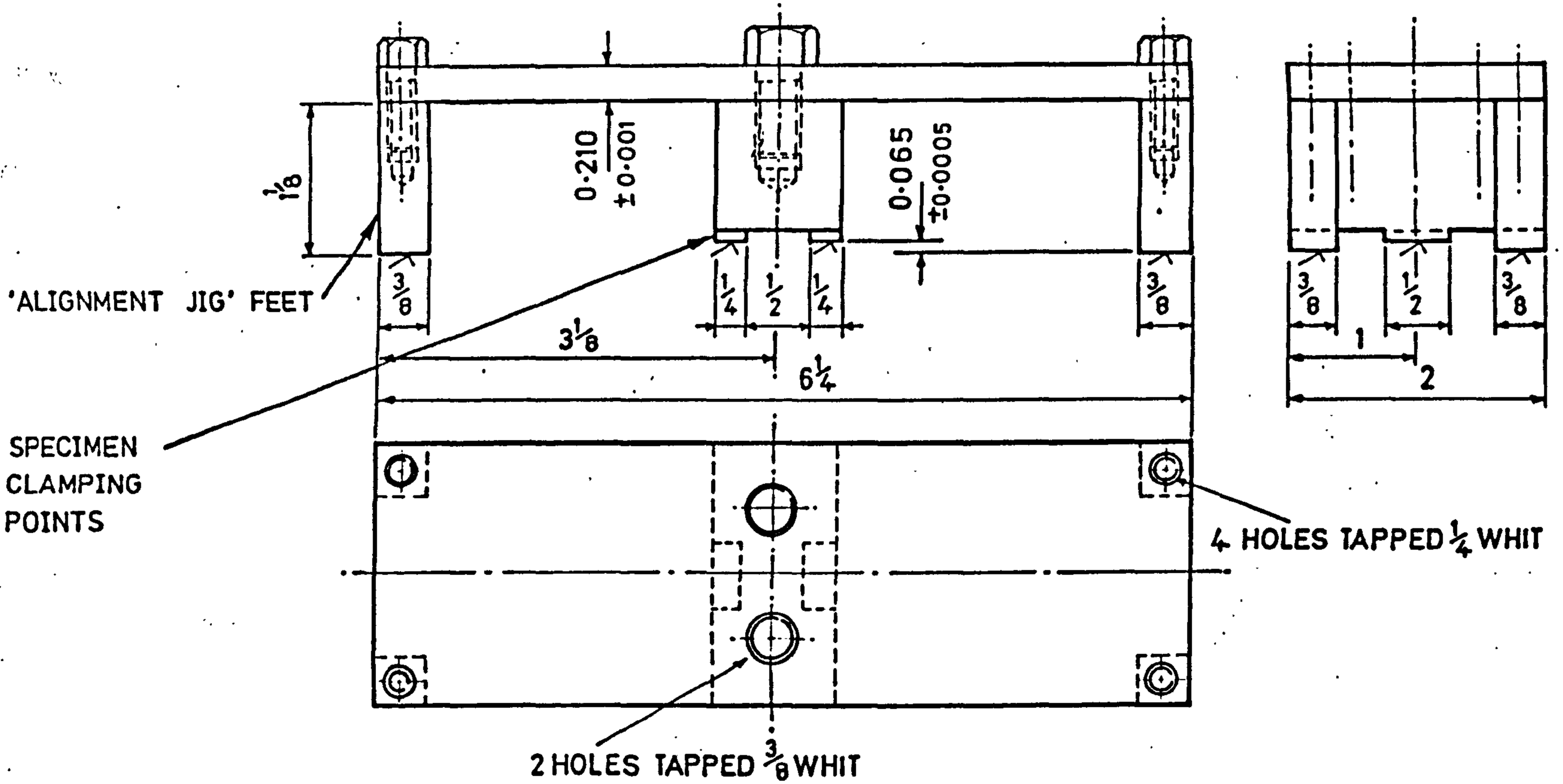

ALL DIMENSIONS IN INCHES

FACES MARKED ⌐ ARE TO BE HARDENED AND GROUND.
TOLERANCES ±0·010 EXCEPT WHERE STATED.

FIG.5.1(c) UNIAXIAL ALIGNMENT JIG

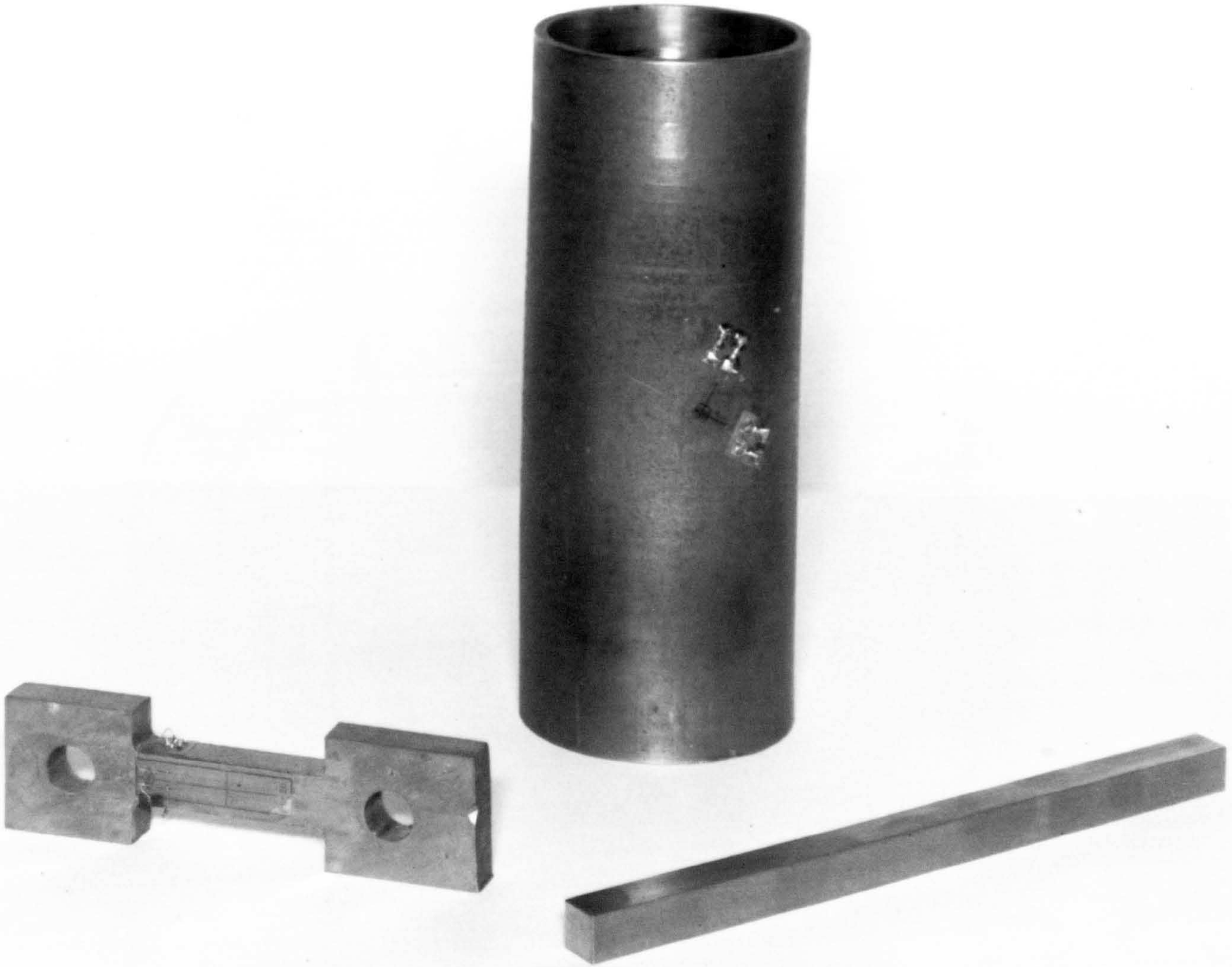

FIG.5.2 UNIAXIAL, BIAXIAL & BEAM SPECIMENS

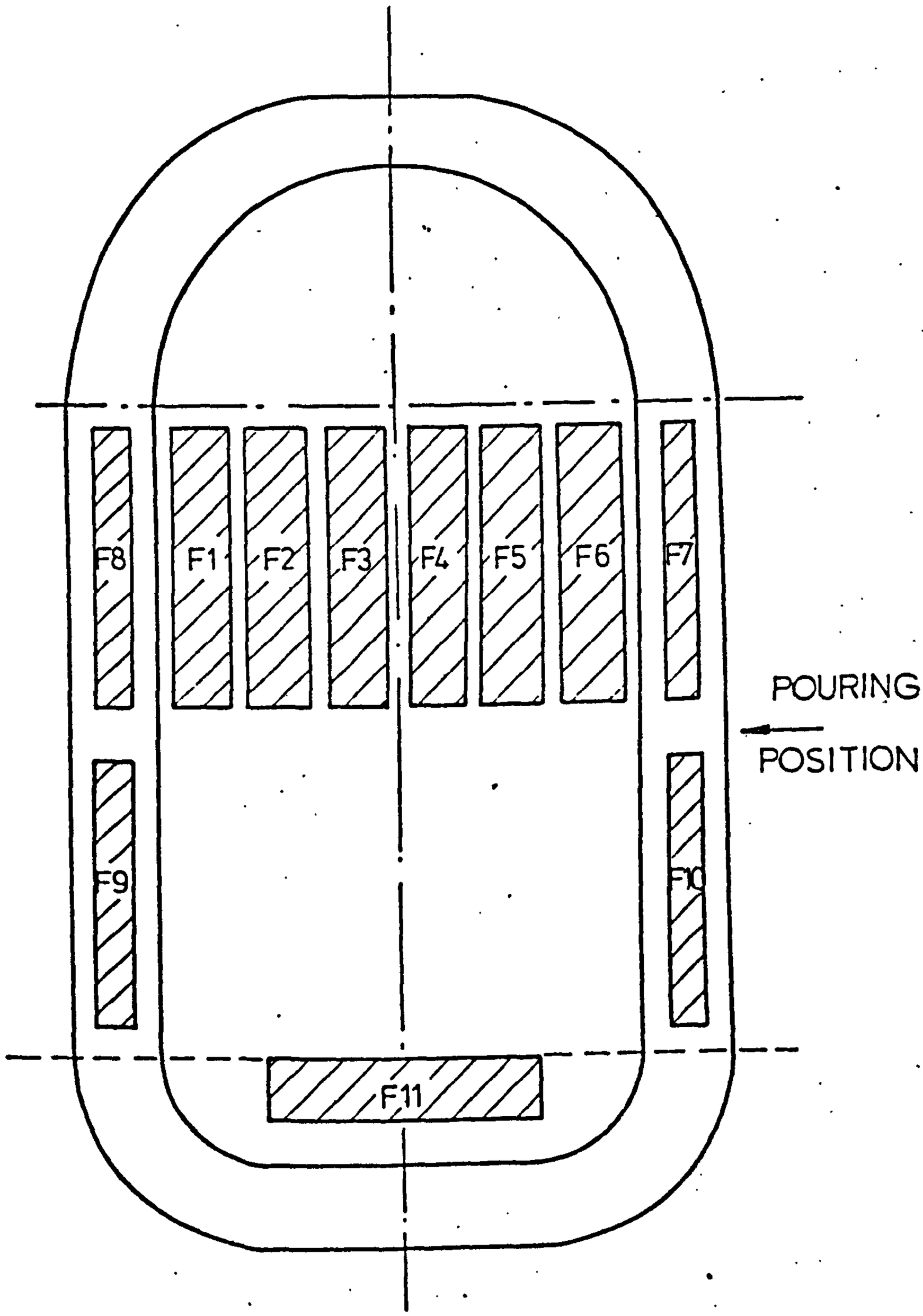

FIG.5.3 POSITIONS FROM WHICH THE SPECIMENS WERE TAKEN IN CASTING 14

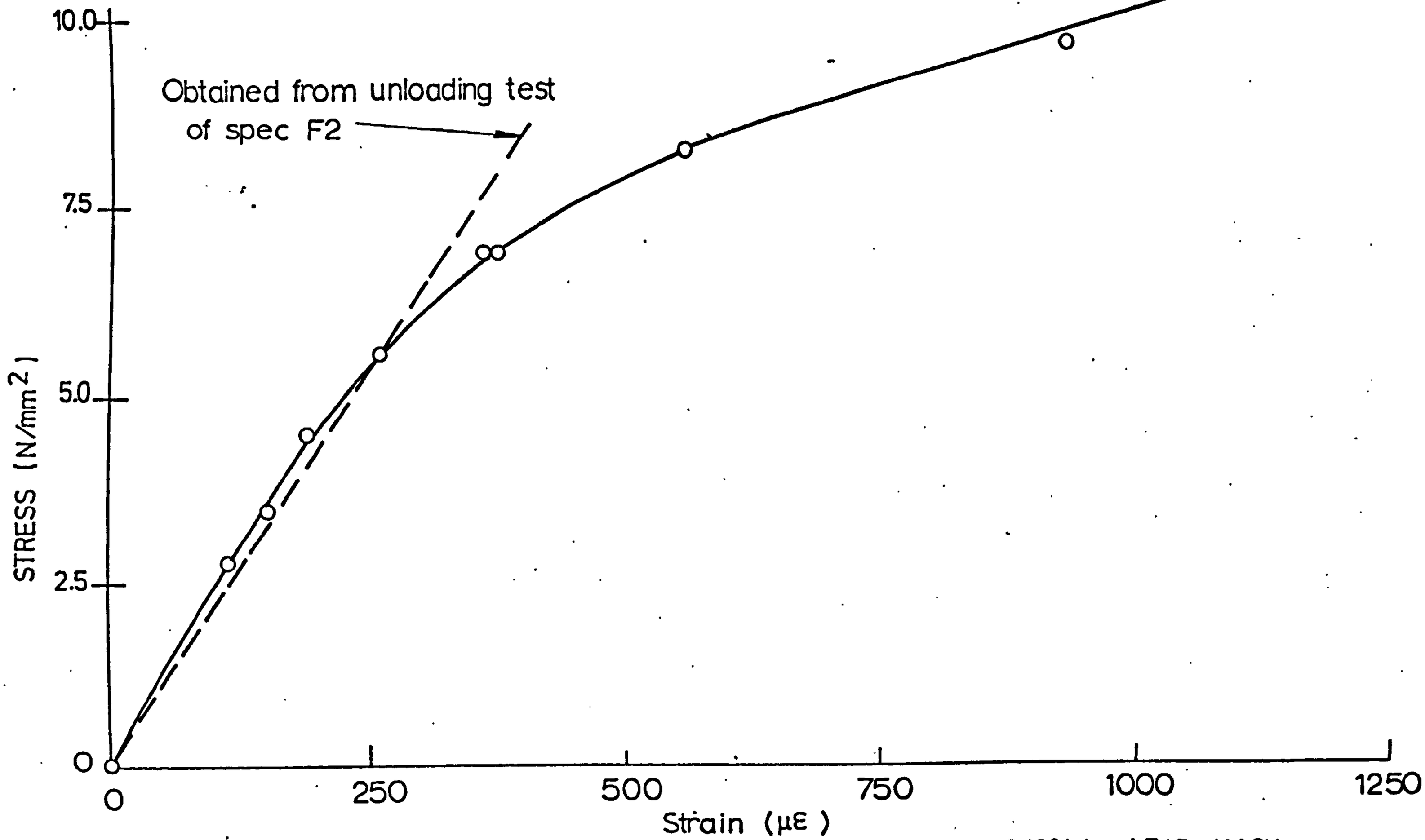

FIG.5.4 LOADING & UNLOADING STRESS STRAIN CURVES FOR 1.2%Sb,0.12%As LEAD ALLOY

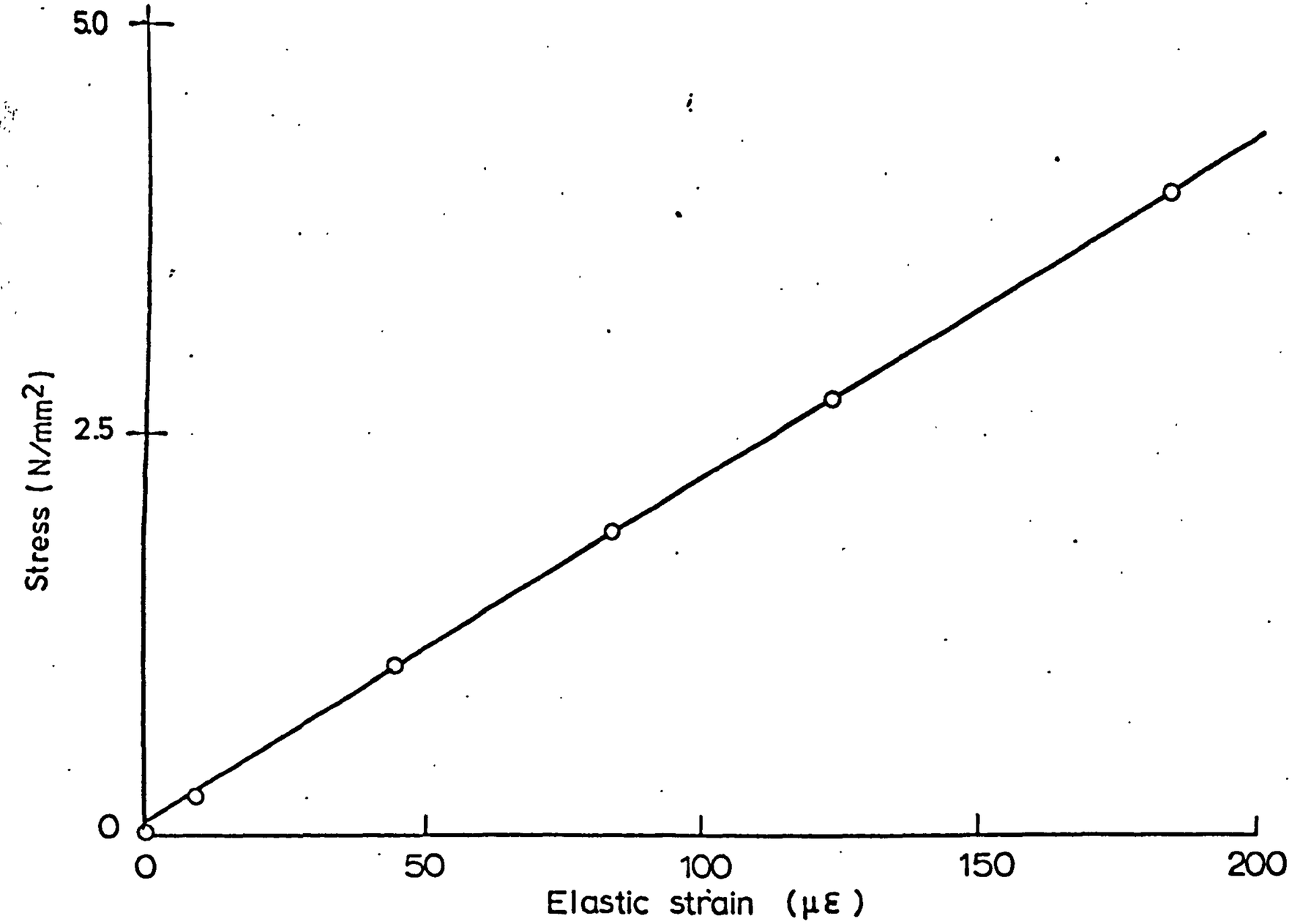

FIG.5.5 ELASTIC STRESS-STRAIN LINE FOR 1.2%Sb, 0.12%As LEAD ALLOY

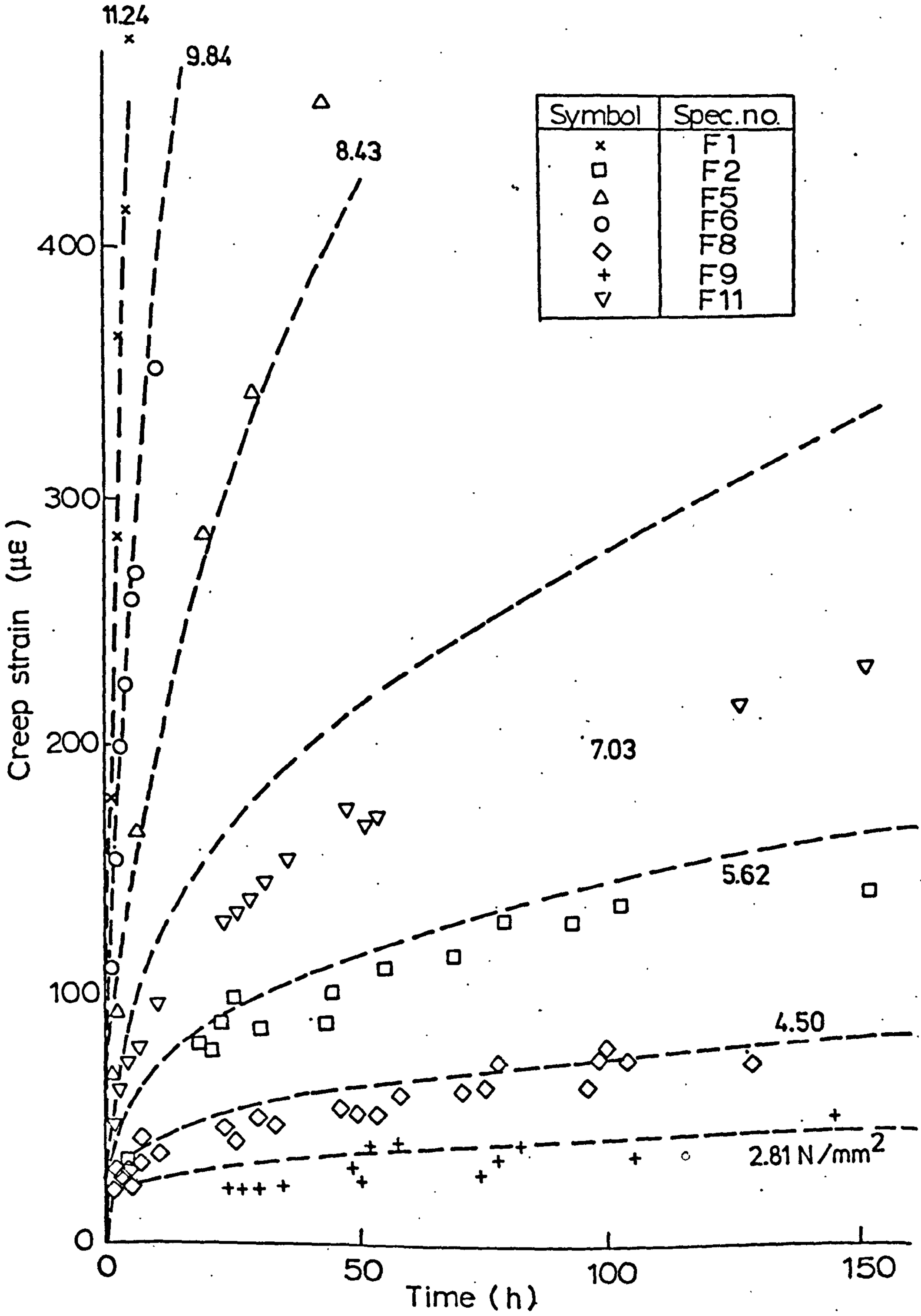

FIG. 5.6 CREEP CURVES FOR 1.2%Sb, 0.12%As LEAD ALLOY

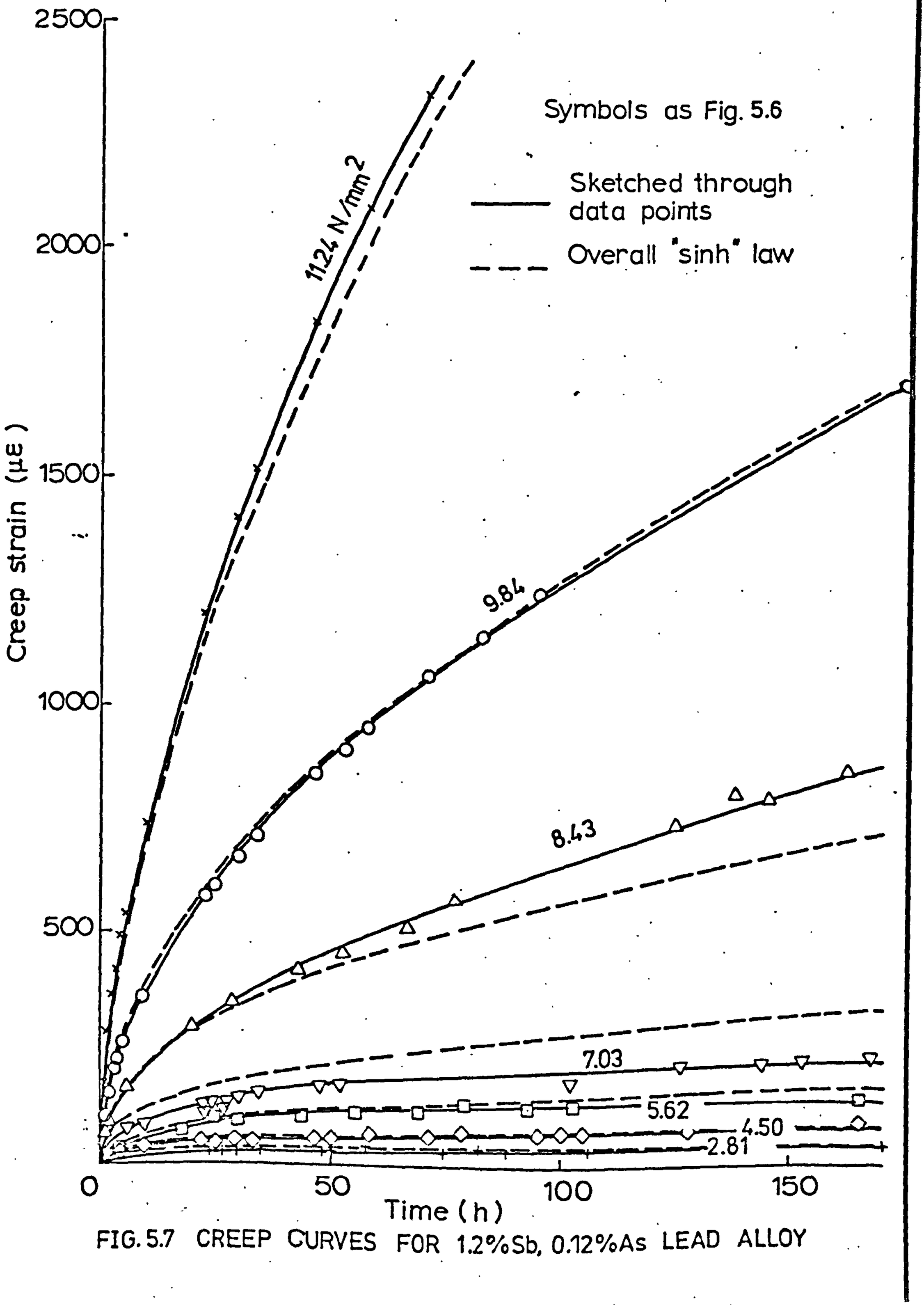

FIG. 5.7 CREEP CURVES FOR 1.2%Sb, 0.12%As LEAD ALLOY

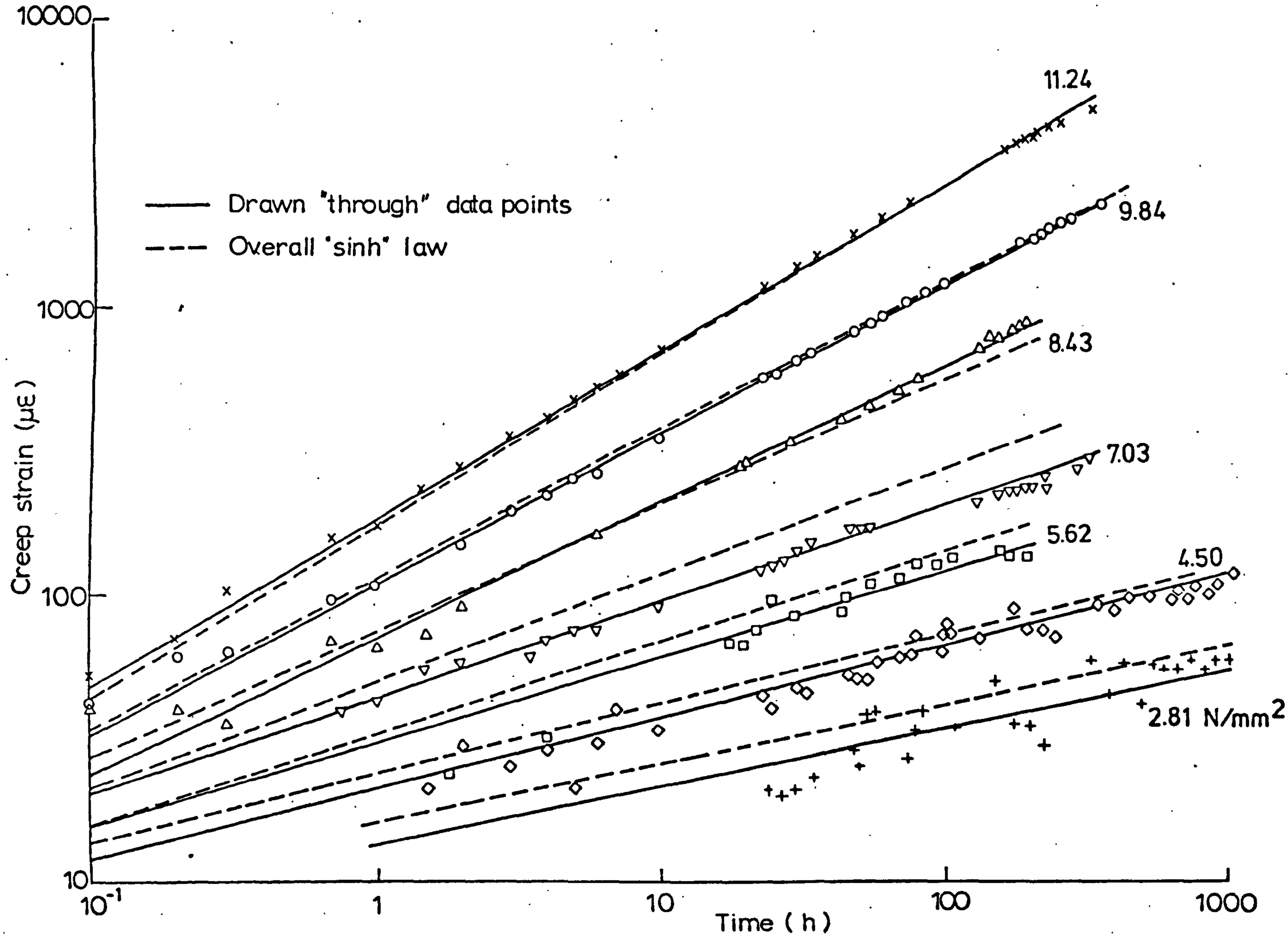

FIG. 5.8 CREEP DATA FOR 1.2%Sb, 0.12% As LEAD ALLOY

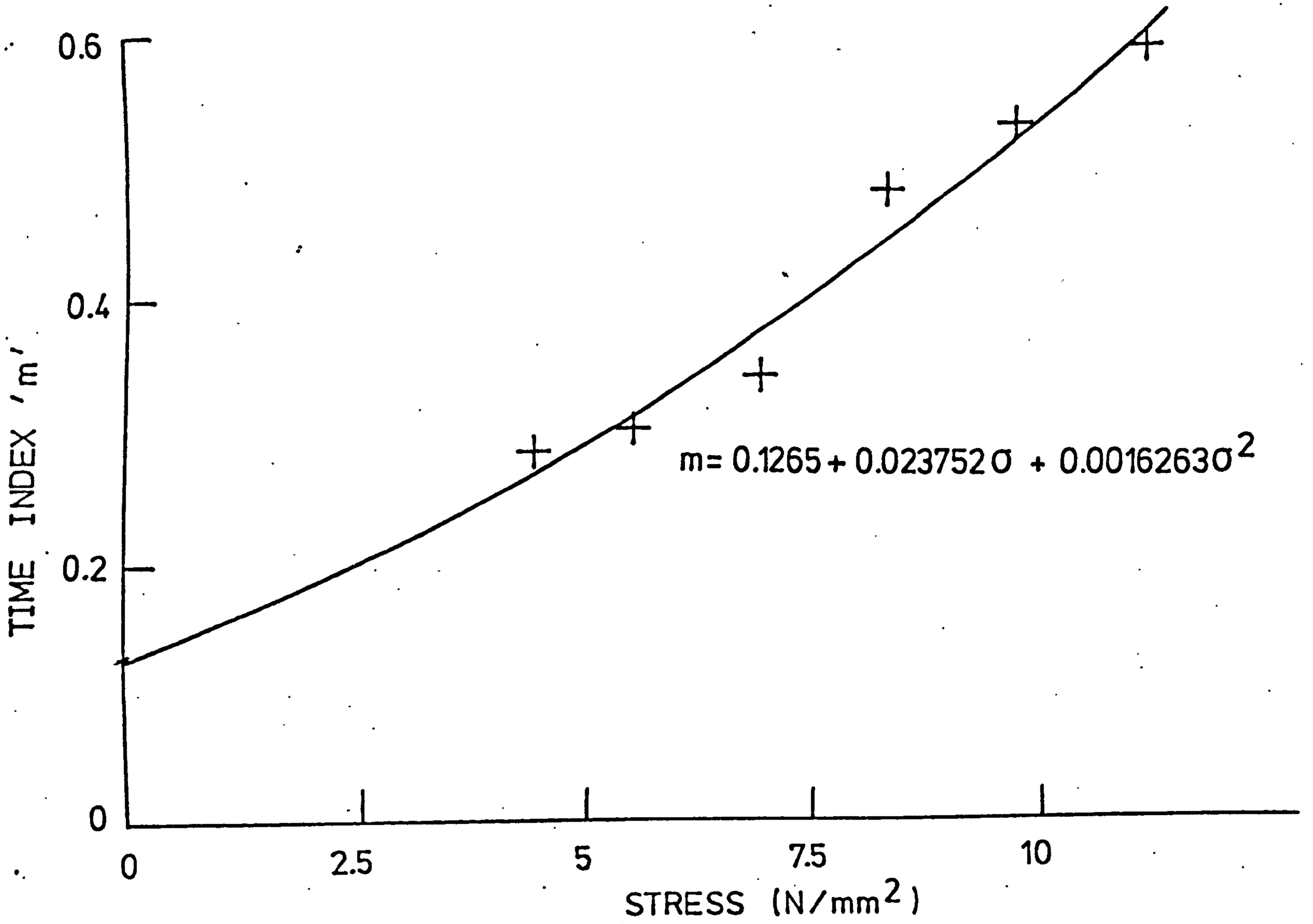

FIG. 5.9 VARIATION OF 'm' WITH STRESS FOR 1.2% Sb, 0.12% As LEAD ALLOY

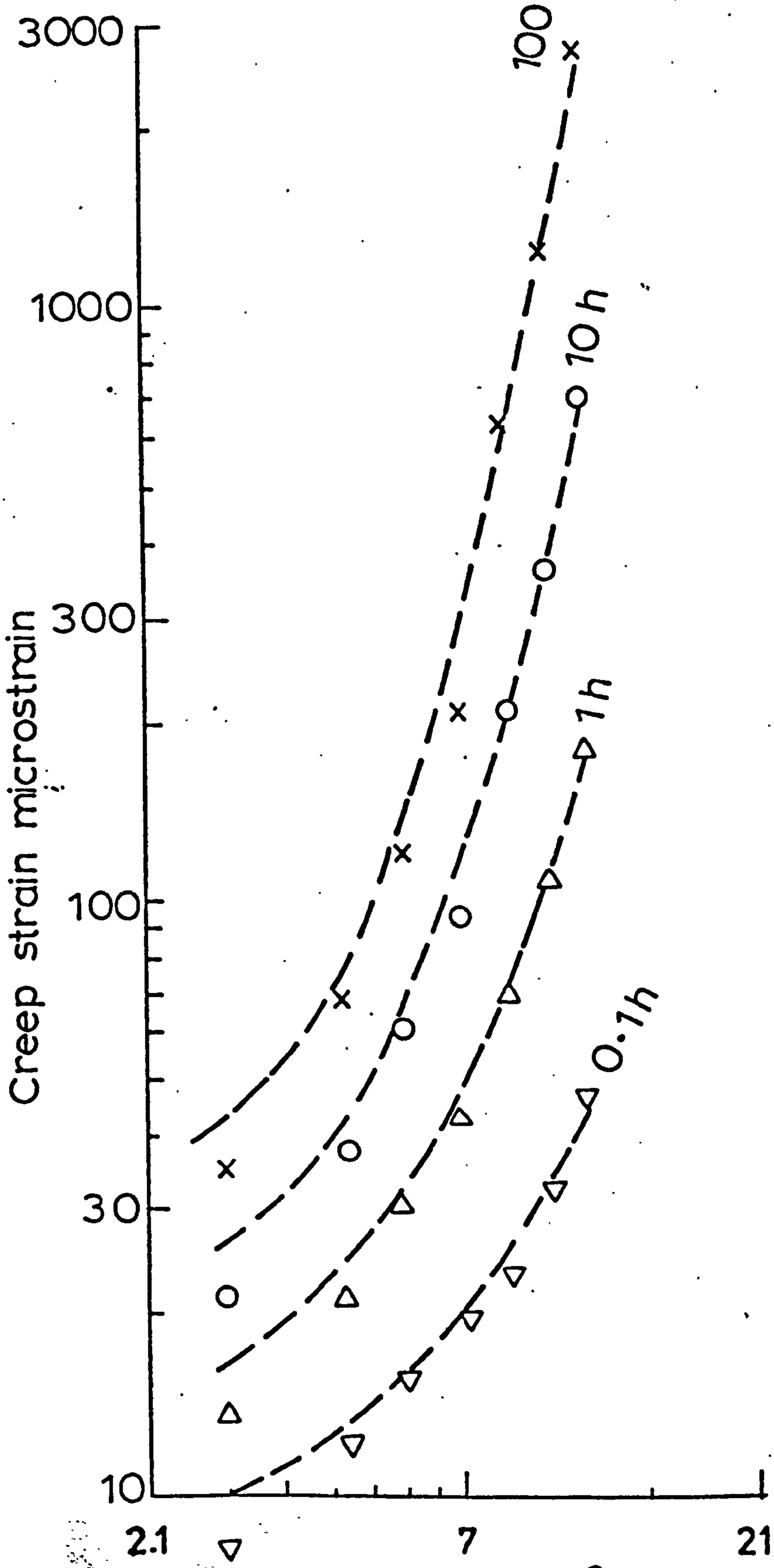

FIG. 5.10 ISOCHRONOUS STRESS-STRAIN CURVES FOR 1.2% Sb, 0.12% As LEAD ALLOY

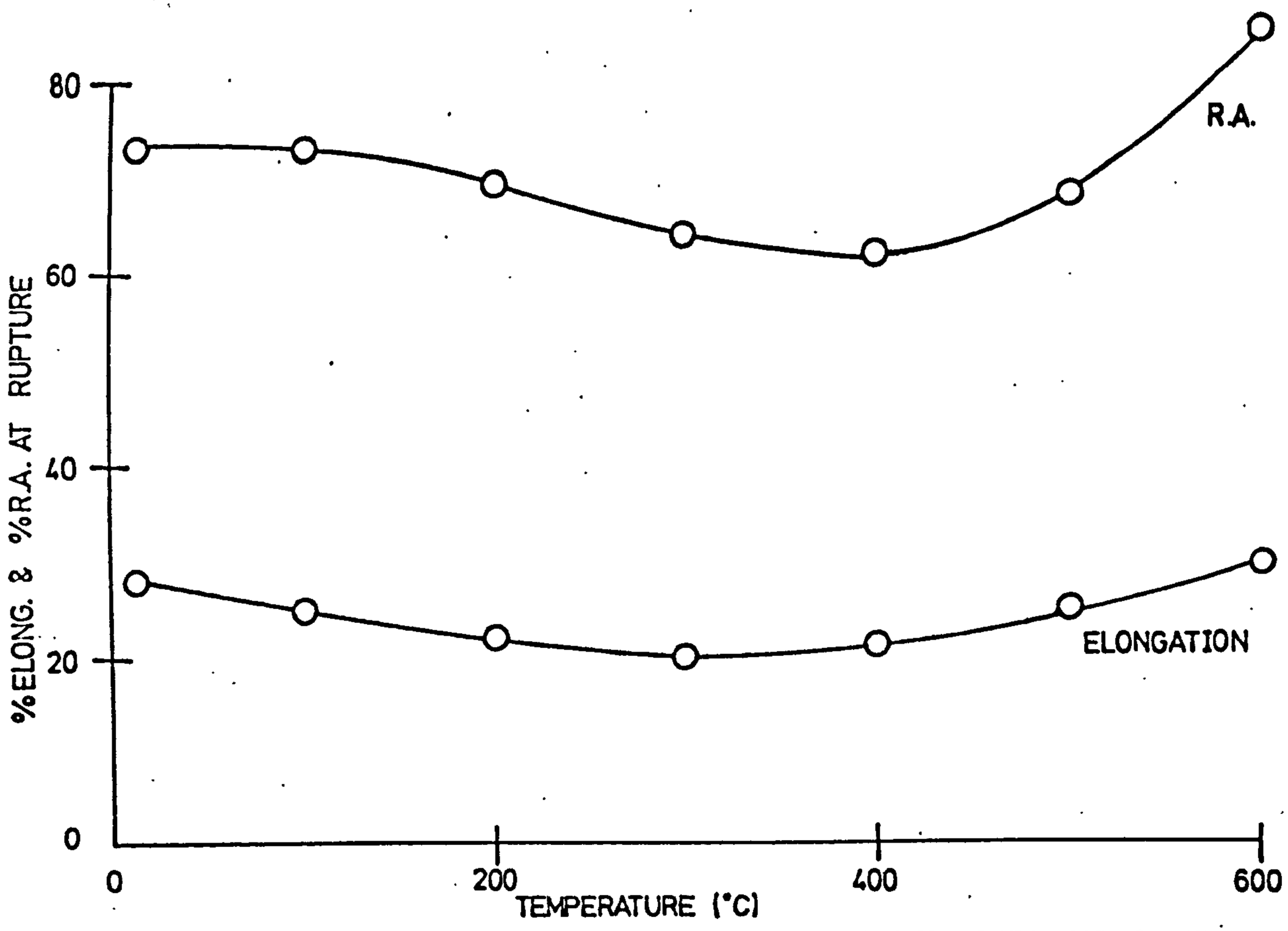

FIG. 5.11 VARIATION OF DUCTILITY WITH TEMPERATURE FOR 2.25CR MO STEEL

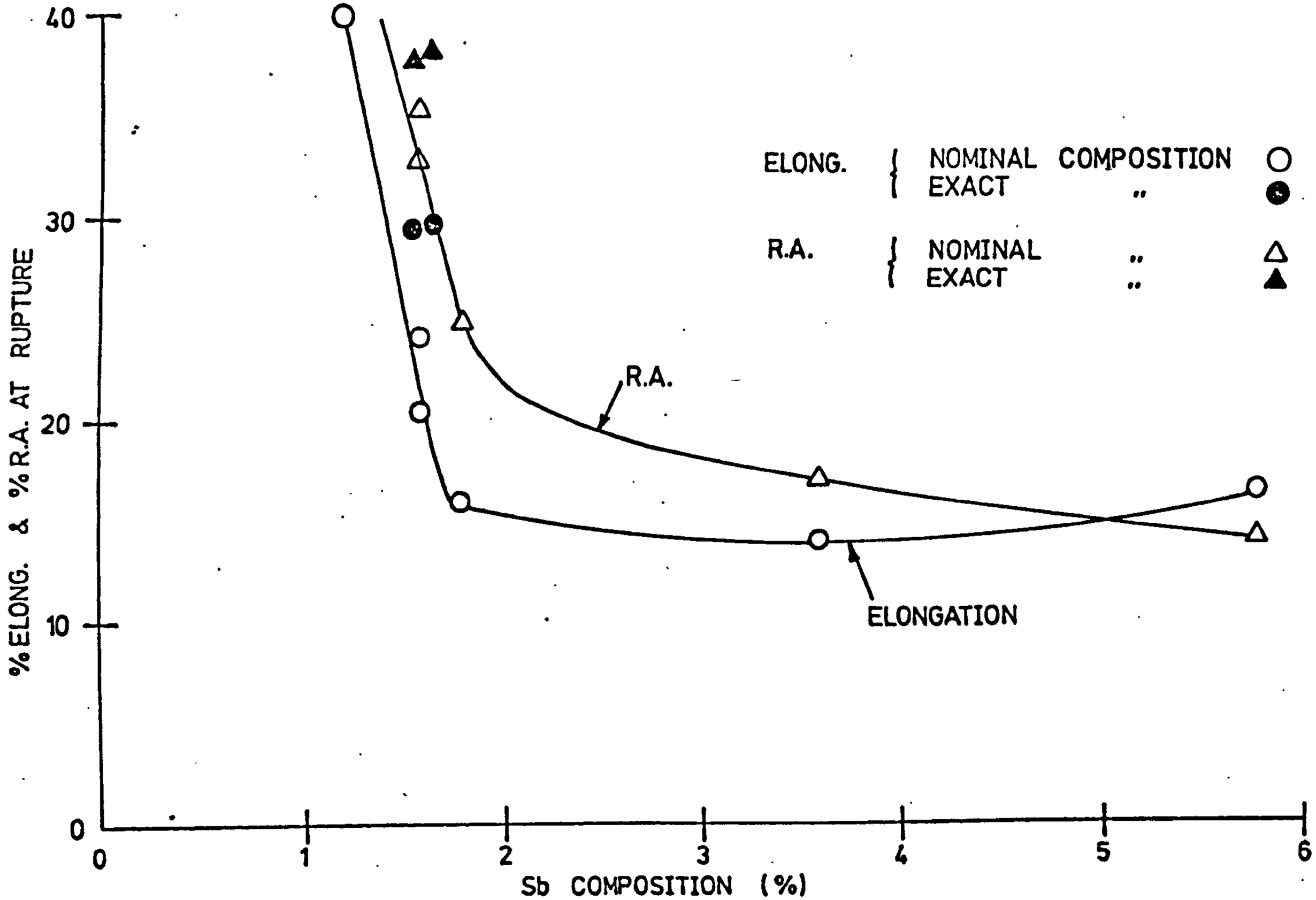

FIG. 5.12 VARIATION OF DUCTILITY WITH Sb COMPOSITION

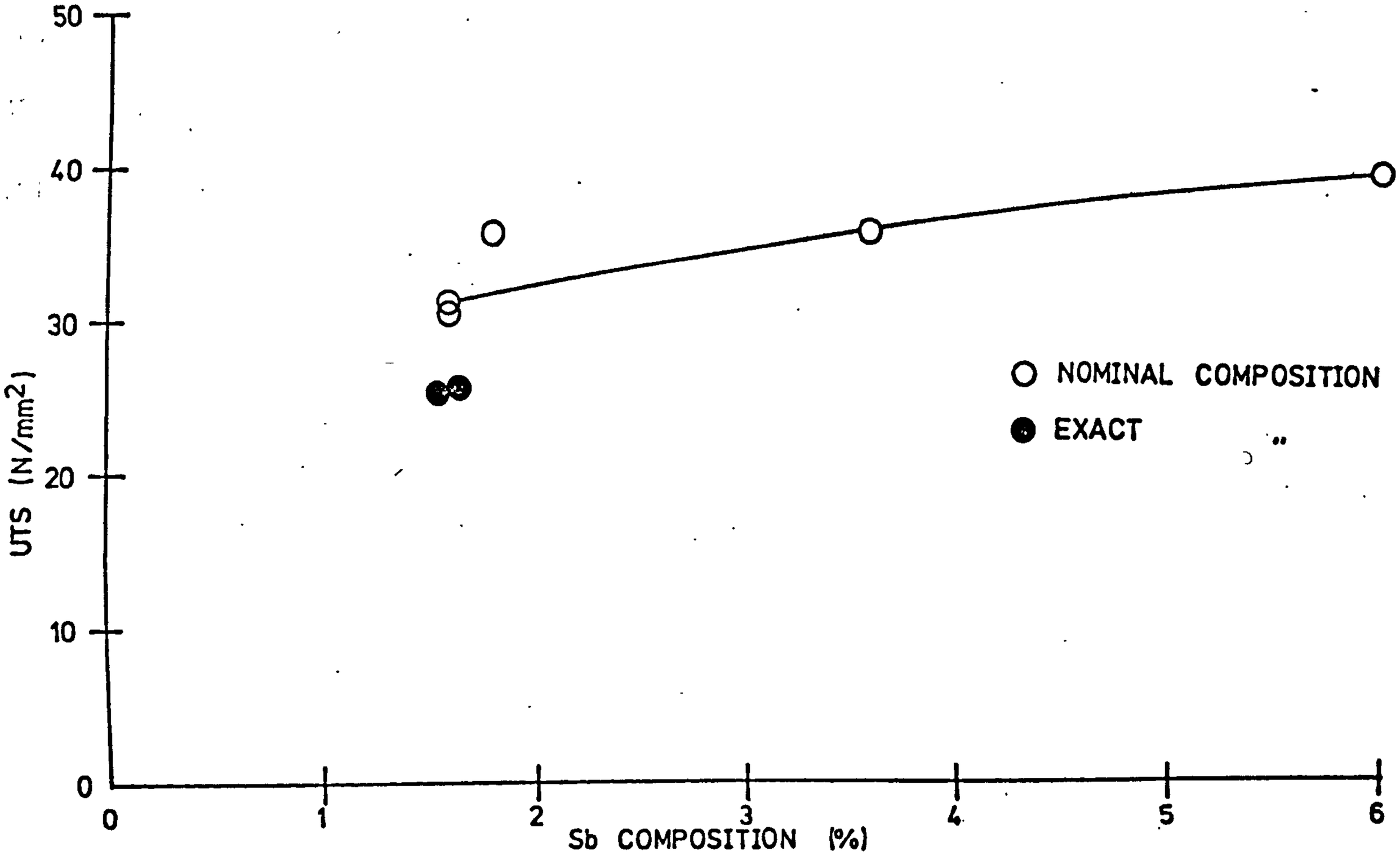

FIG. 5.13 VARIATION OF UTS WITH Sb COMPOSITION

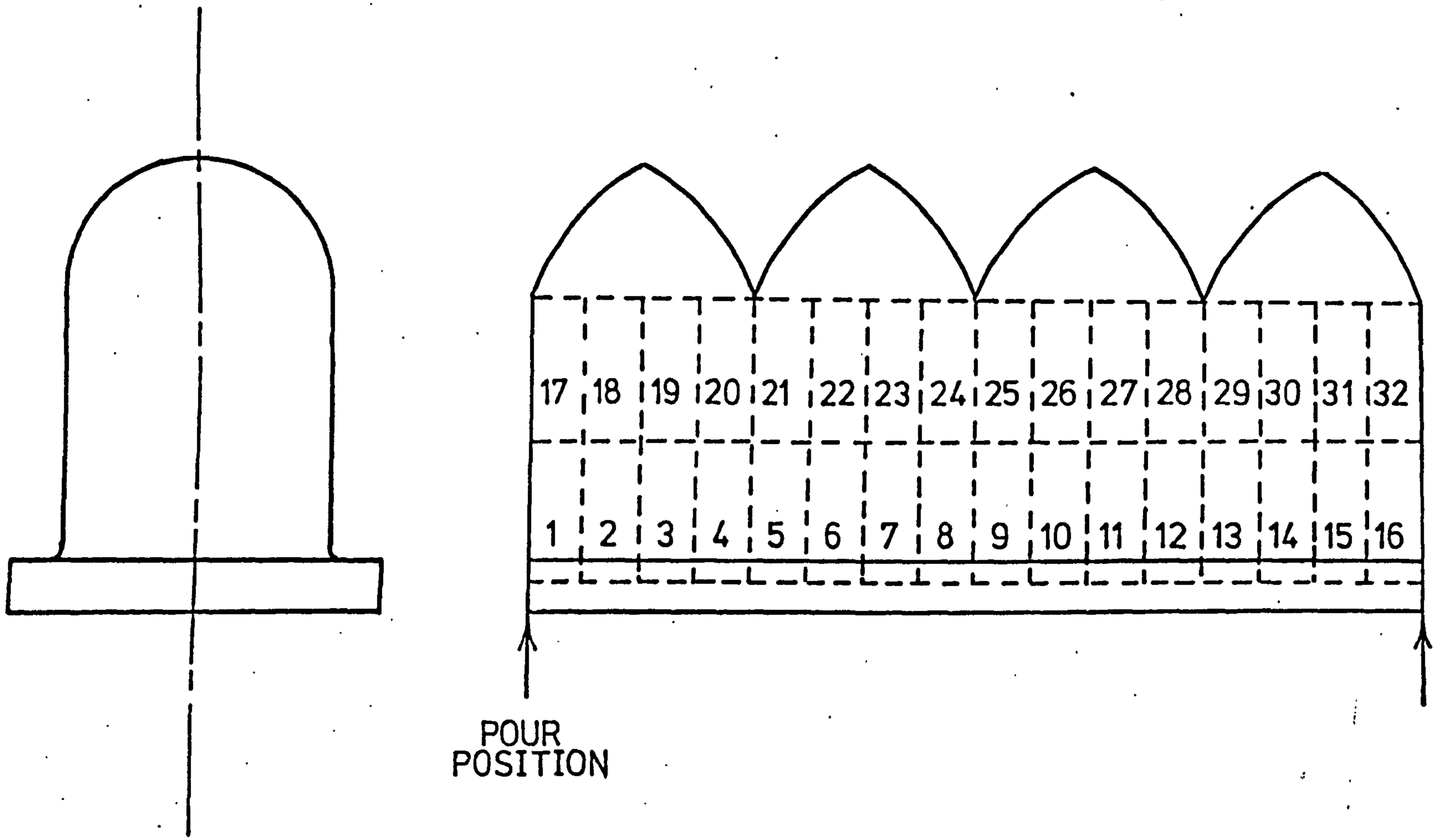

FIG. 5.14 POSITIONS OF THE UNIAXIAL SPECIMENS FROM THE PRESSURE VESSEL CASTINGS

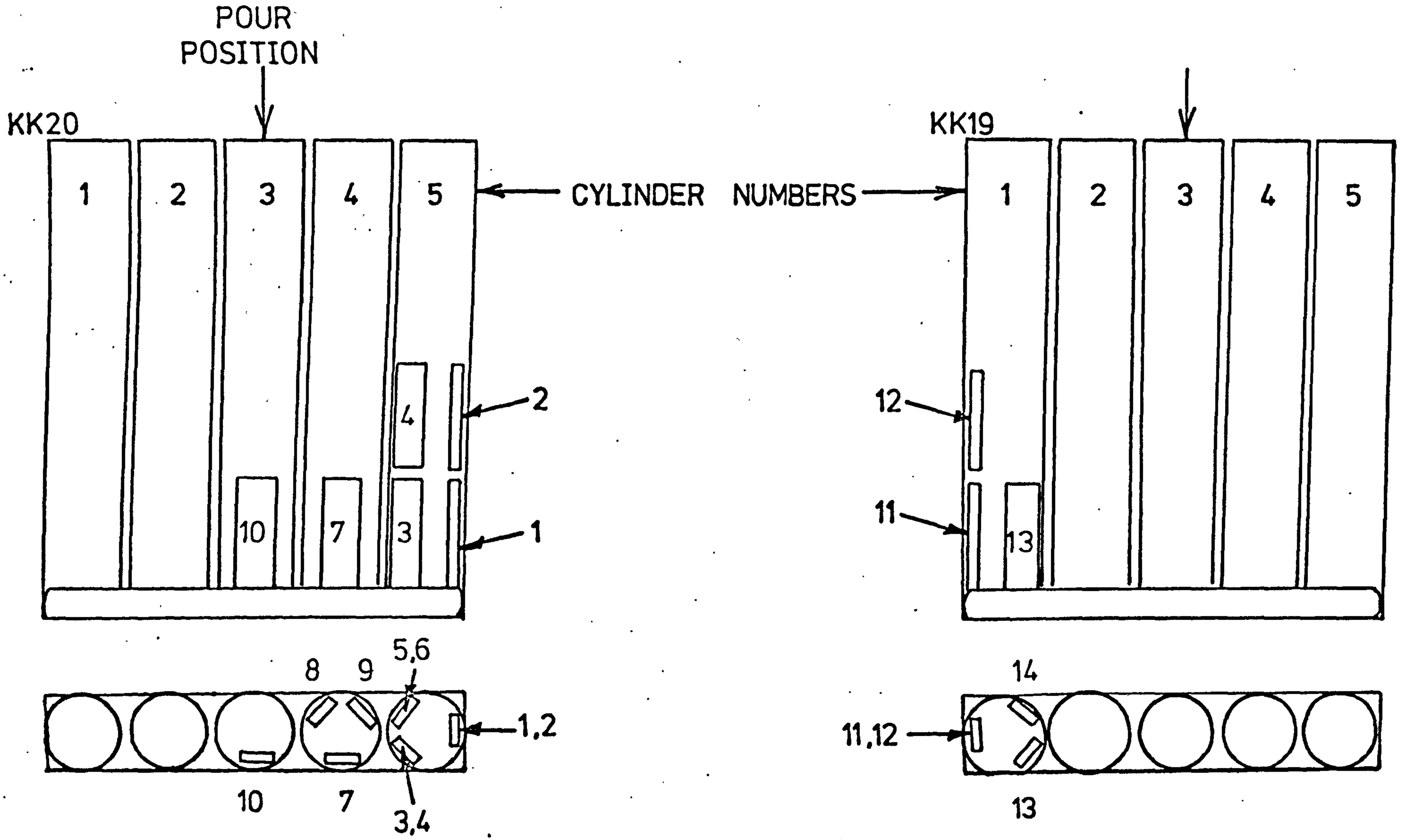

FIG. 5.15 POSITIONS OF THE UNIAXIAL SPECIMENS FROM THE *MULTI-CYLINDERS CASTINGS*

FIG. 5.16(a) LOADING STRAINS

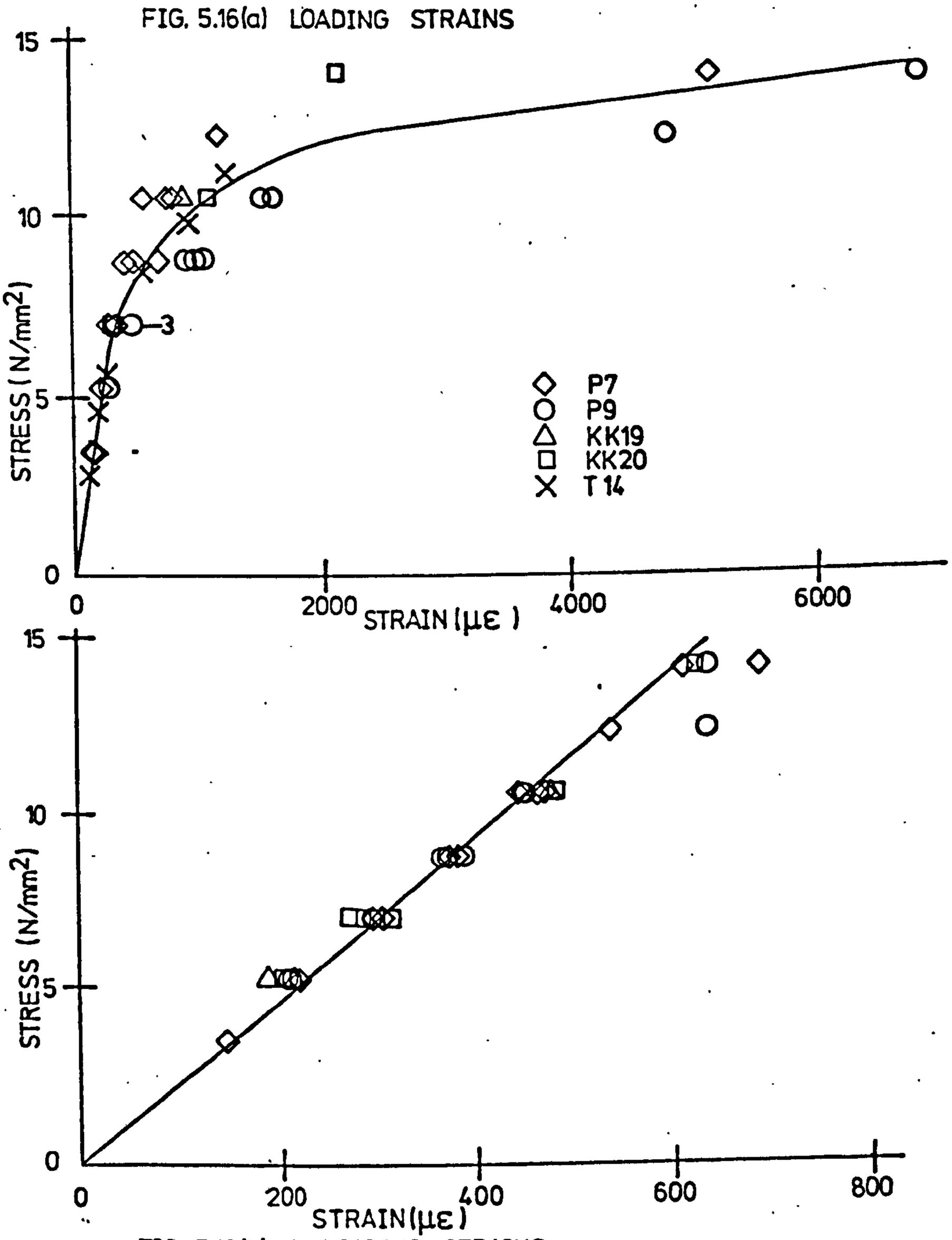

FIG. 5.16(b) UNLOADING STRAINS

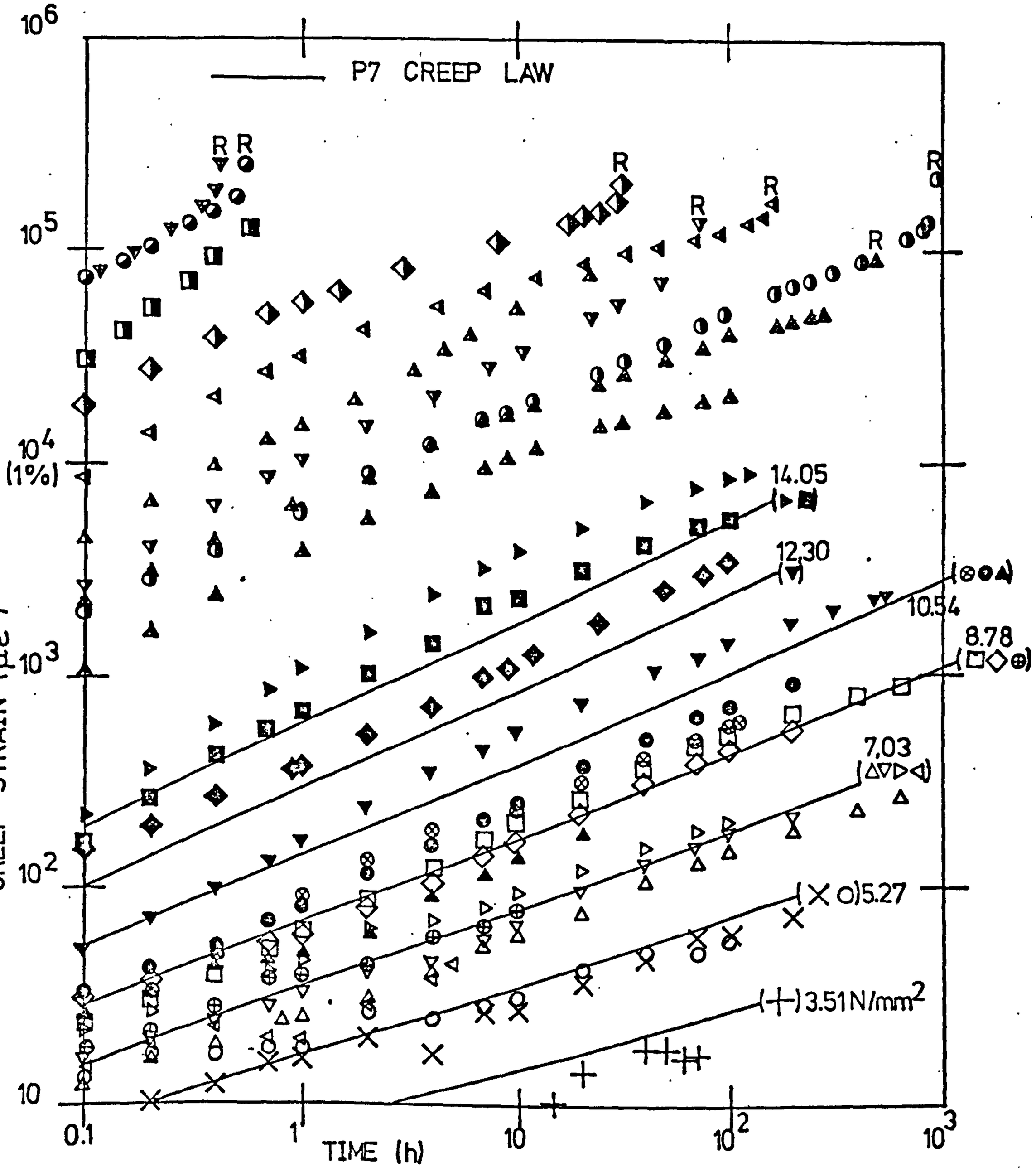

FIG. 5.17(a) P7 CREEP DATA (SYMBOLS, TABLE 5.9)

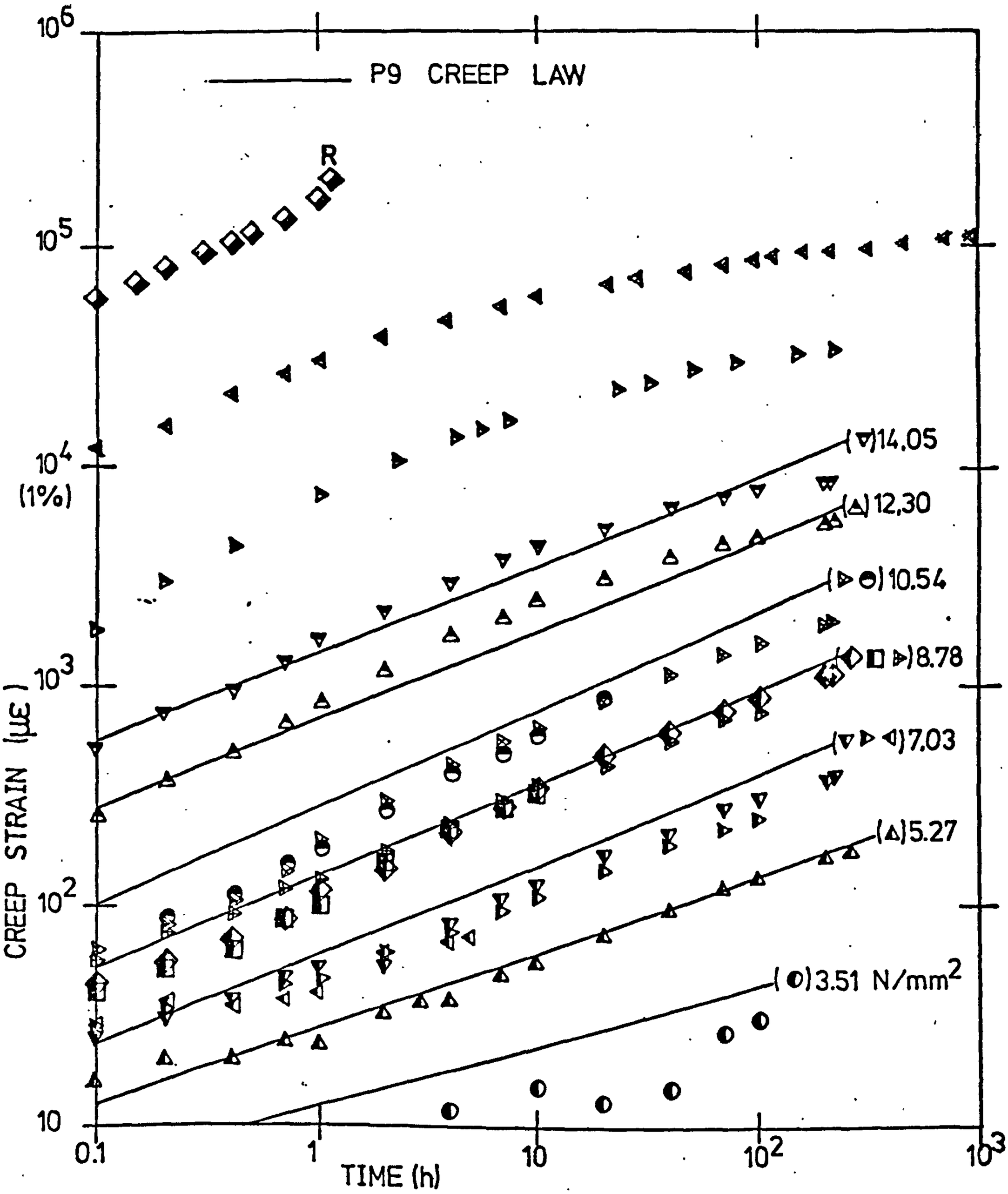

FIG. 5.17(b) P9 CREEP DATA (SYMBOLS, TABLE 5.9)

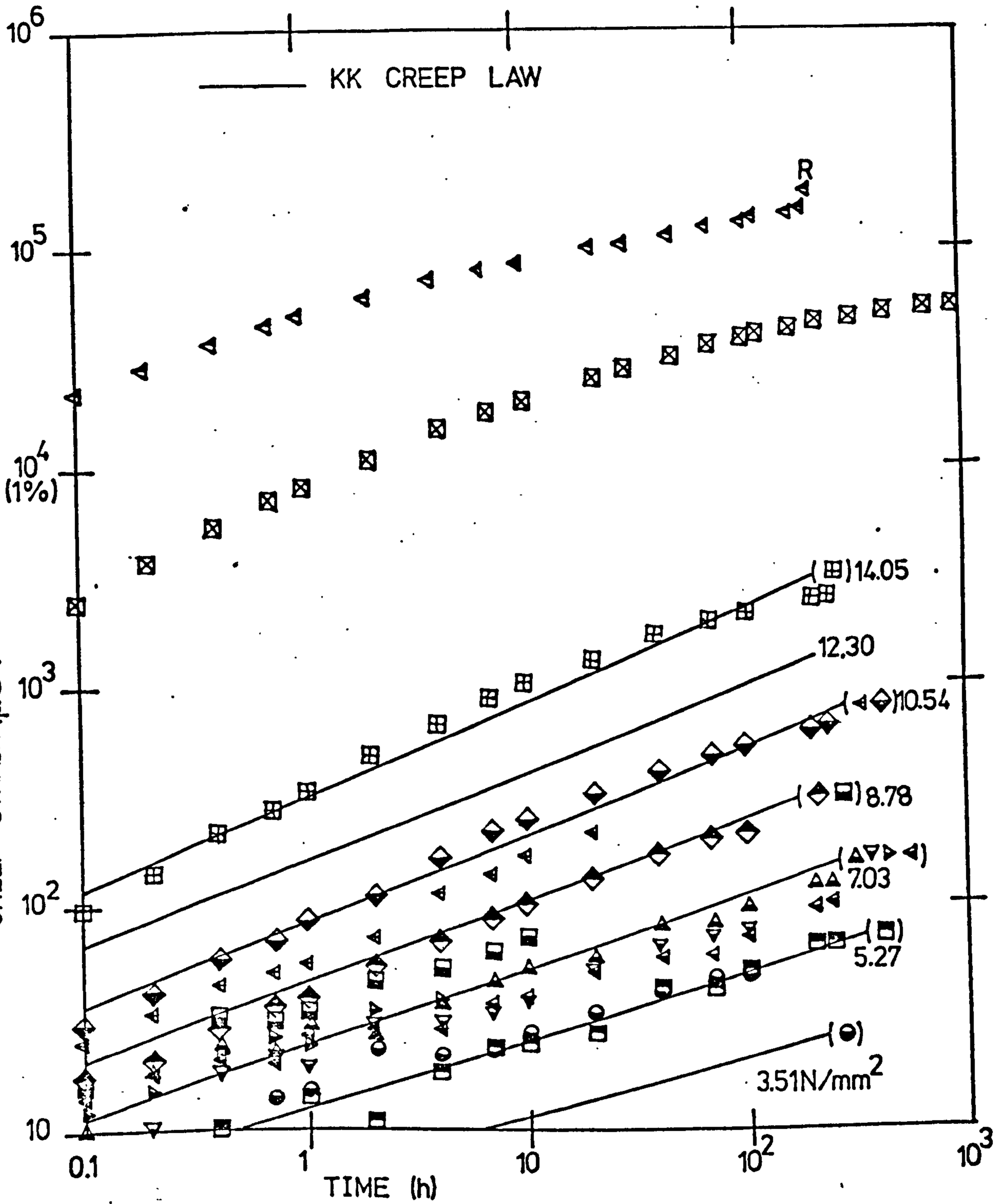

FIG. 5.17(c) KK19 & KK20 CREEP DATA (SYMBOLS, TABLE 5.9)

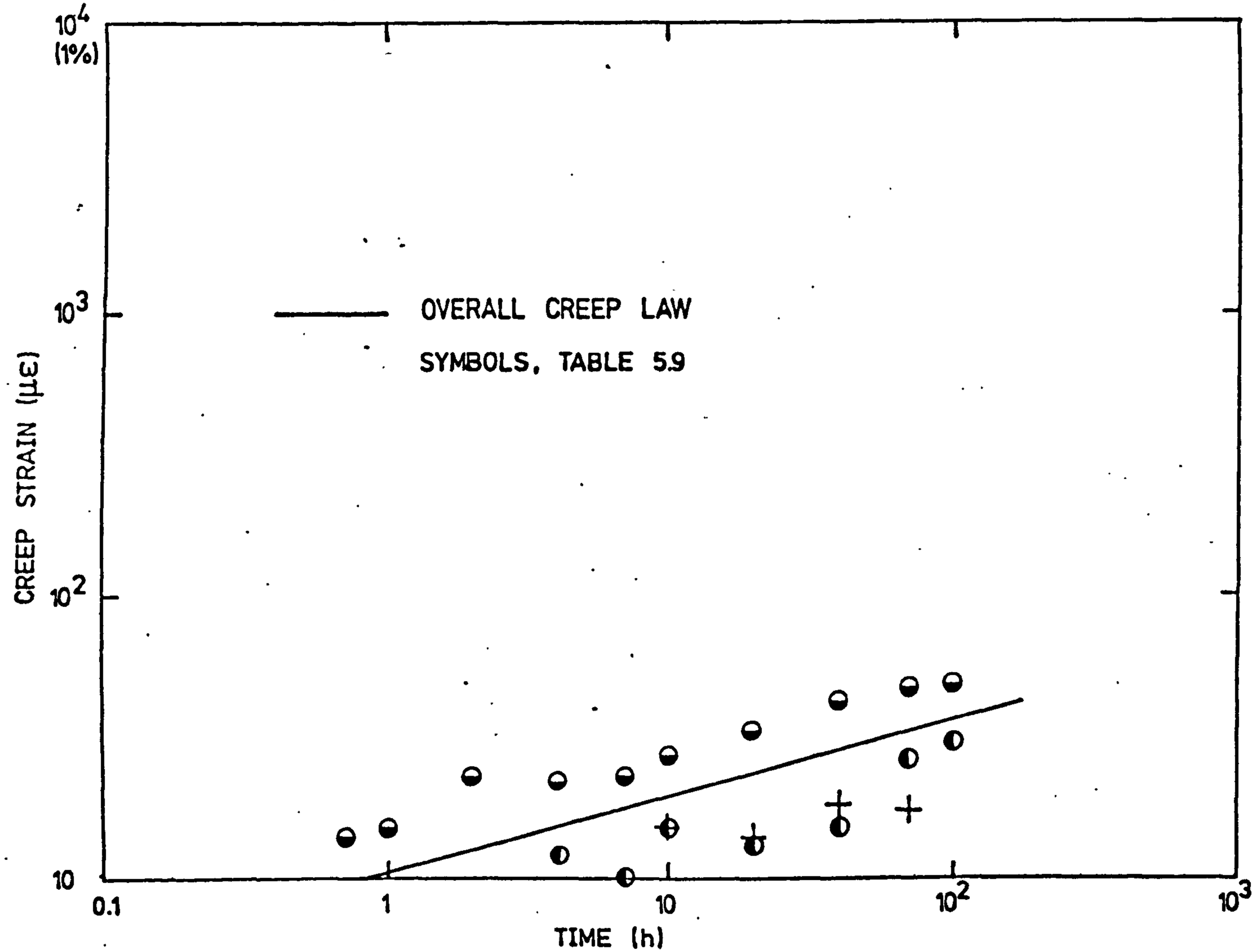

FIG. 5.18(a) CREEP DATA AT 3.51 N/mm^2

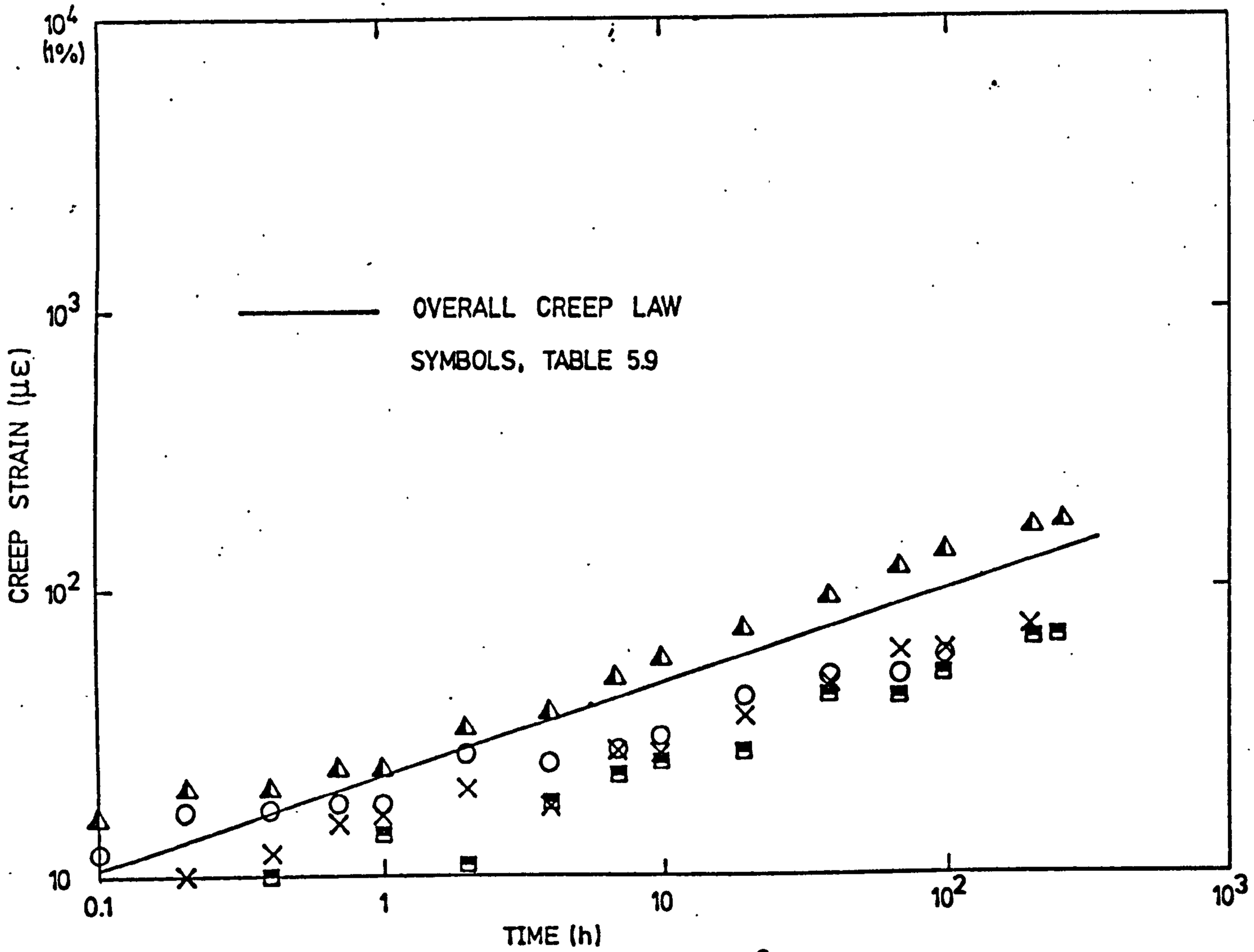

FIG. 5.18 (b) CREEP DATA AT 5.27 N/mm^2

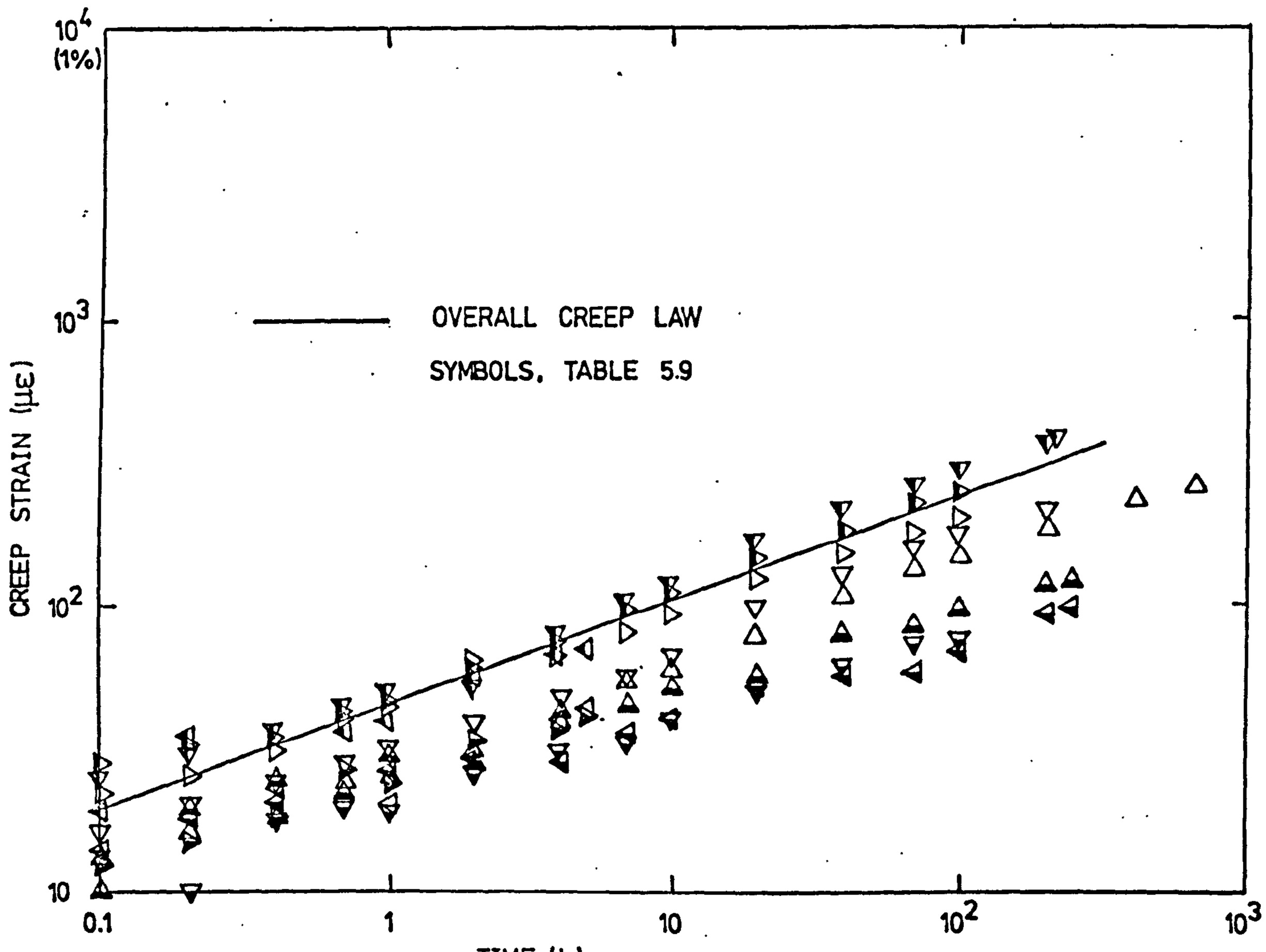

FIG. 5.18(c) CREEP DATA AT 7.03 N/mm^2

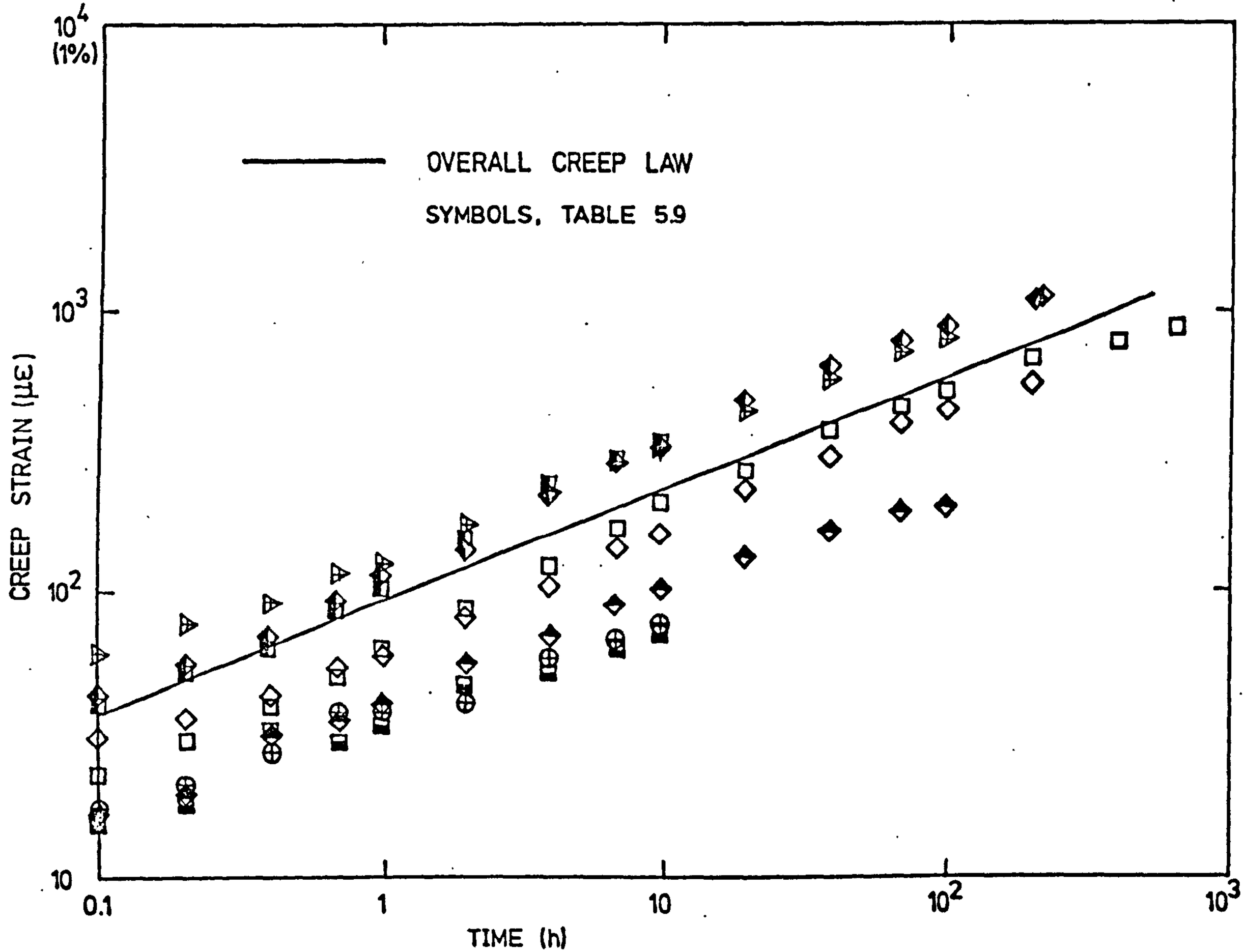

FIG. 5.18(d) CREEP DATA AT 8.78 N/mm^2

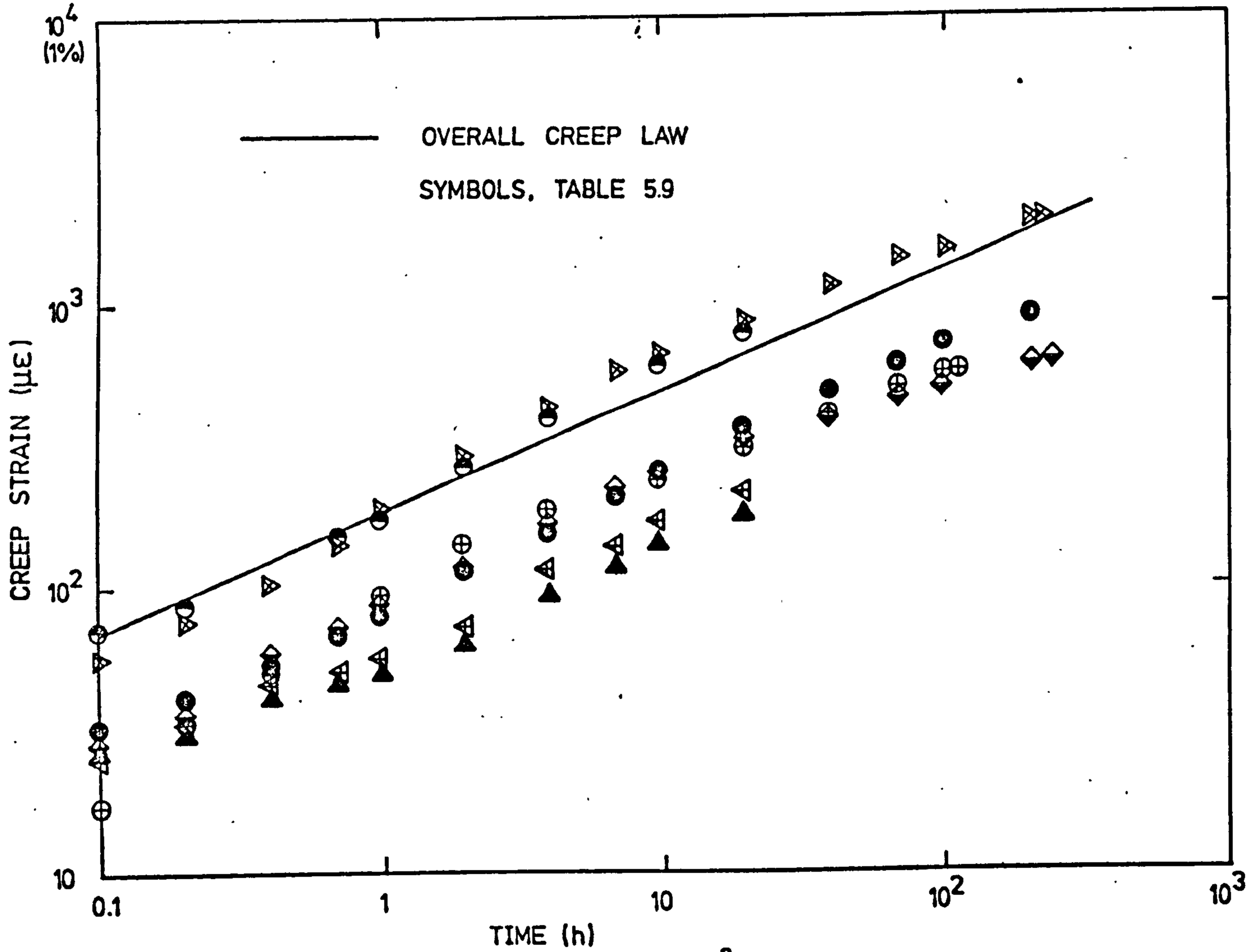

FIG. 5.18(e) CREEP DATA AT 10.54 N/mm^2

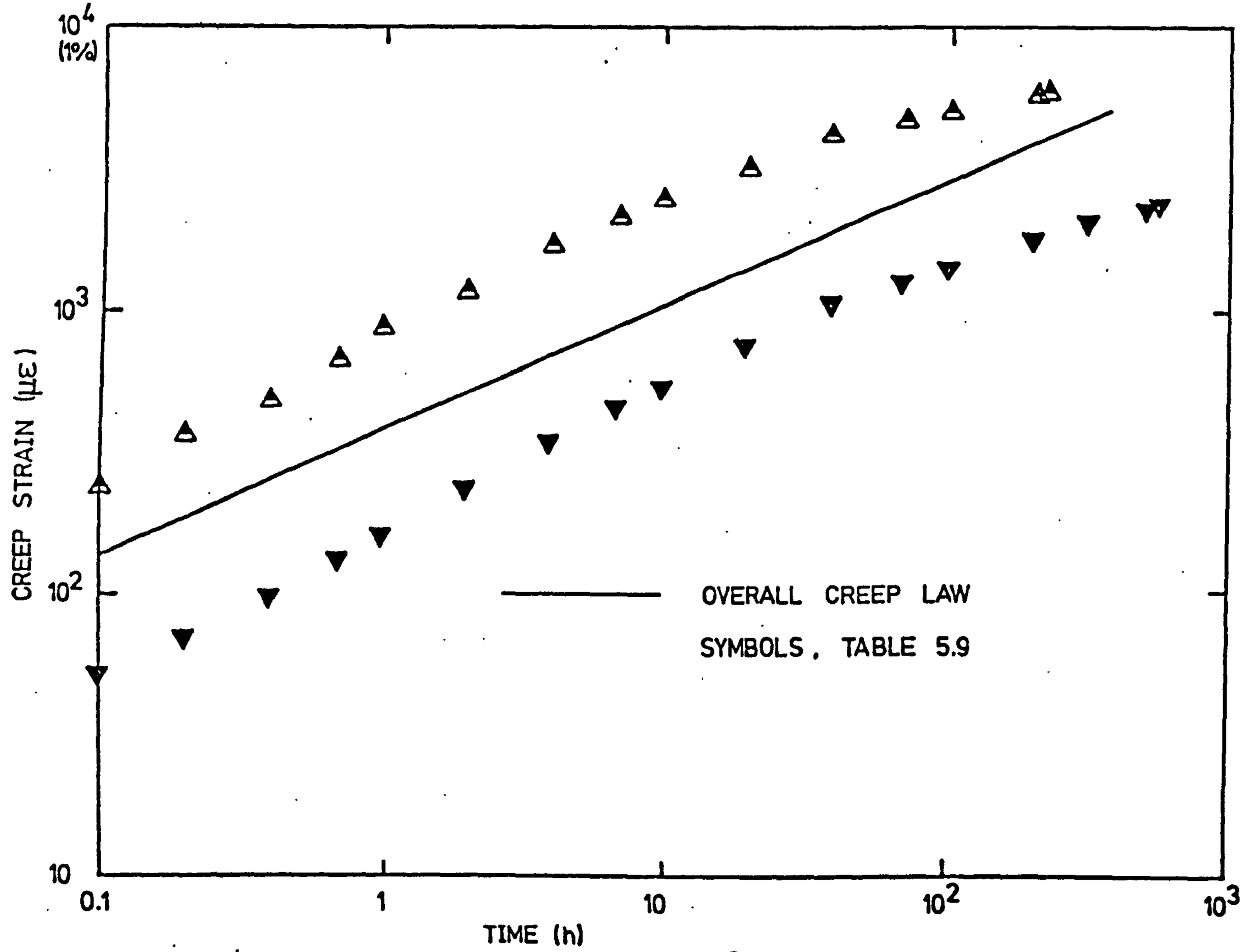

FIG. 5.18(f) CREEP DATA AT 12.30 N/mm^2

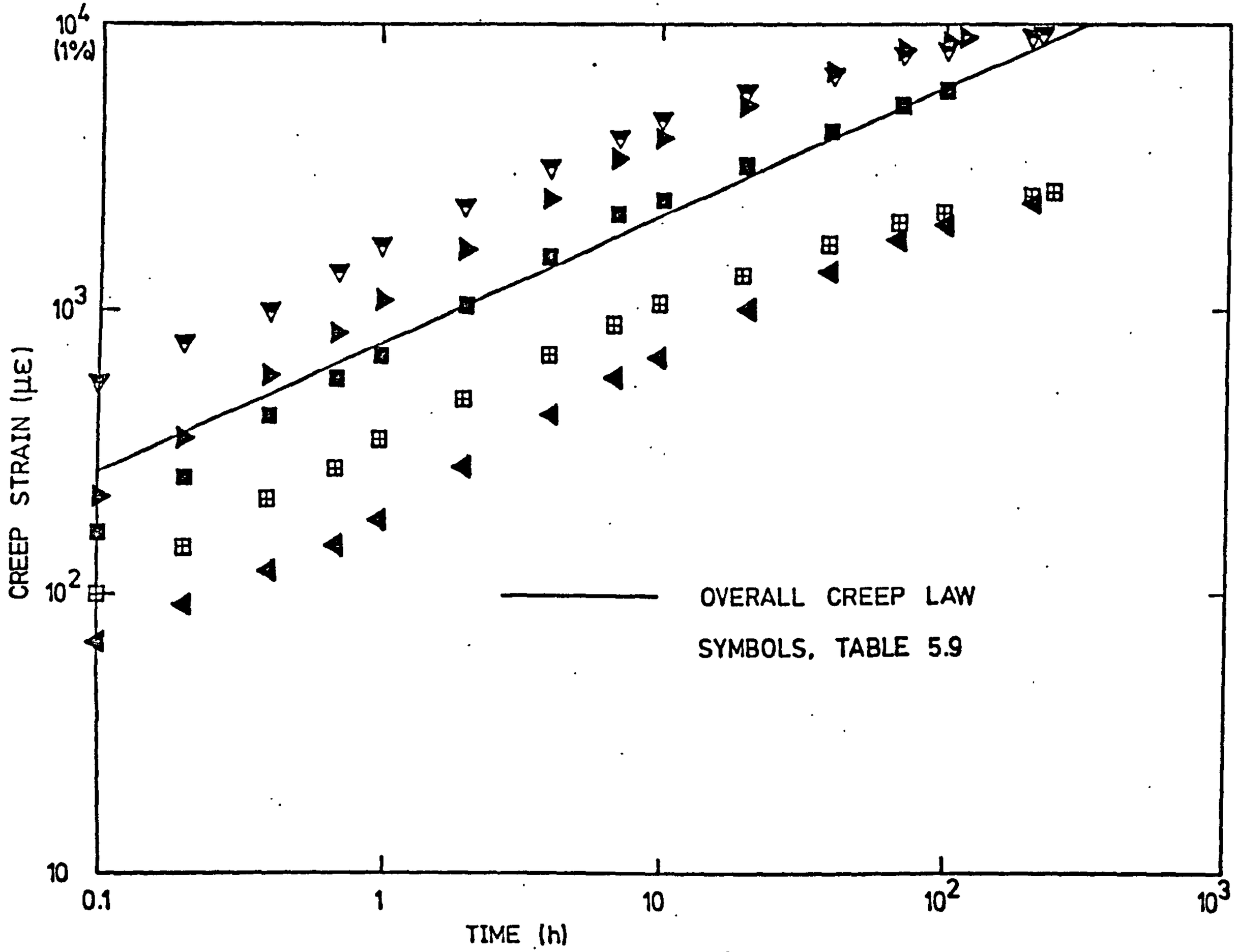

FIG. 5.18(g) CREEP DATA AT 14.05 N/mm^2

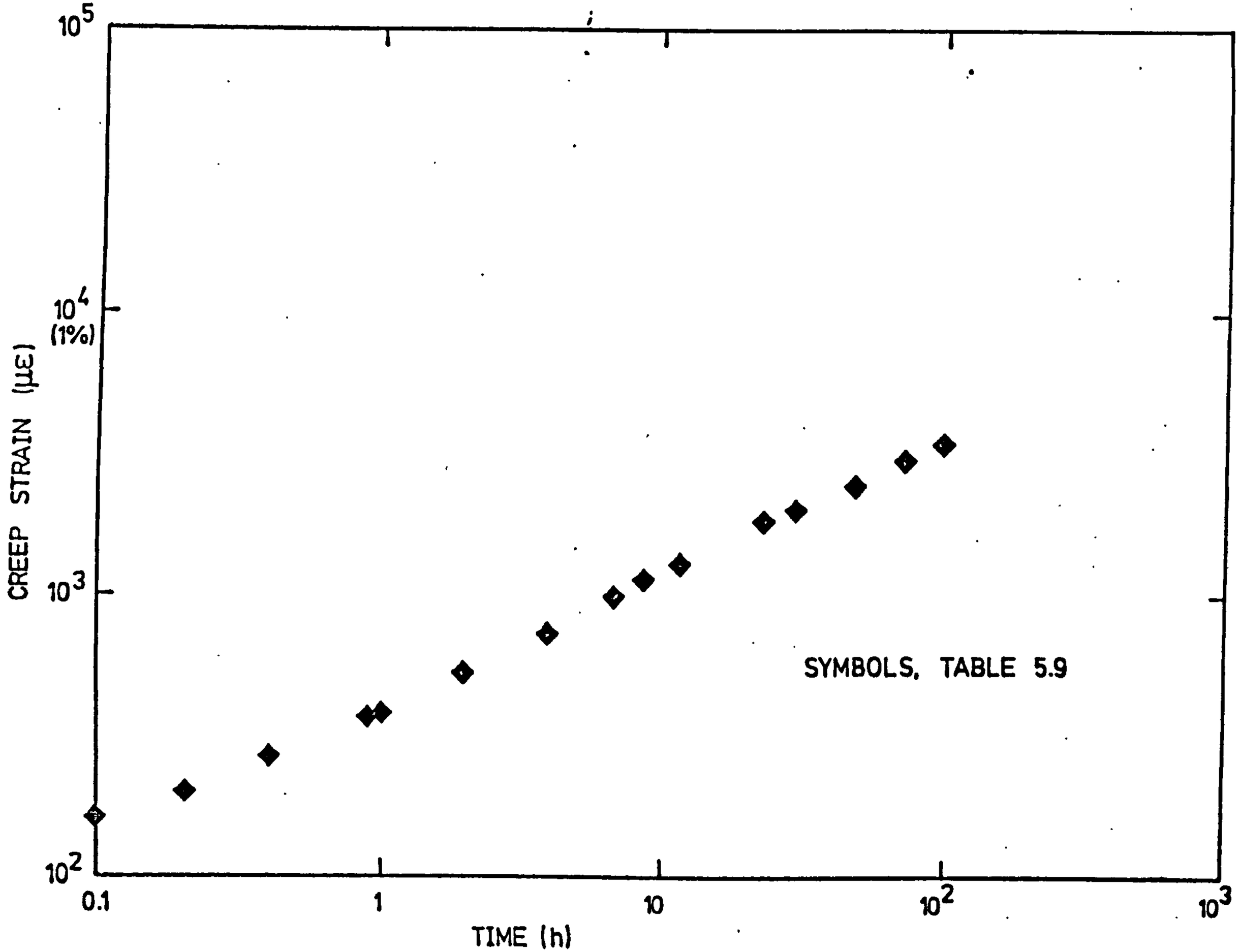

FIG. 5.18(h) CREEP DATA AT 15.81 N/mm^2

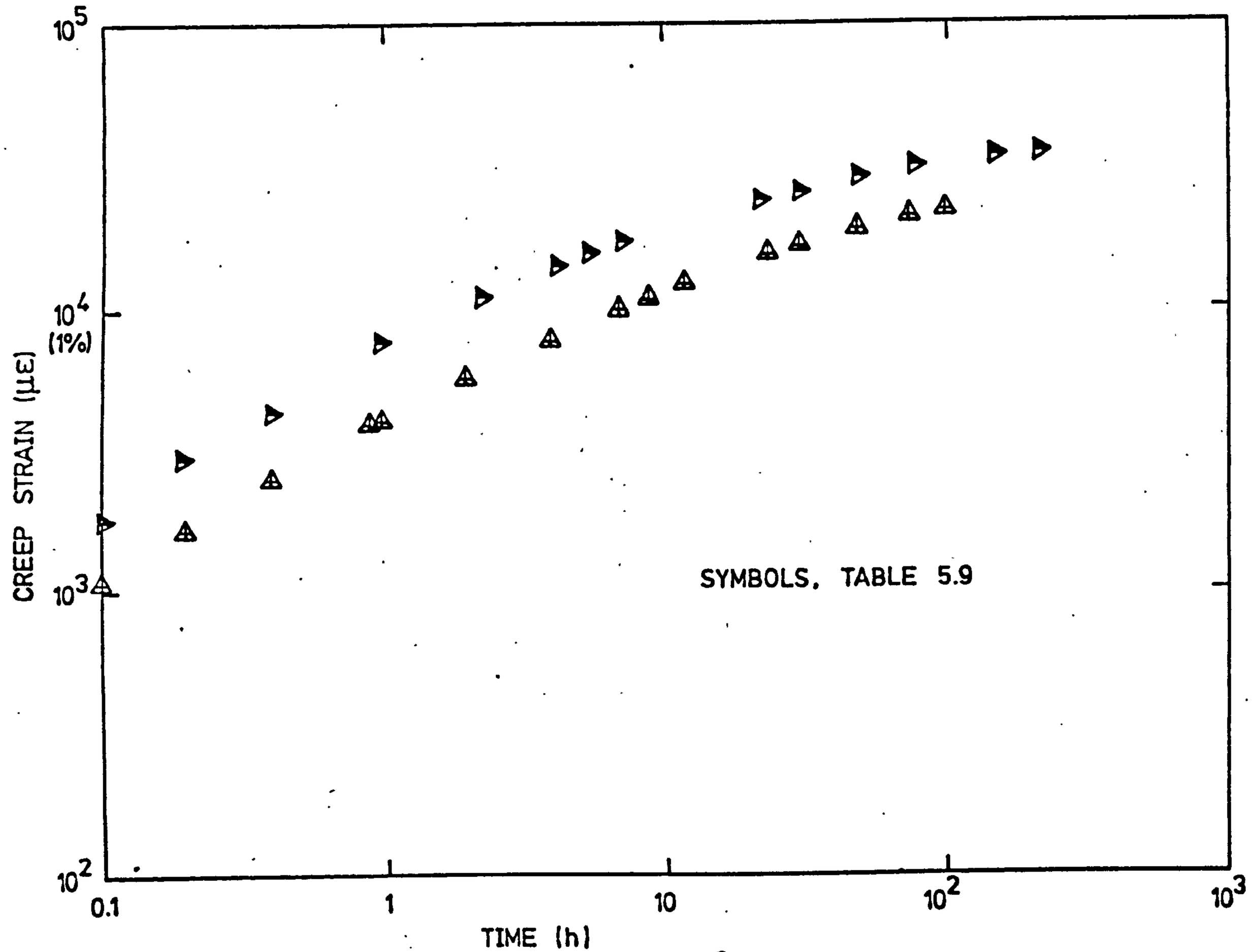

FIG. 5.18(i) CREEP DATA AT 17.57 N/mm^2

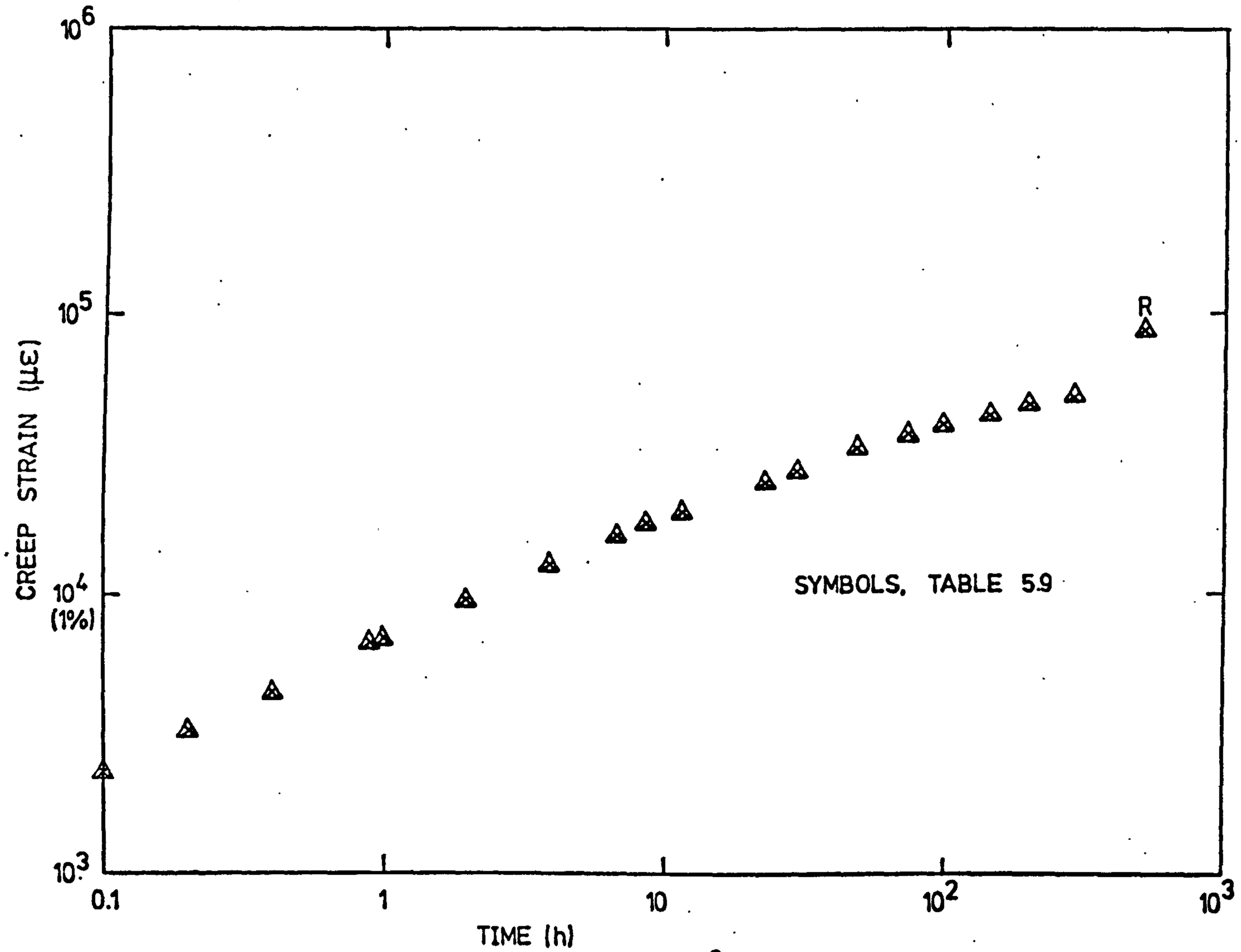

FIG. 5.18(j) CREEP DATA AT 19.32 N/mm^2

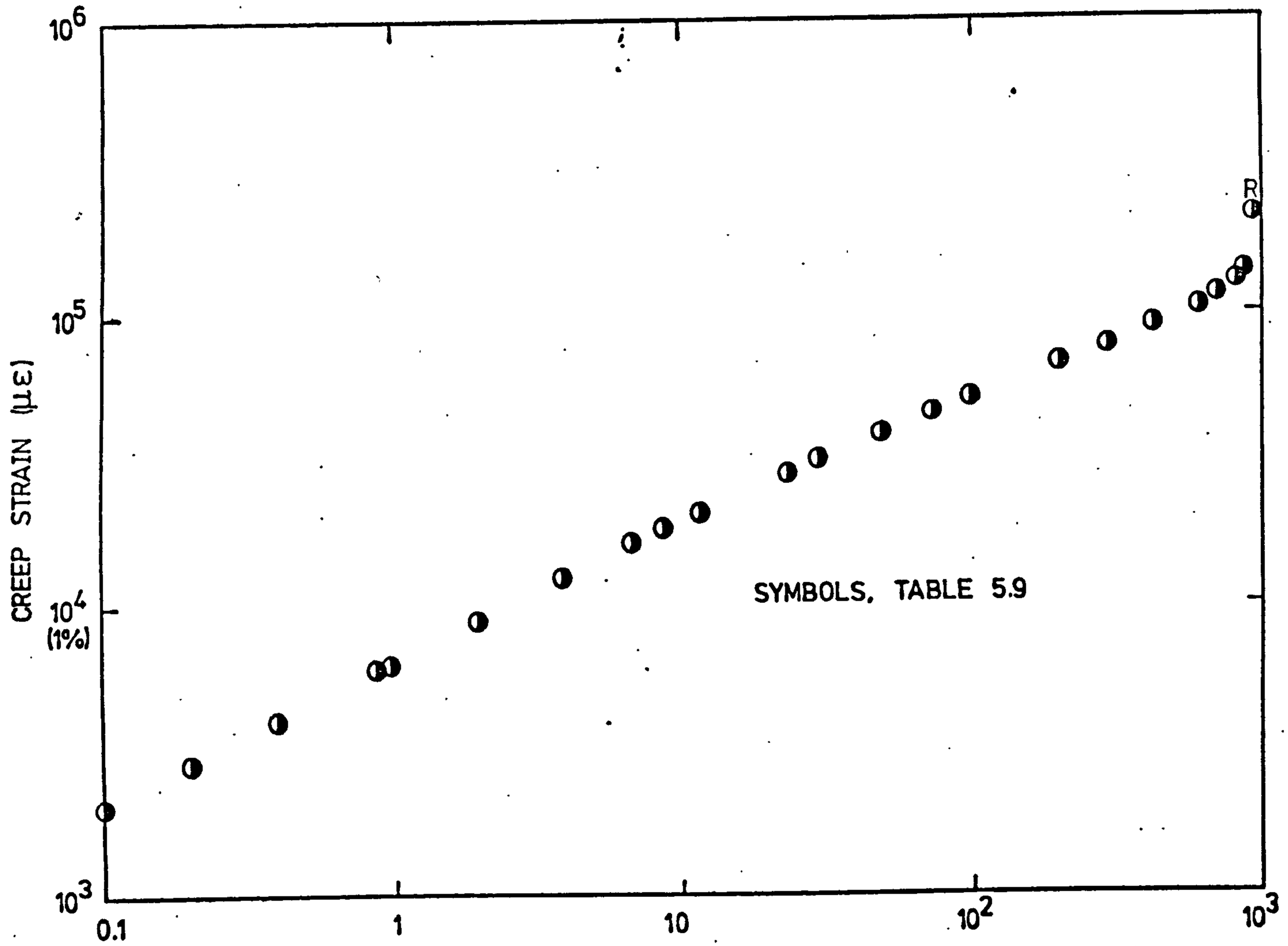

FIG. 5.18(k) CREEP DATA AT 21.08 N/mm^2

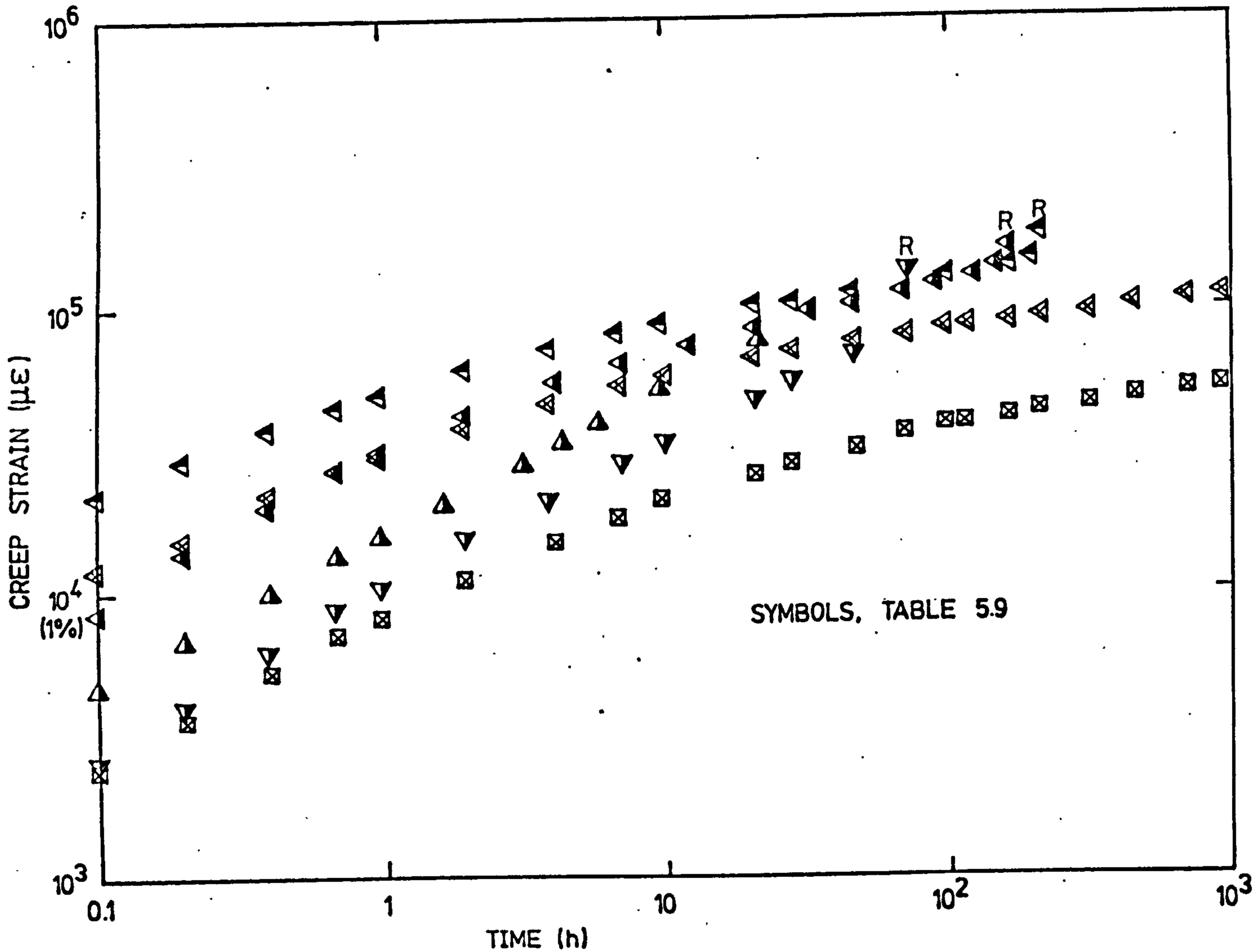

FIG. 5.18(I) CREEP DATA AT 22.84 N/mm^2

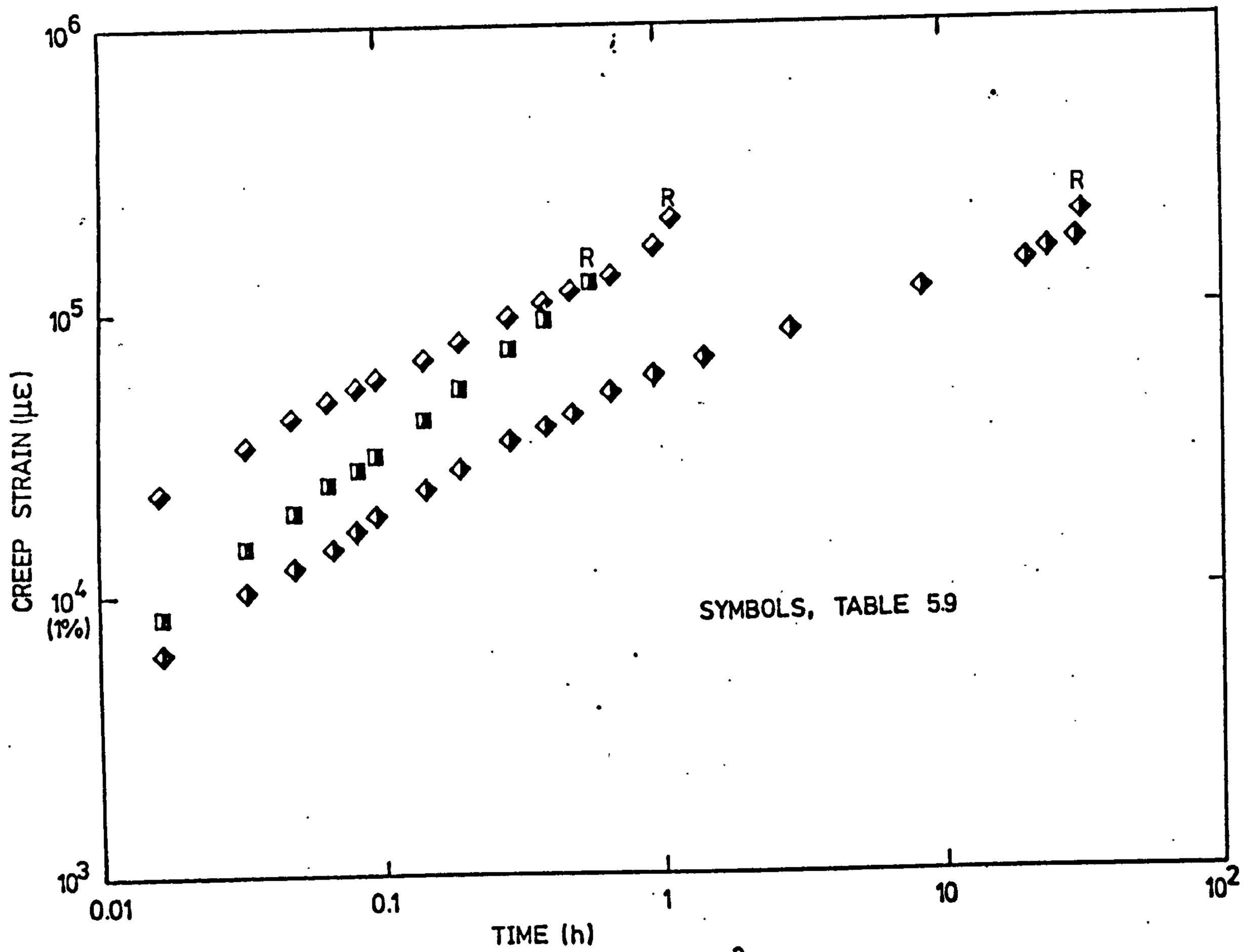

FIG. 5.18(m) CREEP DATA AT 24.59 N/mm^2

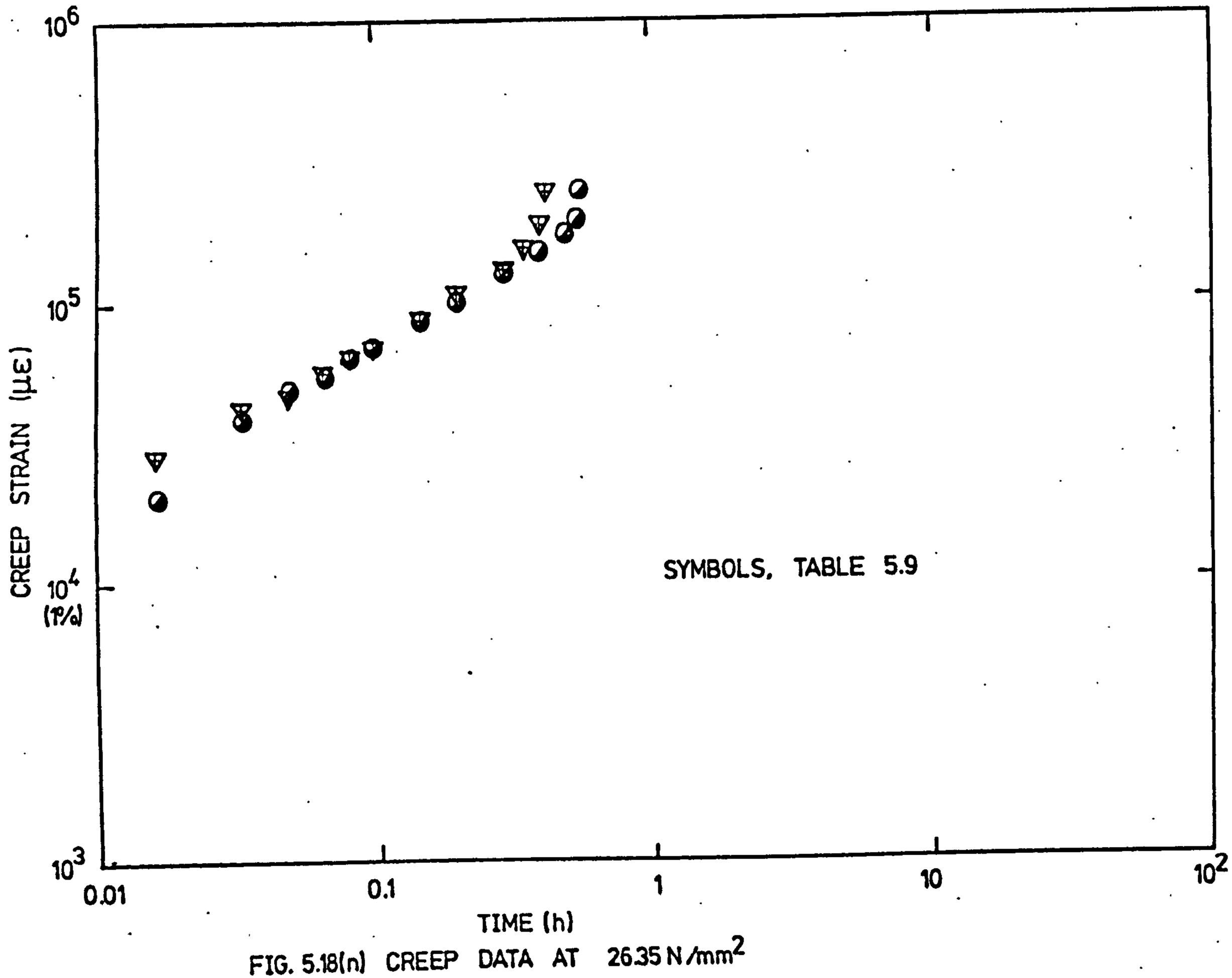

FIG. 5.18(n) CREEP DATA AT 26.35 N/mm^2

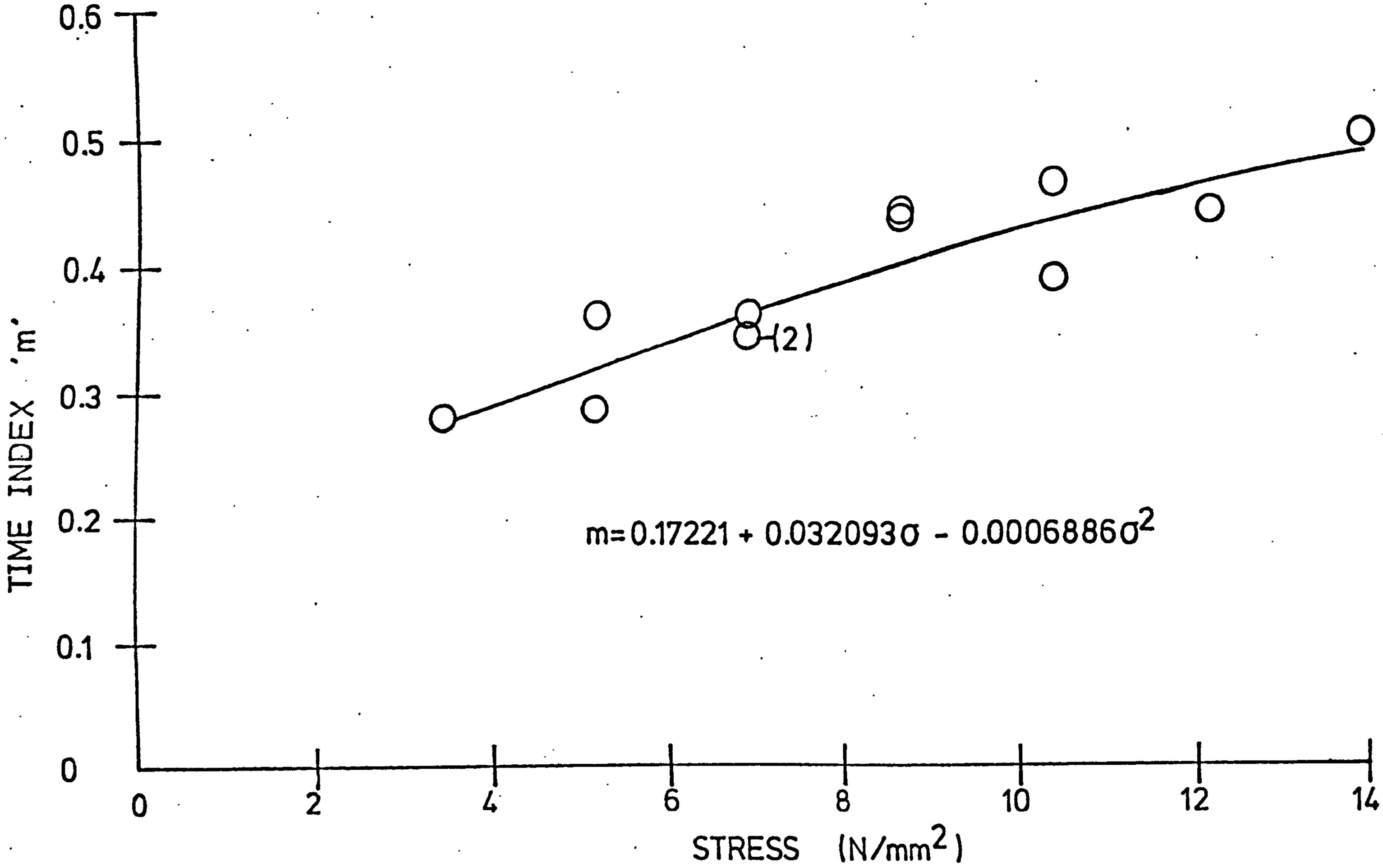

FIG. 5.19(a) VARIATION OF 'm' WITH STRESS FOR CASTING P7

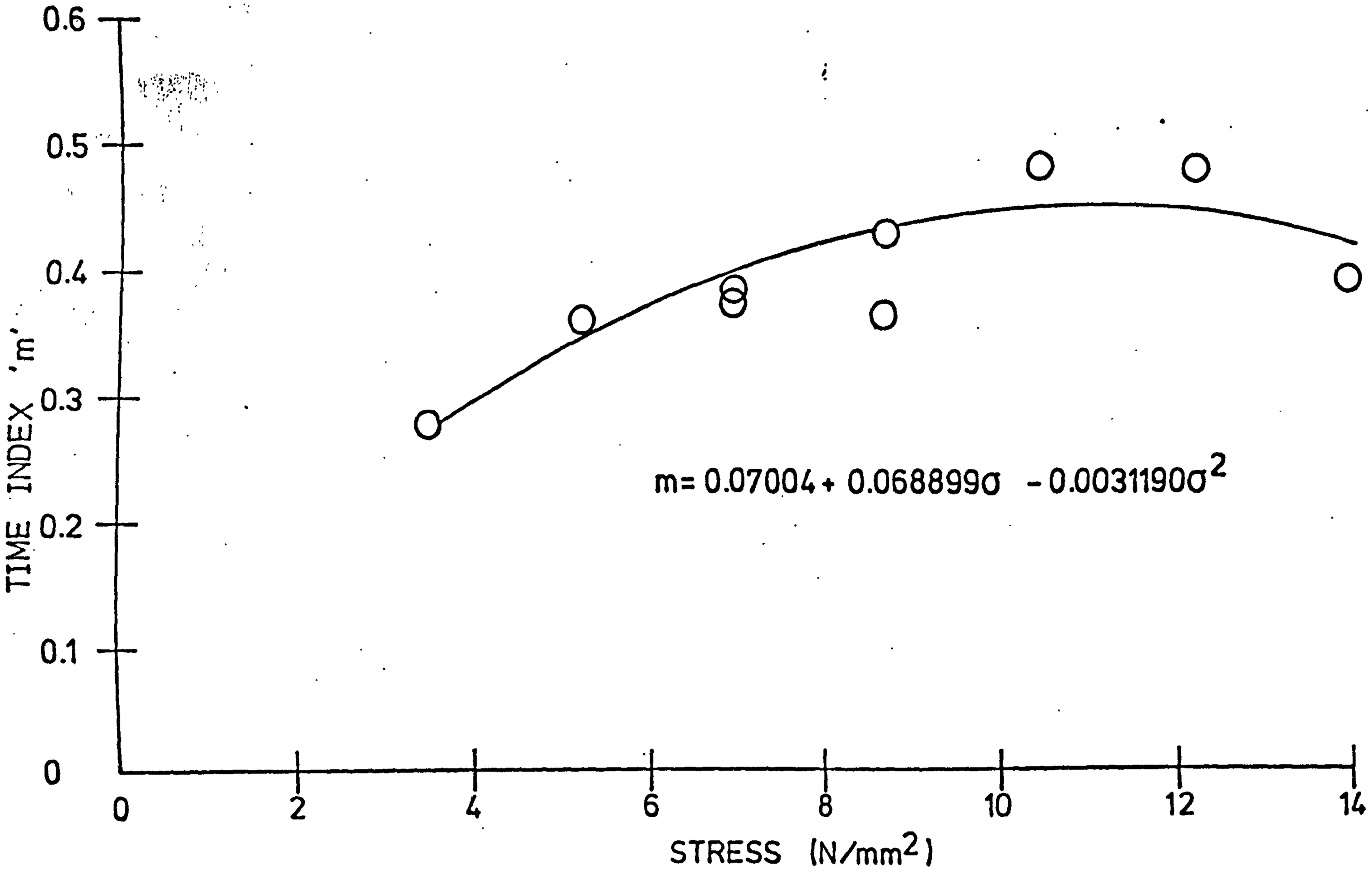

FIG. 5.19 (b) VARIATION OF 'm' WITH STRESS FOR CASTING P9

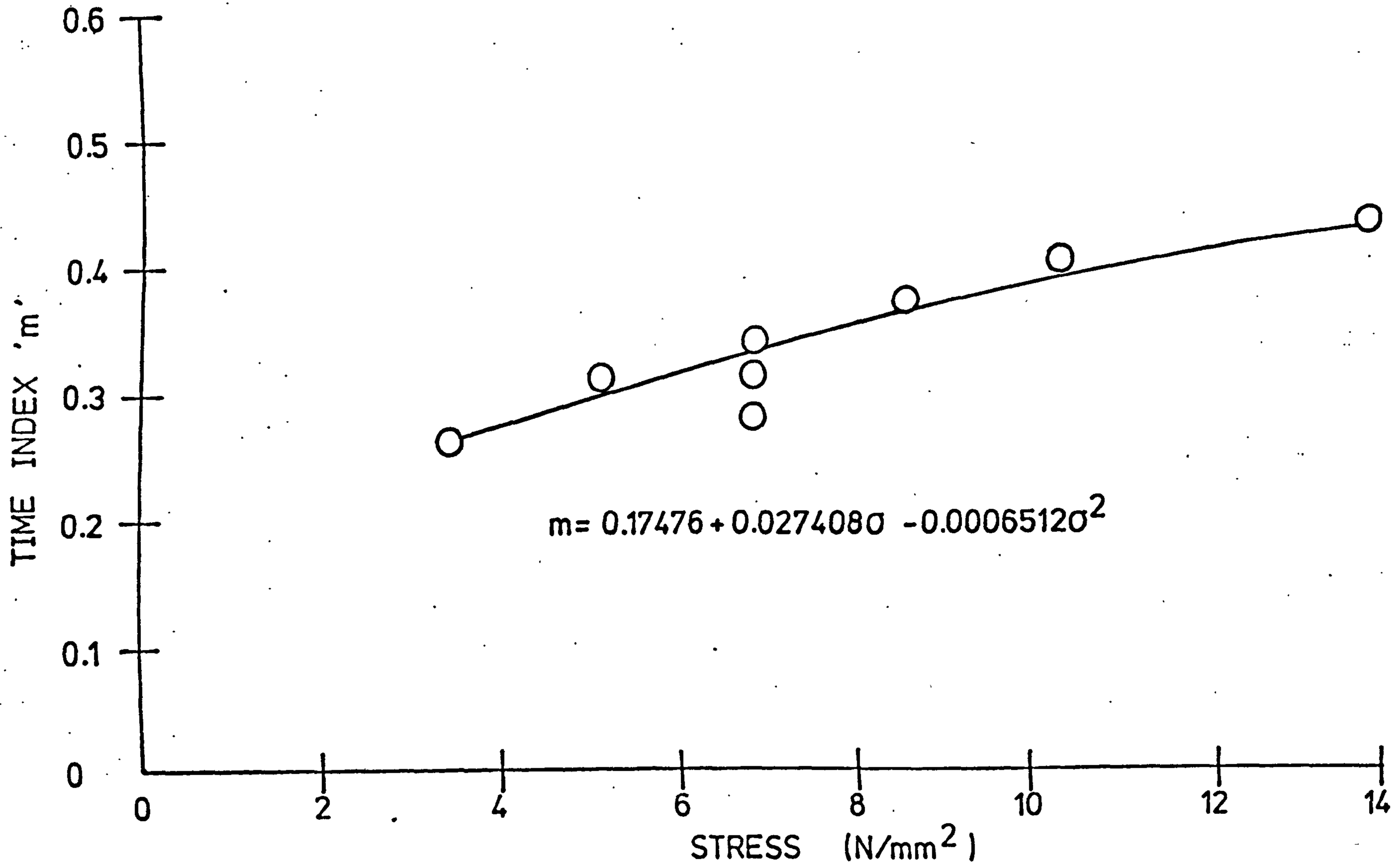

FIG. 5.19(c) VARIATION OF 'm' WITH STRESS FOR CASTINGS KK19 & KK20

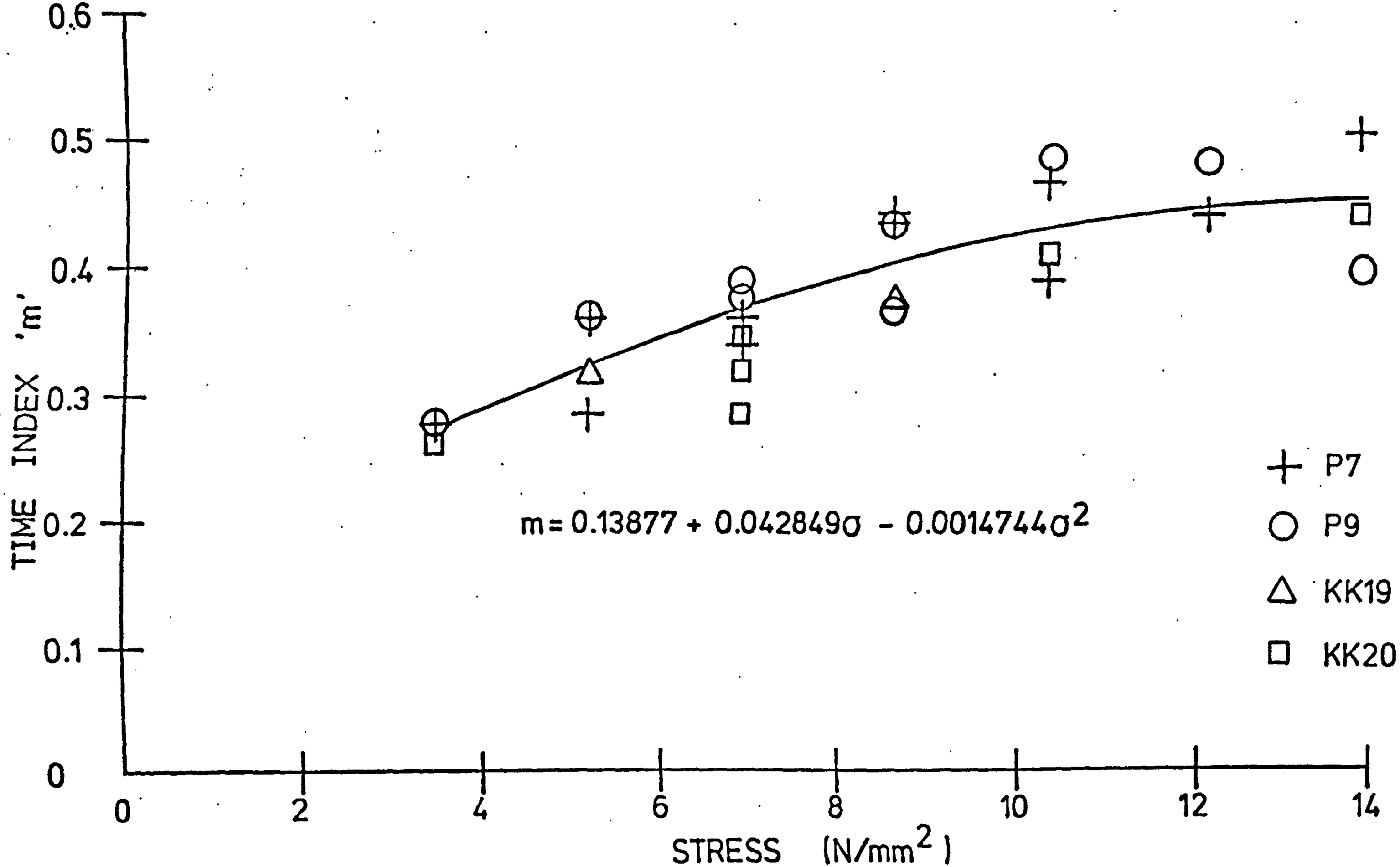

FIG. 5.19(d) VARIATION OF 'm' WITH STRESS (COMBINED DATA)

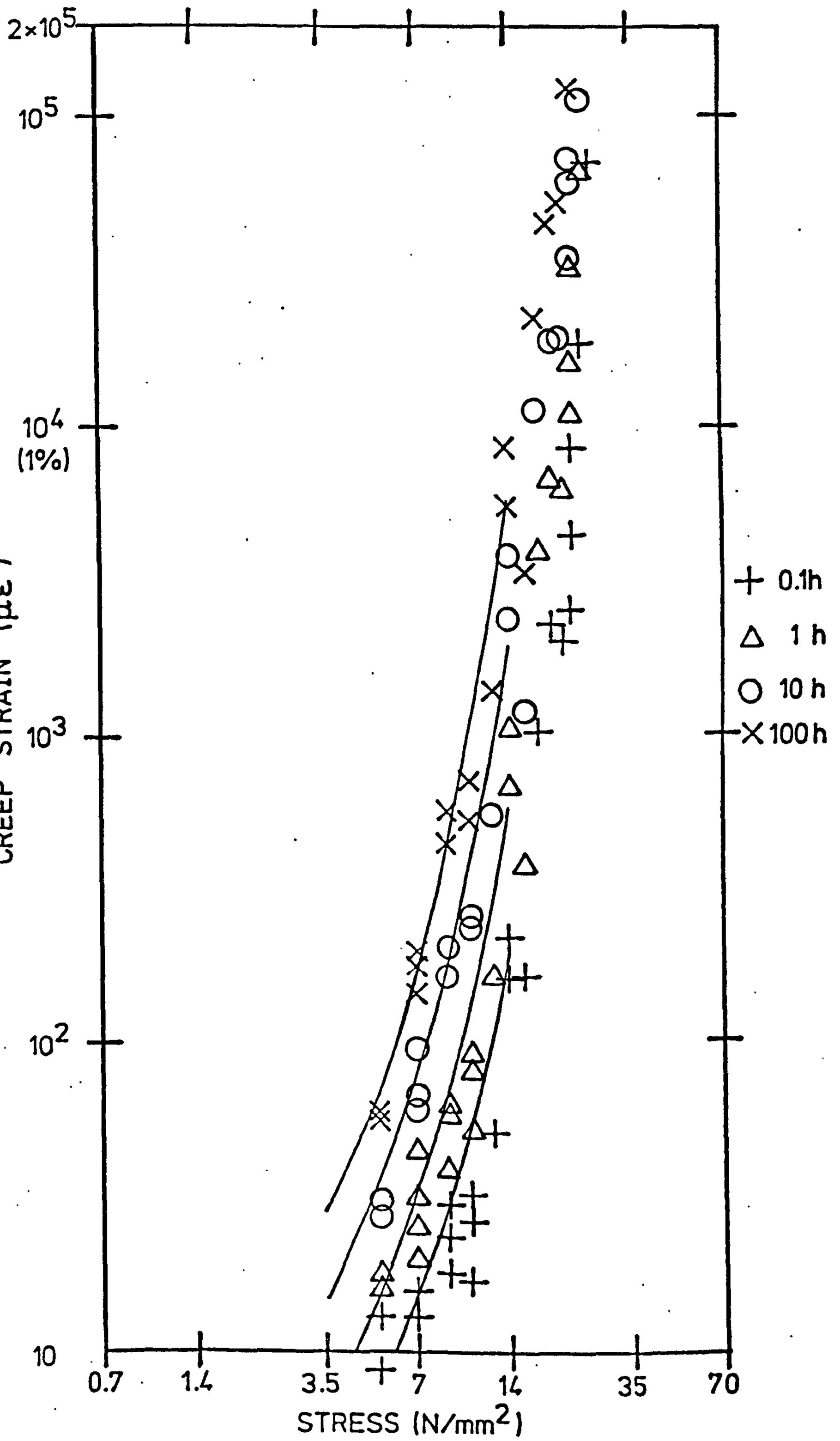

FIG.5.20(a) ISOCHRONOUS STRESS STRAIN CURVES FOR CASTING P7

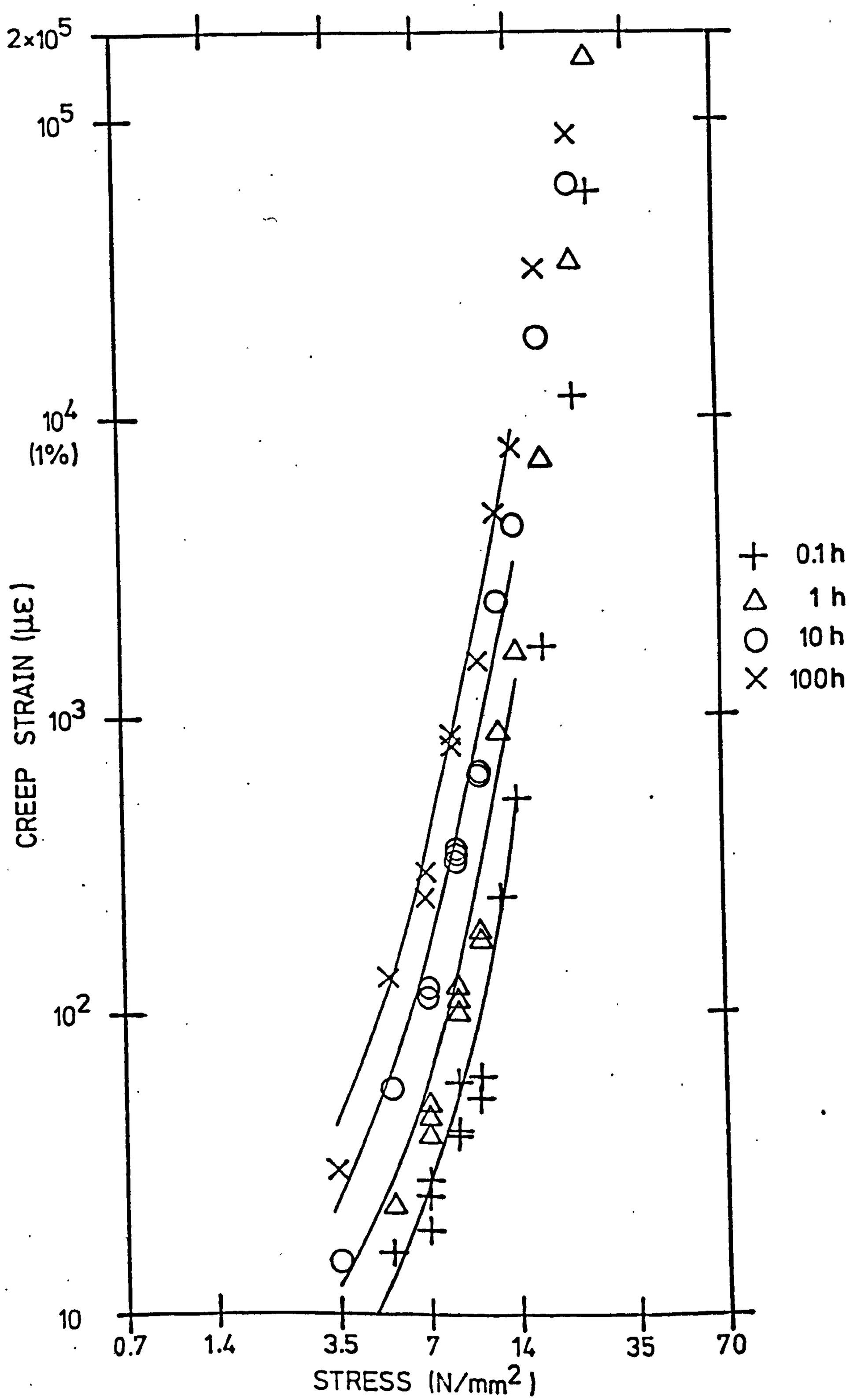

FIG. 5.20(b) ISOCHRONOUS STRESS-STRAIN CURVES FOR CASTING P9

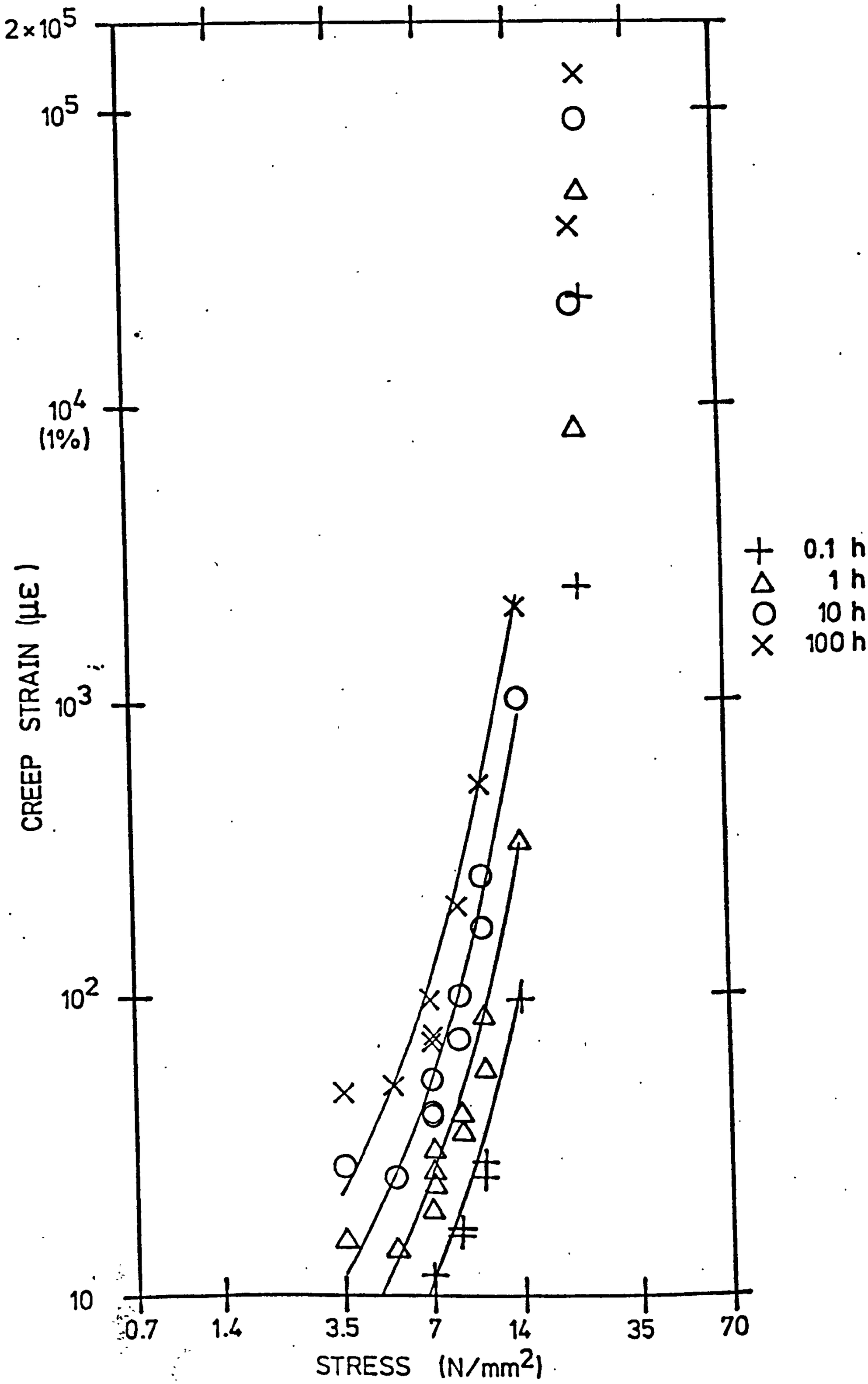

FIG. 5.20(c) ISOCHRONOUS STRESS-STRAIN CURVES FOR CASTINGS KK19 & KK20

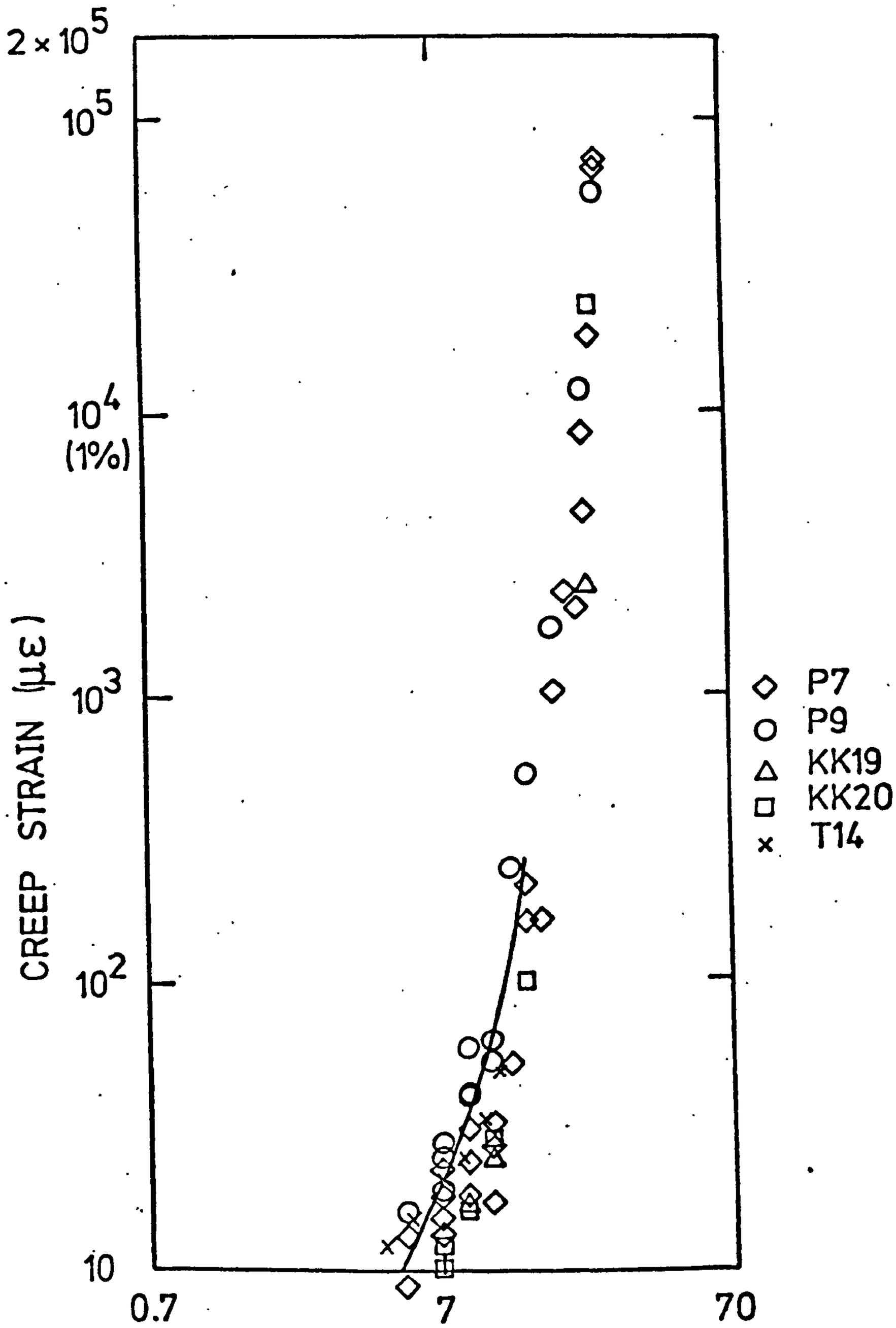

FIG. 5.21(a) OVERALL ISOCHRONOUS DATA AND CREEP LAW AT 0.1h

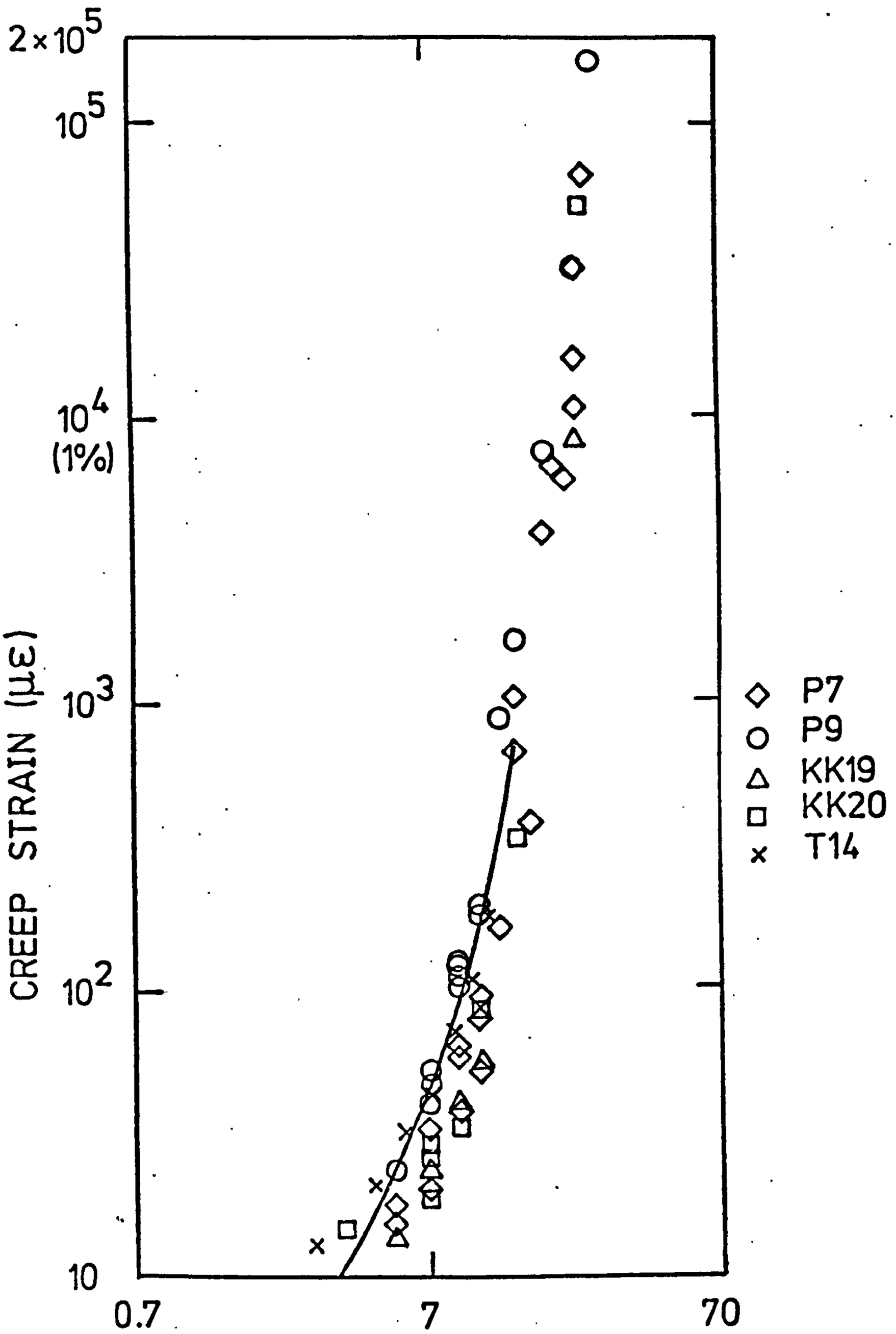

FIG. 5.21(b) OVERALL ISOCHRONOUS DATA AND CREEP LAW AT 1h

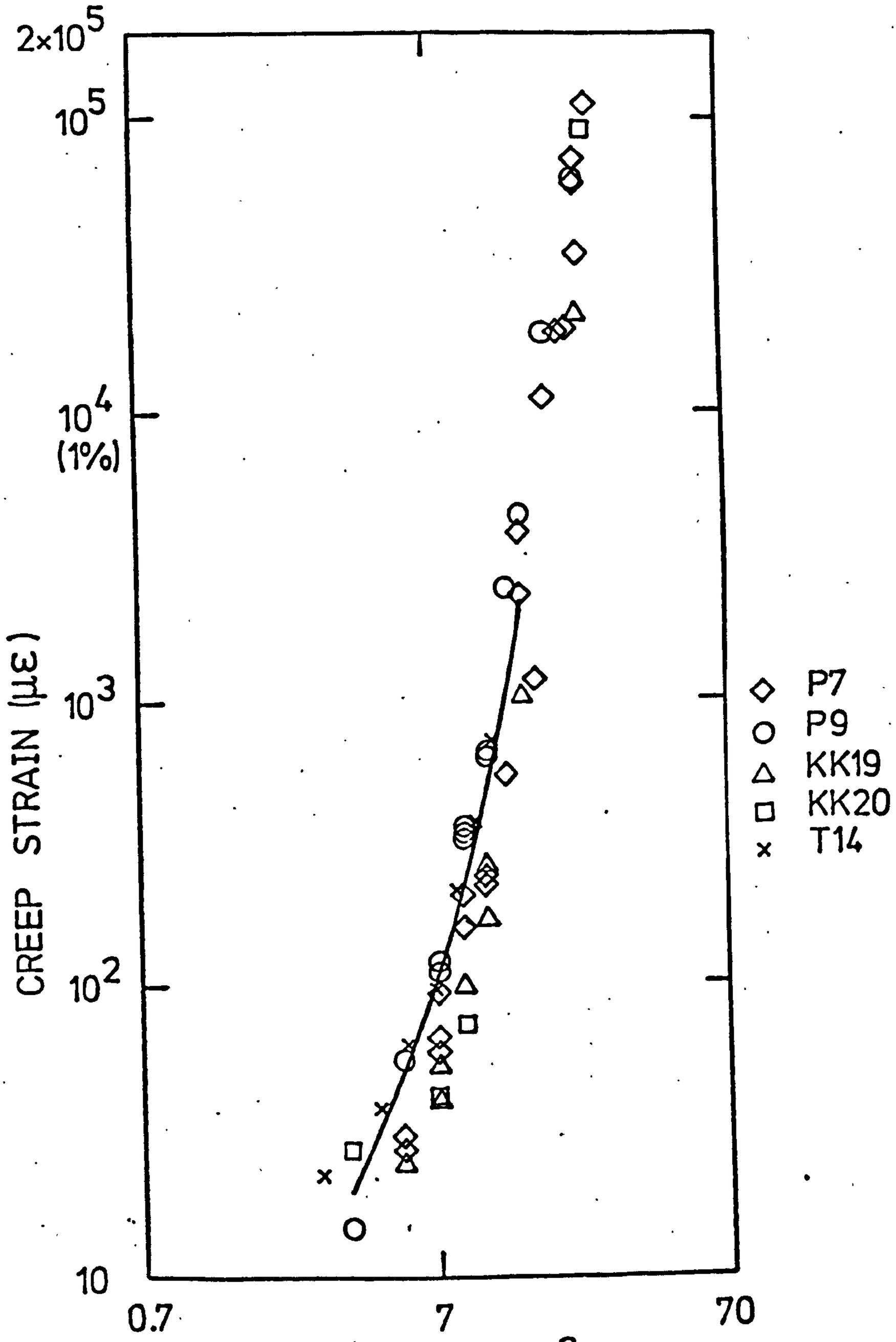

FIG. 5.21(c) OVERALL ISOCHRONOUS DATA AND CREEP LAW AT 10h

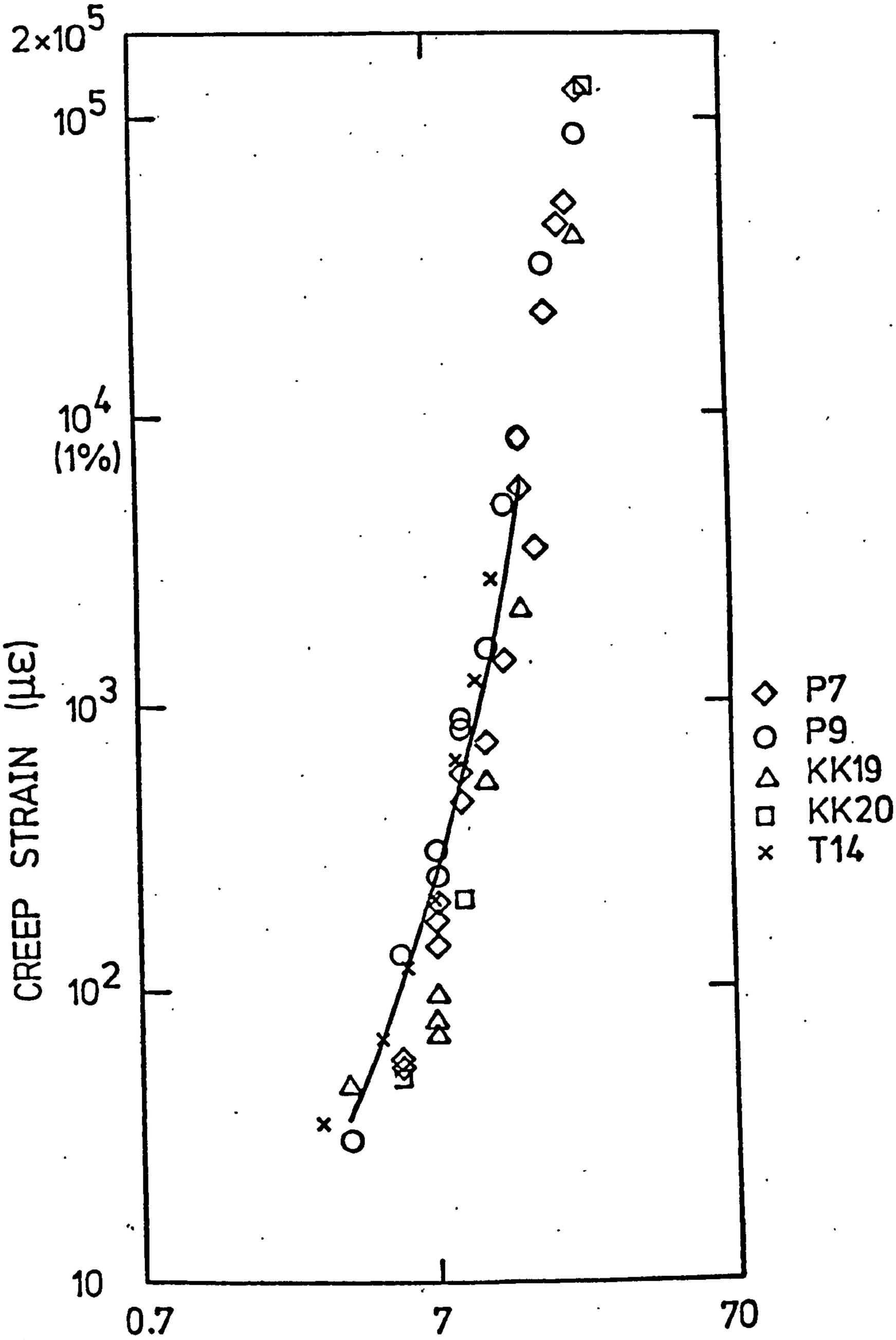

FIG. 5.21(d) OVERALL ISOCHRONOUS DATA AND CREEP LAW AT 100h

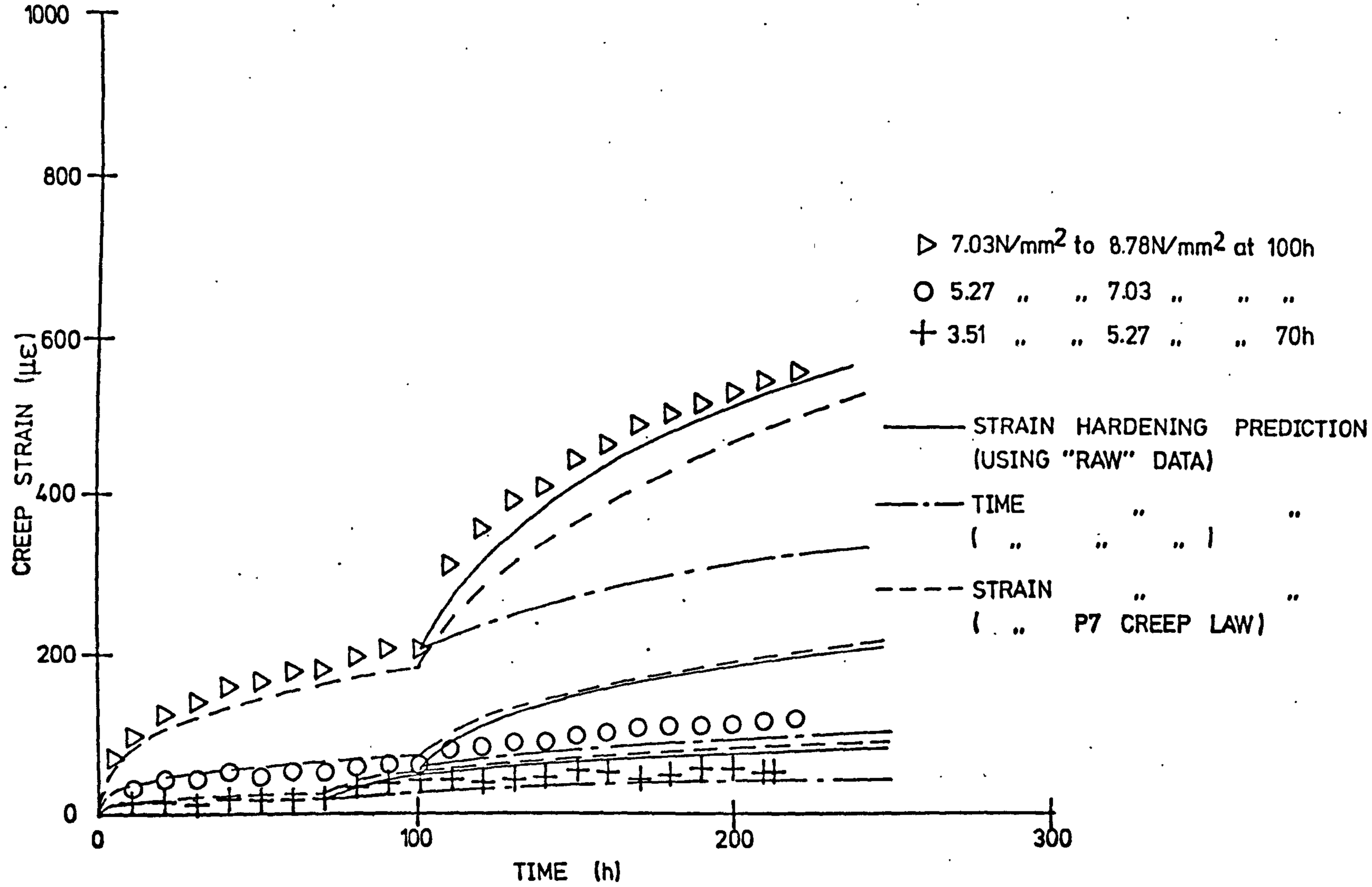

FIG. 5.22(a) P7 'STEPPED UP' CREEP TESTS

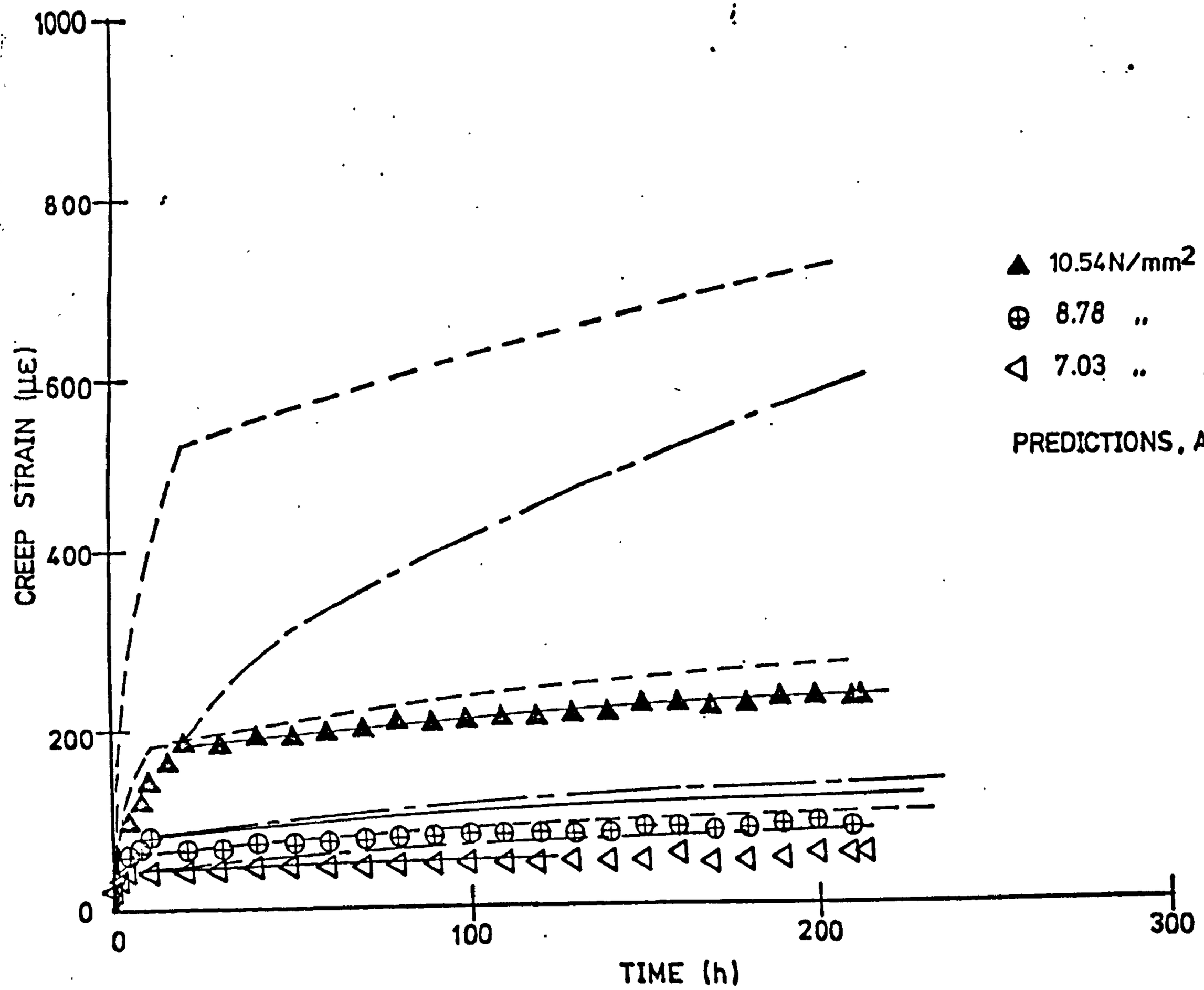

FIG. 5·2 2 (b) P7 'STEPPED DOWN' CREEP TESTS

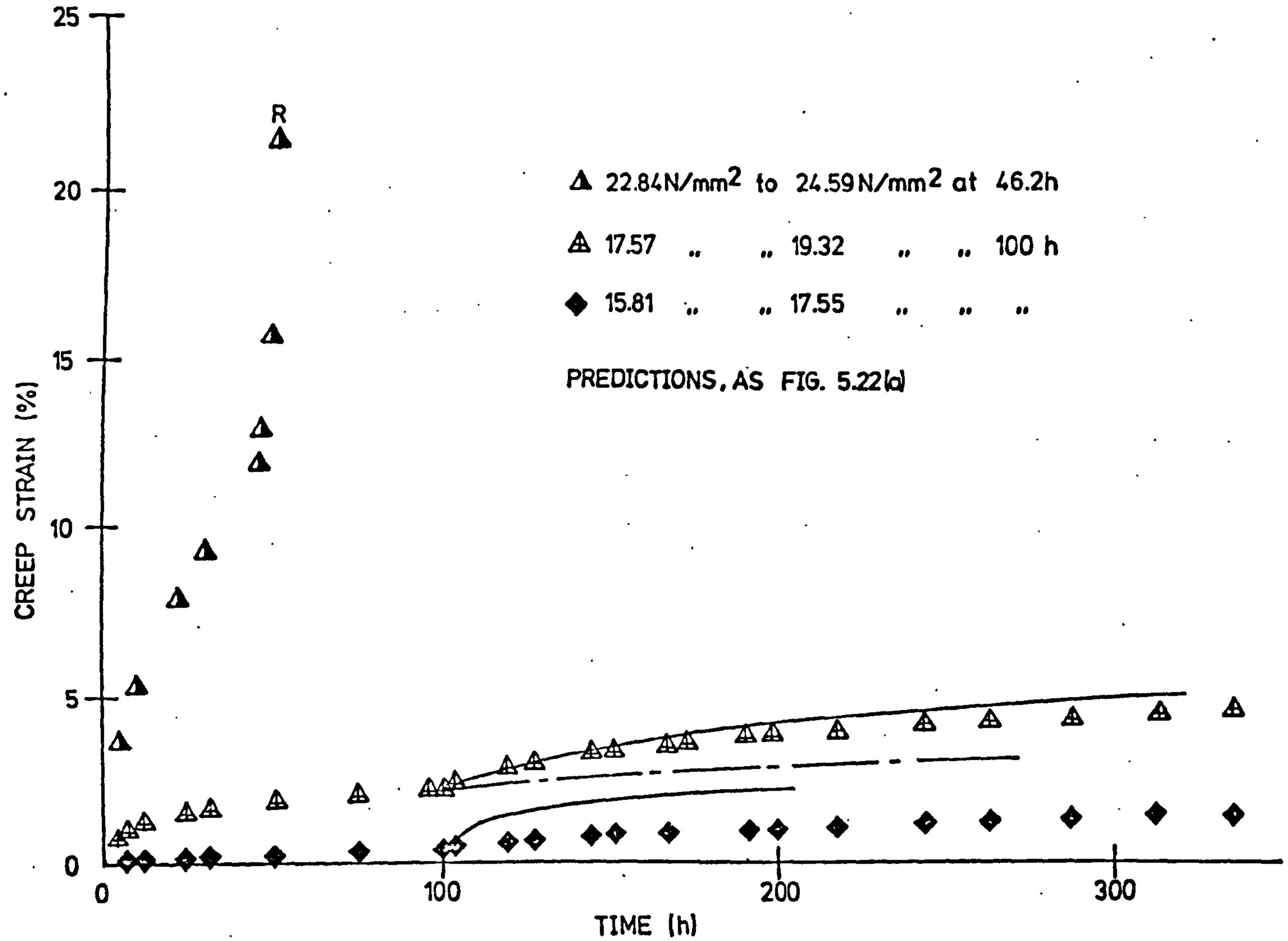

FIG. 5.22(c) P7 'STEPPED UP' CREEP TESTS

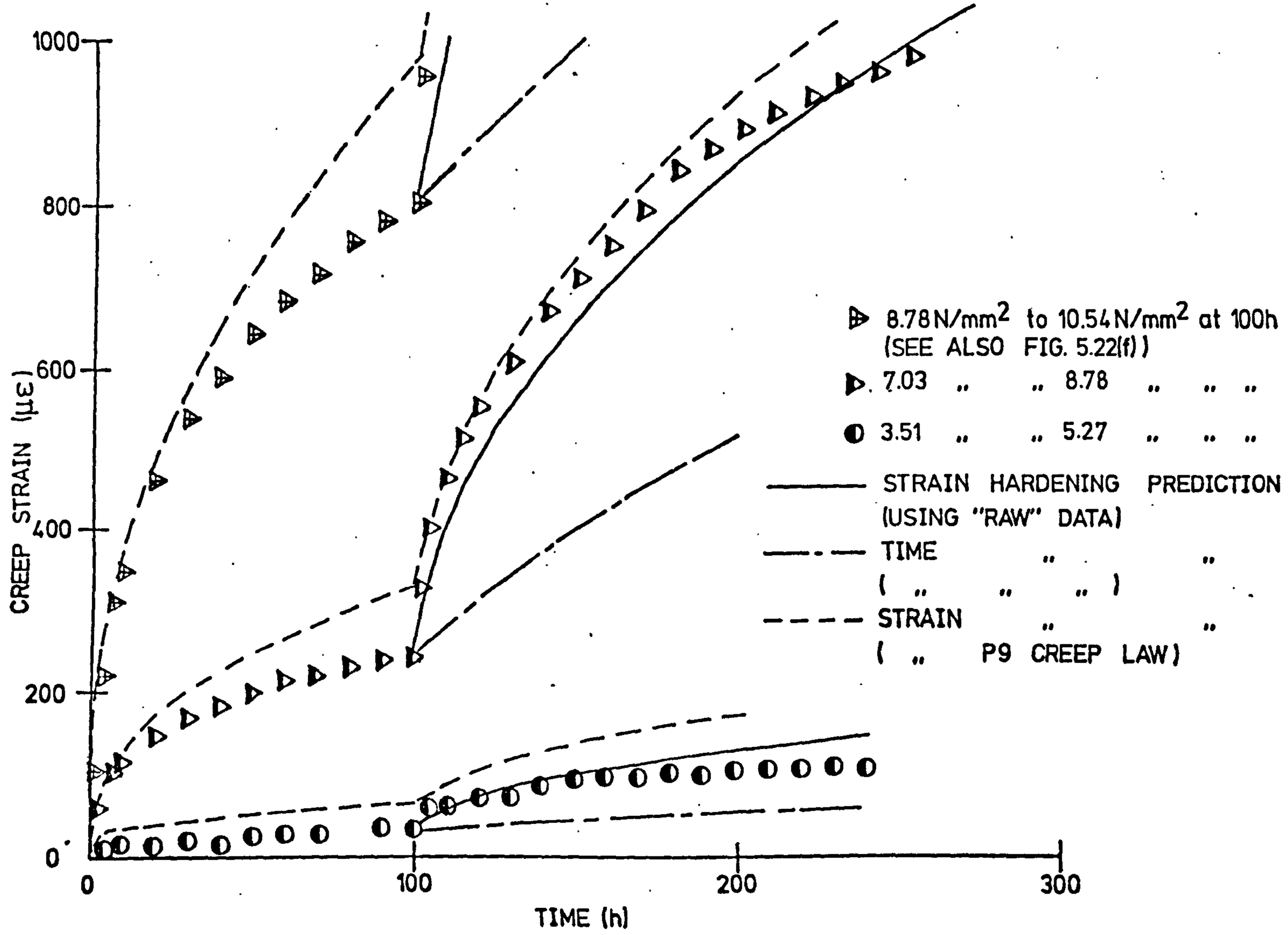

FIG. 5.22(d) P9 'STEPPED UP' CREEP TESTS

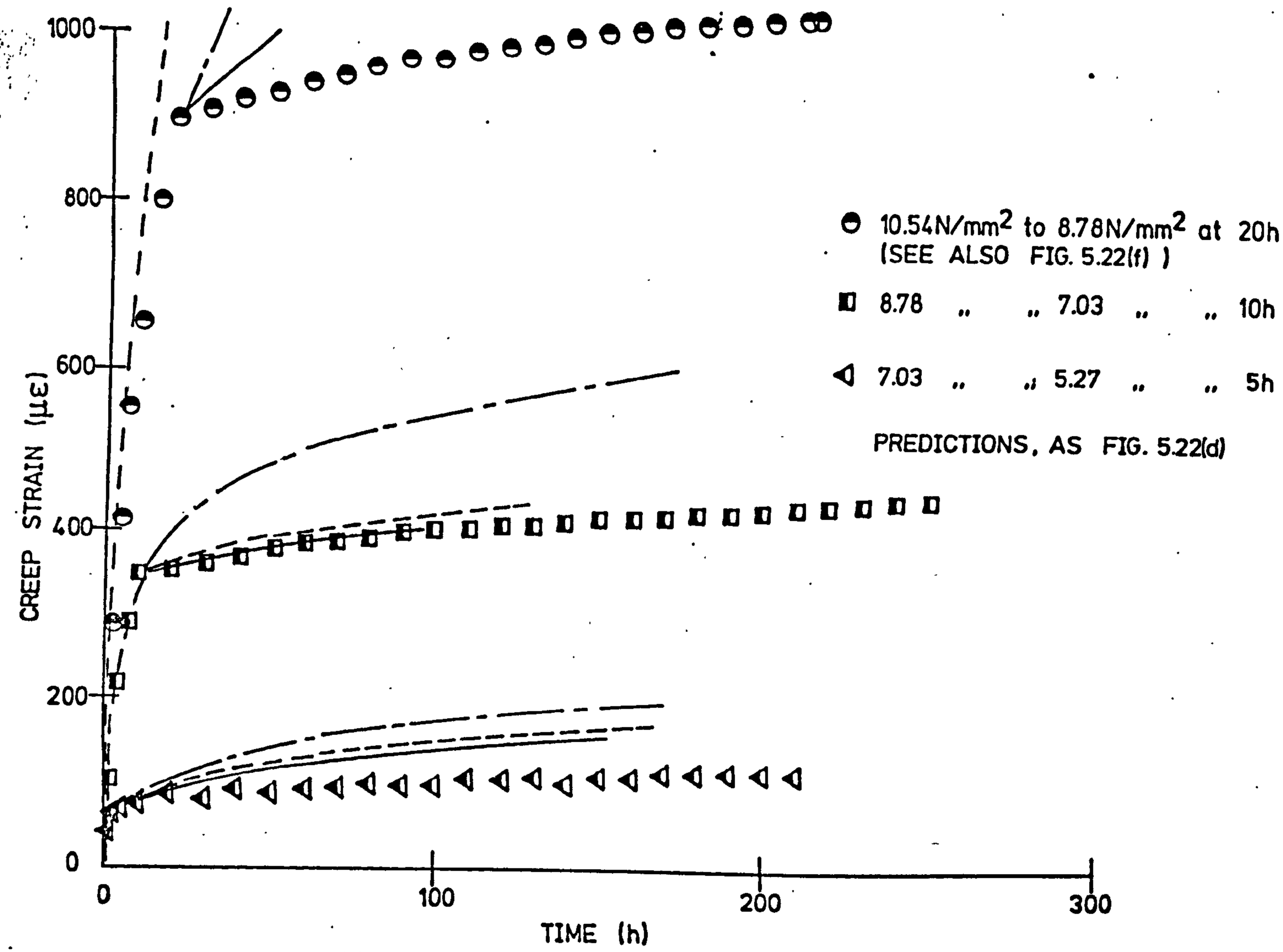

FIG. 5.22(e) P9 'STEPPED DOWN' CREEP TESTS

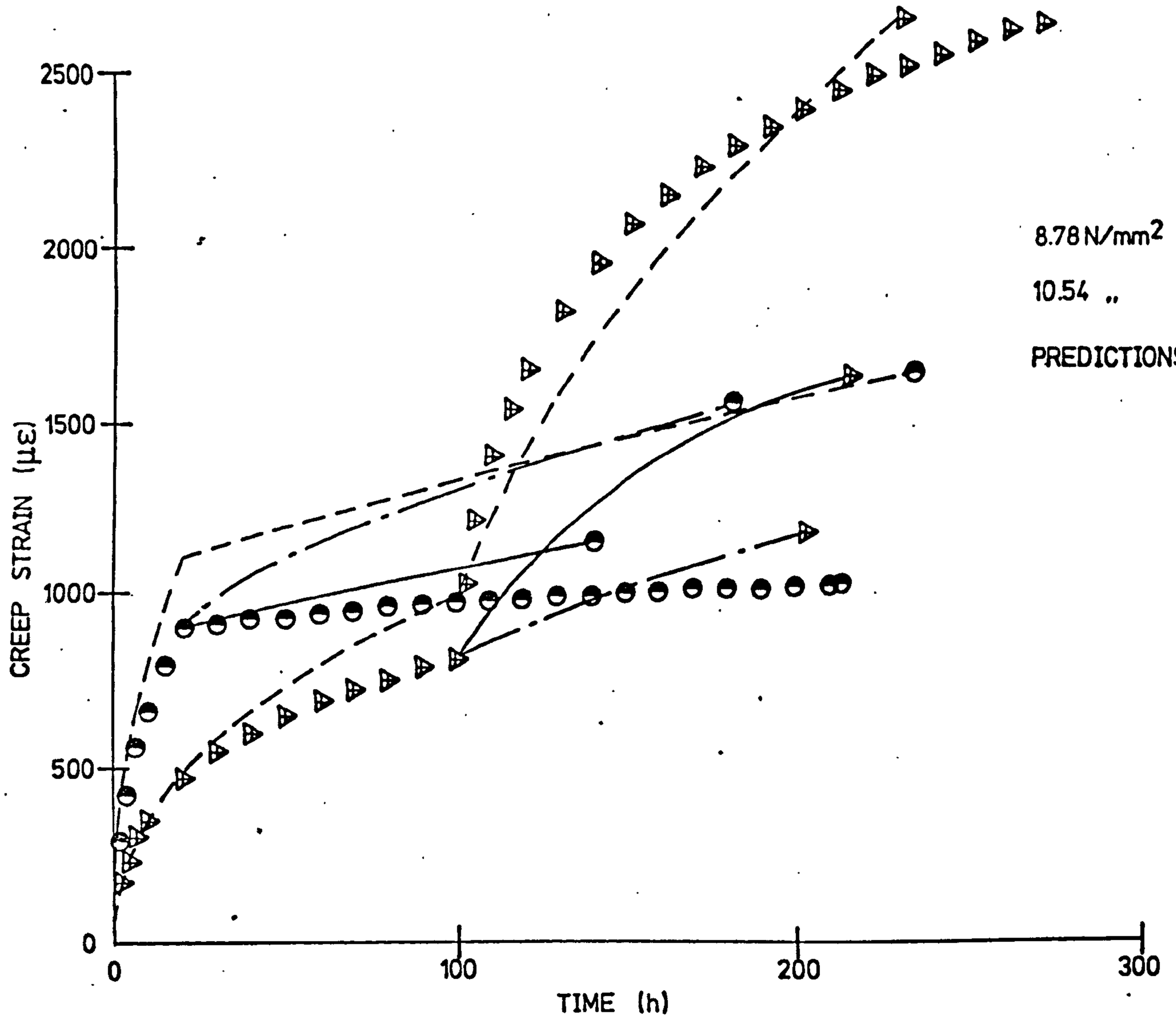

FIG. 5.22(f) P9 'STEPPED LOAD' CREEP TESTS

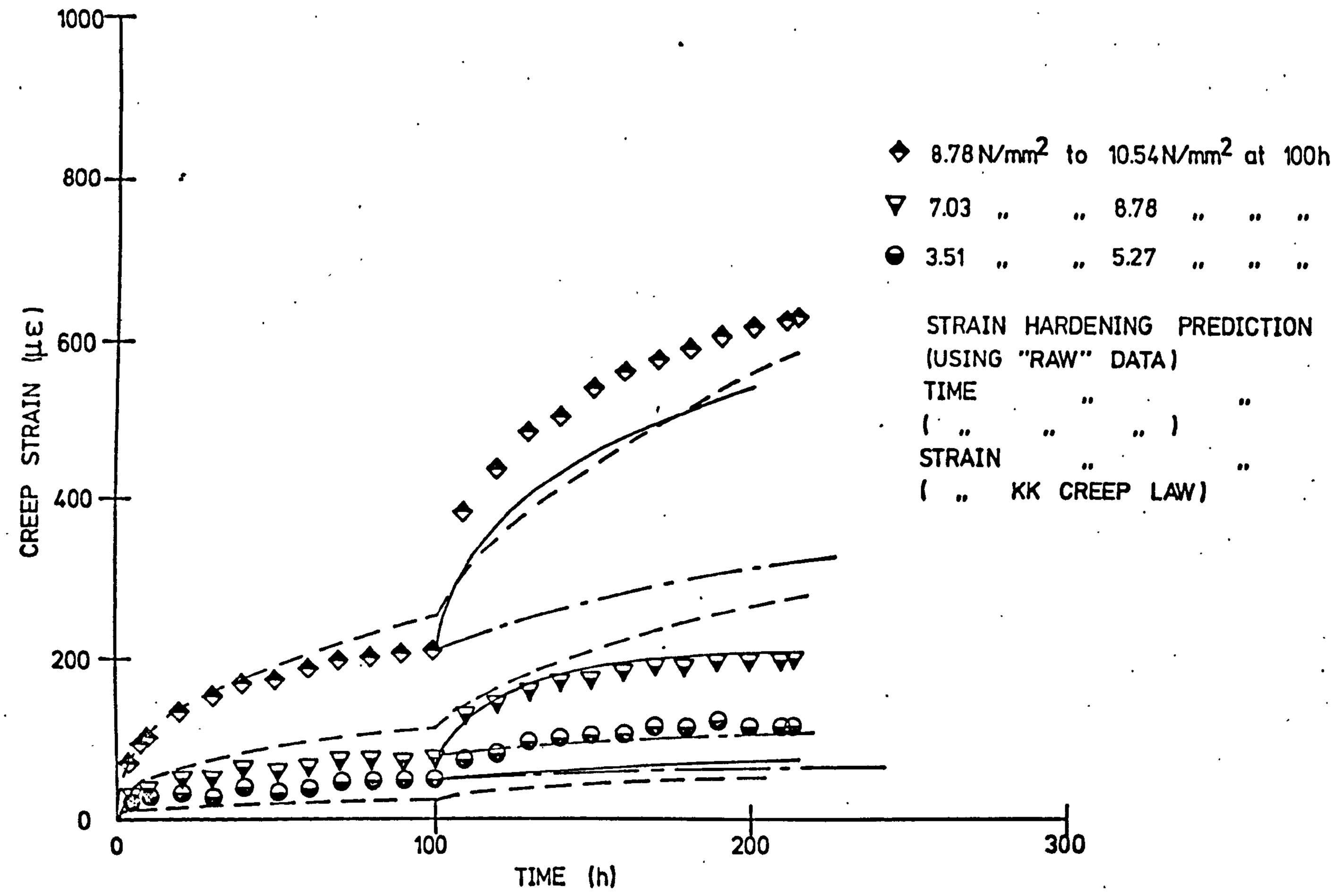

FIG. 5.22(g) KK 'STEPPED UP' CREEP TESTS

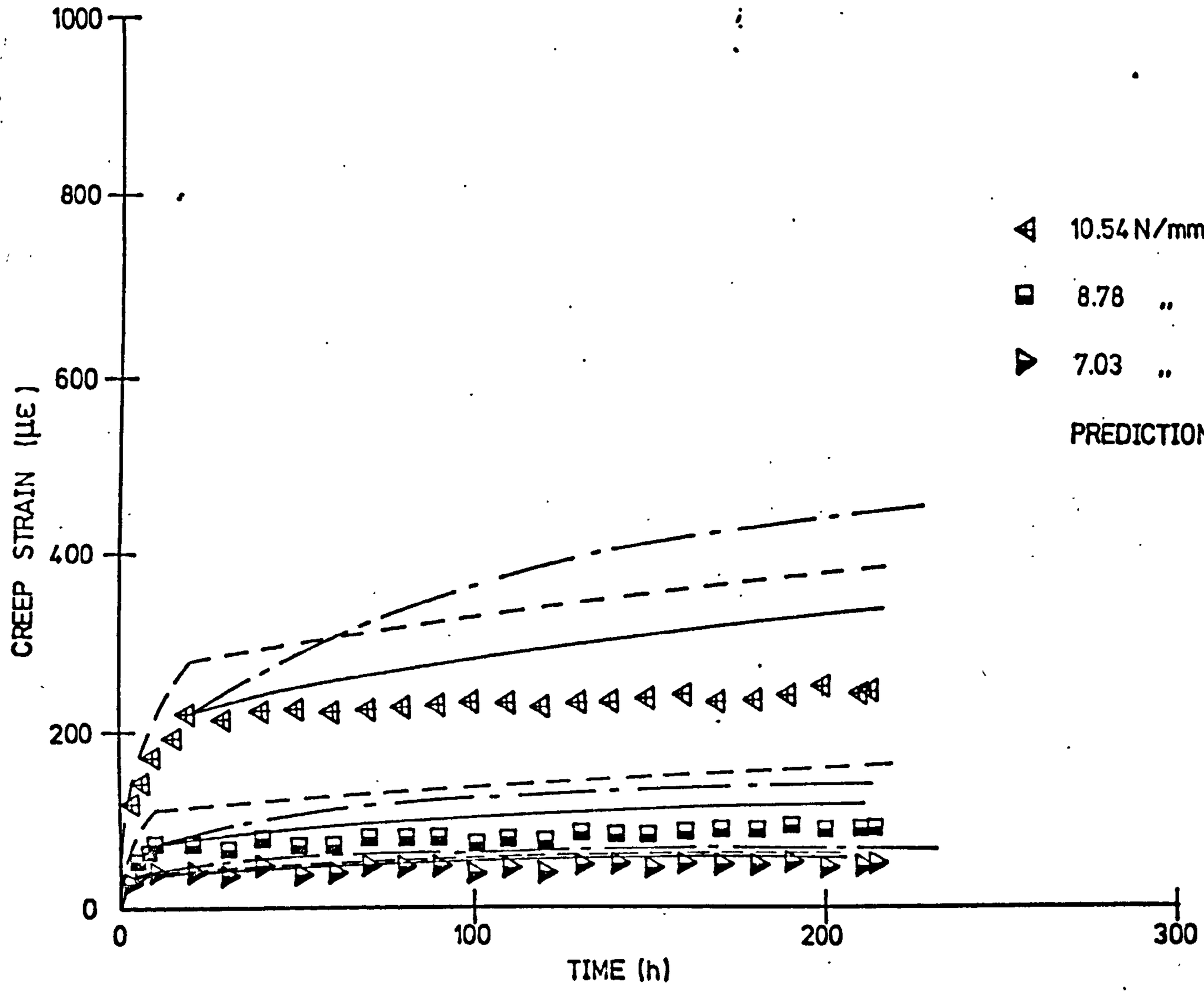

◀ 10.54 N/mm² to 8.78 N/mm² at 20h

■ 8.78 „ „ 7.03 „ „ 10h

▶ 7.03 „ „ 5.27 „ „ 5h

PREDICTIONS, AS FIG.5.22(g)

FIG. 5.22(h) KK 'STEPPED DOWN' CREEP TESTS

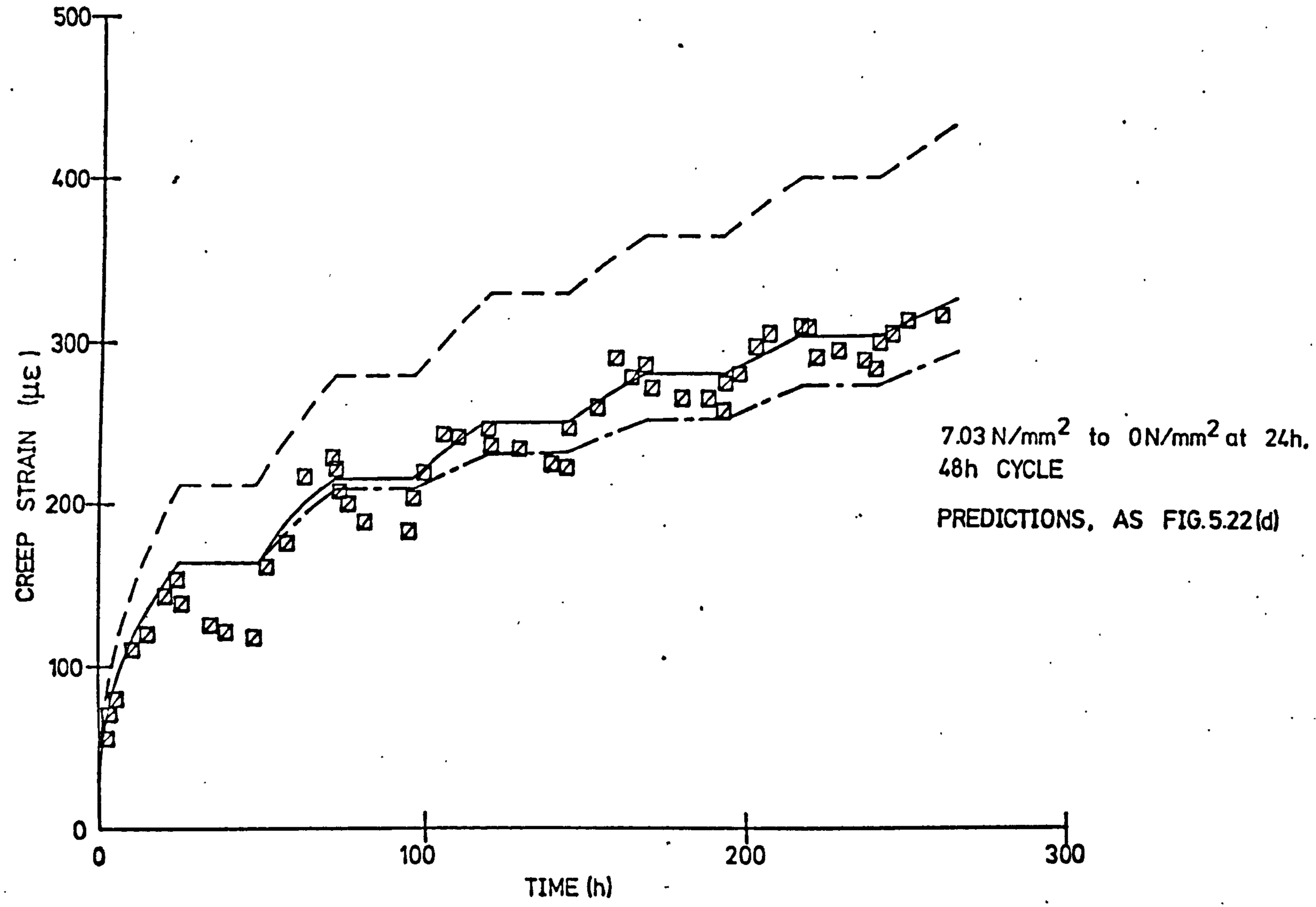

FIG. 5.22(i) P9 'CYCLIC LOAD' CREEP TEST

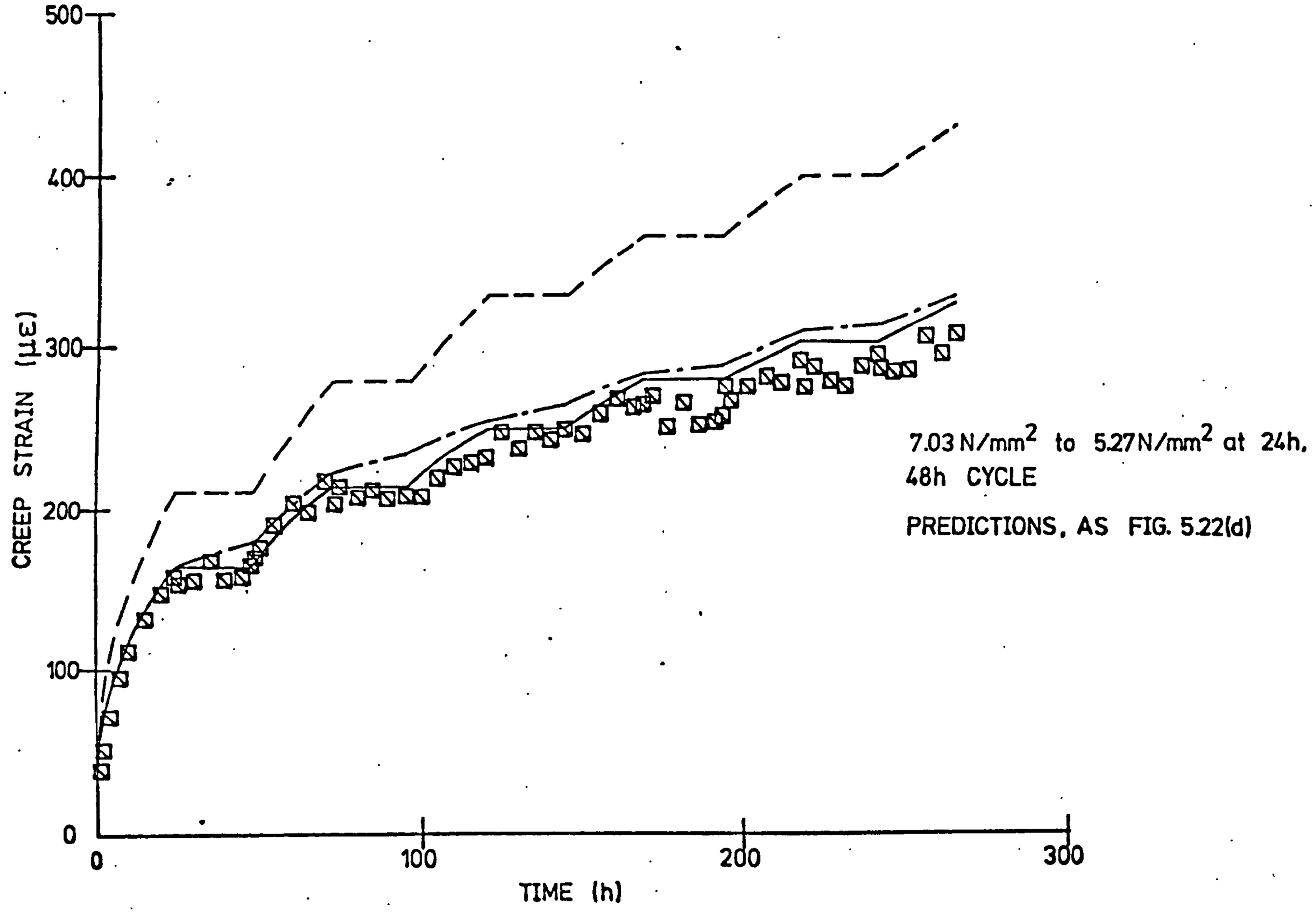

FIG. 5.22(j) P9 'CYCLIC LOAD' CREEP TEST

Table 4.4 Fig 7.14

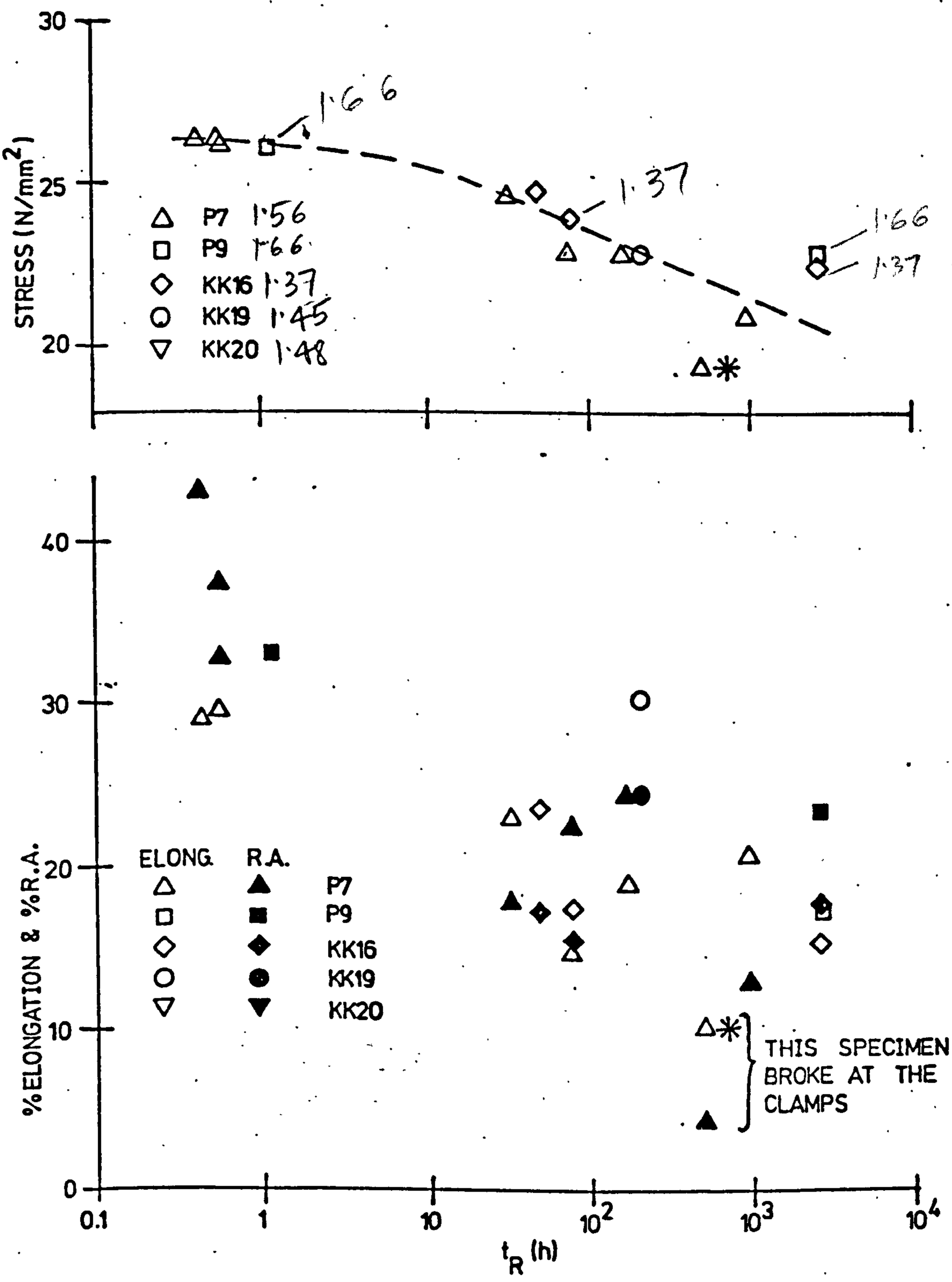

FIG. 5.23(a) CREEP RUPTURE DATA

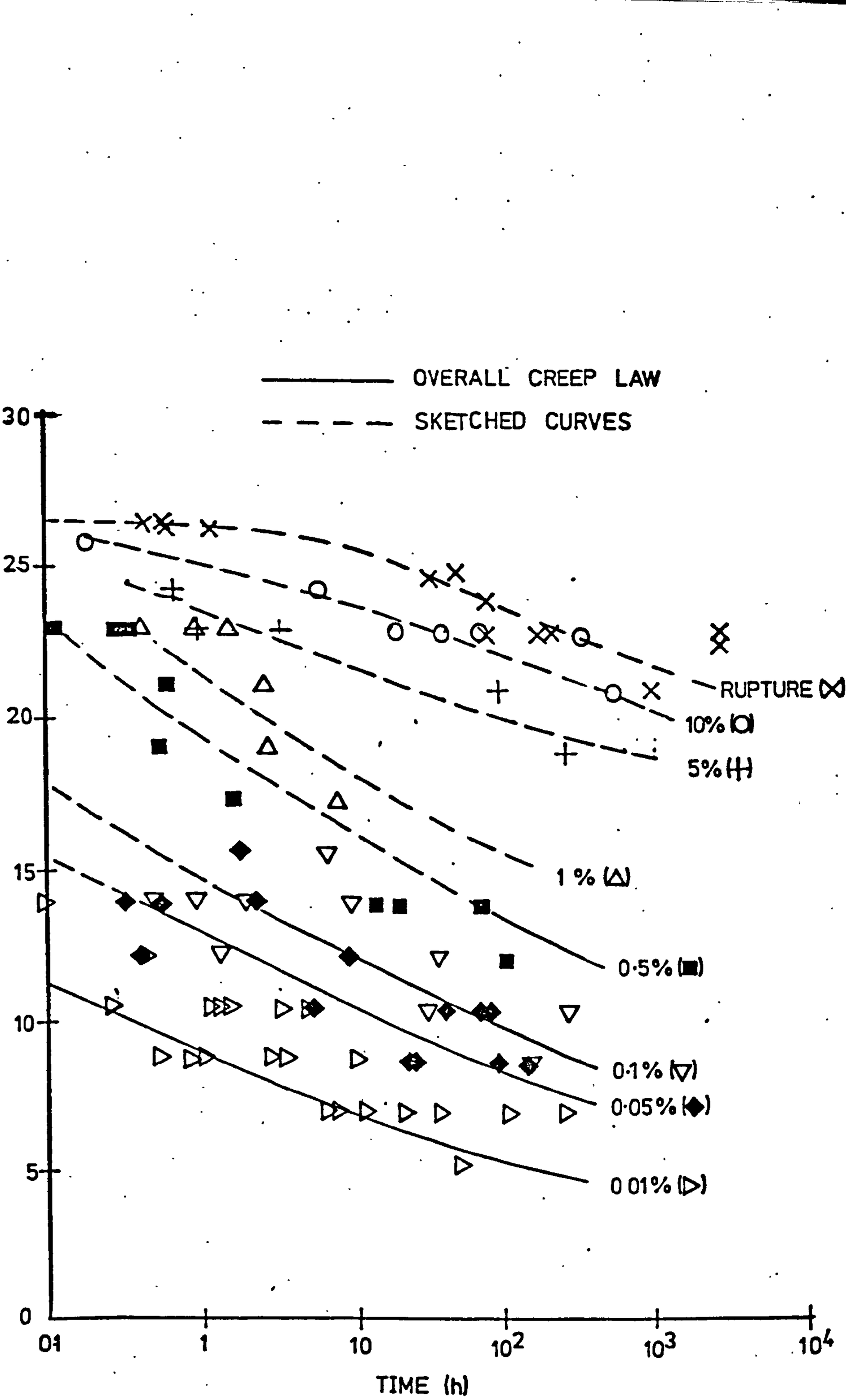

FIG 5·23(b) RUPTURE AND STRAIN CONTOURS

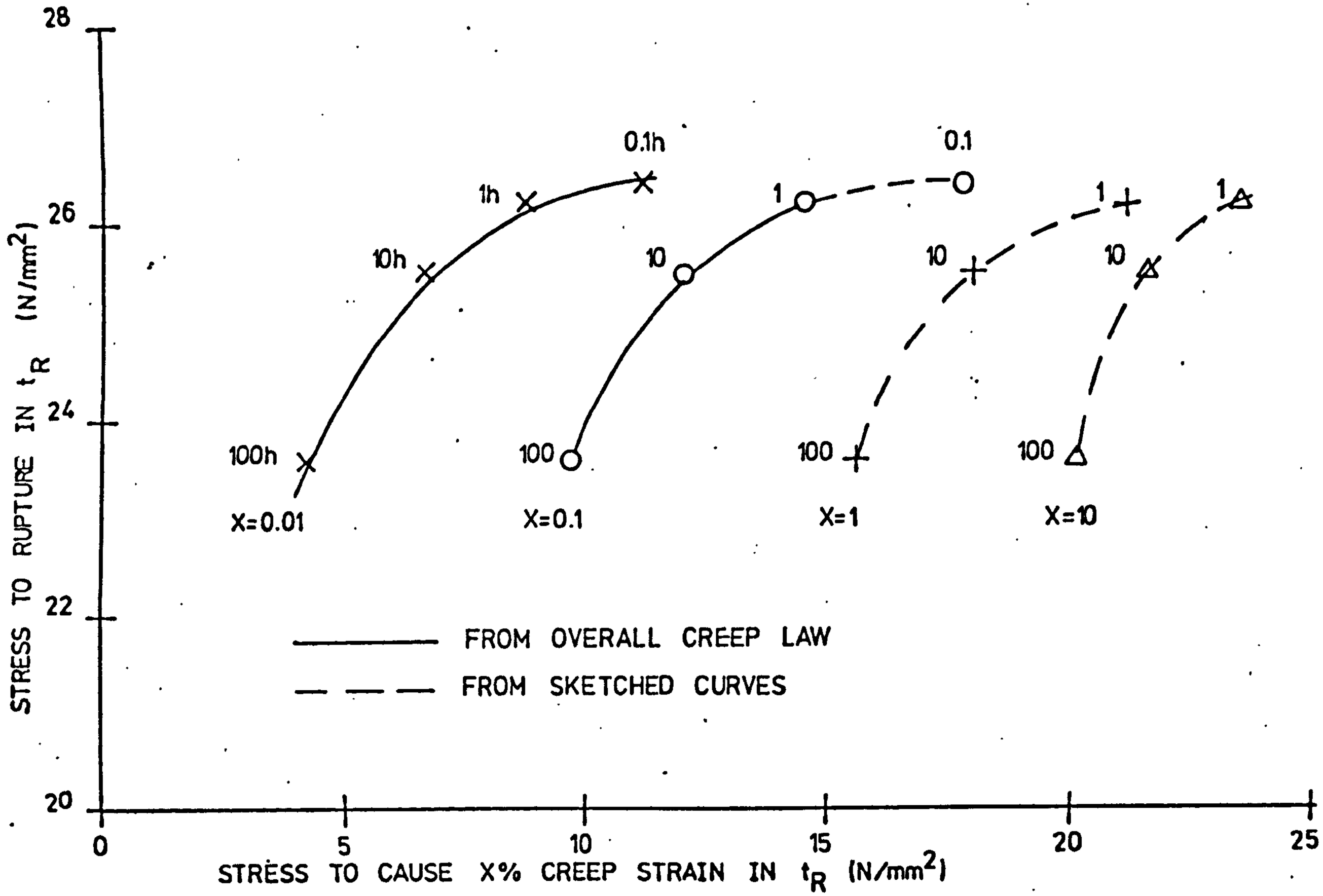

FIG. 5.23(c) MURPHY PLOTS

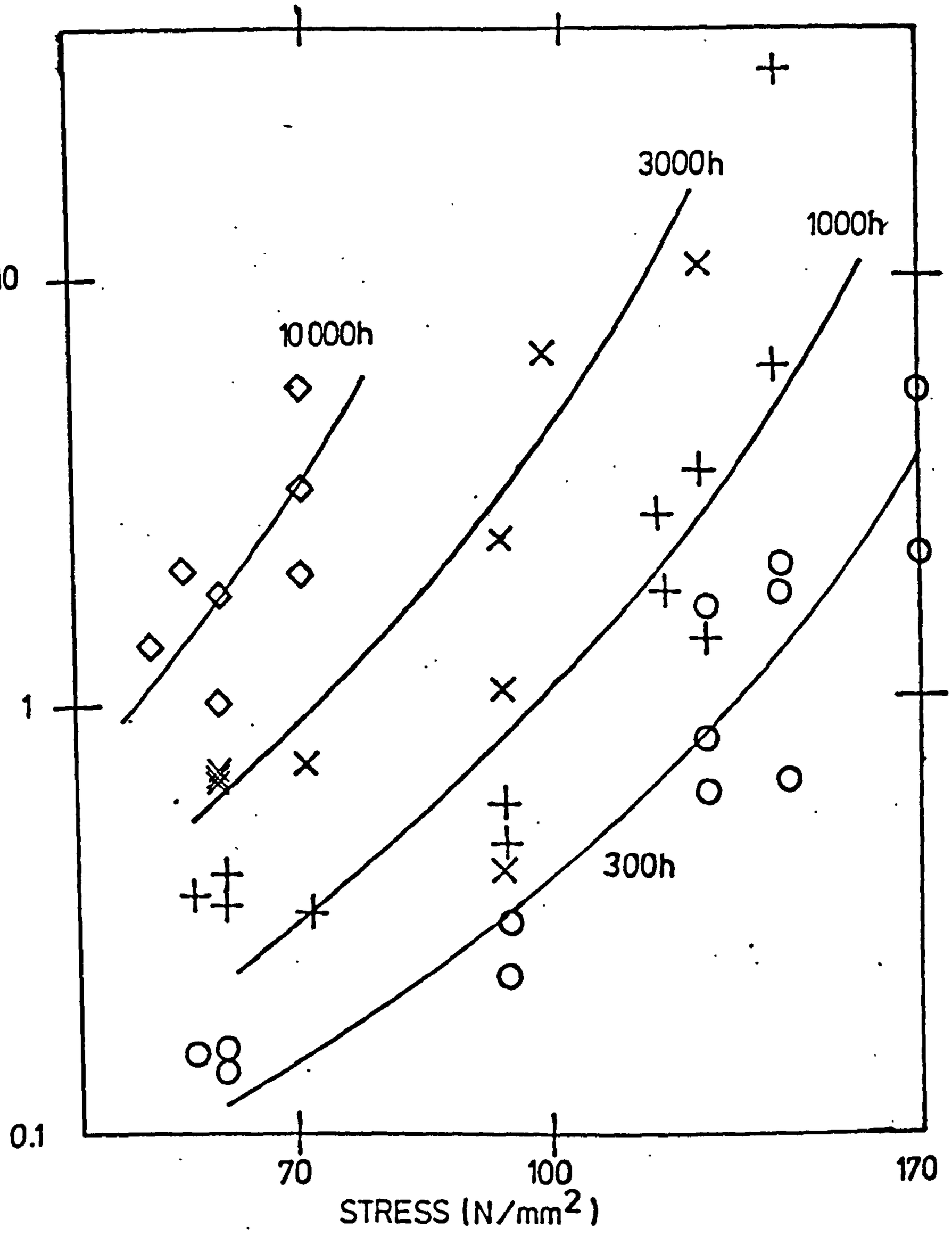

FIG. 5.24 ISOCHRONOUS STRESS-STRAIN CURVES FOR 2.25 CR MO STEEL AT 575°C

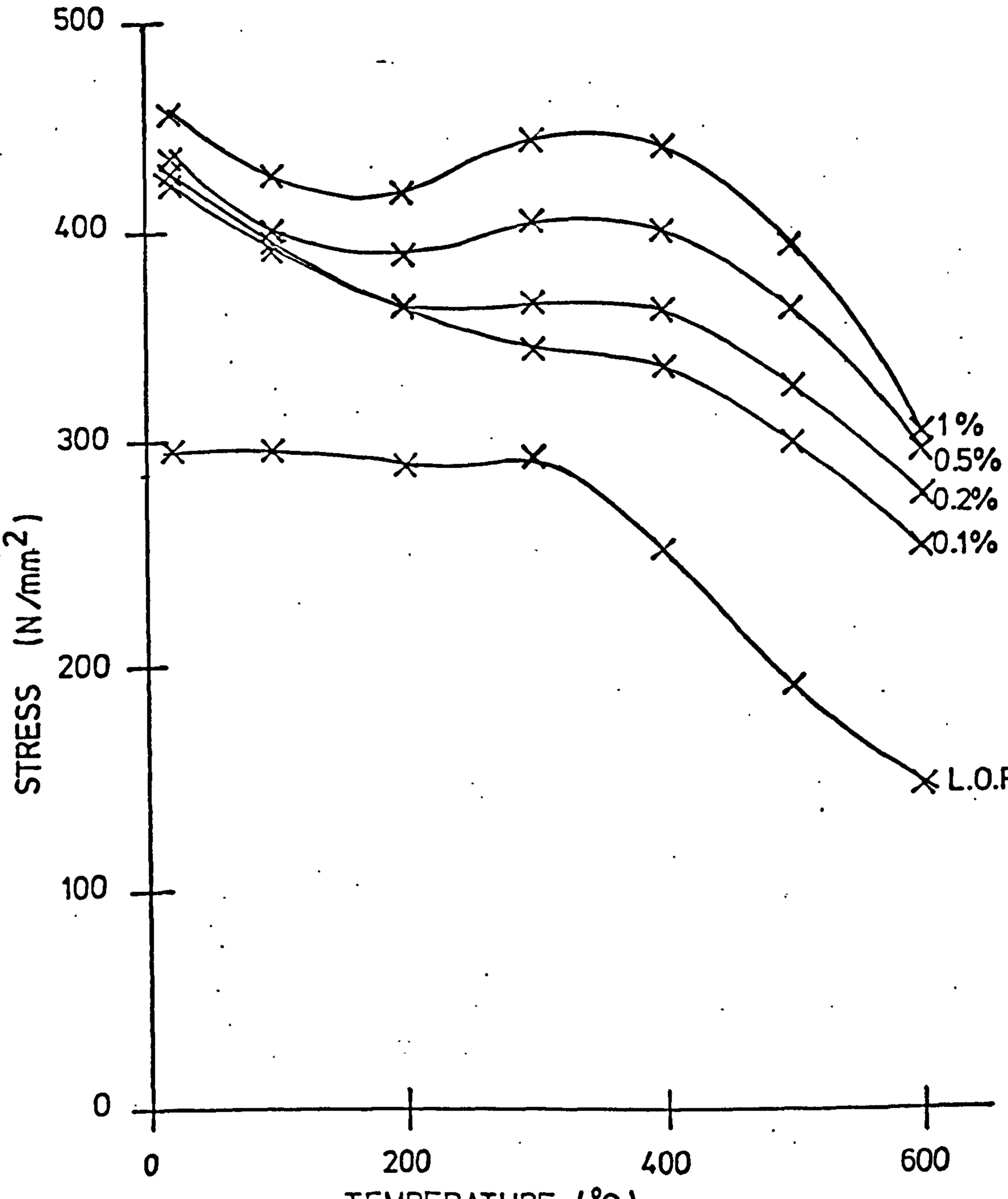

FIG. 5.25 PROOF STRESS V TEMPERATURE FOR 2.25 CR MO STEEL

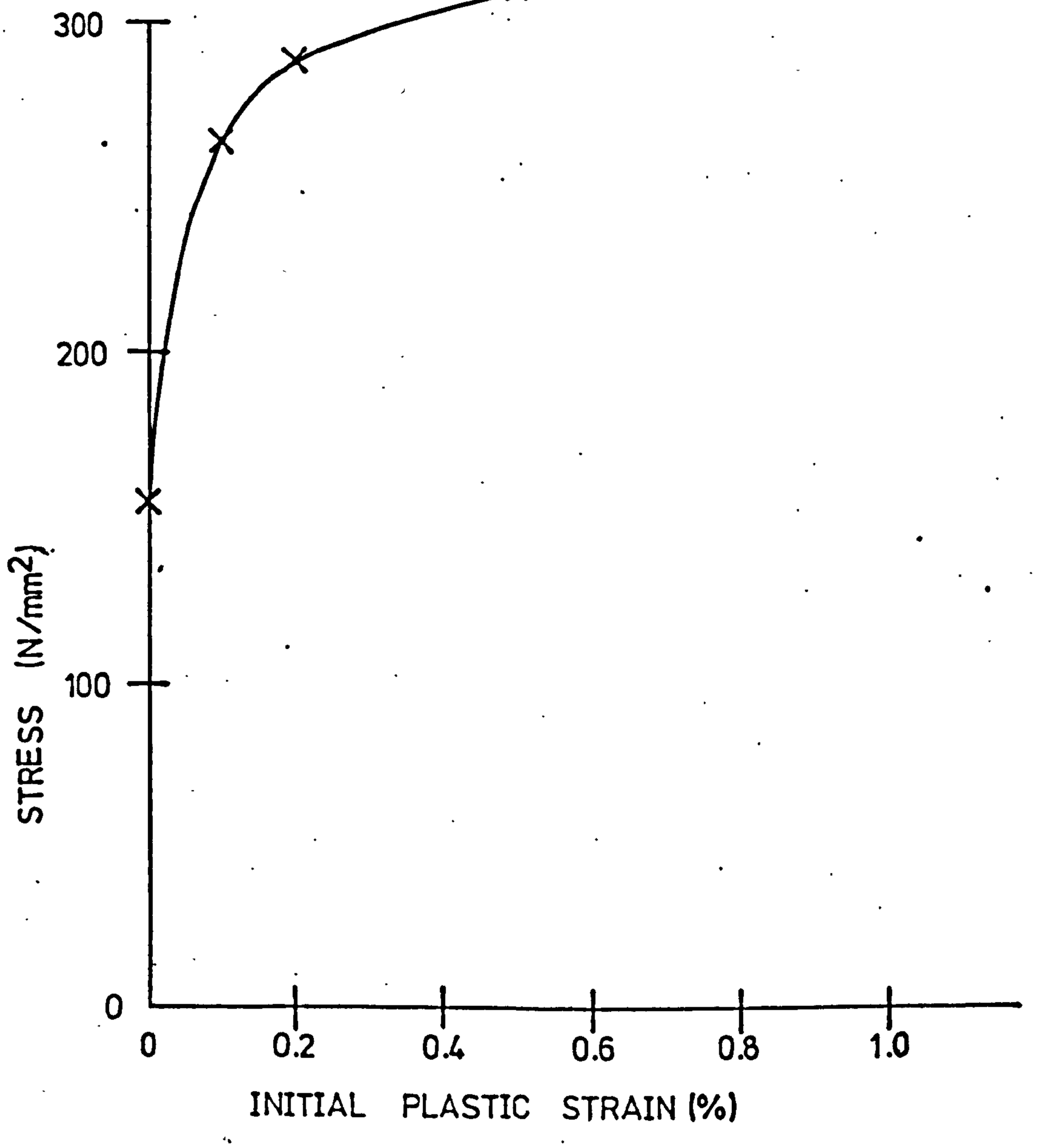

FIG. 5.26 STRESS V INITIAL PLASTIC STRAIN FOR 2.25CR MO STEEL AT 575°C

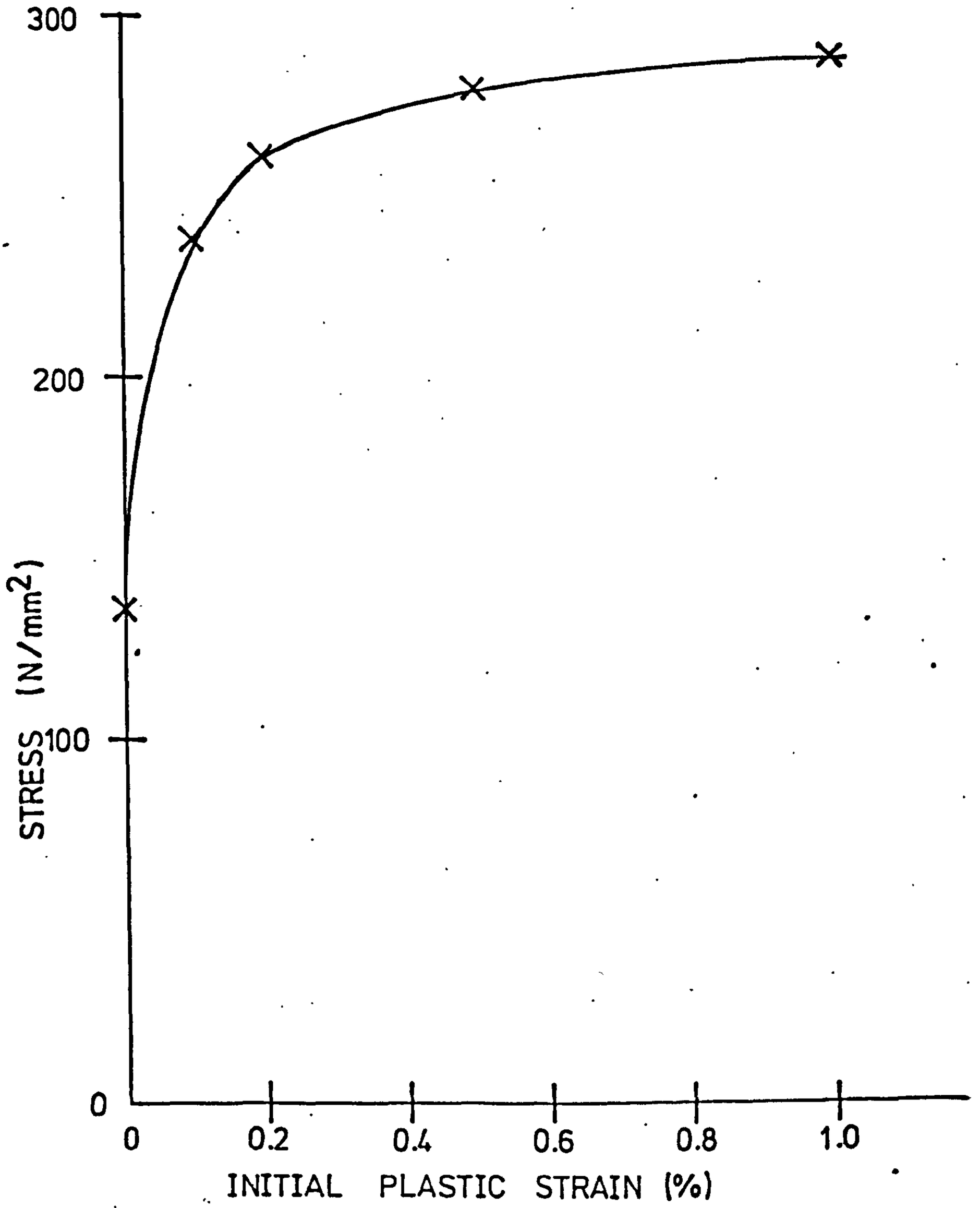

FIG. 5.27 STRESS V INITIAL PLASTIC STRAIN FOR 2.25CR MO STEEL AT 600°C

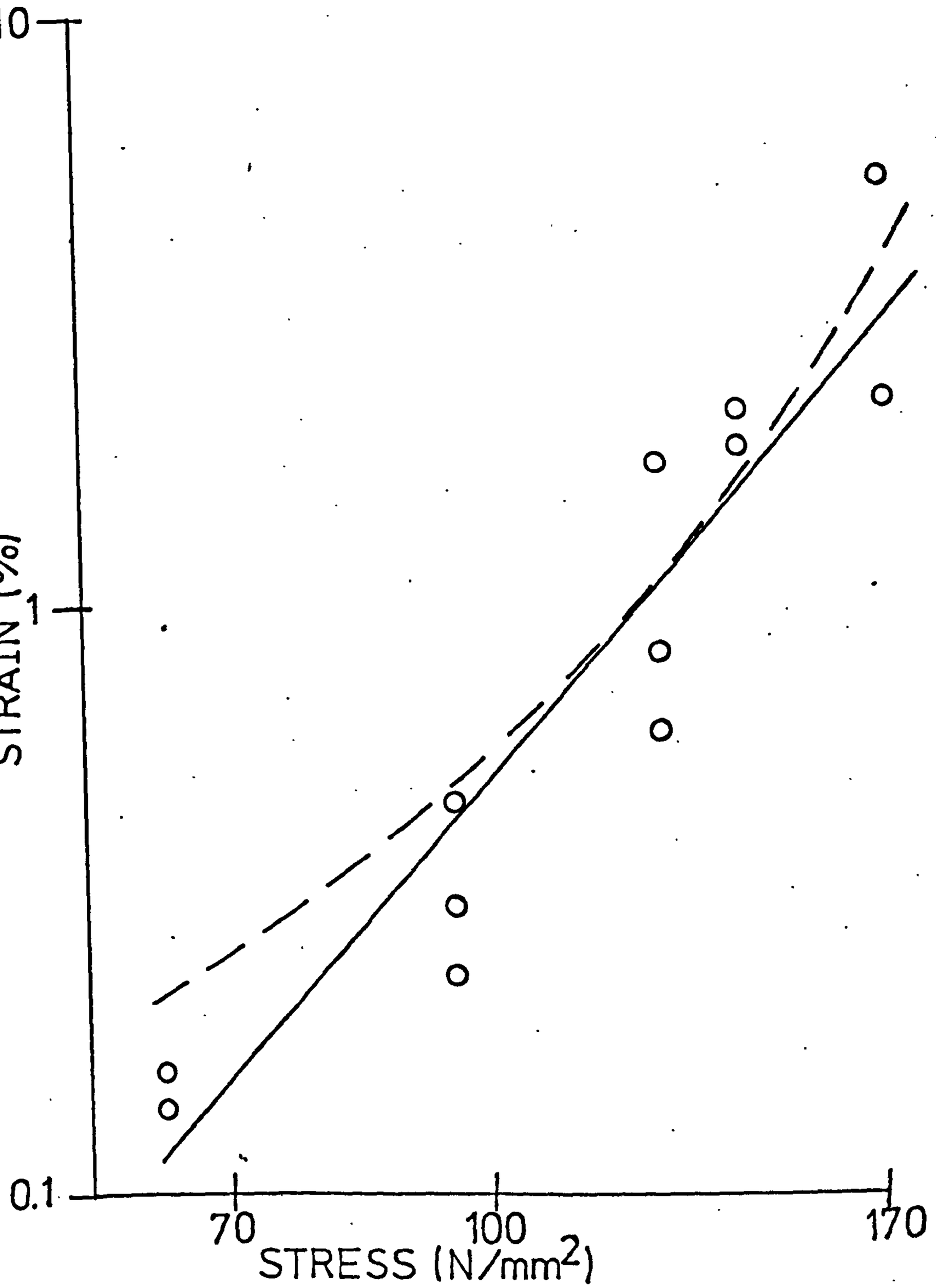

FIG. 5.28 ISOCHRONOUS STRESS-STRAIN CURVES FOR 2.25 CR MO STEEL AT 575°C, 300h

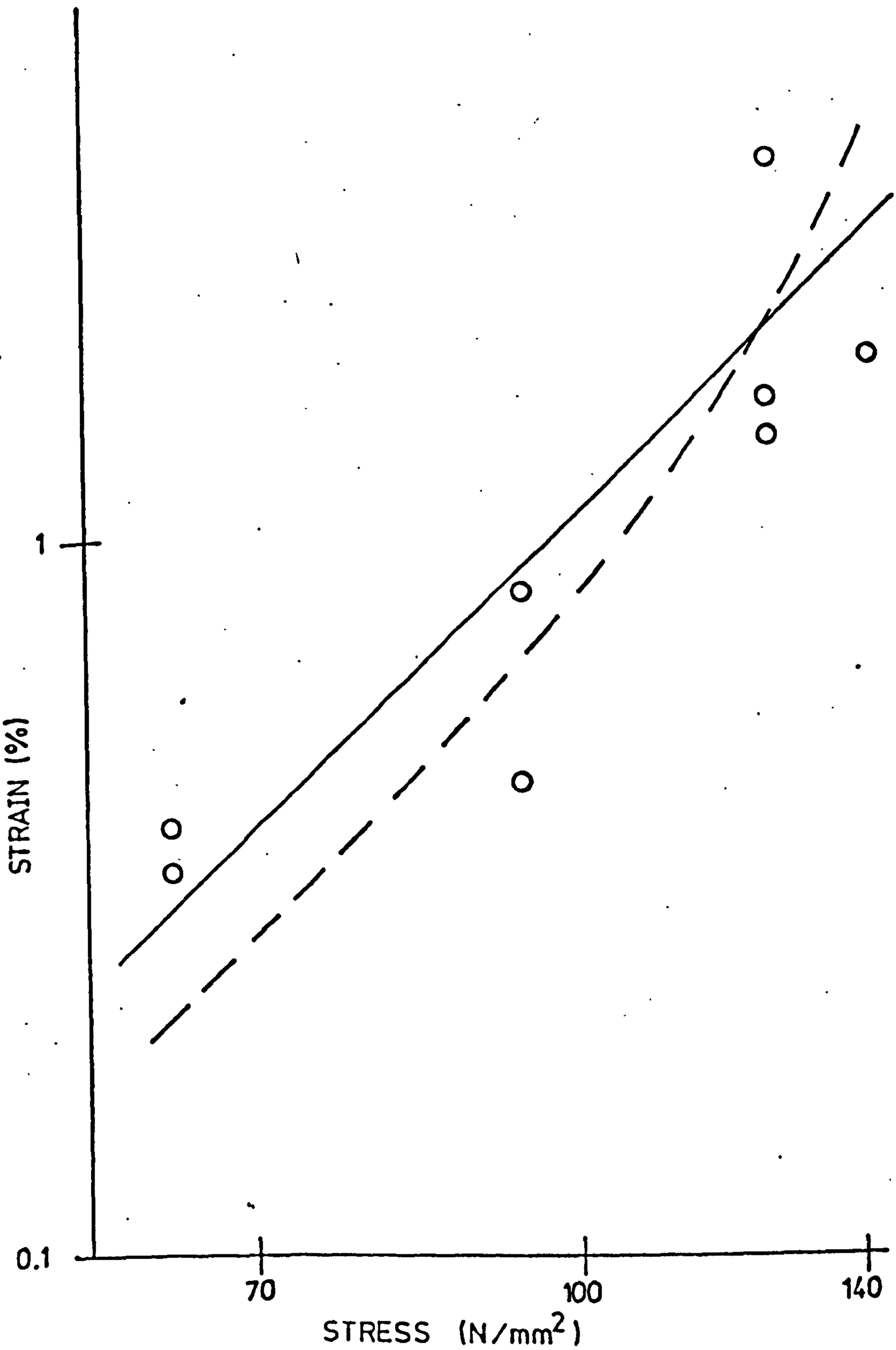

FIG. 5.29 ISOCHRONOUS STRESS-STRAIN CURVES FOR 2.25CR MO STEEL AT 575°C, 1000h

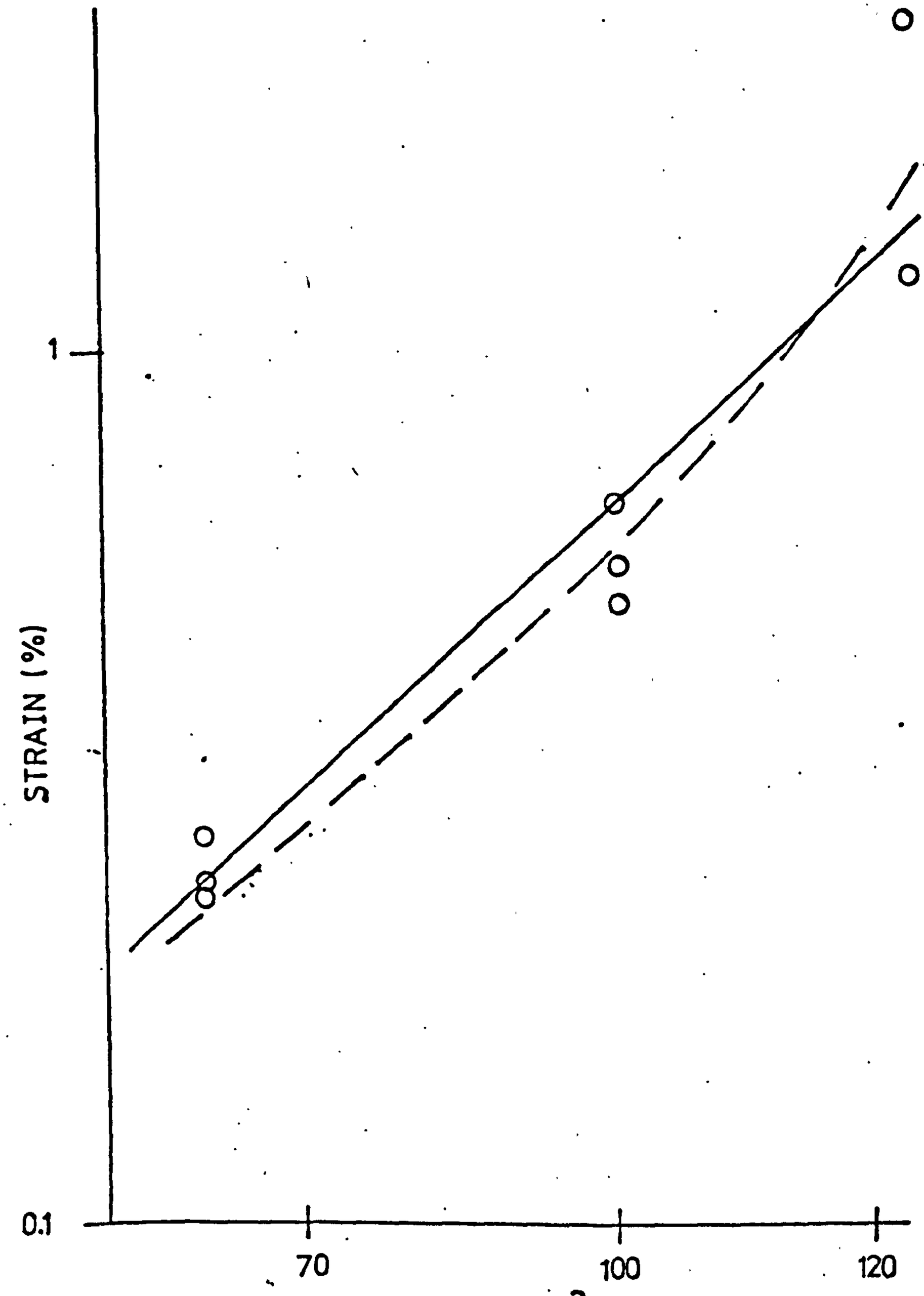

FIG. 5.30 ISOCHRONOUS STRESS-STRAIN CURVES FOR 2.25 CR MO STEEL AT 600°C, 300 h

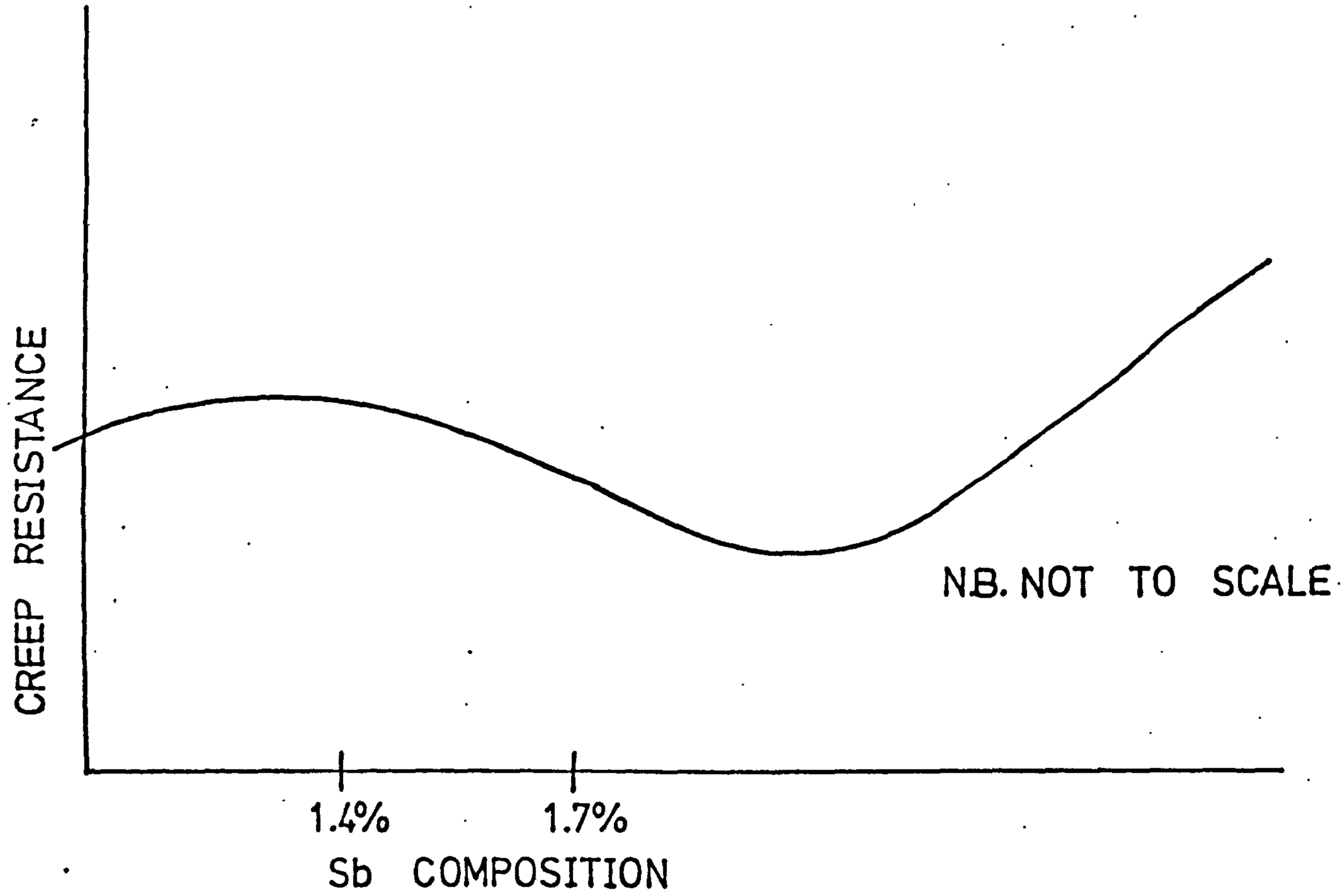

FIG. 5.31 VARIATION OF CREEP RESISTANCE WITH Sb COMPOSITION

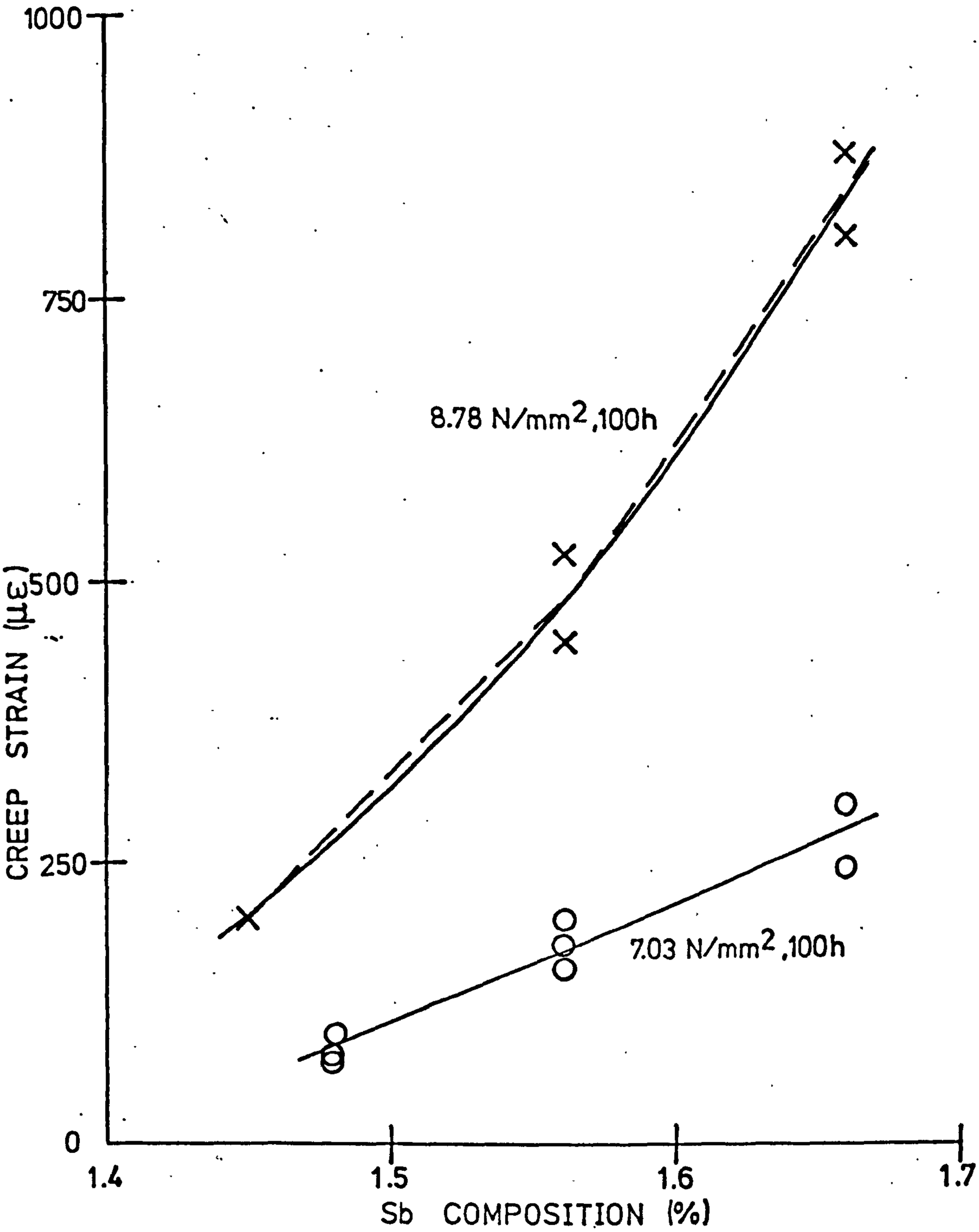

FIG. 5.32 CREEP STRAIN V Sb COMPOSITION

CHAPTER 6

6. BEAM AND CANTILEVER TESTS

6.1 Introduction

The existence of Reference Stresses has been proved for components made of materials having separable stress-time creep laws with simple power stress functions. Since these Reference Stresses are insensitive to the value of the stress exponent, it is a reasonable assumption that these Reference Stresses will also be applicable for materials which do not obey simple creep laws. To test this assumption, tests were carried out on beams in pure bending and cantilevers made from a lead alloy which does not obey a simple creep law. The results of the tests were used to assess the accuracy of the Mackenzie Reference Stress predictions which were obtained for a simple creep law (equation 3.2). The test results were also used to obtain experimental Reference Stresses based upon the three methods described in Chapter 3.

Some variable load tests were carried out on cantilevers to test the applicability of the Reference Stress method to proportional variable loading.

Since the purpose of the tests carried out on the beams and cantilevers was to assess the Reference Stress method and to see whether it is possible to obtain experimental Reference Stresses in practice, it was decided to eliminate "casting-to-casting" scatter by taking all of the uniaxial specimens, beams and cantilevers from the same casting.

6.2 The model material

The uniaxial specimens and the beams were cut from a chill cast 1.66% Sb, 0.16% As lead alloy pressure vessel casting (P9). The initial and unloading strains obtained from the uniaxial specimens are shown in Fig. 6.1 and the creep strains obtained from the constant load creep

tests are shown in Fig. 5.17(b). These strains were obtained from electrical resistance strain gauges used in conjunction with a data logging system capable of taking readings at approximately 0.3 sec intervals. The strains on unloading after the creep tests were used to determine the Young's modulus for the material, which was found to be 3.34×10^4 N/mm^2.

The initial and creep data were used to generate the $\varepsilon_c/\varepsilon_i$ lines and time contours shown in Figs. 3.2 and 3.4 for the single model and two model experimental Reference Stress methods respectively.

6.3 Pure bending model tests

Three nominally identical beams, 8.9 mm square cross-section and 102 mm free length, were tested. The bending moments were chosen so that the anticipated Reference Stresses would be

i) within the instantaneous elastic range (5.17 N/mm^2)

ii) near the elastic-plastic transition (7.03 N/mm^2) and

iii) predominantly plastic. (14.05 N/mm^2).

For a uniform beam in pure bending, a single Reference Stress characterises all deformations.

The loads necessary to produce these bending moments were small enough to be applied by the weight of the steel 'jaws' in the arrangement shown in Figs. 6.2(a)-(b). Surface strains were measured using 30 mm. gauge length electrical resistance strain gauges attached to the tensile and compressive surfaces of the beams.

From the analysis of Appendix 1, it can be seen that the initial and creep strains are given by

$$(\varepsilon_i)_{surface} = 1.48\bar{\varepsilon}_{io} \qquad (6.1a)$$

$$(\varepsilon_c)_{surface} = 1.48\bar{\varepsilon}_{co} \qquad (6.1b)$$

and $$\bar{\sigma}_o = 4.06 \frac{M}{bd^2} \qquad (6.1c)$$

The results for the three test beams are collected in Table 6.1. The value of the nominal stress (M/bd^2) is that used by Mackenzie (37); it is of course 1/6 of the linear elastic surface bending stress.

The experimentally obtained initial surface strains obtained from these tests are given in Table 6.1, together with the initial strains predicted by equation 6.1a for which the values of $\bar{\varepsilon}_{io}$ were obtained from Fig. 6.1 at the Reference Stress given by equation 6.1c. This comparision is by no means trivial because the initial deformations include initial plasticity. These results show that the predictions based on equations 6.1a and 6.1c are accurate and even when a great deal of plastic strain was obtained, the accuracy was better than 20%.

Similarly, equations 6.1b and 6.1c were used to predict the surface creep strains and these are shown compared with the experimentally obtained surface creep strains in Figs. 6.3a and 6.3b. These results show that the analytical predictions based upon Mackenzie's method of obtaining the Reference Stress are very accurate, even when the actual material does not obey a simple creep law.

The experimental Reference Stresses which were obtained using the 'one model' and 'two model' graphical methods described in Chapter 3 are given in Table 6.1 together with the analytical (Mackenzie) and approximate (Sim) values of the Reference Stresses. Since the components (beams and cantilevers) have one-dimensional stress systems (which are independent of Poisson's ratio), the elastic solutions are readily calculated and therefore, in order to use the two model method, there is no necessity to determine the initial deformations from incompressible model tests. Instead, $(\phi_i)_A$ has been calculated using the Young's modulus of the lead alloy model material. Similarly, the initial strains, $(\varepsilon_i)_A$, used to construct Fig. 3.4 were obtained by using the Young's modulus of the lead alloy model material.

The proposed method of prediction of prototype deformations using equation 3.19 requires the determination of the quantity X, as well as the Reference Stress from the model test and model material data. The analytical value of this quantity given by equation 6.1b and the approximate value, obtained from the ratio of the calculated elastic deformation to the elastic strain at the approximate Reference Stress are given in Table 6.1. These are compared with the values for each test beam for the one and two-model methods. For the one model method, $X = \phi_i/\bar{\varepsilon}_{io}$ and for the two model method, $X = (\phi_i)_A/(\bar{\varepsilon}_{io})_A$, where as stated above, A is a linear elastic material with Young's modulus equal to that of the lead alloy.

It was shown (equation 3.23) that two non-creeping models could be used to determine experimental Reference Stresses. Using the initial surface strains obtained from the beam tests as $(\phi_i)_1$, which include some initial plasticity and are therefore non-linear, and using the linear elastic solution for the surface strains as $(\phi_i)_2$ the 'non-creeping model method' of obtaining Reference Stresses may be used. Fig. 3.5 shows the $(\varepsilon_i)_1/(\varepsilon_i)_2$ against σ plot obtained from the ratio of 'total' initial strains from the uniaxial specimens to the 'initial' elastic strains from the uniaxial specimens, based upon the Young's modulus. Reference Stresses obtained by this method are also given in Table 6.1 and the X values given by equation 3.25 are the same as those obtained for the 'two model' method.

Both the one and two model methods provide estimates for the deformation due to stress redistribution and the redistribution time. The values of the two quantities given by the two methods for each test beam are compared in Table 6.1 with theoretical predictions. The predictions of $\Delta\phi$ are based on the work of Penny and Marriott (5), Marriott (24), (25) and Leckie and Martin (26). The predictions of the

redistribution time are based on the work of Calladine (29) i.e. using equation 2.26. The values of stress exponent required for these predictions were obtained from the slopes of log ε_c - log σ curves at the Reference Stress.

6.4 Constant load cantilever model tests

Four nominally identical cantilevers 8.9 mm. square cross-section, 102 mm. long were tested. The loads were again chosen so that the anticipated Reference Stresses to predict the tip deflection would be

i) within the instantaneous elastic range (5.17 N/mm^2),

ii) near the elastic-plastic transition (7.03 N/mm^2) and

iii) in the plastic range (8.62 N/mm^2 and 10.34 N/mm^2).

Loads were applied to the tip of the cantilever and the tip deflection was measured by means of a linear capacitance transducer, as shown in Fig. 6.4.

The results are shown in Table 6.2 and were obtained as explained in connection with Table 6.1 using the appropriate equations from Appendix 3. The measured tip creep deflections ϕ_c are shown in Figs. 6.5(a), (b) together with the analytical predictions based upon Mackenzie's method.

6.5 Assessment of accuracy of predictions of deformations based on experimentally determined Reference Stresses

Predictions for the stationary creep deformation of a prototype are determined from the uniaxial creep data for the prototype material at the Reference Stress and the quantity X defined in equation 3.19. It may be seen from Tables 6.1 and 6.2 that there is considerable scatter in the experimentally determined values of Reference Stress and the quantity X. The effect of this scatter has been determined by comparing predictions based on the experimental value with calculated

deformations for prototype beams made of hypothetical materials with a creep law of the form of equation 3.2

$$\text{i.e.} \quad \varepsilon_c = \sigma^n \Gamma(t)$$

A range of prototype material has been considered by varying the stress exponent n.

The predicted stationary creep deformation of a protytype beam of the same dimensions as the models is:

$$(\phi_{sc})_{\text{prediction}} = X \cdot \bar{\varepsilon}_{co}$$

Substituting for $\bar{\varepsilon}_{co}$ from the prototype material creep law gives:

$$(\phi_{sc})_{\text{prediction}} = X \cdot \bar{\sigma}_o^{\,n} \Gamma(t)$$

The exact solution for the stationary state surface strain of the prototype beam in pure bending, given by Appendix equation A.1.4b, is

$$(\phi_{sc})_{\text{prototype}} = \sigma_{nom}^n \left(4 + \frac{2}{n}\right)^n \Gamma(t)$$

Thus for pure bending deformation,

$$\frac{(\phi_{sc})_{\text{prediction}}}{(\phi_{sc})_{\text{prototype}}} = \frac{X \cdot \bar{\sigma}_o^{\,n}}{\sigma_{nom}^n \left(4 + \frac{2}{n}\right)^n} \qquad (6.2)$$

Similarly the exact stationary state solution for the tip deflection of a prototype cantilever, given by equation A.3.5d, is

$$(\phi_{sc})_{\text{prototype}} = \sigma_{nom}^n \frac{L^2}{d} \frac{2}{n+2} \left(4 + \frac{2}{n}\right)^n \Gamma(t)$$

Thus for the tip deflection of a cantilever:

$$\frac{(\phi_{sc})_{\text{prediction}}}{(\phi_{sc})_{\text{prototype}}} = \frac{X \cdot \bar{\sigma}_o^{\,n}}{\sigma_{nom}^n \frac{2}{n+2} \left(4 + \frac{2}{n}\right)^n \frac{L^2}{d}} \qquad (6.3)$$

The ratios of the predicted deformations to the deformations of the hypothetical prototypes, given by Equations (6.2) and (6.3), are

plotted against the stress exponent of the prototype material in Figs. 6.6 and 6.7 for each of the experimental results in Tables 6.1 and 6.2 for the pure bending and cantilever tests respectively. The errors in the predictions generally increase as the stress exponent n of the prototype material increases. For values of stress exponent up to 5, the predictions are between 0.6 and 2.0 times the prototype deformations. In general the predictions are 'safe' in the sense that they over-estimate the deformation. Although the errors in the predictions are large, predictions of this order of accuracy would still be useful for design purposes.

Predictions based on Mackenzie and Sim type calculations are also plotted in Figs. 6.6 and 6.7. The Mackenzie predictions are obviously good because they are based on the same behaviour law as the hypothetical prototype material. The Sim prediction is good for the beam in pure bending but is the worst prediction for the cantilever tip deflection.

6.6 Variable load cantilever tests

Six nominally identical cantilevers 8.9 mm. square cross-section, 102 mm. long were tested under variable load conditions. The loads were chosen so that the anticipated Reference Stresses to predict the tip deflection would be:

i) 7.03 N/mm^2 to 8.62 N/mm^2 at 100 h (i.e. a stress initially at the elastic-plastic intersection to a stress in the plastic range),

ii) 8.62 N/mm^2 to 7.03 N/mm^2 at 10 h (i.e. a stress initially in the plastic range to a stress at the elastic-plastic intersection),

iii) 7.03 N/mm^2 to 0 N/mm^2 at 24 h, the cycle was then repeated every 48 h (2 tests), and

iv) 7.03 N/mm^2 to 5.27 N/mm^2 at 24 h, the cycle was then repeated every 48 h (2 tests).

The measured tip creep deflections ϕ_c are shown in Figs. 6.8 (a)-(c) together with the analytical predictions based upon Mackenzie's method (Appendix 3). The initial deformations obtained upon loading are given in Table 6.3 and these are compared with the predicted values.

From Fig. 6.8 (a) - (c), it can be seen that the Reference Stress predictions for variable loading are accurate enough for design purposes. The cyclic loading tests show that the hardening in the cantilevers is greater than that in the uniaxial specimen, which results in an overestimate of the prediction (based on uniaxial tests), which becomes progressively greater as the number of cycles increases.

6.7 Conclusions

It has been shown that analytical values of Reference Stress based upon Mackenzie's method give accurate predictions of deformations for both constant and variable proportional loading. More important, it has been shown that for problems for which analytical Reference Stresses cannot be obtained, experimental Reference Stresses may be used to predict deformations to an acceptable degree of accuracy.

Note: Numbers 1 and 2 are strain gauges

TABLE 6.1 BEAMS IN PURE BENDING

Test Beam Number			1	2	3
Quantity	Symbol	Units			
Nominal Stress M/bd^2	σ_{nom}	MN/m^2	1.29	1.72	3.45
<u>Reference Stress Indices</u>					
Analytical	$\bar{\sigma}_o/\sigma_{nom}$		4.06	4.06	4.06
Approx.			4.00(-1)	4.00(-1)	4.00(-1)
Exp. One-model			4.90(+21)	4.61(+14)	4.18(+3)
Exp. Two-model			4.42(+9)	4.18(+3)	3.59(-12)
Exp. non-creep method			4.32(+5)	4.13(+2)	3.74(-8)
<u>The Quantity 'X'</u>					
Analytical	$\phi_i/\bar{\varepsilon}_{io}$		1.48	1.48	1.48
Approx.			1.5(+1)	1.5(+1)	1.5(+1)
Exp. One-model			1.16(-22)	1.11(-25)	1.22(-18)
Exp. Two-model	$(Q_i)_A/(\bar{\varepsilon}_{io})_A$		1.36(-8)	1.44(-3)	1.67(+3)
<u>Initial Deformation</u>					
Analytical	ϕ_i	%	0.040	0.065	0.985
Experimental			0.044(+10)	0.072(+10)	0.807(-18)
<u>Redistribution Deformation</u>					
Exp. One-model	$\Delta\phi$	%	0.004	0.007	0.097
Exp. Two-model			0.002	0.004	0.173
Marriott et al			0.004 to 0.006	0.005 to 0.008	0.045 to 0.095
<u>Redistribution Time</u>					
Exp. One-model	t_{red}	h	2.7	12.4	2
Exp. Two-model			1.0	19.2	6
Calladine			90	22	0.08

Note: Numbers in parenthesis are % deviation from exact solution.

TABLE 6.2 CANTILEVER BEAMS

Test Beam Number			1	2	3	4
Quantity	Symbol	Units				
Nominal Stress WL/bd^2	σ_{nom}	MN/m^2	1.55	2.07	2.59	3.10
Reference Stress Indices						
Analytical	σ_o/σ_{nom}		3.33	3.33	3.33	3.33
Approx.			4.00(+20)	4.00(+20)	4.00(+20)	4.00(+20)
Exp. One-model			3.35(+1)	3.91(+17)	3.41(+2)	3.36(+1)
Exp. Two-model			3.73(+12)	3.90(+17)	3.29(-1)	2.76(-17)
Exp. non-creep method			4.22(+27)	4.16(+25)	3.46(+4)	2.72(-18)
The Quantity 'X'						
Analytical	$\phi_i/\bar{\varepsilon}_{io}$	mm/%	1407	1407	1407	1407
Approx.			1161 (-35)	1161 (-35)	1161 (-35)	1161 (-35)
Exp. One-model			1657(+18)	1227(-13)	1197(-15)	1562 (+11)
Exp. Two-model	$(\phi_i)_A/(\bar{\varepsilon}_{io})_A$		1243(-12)	1191(-15)	1414(0)	1702 (+21)
Initial Deformation						
Analytical	ϕ_i	mm	0.394	0.633	1.358	2.190
Experimental			0.464(+18)	0.920(+31)	1.245(-8)	1.320(-40)
Redistribution Deformation						
Exp. One-model	$\Delta\phi$	mm	0.093	0.179	0.269	0.083
Exp. Two-model			0.025	0.092	0.125	0.128
Marriott et al			0.021 to 0.029	0.041 to 0.064	0.091 to 0.202	
Redistribution Time						
Exp. One-model	t_{red}	h	2	20	3	1
Exp. Two-model			30	8	7	5
Calladine			320	15	4	1

Note:- Numbers in parenthesis are % deviations from exact solution.

Table 6.3 Initial Cantilever Tip Deflections

σ_{nom} (N/mm^2)	2.07	2.07	2.07	2.07	2.07	2.59
Measured Deflection (mm)	0.920	0.594	0.551	0.946	0.757	1.738
Predicted Deflection (mm)	0.633	0.633	0.633	0.633	0.633	1.358

$$\sigma_{nom} = \frac{WL}{bd^2}$$

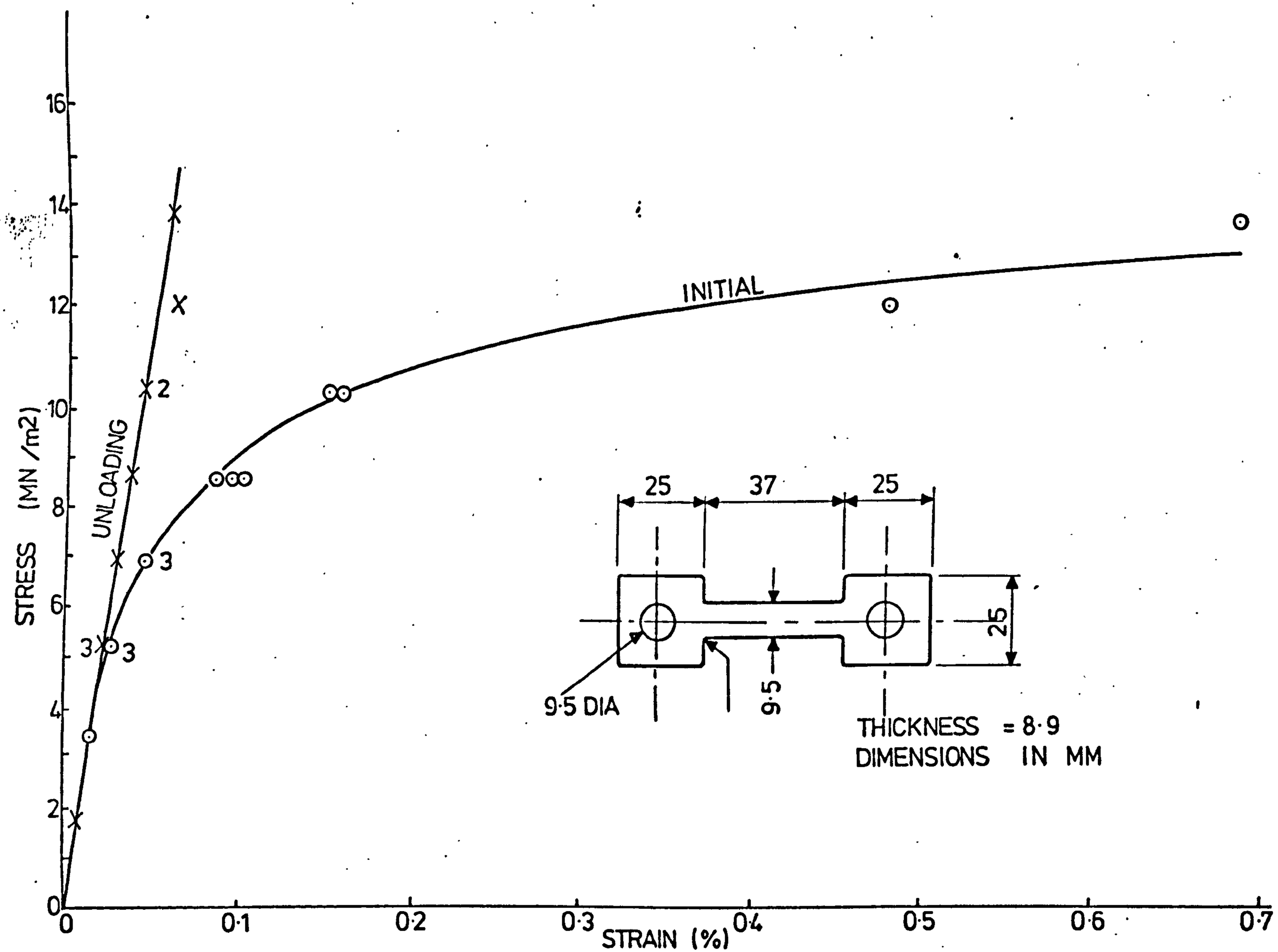

FIG. 6.1 INITIAL AND UNLOADING STRAINS FOR CASTING P9

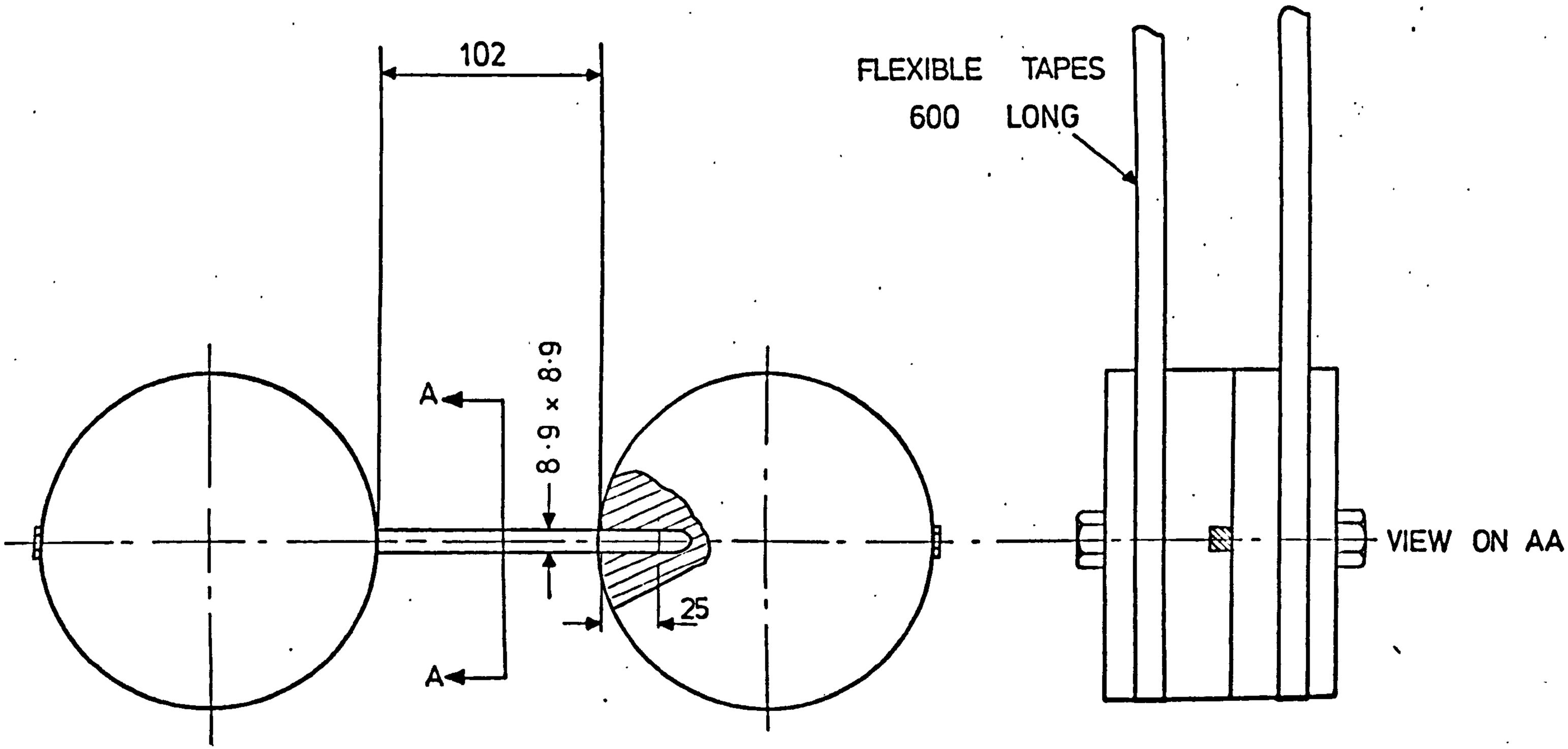

FIG. 6.2(a) THE PURE BENDING TEST RIG

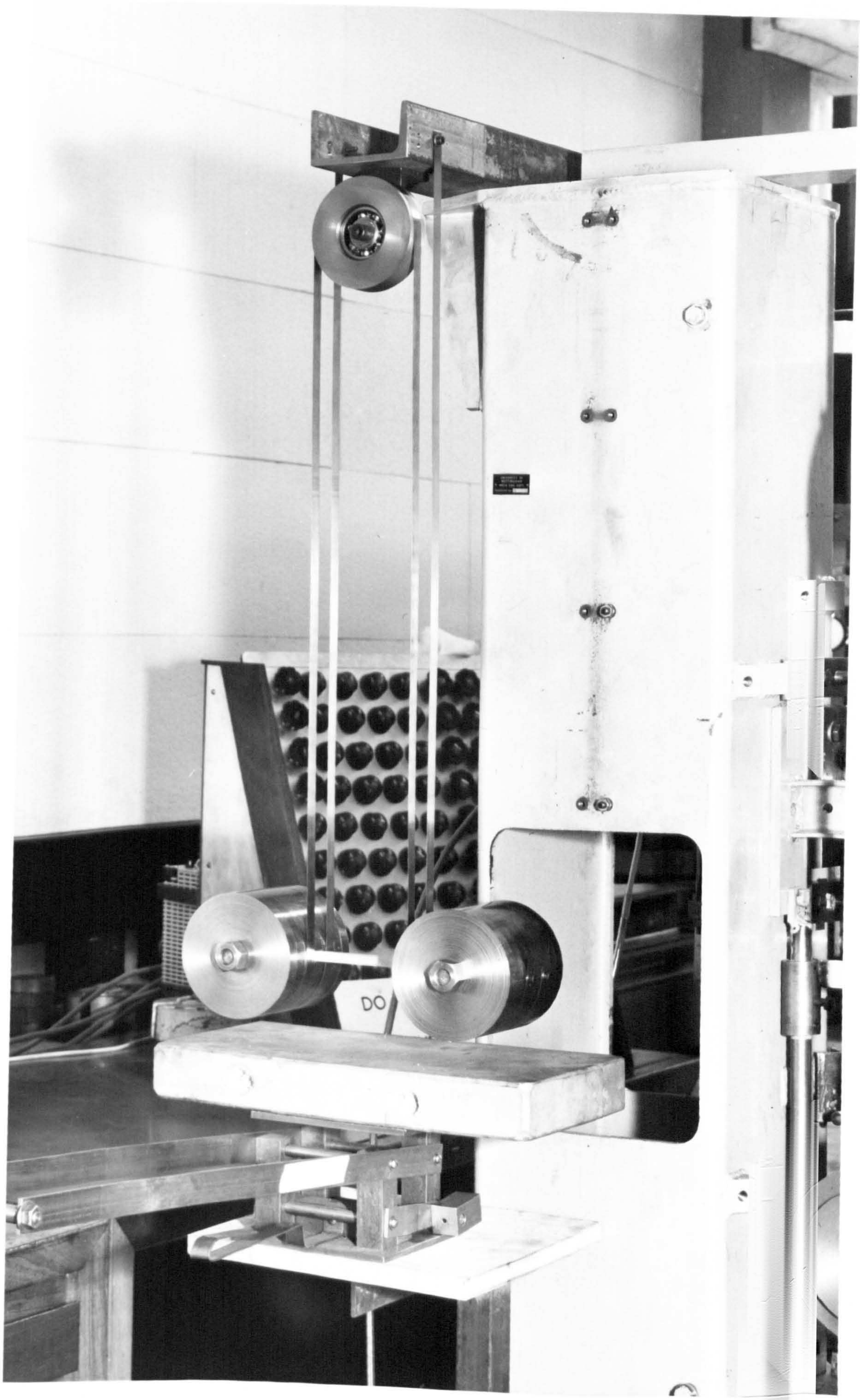

FIG. 6.2(b)

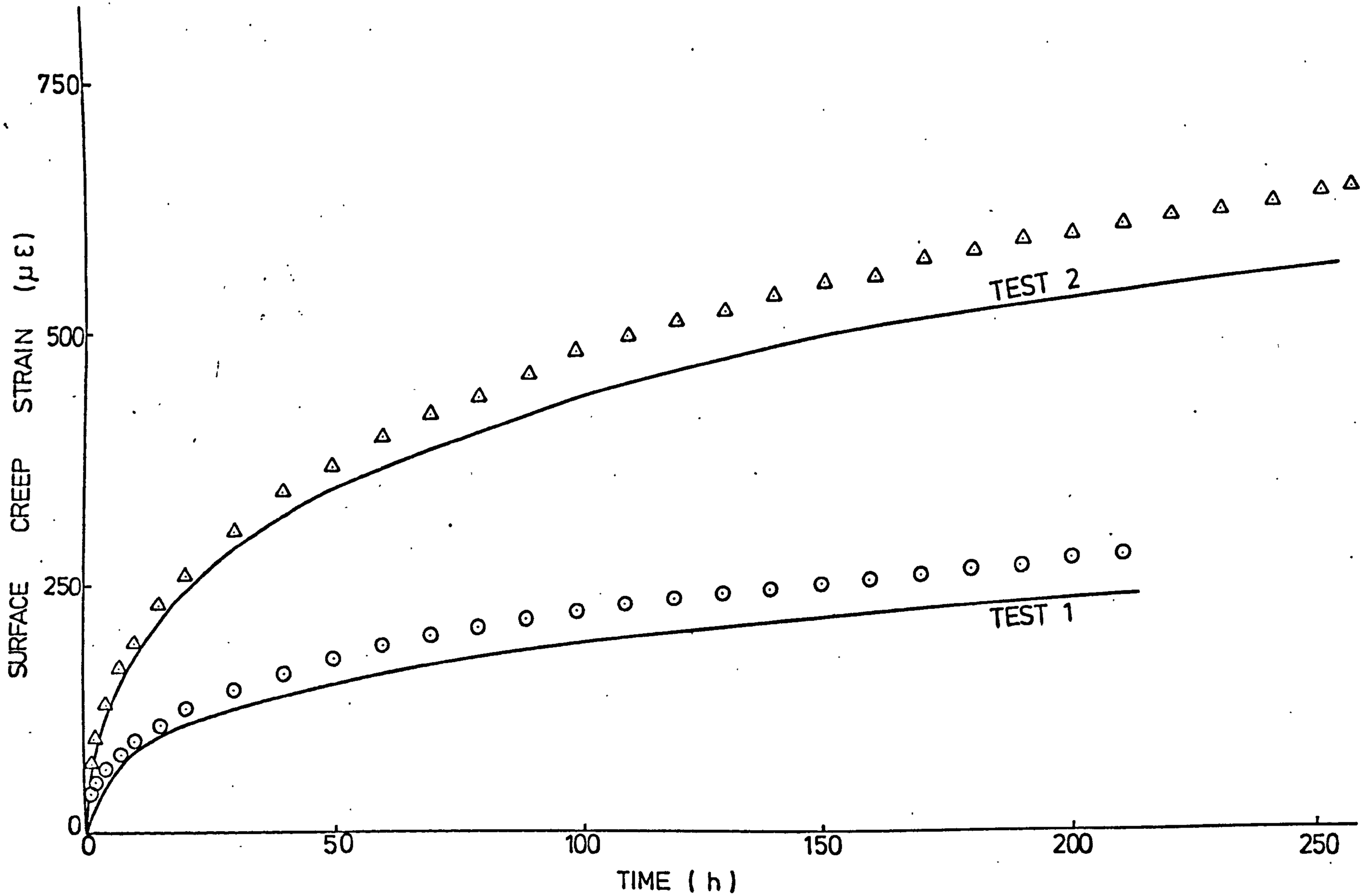

FIG. 6.3(a) PURE BENDING TEST RESULTS AND PREDICTIONS

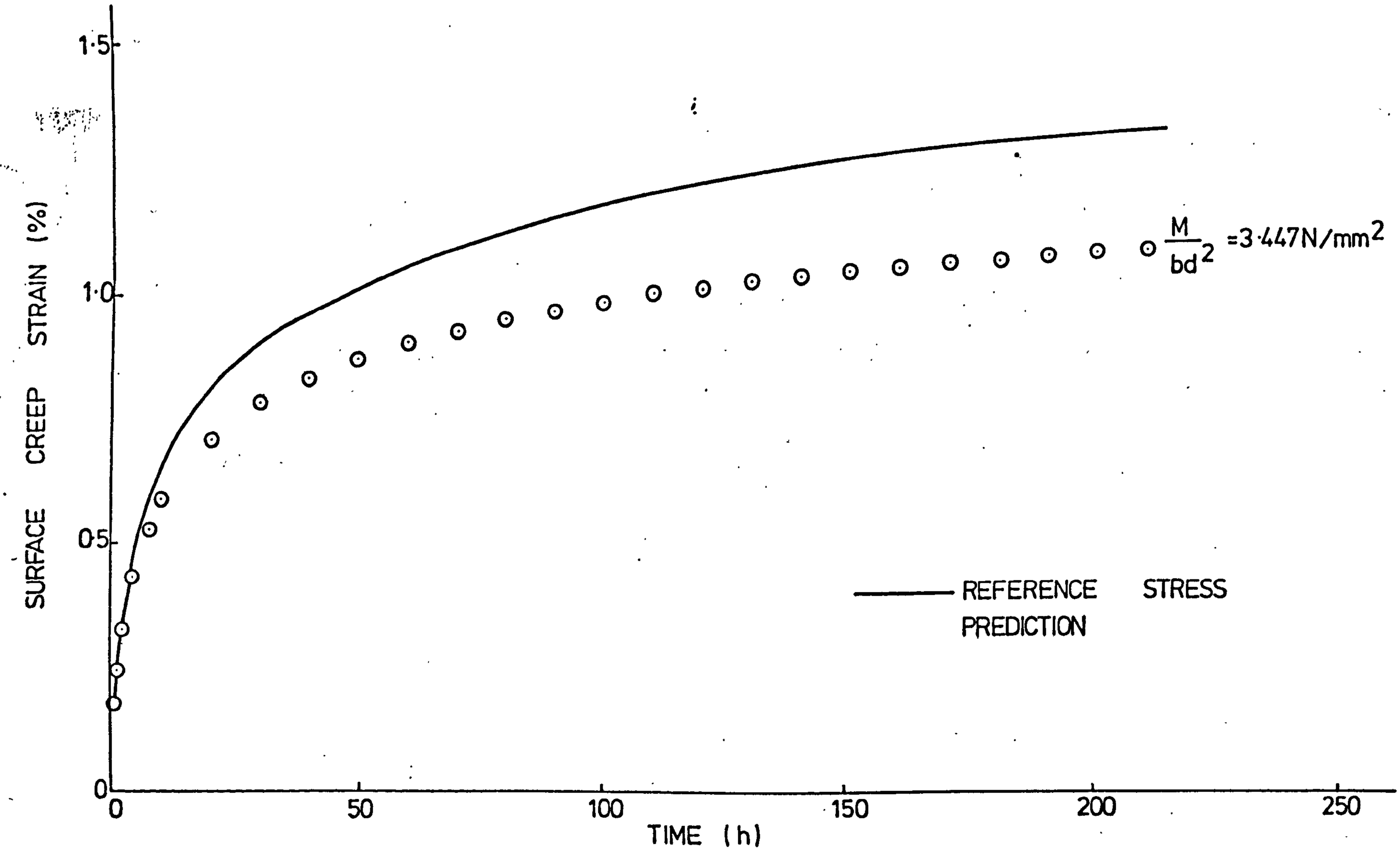

FIG. 6.3(b) PURE BENDING TEST RESULTS

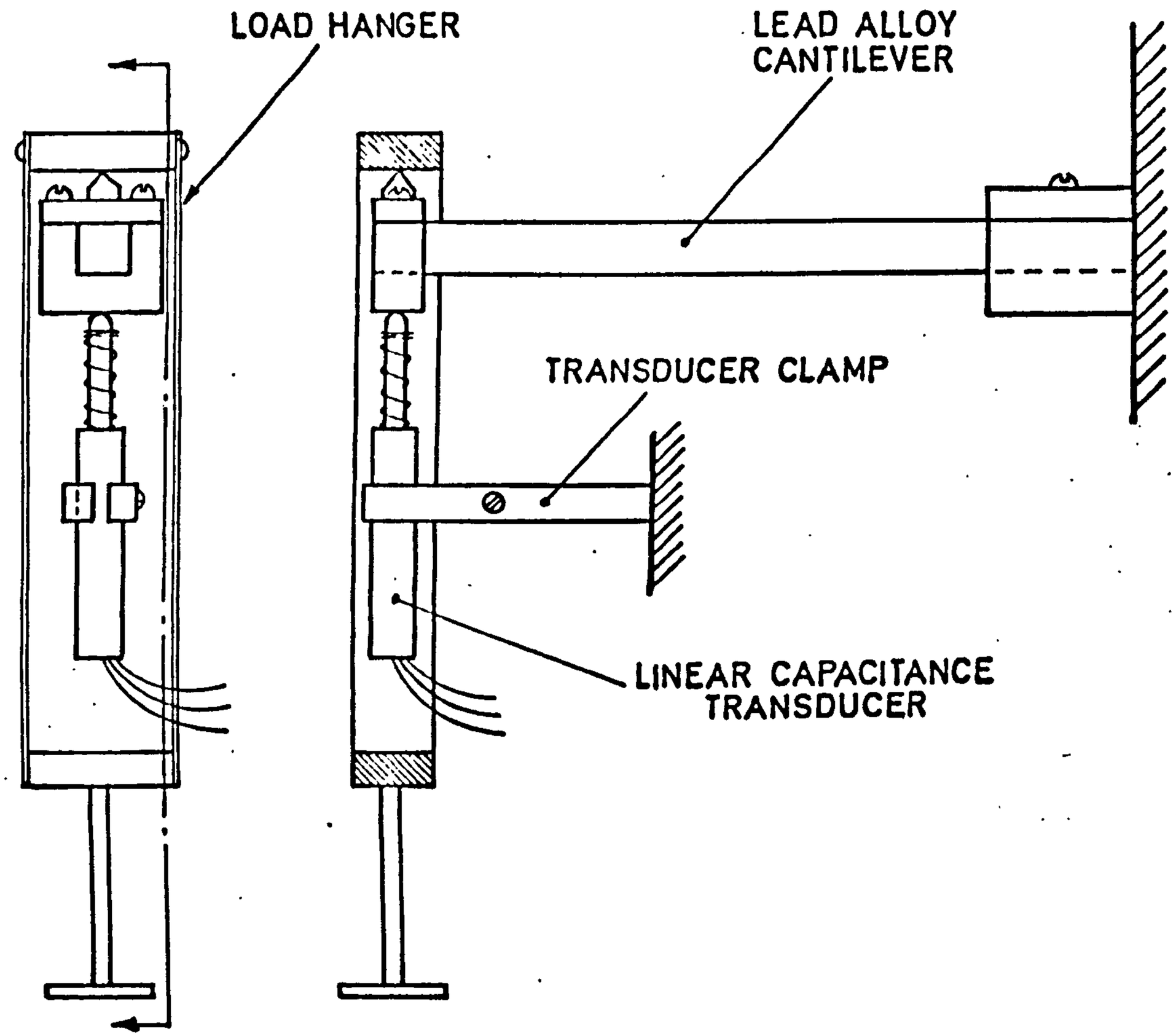

FIG. 6.4 CANTILEVER TEST EQUIPMENT

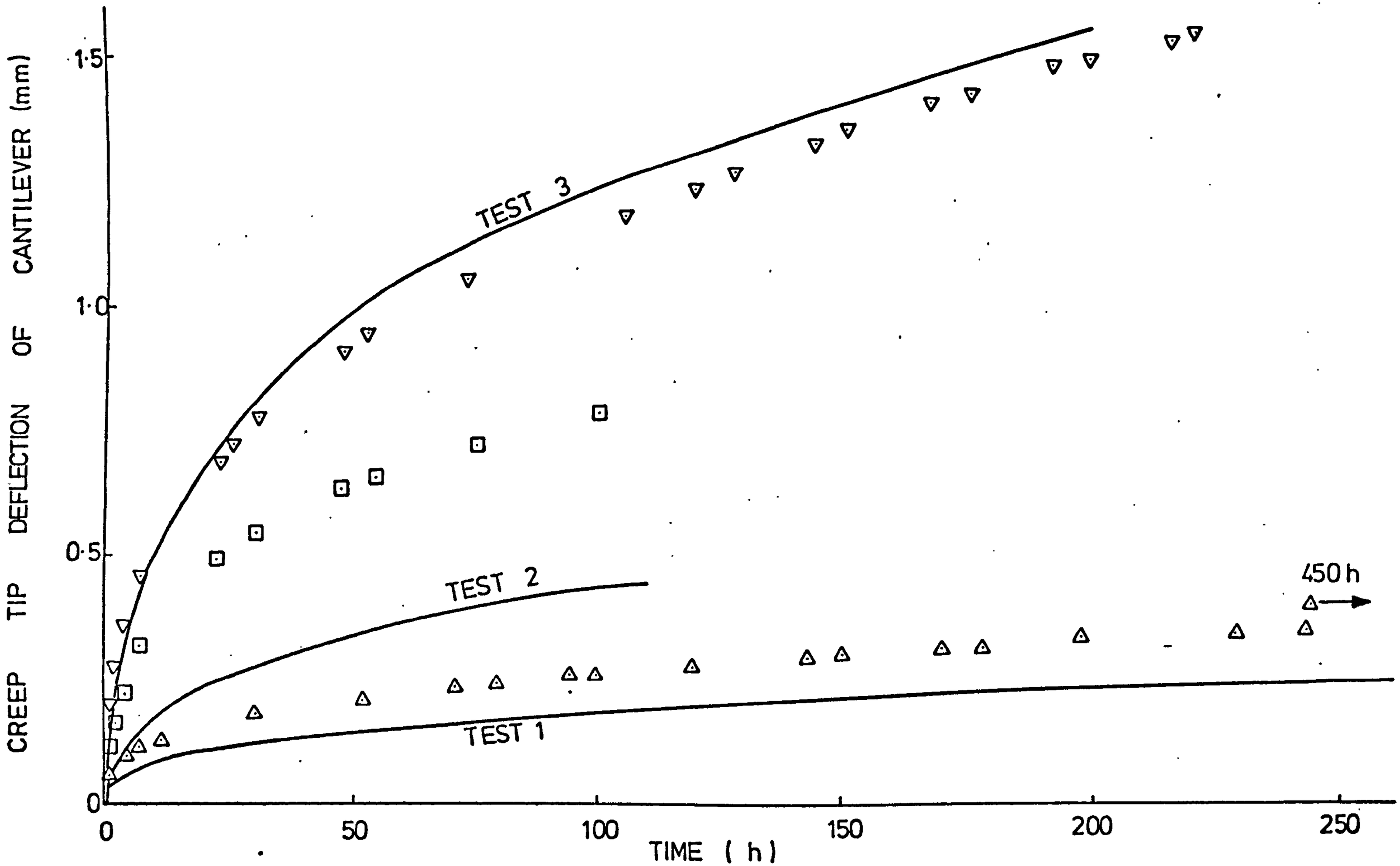

FIG. 6.5(a) CANTILEVER TEST RESULTS AND PREDICTIONS

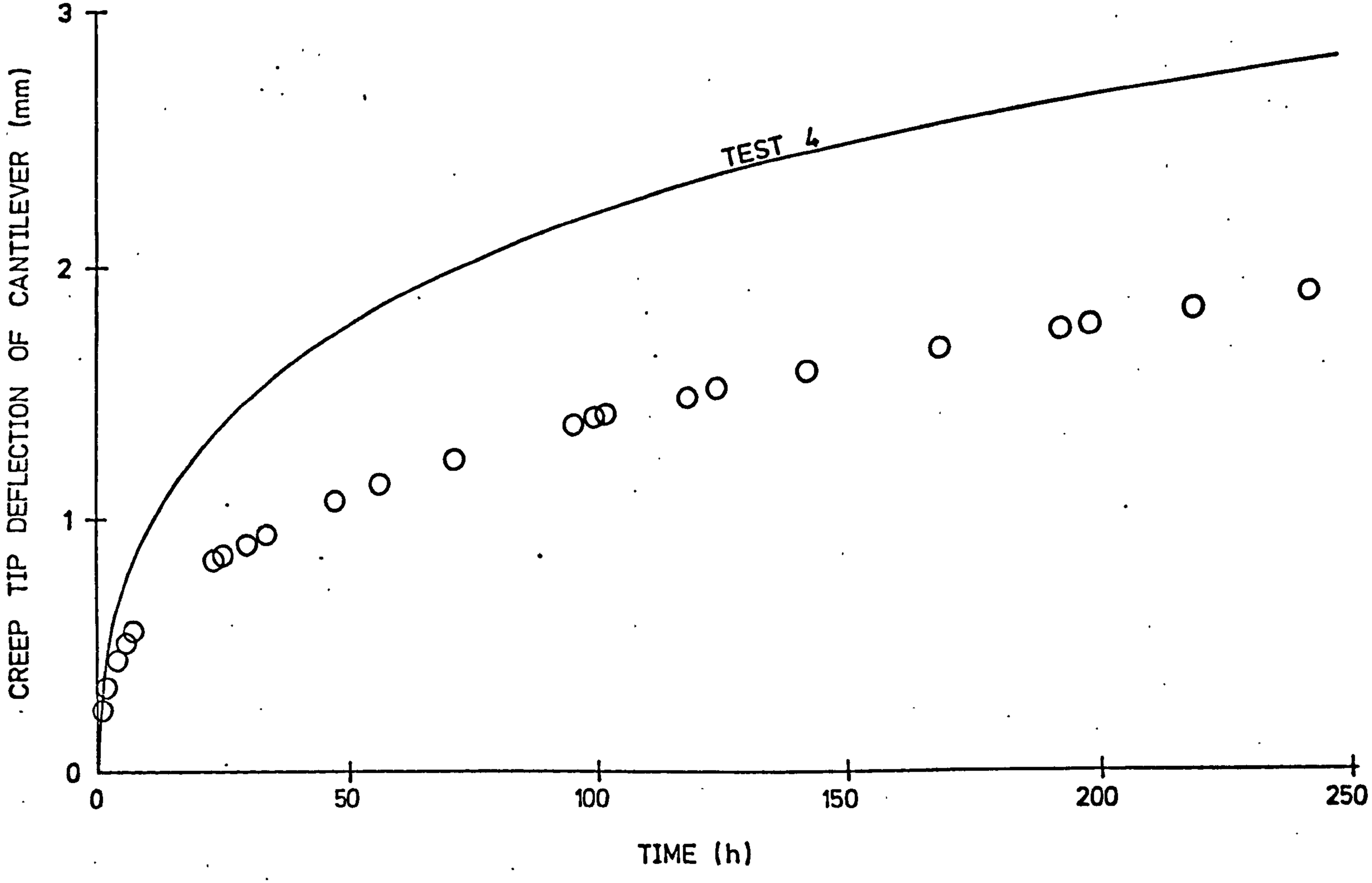

FIG. 6.5(b) CANTILEVER TEST RESULTS AND PREDICTIONS

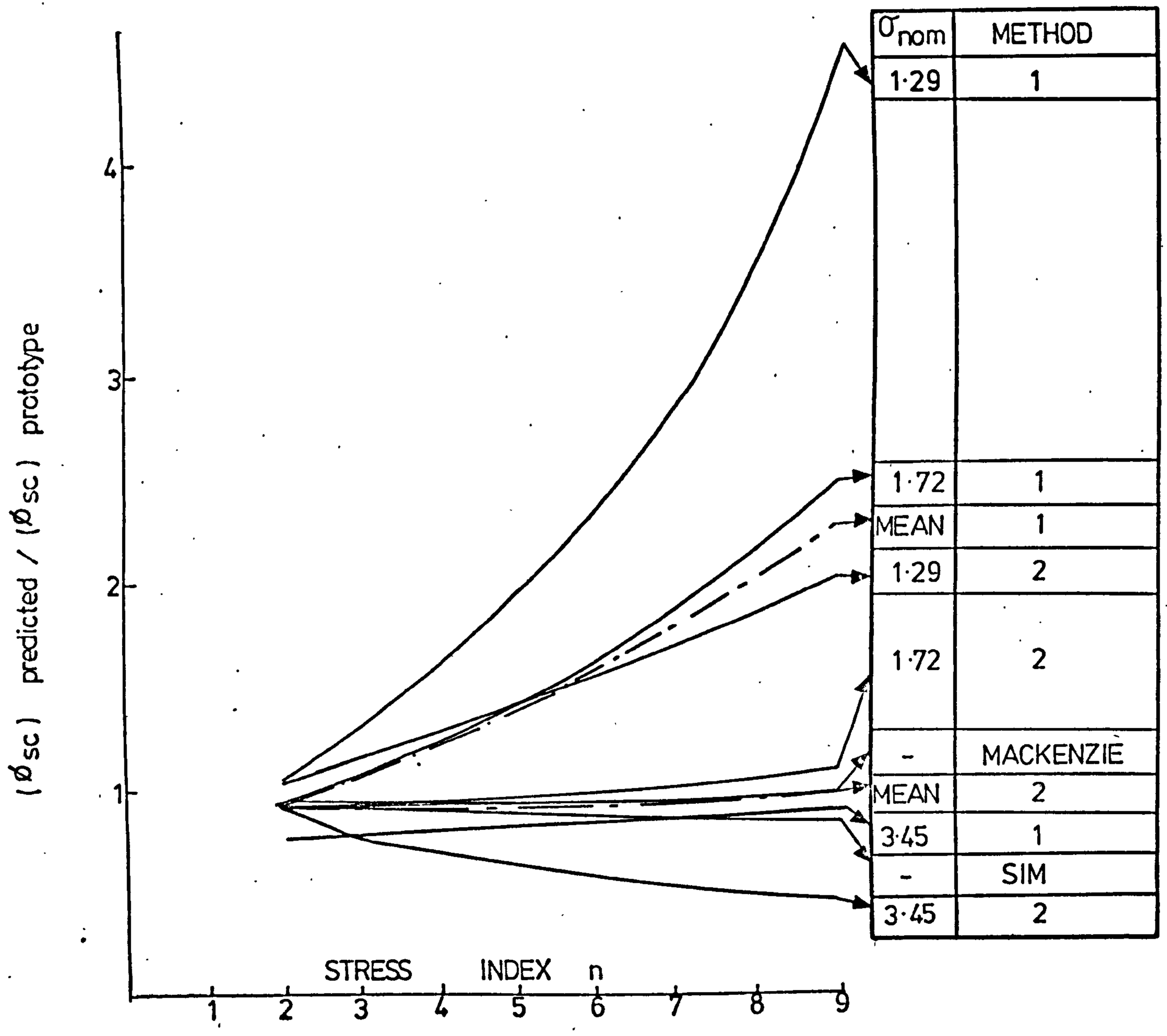

FIG. 6.6 ASSESSMENT OF PURE BENDING PREDICTIONS

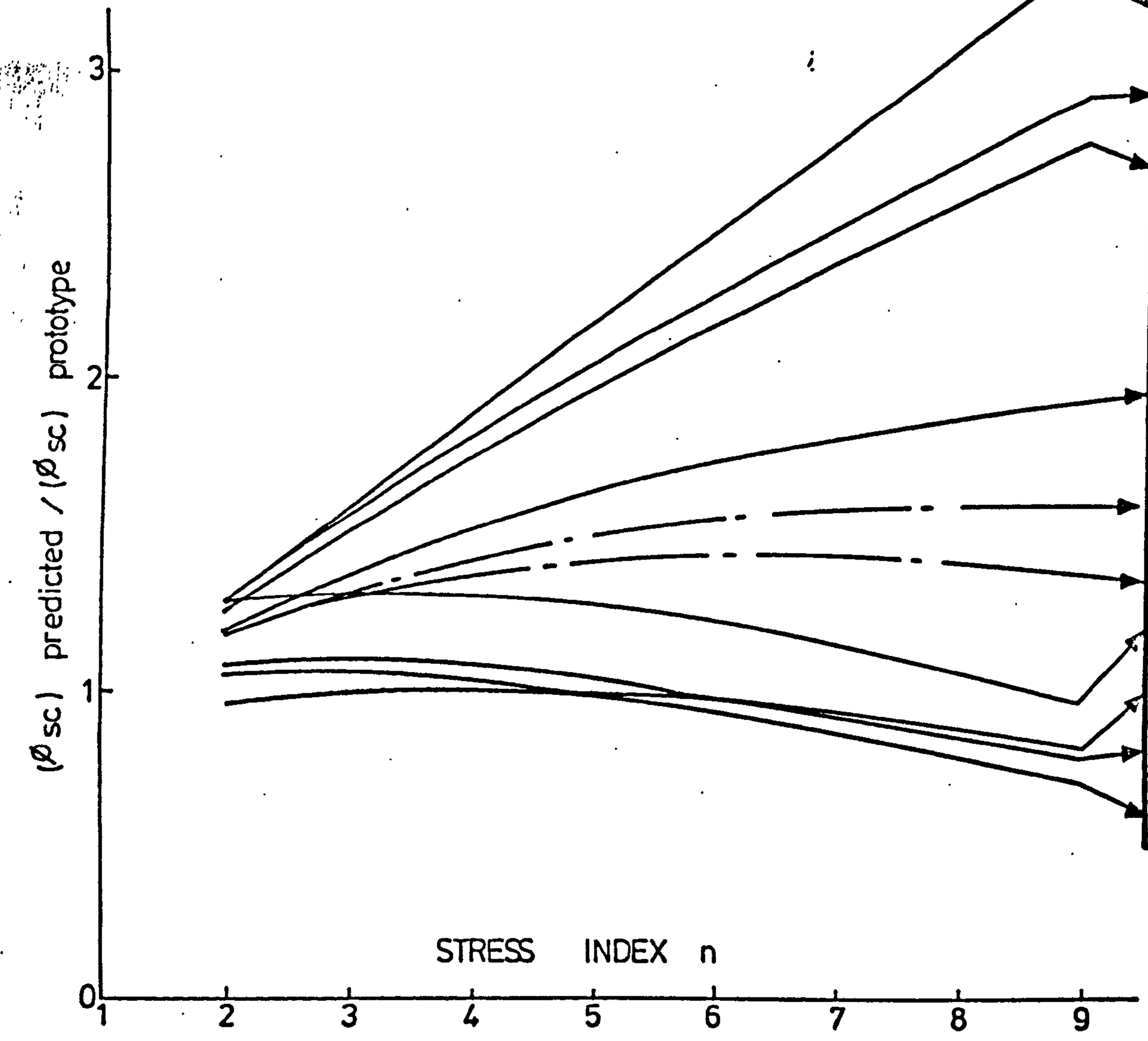

σ_{nom}	METHOD
-	SIM
2·07	1
2·07	2
1·55	2
MEAN	2
MEAN	1
1·55	1
2·59	1
-	MACKENZIE
2·59	2

FIG. 6.7 ASSESSMENT OF CANTILEVER PREDICTIONS

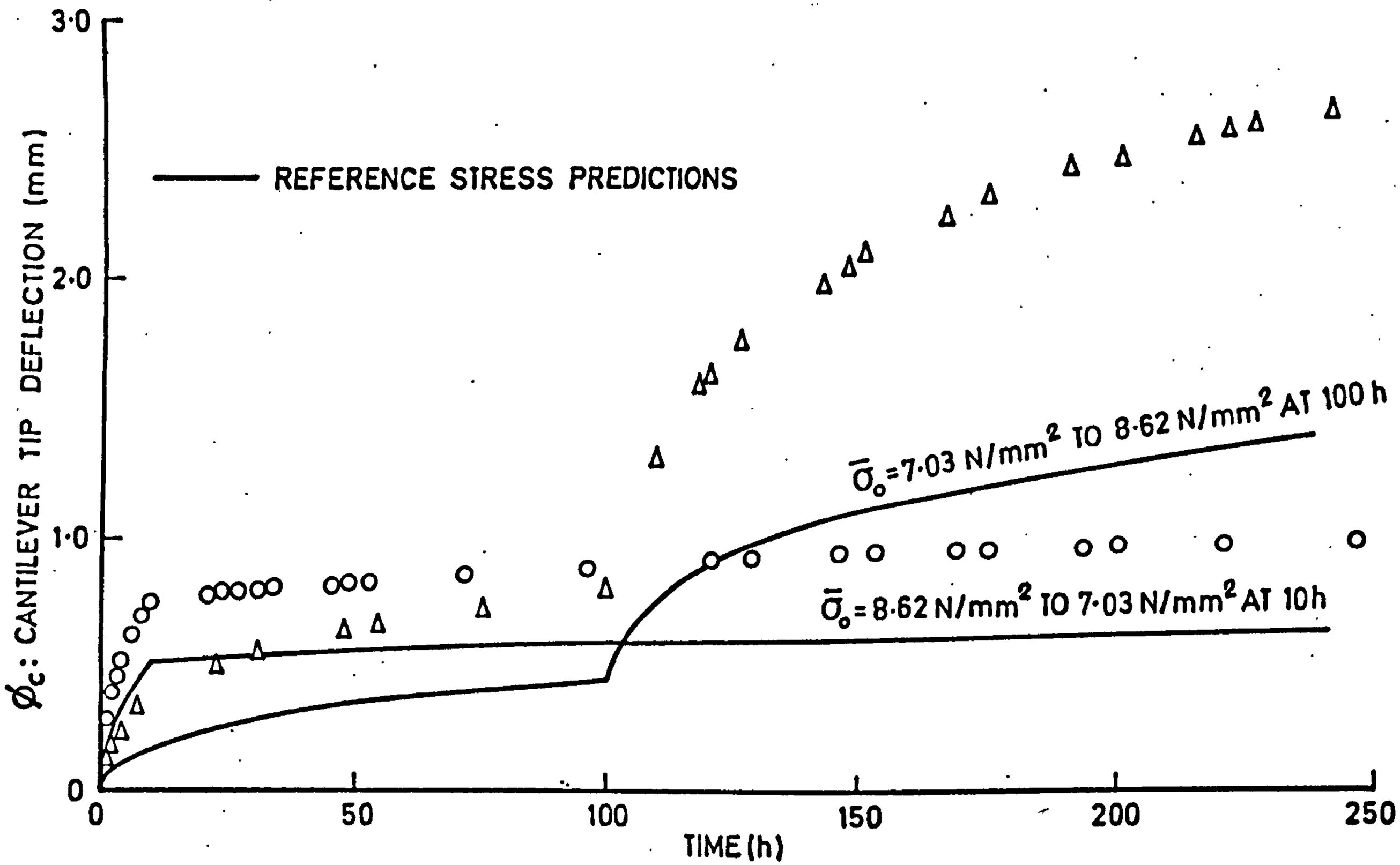

FIG.6.8(a) STEPPED LOAD CANTILEVER TESTS.

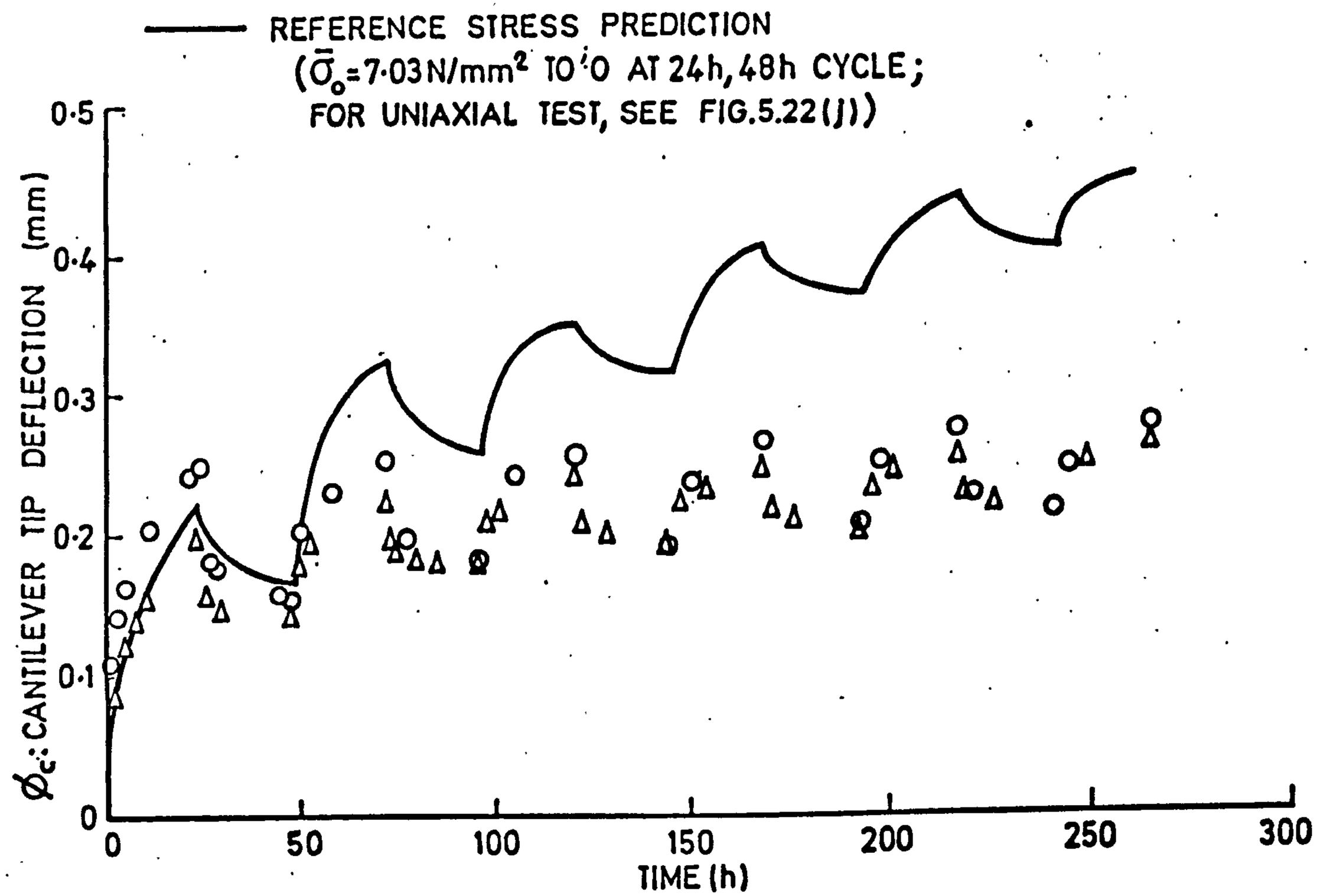

FIG.6.8(b) CYCLIC LOAD CANTILEVER TEST.

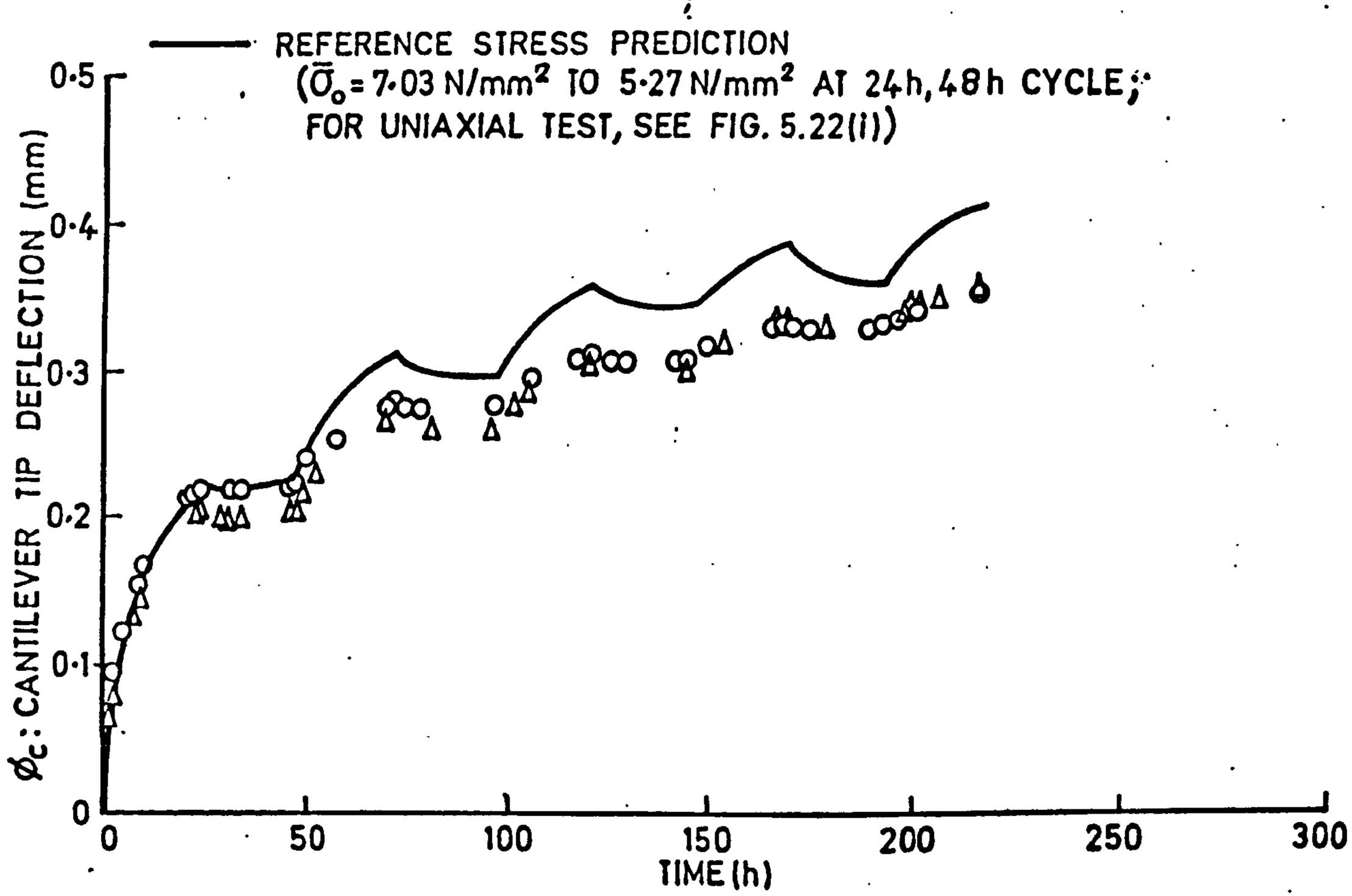

FIG. 6.8(c) CYCLIC LOAD CANTILEVER TEST.

CHAPTER 7

7. THE BIAXIAL CREEP PROPERTIES OF CHILL CAST 1.6% Sb, 0.16% As LEAD

7.1 Selection of the test specimen

When choosing the biaxial test specimen, the following requirements were considered:

(i) A uniform stress field must be produced so that there is no redistribution of stress.

(ii) The specimen shape must be simple so that casting and machining are easy.

(iii) There must be as wide a range of biaxial stress ratios as possible.

(iv) The loads should be conveniently small and easy to apply accurately.

(v) The specimen should not rupture at the grips.

Cruciform plates were considered but were discarded because of the possibility of buckling under compressive loads, which restricted the application to the tensile-tensile quadrant (see Fig. 7.1(a)). Also, cruciform plates would require a lot of machining as they could not be cast to size.

Thin cylinders under the action of combined

(i) tension and internal pressure,

(ii) tension and torsion, and

(iii) internal pressure and torsion

were considered because of the ease of manufacture.

The outside diameter can be cast to size and the inside diameter bored to the required size.

The thin cylinder under combined tension and internal pressure was discarded because the stresses were restricted to the tensile-

tensile quadrant (Fig. 7.1(b)). Of the other two methods, the thin cylinder under internal pressure and torsion was considered to be the best because it has a wider stress range (Figs. 7.1(c) and (d)). The combined tension and torsion specimen is restricted to the tensile-compressive quadrant whereas the combined internal pressure and torsion specimen covers the same tensile-compressive range, but also covers part of the tensile-tensile quadrant. Since the hemispherical end of the pressure vessel castings when pressurised, may be used to produce a 1:1:0 stress ratio, it was decided that the stress ratics were sufficiently covered in the tensile-tensile quadrant by the thin cylinder under combined internal pressure and torsion. Also, the combined internal pressure and torsion specimen does not require the accurate alignment of an axial load but only requires the application of a steady pressure.

Because it is desirable to keep the variation in stress across the walls as small as possible, the wall thickness of the thin cylinder must be as small as possible. However, because of the limitations of the casting process (the grain density is between 2 and 8 grains per mm), it was decided that a wall thickness of about 3 mm was the smallest that could be tolerated.

Having decided upon a wall thickness of 3 mm, the inside diameter and length of the cylinder were chosen so that a reasonably uniform stress distribution was obtained in the central portion. To this end, a series of elastic finite element solutions were obtained (using PAFEC 70+, ref.64) for various inside diameters and cylinder lengths, in the ranges $1 < \frac{L}{d} < 2$, $8 < \frac{d}{t} < 20$, the cylinders being assumed to be rigidly clamped at the ends and loaded by internal pressure. From these finite element solutions, it was decided that a diameter to thickness ratio of about 16 should be used together with a cylinder gauge length of 102 mm, which is twice the internal diameter. The

elastic finite element solution to the problem with the chosen dimensions (shown in Fig. 7.2 and 5.2) is shown in Fig. 7.3.

The analytical initial elastic and stationary state solutions are presented in Appendices 4 and 5 for internal pressure and torsion respectively from which it can be seen that for the selected $\frac{d}{t}$ value, the difference between the mean stresses and the exact stresses at the outside surface are small for a range of values of n. Under internal pressure, the maximum error in creep strain predictions based on mean stresses (KK18/1 and KK 19/5) is 19.3% and under pure torsion, the maximum error in creep strain predictions based on mean stresses (KK 9/1) is 5.1%.

7.2 The biaxial loading equipment

7.2.1 The clamping system

The clamping system is shown in Fig. 7.4. Grip of the thin cylinder is achieved by tightening the four 'clamping ring' bolts causing the lead to be extruded into the circumferential grooves in the sealing and 'clamping plugs' and the axial grooves in the 'clamping quadrants'. 'O'-rings are used to prevent oil leakage when the cylinder is pressurised. With this clamping system, a pressure of 4 N/mm^2 and a torque of 250 Nm have been applied without any leakage occurring. An Araldite cylinder is placed inside the thin cylinder specimen to reduce the amount of oil inside the specimen.

7.2.2 The torsion system

A schematic diagram of the torsion system is shown in Fig. 7.5. The 'load application straps' and the 'upper pulley support straps' are made of thin steel strips (0.3 mm thick) which offer very little resistance to bending. Therefore, since the 'upper pulley support straps' are long compared with the axial movements expected from the thin cylinders, the 'upper pulley' is free to move in the axial direction without applying any axial restraint to the cylinder.

The 'upper pulley' is mounted on a roller bearing and it is balanced so that resistance to rotary motion is negligible.

As the cylinders are mounted horizontally, it is necessary to eliminate the bending effect caused by the weight of the 'lower pulley'. This is done by adding a balance weight to the 'load applying bar'. The balance weight has the effect of eliminatingthe vertical force applied to the end of the thin cylinder but introduces a small initial torque to the cylinder. However, this torque is easily calculated and may be included (along with the 'load applying bar' and 'load hanger') in the total torque being applied to the thin cylinder.

The load on the 'load hanger' is distributed equally to the straps on either side of the 'load applying bar', by having a knife edge in the centre of the 'load applying bar'.

Before applying the torque, the total weight (i.e. load, load hanger, load applying bar and balance weights) is supported by two levers mounted on a platform (shown in Fig. 7.6). During this time the 'lower pulley' is balanced by an additional set of balance weights. The application of the torque then requires the simultaneous lowering of the 'load applying bar' and raising of the additional set of balance weights.

7.2.3 The Pressure System

A schematic diagram of the pressure system is shown in Fig. 7.7. The pump motor obtains its power supply via a pressure switch. In normal use, the electrical power will only be supplied to the pump motor if the pressure in the system is above a minimum level, which may be set by a pressure switch to any convenient pressure. The pressure switch is normally set about 0.1 N/mm^2 less than the pressure required in the thin cylinder specimen. If the pressure should drop

below that set on the pressure switch, due to rupture of the specimen or excessive leakage from the system, the pump will cut out and the pressure will fall to zero. For starting up purposes, the pressure switch has a by-pass switch to allow the pressure to build up to a value greater than the pressure set on the pressure switch.

The pump is used to supply the pressure to the thin cylinder (or pressure vessel) and a pressure relief valve is used to control the pressure. A bleed valve is also incorporated to ensure a flow of oil and thus eliminate the possibility of overheating the pump.

Because of the accuracy with which the pressure must be set, a seal-less piston is incorporated. The pistons cross-sectional area is accurately known, therefore by adding the required weights to the piston, the correct pressure can be obtained by altering the pressure relief valve until the seal-less piston just begins to rise, with the piston being slowly turned to eliminate friction. When the correct pressure is obtained, an additional small weight is added to the seal-less piston which causes it to fall to the bottom of its travel. This small weight sets the maximum pressure which may be applied, i.e. a weight is added so that a pressure increase of 0.01 N/mm^2 will cause the piston to rise. The piston has microswitches attached to it so that when the piston rises to a pre-determined height a solenoid valve is activated and closes off the pump supply. Due to leakage in the system the piston will slowly fall until it reaches a microswitch which will open the solenoid valve. If the pressure is still above the required value the piston will again rise. However, it should be noted that the main use of the piston is for setting the pressure and its use as a control of the solenoid valve is merely an emergency measure.

Because some of the cylinders and pressure vessels will be required to be tested in the plastic range, it is important that pressure surges are eliminated. Fig. 7.8 shows the effect of pressure surges. A hydraulic accumulator and a restrictor (in the form of a needle valve) were used for this purpose, as shown in Fig. 7.7. The restriction to flow ensures that pressure fluctuations are absorbed by the accumulator. The pressure is applied to the thin cylinder(or pressure vessel) by building up the pressure to the required value and then slowly opening the cylinder (or pressure vessel) supply valve. The complete loading system is shown in Fig. 7.6.

7.3 The strain measuring equipment

7.3.1 Deformation measurement requirements

As in the case of the uniaxial test rig, it was decided that the biaxial test rig should be capable of testing cylinders at both high and low stresses. Therefore, it was necessary to incorporate mechanical strain measuring systems for taking readings outside the scope of electrical resistance strain gauges, i.e. deformation measurements of the thin cylinders must also be possible so that large strains can be calculated. To obtain the principal strains for the biaxial stress system it is necessary to measure three components of strain, the axial strain, hoop strain and the shear strain associated with the axial deformation, radial deformation and twist of the thin cylinder, i.e. it is assumed that end effects are negligible and that

$$\varepsilon_\theta = \frac{\text{Radial expansion}}{\text{Outside radius}} = \frac{\Delta_r}{R_o} \qquad (7.1a)$$

$$\varepsilon_a = \frac{\text{Axial extension}}{\text{Specimen length}} = \frac{\Delta_a}{L} \qquad (7.1b)$$

and $$\gamma = \text{Angular Twist} \times \frac{R_o}{L} = \frac{R_o\theta}{L} \qquad (7.1c)$$

From the surface strains the radial strain may be obtained by assuming creep to be a constant volume process. This assumption is necessary because it is not possible to measure the change in wall thickness during the tests.

Appendices 4 and 5 show that slight variations in stress occur through the thickness and that the radial stress is not zero. However, because the variations in stress through the thickness are small and because the radial stress is small and zero at the outer surface where the measurements were made, the mean stresses were assumed to apply. The mean stresses are

$$\sigma_\theta = \frac{pR_i}{t} \qquad (7.2a)$$

$$\sigma_a = \frac{pR_i^2}{2R_m t} \qquad (7.2b)$$

$$\tau = \frac{T}{2\pi R_m^2 t} \qquad (7.2c)$$

where σ_θ, σ_a and τ are the hoop, axial and shear stresses respectively,

R_o, R_i and R_m are the outside, inside and mean radii respectively,

$t = R_o - R_i$, the wall thickness,

p, T are the internal pressure and torque respectively.

The errors introduced by assuming that the mean stresses act on the outer surface are small, as can be seen from Appendices 4 and 5. When initial plastic strains occur, the errors due to using these mean stresses will be reduced even further.

7.3.2 Strain measurements using electrical resistance strain gauges

Bellamy (56) investigated the adhesion and reinforcement effects of electrical resistance strain gauges on lead and concluded that adhesion was good and that reinforcement was negligible for lead of thickness

10 mm. Strain gauging was therefore considered to be acceptable for the present application, the smallest thicknesses being about 3 mm.

The multi-half-bridge system of strain gauging shown schematically in Fig. 7.9 was used in conjunction with a data logging system, capable of taking readings at intervals of about 0.3 sec. Wherever possible, electrical symmetry was maintaineed, i.e. the live and dummy circuits were made as similar as possible and were subjected to the same conditions.

The dummy gauge corresponding to each live gauge was of the same type and attached to the same material so that thermal strains and heat dissipation rates would be the same. The screened cables from the bridge balance box to the strain gauges were made the same length for both the live and dummy circuits and the number of soldered joints, which can act as thermocouples, were kept the same for both the live and dummy circuits. All of the circuits were continuously energised by a stabilised voltage supply, set at 4V, which was the maximum input that did not cause drift due to the electrical heating of the strain gauges. The apex system of bridge balancing was used with a switching device operated by the data transfer unit, outside the bridge circuits so that the switch resistance cannot affect the output voltage.

With the room temperature maintained at $20 \pm \frac{1}{2}^{o}C$, drift of the system was kept within $\pm$ 10$\mu\varepsilon$ over a period of 300h. Compensation for this drift was made by incorporating a 'drift gauge' in the system. A drift gauge is a gauge incorporated in the system which has no load applied to it, any change in the output is assumed to be due to drift and is taken to be the same for all of the live gauges.

7.3.3 Radial deformation

The hoop strain is calculated from the increase in the outside diameter of the thin cylinder by using equation 7.1a. The increase in

diameter is measured by use of two pairs of opposing linear capacitance transducers with a 5 mm. range (shown in Fig. 7.10). Because of the possibility of the cylinders being 'out of round', it is necessary that the diametral measurements be made at the same positions at all times (an 'out of roundness' of 0.025 mm. would imply a strain of about 500$\mu\varepsilon$). In order to ensure that the diametral measurements are made at the same position at all times, the transducers are mounted on a ring which rolls on four bearings such that its centre is coincident with the centre of the thin cylinder. During torsion, the transducers mounting ring is then driven by the thin cylinder through one of the feet of the transducers placed next to a small araldite step, glued to the thin cylinder. The glue is very flexible, enabling the system to be used to measure large strains. The bearings on which the transducer mounting ring is supported are such that the frictional resistance to the motion of the thin cylinder is negligible. Using this method, the sensitivity of the hoop strain measurements is 17$\mu\varepsilon$/division of unit output from the tranducers.

Provision was also made for the use of dial gauges (1 division $\equiv$ 0.0001 in) with this system (shown in Figs. 7.6 and 7.11). With these dial gauges, the sensitivity is reduced to 88$\mu\varepsilon$/division.

7.3.4 Axial Deformation

The axial strain is obtained by using equation 7.1b, which requires the axial deformation to be measured. This deformation is measured with a dial gauge, (1 division $\equiv$ 0.0001 in) the foot of which is placed at the centre of the 'lower pulley', i.e. along the axis of the cylinder. Measuring the deformation along the axis of the cylinder allows the average axial strain to be obtained. Figs. 7.6 and 7.11 show this dial gauge. With this system, the sensitivity is 25$\mu\varepsilon$/division.

7.3.5 Angular deformation

The angular deformation of the thin cylinder is obtained by measuring the amount by which the load falls. This is done by means of a dial gauge (1 division ≡ 0.0001 in) whose foot rests on the hook at the centre of the 'load applying bar'. Taking measurements at the centre of the 'load applying bar' compensates for any bending of the cylinder which may occur (bending will cause the ends of the 'load applying bar' to move by the same amount, but in opposite directions). This system of measuring the twist of the thin cylinder (shown in Figs. 7.6 and 7.11) allows the shear strain to be obtained by using the formula

$$\gamma = \frac{R_o}{LR_p}\Delta_\theta \qquad (7.3)$$

where Δ_θ is the displacement of the centre of the 'load applying bar' and R_p is the radius of the 'lower pulley'. The sensitivity of this measuring system is $6\mu\varepsilon$/division.

7.3.6 Assessment of the Biaxial Rig

Tests were carried out on an aluminium cylinder which had four strain gauge rosettes placed at the centre and ends on opposite sides of the cylinder. The results showed that, under torsion the end effects are not noticeable but, as was expected from the finite element results (Fig. 7.3), the strains measured under internal pressure at the ends were different to those measured at the centre. However, since the major effect of these end effects is on the axial deformation of the cylinder, which was expected to be practically zero for all of the tests, this was not considered to be of great significance. These tests also showed that there was no bending in the system.

7.4 Results

7.4.1 Initial strains

From the thin cylinder tests (identified by KK), results were obtained for stress ratios, shown in Table 7.1. In addition, the tests of the pressure vessels provided information for two stress ratios (1:1:0 and 1:0.47:0). The number of tests carried out at each biaxial stress ratio is shown in Table 7.1, together with the casting number from which the specimens were taken and the von Mises effective stress at which the tests were carried out. With the biaxial test rig, it was not possible to apply the pressure and torsion loads simultaneously.

Of the 18 biaxial tests carried out, 14 needed the application of a single load only, i.e. either pure internal pressure (of cylinders or pressure vessels) or pure torsion (of cylinders). This ensured that during loading, the stress path in 'stress space' was radial. One of the other tests was carried out with a von Mises effective stress of 7.03 N/mm^2 which is just beyond the elastic limit and it is therefore unlikely that a non-radial path will have had much effect on the plastic and creep strains obtained. For the other three tests, the von Mises effective stress was 14.06 N/mm^2 which is in the plastic range. It was therefore necessary to apply the torsion and pressure loads slowly (about 10 sec) in order to obtain radial stress paths. The initial deformations obtained from the 18 tests are shown in Table 7.2.

Two thin cylinders tested under pure internal pressure were unloaded at the end of the tests and the unloading strains were used to obtain a value of Poisson's ratio, using the simple relationship

$$\nu = \frac{\left[\frac{\varepsilon_1}{\varepsilon_2}\right]^{k-1}}{\left[\frac{\varepsilon_1}{\varepsilon_2}\right]^{-k}} \qquad (7.4)$$

where ε_1 and ε_2 are the principal unloading strains (elastic) and $k = \sigma_2/\sigma_1$, which for the internal pressure case is 0.47

$$\text{i.e. } \nu = \frac{0.47(\varepsilon_1/\varepsilon_2) - 1}{(\varepsilon_1/\varepsilon_2) - 0.47}$$

For the two tests, $(\varepsilon_1/\varepsilon_2)$ were measured and found to be 26.3 and 27.0, giving values of Poissons ratio of 0.439 and 0.435. On the basis of these results, a Poissons ratio of 0.44 was assumed for the subsequent calculations. Using this value of Poissons's ratio and a Young's Modulus of 2.32×10^4 N/mm^2, obtained from the uniaxial calibration of the material, elastic components of strain were calculated for each of the biaxial tests, using the relationships

$$(\varepsilon_1) = \frac{1}{E}(\sigma_1 - \nu\sigma_2)$$

$$(\varepsilon_2) = \frac{1}{E}(\sigma_2 - \nu\sigma_1)$$

These were subtracted from the measured total initial strains to give the plastic components of strain which are given in Table 7.2. To assess the accuracy of the Prandtl-Reuss relationships for predicting plastic strain components, the theoretically determined ratio of principal plastic strains is compared with the experimentally obtained ratio (given in Table 7.2). This comparison shows that in the tension-compression quadrant, the Prandtl-Reuss relationships give accurate predictions but in the tension-tension quadrant the correlation is not so good. This is almost certainly due to inaccuracies in the cal lated values of small plastic strain components. A small error in either the measured $\varepsilon_1/\varepsilon_2$ value or the k value (0.47), which is based upon average stresses, will change the value of Poisson's ratio, which can cause a significant error in the calculated small plastic strains, particularly for the stress ratio of 1:0.47:0, e.g. if k = 0.5 is used, a Poissons ratio of 0.47 is obtained, which leads to a plastic strain ratio of -22.1 instead of -30.45 obtained with $\nu = 0.44$, for specimen

KK18/1. Another possibility is that the through-thickness properties may be different to those perpendicular to the radius. Anisotropy of this type would have very little effect in the tension-compression quadrant where the 'through thickness' strains are relatively small but would have a significant effect in the tension-tension quadrant where the 'through thickness' strains are relatively large. However, since accurate results are obtained for the 1:1:0 ratio, this is unlikely.

An average stress-strain curve, for the various alloying compositions was drawn through the experimental data shown in Fig. 5.16(a). This average stress strain curve was used in conjunction with the von Mises yield criterion and the Prandtl-Reuss relationships to obtain theoretical predictions of the plastic strains. The predictions obtained by this method were of the correct order of magnitude but, because of the sensitivity of the limit of proportionality and plastic strains to the antimony composition, it was not possible to obtain any consistent correlation between the theoretical and experimental results by this method.

7.4.2 Creep strains

The creep strains obtained from the biaxial tests are shown plotted against time in Figs. 7.12(a)-(r). The overall uniaxial creep law was used in conjunction with the mean stresses and the von Mises (equations 2.17(a), 2.17(b)) and Tresca (equations 2.18(a), 2.18(b)) criteria to obtain the multiaxial creep strain predictions, which are also shown in Figs. 7.12(a)-(r). Appendices 4 and 5 show that these predictions should slightly underestimate the creep strains. The discrepancies between the experimental and predicted creep strains for both the von Mises and Tresca criteria are of the same order of magnitude as those obtained in the uniaxial results. The von Mises criterion gives the better correlation in the tension-compression quadrant (Figs. 5.12(m)-(q)) whereas there is little to choose between the two criteria in the tension-tension quadrant (Figs.5.12(a)-(l)).However, it can be seen that the von Mises criterion gives t

closest overall correlation.

Because the von Mises criterion generally underestimates the creep strains in the tension-tension quadrant by a lot more than that indicated in Appendices 4 and 5, it was decided that the effect of hydrostatic tension on creep should be investigated. Although somewhat arbitrary, the basis for the investigation was chosen to be the maximum principal creep strain after 100 h. In order to obtain comparison between all of the biaxial results, the hydrostatic stress was normalised with respect to the von Mises effective stress ($\sigma_{kk}/3\sigma^*_{VM}$), shown tabulated in Table 7.1. The predicted maximum principal creep strains in 100 h, based upon the overall uniaxial creep law, were normalised with respect to the measured creep strain in 100 h, i.e. $\frac{(\varepsilon_c)_{\text{predicted in 100h}}}{(\varepsilon_c)_{\text{actual in 100 h}}}$. The predicted to actual strain ratios are shown plotted against the normalised hydrostatic tension components of stress in Fig. 7.13(a). Also shown in Fig.7.13(a) is the range of the predicted to actual strain ratios obtained from the uniaxial creep tests, from which it can be seen that in the tension-tension quadrant (i.e. when $\sigma_{kk}/3\sigma^*_{VM}>0.33$) the creep strain predictions are too small whereas in the tension-compression quadrant the creep strain predictions are reasonably accurate. As shown by the uniaxial creep data, the creep strains are dependent upon the antimony composition. In order to take the antimony composition into account, the uniaxial creep strains at 100 h for the required stresses were plotted against the antimony composition as shown in Fig. 7.14. This figure was then used to obtain the 100 h biaxial creep strain predictions instead of the overall uniaxial creep law. These antimony corrected predictions were used to construct Fig. 7.13(b), which confirms the effect of hydrostatic tension in the tension-tension quadrant. Four

of the biaxial tests were carried out on specimens which had antimony compositions (1.31-1.34% Sb) outside the range for which uniaxial data was available. However, some creep tests were carried out on a nominally 1.2% Sb, 0.12% As lead alloy casting (T14), which was not cast by the author and therefore the exact composition was not known. Using this data, the curves shown in Fig. 7.14 were extended (shown by a chain dotted line) to include the 1.31 to 1.34% Sb compositions. Because of the uncertainty of the exact composition of the nominally 1.2% Sb, 0.12% As lead alloy and because of the degree of approximation involved in sketching the curves (Fig. 7.14) between the 1.2% Sb and 1.4% Sb compositions, it was difficult to obtain accurate predictions of uniaxial creep strains for this region of antimony compositions. However, it can be seen that in the range 1.31 to 1.34% Sb, the creep properties are similar to those in the range 1.45 to 1.48% Sb and therefore, the KK19 and KK20 uniaxial creep law (which was obtained from uniaxial specimens with 1.45 to 1.48% Sb compositions) was assumed to apply in this region. The results of the four biaxial tests in the 1.31% to 1.34% Sb region are also shown in Fig. 7.13(b) (identified by having crosses through the data points) and can be seen to fall roughly into line with the other biaxial tests.

Fig. 7.13(b) shows that the effect of the hydrostatic tension component of stress is more dominant at the higher values of effective stress.

The results of tests carried out on two large grained specimens, KK9/3 and KK19/3, having 2 to 3 grains through the wall thickness, did not indicate any effect due to grain size.

7.4.3 Rupture tests

For three of the biaxial tests, the stresses were increased to much greater values and the specimens were allowed to creep until rupture.

Table 7.3 gives the specimens, the increased stresses, rupture strains and the times to rupture (at the increased stresses). The rupture time for the internal pressure test (KK9/3) was taken as the time at which leakage from the pressure vessel was first noticed. It is possible that rupture may have occurred before the leakage was noticed therefore this time must be taken as an upper bound. Because of the small amount of energy stored in the system (due to the use of a large core which almost filled the thin cylinder), the crack propagation for this test will be slow. The tests on the pressure vessels described later in which a large amount of energy was stored, produced rapid fracture, therefore the rupture time was more easily indentified.

Ruptured specimens are shown in Fig. 7.15. Since the rupture strains are at least 30 timesthe strains obtained during the creep tests carried out at the lower stresses, it is likely that the effect of the low stress creep tests on the subsequent rupture times of the higher stresses was negligible. With the available data the effect had to be ignored. There is no close correlation between the uniaxial rupture data and the biaxial rupture data when based upon the maximum principal stress or the von Mises effective stress, the von Mises criterion gave the best correlation and is shown in Fig. 7.16. However, as can be seen, this method tends to overestimate the rupture time by more than an order of magnitude. It was noticed that rupture was initiated in the region of the specimen where the two halves of the multi cylinder mould join together. In this region a small step is produced (about 0.05 mm) which could account for a slight reduction in the rupture life of the specimen. However, due to the ductility of the material, it is unlikely that a large enough stress concentration could be created in this region to cause the observed discrepancy between the uniaxial and biaxial rupture properties. At rupture, the mean hoop strain of the pure internal pressure test (KK9/3) was found to be 5.6% which would increase the maximum principal stress and von

Mises effective stress by about the same amount. This increase in stress could significantly effect the rupture time, but this is also unlikely to account for the observed discrepancy between the uniaxial and biaxial rupture properties. No significant geometry changes occurred in the torsion specimens (until the instant of rupture, when the specimens collapsed). Therefore, it was concluded that a multi-axial state of stress can cause a drastic reduction in rupture time. Further, the reduction in rupture time appears to be as great in the tension-compression quadrant (1:0:-1) as in the tension-tension quadrant (1:0.47:0).

Fig. 7.17 shows the rupture data presented in the manner suggested by Hayhurst (18), which is described in section 2.4.2. From Fig. 7.17, it can be seen that the creep rupture of the two torsion specimens indicate that the maximum shear stress criterion applies whereas the creep rupture test on the thin cylinder under internal pressure appears to be represented more closely by the von Mises effective stress criterion. It is also apparent from Fig. 7.17 that the maximum principal stress and hydrostatic stress criteria do not apply. The formulation suggested by Hayhurst (18) was in terms of the maximum principal stress, the hydrostatic stress and the von Mises effective stress but did not have a term related to the maximum shear stress. On the basis of the limited number of tests carried out on lead alloy specimens, it appears that an extra term should be included in Hayhurst's formulation, namely a maximum shear stress term.

7.5 Discussion

The suitability of the biaxial test rig was proved for both creep and creep rupture testing. The rig would be improved if a simple method were devised for accurately applying the torsion and pressure loads simultaneously and if the pressure and torque applied to the cylinder could be continuously adjusted as the diameter of the cylinder

increases. However, neither of these drawbacks is considered to have had a significant effect on the creep results. This is because most of the tests were performed with the application of a single load and the total strains, even at the end of the creep tests, were small. The rupture data were obtained from single load tests and the mean hoop rupture strain for the pressure test was only 5.6%, therefore even the results obtained from the rupture tests are likely to be as accurate as the uniaxial rupture data, in which significant reductions in cross-sectional area are usually obtained. In high strain tests performed by Finnie (17) on aluminium at 250°C, measurements were made of dimensional changes and the internal pressure was continuously adjusted to maintain constant average stress. However, these tests only lasted for between 7 and 14 hours which makes manual adjustment feasible whereas for tests of up to 300 hours (such as those performed by the author) it was not considered feasible or necessary, because of the small strains. Finnie also presents some small strain biaxial creep results for lead containing 6% Sb at 70°C for which no load adjustments were made. The specimens used by Finnie for the tests on aluminium had the same diameter to thickness ratio as those used for the present tests (i.e. 16:1) but the gauge length to diameter ratio used by Finnie was about 3.5:1 whereas that used for the present tests was 2:1. For the tests on the 6% Sb lead, Finnie used a larger diameter to thickness ratio (20:1) in conjunction with a larger gauge length to diameter ratio (4.5:1) for pressure tests but a shorter gauge length to diameter ratio for torsion tests (1.5:1).

From the biaxial test results, it is apparent that the von Mises effective stress criterion greatly underestimates creep strains in the tension-tension quadrant, where high hydrostatic tensile stress components are found. The stress systems in the tension-tension quadrant are

likely to encourage the formation of voids within the material. These would account for the underestimation of the creep strains when based upon the uniaxial data used in conjunction with the von Mises effective stress. The results of Finnie (17) show a similar effect due to hydrostatic stress in the tension-tension quadrant and the results of Johnson et al (9) and Finnie (17) in the tension-compression quadrant support the results of the present work and show that reasonably accurate predictions of creep strains can be obtained in the tension-compression quadrant by using the von Mises effective stress criterion.

The Prandtl-Reuss flow rule gives accurate predictions of the relative magnitudes of the components of creep strains and initial plastic strains. The apparent large error in the relative magnitudes of initial plastic and creep strain components for the internal pressure only tests is put down to the fact that a small variation in the ratio of the calculated mean stress ratio, (1:0.47:0) or the value of Poissons' ratio (used in the calculation of the initial plastic strains) can have a significant effect on the axial strain component, whilst having little effect on the hoop strain component.

The limited number of rupture tests performed were not enough to draw any firm conclusions from, but the results indicate that the maximum tensile stress and the hydrostatic stress have little effect on the creep rupture times. The normalised rupture data (using the method suggested by Hayhurst (18)), indicates that the von Mises effective stress and the maximum shear stress may be used to bound the creep rupture results.

The rupture strains under biaxial conditions in both the tension-tension and tension-compression quadrants were found to be significantly less than those obtained from uniaxial tests.

7.6 Conclusions

(i) The biaxial test rig proved to be suitable for both creep and creep rupture testing.

(ii) The Prandtl-Reuss flow rule was found to be applicable, to an acceptable degree of accuracy, for both initial plastic and creep strains.

(iii) The von Mises effective stress criterion produced reasonably accurate predictions of creep strains in the tension-compression quadrant but underestimated creep strains in the tension-tension quadrant.

(iv) On the basis of two torsion creep rupture tests and one internal pressure creep rupture test together with the uniaxial creep rupture data, the criterion for creep rupture appears to be bounded by the von Mises effective stress criterion and the maximum shear stress creterion. The maximum tensile stress and the hydrostatic component of stress do not appear to significantly effect the creep rupture properties.

Table 7.1 Biaxial Tests

STRESS RATIO / σ^*_{VM}	1:1:0	1:0.47:0	1:0.25:0	1:0:0	1:0:-0.5	1:0:-1
5.27 N/mm^2	P14					
7.03	P16 P10	KK9/3		KK20/1		KK9/1
9.14		P14				
9.84	P12					
10.54						KK18/5
12.18		P16 P10				
14.05		KK18/1 KK19/5	KK20/2	KK19/3	KK19/4	KK19/2
17.05		P12				
$\sigma_{kk}/3\sigma^*_{VM}$	0.667	0.567	0.462	0.333	0.126	0

σ^*_{VM} is the von Mises effective stress

Table 7.2 Initial Deformations

STRESS RATIO	SPEC-IMEN	σ^*_{VM} (N/mm^2)	INITIAL PRINCIPAL STRAINS, $\varepsilon_1, \varepsilon_2$ ($\mu\varepsilon$)						PRINCIPAL PLASTIC STRAIN RATIO $(\varepsilon_1/\varepsilon_2)_{pl}$	
			OUTSIDE			INSIDE			EXPERI-MENTAL	THEORETICAL
			TOTAL	ELASTIC	PLASTIC	TOTAL	ELASTIC	PLASTIC		
1:1:0	P10	7.03	475, 458	167, 167	308, 291	560, 591	167, 167	393, 424	1.06(0.93)	1.0
	P12	9.84	1150, 1211	234, 234	916, 977	1229, 1298	234, 234	995, 1064	0.94(0.94)	
	P14	5.27	146, 115	125, 125	21, -10	122, 125	125, 125	-3, 0	-2.1 ( )*	
	P16	7.03	491, 408	167, 167	324, 241	262, 262	167, 167	95, 95	1.34(1.0)	
1:0.47:0	P10	12.18	8630, 260	407, 15	8223, 245	11154, -790	407, 15	10747, -805	33.6(-14.1)	-28.4
	P12	17.05	2.06%, -	657, 24	1.99%, -	-, -	657, 24	-, -	-	
	P14	9.14	1818, 127	352, 13	1466, 114	1900, -128	352, 13	1548, -141	12.9(-11.0)	
	P16	12.18	5921, 310	407, 15	5514, 295	6816, -209	407, 15	6409, -224	18.17(-28.6)	
	KK9/3	7.03	311, -46	271, 10	40, -56				-0.71*	
	KK18/1	14.05	2004, -68	542, 20	1462, -48				-30.45	
	KK19/5	14.05	3707, 152	542, 20	3165, 132				24.0	
1:0.25:0	KK20/2	14.05	1360, 531	588, -125	772, -406				-1.90	-3.51
1:0:0	KK19/3	14.05	1453, -1090	595, -262	858, -828				-1.04	-2.0
	KK20/1	7.03	450, -309	298, -131	152, -178				-0.87	
1:0:-0.5	KK19/4	14.05	1528, -1265	275, -212	1253, -1053				-1.19	-1.25
1:0:-1	KK9/1	7.03	333, -337	247, -247	86, -90				-0.96	-1.0
	KK18/5	10.54	647, -642	371, -371	276, -271				-1.02	
	KK19/2	14.05	6583, -7743	494, -494	6089, -7349				-0.83	

* based on small strains, therefore likely to be inaccurate.

( ) inside ratio

N.B. Inside strains were not measured on the KK specimens.

Table 7.3 Biaxial Rupture Tests

Specimen number	Stress Ratio	σ^*_{VM} (N/mm^2)	$\hat{\sigma}$ (N/mm^2)	t_R (h)	Rupture Strains * (%)
KK9/1	1:0:-1	21.08	12.19	24.1	5.5
KK9/3	1:0.47:0	24.59	28.36	2.67	5.6
KK19/2	1:0:-1	24.59	14.19	1.63	7.5

* Mean hoop strain at rupture for the pressure test and the engineering shear strain just before the specimen collapsed.

torsion

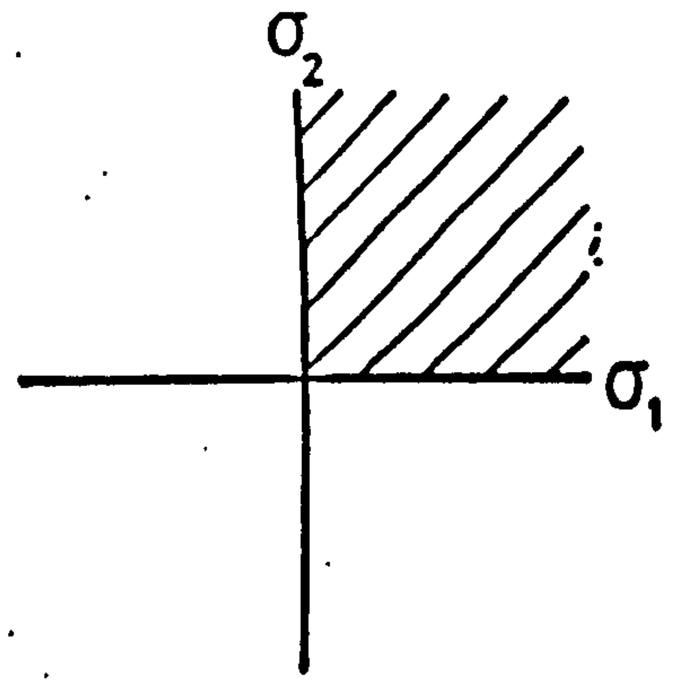

(a) CRUCIFORM PLATE

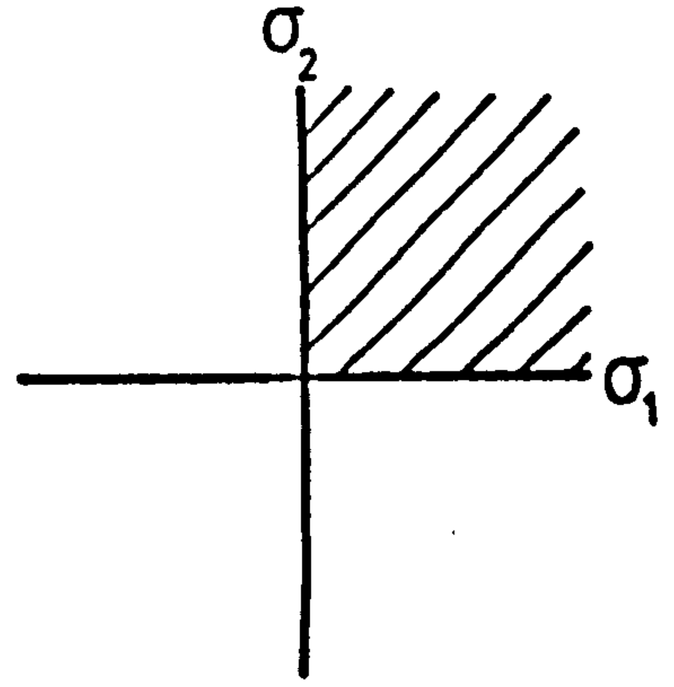

(b) THIN CYLINDER UNDER COMBINED PRESSURE AND TENSION.

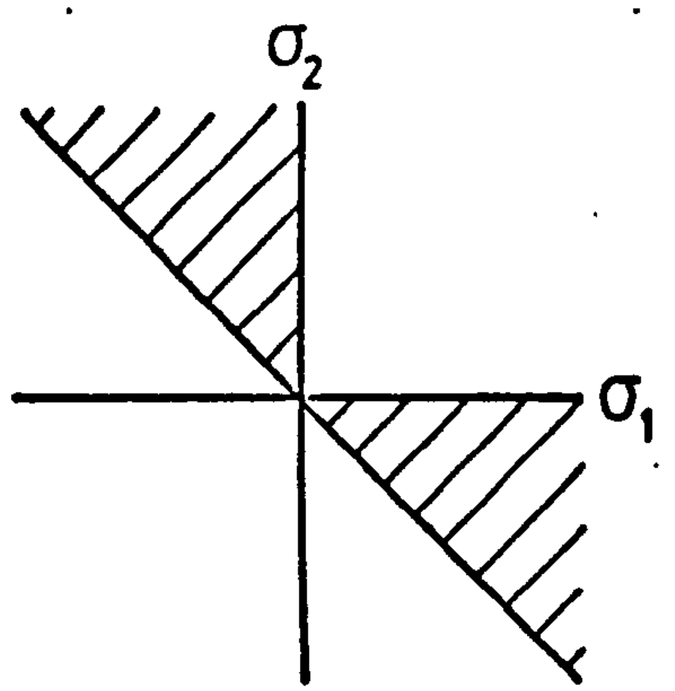

(c) THIN CYLINDER UNDER COMBINED TORSION AND TENSION.

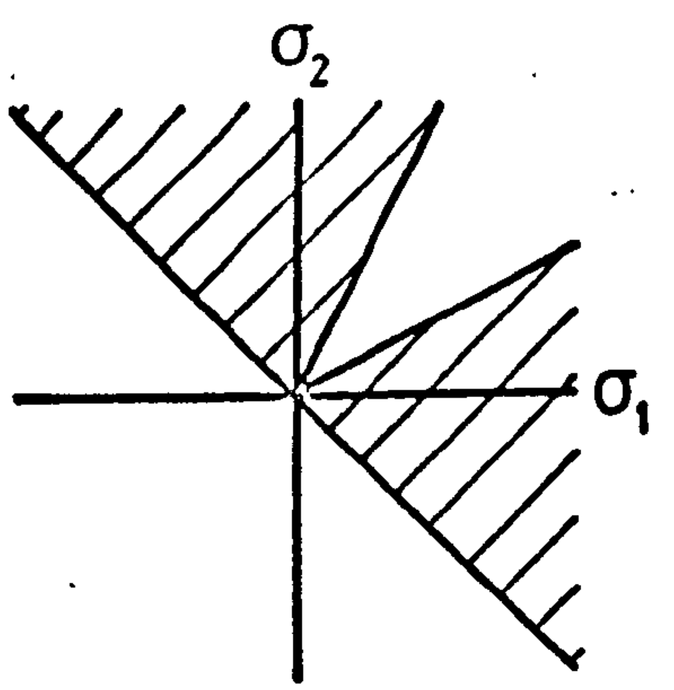

(d) THIN CYLINDER UNDER COMBINED PRESSURE AND TORSION.

FIG. 7.1 BIAXIAL STRESS RANGES

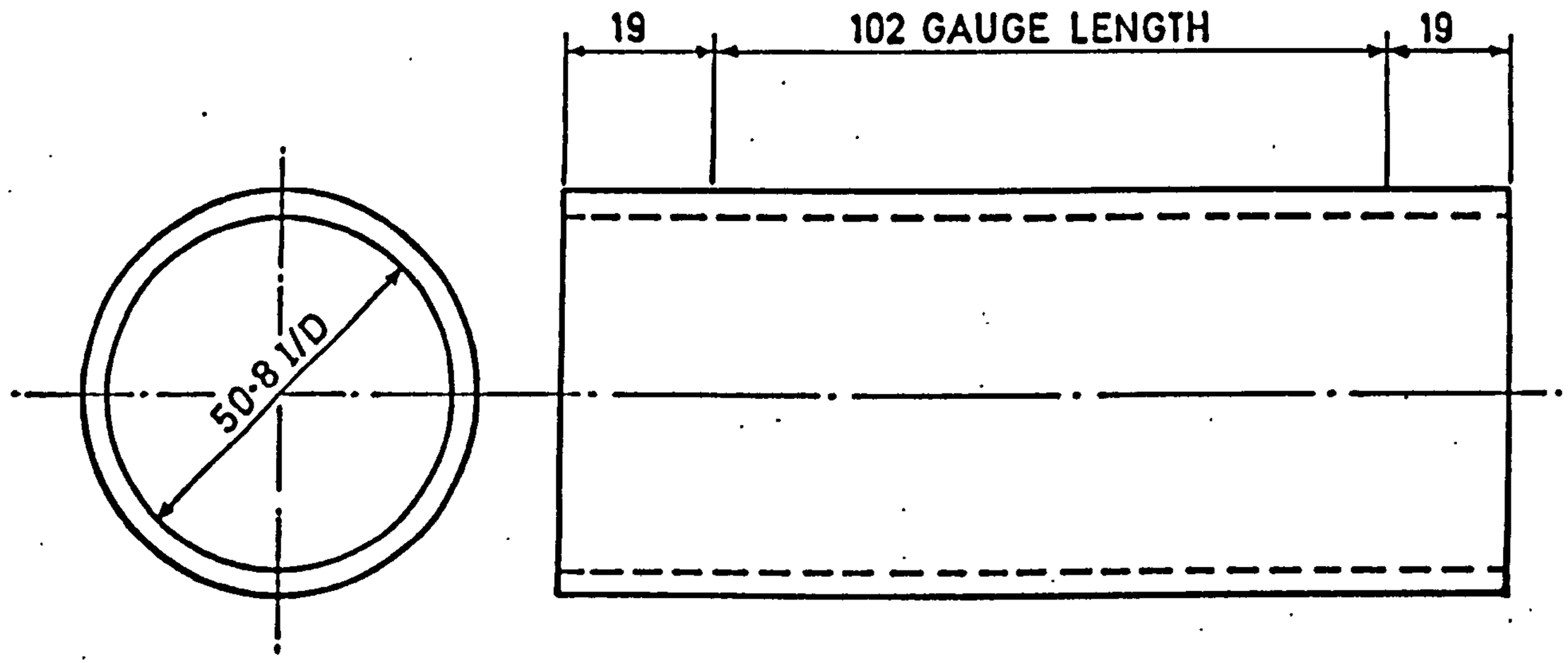

WALL THICKNESS 3mm
ALL DIMENSIONS IN MILLIMETRES

FIG. 7.2 THE BIAXIAL SPECIMEN

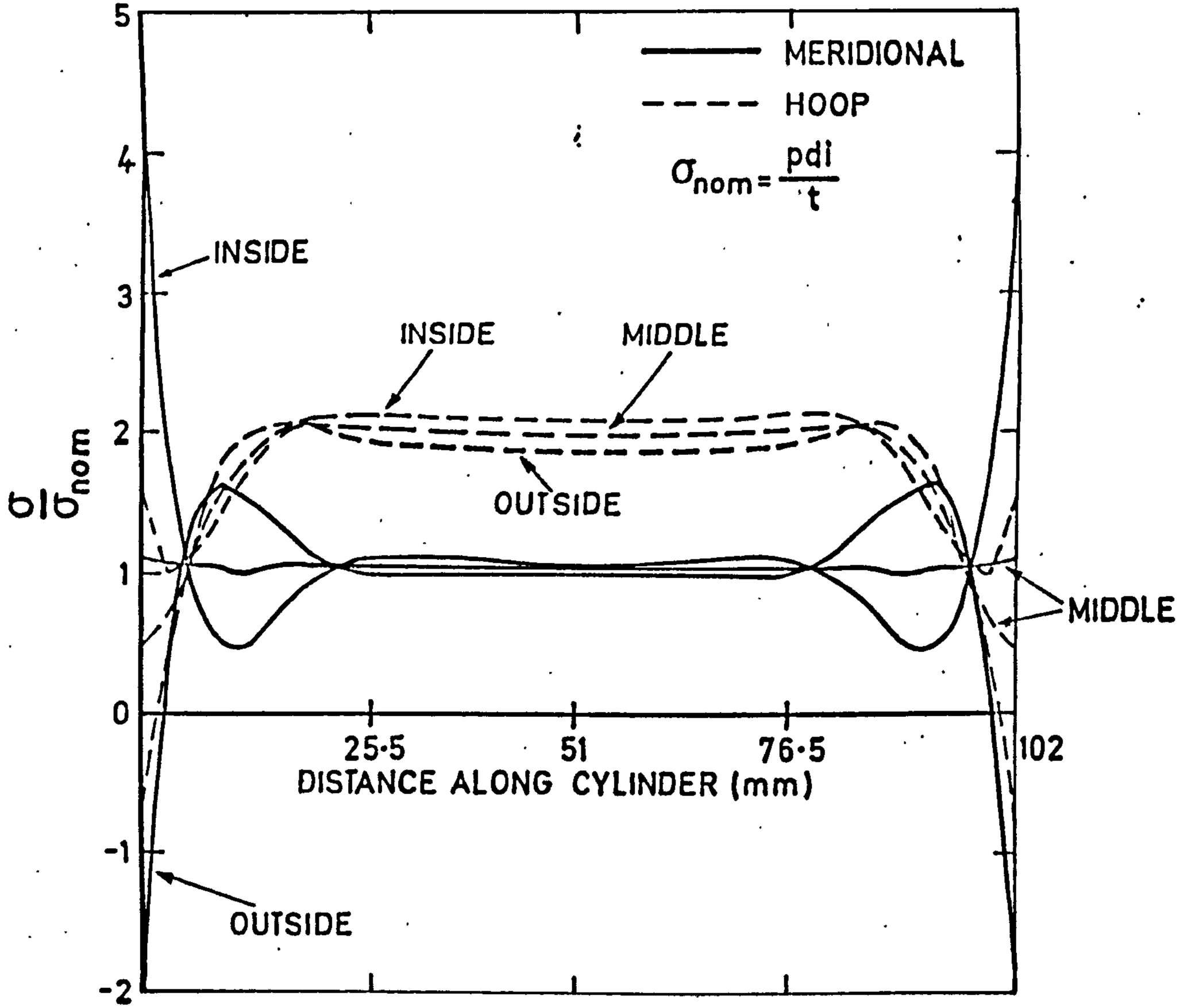

FIG. 7.3 ELASTIC STRESS DISTRIBUTION IN THE THIN CYLINDER UNDER INTERNAL PRESSURE

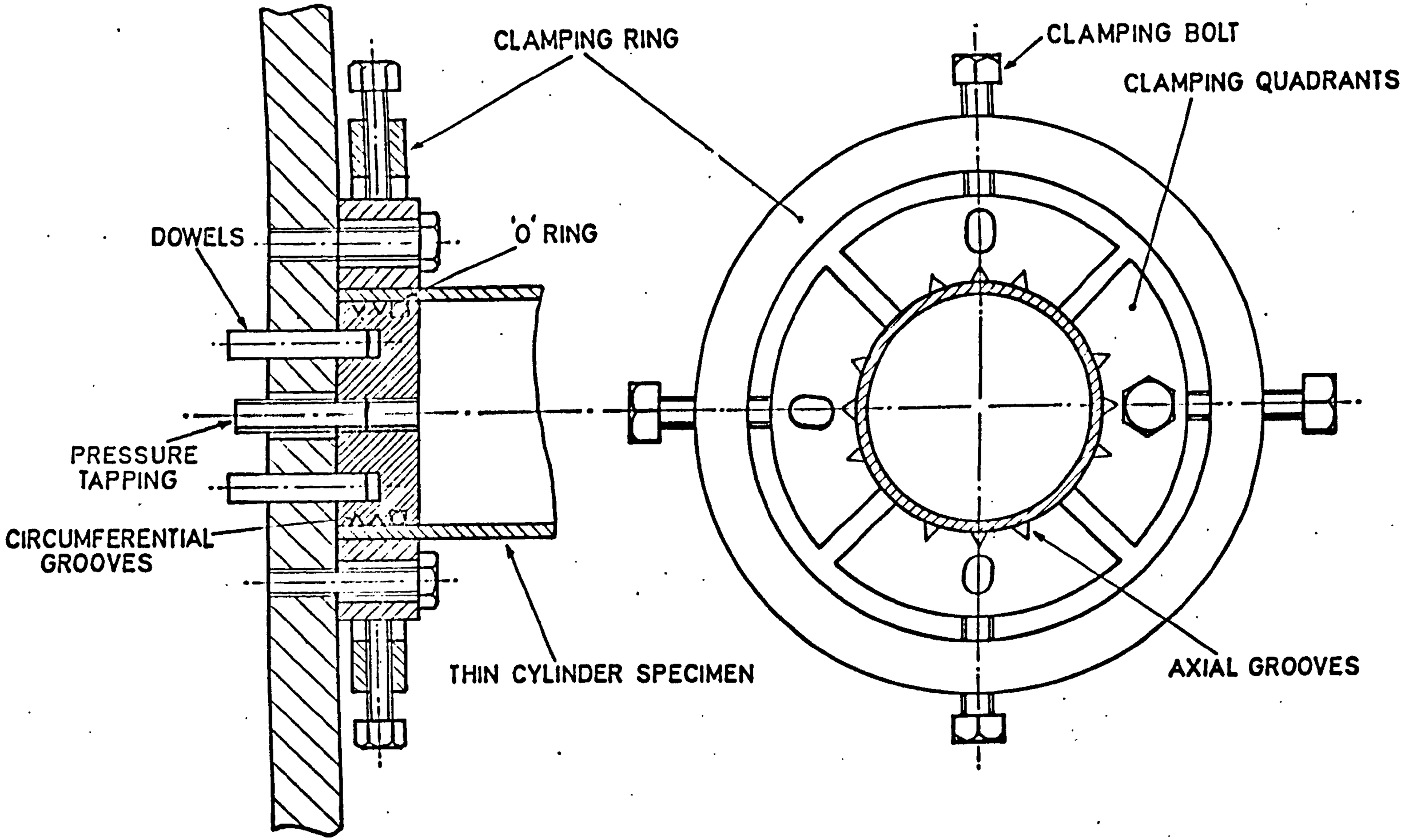

FIG. 7.4 THE CYLINDERS CLAMPING SYSTEM

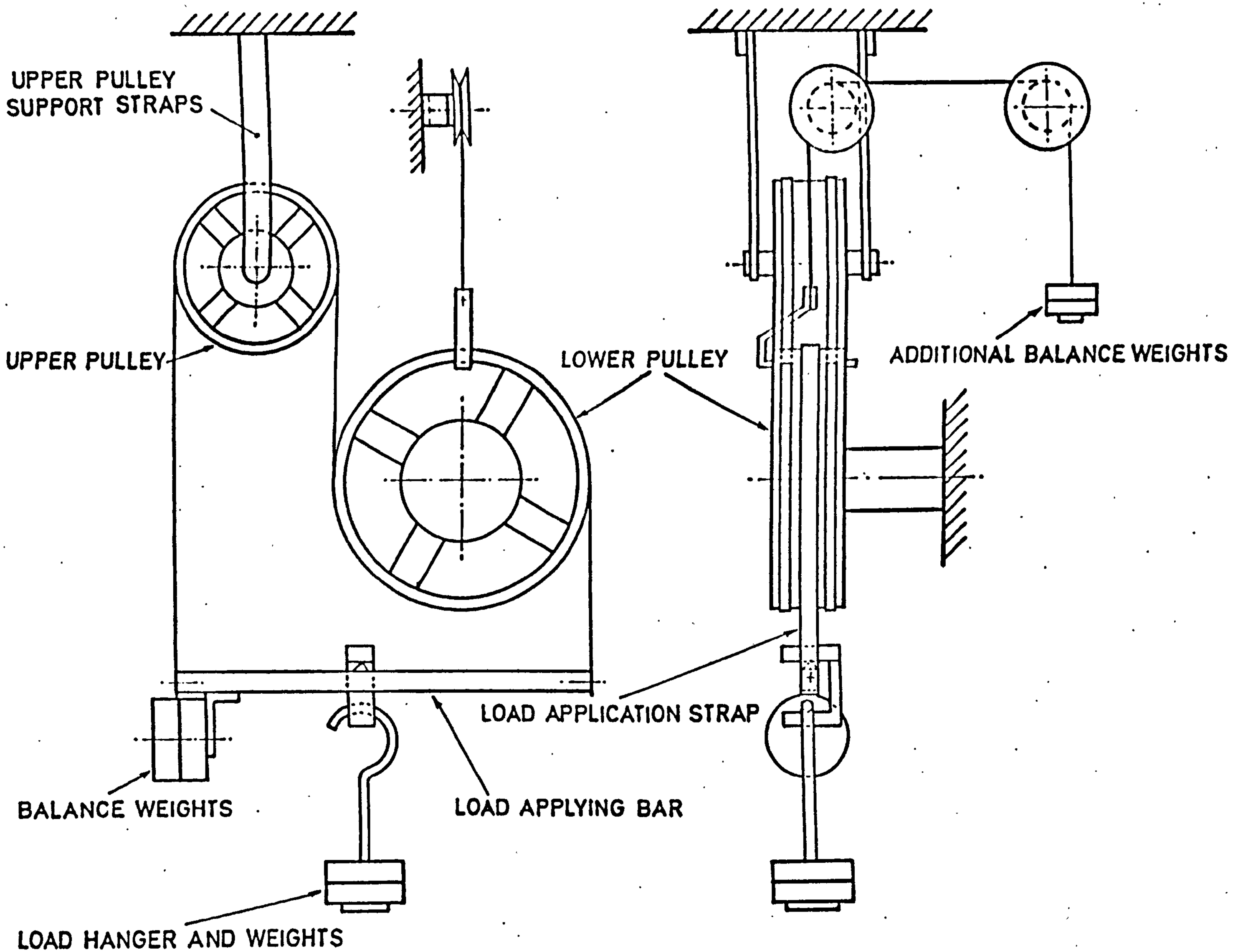

FIG. 7.5 THE TORSION SYSTEM

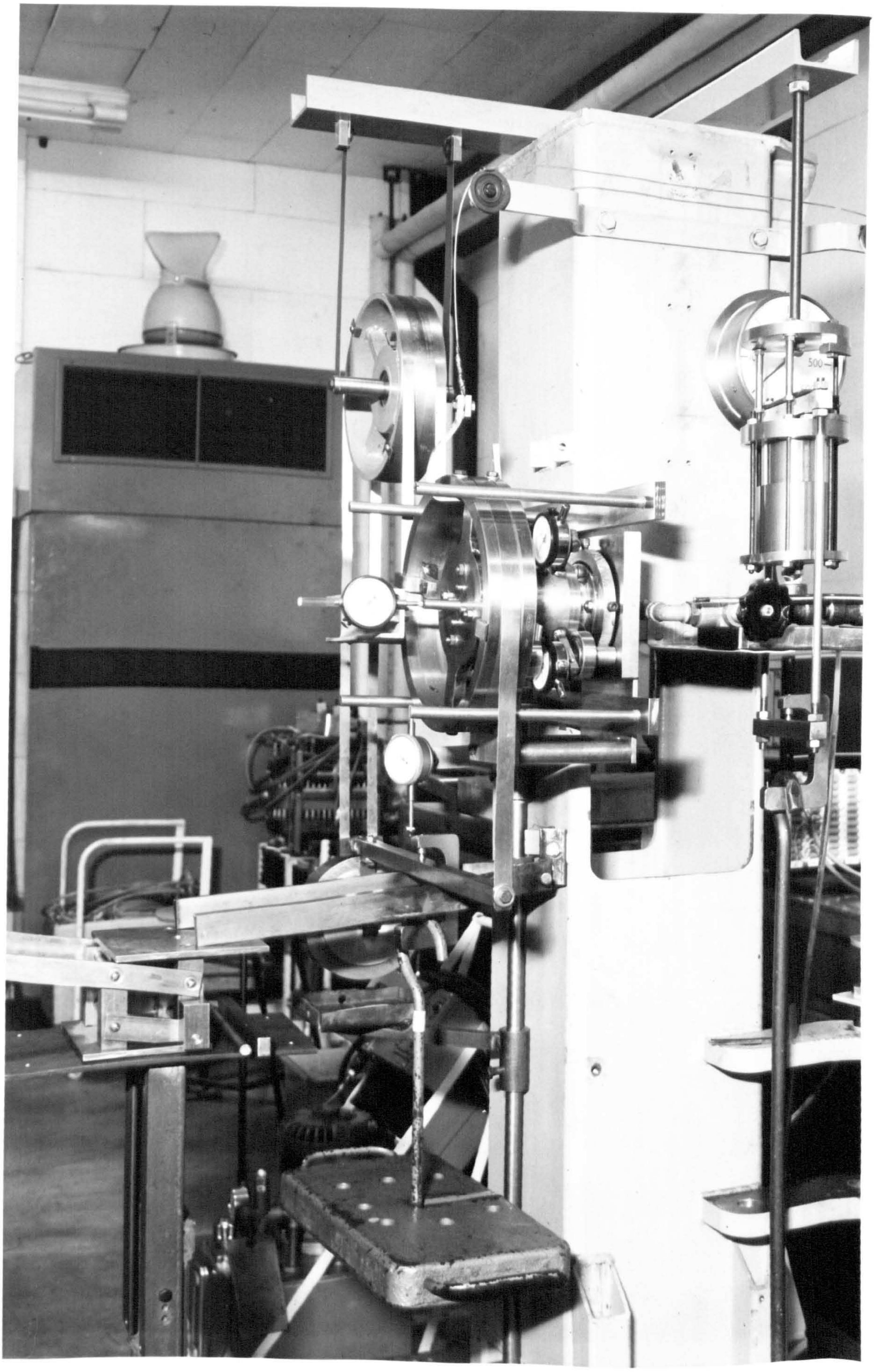

FIG. 7.6 BIAXIAL TEST RIG & SUPPORT LEVERS

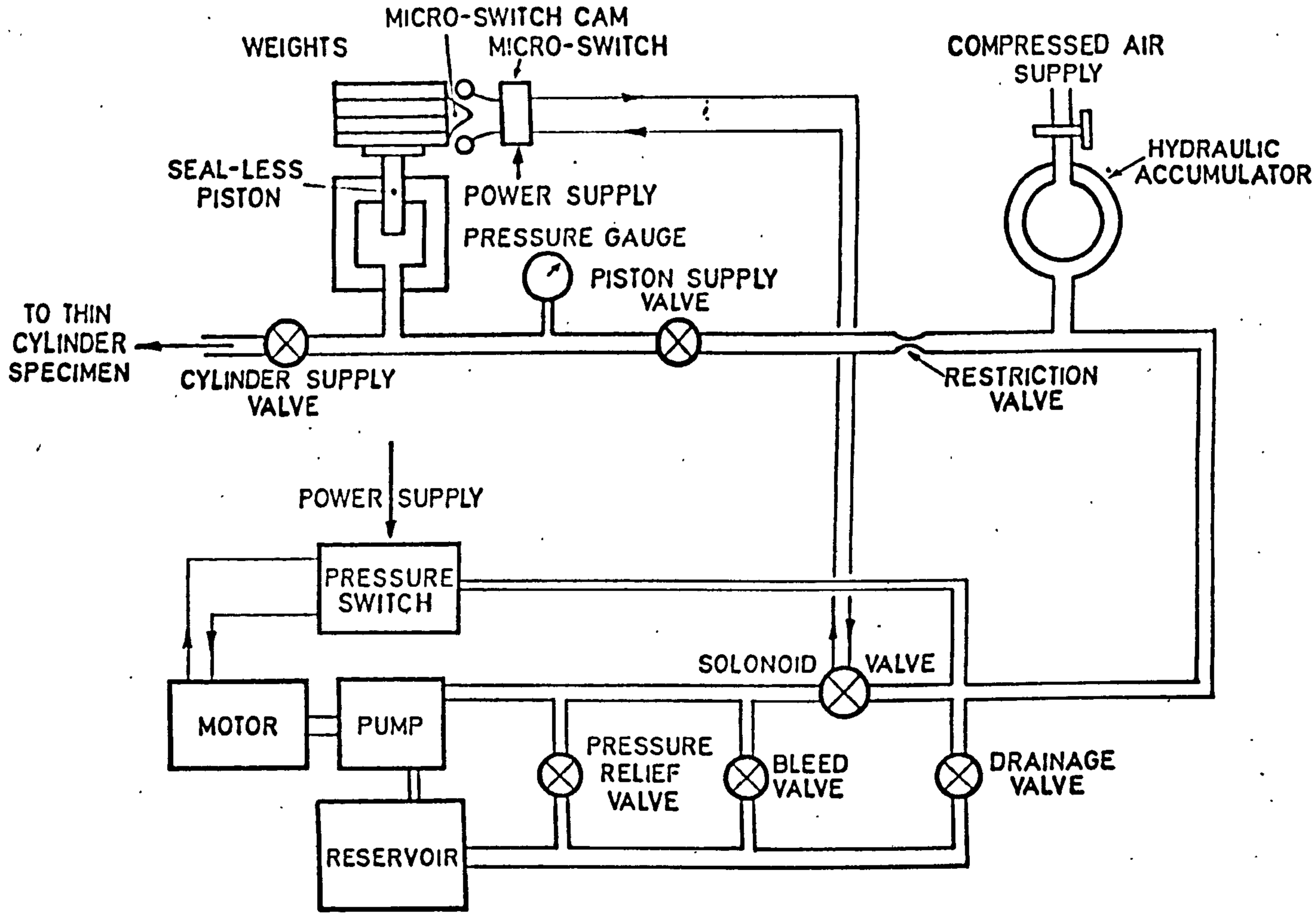

FIG. 7.7 THE PRESSURE SYSTEM

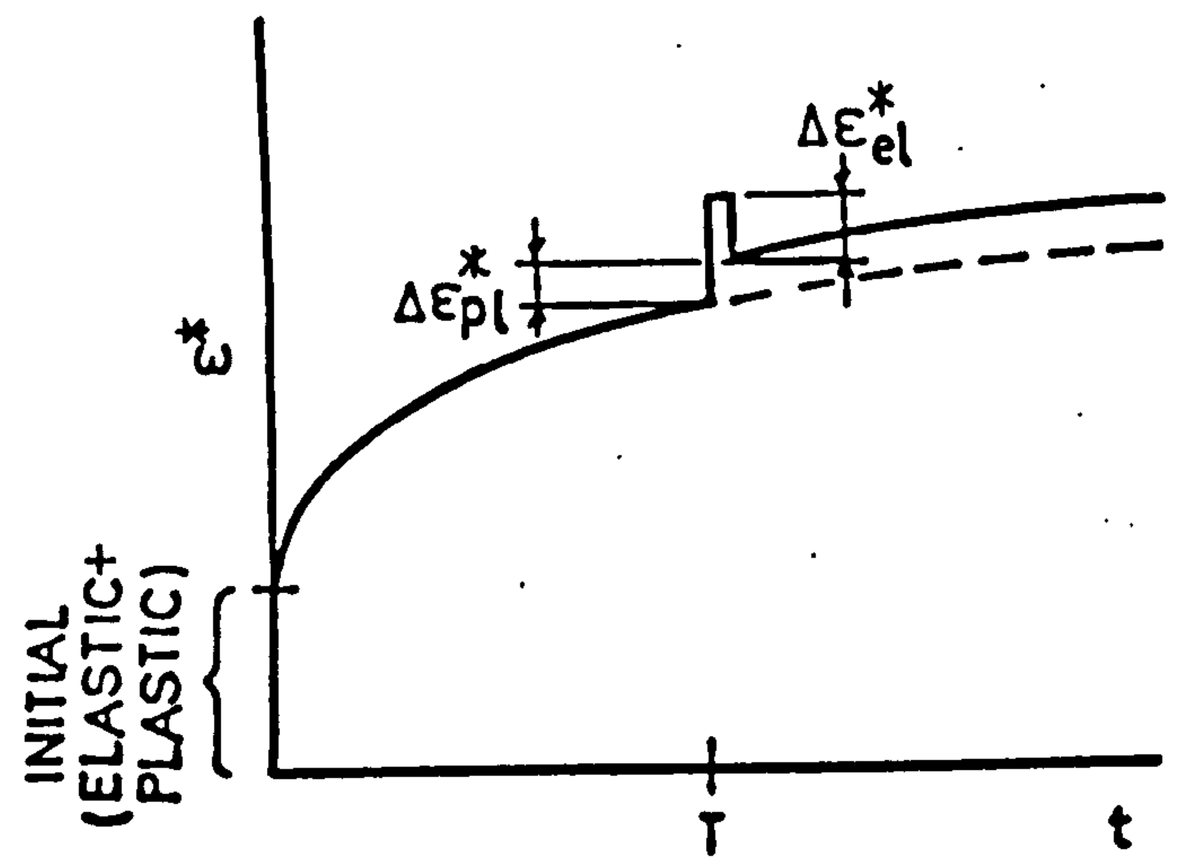

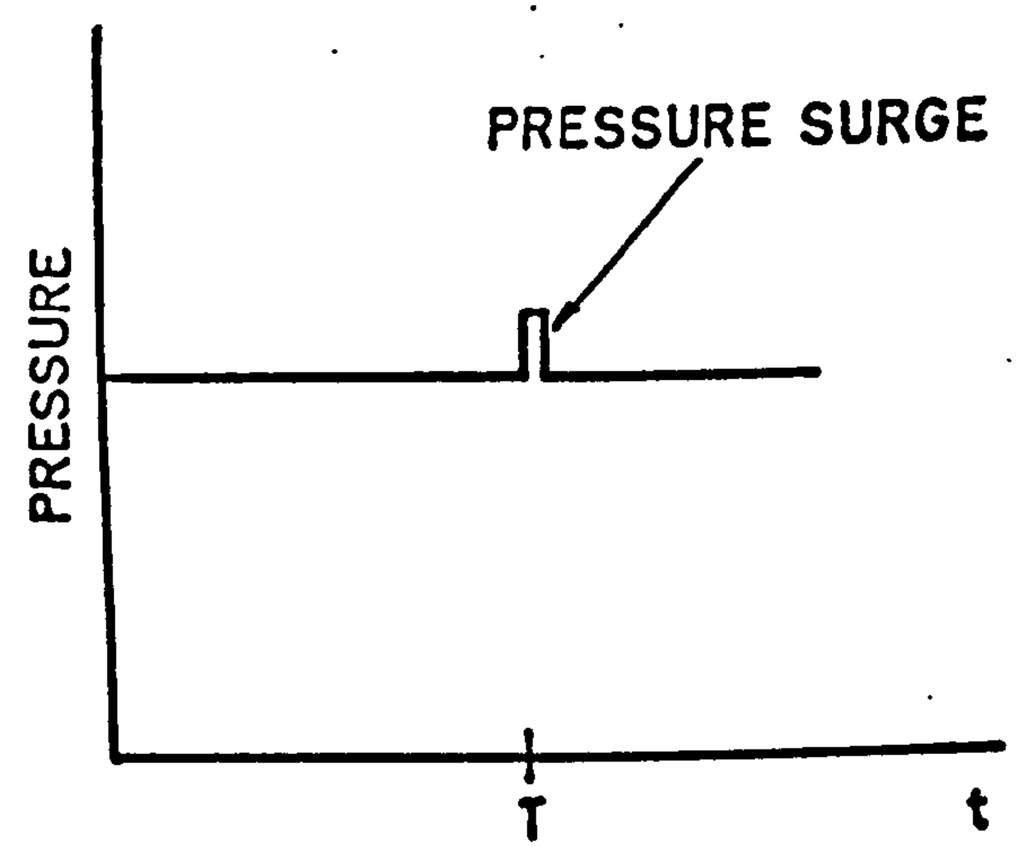

FIG. 7.8 EFFECT OF PRESSURE SURGES

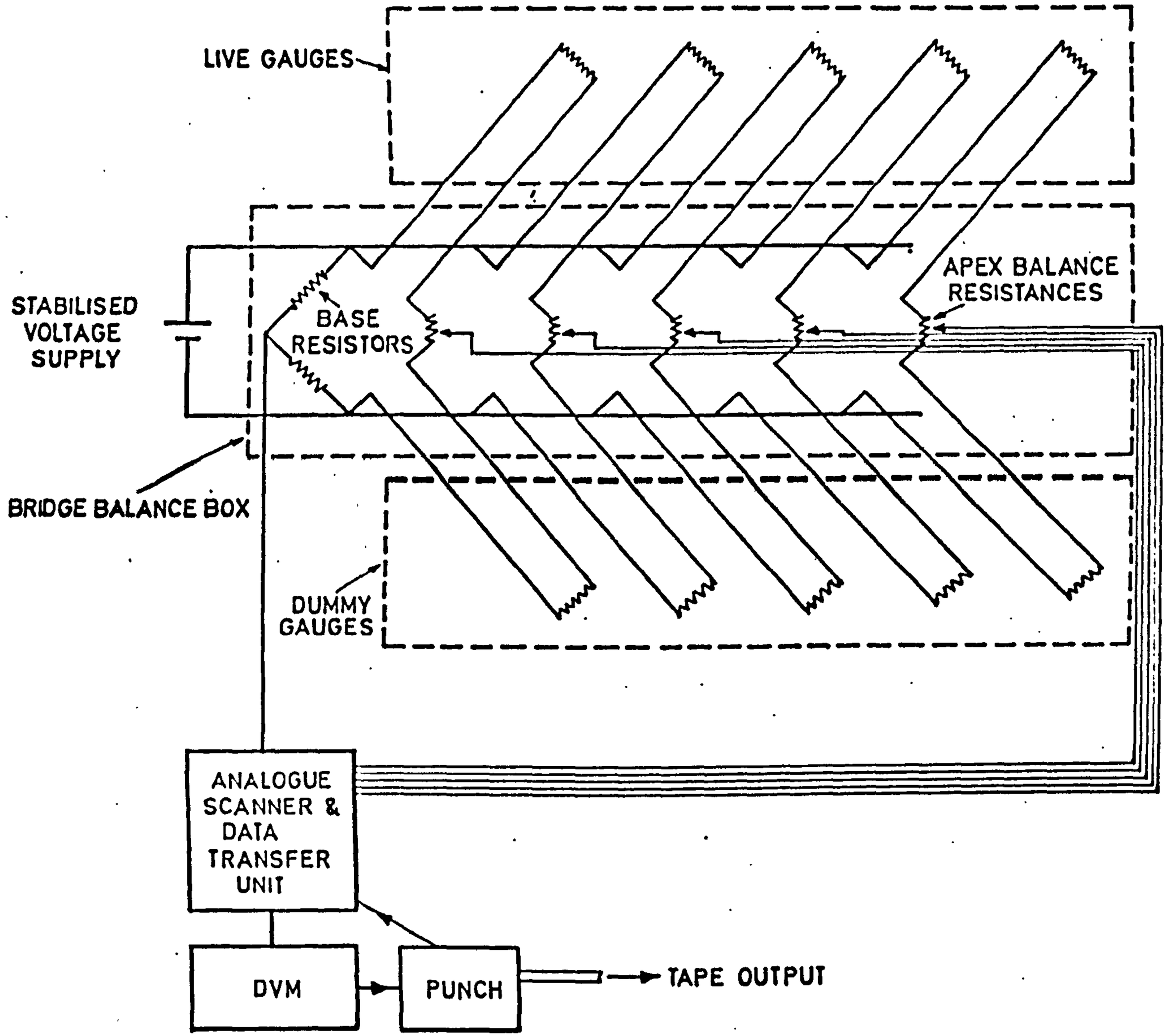

FIG.7.9 ELECTRICAL STRAIN MEASUREMENT AND RECORDING

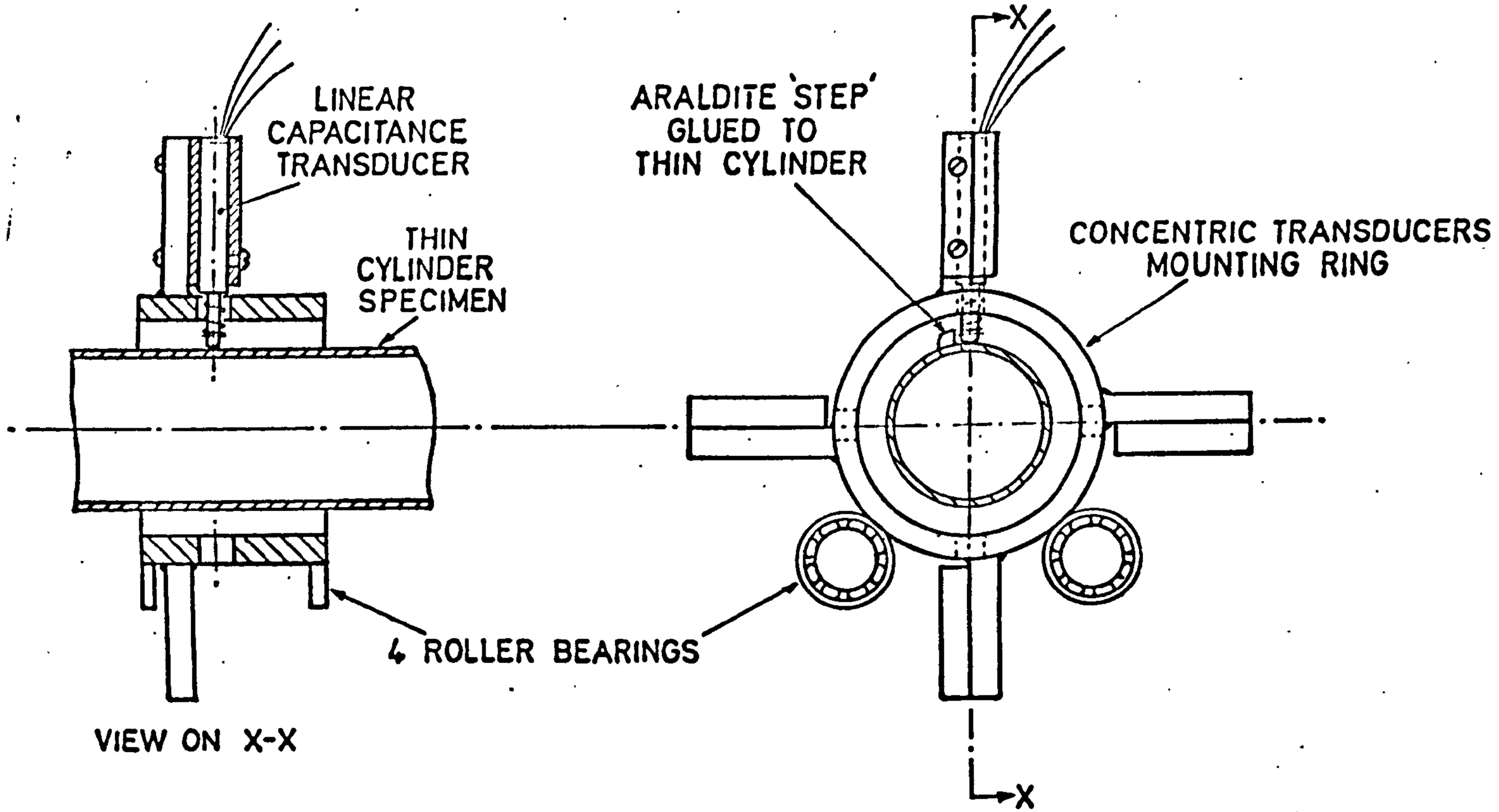

FIG. 7.10 THE RADIAL DEFORMATION MEASURING SYSTEM

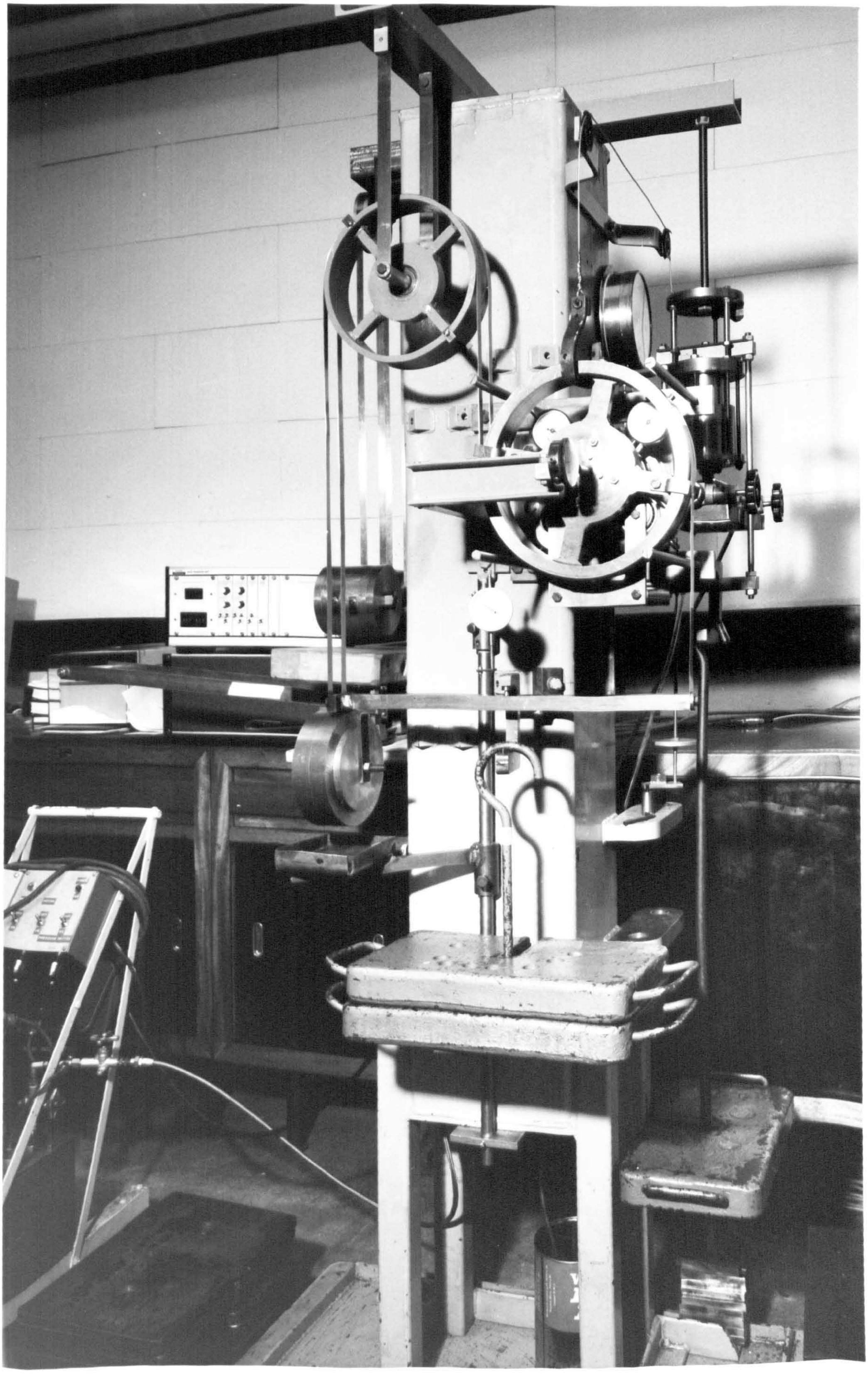

FIG. 7.11 BIAXIAL TEST RIG

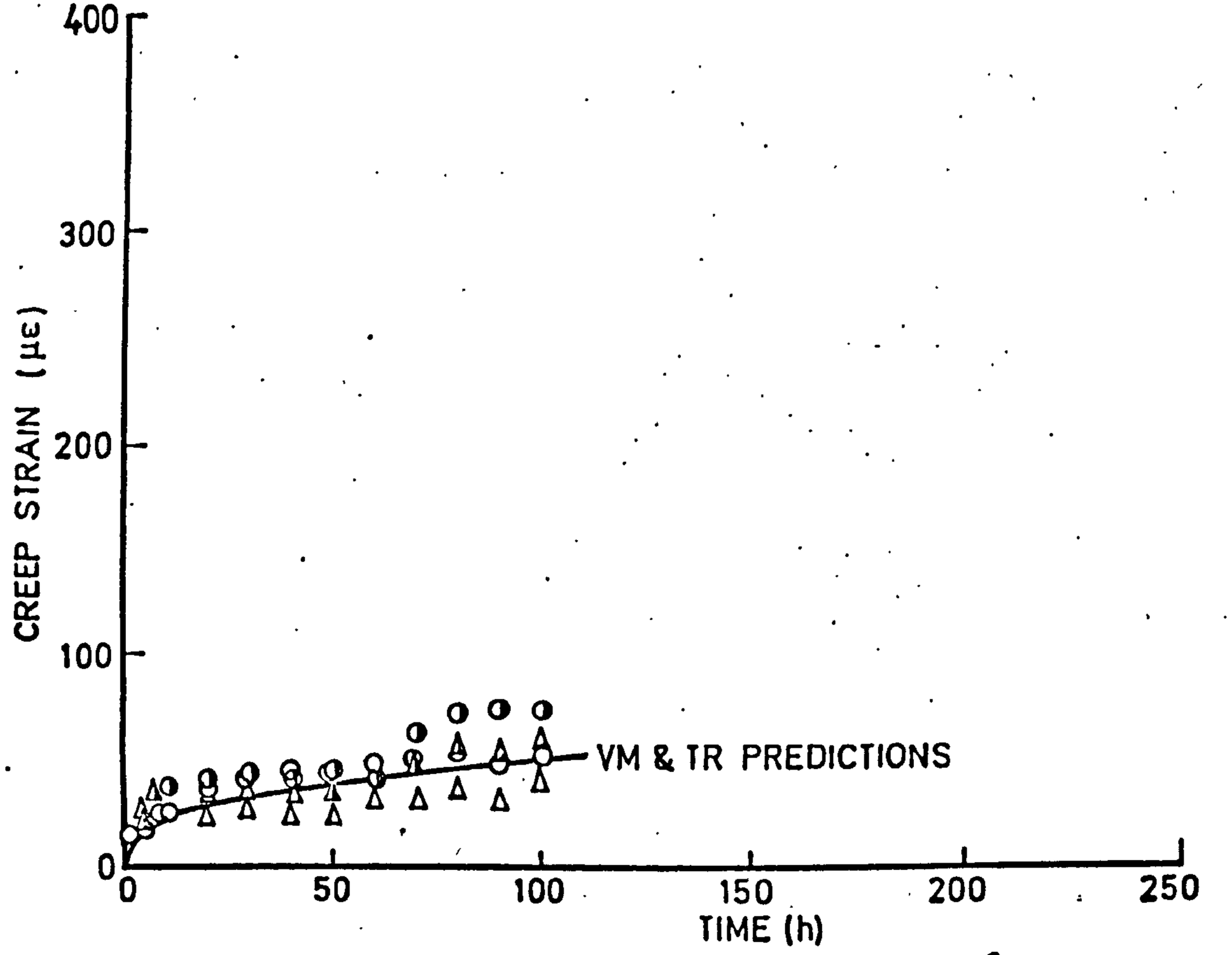

FIG. 7.12(a) BIAXIAL STRESS RATIO 1:1:0

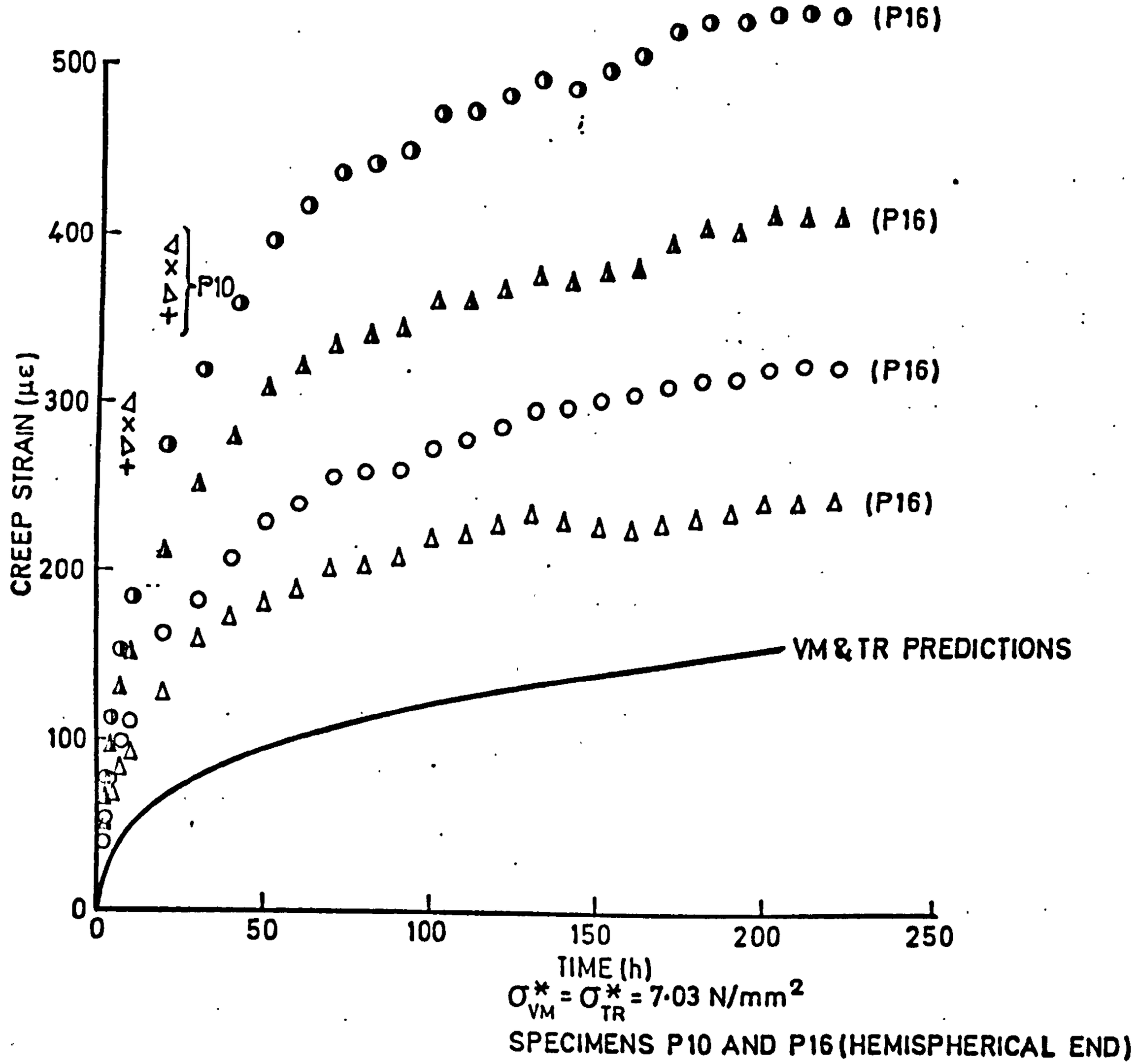

FIG. 7.12(b) BIAXIAL STRESS RATIO 1:1:0

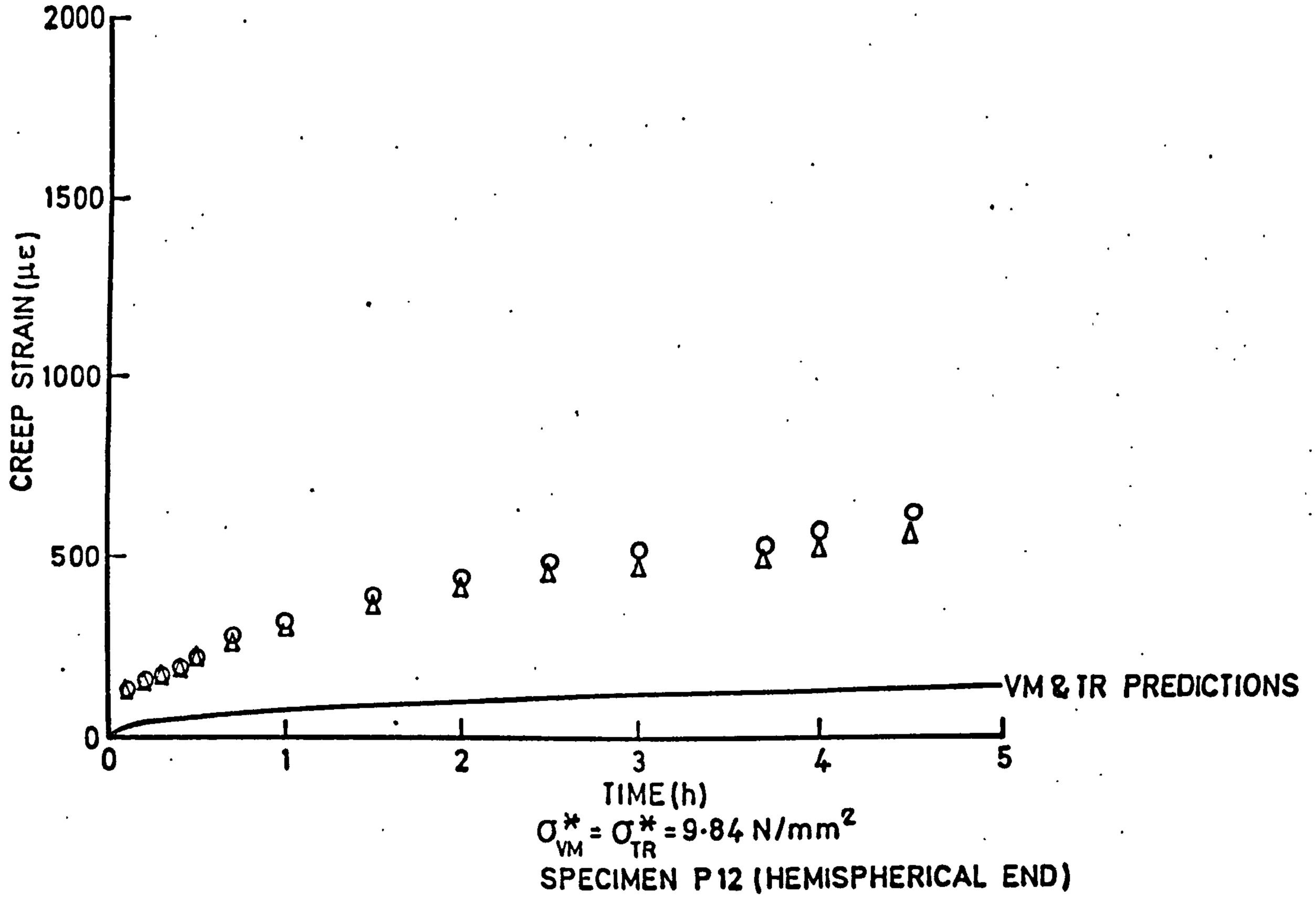

FIG. 7.12(c) BIAXIAL STRESS RATIO 1:1:0

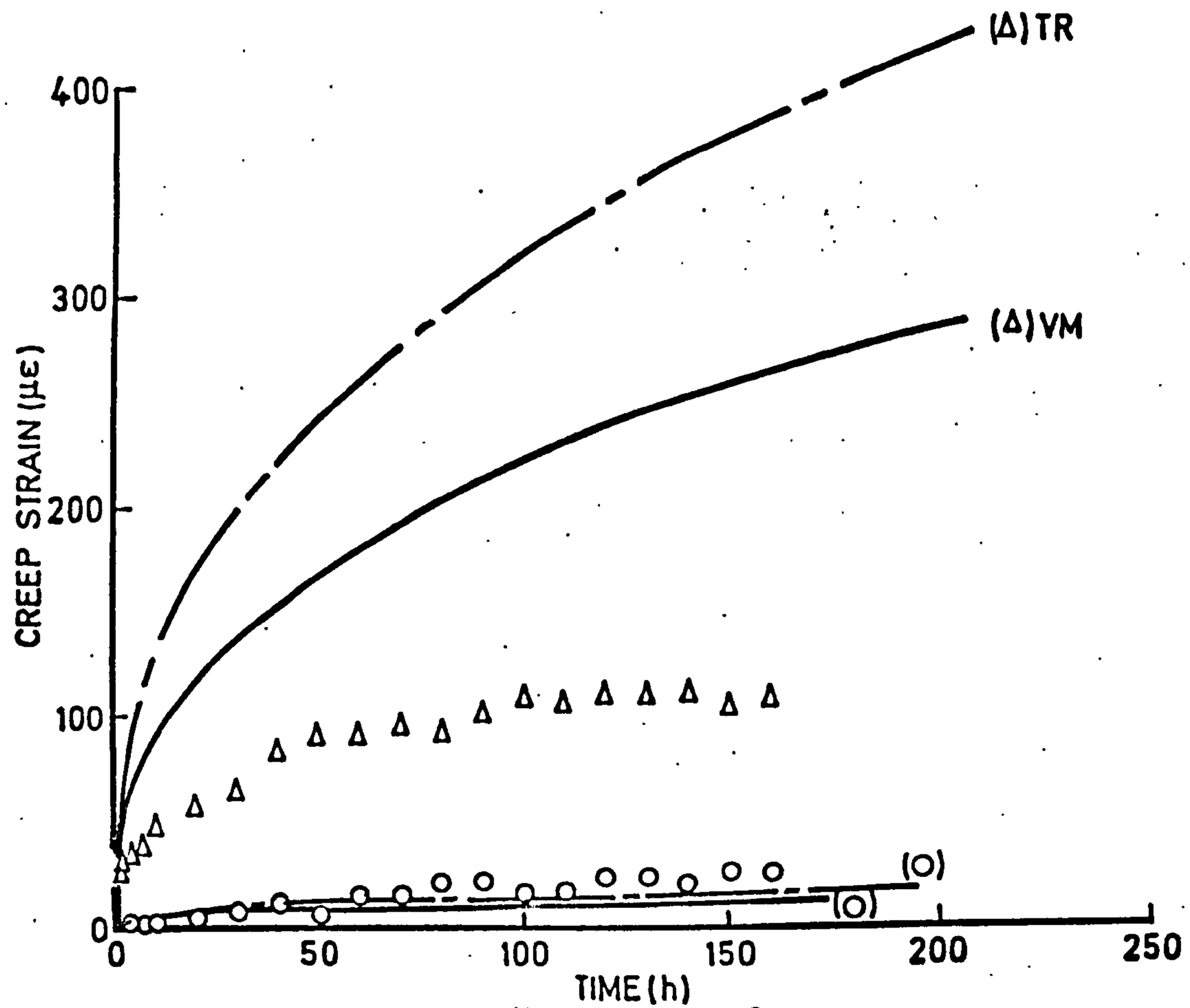

FIG. 7.12(d) BIAXIAL STRESS RATIO 1:0·47:0

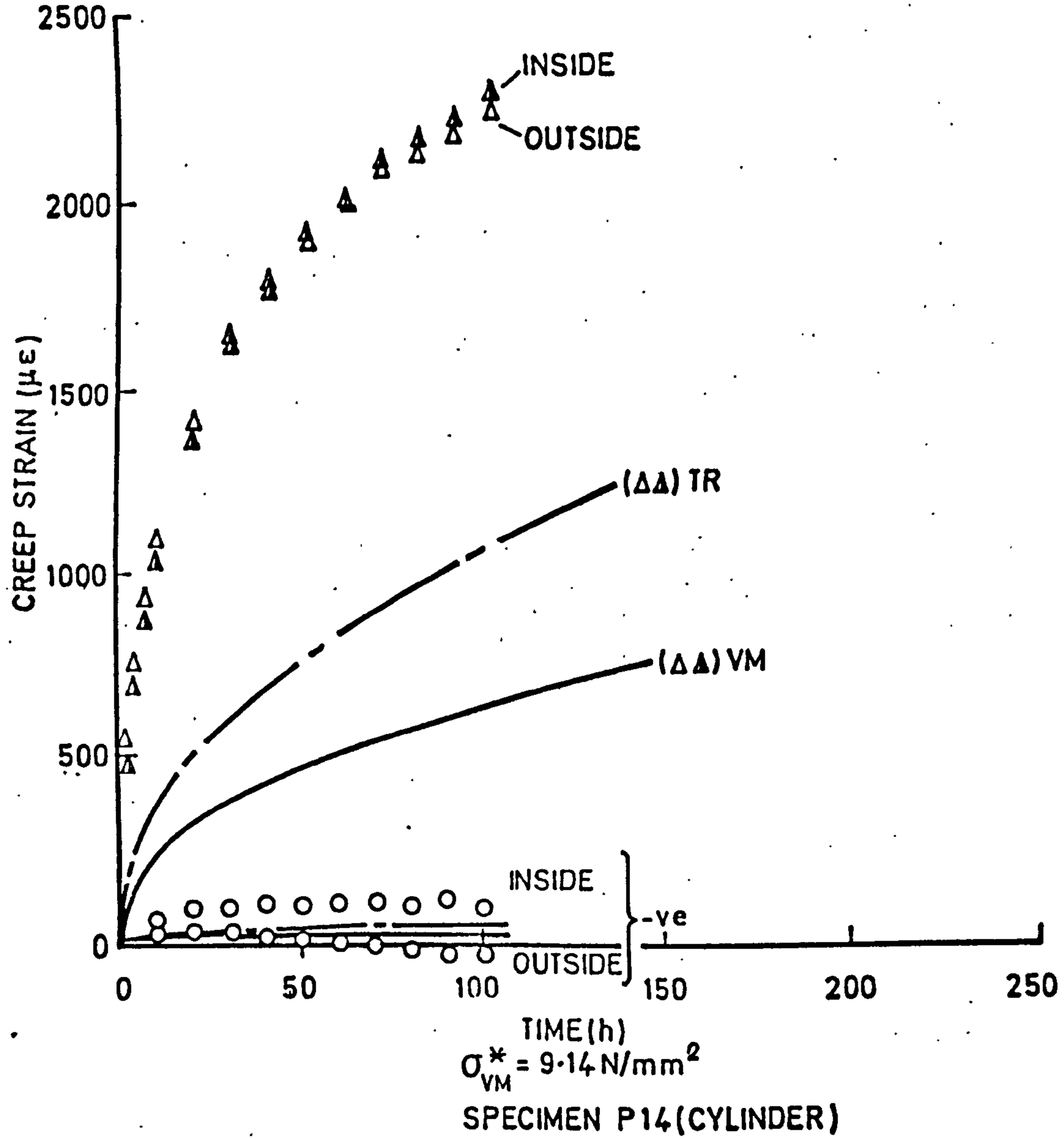

FIG.7.12(e) BIAXIAL STRESS RATIO 1:0·47:0

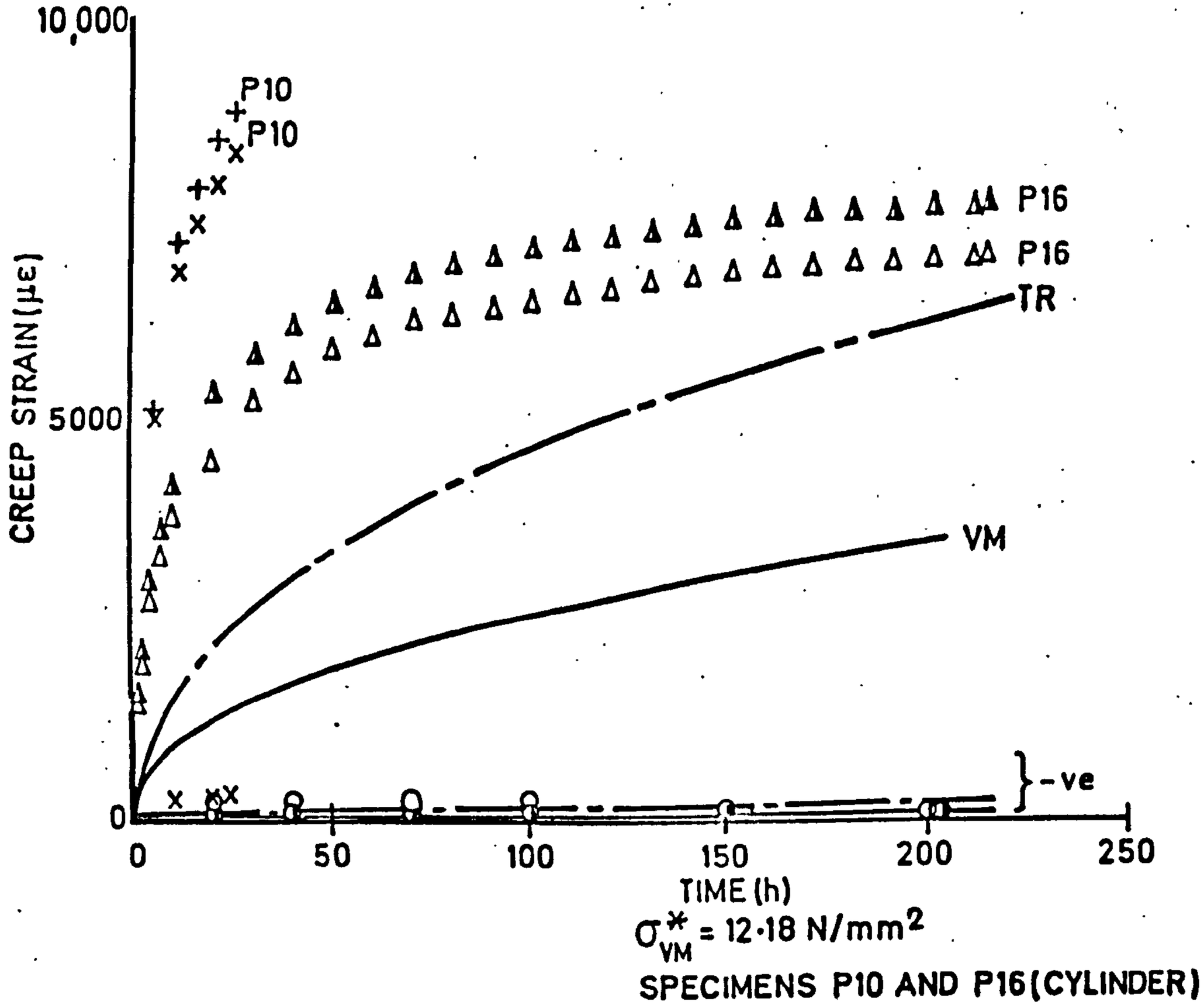

FIG.7.12(f) BIAXIAL STRESS RATIO 1:0·47:0

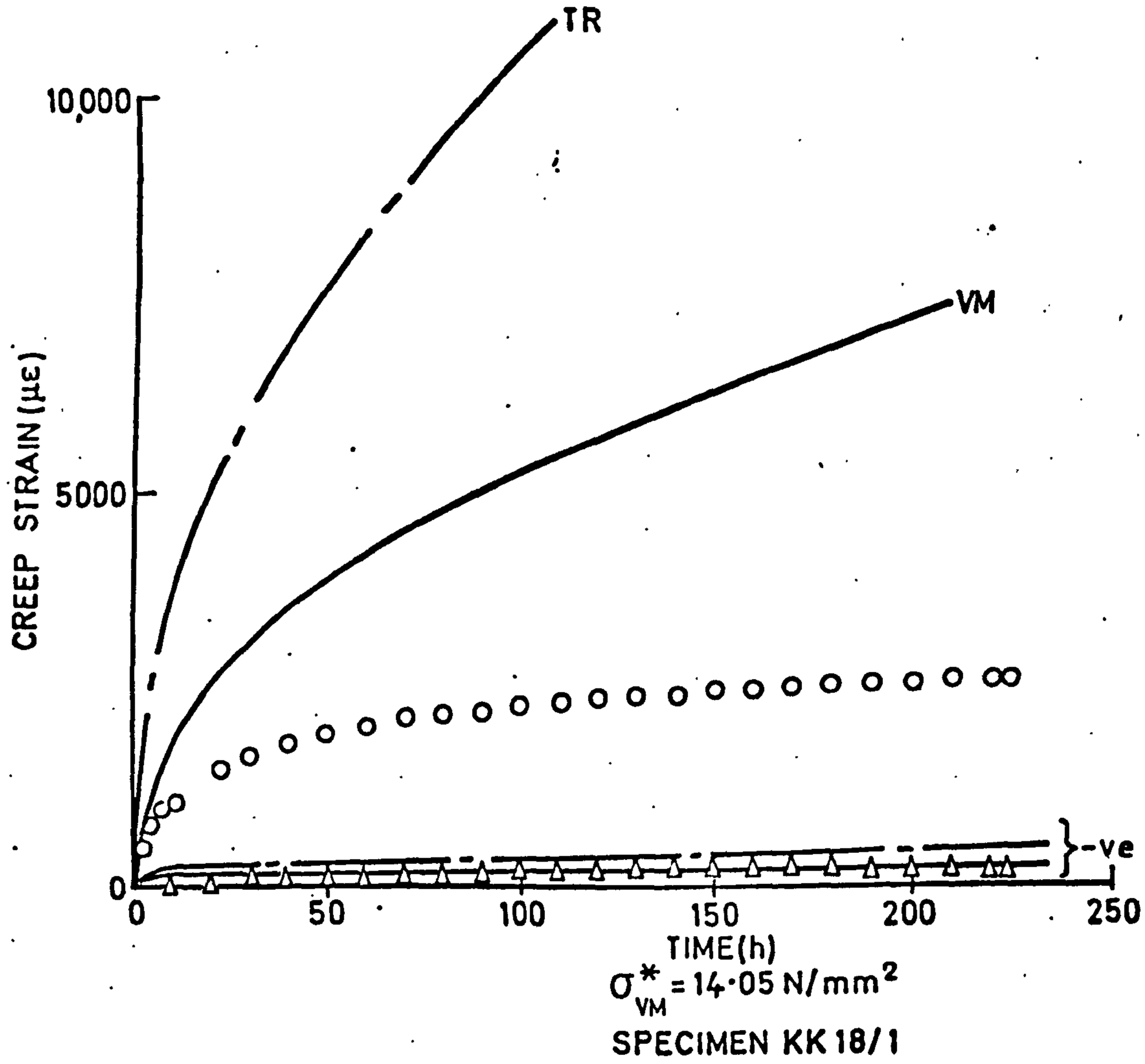

FIG.7·12(g) BIAXIAL STRESS RATIO 1:0·47:0

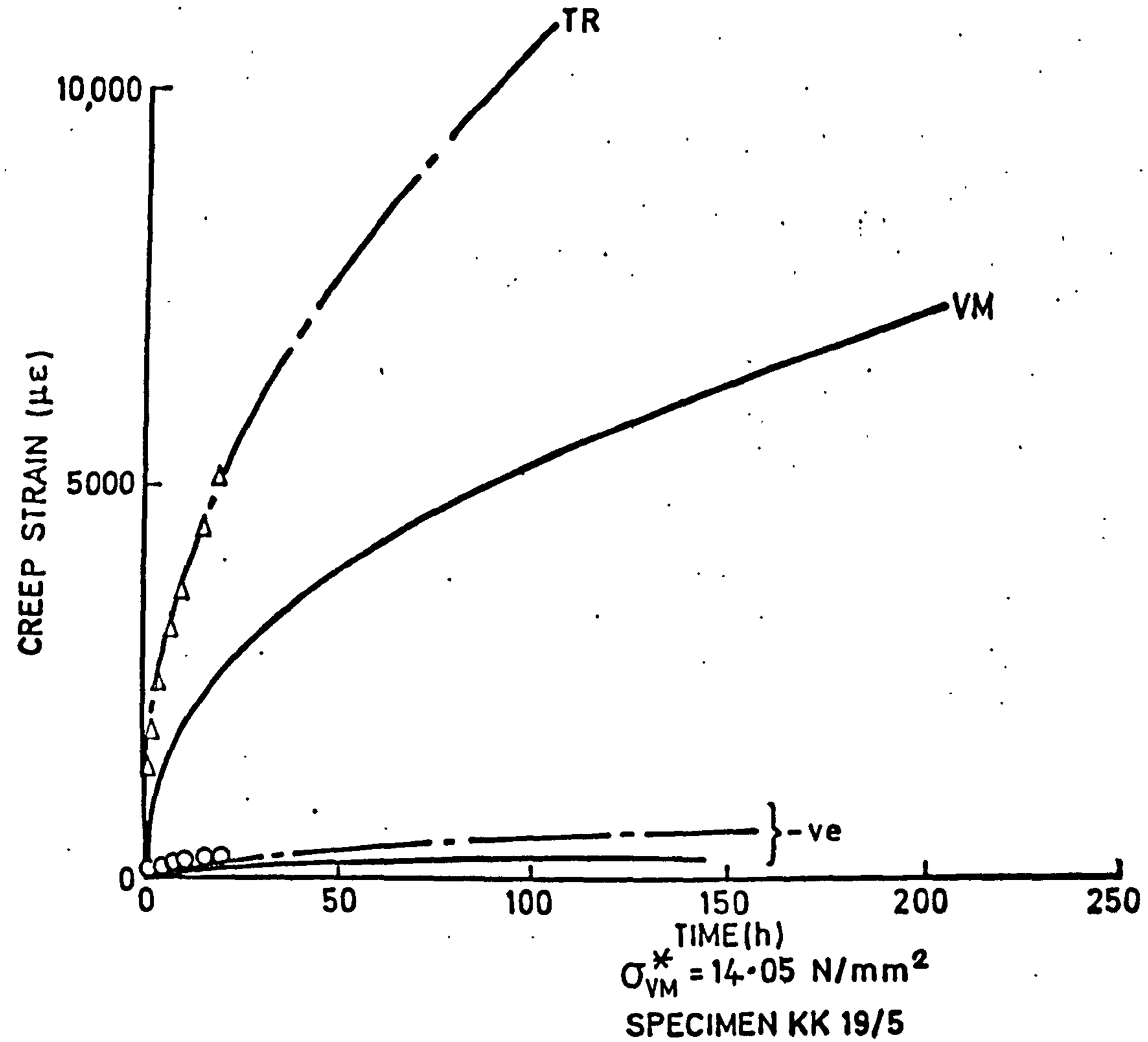

FIG. 7.12(h) BIAXIAL STRESS RATIO 1:0·47:0

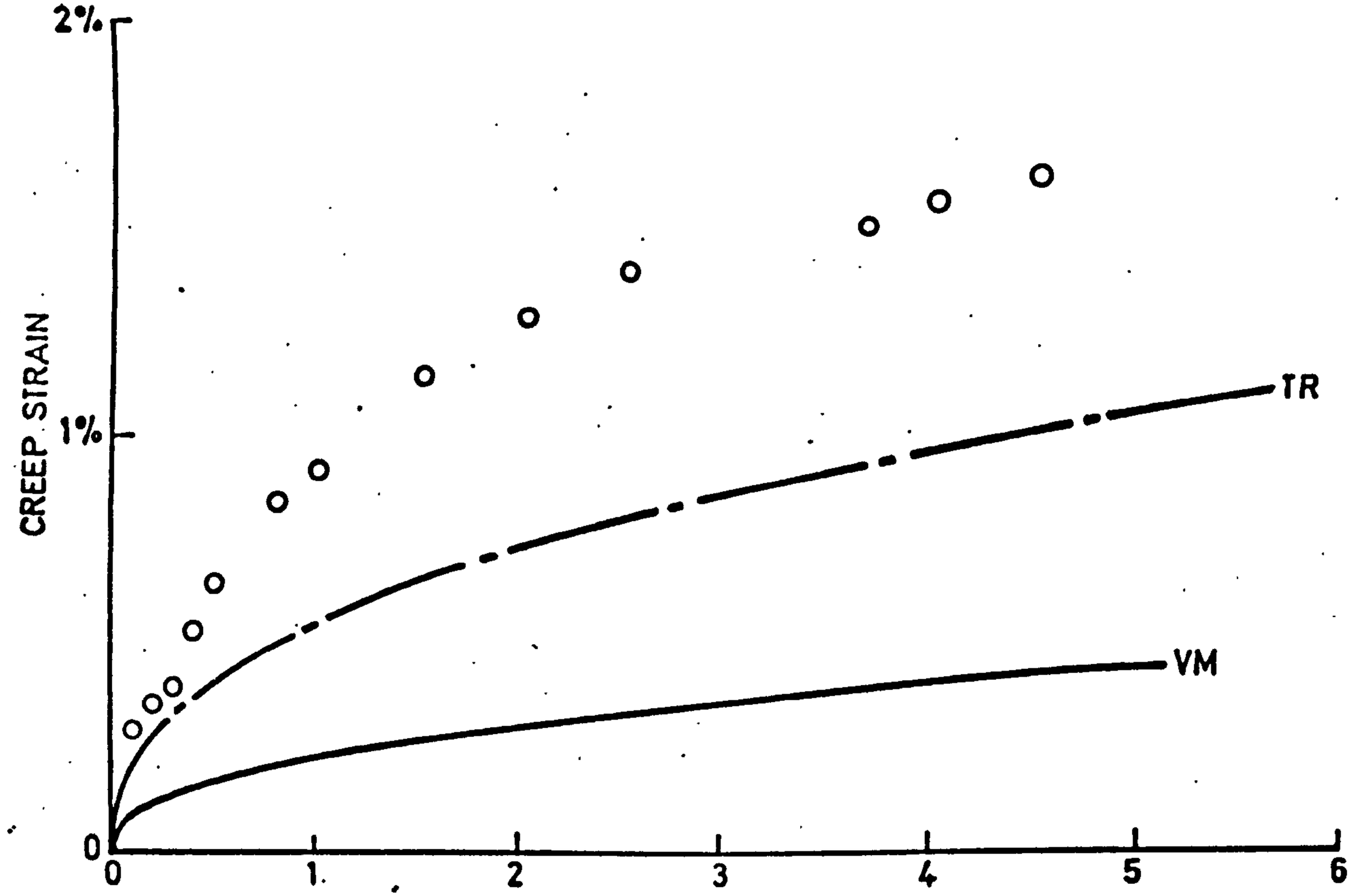

σ^{*}_{VM} = 17·05 N/mm^2

SPECIMEN P12(CYLINDER)

FIG.7·12(i) BIAXIAL STRESS RATIO 1:0·47:0

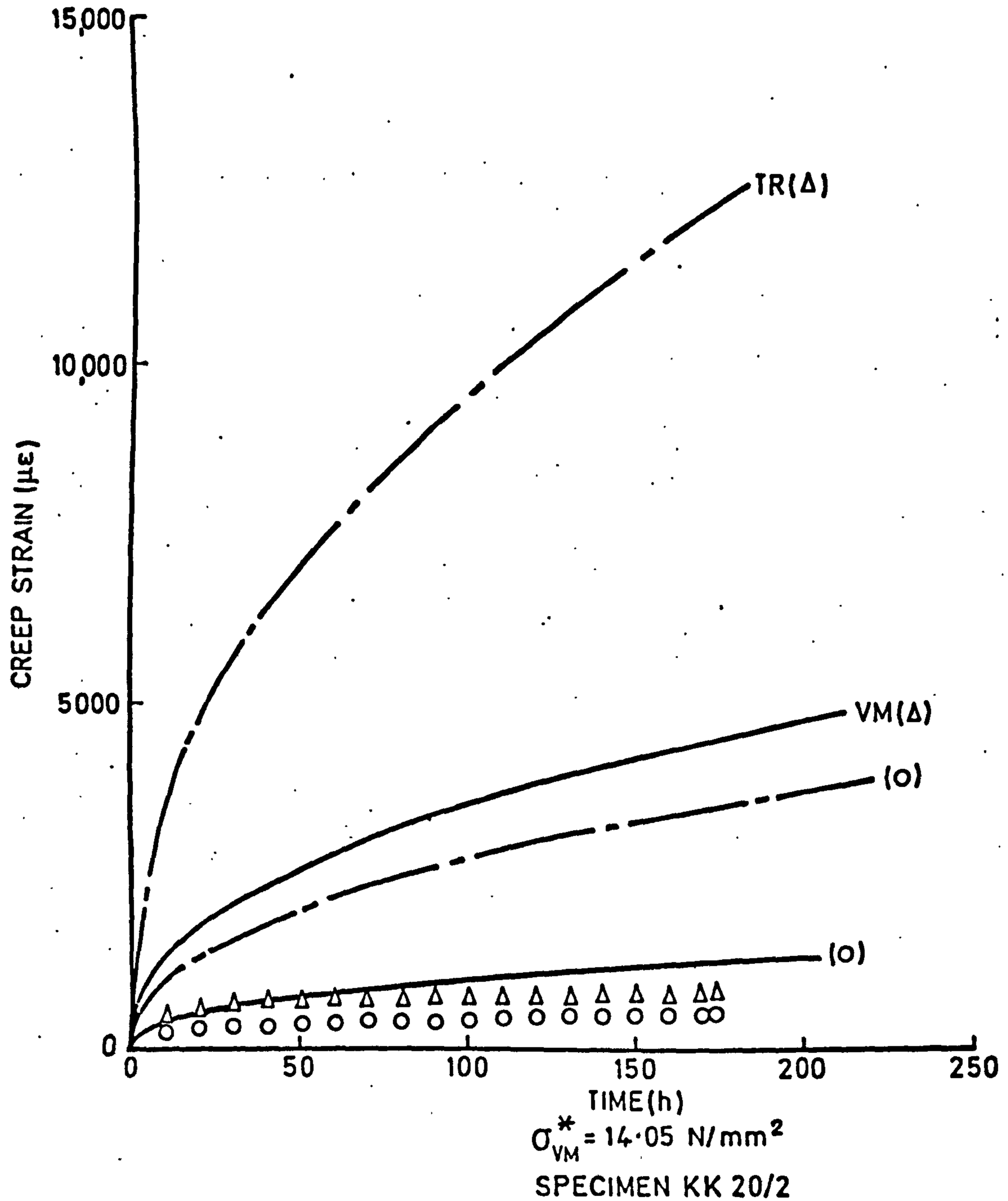

FIG. 7.12(J) BIAXIAL STRESS RATIO 1:0·25:0

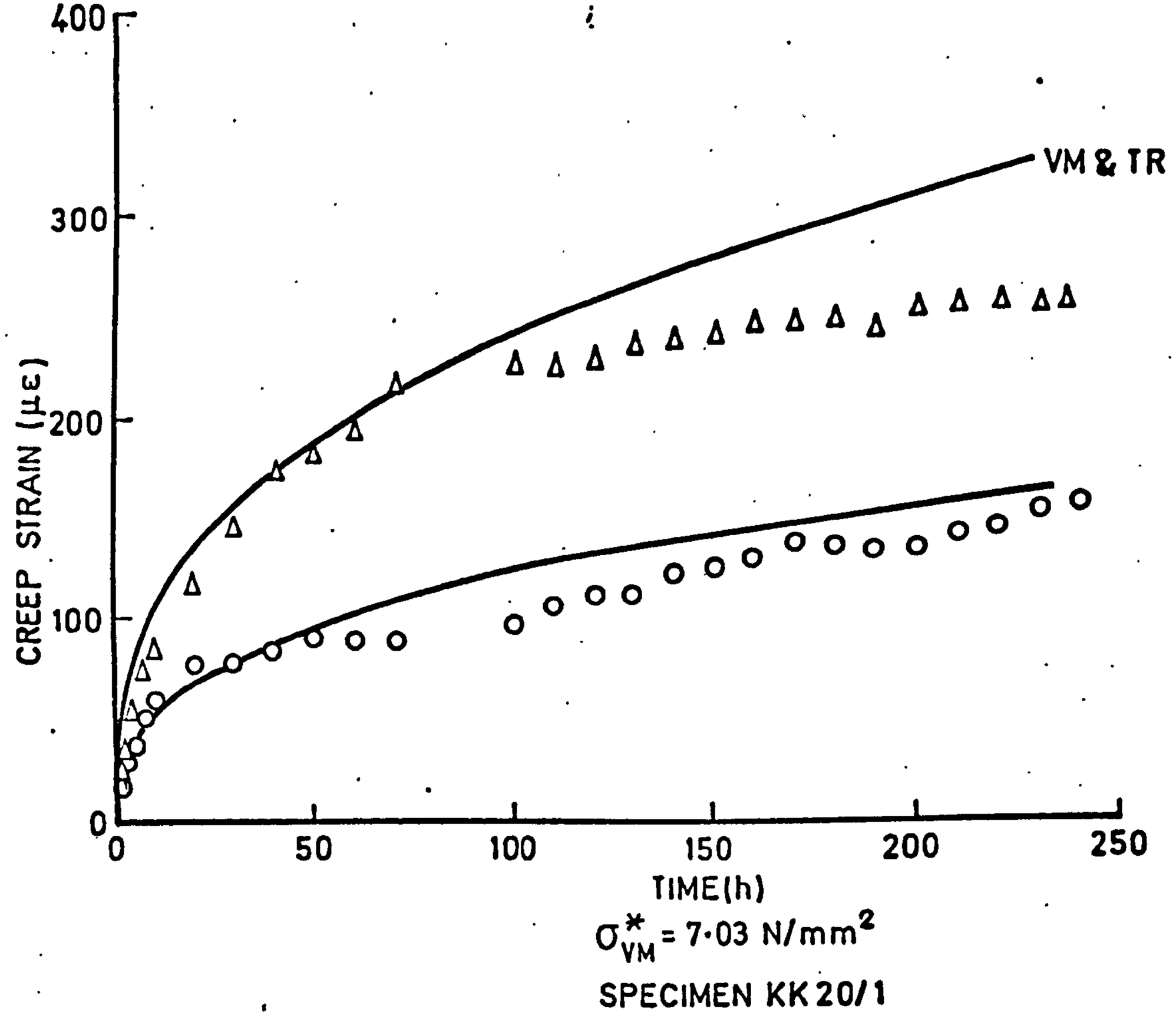

FIG.7.12(k) BIAXIAL STRESS RATIO 1:0:0

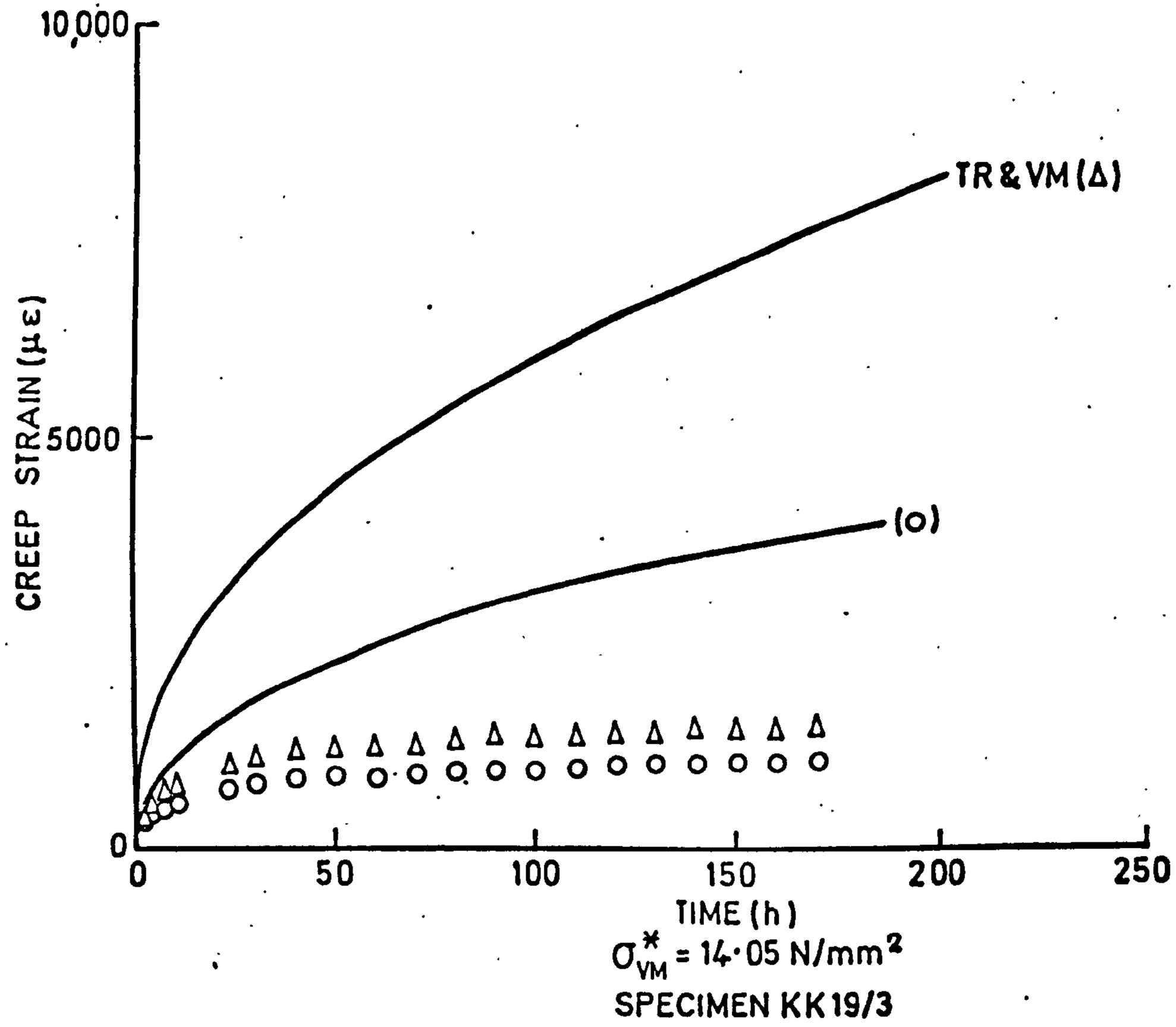

FIG. 7.12(l) BIAXIAL STRESS RATIO 1:0:0

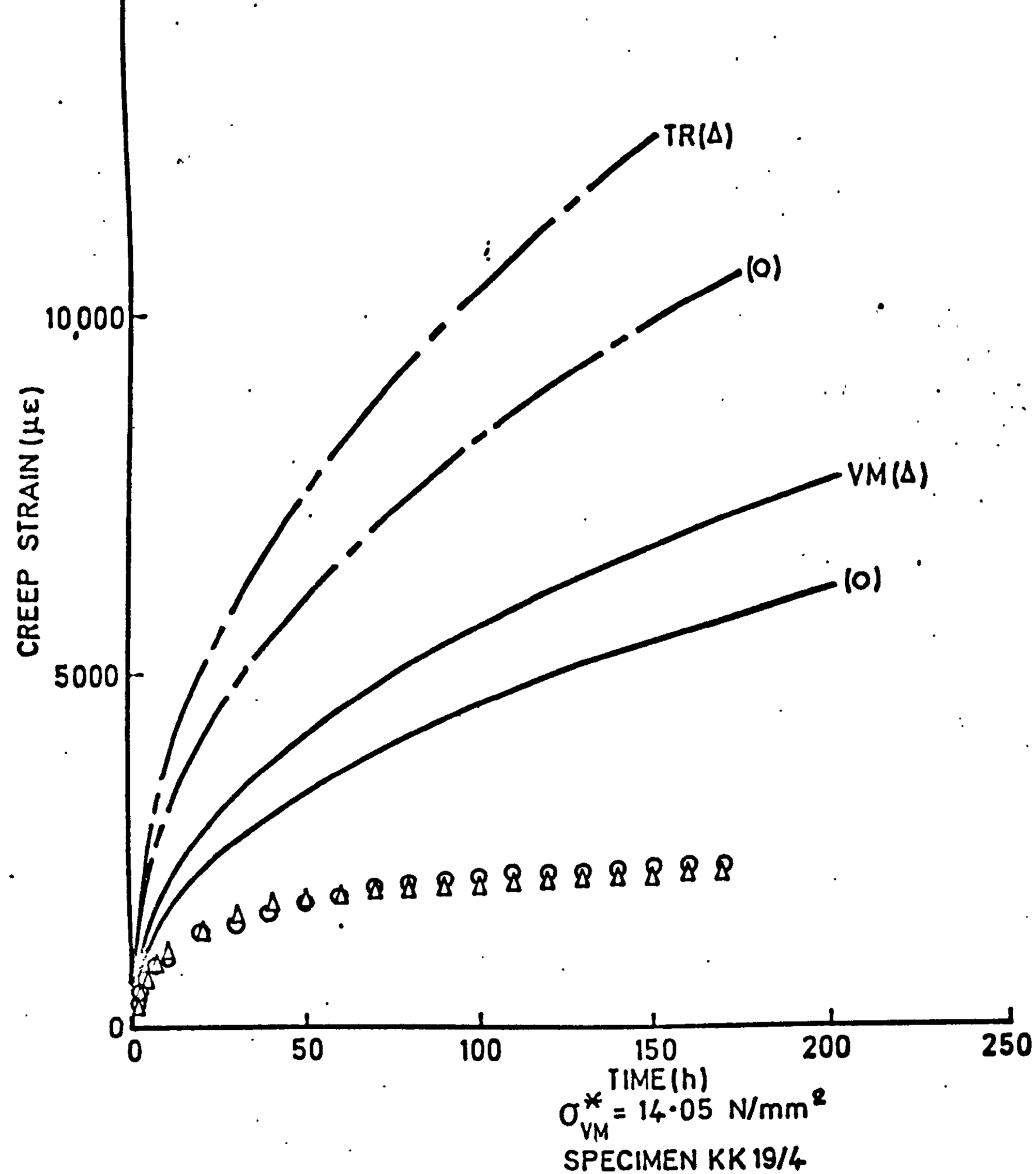

FIG. 7.12(m) BIAXIAL STRESS RATIO 1:0: -1/2

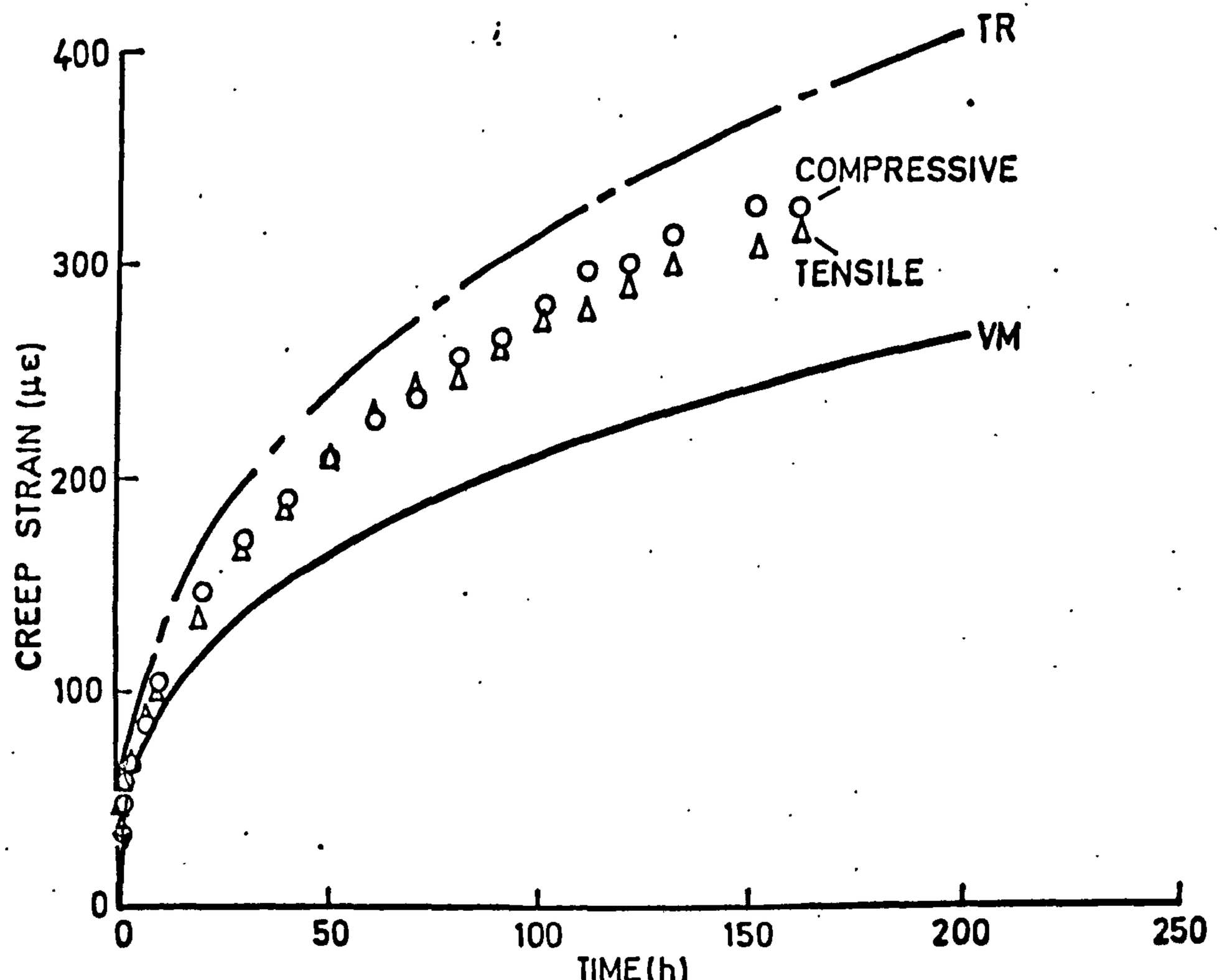

FIG. 7.12(n) BIAXIAL STRESS RATIO 1:0:-1

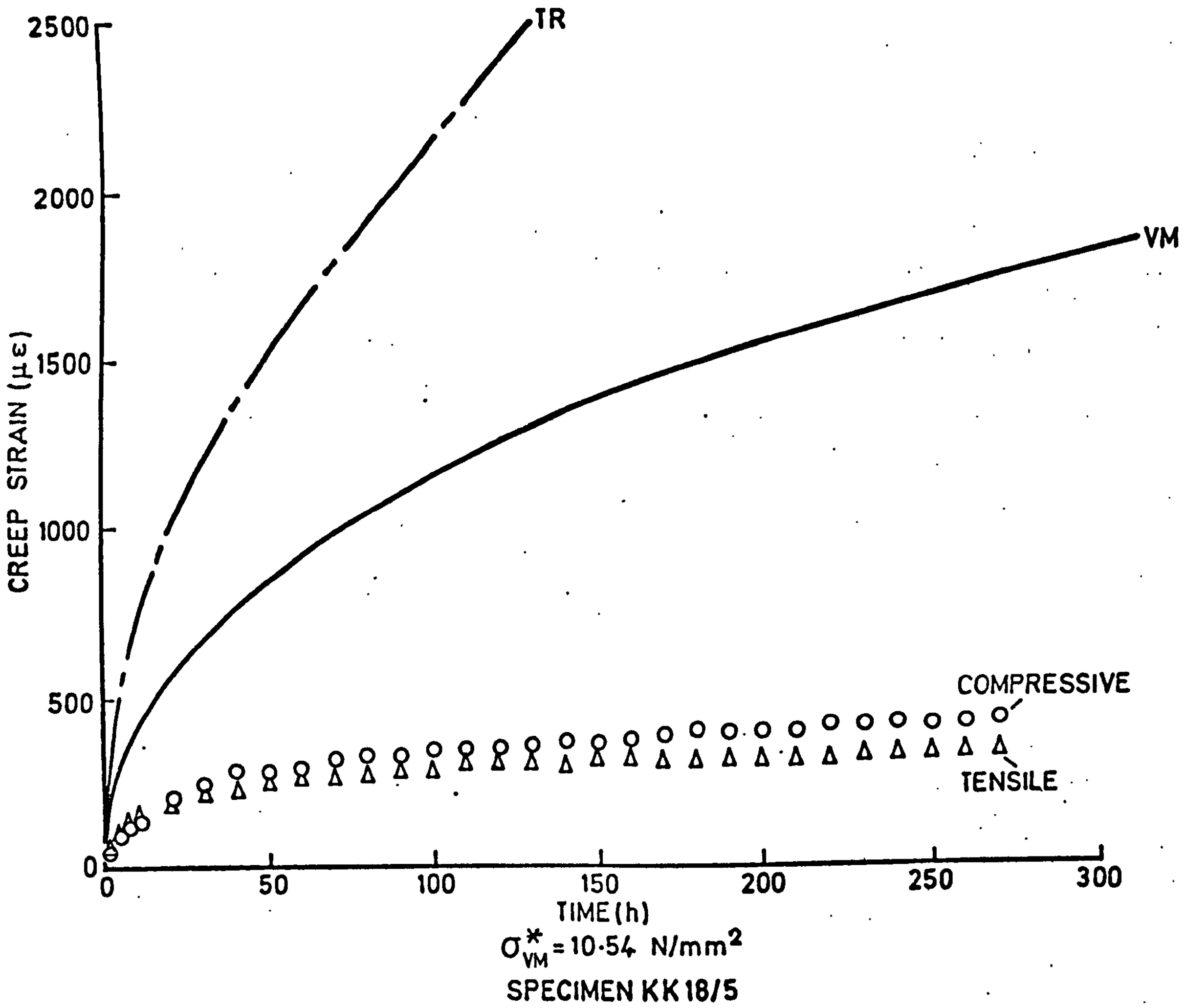

FIG. 7.12(p) BIAXIAL STRESS RATIO 1:0:-1

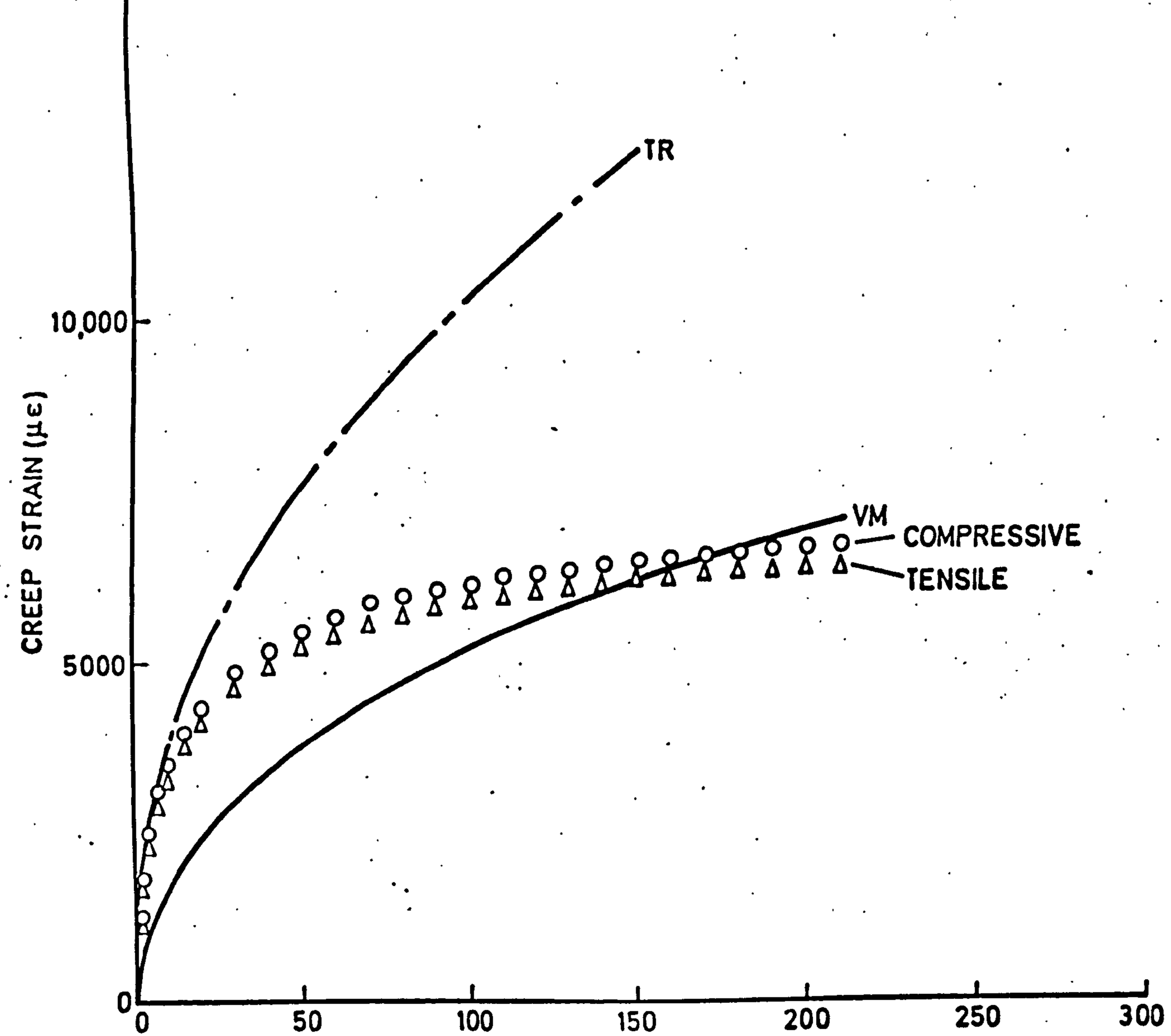

FIG. 7.12(q) BIAXIAL STRESS RATIO 1:0:-1

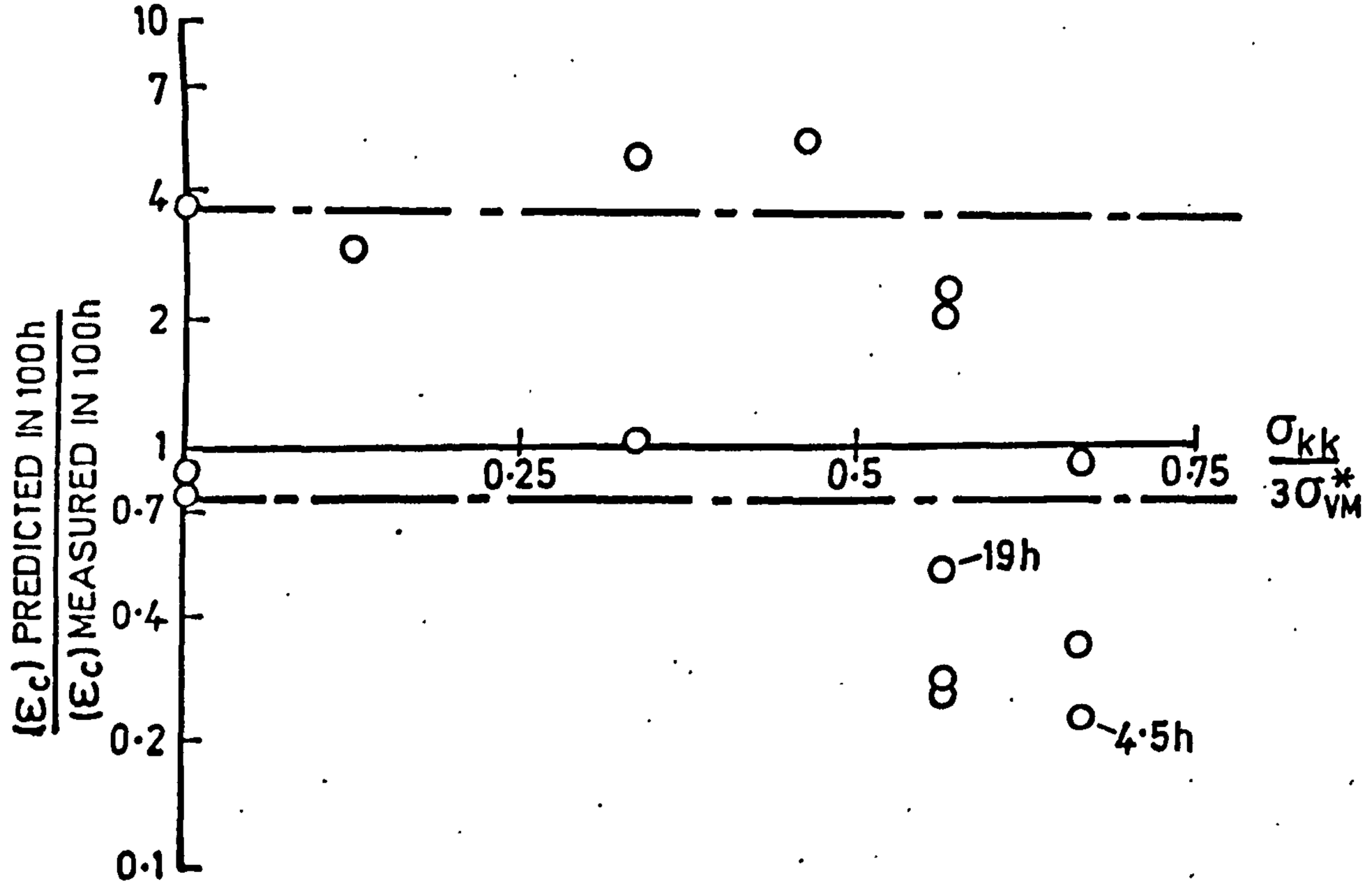

——·—— BOUNDS PREDICTED BY THE UNIAXIAL DATA.

ALL DATA POINTS BASED ON 100h, EXCEPT WHERE STATED.

FIG.7.13(a) EFFECT OF HYDROSTATIC STRESS ON BIAXIAL CREEP STRAINS.

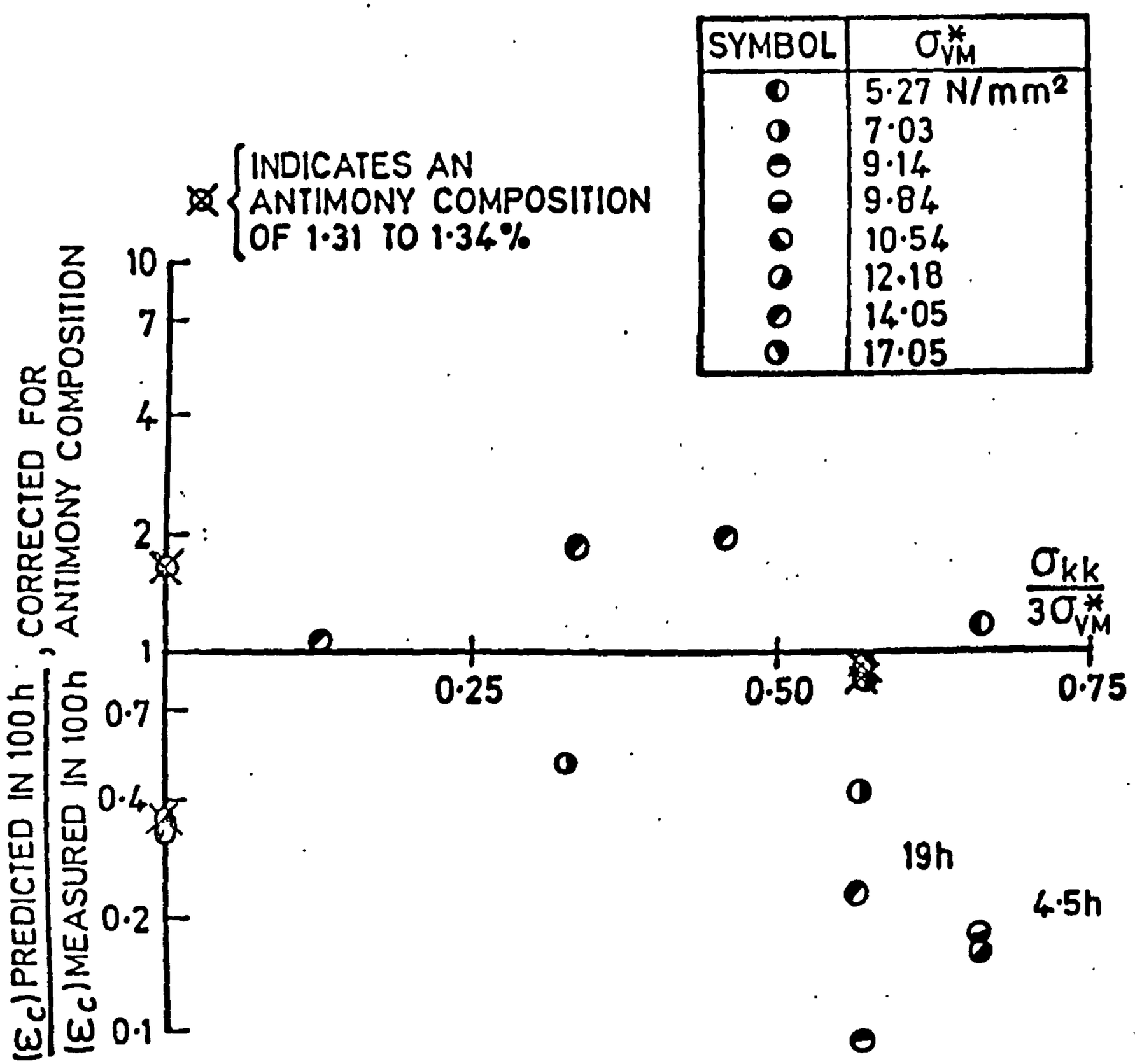

ALL DATA POINTS BASED ON 100h, EXCEPT WHERE STATED.

FIG. 7.13(b) EFFECT OF HYDROSTATIC STRESS ON BIAXIAL CREEP STRAINS (CORRECTED FOR ANTIMONY COMPOSITION)

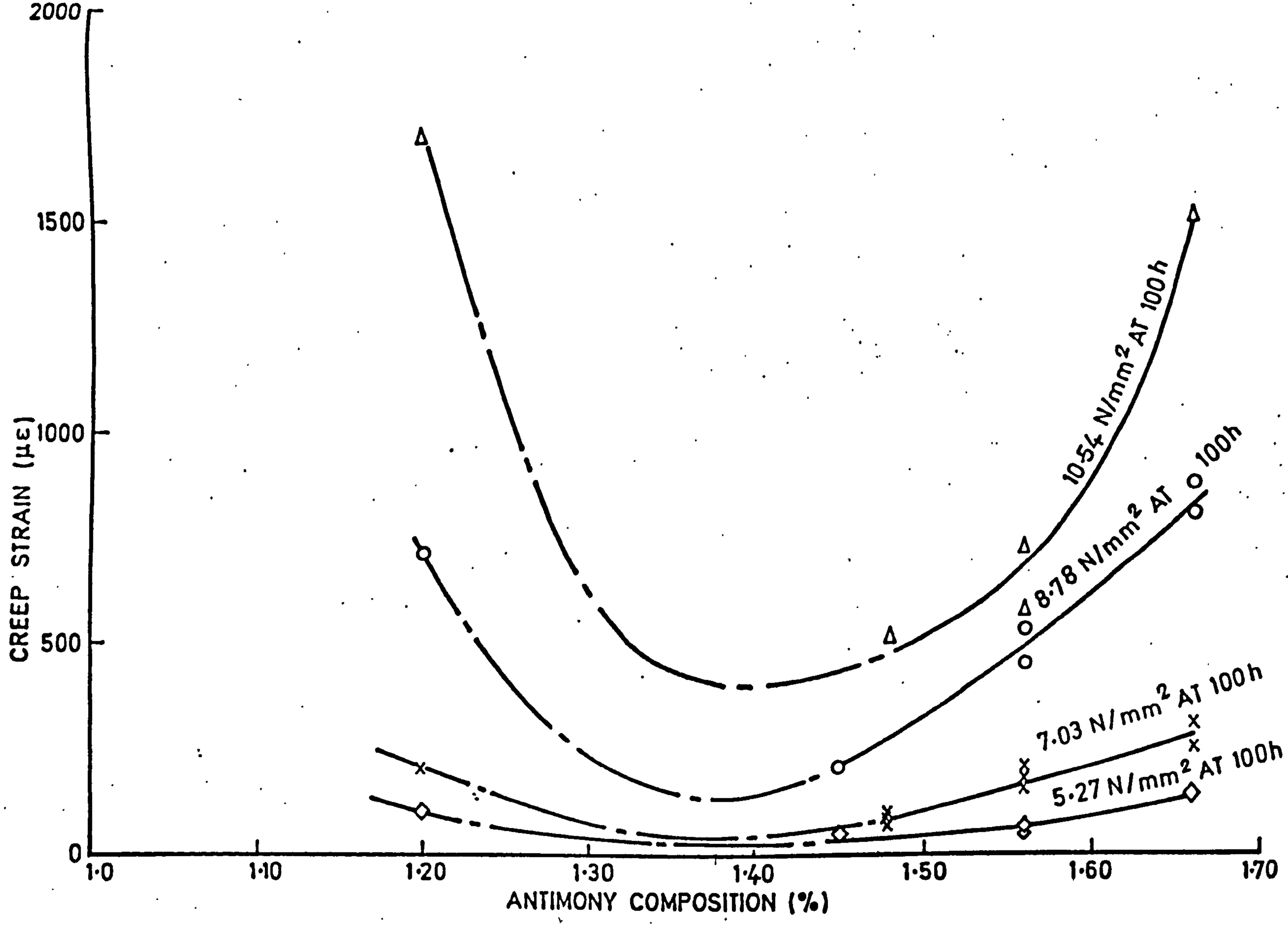

FIG. 7.14 . CREEP STRAIN v ANTIMONY COMPOSITION.

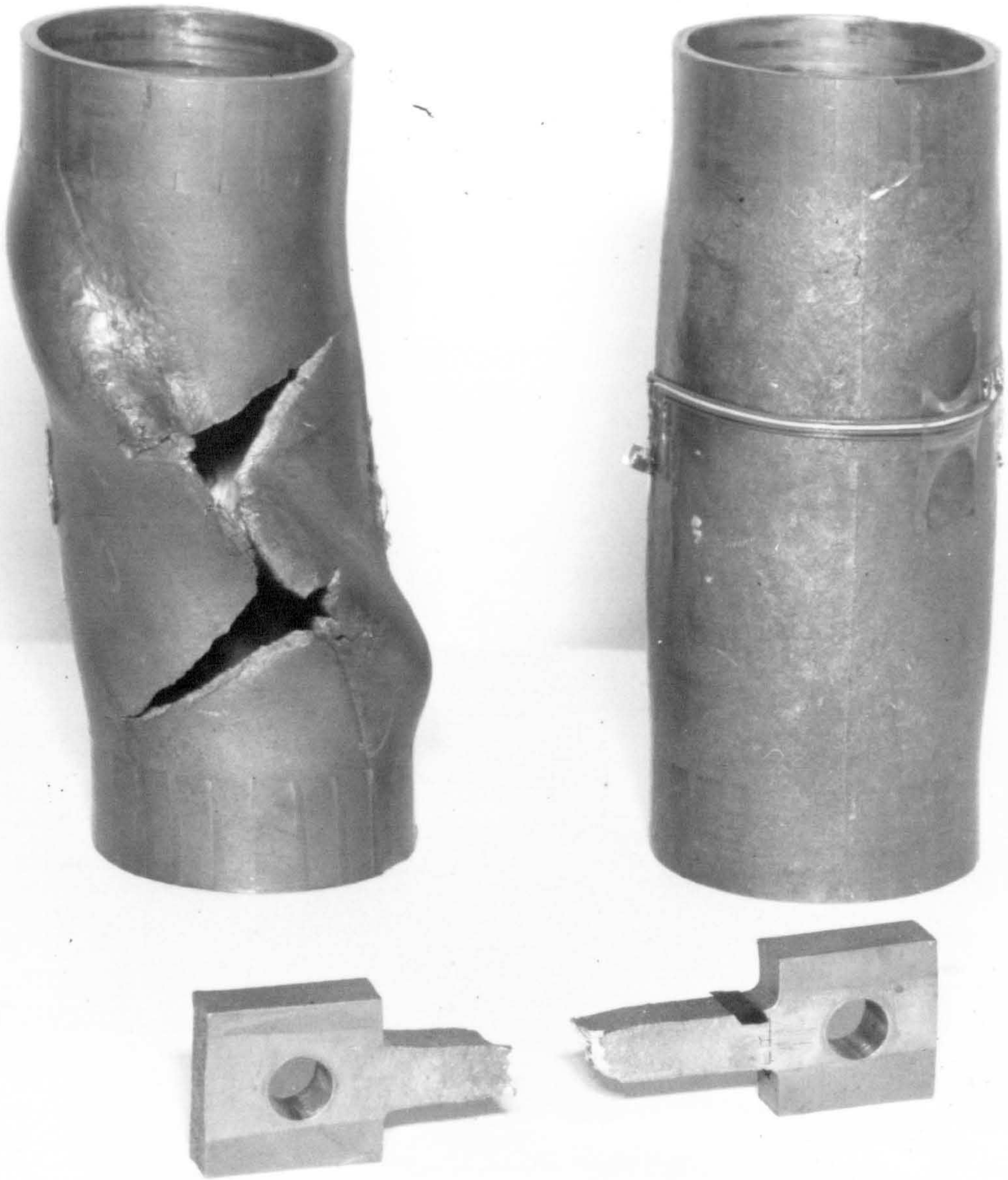

FIG. 7.15 RUPTURED TEST SPECIMENS

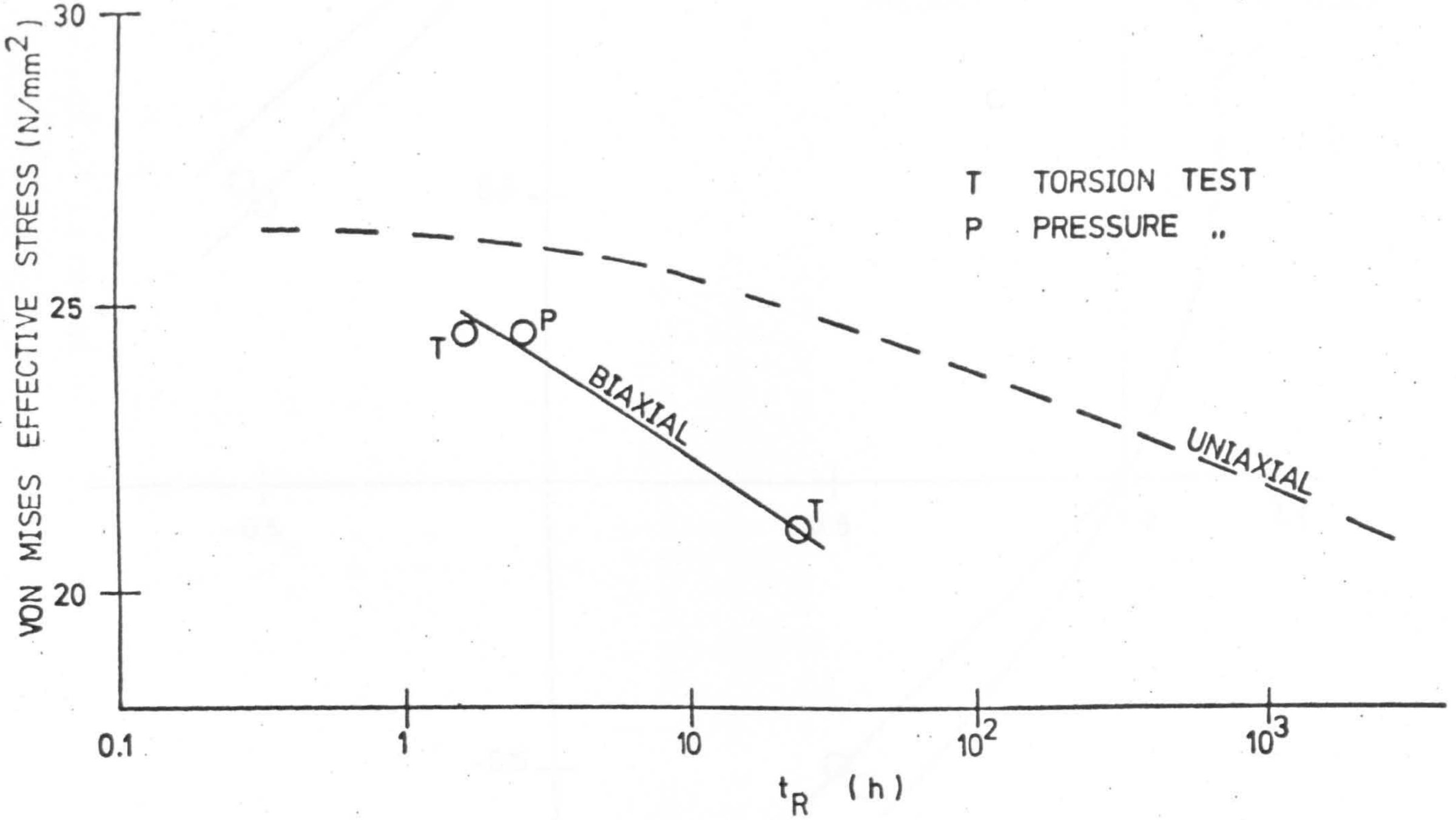

FIG. 7.16 BIAXIAL RUPTURE DATA

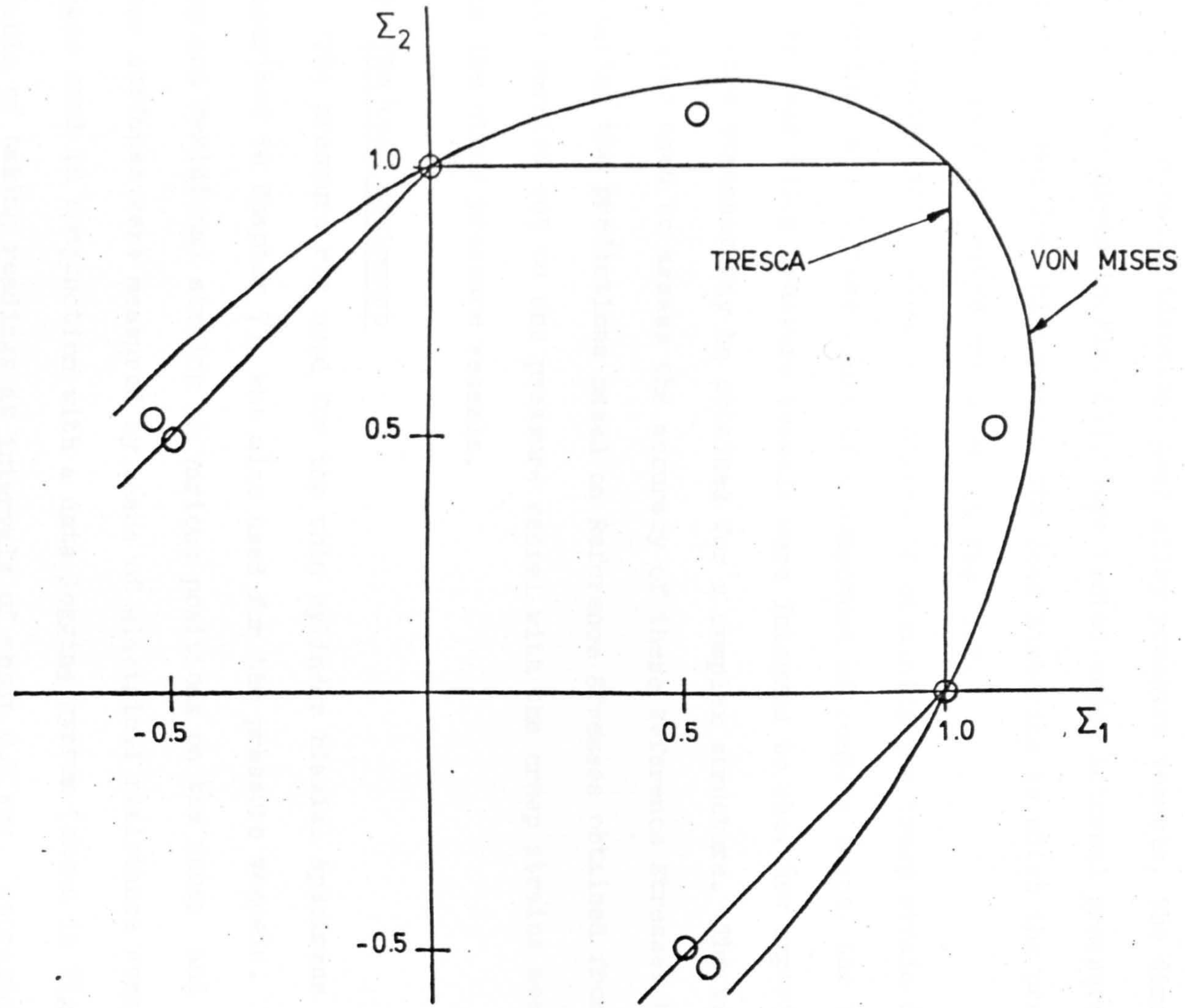

FIG. 7.17 NORMALISED BIAXIAL RUPTURE DATA

CHAPTER 8

8. THE PRESSURE VESSEL TESTS

8.1 Introduction

Four nominally identical lead alloy pressure vessels, the dimensions of which are given in Fig. 8.1, were tested under internal pressure with different load histories. The load histories to which the pressure vessels were subjected are shown in Fig. 8.2.

Besides the obvious objectives of obtaining the creep strain distributions and rupture times of a component of complex shape, the tests on the lead alloy pressure vessels were intended to show how experimental Reference Stresses may be obtained for a complex structure. The tests were also used to assess the accuracy of these Reference Stresses by comparing the predictions based on Reference Stresses obtained from tests carried out on one pressure vessel with the creep strains measured from the other pressure vessels.

8.2 The test equipment

The pressure rig used for the thin cylinder biaxial specimens (described in Chapter 7), was also used for the pressure vessels. The hoop and meridional strains at various positions on the inner and outer surfaces were measured by means of electrical resistance strain gauges used in conjunction with a data logging system (shown in Fig. 7.9), capable of taking readings at intervals of about 0.3 sec. Approximately 76 gauges were put on each of the vessels, which resulted in a scan time of about 23 sec. The order of magnitude of the error in creep strain measurements caused by not taking the initial readings at the instant of loading is given by

$$\left\{\begin{matrix}\%\text{ error in creep reading} \\ \text{at time } t\end{matrix}\right\} \simeq \left[\frac{\Delta t}{t}\right]^m \times 100 \qquad (8.1)$$

where Δt is the time between loading and taking the first reading and m

is the time index. Therefore, the maximum order of magnitude of the errors in the creep readings at 0.1, 1, 10 and 100 h are 25%, 8%, 3% and 1% respectively, taking $m = \frac{1}{2}$. It can be seen that, although large errors may be involved at short times, they soon become negligible, therefore, the scan time was considered to be adequate.

The clamping conditions shown in Fig. 8.3(a) were decided upon after a series of elastic finite element solutions (using PAFEC 70+, ref. 64) with different end conditions showed that these conditions were the closest to those of an encastré cylinder, which would simplify any future finite element calculations (i.e. plastic or creep) on this structure. The flange of the pressure vessel is placed inside a steel clamping ring and a layer of araldite is used to stick the two together before the end of the flange is machined flat.

The system of leading the internal gauge leads from the inside of the pressure vessels to the outside is also shown in Fig. 8.3 (a). An 'O'-ring is used to seal the pressure vessel. With this system, a pressure of 7 N/mm^2 has been applied without any leakage being observed from either the 'O'-ring seal or the silicon rubber bung through which the varnish covered strain gauge leads pass.

Because of the difficulty of accurately positioning strain gauges on the inside of the pressure vessels, to measure the exact positions after the tests, it was necessary to lightly scribe a reference grid on the inside so that the pressure vessels could be cut up after the tests and the positions of the gauges relative to these grids measured. Figs. 8.3(b) and (c) show some strain gauges on the inside and outside surfaces of a pressure vessel and the steel ring attached to the flange of the pressure vessel.

8.3 The elastic stress distribution

The elastic stress distribution in the pressure vessel was obtained by both the finite element and frozen stress photoelastic methods, the results of which are shown in Figs. 8.4(a) and (b). For the finite element analysis, the structure was idealised by 22-8 node axisymmetric elements as shown in Fig. 8.5. The photoelastic model (shown in Fig. 8.6) was cast in the same mould as the lead alloy models, the aluminium core was replaced by an undersize silicon rubber core. It was then necessary to machine the inside of the Araldite model to produce the correct wall thickness.

The initial plastic strains and creep strains are dependent upon the von Mises effective stress and the deviatoric stress components which are shown in Figs. 8.7(a) and (b) respectively. These were obtained by using the photoelastic stresses. As expected, these results show that the greatest initial plastic and creep strains will be the hoop strains obtained in the cylinder. However, the results also show that some relatively large hoop strains as well as large meridional strains may be obtained in the region of the cylinder to hemisphere intersection i.e. fairly high values of s_{ij}/σ^* are present in this region. These findings are based on initial elastic stresses whereas in the actual tests on the lead alloy models, initial plasticity will modify the stress distribution and redistribution of stresses during creep will occur. However, as Parkes and Webster (23) have shown, for an axisymmetric pressure vessel under creep, it is possible for high effective stresses to increase even though the actual stress components are decreasing during redistribution. This means that although the s_{ij}/σ^* values may reduce during redistribution, an increase in σ^* may occur which will cause high creep strain rates to be maintained.

8.4 Results

The load histories to which the pressure vessels were subjected are shown in Fig. 8.2.

8.4.1 Initial strains

The initial strains obtained when the pressure vessels were first loaded are shown in Figs. 8.8(a)-(d). The initial pressure of 1.32 N/mm^2 applied to the P14 pressure vessel (Test 2) was intended to give purely elastic strains in the hemisphere and in the region of the hemisphere to cylinder intersection. The initial pressure applied to the P10 and P16 pressure vessels (Tests 4 and 1 respectively) was 1.76 N/mm^2, which was intended to give strains in the hemisphere near the elastic-plastic transition. Test 3 on the P12 pressure vessel was carried out with an internal pressure of 2.64 N/mm^2 which produced plastic strains at all parts of the pressure vessel.

From Figs. 8.8(a)-(d) it can be seen that the general appearance of the strain distribution is not greatly affected by the magnitude of the internal pressure. By far the largest initial strains obtained in all of the tests were the hoop strains on the inside surface of the cylinder. The meridional strains obtained on the inside surface at the position of peak meridional stress (in the hemisphere, near the hemisphere to cylinder intersection as shown by Fig. 8.4(b)) are about 25% of the maximum hoop strains in the cylinders, these meridional strains being more significant at the lowest pressures.

In test 3, which was carried out at the highest pressure a relatively large hoop strain was obtained in the cylinder, near the hemisphere to cylinder intersection.

8.4.2 Creep strain distributions

The creep strain distributions at various times during the initial constant load phases of the pressure vessel tests are shown in Figs. 8.9(a)-(h). Figs. 8.9(a) and (b) show the hoop and meridional creep

strain distributions in pressure vessel P14 (Test 2) at times 0.1, 1, 10 and 100 h, under an internal pressure of 1.32 N/mm^2. Figs. 8.9(c) and (d) show the hoop and meridional creep strain distributions in pressure vessel P10 (Test 4) at times 0.1, 1, 10 and 24 h under an internal pressure of 1.76 N/mm^2. Figs. 8.9(e) and (f) shown the hoop and meridional creep strain distributions in pressure vessel P16 (Test 1) at times 0.1, 1, 10, 100 and 213 h under an internal pressure of 1.76 N/mm^2. Figs. 8.9(g) and (h) show the hoop and meridional creep strain distributions in pressure vessel P12 (Test 3) at time 0.1, 1 and 4.5 h under an internal pressure of 2.64 N/mm^2. The general shape of the creep strain distribution curves are similar to those obtained for the initial deformations. The main difference is that a peak hoop creep strain is present in the cylinders near the hemisphere to cylinder transition which is not present in the initial strains, except at the highest load (i.e. Test 3). The implication of this is that the existence of a peak value requires the strain (either initial or creep) to be strongly dependent upon stress (i.e. q and n must be large). The greatest creep strains were found to be the hoop strains on the inside surface of the cylinders.

8.4.3 Rupture times

After the creep tests had been performed on the P10, P14 and P16 pressure vessels, the pressure was increased to a much higher value and the pressure vessels were allowed to creep under this pressure until rupture occurred. The P12 pressure vessel was initially loaded with a pressure of 2.64 N/mm^2 and this pressure was held constant until rupture occurred. For the purpose of trying to correlate the rupture data for these pressure vessels, it was necessary, because of the lack of data to assume that any damage caused during the creep tests (i.e. when the pressures were relatively low) was negligible and that only the final pressure had a significant effect on the rupture times of the pressure

vessels. This assumption is reasonable because the maximum creep strains during the creep tests are only about 20% of the rupture strains.

Table 8.1 shows the final pressures applied to the pressure vessels, the times for which the pressure vessels lasted under these pressures. Attempts were made to try and relate these rupture times to

(i) the nominal hoop stress in the cylinder, based on initial dimensions,

(ii) the experimentally determined maximum Reference Stress,

(iii) the theoretically determined maximum Reference Stress, and

(iv) the approximate (Sim) Reference Stress.

None of these methods gave accurate results and Table 8.1 shows that the rupture times predicted by these methods are many orders of magnitude too large. Fig. 7.16 obtained from biaxial tests on thin cylinders indicates a similar effect but the deviation was not as great.

It was therefore decided that the reverse procedure should be tried i.e. the uniaxial stress which causes rupture in the same time as the pressure vessel was obtained, using Fig. 5.23(a). This associated uniaxial stress may be regarded as an experimentally determined 'Rupture' Reference Stress $(\bar{\sigma}_o)_R$. The results are shown in Table 8.2 and Fig. 8.10.

It may be seen from the values of $(\bar{\sigma}_o)_R/\sigma_{nom}$ in Fig. 8.10 that the Rupture Reference Stress is not linearly dependent upon the load (which is the case with the deformation Reference Stress), but reduces almost linearly with pressure. This is probably due to the rupture ductility of the material being dependent upon the magnitude of the biaxial stress system in a different way to that in a uniaxial stress system. Because of the short cylinder length of the pressure vessels, the end restraints have a significant effect on the rupture times and it was not possible to obtain biaxial rupture data from the pressure vessels.

Axial cracks in the cylinder of the pressure vessel were the eventual cause of failure. An example of the rupture is shown in Fig. 8.3(c). The length of these cracks varied from 36 to 71 mm but as Table 8.3 shows, these do not appear to depend upon the magnitude of the pressure. It was noticed that failure occurred quite suddenly whereas the failure of the thin cylinder pressure vessels was very slow, during which time a small leakage developed. This was attributed to the much greater energy stored in the oil in the pressure vessel (which for experimental convenience had no core) to that stored in the oil in the thin cylinders (which did have a core). The axial cracks started somewhere near the centre of the cylinder, where the maximum hoop strains were present, these cracks then travelled towards the flange end of the cylinder. Around the main crack, which caused eventual failure, some smaller axial cracks were also present, as may be seen in Fig. 8.3(c).

8.5 Reference Stresses for the pressure vessels

In chapter 6, it was shown that experimental Reference Stresses could be obtained for simple structures (made from pressure vessel casting P9), having one dimensional stress systems. The P9 and P14 pressure vessels were found to have almost indentical antimony compositions i.e. 1.66% Sb and 1.67% Sb respectively. Therefore, the necessary uniaxial calibration for the experimental Reference Stress method obtained from specimens taken from the P9 pressure vessel casting (shown in Figs. 3.2 and 3.4) was suitable for use in conjunction with the deformations measured during the P14 pressure vessel test to obtain experimental Reference Stresses at various positions in the pressure vessel.

Although the single model method is not directly applicable to the pressure vessel tests, because $\nu \neq \frac{1}{2}$, Reference Stresses were obtained by this method and these were compared with the Reference Stresses obtained by the two model method.

Reference Stresses were obtained for eight strains in the pressure vessel, these being chosen to be

(i) the outside surface at the apex of the pressure vessel, where the Reference Stress is known (Appendix 6)

(ii) inside and outside hoop strains at the mid-cylinder position, which also has an anlytical solution (Appendix 4)

(iii) at a position where the rate of change of strain with position is large, i.e. the hoop strains 25 mm from the flange on the inside surface,

(iv) the hoop and meridional strains at the positions of the maximum and minimum meridional strains on the inside surface, near the hemisphere to cylinder intersection.

These positions are shown and numbered in Fig. 8.11.

The results obtained by both the single and two model methods are displayed in Table 8.4 and, where analytical solutions exist, these results are also displayed. From these results, it can be seen that the single model and two model methods give similar results for Reference Stresses except at positions where the plastic strains are small, i.e. the single model method gives good results if reasonably large strains exist, which is probably because plastic deformations occur at constant volume.

Because the P16 pressure vessel ruptured after about 2 min. only, the pressure applied to this vessel was considered to be close to the limit load. This ultimate pressure, P_{ult}, was used to obtain the approximate Reference Stress for the structure given by

$$\bar{\sigma}_o = \frac{P}{P_{ult}} \quad \sigma_{ult}.$$

Using this approximate method, $\bar{\sigma}_o/\sigma_{nom} = 1.118$, which may be seen to be close to the Reference Stresses obtained for the cylinder hoop strains but was very inaccurate for the Reference Stresses to predict strains at other points in the pressure vessel. This value of $\bar{\sigma}_o/\sigma_{nom}$ is also close to the high load values obtained in the rupture tests (Table 8.2 and Fig. 8.10).

Although it has not been analytically proved, the Reference Stresses obtained for both the meridional and hoop strains at the same point in the pressure vessel were found to be very similar, which implies that a single Reference Stress may be used to predict all strains at a particular point and only the 'X' value defined in section 6.3 is different.

In order to estimate the accuracy of the experimentally determined Reference Stresses obtained from the results of the P14 pressure vessel, they were used to predict the variable load creep deformations of the P10, P14 and P16 pressure vessel tests. These predictions are shown in Figs. 8.12(a)-(f). Since the Reference Stresses were obtained from the initial constant load data from the P14 test, the variable load predictions of the P14 creep strains may be used to test the hardening law which is used. The predictions were based upon the uniaxial creep laws obtained in Chapter 5 with a correction for differences in antimony composition. The method of correcting for antimony composition is described in Section 7.4.2 in connection with the biaxial tests. The material was also assumed to be strain hardening, which is shown to be reasonably accurate in Chapter 5. The results of thesepressure vessel Reference Stress predictions show that the pressure vessel deformations can be predicted accurately for both steady and variable load conditions. The predictions of pressure vessel deformations were within 2 to 1, which is the same order of accuracy as the beam and cantilever predictions. When it is considered

that the scatter on actual prototype material data may be of the order of 10 to 1, these predictions based upon the experimental Reference Stresses are acceptable for design purposes.

8.6 Conclusions

As in the case of structures with one-dimensional stress systems, it has been shown that experimental Reference Stresses may be obtained for structures with complex stress systems and that the likely error, excluding scatter of the prototype material, in prototype deformations is about 2 to 1, even under variable load conditions. It has also been shown that, even though the single model method is capable of producing reasonable predictions, the method is inaccurate for the smaller strains (i.e. accurate Reference Stresses could not be obtained for some of the meridional strains). The Reference Stresses obtained for strains in different directions at the same point indicate that the Reference Stress may be constant for a particular mode of deformation. The 'X' values however, were found to be different for different strain components at the same point in a structure.

The agreement between the Reference Stresses obtained by the two model method and the Reference Stresses obtained analytically, for points at which analytical solutions are possible (i.e. mid-cylinder and apex of hemisphere), was very good, i.e. all experimental Reference Stresses were within 15% of the theoretical values.

The predictions of rupture times for the pressure vessels, based upon the experimental, approximate and theoretical Reference Stresses was found to be very poor. This was attributed to the dependence of rupture ductility on stress being different under multiaxial stress systems than under a uniaxial stress system.

Table 8.1

Test	Pressure N/mm^2	Measured Rupture Time (h)	Rupture Time Predictions (h)			
			$(\sigma_\theta)_{max}$	$(\bar{\sigma}_o)_{exp}$	$(\bar{\sigma}_o)_{theor.}$	$(\bar{\sigma}_o)_{approx.}$
1 (P16)	2.95	0.03	200	0.75	> 2000	0.33
2 (P14)	2.64	0.78	> 2000	270	> 2000	220
3 (P12)	2.46	4.6	> 2000	1400	> 2000	1300
4 (P10)	2.36	11.5	> 2000	> 2000	> 2000	> 2000

Table 8.2

Test	Pressure N/mm^2	Measured Rupture Time (h)	$(\bar{\sigma}_o)_R / \sigma_{nom}$
1	2.95	0.03	1.131
2	2.64	0.78	1.240
3	2.46	4.6	1.314
4	2.36	11.5	1.354

$\sigma_{nom} = pd_i/2t$

Table 8.3

TEST	RUPTURE STRAINS (%)		CRACK LENGTH
	MEAN HOOP	RED. IN AREA AT FRACTURE	mm
1	3.58	19.0	56.1
2	3.98	8.6	35.6
3	4.04	16.7	70.9
4	4.06	15.0	54.9

Table 8.4 P14 Pressure Vessel Results

Position in Pressure Vessel			1 outside	2 inside hoop	2 inside merid.	3 inside hoop	3 inside merid.	4 outside hoop	5 inside hoop	6 inside hoop
Quantity	Symbol	Units								
Nominal Stress $pd_i/2t$	σ_{nom}	$\frac{MN}{m^2}$	10.34							
Ref. Str. Indices										
Theoretical	$\bar{\sigma}_o/\sigma_{nom}$		0.500					0.866	0.866	
One-model			0.550	0.837	0.800	0.840	1.33	1.029	1.016	1.004
Two-model			0.460	0.847	0.826	0.850	0.829	1.107	1.110	0.951
The Quantity 'X'										
Theoretical	$\phi_i/\bar{\varepsilon}_{io}$		0.500					0.866	0.866	
One-model			0.413	0.442	0.820	1.274	-	0.977	1.092	0.708
Two-model	$(\phi_i)_A/(\bar{\varepsilon}_{io})_A$		0.543	0.283	0.593	0.964	0.189	0.678	0.676	0.757
Initial Deformation	ϕ_i	$\mu\varepsilon$	124	371	623	1070	-22	1818	1900	1189
Redistribution Deformation										
One-model	$\Delta\phi$	$\mu\varepsilon$	4	20	81	61	-	283	312	95
Two-model			0	93	2	162	0	0	14	60
Redistribution Time										
One-model	t_{red}	h	15	12	7	10	-	3	5	7
Two-model			0	7	1	10	0	0	1	4

$$\bar{\sigma}_o/\sigma_{nom} \text{ approx.} = \frac{P}{P_{ult}} \frac{\sigma_y}{\sigma_{nom}} = 1.118$$

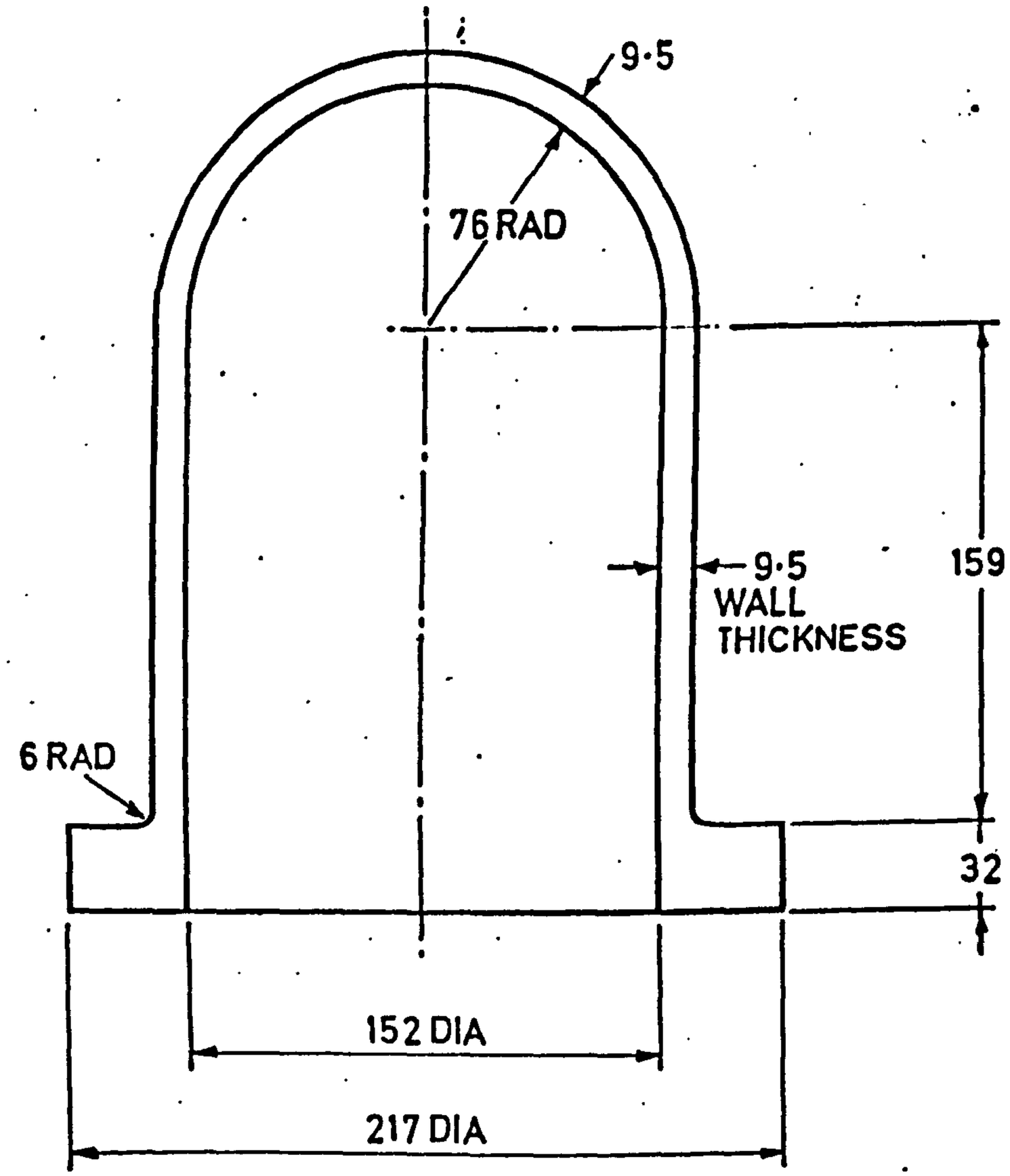

ALL DIMENSIONS IN mm

FIG.8.1 NOMINAL PRESSURE VESSEL DIMENSIONS.

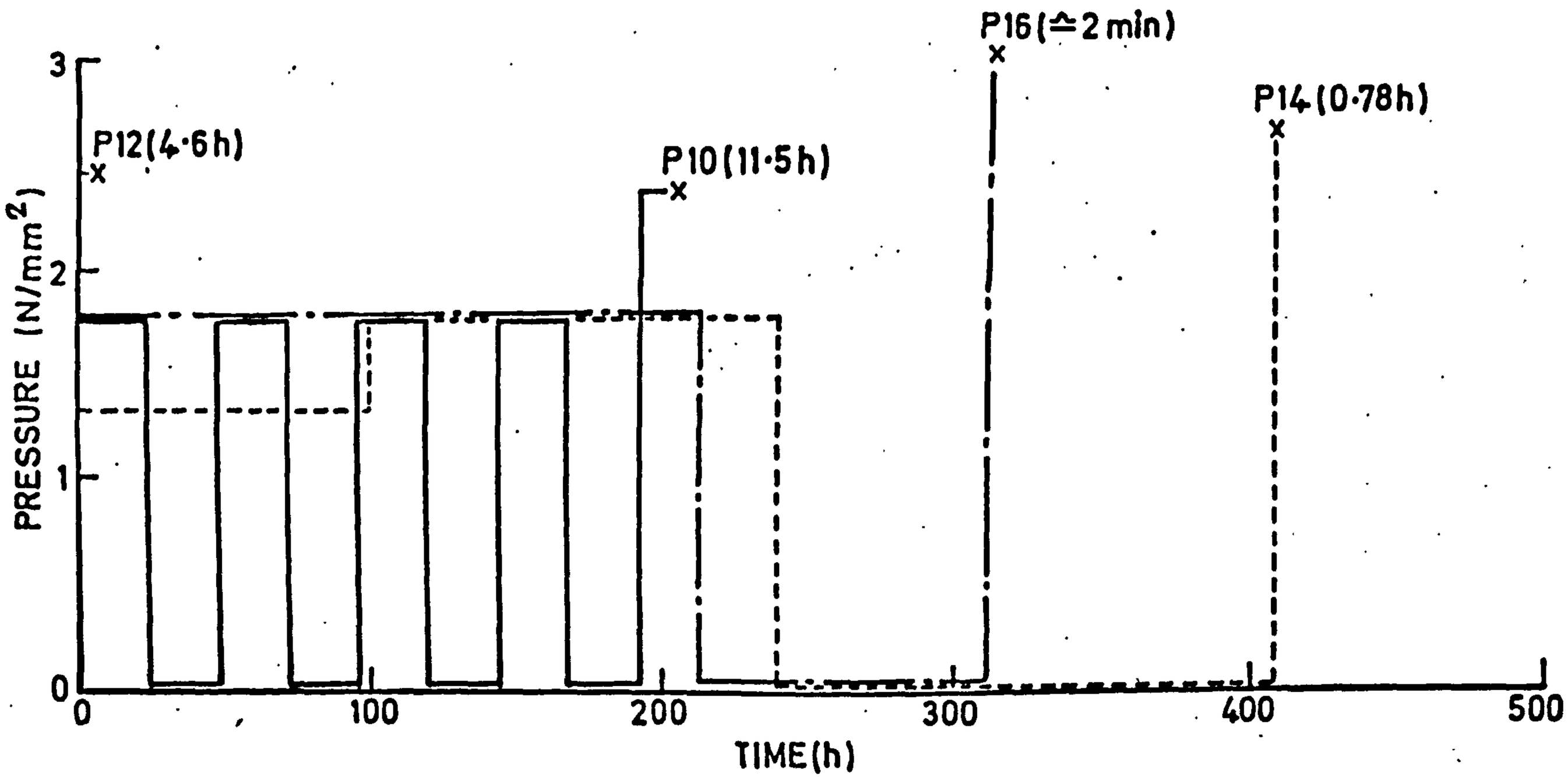

FIG.8.2 LOAD HISTORY FOR THE PRESSURE VESSELS.

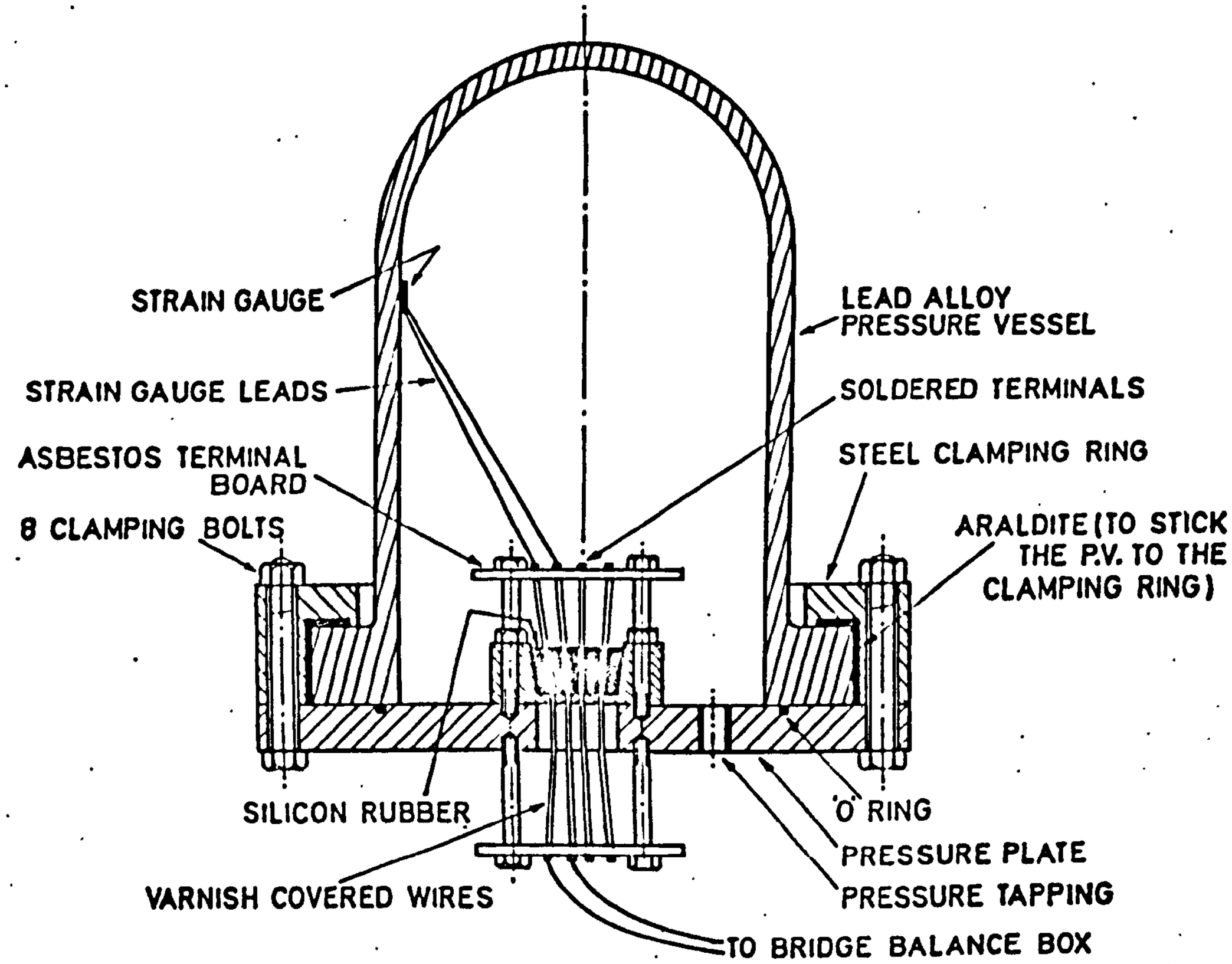

FIG. 8.3(d) THE PRESSURE VESSEL CLAMPING AND STRAIN GAUGING SYSTEM

FIG. 8.3(b) INTERNAL STRAIN GAUGES

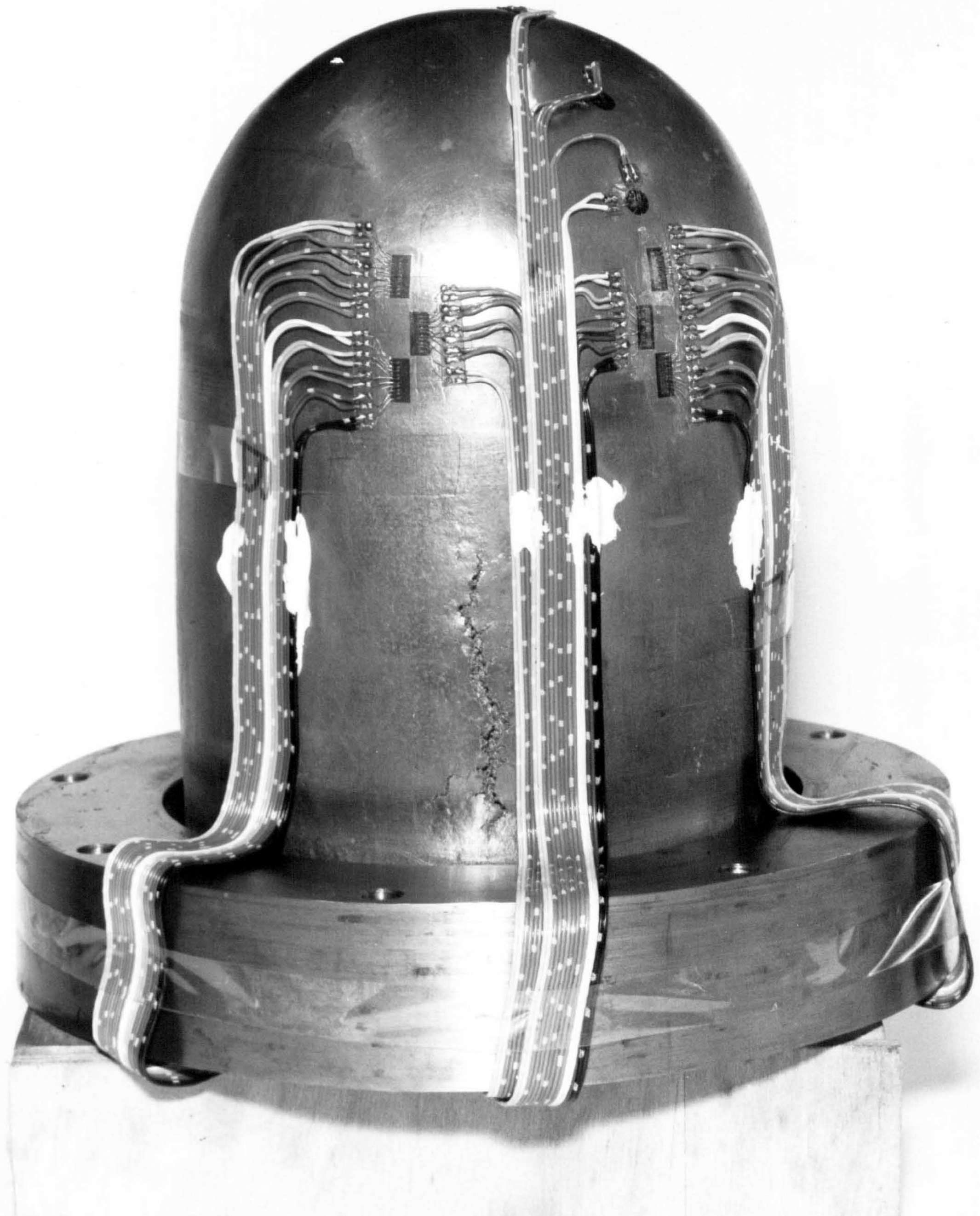

FIG. 8.3(c) A RUPTURED PRESSURE VESSEL

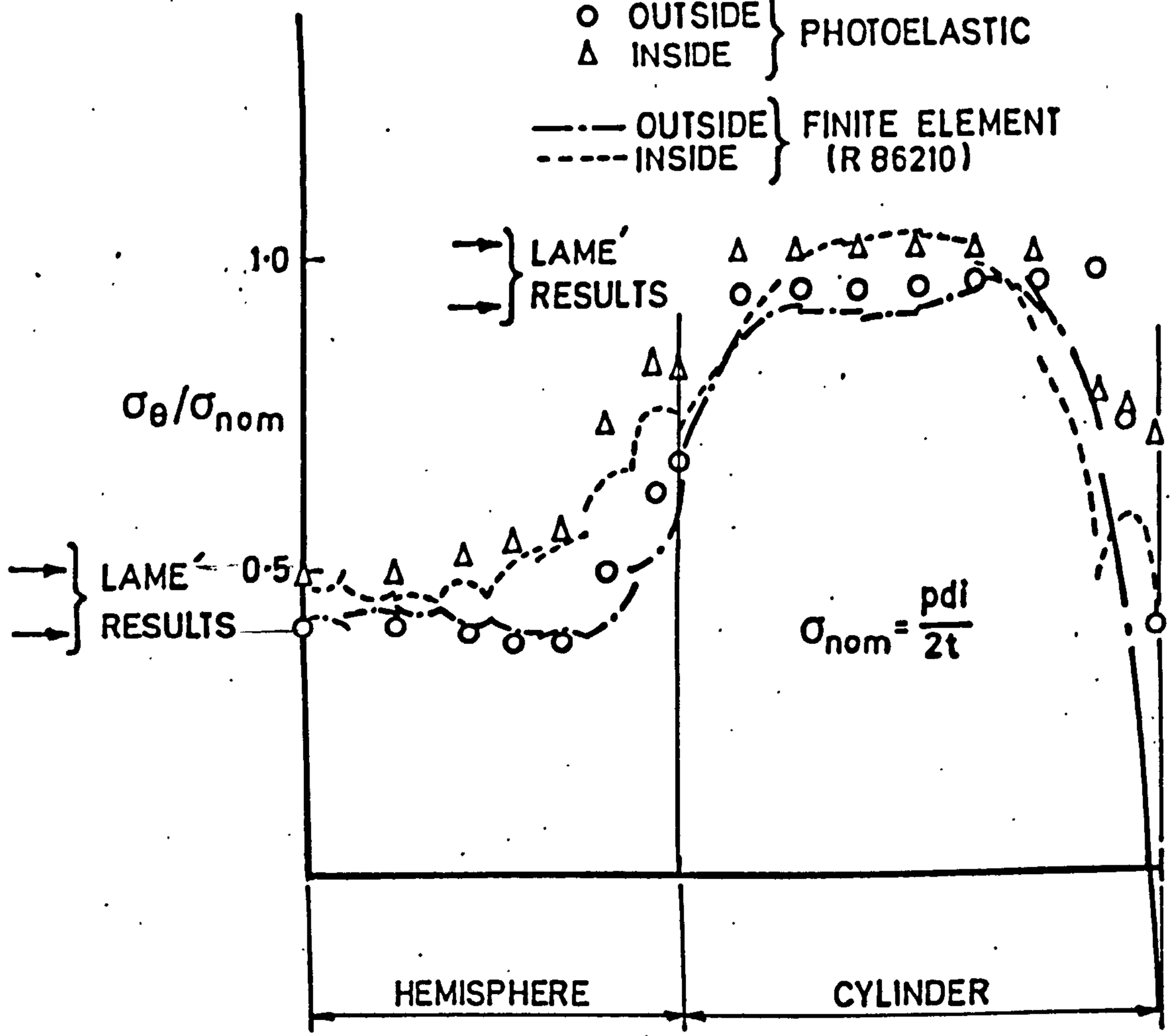

FIG.8.4(a) ELASTIC HOOP STRESS DISTRIBUTION.

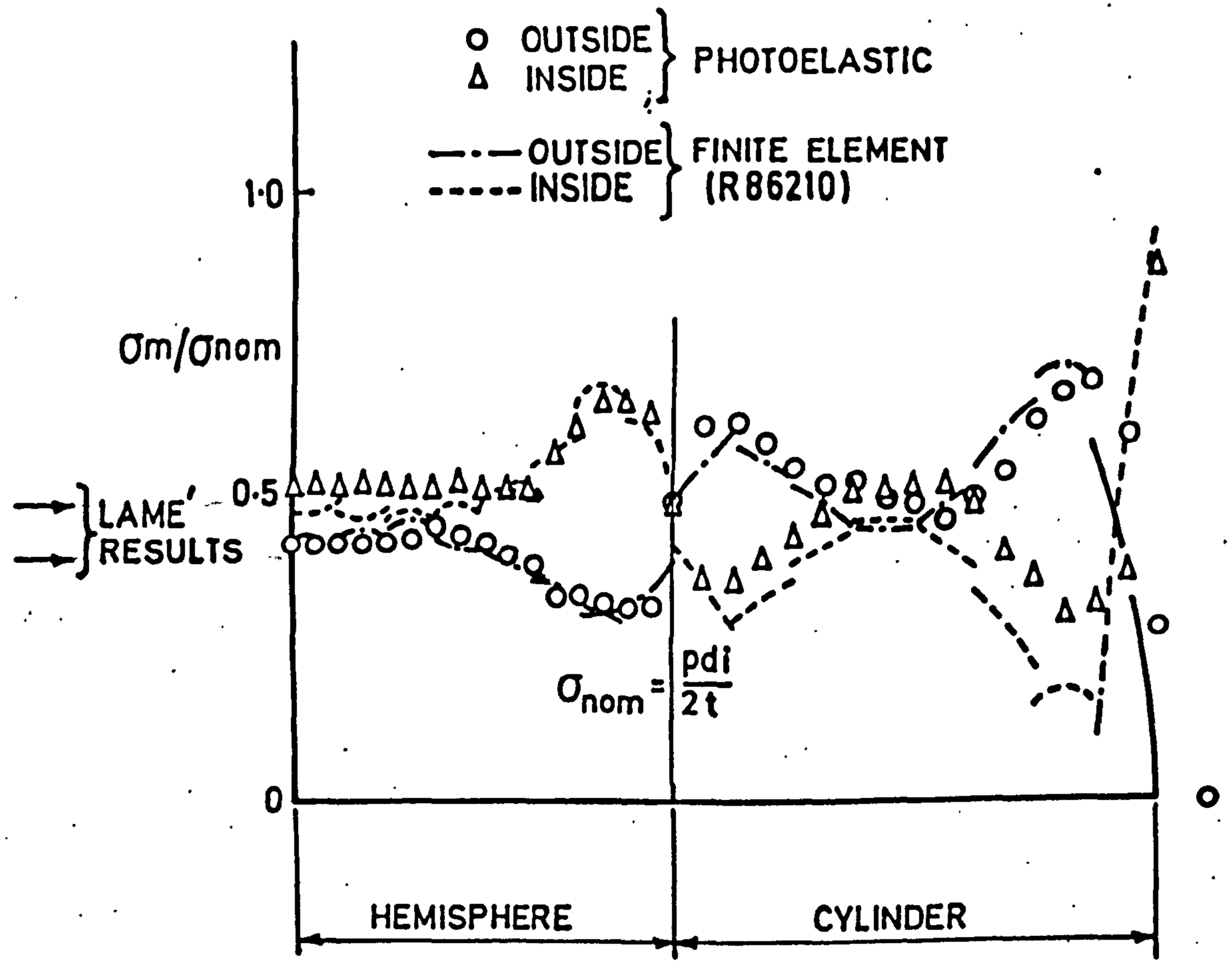

FIG. 8.4(b) ELASTIC MERIDIONAL STRESS DISTRIBUTION.

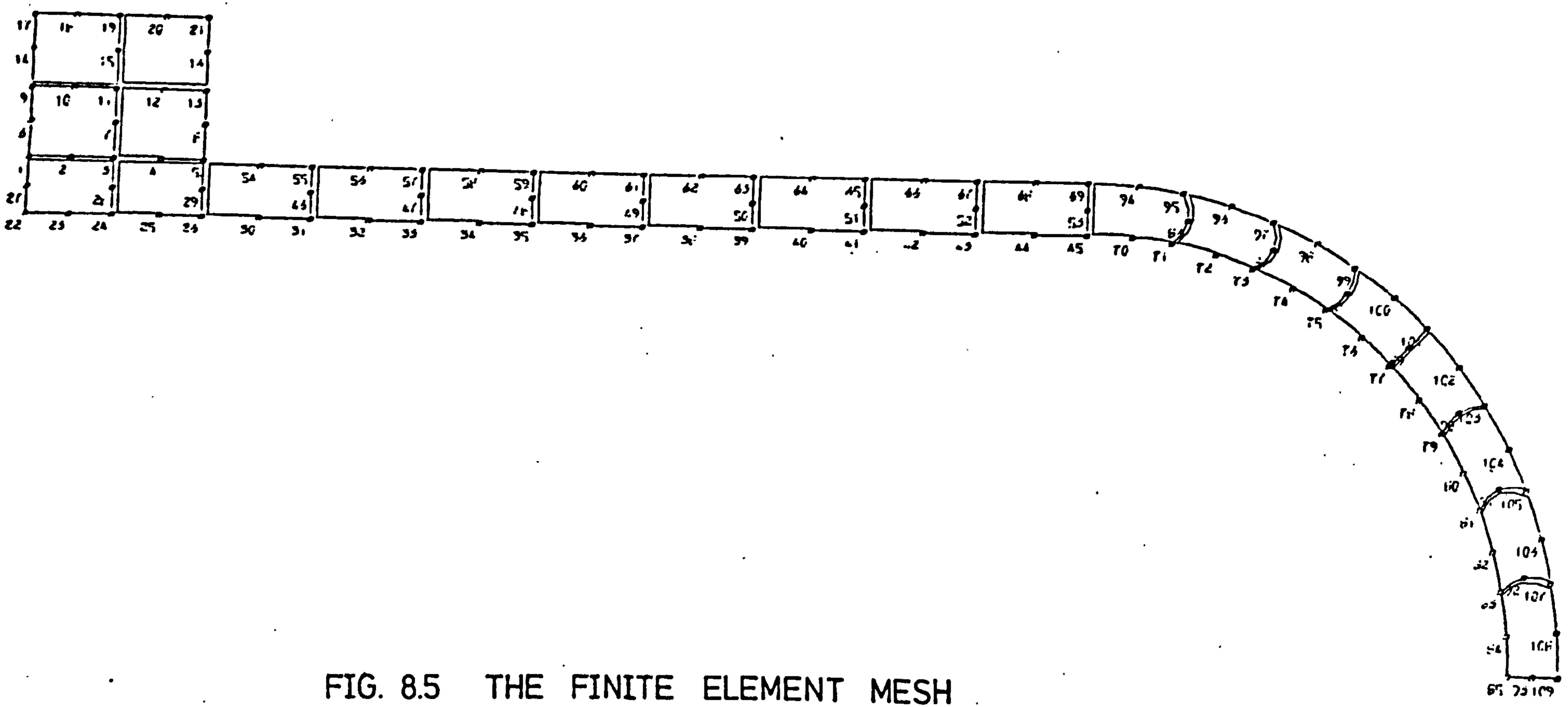

FIG. 8.5 THE FINITE ELEMENT MESH

FIG. 8.6 AN ARALDITE PRESSURE VESSEL

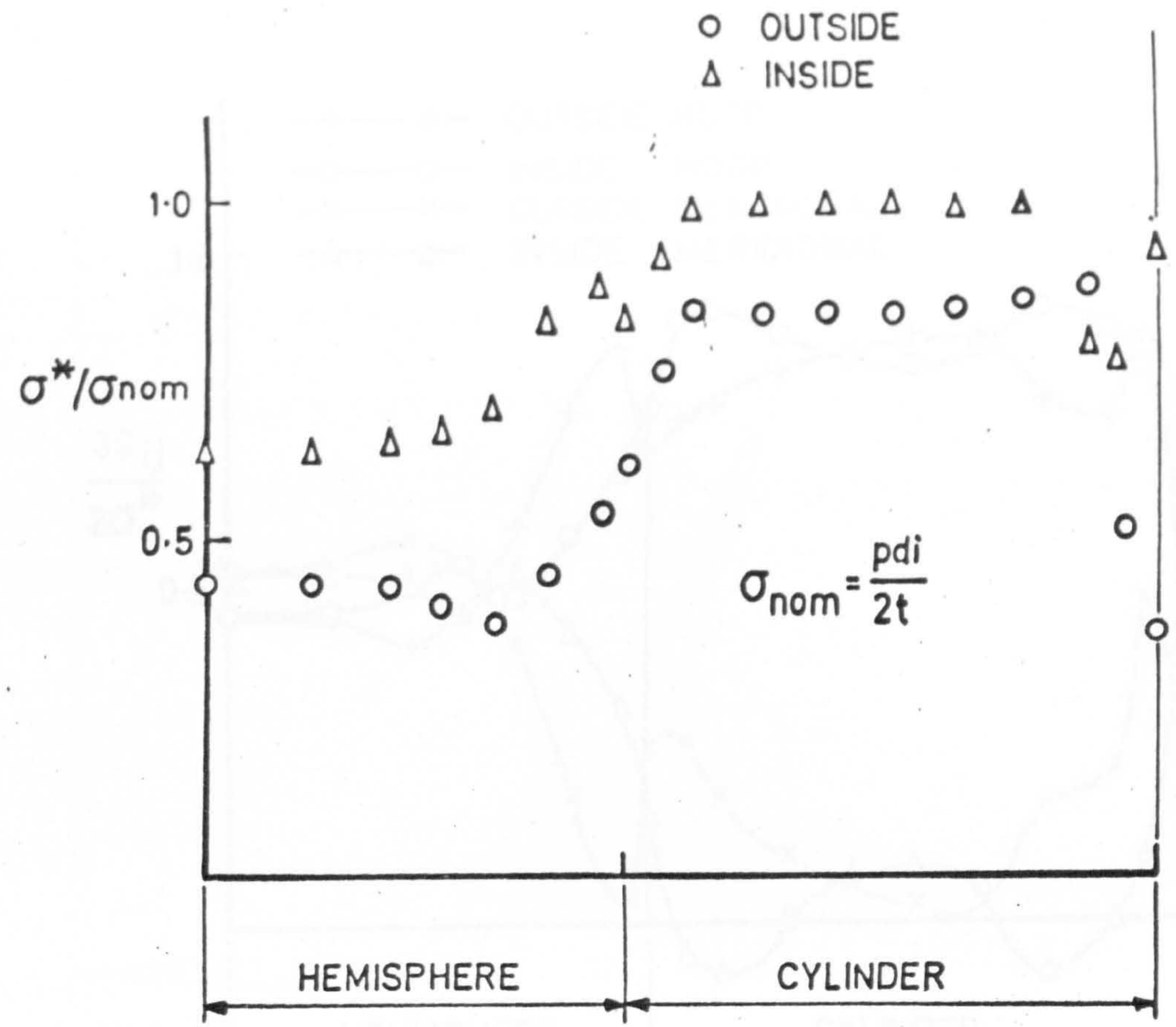

FIG.8.7(a) EFFECTIVE STRESS DISTRIBUTION.

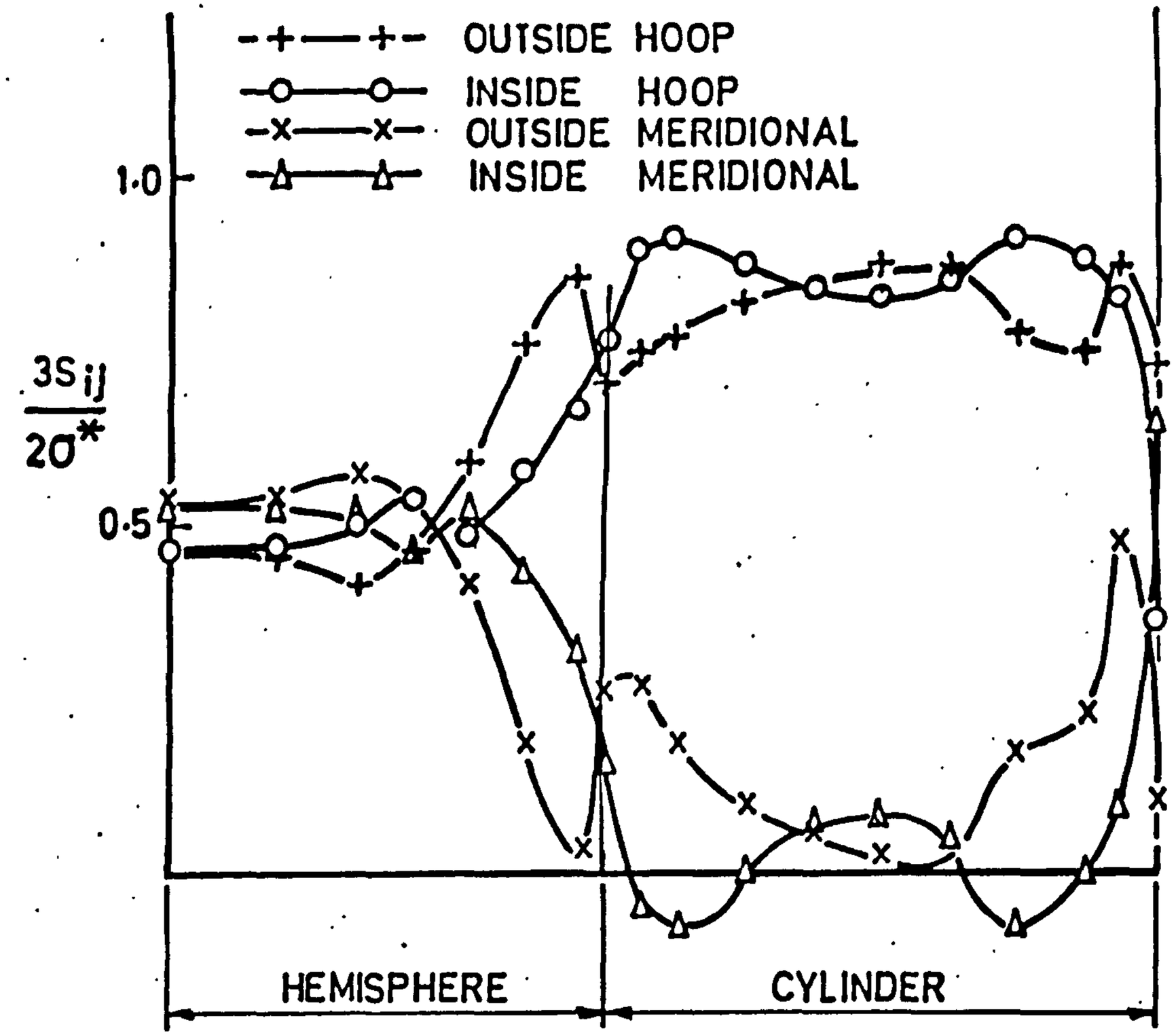

FIG.8.7(b) DEVIATORIC STRESS DISTRIBUTION.

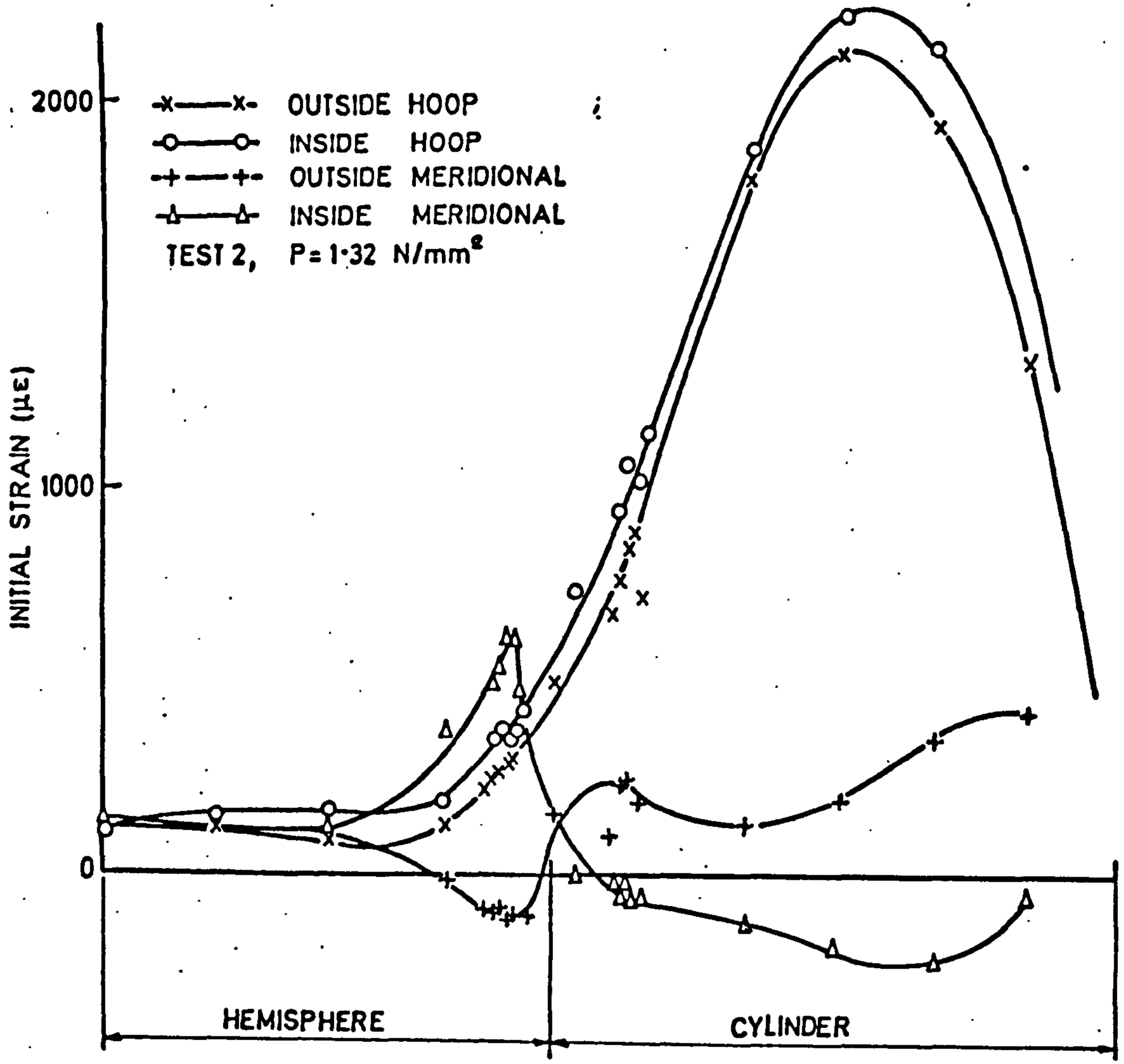

FIG. 8.8(a) INITIAL STRAIN DISTRIBUTIONS (P14)

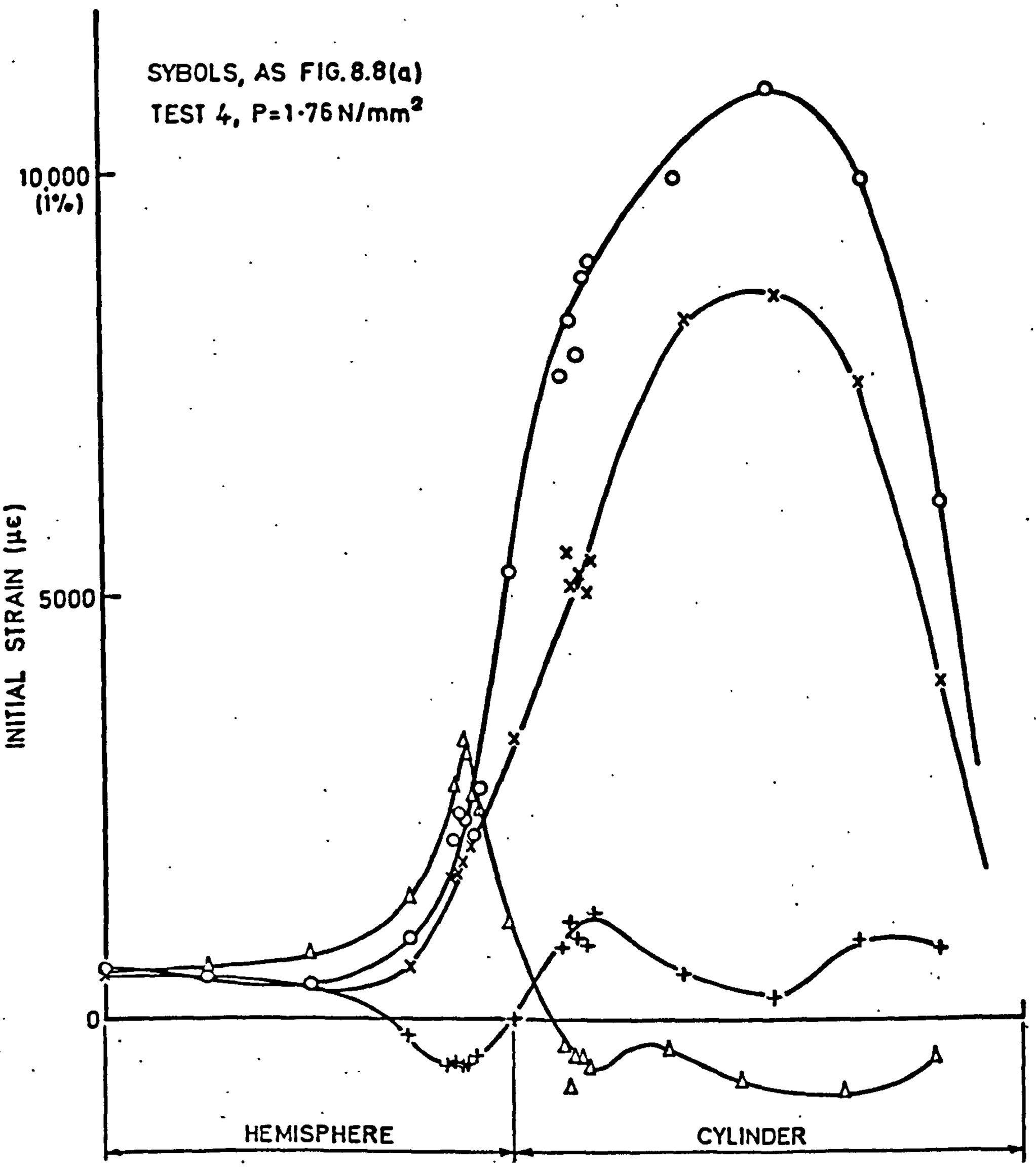

FIG.8.8(b) INITIAL STRAIN DISTRIBUTIONS. (P10)

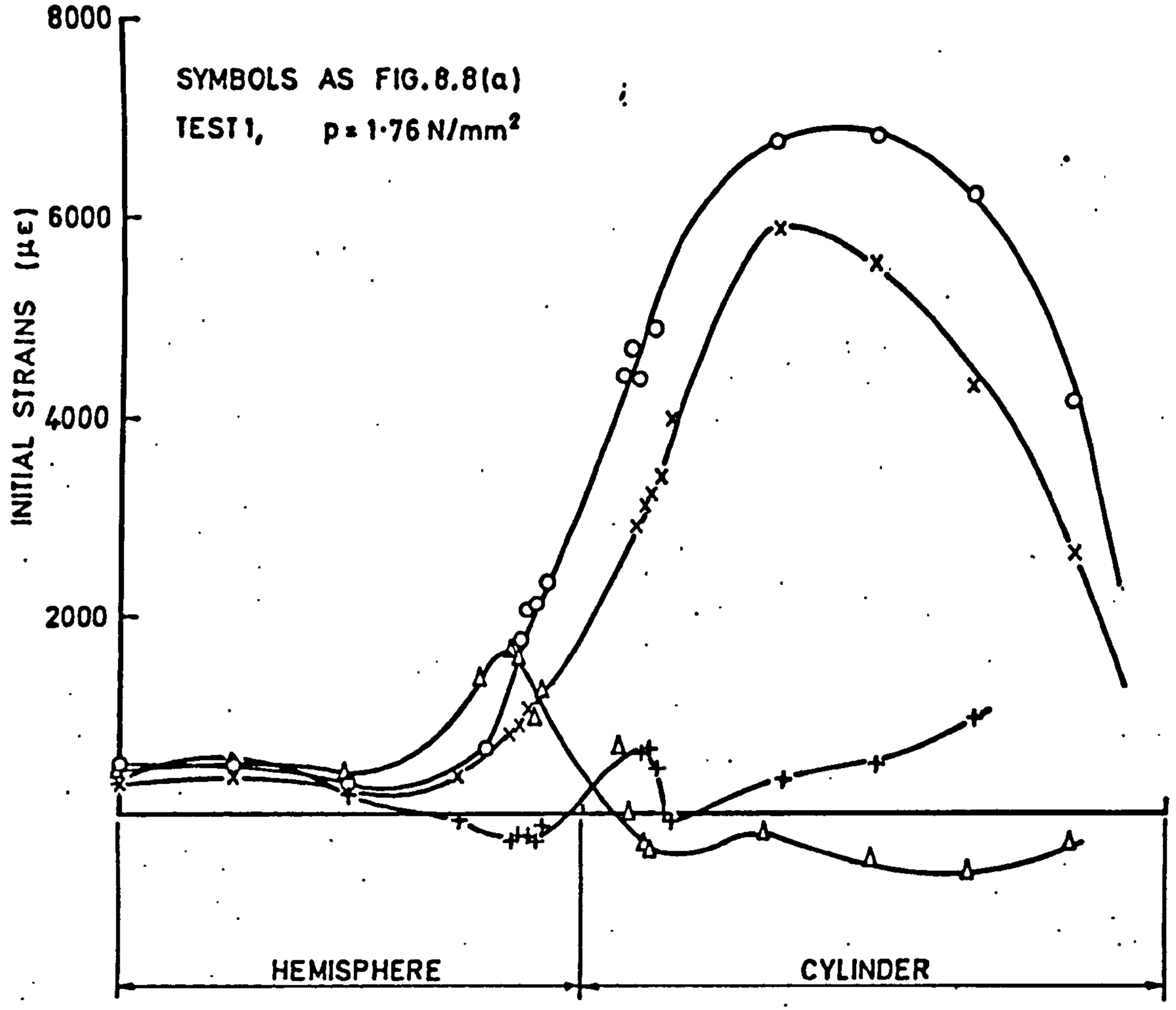

FIG. 8.8(c) INITIAL STRAIN DISTRIBUTIONS (P16)

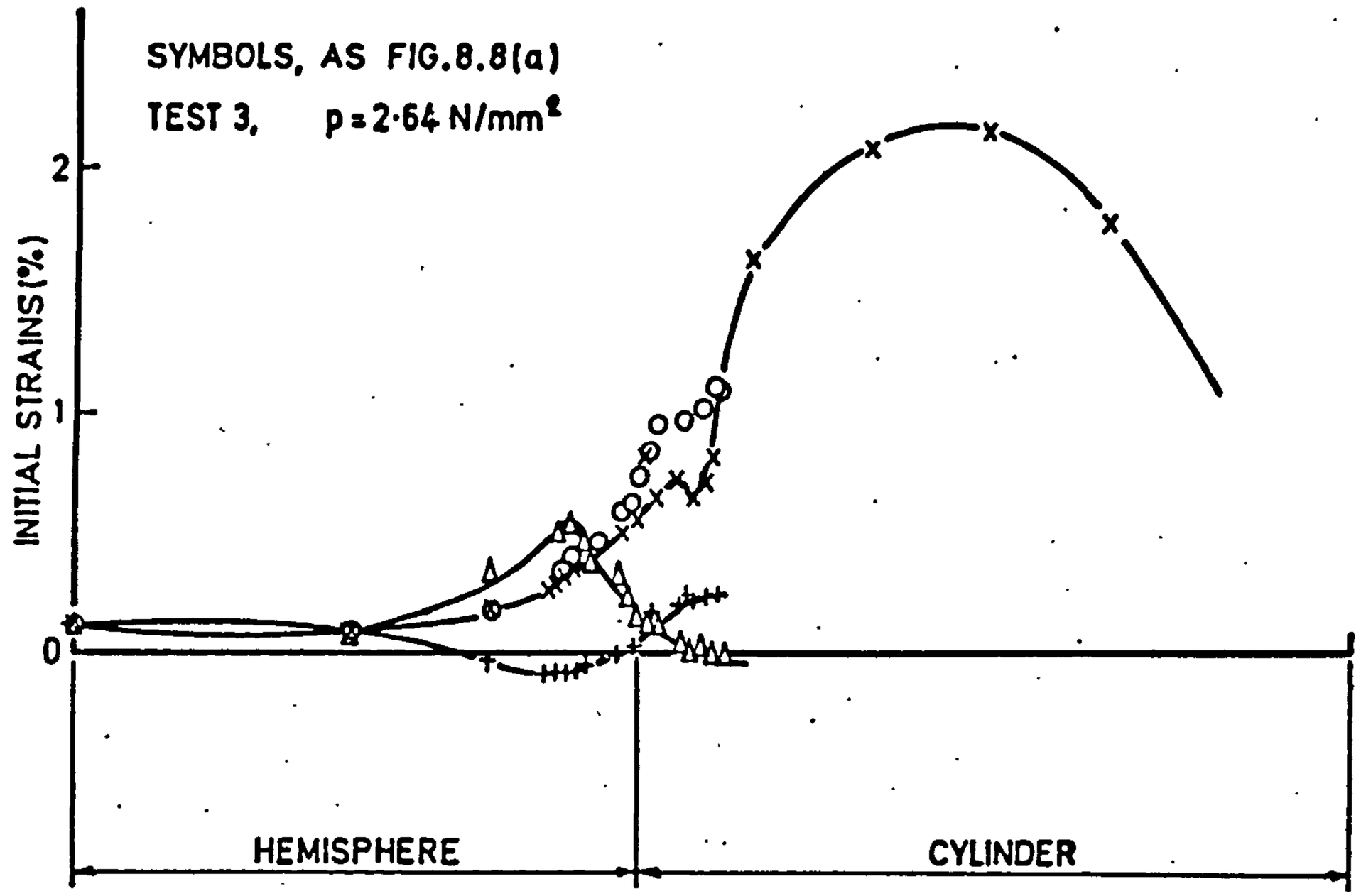

FIG. 8.8(d) INITIAL STRAIN DISTRIBUTIONS (P12)

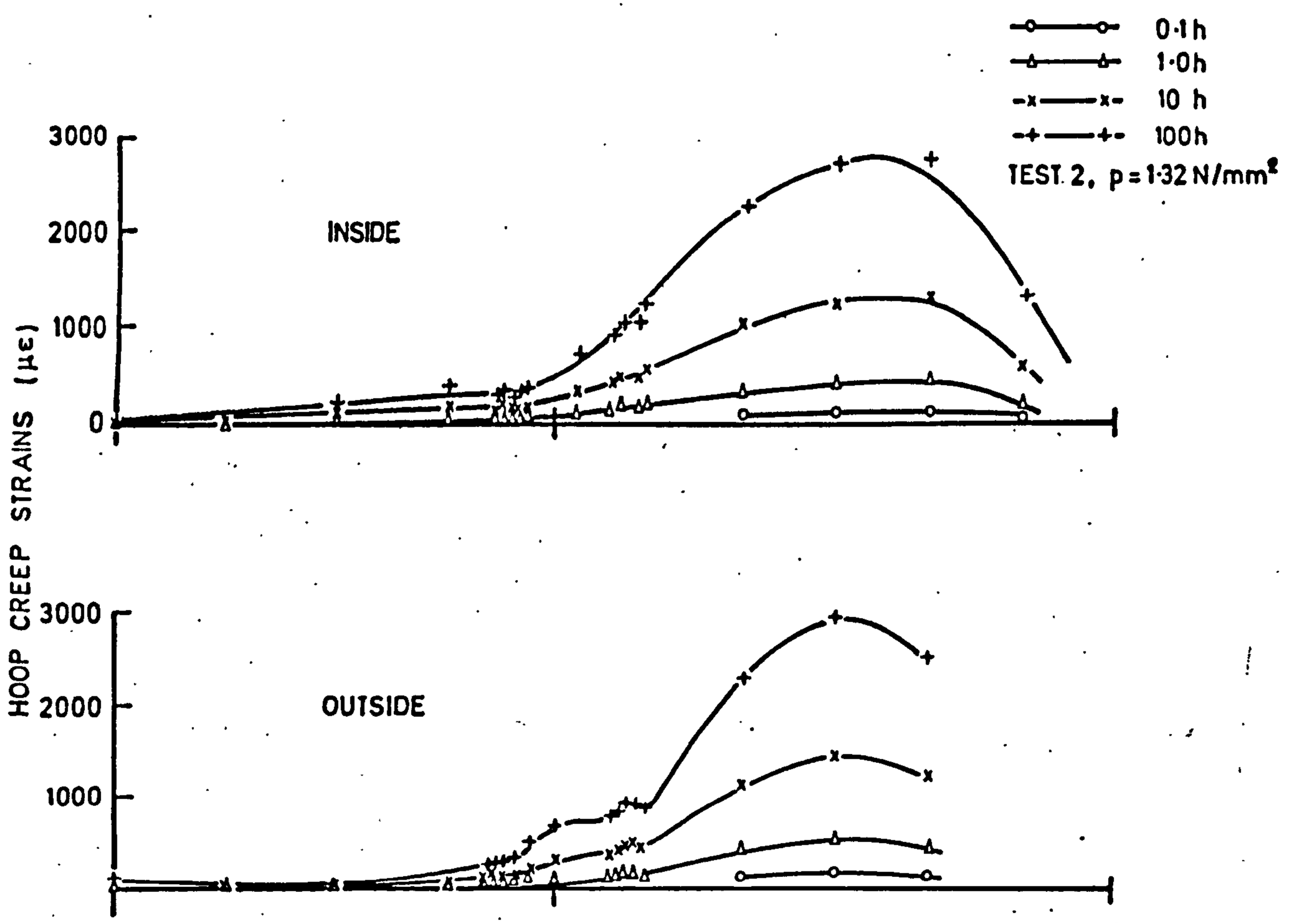

FIG.8.9(a) HOOP CREEP STRAIN DISTRIBUTIONS (P14)

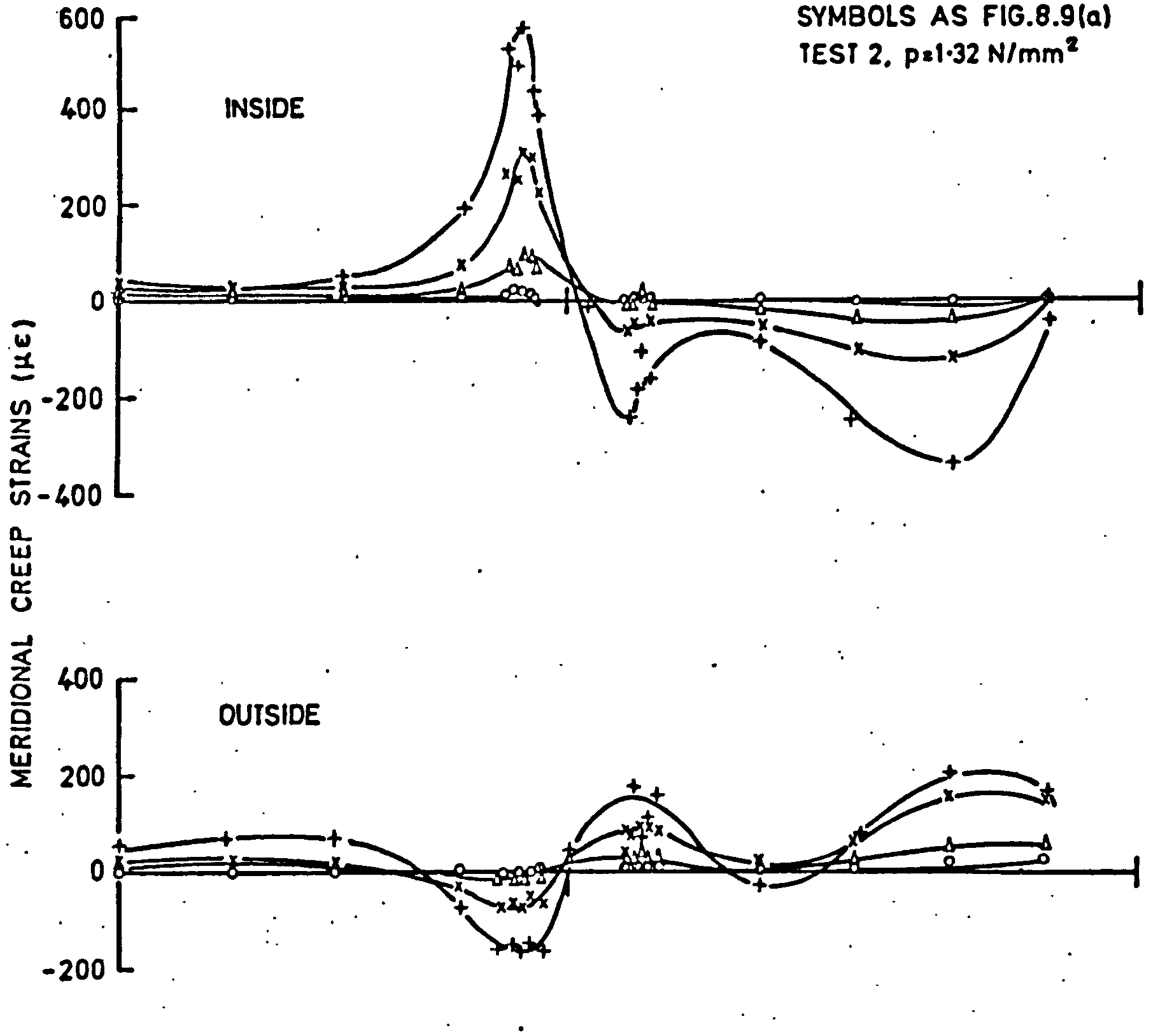

FIG. 8.9(b) MERIDIONAL CREEP STRAIN DISTRIBUTIONS (P 14)

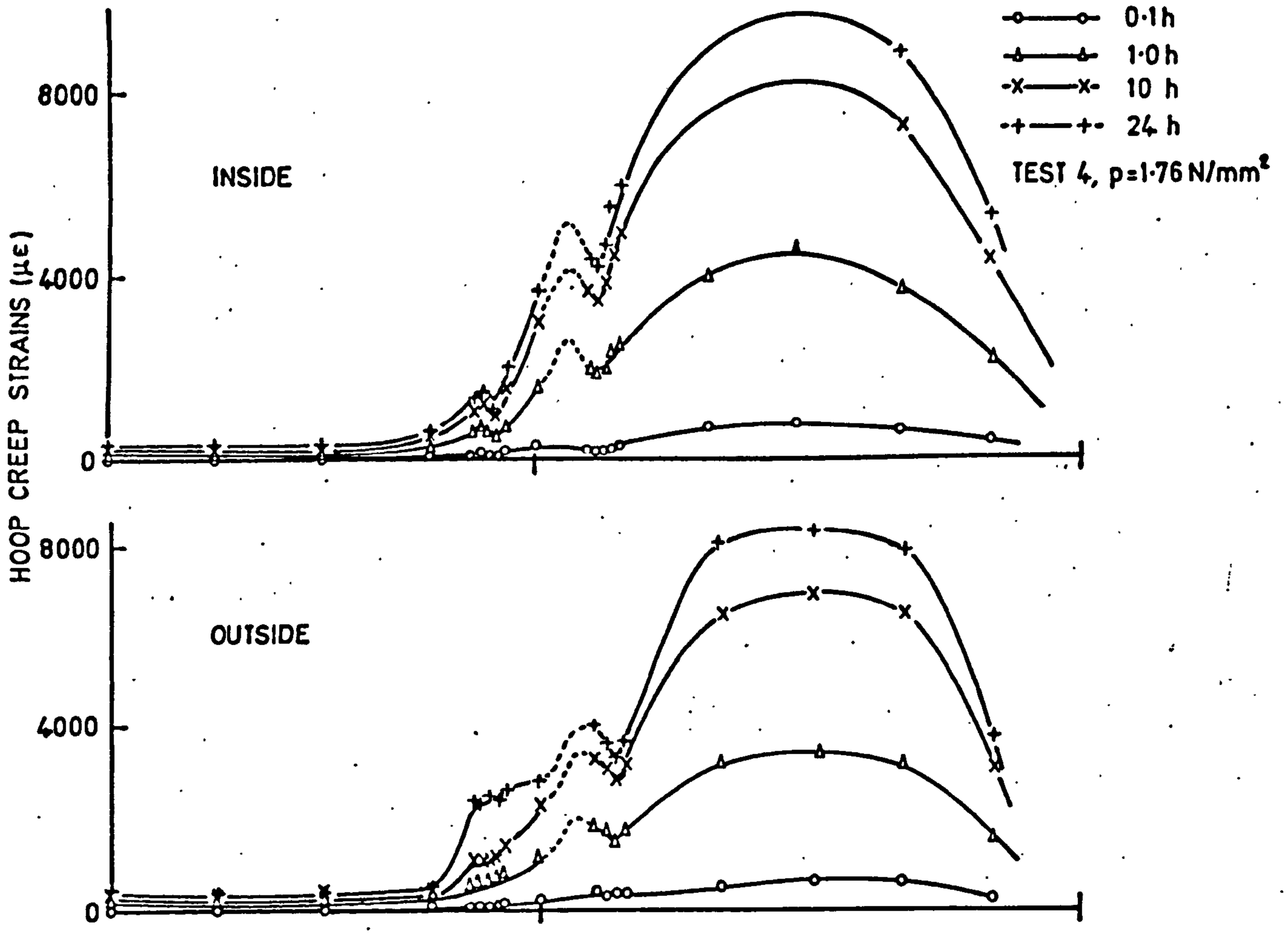

FIG. 8.9(c) HOOP CREEP STRAIN DISTRIBUTIONS (P10)

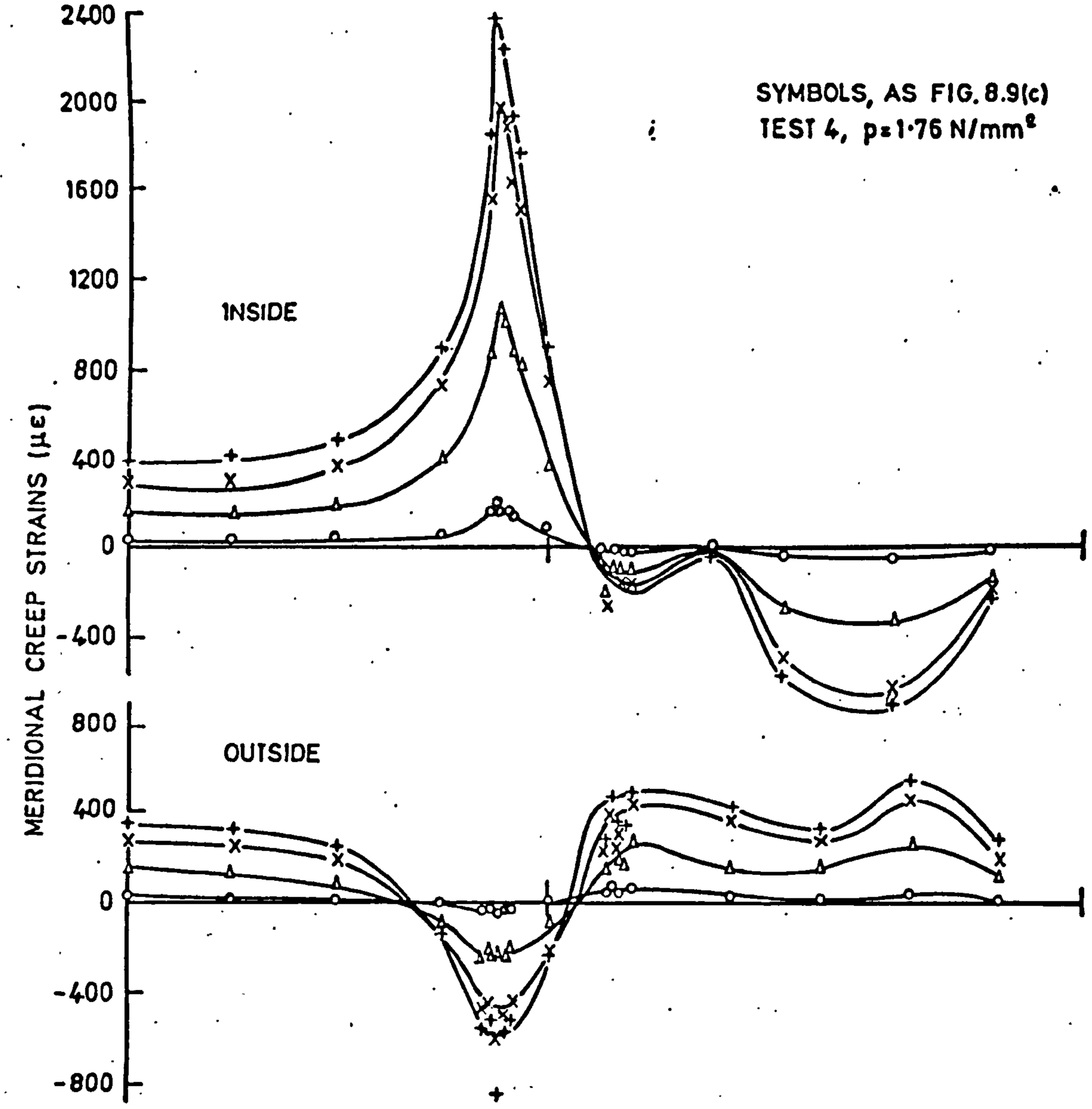

SYMBOLS, AS FIG. 8.9(c)
TEST 4, $p = 1{\cdot}76\ N/mm^2$

FIG. 8.9(d) MERIDIONAL CREEP STRAIN DISTRIBUTIONS (P10)

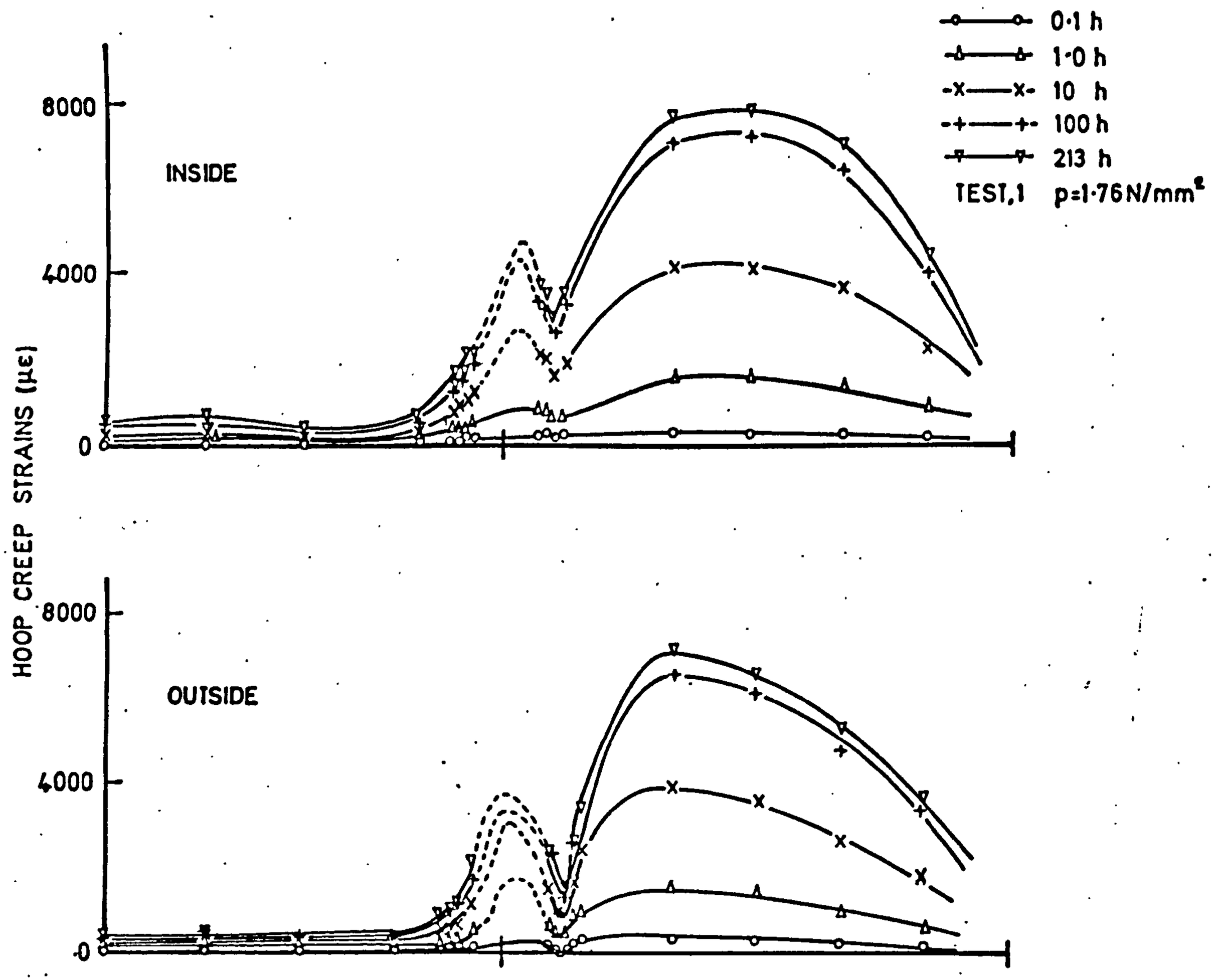

FIG.8.9(e) HOOP CREEP STRAIN DISTRIBUTIONS (P16)

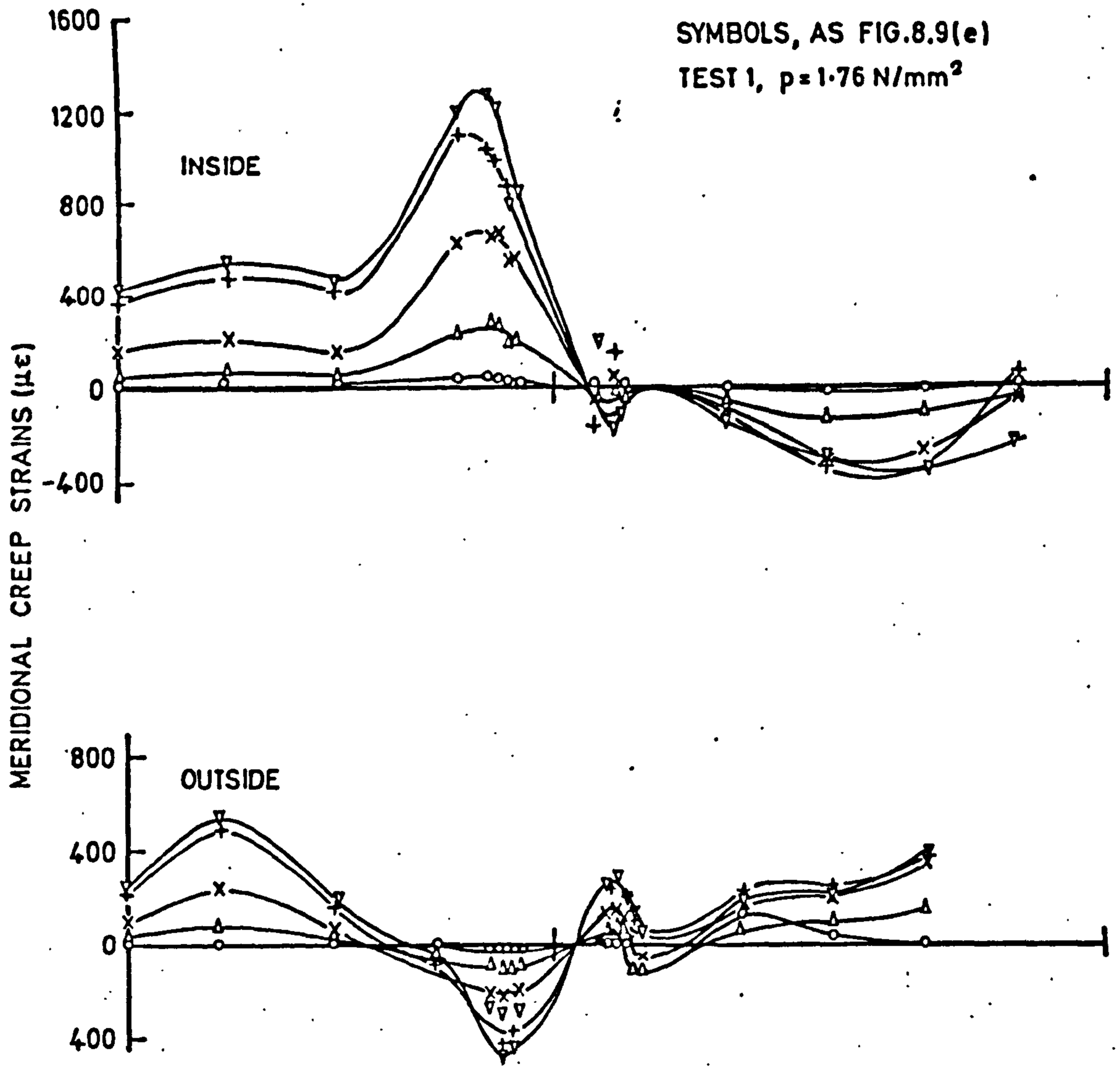

FIG.8.9(f) MERIDIONAL CREEP STRAIN DISTRIBUTIONS (P16)

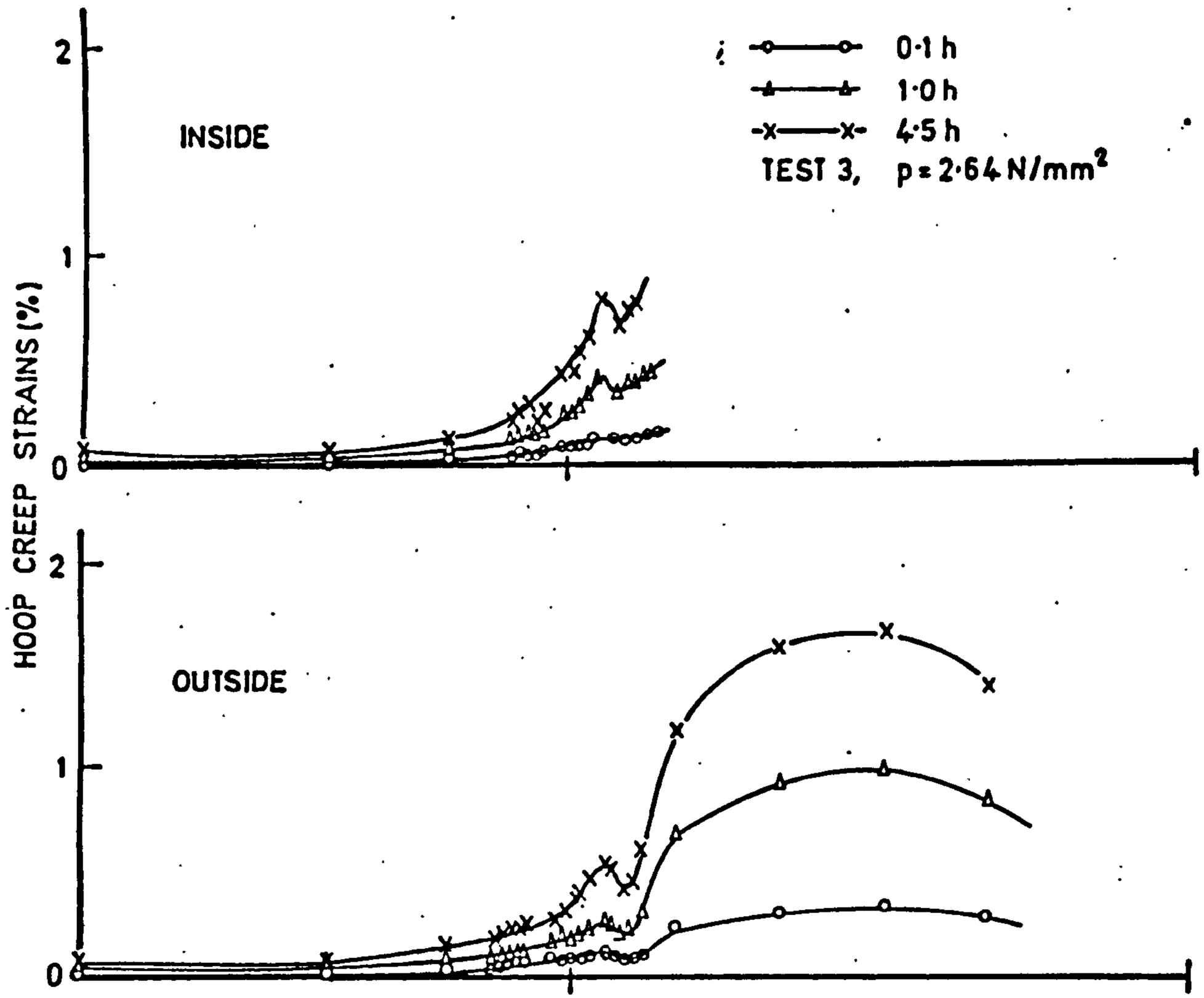

FIG.8.9(g) HOOP CREEP STRAIN DISTRIBUTIONS (P12)

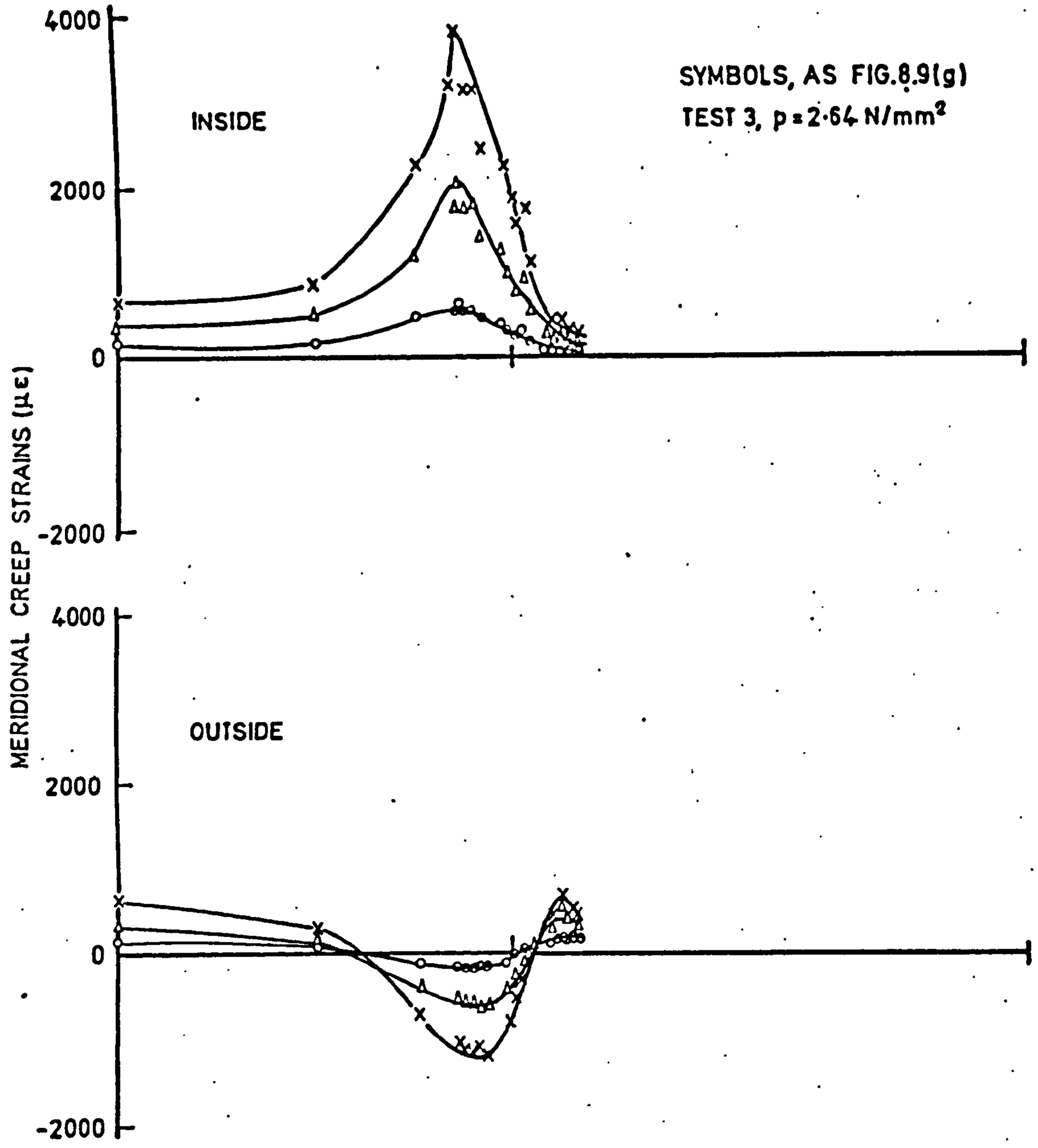

FIG.8.9(h) MERIDIONAL CREEP STRAIN DISTRIBUTIONS (P12)

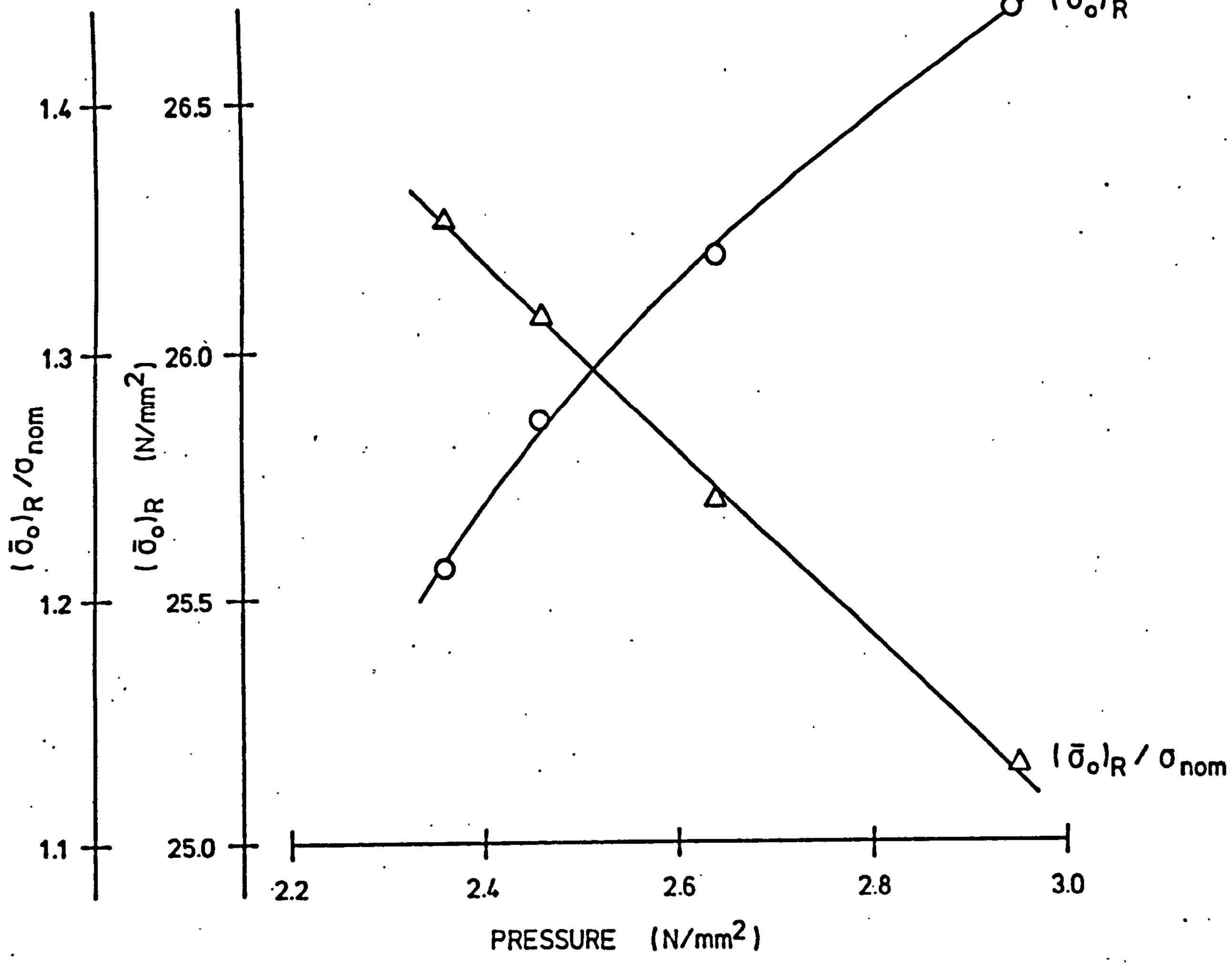

FIG. 8.10 PRESSURE VESSELS RUPTURE DATA

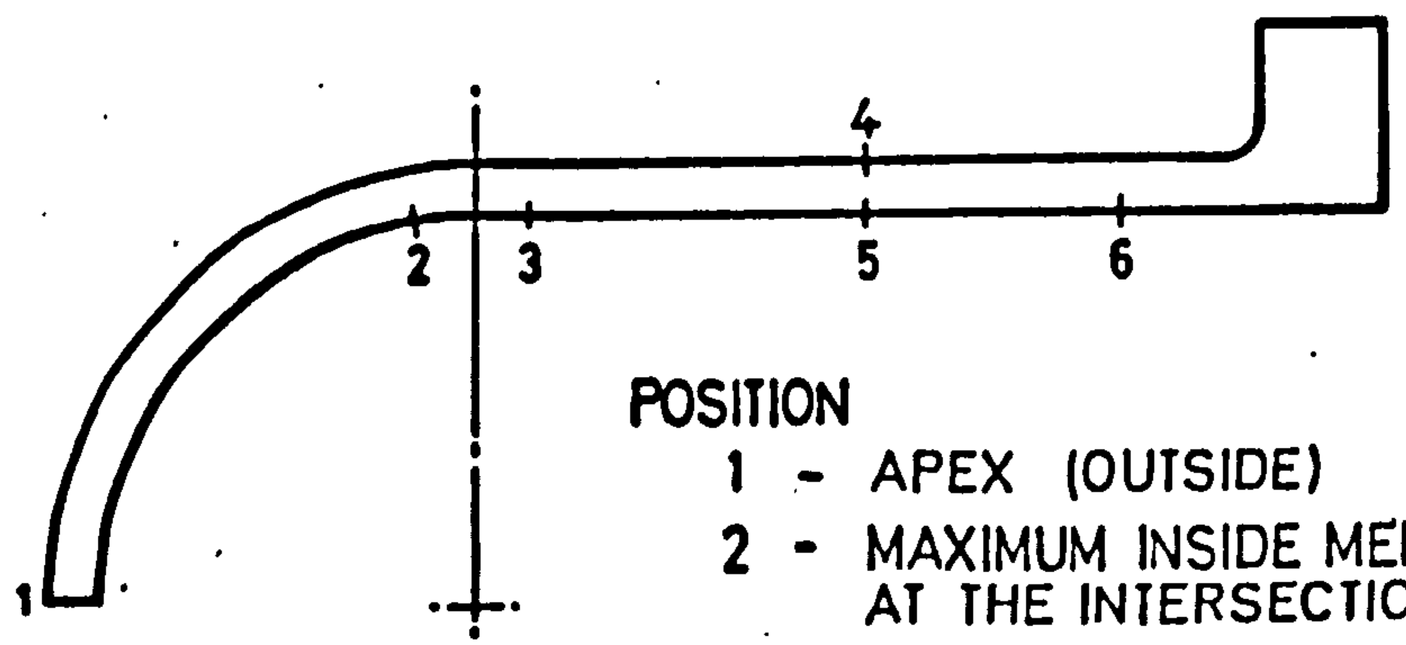

POSITION

1 - APEX (OUTSIDE)

2 - MAXIMUM INSIDE MERDIONAL STRAIN AT THE INTERSECTION.

3 - MINIMUM INSIDE MERIDIONAL STRAIN AT THE INTERSECTION.

4 - MID-CYLINDER (OUTSIDE)

5 - MID-CYLINDER (INSIDE)

6 - 25mm FROM FLANGE (INSIDE)

FIG.8.11 POSITIONS FOR THE REFERENCE STRESS PREDICTIONS.

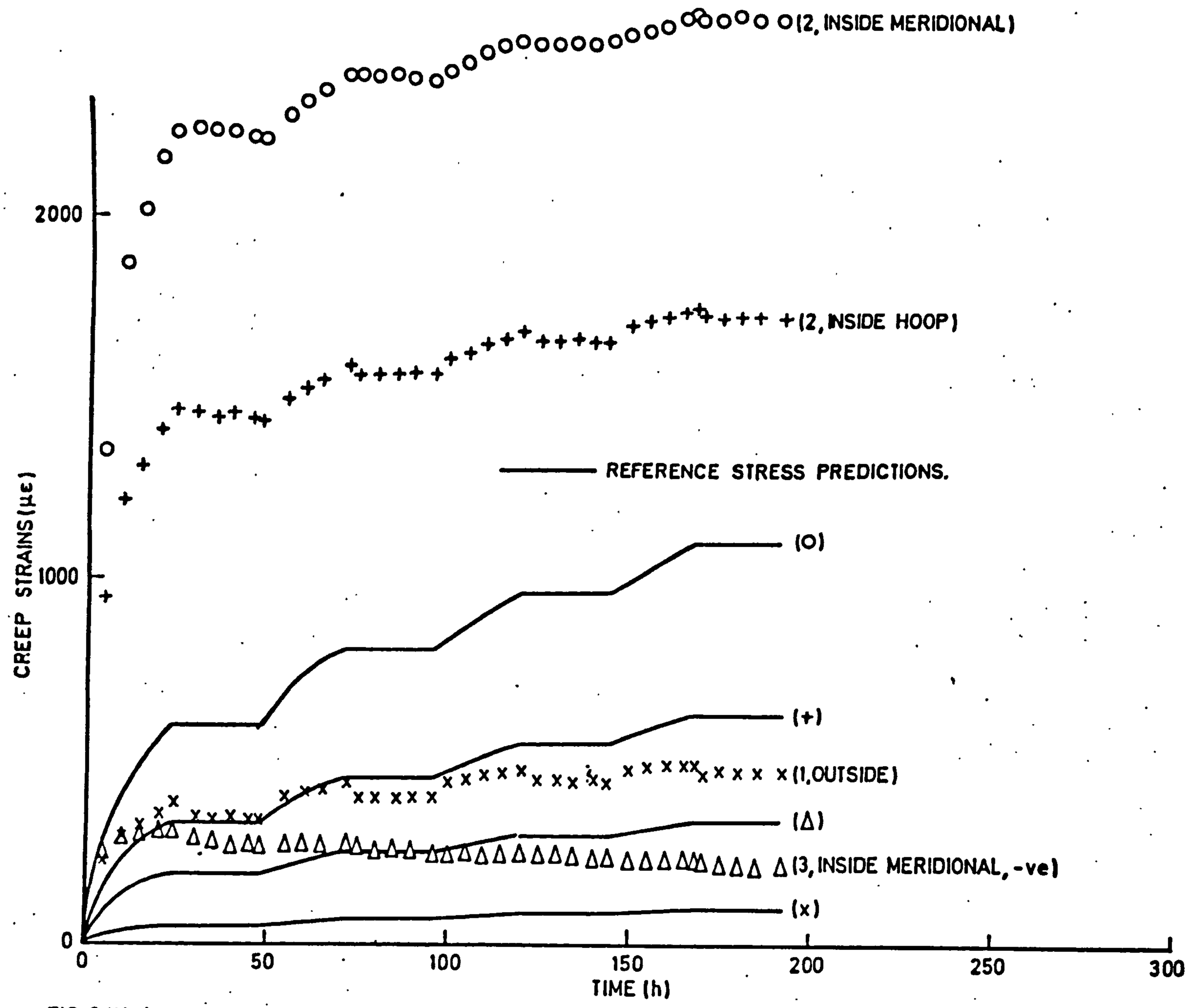

FIG. 8.12(a) CREEP STRAINS FOR P10 (POSITIONS SHOWN ON FIG. 8.10)

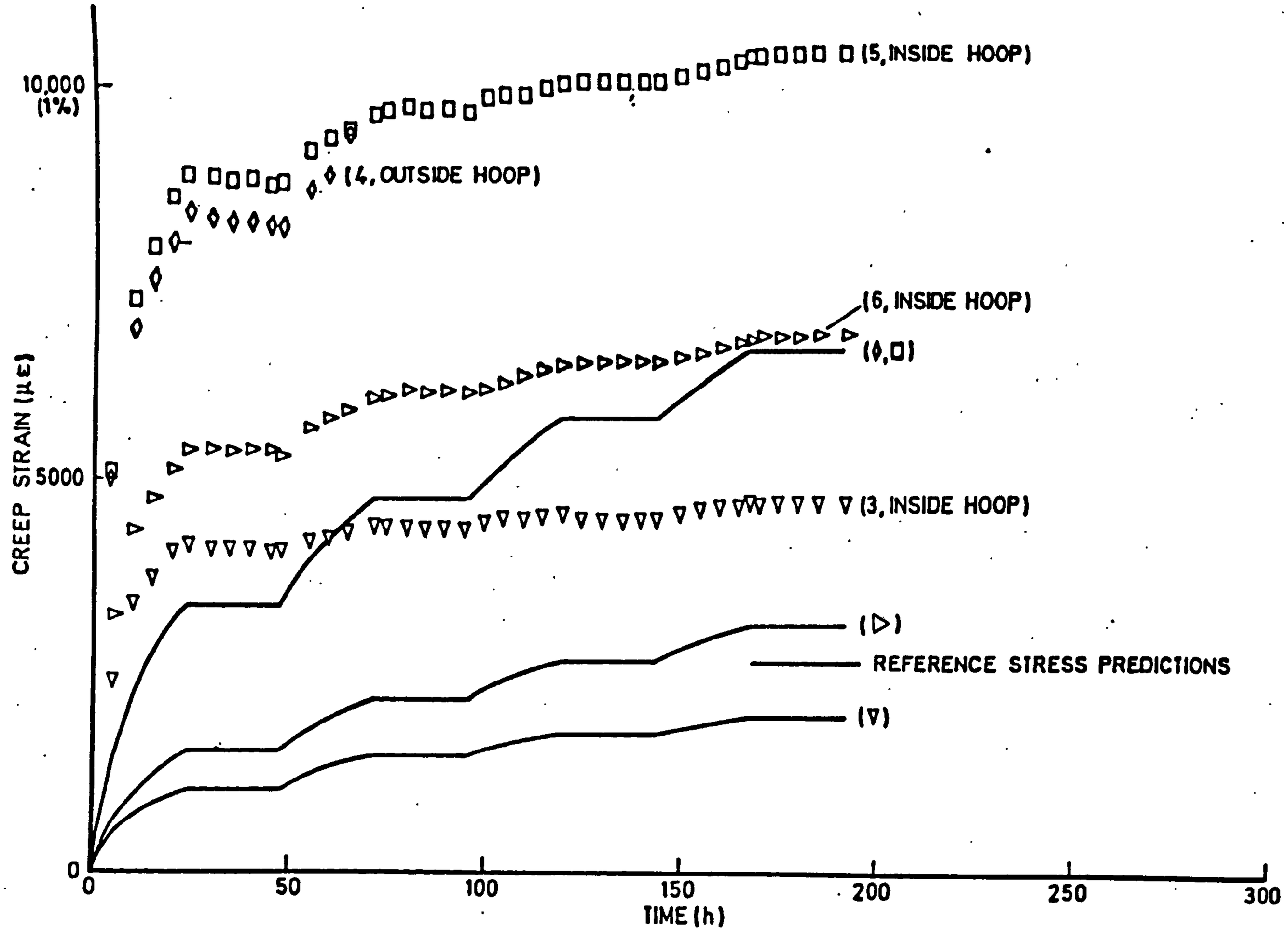

FIG. 8.12(b) . CREEP STRAINS FOR P10 (POSITIONS SHOWN IN FIG. 8.10)

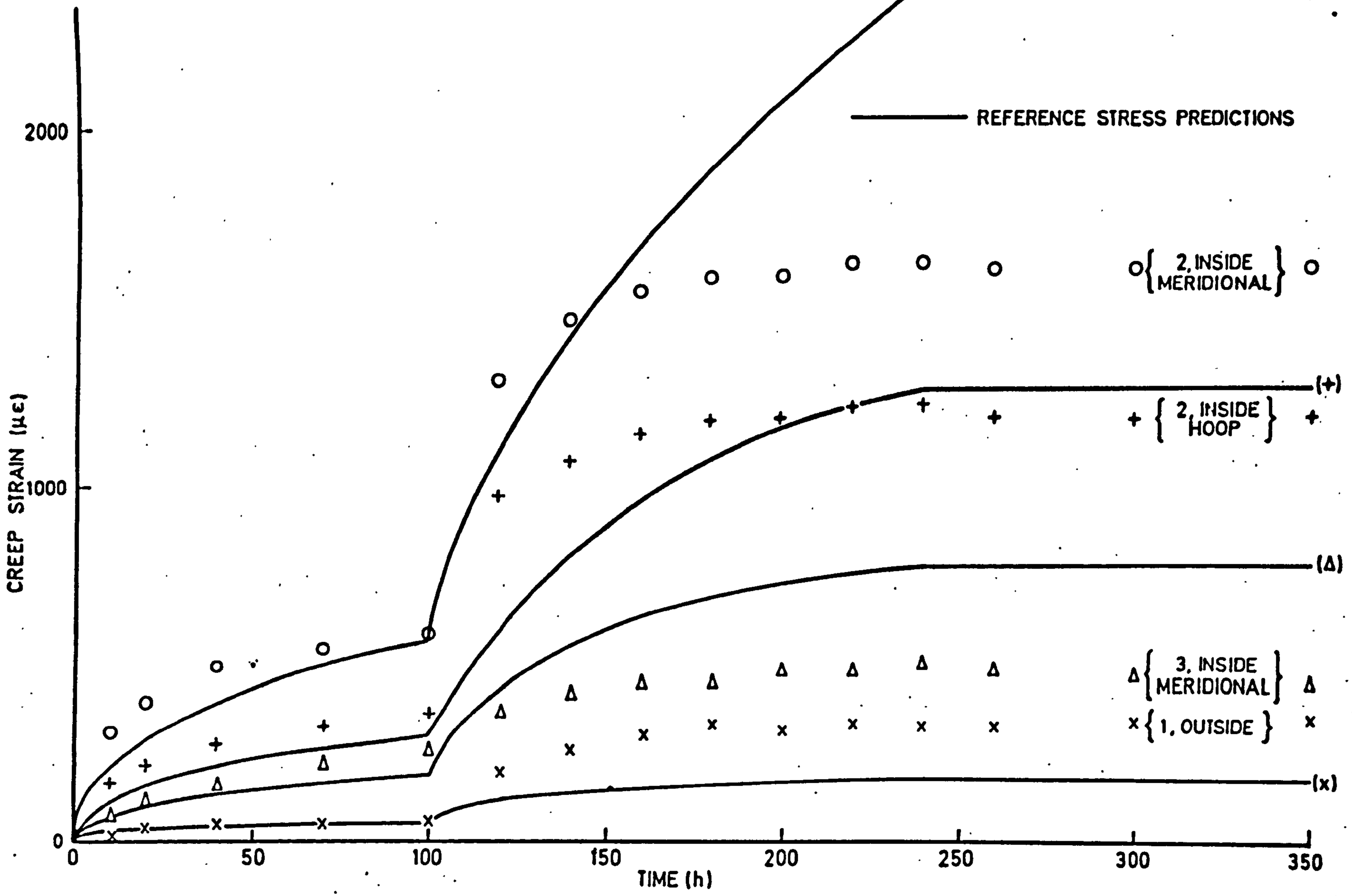

FIG. 8.12(c) CREEP STRAINS FOR P14 (POSITIONS SHOWN IN FIG. 8.10

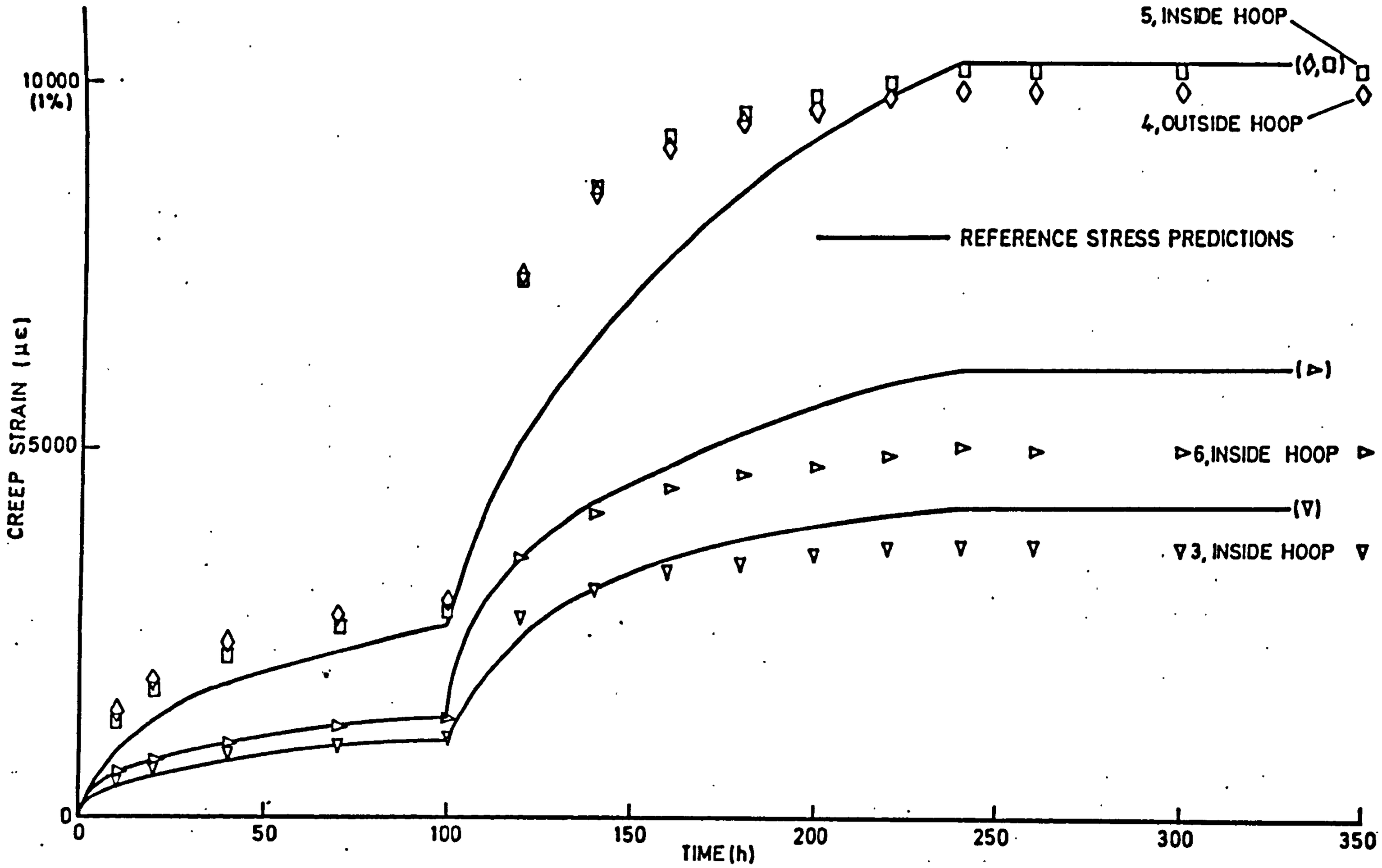

FIG.8.12(d) CREEP STRAINS FOR P14 (POSITIONS SHOWN IN FIG.8.10)

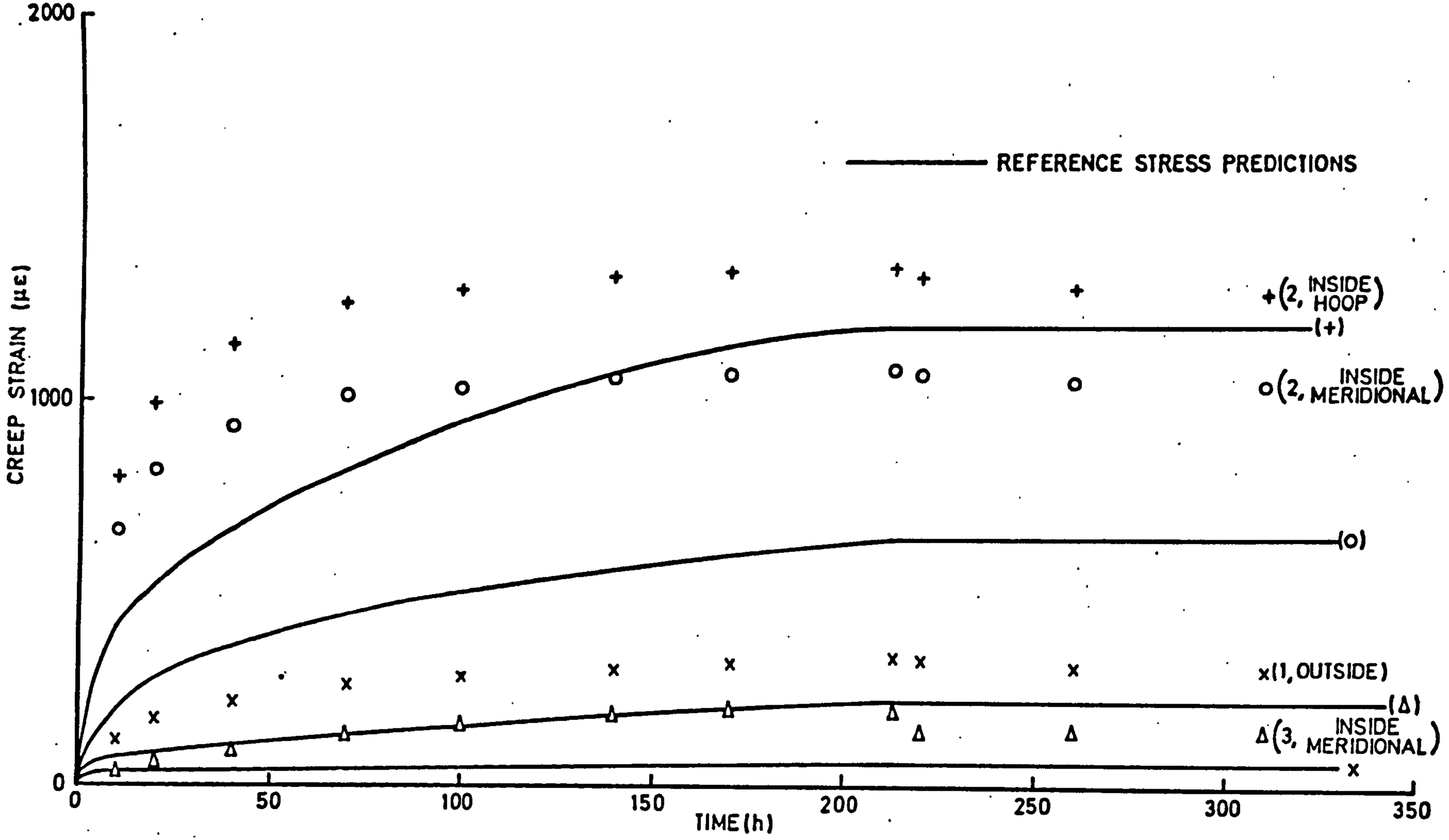

FIG. 8.12(e) CREEP STRAINS FOR P16 (POSITIONS SHOWN IN FIG. 8.10)

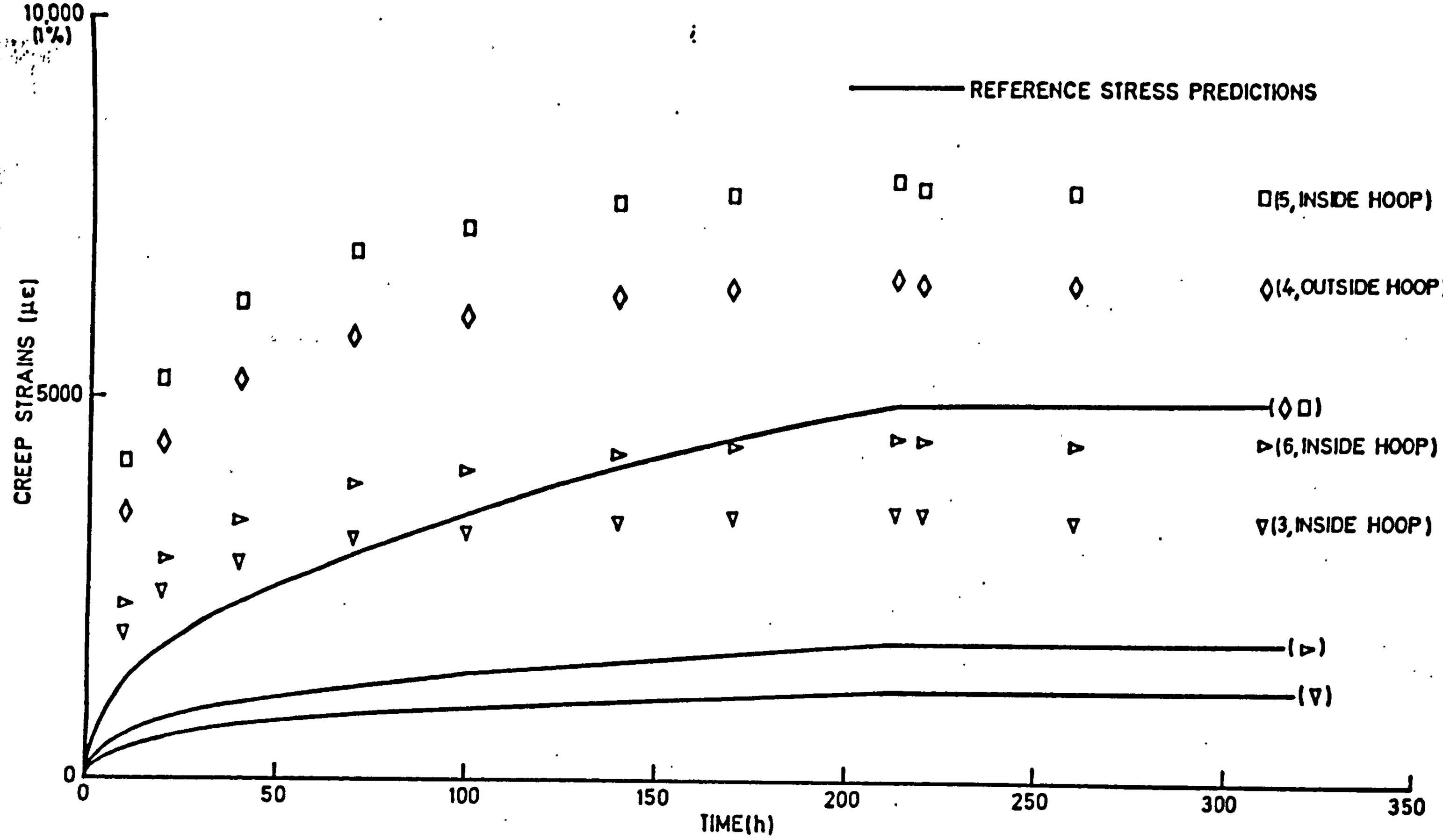

FIG.8.12(f) CREEP STRAINS FOR P16 (POSITIONS SHOWN IN FIG.8.10)

CHAPTER 9

9. DISCUSSION

9.1 Introduction

Various methods of creep analysis are outlined in chapter 2, one of the most promising being the Reference Stress method. In chapter 3, an experimental method of obtaining Reference Stresses from tests of models made of a creeping model material is described. The production of lead-antimony-arsenic alloy models suitable for such tests is described in chapter 4 and the uniaxial calibration of this material is described in chapter 5. Tests performed on some simple components with one dimensions stress systems (beams in pure bending and tip loaded cantilevers) were used in conjunction with uniaxial data to obtain experimental Reference Stresses and these were compared with theoretically determined Reference Stresses in chapter 6. Chapter 7 describes biaxial tests performed on the model material. In chapter 8, the experimental Reference Stress method used for the simple components of chapter 6, was used to obtain Reference Stresses at various positions in a more complex component, namely a cylindrical pressure vessel with a hemispherical end closure.

9.2 Theoretical ideas

Previously, Reference Stresses have been obtained for some simple components under simple loading conditions by analytical and numerical methods (22), (36), (37), (39), (40). By using the finite element method, it may be possible to extend the numerical methods of obtaining Reference Stresses to more complex components and loadings. However, numerical calculations are expensive in both development and computer

time. As an alternative to these numerical methods, approximate Reference Stresses (42) based upon limit analysis have been used, but this method does not account for the possibility of there being different Reference Stresses for different positions and modes of deformation in a component.

The experimental method of obtaining Reference Stresses from tests of model components is proposed as an alternative to the numerical methods and the approximate method.

Penny and Marriott (5) showed that the Reference Stress is the stress for which the material uniaxial data and the initial and stationary creep deformations satisfy the relationship

$$\frac{\phi_{sc}}{\phi_i} = \frac{\bar{\varepsilon}_{co}}{\bar{\varepsilon}_{io}} \qquad (9.1)$$

It has been shown that this relationship is only strictly applicable if the material behaviour laws for both initial deformations and creep deformations are of similar form. Creep and plastic deformations of materials are generally incompressible but for most materials the initial elastic deformation is not incompressible. The important deformations of components with one-dimensional stress systems are those which are not influenced by the material compressibility. Thus equation 9.1 is valid for components whose material is initially incompressible and for the important deformations of components with one-dimensional stress systems.

Most materials are initially compressible and it has been shown that the stationary creep deformation of a component (or model) may be related to the initial deformation of a model made from an incompressible material and the uniaxial data for the two materials at the Reference Stress. The relationship is:

$$\beta_{AL} \cdot \frac{(\phi_{sc})_L}{(\phi_i)_A} = \frac{(\bar{\varepsilon}_{co})_L}{(\bar{\varepsilon}_{io})_A} \qquad (9.2)$$

where L and A refer to the creep and initially incompressible materials respectively. Equation 9.2 is more general than equation 9.1 because it relates the deformations of two components and their material properties. If the material L is initially incompressible or the component has a one-dimensional stress system, then A can be replaced by L in equation 9.2.

Equations 9.1 and 9.2 may be used to determine Reference Stresses from experimental results. Alternatively they may be used to predict the stationary creep deformation of a component. The advantage of the Reference Stress approach for the prediction of a prototype deformation is that the uniaxial data of the prototype material at the Reference Stress only is required.

The Reference Stresses for stationary creep and plasticity are the same and thus may be used to predict plastic deformations.

Since Reference Stresses are insensitive to material behaviour laws, the choice of model materials is one of convenience. Araldite at a temperature above the stress freezing temperature and a chill cast antimony-arsenic alloy of lead (nominally 1.6% Sb, 0.16% As) were chosen as the two model materials for the work described in this thesis.

9.3 Experimental equipment

The casting procedure developed for the 1.6% Sb, 0.16% As lead alloy allowed uniform grained castings to be produced. For the Þ castings and for the volumes of interest in the KK castings, the grain density was found to be between 2 and 7 grains per mm. Low strain creep tests (less than 1% in 200 h) of specimens from different positions within the castings, having different grain densities (2 to

7 grains per mm), indicated that grain size had little effect on creep properties. It was found that the greater the amount of antimony present in the castings, the less critical were the casting conditions (i.e. mould and melt temperatures). The mould and melt temperatures and the cooling rate of the casting after pouring could be repeated so as to produce nominally identical castings. However, adequate control over the alloying composition was found to be difficult, Table 4.4 shows the variations in composition. It was found that creep properties were dependent upon the alloy composition.

The uniaxial test rigs are capable of applying axial loads to within 0.03 mm. of the axis of the gauge length which, for specimens with minimum cross-sectional dimensions of 8.9 mm. reduces the bending effect to negligible proportions.

Tests performed with the combined internal pressure and torsion rig on an aluminium thin cylinder showed that a uniform stress distribution can be produced in the central portion of the thin cylinders. The aluminium thin cylinder tests also showed that the torsion system did not apply any measurable (using electrical resistance strain gauges) bending. The results of the biaxial lead alloy creep tests proved the biaxial rig to be capable of both creep and creep rupture testing.

For the beams in pure bending, electrical resistance strain gauges were used to measure the initial and creep strains. The initial and creep strains of the pressure vessels and thin cylinders up to 2% were also obtained from electrical resistance strain gauges. For strains greater than 2% in the pressure vessels, which only occurred near the centre of the cylinder, and for the hoop strains in the thin cylinders, linear capacitance transducers were used to measure changes in diameter from which hoop strains were deduced. The tip deflections

of the cantilevers were also measured using linear capacitance transducers. The linear capacitance transducer and electrical resistance strain gauge methods of measurement are both very accurate, depending mainly upon the stability of the voltage supply and accuracy of the gauge factor. Therefore, errors in deformation measurements due to the equipment were negligible compared with material property scatter.

The loads for the uniaxial specimens, beams in pure bending and tip loaded cantilevers and the torsion load for the thin cylinders were all produced by means of dead weights. The accuracy of the weights was within $\pm \frac{1}{4}\%$, therefore even for high stress tests where the tangent n value (slope of the $\log \varepsilon_c$ - $\log \sigma$ plot) is large, the errors in creep strains due to the loading is small compared with the material property scatter. Stepped loading was achieved by the smooth application or removal of weights, which because of the small loads used, could be done manually.

The pressure loading of the thin cylinder specimens and the pressure vessels was achieved by the application of a dead load to a seal-less piston supplied by a continuously running pump. The weights used were accurate to within $\pm \frac{1}{4}\%$, therefore the pressure loading should be accurate to within $\pm \frac{1}{4}\%$. However, variations in supply pressure and friction in the seal-less piston, caused pressure variations. The pressure was recorded at intervals during the tests and up until rupture of the thin cylinders and pressure vessels, when the leakage caused a reduction in pressure, the pressure variation was found to be within $\pm$ 1%. Because this pressure variation was not consistently above or below that set by the dead weight loads it is not possible to estimate whether the measured creep strains are above or below those which would have been obtained with constant pressure tests. The greatest error would be caused if the pressure were 1% too high during the whole of the test period (N.B. this did not actually happen). However, even if these conditions were to

exist for a high load test (i.e. when the tangent n-value is large), the error in creep strain is only about 10%, which is of the same order of magnitude as the scatter of material data within a single casting and is much less than the casting to casting scatter obtained.

9.4 Material Properties

Because Reference Stresses are insensitive to material properties, the model material may be chosen to suit experimental convenience. Lead-antimony-arsenic alloys can be cast in the laboratory and creep at room temperature under relatively small stresses, therefore they are a good choice as model materials. The actual antimony and arsenic compositions (1.6% Sb, 0.16% As), were decided upon after a series of tests on uniaxial specimens with different compositions showed that this alloy had similar ductility properties to those of some steels at elevated temperature. Therefore, the material may be suitable for rupture model tests.

It was found that grain sizes varied within castings (the largest grains being found near the pour position) but creep tests did not indicate any large variation in properties due to grain size. The implication of this is that the major contribution to creep is due to the deformation of grains rather than grain boundary sliding. Also, it was found to be very difficult to accurately control the alloying composition.and it was found that the creep properties of the material are dependent upon the alloying composition.

An attempt at fitting a uniaxial creep law to the data showed that a simple power function of stress was not adequate and that seperable stress and time functions did not exist. The best fit to the data was found to be given by a law of the form

$$\varepsilon_c = A \sinh \left[\frac{\sigma}{B}\right] t^{m(\sigma)}$$

where $m(\sigma) = a + b\sigma + c\sigma^2$.

From stepped load tests, the material was found to closely follow a strain hardening law.

The results of the biaxial tests showed that on the whole the von Mises formulation of the creep law (equations 2.17(a) and 2.17(b)) gives accurate predictions. However in the tensile-tensile quadrant (i.e. when $\sigma_{kk}/\sigma_{vm}^* > 1$), the predictions greatly underestimate the creep strains.

The uniaxial creep rupture test results (shown in Fig.23), show that at high stress the ductility is much greater than the ductility at lower stresses. Also, scatter in rupture times appears to increase as the rupture time increases (i.e. at relatively low stresses). On the basis of only three biaxial tests of thin cylinders, one under internal pressure and two in pure torsion, the rupture criterion appears to fall somewhere between the maximum shear stress criterion and the von Mises effective stress criterion.

9.5 Results of component tests

Using the uniaxial data in conjunction with the measured deformations of components, a graphical method based on equations 9.1 and 9.2 was developed which allowed experimental Reference Stresses and 'X'-values to be obtained, where stationary creep deformations are given by $\phi_{sc} = X\bar{\varepsilon}_{co}$.

For simple components with analytical solutions for Reference Stresses and 'X'-values (i.e. beams in pure bending and tip loaded cantilevers), accurate values of $\bar{\sigma}_o$ and X were obtained. An assessment of the accuray of the experimentally determined Reference Stresses for these simple components was made by comparing predictions based on these Reference Stresses with analytical predictions for materials having simple creep laws (i.e. $\varepsilon_c = \sigma^n \Gamma(t)$). This showed that

for n values up to 5, the Reference Stress predictions fell within 0.6 and 2 times the analytical predictions, which, for design purposes, would be adequate, because scatter of steel data is usually greater than this.

The measured values of redistribution deformation $\Delta\phi$, were expected to be smaller than the theoretical estimates (which are based on an initial elastic stress distribution); because of initial plasticity. This is not the case for most of the test results given in Tables 6.1 and 6.2. However, the experimental value of $\Delta\phi$ are close enough to the theoretically determined values of $\Delta\phi$ to be confident in using the experimental values of $\Delta\phi$ to predict the order of magnitude of $\Delta\phi$ in prototype components.

The experimental determination of the redistribution time is difficult when $\Delta\phi$ is small; this accounts for the discrepancies at low loads for both pure bending and cantilever tests. The results for the other tests agree quite well except for the case of the beam in pure bending with very large initial plasticity.

From the results of the tests on these simple components made from a material which does not obey a simple creep law, it was concluded that Reference Stresses exist for components made of materials which obey more complex creep laws and that these Reference Stresses may be obtained experimentally from tests carried out on components which are made of materials which do not have simple creep laws.

The initial and creep strains were measured in cylindrical pressure vessels with hemispherical end closures. The strains obtained from one of the tests (P14) were used to obtain Reference Stresses and 'X'-values for the prediction of creep strains at various positions. The results showed that Reference Stresses vary with position. Analytical solutions which exist for cylinders and spheres under internal pressure compared favourably with the experimentally determined values of Reference Stresses and 'X'-values for the cylinder and apex of the sphere. For the statically

indeterminate positions in the pressure vessel (e.g. the cylinder to sphere intersection), theoretical Reference Stresses could not be obtained. Therefore, in order to assess the accuracy of these Reference Stresses and 'X'-values, obtained from the P14 pressure vessel, they were used to predict variable load deformations in the other pressure vessels (at different pressures). The accuracy of these predictions for both constant and variable loads were of the same order of magnitude as that for the simple components. Therefore, it was concluded that the experimental Reference Stress method is also applicable to more complex components under complex loading conditions.

9.6 Suggestions for further work

The experimental Reference Stress method has been shown to be suitable for the prediction of deformations of isothermal steadily and unsteadily loaded structures. Many components do not operate under isothermal conditions. It is suggested that the experimental Reference Stress technique should be developed to predict Reference Stresses for components to which thermal gradients are also applied.

CHAPTER 10

10. SUMMARY OF CONCLUSIONS

1. Reference Stresses can be determined experimentally for components with one dimensional stress systems by tests of a single model which creeps, together with the uniaxial properties of the model material.

2. Reference Stresses can be determined experimentally for components with complex stress systems by tests of two models, one of which deforms initially at constant volume and the other model creeps, together with the uniaxial properties of the two materials. If the creeping model also deforms initially at constant volume, then the one model method may be used.

3. Simple graphical methods can be used to obtain experimental Reference Stresses.

4. The experimental Reference Stress method also yields the redistribution deformation, $\Delta\phi$, and the redistribution time, t_{red}.

5. Reference Stresses vary with position and are different for each mode of deformation at each position.

6. Experimental Reference Stresses obtained from the beam and cantilever tests showed that, for values of stress exponent up to 5, the predictions are between 0.6 and 2 times the prototype deformations. The predictions of prototype deformations obtained from tests of pressure vessels were between about 0.5 and 1 times the actual values. The above predictions do not take scatter of prototype material into account.

7. Experimental Reference Stresses and "X'- Values can be obtained from tests of models made of materials which obey complex creep

laws. These Reference Stresses and 'X'-values agree closely with analytical solutions based upon creep laws with seperable stress and time functions with a simple power stress function. This confirms the insensitivity of Reference Stresses to material creep properties.

8. Sim's approximate Reference Stress, $\frac{P\sigma_y}{Pult}$, does not account for variation with position and mode of deformation and can greatly overestimate creep deformations.

9. For a nominally 1.6% Sb, 0.16% As lead alloy (which has room temperature ductility properties similar to those of structural steels at elevated temperature), the technique of chill casting small grained, homogeneous model components was developed.

10. The uniaxial creep data showed that the creep model material does not have separable stress and time functions with a simple power stress function. A good fit to the data was obtained with a law of the form

$$\varepsilon_c = A \sinh \left[\frac{\sigma}{B}\right] t^{m(\sigma)}$$

where $m(\sigma) = a + b\sigma + c\sigma^2$.

11. The creep properties were found to be dependent upon antimony composition but were not found to be strongly dependent upon casting conditions and grain size.

12. The Prandtl-Reuss flow rule was found to be accurate for both initial plastic and creep strains.

13. The von Mises effective stress was found to give accurate biaxial creep predictions except at high values of hydrostatic stress (i.e. when $\sigma_{kk}/\sigma^*_{vm} > 1$), where the predictions underestimate creep strains.

14. The uniaxial and biaxial test rigs proved to be adequate for both creep and creep rupture testing.

15. The multiaxial creep rupture criterion appears to lie somewhere between the maximum shear stress criterion and the von Mises effective stress criterion.

ACKNOWLEDGEMENTS

The author wishes to thank Professor A. G. Smith, Head of the Department of Mechanical Engineering, for providing the facilities for this research. The author also wishes to thank Professor H. Fessler and Dr. J. J. Webster for their encouragement and guidance during the project.

The Science Research Council supported this work by awarding me a studentship.

The helpful assistance of the technicians of the Faculty of Applied Science is much appreciated, particularly B. Mynett, R. Pickard, S. Raines and B. K. Stockaj.

The steel data supplied by the British Steelmakers Creep Committee and Babcock and Wilcox was very useful.

Finally, the author wishes to thank Mrs. A. Fairless for typing this thesis.

References

1. Rotherham, L. "Creep of Metals". Inst. of P., 1951

2. Hoffmann, W. "Lead and Lead Alloys".

3. Finnie, I. and Heller, W.R. "Creep of Engineering Materials" McGraw-Hill, New York, 1959

4. Hult, J. "Creep of Engineering Structures" Blaisdell, Waltham, Mass., 1966

5. Penny, R.K. and Marriott, D.L. "Design for Creep" McGraw-Hill, Maidenhead, 1971

6. Dorn, J.E. "Some Fundamental Experiments on High Temperature Creep" J.Mech.Phys. Solids, 3, 1955

7. Larson, F.R. and Miller, J. "A Time-Temperature Relationship for Rupture and Creep Stresses" Trans. A.S.M.E., 174(No.5) July 1952

8. Graham, A. and Walles, K.F.A. "Relationships between Long- and Short-Time Creep and Tensile Properties of a Commercial Alloy" J. Iron and Steel Inst., 179, 1955

9. Johnson, A.E., Henderson, J and Khan, B "Complex Stress Creep, Relaxation and Fracture of Metallic Alloys" H.M.S.O. Edinburgh, 1962

10. Kachanov, L.M. "Rupture Time under Creep Conditions" Contrib. to Problems of Continuum Mechanics, Philadelphia, 1961

11. Hayhurst, D.R., Kelly, D.A., Leckie, F.A., Morrison, C.J., Ponter, A.R.S. and Williams, J.J. "Approximate Design Methods for Creeping Structures" I.Mech.E., Inst. conf. on creep and fatigue in elevated temp. applications, Philadelphia, 1973

12. Murphy, M.C. "Rating the Creep Behaviour of Heat-Resistant Steels for Steam Power Plant" Q.Metals Eng., Feb., 1973

13. Rabotnov, Y.N. "On the Equation of State of Creep" Proc. I.Mech.E., 1963-65, Vol.178, Pt.3A

14. Rabotnov, Y.N. "Some Problems of the Theory of Creep" N.A.C.A. Tech. Memo. 1353, 1948

15. Greenwood, G.W. "The Influence of Complex Stress on High Temperature Deformation Processes" Joint Metals Soc./I.O.P./I.Mech.E.Meeting, Prediction of Component Life at High Temperatures, May, 1975

16. Dyson, B.F. "The Inadequacy of Tensile Creep Data" Joint Metals Soc./I.O.P./I.Mech.E. Meeting, Prediction of Component Life at High Temperatures, May, 1975

17. Finnie, I. "An Experimental Study of Multiaxial Creep in Tubes" Proc.I.Mech.E., 1963-64, Vol.178, Pt.3A

18. Hayhurst, D.R. "Creep Rupture under Multi-Axial States of Stress" J.Mech.Phys. Solids, 20, 1972

19. Marriott, D.L. and Leckie, F.A. "Some Observations on the Deflections of Structures During Creep" Proc. I.Mech.E. 1963-64, Vol.178, Pt.3L

20. Frederick, C.O. and Lewis, D.J. "Primary Creep Deformation of Beams" Proc. I.Mech.E. 1963-64, Vol.178, Pt. 3L

21. Sim, R.G. "Plane Strain Creep Behaviour of Thick walled Cylinders" Inst. J.Mech.Sci., 13, 1971

22 Sim, R.G. "Reference Stress Concepts in the Analysis of Structures During Creep" Int. J.Mech.Sci.,12, 1970

23. Parkes, D.A.C. and Webster, J.J. "Finite Element Solutions for Two Transient Creep Problems" I.Mech.E., Int.conf. on creep and fatigue in elevated temp. applications, Philadelphia, 1973

24. Marriott, D.L. "Approximate Analysis of Transient Creep Deformations" J.S.A., Vol.3, No. 4, 1968

25. Marriott, D.L. "Approximate Estimation of Strain-Hardening Creep Deformation" J.S.A., Vol.3, No. 4, 1968

26. Leckie, F.A. and Martin, J.B. "Deformation Bounds for Bodies in a State of Creep" J.App.Mech., June, 1967

27. Leckie, F.A. and Ponter, A.R.S. "Deformation Bounds for Bodies which Creep in the Plastic Range" Trans. A.S.M.E., June, 1970

28. Ponter, A.R.S. and Leckie, F.A. "The Application of Energy Theorems to Bodies which Creep in the Plastic Range" J.App.Mech, Sept., 1970

29. Calladine, C.R. — "Time-Scales for Redistribution of Stress in Creep of Structures" Proc. Roy. Soc., A.309, 1969

30. Hoff, N.J. — "Approximate Analysis of Structures in the Presence of Moderately Large Creep Deformations" Q.J.App.Math., 12, 1954

31. Calladine, C.R. and Drucker, D.C. — "Nesting Surfaces of Constant Rate of Energy Dissipation in Creep" Q.J.App.Math., 20, 1960

32. Calladine, C.R. and Drucker, D.C. — "A Bound Method for Creep Analysis of Structures : Direct use of Solutions in Elasticity and Plasticity" J.Mech.Eng.Sci, Vol.4, No.1, 1962

33. Calladine, C.R. — "Stress Concentration in Steady Creep : Interpolation between Solutions in Elasticity and Plasticity" Proc. I.Mech.E., 1963-64, Vol.178, Pt.3A

34. Martin, J.B. — "A Note on the Determination of an Upper Bound on Displacement Rates for Steady Creep Problems" Trans.A.S.M.E., March, 1966

35. Palmer, A.C. — "A Lower Bound on Displacement Rates in Steady Creep" Trans. A.S.M.E., March, 1967

36. Anderson, R.G., Gardner, L.R.J. and Hodgkins, W.R. — "Deformation of Uniformly Loaded Beams Obeying Complex Creep Laws" J.Mech.Eng.Sci., 5, 1965

37. Mackenzie, A.C. — "On the use of a Single Uniaxial Test to Estimate Deformation Rates in Some Structures Undergoing Creep" Int.J.Mech.Sci., 10, 1968

38. Johnson, A — "An Alternative Definition of Reference Stress for Creep" I.Mech.E., Int.conf. on creep and fatigue in elevated temp.applications. Philadelphia, 1973

39. Sim, R.G. — "Evaluation of Reference Stress Parameters for Structures Subject to Creep" J.Mech.Eng.Sci., Vol.13, No.1, 1971

40. Sim, R.G. — "Reference Results for Plane Strain Creep Behaviour" J.Mech.Eng.Sci., Vol.14, No.6, 1972

41. Fairbairn, J. — "Applications of the Reference Stress Concept" N.E.L. Report No. 436, Oct.1969

42. Penny, R.K. and Marriott, D.L. — "Creep of Pressure Vessels" I.Mech.E., Int. conf. on creep and fatigue in elevated temp. applications, Philadelphia, 1973

43. Chubb, E.J. — "Computation of the Behaviour of Structures that are subject to Cyclic Loadings and High Temperatures" I.Mech.E., conf. on creep behaviour of piping, Feb.1974

44. Frederick, C.O. and Armstrong, P.J. — "Convergent Internal Stresses and Steady cyclic States of Stress" J.S.A., Vol.1, No. 2, 1966

45. Sim, R.G. — "Reference Stresses and Temperatures for cylinders and Spheres under Internal Pressure with a Steady Heat Flow in the Radial Direction" Int. J.Mech.Sci., 1973

46. Carlton, R.G., Poynor, J. and Townley, C.H.A. — "Creep Data Requirements for the Design of Power Plant" British Steelmakers Creep Committee, Proc. of the Symposium, 5-6 Oct. 1971

47. Martin, J.B. and Leckie, F.A. — "On the Creep Rupture of Structure" J.Mech.Phys. Solids, Vol.20, 1972

48. Goodall, I.W. and Cockroft, R.D.H. — "On Bounding the Life of Structures Subjected to Steady Load and Operating within the Creep Range" Int.J.Mech.Sci., Vol.15, 1973

49. Goodall, I.W. — "The Creep of Branch Connections" I.Mech.E., Conf. on creep behaviour of piping, Feb.1974

50. Frederick, C.O. — "Model Correlations for Investigating Creep Deformation and Stress Relaxation in Structures" J.Mech.Eng. Sci. Vol.7, No. 1, 1965

51. Fessler, H., Gill, P.A.T. and Stanley, P. — "A Material for Accelerated Creep Testing with Models" Conf. on Recent Advances in Stress Analysis, Roy.Aero.Soc., March 1968

52. Fessler, H. and Bellamy, R.A. — "Use of Models for the Prediction of Creep Behaviour of Components" I.Mech.E., Int.conf. on creep and fatigue in elevated temp. applications Philadelphia, 1973

53. Gulvin, T.F., Hacon, J., Hazra, L.K. and Mares, H.W. — "The Creep Properties of Carbon Steels to BS 1501-161 and 224 Grades" The Presentation of Creep Strain Data, B.S.C.C., Proc. of the Symposium, 5-6 Oct. 1971

54. Glen, J. and Hazra, L.K.
"Some Information of Creep Behaviour of Low Alloy Steels"
The Presentation of Creep Strain Data
B.S.C.C., Proc. of the Symposium, 5-6 Oct. 1971

55. Branch, G.
"The Assessment and Extrapolation of Creep Strain Data from a CrMoV Rotor Forging"
The Presentation of Creep Strain Data,
B.S.C.C., Proc. of the Symposium, 5-6 Oct. 1971

56. Bellmay, R.A.
"The Development of Model Techniques for Prediction of Creep Strains Applied to Steam Turbine Casings"
Ph.D. Thesis, 1973, Nottingham Univ.

57. Fessler, H., Webster, J.J. and Parkes, D.A.C.
"Creep Deformation of Simplified Steam Turbine Casings"
Final Report to the Science Research Council on Grant Ref. B/SR/5741.4, July, 1975

58. Tannahill, A.L.
"5% Proof Stress of Power Plant Steels"
Babcock and Wilcox Report No. 1/72/550

59.
"Creep Data from B.S.C.C."
Ref. T.I.S.T.D.D.E.D. Supplied by Mr. J.C. Guest on 18.1.74

60.
"The Presentation of Creep Strain Data"
British Steelmakers Creep Committee,
Proc. of the Symposium, 5-6 Oct. 1971

61. Smith, A.I.
"Interim Report on Long Time Creep Tests Undertaken in Collaboration with the B.S.C.C., on a Range of Carbon, Low Alloy and Austenitic Steels"
N.E.L. Report No. Z3/17/71

62. Penny, R.K. and Leckie, F.A.
"The Mechanics of Tensile Testing"
Int. J.Mech. Sci., Vol.10, 1968

63. Brealey, G.
"Creep of a Lead Alloy"
B.Sc. Thesis, 1975, Nottingham Univ.

64. Henshell, R.D.
"Pafec 70+"
Finite Element Manual, Nottingham Univ.

APPENDIX 1

Beams in Pure Bending

For a rectangular beam in pure bending, the equations of equilibrium and compatability are

$$M = 2b \int_0^{\frac{d}{2}} \sigma(y) y \, dy \qquad \text{(A.1.1.)}$$

and $$\varepsilon(y) = \frac{y}{R} \qquad \text{(A.1.2)}$$

where M is the pure bending moment applied to a beam b(wide) x d(deep) and $\varepsilon(y)$ is the maximum direct strain at a distance y from the neutral axis when the radius of curvature of the beam is R.

The constitutive equation which governs the initial deformation is

$$\varepsilon_i = k\sigma^q \qquad \text{(A.1.3a)}$$

(where $k = \frac{1}{E}$ and q = 1 for the linear elastic case) and the constituitive equation which govers the stationary creep deformation is

$$\varepsilon_c = \sigma^n \Gamma(t) \qquad \text{(A.1.3b)}$$

Using equations A.1.1, A.1.2 and A.1.3a the initial curvature, $\left[\frac{1}{R}\right]_i = K_i$, is given by

$$K_i = 2^{q+1} \left[\frac{2q+1}{q}\right]^q \left[\frac{M}{bd^2}\right]^q \frac{1}{d} \, k \qquad \text{(A.1.4a)}$$

Similarly, the stationary creep curvature is given by

$$K_{sc} = 2^{n+1} \left[\frac{2n+1}{n}\right]^n \left[\frac{M}{bd^2}\right]^n \frac{1}{d} \Gamma(t) \qquad \text{(A.1.4b)}$$

Substituting back into the original equations, the initial and stationary state stress distributions are obtained i.e.

$$\sigma_i(y) = \frac{4q+2}{q} \frac{M}{bd^2} \left[\frac{2y}{d}\right]^{\frac{1}{q}} \qquad \text{(A.1.5a)}$$

$$\sigma_{ss}(y) = \frac{4n+2}{n} \frac{M}{bd^2}\left[\frac{2y}{d}\right]^{\frac{1}{n}} \qquad (A.1.5b)$$

Using Mackenzies method of obtaining Reference Stresses, equations (A.1.4a) and (A.1.4b) reduce to

$$K_i = \frac{12}{\alpha d}\,\bar{\varepsilon}_{io} \qquad (A.1.6a)$$

$$K_{sc} = \frac{12}{\alpha d}\,\bar{\varepsilon}_{co} \qquad (A.1.6b)$$

where $\bar{\varepsilon}_{io}$ and $\bar{\varepsilon}_{co}$ are the initial and creep strains obtained from a uniaxial specimen when it is subjected to the Reference Stress $\bar{\sigma}_o$, where

$$\bar{\sigma}_o = \left[\frac{2^{p+1}}{12}\left[\frac{2p+1}{p}\right]^p\right]^{\frac{1}{p-1}} \frac{M}{bd^2} = \alpha\frac{M}{bd^2} \qquad (A.1.7)$$

and p is a particular value of n or q which is chosen for the particular application. The value of α is weakly dependent upon p , as Table A.1.1 shows.

TABLE A.1.1

p	2	3	5	7
α	4.167	4.115	4.072	4.049

The surface strains of the beam in pure bending may be predicted by the same Reference Stress and equations (A.1.6a) and (A.1.6b) become

$$(\varepsilon_i)_{surface} = \frac{6}{\alpha}\bar{\varepsilon}_{io} \qquad (A.1.8a)$$

$$(\varepsilon_{sc})_{surface} = \frac{6}{\alpha}\bar{\varepsilon}_{co} \qquad (A.1.8b)$$

Using Sim's approximate method,

$$\bar{\sigma}_o = \frac{P}{Pult}\sigma_y = \frac{M}{\frac{(bd^2\sigma_y)}{4}}\sigma_y$$

$$\text{i.e. } \bar{\sigma}_o = \frac{4M}{bd^2} \qquad (A.1.9)$$

APPENDIX 2

2-Bar Structure

For the 2-bar structure shown in Fig. A.2.1, the equations of equilibrium and compatability are

$$W = A_1\sigma_1 + A_2\sigma_2 \qquad \text{(A.2.1)}$$

$$\delta = \varepsilon_1 L_1 = \varepsilon_2 L_2 \qquad \text{(A.2.2)}$$

where W is the load applied to the structure and δ is the deflection under the load.

The two bars are made of the same material and the constitutive equations which govern the initial and creep deformations are

$$\varepsilon_i = k\sigma^q \qquad \text{(A.2.3a)}$$

and $$\varepsilon_c = \sigma^n \Gamma \qquad \text{(A.2.3b)}$$

respectively.

From these equations, the initial and stationary creep deformations are found to be

$$\delta_i = \left[\frac{W}{\frac{A1}{L_1^{\frac{1}{q}}} + \frac{A_2}{L_2^{\frac{1}{q}}}}\right]^q k \qquad \text{(A.2.4a)}$$

$$\delta_{sc} = \left[\frac{W}{\frac{A_1}{L_1^{\frac{1}{n}}} + \frac{A_2}{L_2^{\frac{1}{n}}}}\right]^n \Gamma(t) \qquad \text{(A.2.4b)}$$

Substituting back into the original equations, the initial and stationary state stresses are found to be

$$(\sigma_i)_1 = \left[\frac{W}{\frac{A1}{L_1^{\frac{1}{q}}} + \frac{A_2}{L_2^{\frac{1}{q}}}}\right] \frac{1}{L_1^{\frac{1}{q}}} \qquad \text{(A.2.5a)}$$

$$(\sigma_i)_2 = \left[\frac{W}{\frac{A1}{L_1^{\frac{1}{q}}} + \frac{A_2}{L_2^{\frac{1}{q}}}}\right] \frac{1}{L_2^{\frac{1}{q}}} \qquad \text{(A.2.5b)}$$

$$(\sigma_{ss})_1 = \left[\frac{W}{\frac{A_1}{L_1^{\frac{1}{n}}} + \frac{A_2}{L_2^{\frac{1}{n}}}}\right] \frac{1}{L_1^{\frac{1}{n}}} \qquad (A.2.5c)$$

$$(\sigma_{ss})_2 = \left[\frac{W}{\frac{A_1}{L_1^{\frac{1}{n}}} + \frac{A_2}{L_2^{\frac{1}{n}}}}\right] \frac{1}{L_2^{\frac{1}{n}}} \qquad (A.2.5d)$$

For the specific case when

$A_1 = 2A$, $A_2 = A$, $L_1 = L$ and $L_2 = 2L$

Mackenzies method of obtaining Reference Stresses reduces equations (A.2.4a) and (A.2.4b) to

$$\delta_i = \frac{2L}{5\alpha} \bar{\varepsilon}_{io} \qquad (A.2.6a)$$

$$\delta_{sc} = \frac{2L}{5\alpha} \cdot \bar{\varepsilon}_{co} \qquad (A.2.6b)$$

where $\bar{\varepsilon}_{io}$ and $\bar{\varepsilon}_{co}$ are the initial and creep strains obtained from a uniaxial specimen when it is subjected to the Reference Stress $\bar{\sigma}_o$,

where

$$\bar{\sigma}_o = \left[\frac{5}{2(2 + \frac{1}{2^{\frac{1}{p}}})^p}\right]^{\frac{1}{p-1}} \frac{W}{A} = \alpha \frac{W}{A} \qquad (A.2.7)$$

and p is a particular value of n or q which is chosen for the particular application. The value of α is weakly dependent upon p, as Table A.2.1 shows.

Table A.2.1

p	2	3	5	7
α	0.341	0.339	0.337	0.336

Using Sim's approximate method,

$$\bar{\sigma}_o = \frac{P}{Pult} \sigma_y = \frac{W}{(2A\sigma_y + A\sigma_y)} \sigma_y$$

i.e. $$\bar{\sigma}_o = \frac{W}{3A} \qquad (A.2.8)$$

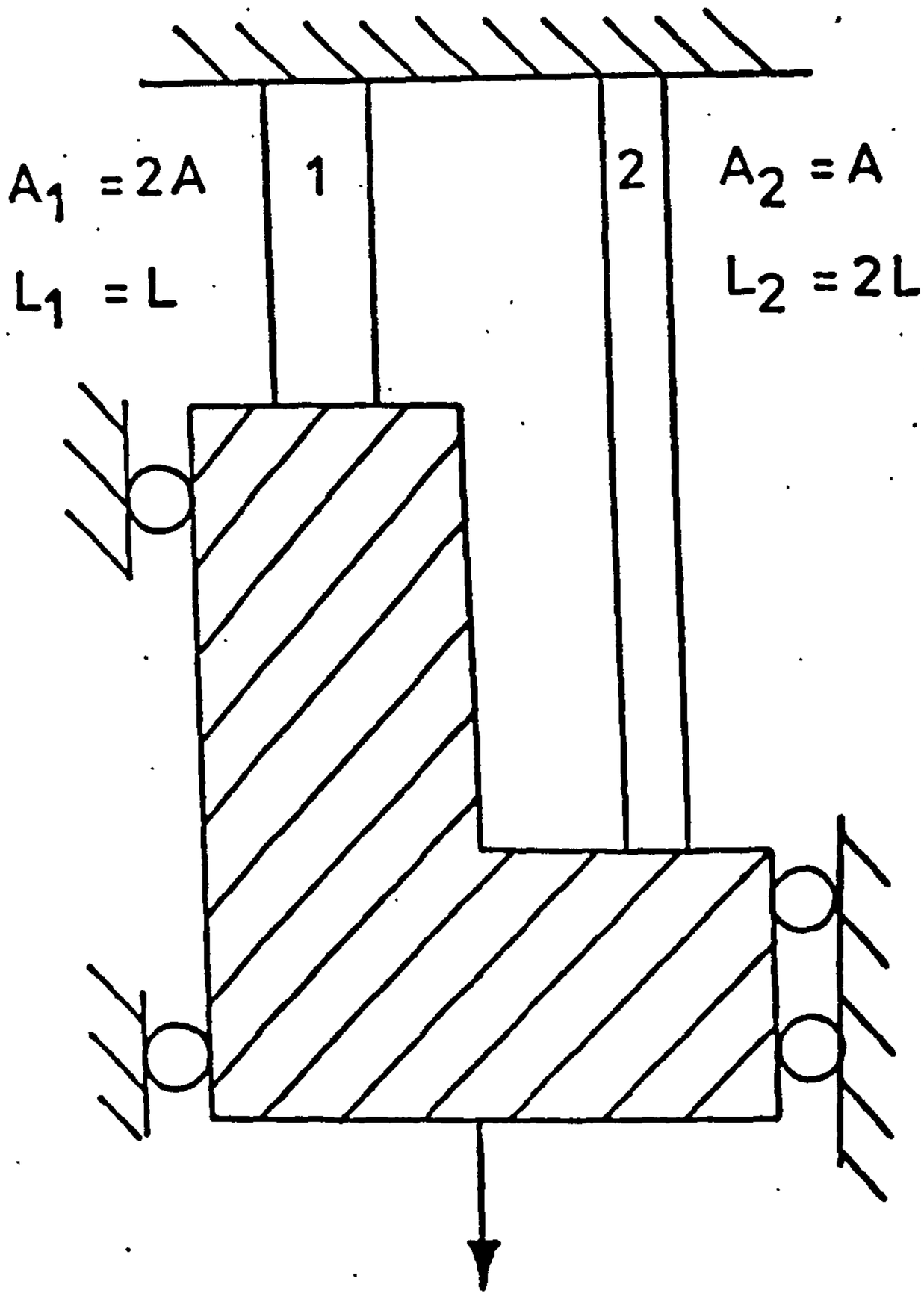

FIG. A.2.1 2 - BAR STRUCTURE

APPENDIX 3

Cantilevers With Transverse End Loads

Using equations A.1.4a and A.1.4b, the initial and stationary creep curvatures at a distance x from the free end of a cantilever of length L, with a transverse end load W are

$$Ki(x) = 2^{q+1}\left[\frac{2q+1}{q}\right]^{q}\left[\frac{Wx}{bd^2}\right]^{q}\frac{1}{d}\,k \qquad (A.3.1a)$$

$$Ksc(x) = 2^{n+1}\left[\frac{2n+1}{n}\right]^{n}\left[\frac{Wx}{bd^2}\right]^{n}\frac{1}{d}\,\Gamma(t) \qquad (A.3.1b)$$

Also, the initial and stationary state stress distribution are given by

$$\sigma_i(x,y) = \left(\frac{4q+2}{q}\right)\frac{Wx}{bd^2}\left(\frac{2y}{d}\right)^{\frac{1}{q}} \qquad (A.3.2a)$$

$$\sigma_{ss}(x,y) = \left(\frac{4n+2}{n}\right)\frac{W}{bd^2}\left(\frac{2y}{d}\right)^{\frac{1}{n}} \qquad (A.3.2b)$$

Similarly, the initial and stationary creep curvature at any section of the cantilever are given by

$$K_i = \frac{12}{\alpha d}\,\bar{\varepsilon}_{io} \qquad (A.3.3a)$$

and $$K_{sc} = \frac{12}{\alpha d}\,\bar{\varepsilon}_{co} \qquad (A.3.3b)$$

where $\bar{\varepsilon}_{io}$ and $\bar{\varepsilon}_{co}$ are the initial and creep strains obtained from a uniaxial specimen subjected to the Reference Stress $\bar{\sigma}_o$, where

$$\bar{\sigma}_o = \alpha\frac{Wx}{bd^2} \qquad (A.3.4)$$

Therefore, it can be seen that the Reference Stress to predict the curvature at a particular point and, therefore, the surface strain also, is linearly dependent upon the distance from the free end. The value of α in equations A.3.3a, A.3.3b and A.3.4 are given in Table A.1.1.

For small deflections, the initial and stationary creep curvatures may be approximated as follows

$$K_i = \frac{d^2 v_i}{d x^2} \quad \text{and} \quad K_{sc} = \frac{d^2 v_{sc}}{d x^2}$$

substituting these relationships and the boundary conditions in equations A.3.1a and A.3.1b and integrating gives the slope and deflection relationships at any point along the cantilever

$$\left[\frac{d v}{d x}\right]_i = \frac{1}{p+1} \quad Q \quad (x^{p+1} - L^{p+1}) \qquad \text{(A.3.5a)}$$

$$\left[\frac{d v}{d x}\right]_{sc} = \frac{1}{n+1} \quad Q \quad (x^{n+1} - L^{n+1}) \qquad \text{(A.3.5b)}$$

$$(v)_i = \frac{1}{p+1} \quad Q \quad \left(\frac{x^{p+2}}{p+2} - L^{p+1}\right) \qquad \text{(A.3.5c)}$$

$$(v)_{sc} = \frac{1}{n+1} \quad Q \quad \left(\frac{x^{n+2}}{n+2} - L^{n+2}\right) \qquad \text{(A.3.5d)}$$

where

$$Q = \left[\frac{W}{bd^2}\right]^r \quad \frac{1}{d} \left[2^{r+1} \left[\frac{2r+1}{r}\right]^r\right] \quad S$$

with r=q and s=k for equations A.3.5a and A.3.5b and r=n and s= $\Gamma(t)$ for equations A.3.5c and A.3.5d.

Using Mackenzies Reference Stress method, the slope of the cantilever tip is given by

$$\left[\frac{dv}{dx}\right]_{i(x=o)} = \frac{6}{\alpha} \quad \frac{L}{d} \quad \bar{\varepsilon}_{io} \qquad \text{(A.3.6a)}$$

$$\left[\frac{dv}{dx}\right]_{sc(x=o)} = \frac{6}{\alpha} \quad \frac{L}{d} \quad \bar{\varepsilon}_{co} \qquad \text{(A.3.6b)}$$

where

$$\bar{\sigma}_o = \left[\frac{2^{p+1} \quad \left[\frac{2p+1}{p}\right]^p}{6(p+1)}\right]^{\frac{1}{p-1}} \qquad \frac{WL}{bd^2} = \alpha \frac{WL}{bd^2} \qquad \text{(A.3.7)}$$

and p is a particular value of n or q chosen for the particular application.

The value of α is weakly dependent upon p, as Table A.3.1 shows, but the dependence is stronger than that in the previous two examples (Appendices A.1 and A.2)

Table A.3.1

p	2	3	5	7
α	2.778	2.910	3.094	3.216

Similarly, using Mackenzies' Reference Stress method for the deflection of tip of the cantilever,

$$(v_i)_{x=o} = \frac{4}{\alpha^1} \frac{L^2}{d} \bar{\varepsilon}_{io} \qquad \text{(A.3.8a)}$$

$$(v_{sc})_{x=o} = \frac{4}{\alpha^1} \frac{L^2}{d} \bar{\varepsilon}_{co} \qquad \text{(A.3.8b)}$$

where

$$\bar{\sigma}_o = \left[\frac{2^{p+1} \left[\frac{2p+1}{p}\right]^p}{4(p+2)} \right]^{\frac{1}{p-1}} \qquad \frac{WL}{bd^2} = \alpha^1 \frac{WL}{bd^2} \qquad \text{(A.3.9)}$$

where p is a particular value of n or q which is chosen for the particular application. The value of α^1 is weakly dependent upon p as Table A.3.2 shows

Table A.3.2

p	2	3	5	7
α^1 at x = o	3.125	3.188	3.294	3.374
α^1 at x = $\frac{L}{4}$	2.815	2.940	3.110	3.227
α^1 at x = $\frac{L}{2}$	2.936	3.021	3.160	3.263
α^1 at x = $\frac{3L}{4}$	3.058	3.125	3.238	3.323

Similarly, Reference Stresses may be found to predict the deflections at other points in the cantilever. Table A.3.2 shows the values of α^1 for x =o, $\frac{L}{4}$, $\frac{L}{2}$ and $\frac{3L}{4}$. Table A.3.2 shows that although the Reference Stresses for predicting deflections are more nearly constant (with position) than the Reference Stresses for predicting strains, the variation is still quite significant.

Using Sim's approximate method,

$$\bar{\sigma}_o = \frac{P}{Pult}\sigma_y = \frac{WL}{(\frac{bd^2\sigma_y}{4})}$$

$$\text{i.e. } \bar{\sigma}_o = \frac{4WL}{bd^2} \qquad \text{(A.3.10)}$$

APPENDIX 4

Internal Pressurisation of Long Closed End Cylinders

a) Thin Cylinders (inside diameter d, wall thickness t)

In this statically determinate problem, the initial and stationary state creep stresses are the same and there is no stress redistribution (i.e. $\Delta\phi = 0$), therefore,

$$\sigma_\theta = \frac{pd}{2t} \qquad \text{(A.4.1a)}$$

$$\sigma_a = \frac{pd^2}{4t(d+t)} \qquad \text{(A.4.1b)}$$

and if $d \gg t$, then $\sigma_\theta = \frac{pd}{2t}$ and $\sigma_a = \frac{pd}{4t}$ and the initial elastic and creep strains are given by

$$(\varepsilon_\theta)_i = \frac{pd}{4Et}(2 - \nu) \qquad \text{(A.4.2a)}$$

$$(\varepsilon_a)_i = \frac{pd}{4Et}(1 - 2\nu) \qquad \text{(A.4.2b)}$$

$$(\varepsilon_\theta)_c = \left[\frac{3}{4}\right]^{\frac{n+1}{2}} \left[\frac{pd}{2t}\right]^n \Gamma(t) \qquad \text{(A.4.2c)}$$

$$(\varepsilon_a)_c = 0 \qquad \text{(A.4.2d)}$$

In this simple example, the Reference Stress for predicting the hoop creep strains is the effective stress

$$\text{i.e. } \bar{\sigma}_o = \frac{\sqrt{3}}{4} \frac{pd}{t} \qquad \text{(A.4.3)}$$

and the hoop creep strain is given by

$$(\varepsilon_c) = \frac{\sqrt{3}}{2} \bar{\varepsilon}_{co} \qquad \text{(A.4.4)}$$

b) Thick Cylinders (inside radius Ri, outside radius Ro)

The initial elastic and stationary state creep stresses are given by

$$(\sigma_\theta)_i = \frac{pRi^2}{Ro^2-Ri^2}\left(1 + \frac{Ro^2}{r^2}\right) \qquad (A.4.5a)$$

$$(\sigma_a)_i = \frac{pRi^2}{Ro^2-Ri^2} \qquad (A.4.5b)$$

$$(\sigma_r)_i = \frac{pRi^2}{Ro^2-Ri^2}\left(1 - \frac{Ro^2}{r^2}\right) \qquad (A.4.5c)$$

$$(\sigma_\theta)_{ss} = \frac{\left[\frac{2-n}{n}\right]\left[\frac{Ro}{r}\right]^{\frac{2}{n}} + 1}{\left[\frac{Ro}{Ri}\right]^{\frac{2}{n}} - 1}\, p \qquad (A.4.5d)$$

$$(\sigma_a)_{ss} = \frac{\left[\frac{1-n}{n}\right]\left[\frac{Ro}{r}\right]^{\frac{2}{n}} + 1}{\left[\frac{Ro}{Ri}\right]^{\frac{2}{n}} - 1}\, p \qquad (A.4.5e)$$

$$(\sigma_r)_{ss} = \frac{1 - \left[\frac{Ro}{r}\right]^{\frac{2}{n}}}{\left[\frac{Ro}{Ri}\right]^{\frac{2}{n}} - 1}\, p \qquad (A.4.5f)$$

For the specific case of the cylinders used for the biaxial tests and the cylinders of the pressure vessels, Ro/Ri = 1.125 and the ratio of the stationary state hoop stress to the mean hoop stress at the outside surface is given by:

$$\text{outside hoop stress ratio} = Re(n) = \frac{1}{4n\left(\left(\frac{9}{8}\right)^{\frac{2}{n}} - 1\right)} \qquad (A.4.6)$$

Table A.4 shows the value of Re for a range of values of n.

TABLE A.4

n	1	2	3	5	7	9
$R_\theta(n)$	0.941	1.000	1.020	1.036	1.044	1.047

The maximum effective stress used in the biaxial pressure tests was 14.05 N/mm^2. Taking the tangent to the $\log \varepsilon_c - \log \sigma$ data at 100 h (Fig. 5.21(d)) at a stress of 14.05 N/mm^2 as the maximum possible n value, $\hat{n}$, we find that the maximum possible error in the creep strain predictions based upon mean stresses is given by

$$\text{maximum \% error} = ((R_\theta(\hat{n}))^{\hat{n}} - 1) \times 100$$

$$= 19.3\% \text{ (low)}$$

APPENDIX 5

Torsion of Cylinders

a) Thin Cylinders (mean diameter d, wall thickness t)

In this statically determinate problem, the initial and stationary state creep stresses are the same and there is no stress redistribution (i.e. $\Delta\phi = 0$), therefore,

$$\tau = \frac{2T}{\pi d^2 t} \qquad (A.5.1)$$

The principal stresses are $\pm\tau$

The initial and creep twists (θ/unit length) are given by

$$\theta_i = \frac{4T}{\pi d^3 tG} \qquad (A.5.2a)$$

$$\theta_c = \frac{6}{d}\left[\sqrt{3}\right]^{n-1}\left[\frac{2T}{\pi d^2 t}\right]^n \Gamma(t) \qquad (A.5.2b)$$

In this simple example, the Reference Stress for predicting the creep strains is the effective stress

$$\text{i.e. } \bar{\sigma}_o = \frac{2\sqrt{3}T}{\pi d^2 t} \qquad (A.5.3)$$

and the creep twist is given by

$$\theta_c = \frac{2\sqrt{3}}{d}\,\bar{\varepsilon}_{co} \qquad (A.5.4)$$

b) Thick Cylinders (inside radius R_i, outside radius R_o)

The initial elastic and stationary state creep stresses are given by:

$$\tau_i = \frac{2Tr}{\pi(R_o^4 - R_i^4)} \qquad (A.5.5a)$$

$$\tau_{ss} = \frac{(3+\frac{1}{n})}{2\pi\left[1-(\frac{R_i}{R_o})^{3+\frac{1}{n}}\right]}\,\frac{T}{R_o^3}\left[\frac{r}{R_o}\right]^{\frac{1}{n}} \qquad (A.5.5b)$$

For the specific case of the cylinders used for the biaxial tests, $R_o/R_i = 1.125$ and the ratio of the stationary state shear stress to the mean shear stress at the outside surface is given by:

$$\text{Outside shear stress ratio} = R_\tau = 0.09911 \quad \frac{3+\frac{1}{n}}{1-(\frac{8}{9})^{3+\frac{1}{n}}}$$

Table A.5.1 shows the value of R_τ for a range of values of n

TABLE A.5.1

n	1	2	3	5	7	9
R_τ	1.055	1.027	1.017	1.010	1.007	1.005

By a similar method to that used in Appendix 4, the maximum error in creep strains predicted by using the mean shear stress is 5.1% (low).

The initial and stationary state creep twists (θ/unit length) are given by:

$$\theta_i = \frac{2T}{\pi(R_o^4 - R_i^4)G} \qquad \text{(A.5.7a)}$$

$$\theta_{sc} = (3\tfrac{n}{2} \left[\frac{(3+\frac{1}{n})}{2\pi(1-(\frac{R_i}{R_o})^{3+\frac{1}{n}})}\right]^n \left[\frac{T}{R_o^3}\right]^n \frac{3}{R_o} \Gamma(t) \qquad \text{(A.5.7b)}$$

Using Macknezies method, a Reference Stress can be obtained for predicting the stationary creep twist ie. for a solid cylinder

$$\text{i.e.} \quad \theta_{sc} = \frac{3.308}{\alpha R_o} \bar{\varepsilon}_{co} \qquad \text{(A.5.8)}$$

$$\text{where} \quad \bar{\sigma}_o = \left[\frac{(3\tfrac{p}{2} \left[\frac{(3+\frac{1}{n})}{2\pi}\right]^p \pi}{2\sqrt{3}}\right]^{\frac{1}{p-1}} \frac{T}{R_o^3} = \frac{\alpha T}{R_o^3} \qquad \text{(A.5.9)}$$

and p is a particular value of n which is chosen for the particular application.

The value of α is weakly dependent upon p, as Table A.5.2 shows

TABLE A.5.2

p	2	3	5	7
α	0.844	0.839	0.834	0.832

Using Sim 's approximate method,

$$\bar{\sigma}_o = \frac{P}{Pult}\,\sigma_y = \frac{T}{\frac{\pi R_o^3 \sigma_y}{3}}\,\sigma_y$$

i.e. $$\bar{\sigma}_o = \frac{3}{\pi}\,\frac{T}{R_o^3} \qquad (A.5.10)$$

APPENDIX 6

Internal Pressurisation of spheres

a) Thin Spheres (inside diameter d, wall thickness t)

In this statically determinate problem, the initial and stationary state creep stresses are the same and there is no stress redistribution (i.e. $\Delta\phi = 0$), therefore,

$$\sigma_\theta = \frac{pd^2}{4t(d+t)} \qquad (A.6.1)$$

and if $d \gg t$, then $\sigma_\theta = \frac{pd}{4t}$ and the initial elastic and creep strains are given by

$$(\varepsilon_\theta)_i = \frac{pd}{4Et}(1-\nu) \qquad (A.6.2a)$$

$$(\varepsilon_\theta)_c = \frac{1}{2}\left(\frac{pd}{4t}\right)^n \Gamma(t) \qquad (A.6.2b)$$

In this example, the Reference Stress for predicting the hoop creep strain is the effective stress

i.e. $$\bar{\sigma}_o = \frac{pd}{4t} \qquad (A.6.3)$$

and the hoop strain is given by

$$(\varepsilon_\theta)_c = \frac{1}{2}\bar{\varepsilon}_{co} \qquad (A.6.4)$$

b) Thick Spheres (inside radius R_i, outside radius R_o)

The initial elastic and stationary state creep stresses are given by

$$(\sigma_\theta)_i = \frac{pR_i^3}{R_o^3 - R_i^3}\left[1 + \frac{R_o^3}{2r^3}\right] \qquad (A.6.5a)$$

$$(\sigma_r)_i = \frac{pR_i^3}{R_o^3 - R_i^3}\left[1 - \frac{R_o^3}{r^3}\right] \qquad (A.6.5b)$$

$$(\sigma_\theta)_{ss} = \frac{((3-2n)(2n)(R_o/r)^{\frac{3}{n}} + 1}{(R_o/R_i)^{\frac{3}{n}} - 1} \cdot p \qquad (A.6.5c)$$

$$(\sigma_r)_{ss} \doteq -p \cdot \frac{(R_o/r)^{\frac{3}{n}} - 1}{(R_o/R_i)^{\frac{3}{n}} - 1} \qquad (A.6.5d)$$

For the specific case of the hemispherical end of the pressure vessels, $R_o/R_i = 1.125$ and the ratio of the stationary state hoop stress to the mean hoop stress at the outside surface is given by:

$$\text{outside hoop stress ratio } R_\theta = \frac{51}{128n((\frac{9}{8})^{\frac{3}{n}} - 1)} \qquad (A.6.6)$$

Table A.6 shows the value of R_θ for a range of values of n

TABLE A.6

n	1	1.5	2	3	5	7	9
R_θ	0.940	1.000	1.031	1.063	1.088	1.099	1.106

By a similar method to that used in Appendix 4, the maximum error in creep strains predicted by using the mean hoop stress is 31.1% (low).